FOR REFERENCE ONLY

FOR REFERENCE ONLY

42 0022593 X



ProQuest Number: 10183433

All rights reserved

INFORMATION TO ALL USERS
The quality of this reproduction is dependent upon the quality of the copy submitted.

In the unlikely event that the author did not send a complete manuscript
and there are missing pages, these will be noted. Also, if material had to be removed,
a note will indicate the deletion.



ProQuest 10183433

Published by ProQuest LLC (2017). Copyright of the Dissertation is held by the Author.

All rights reserved.
This work is protected against unauthorized copying under Title 17, United States Code
Microform Edition © ProQuest LLC.

ProQuest LLC.
789 East Eisenhower Parkway
P.O. Box 1346
Ann Arbor, MI 48106 – 1346

Chemical and Structural Studies of Aluminium and Zirconium Aqueous Chemistry

Kirill L. Shafran, Dipl. Chem.

A thesis submitted in partial fulfilment of the requirements of The Nottingham Trent University for the degree of Doctor of Philosophy

September 2003

Department of Chemistry
The Nottingham Trent University

10369587

THE NOTTINGHAM TRENT UNIVERSITY LIS

REF | PH.D/CP/03 SHA

S.L.

For my parents, wife, daughter and son

Acknowledgements

I would like firstly to thank my supervisor Dr. Carole C. Perry for the opportunity to carry on this project, constant support and guidance she has given to me throughout my postgraduate studies, Dr. Robert Polywka, Dr. Ian Smith and Dr. David Duncalf of the Unilever Research, Port Sunlight, Wirral, UK for their help and guidance throughout this project.

I am much indebted to members of the Inorganic Chemistry Research Group, Martin Gardener, Chris McLean-Tucke, David Eglin, Simon Thompson, David Belton, Paul Roach, Neil Shirtcliffe for their support and help.

I am also grateful to all technical staff at the Nottingham Trent University in the department of Chemistry and Physics for their help and support with various equipment and sample characterisation.

Finally, I would like to take this opportunity to especially thank my wife and my parents for the continuing support, encouragement and patience they have shown to me.

CONTENTS

CHAPTER I. Aqueous chemistry of aluminium and zirconium: a literature review and theoretical considerations

1.1. Preamble 1
1.2. Aluminium and zirconium: the elements 2
1.3. Aqueous chemistry of aluminium and zirconium 2
1.3.1. Thermodynamic equilibrium constants for aluminium ions 3
1.3.2. Thermodynamic equilibrium constants of zirconium-ions 10
1.3.3. The Partial charge model 12
1.3.4. Hydrolysis of monomeric ions of aluminium and zirconium; Partial charge model considerations 15
1.3.5. General condensation pathways of hydrolysed metal ions 20
1.3.6. Condensation pathways of aluminium ions 22
1.3.7. Condensation pathways of zirconium ions 30
1.4. Kinetics of hydrolysis and condensation of Al^{3+} and Zr^{4+} aqueous solutions 35
1.5. Colloidal and solid phases formed by hydrolysis of Al^{3+} and Zr^{4+} ions 38
1.6. Effect of anions on the properties of molecular precursors and the resulting Al- and Zr-containing solid phases 45
1.7. Conclusions 52
References 54

CHAPTER II. Materials and Methods

2.1. The choice of model systems 58
2.2. The choice of methods 58
2.3. Potentiometry 60
2.3.1. Potentiometric titrations. Principles and instrumentation 61
2.3.2. Potentiometric titrations for standardisation of stock solutions of acids alkalis 62
2.3.3. Single-batch potentiometric titration setup 63
2.3.4. Time-resolved potentiometric titrations 64
2.4. Multi-batch titrations 65
2.4.1. Multi-batch titrations of aluminium salt solutions at room temperature 66
2.4.2. Multi-batch titrations of aluminium chloride with potassium hydroxide at 90 °C 67
2.4.3. Multi-batch titrations of zirconium solutions with different alkalis at 90 °C 69
2.5. UV-Vis spectroscopy 75
2.5.1. Principles and instrumentation of UV-Vis spectroscopy 75
2.5.2. Organic reagent assays for speciation studies of aluminium and zirconium 77
2.5.3. Xylenol Orange organic reagent assay for zirconium-ions 78
2.6. Dynamic light scattering 80
2.6.1. Principles and instrumentation of dynamic light scattering 80
2.6.2. Dynamic light scattering. Experimental procedure 84
2.7. Solution NMR spectroscopy 85
2.7.1. Theory and instrumentation of NMR spectroscopy 85
2.7.2. Features of ^{27}Al NMR spectroscopy 88
2.7.3. ^{27}Al NMR spectra of the Al-containing samples prepared at room temperature 89
2.7.4. ^{27}Al NMR spectra of the Al-containing samples prepared at

high temperature 89
2.7.5. *In-situ* ^{27}Al NMR kinetic measurements of Al hydrolysis at 90°C 89
2.8. Spray-freeze-drying 91
2.9. FT-IR spectroscopy 93
2.9.1. Principles and instrumentation of FT-IR spectroscopy 94
2.9.2. FT-IR spectra of solid samples 95
2.10. Powder X-ray diffraction measurements 95
2.10.1. Principles and instrumentation of PXRD 96
2.10.2. Preparation and measurement of the solid samples for PXRD 97
2.11. Generalised two-dimensional correlation analysis 97
2.11.1. Theory of two-dimensional correlation spectroscopy 98
2.11.2. A new method for correlation analysis of the dynamic spectra 102
2.12. List of reagents and materials 103
References 105

CHAPTER III. Solution speciation studies of hydrolysed aluminium ions
3.1. Solution studies of aluminium speciation at room temperature 107
3.1.1. Potentiometric titrations of aluminium solutions at room temperature 107
3.1.1.1. Effect of aluminium and alkali concentration on the speciation of Al-ions 110
3.1.1.2. Effect of anions and alkali strength 110
3.1.1.3. Time-resolved potentiometric titrations of Al solutions 114
3.1.2. Results from ^{27}Al NMR spectroscopy 121
3.1.3. Results from dynamic light scattering 126
3.1.4. Discussion 127
3.1.5. Conclusions 139
3.2. Solution studies of aluminium speciation at high temperature 139
3.2.1. Hydrolysis at elevated temperature as monitored by ^{27}Al NMR spectroscopy 140
3.2.2. Quantification of the ^{27}Al NMR spectra 141
3.2.3. Discussion of the methods for quantification of ^{27}Al NMR spectra 147
3.2.4. Kinetic studies of aluminium-ion hydrolysis at elevated temperature using *in-situ* ^{27}Al NMR monitoring 148
3.2.5. Discussion 161
3.2.6. Conclusions 164
3.3. Multi-batch titration of Al-ions at high temperature (series AMK1): results of solution studies 165
3.3.1. Potentiometric measurements in the series AMK1 166
3.3.2. Dynamic light scattering measurements of the series AMK1 168
3.3.3. Results of ^{27}Al NMR characterization of the series AMK1 169
3.3.4. Discussion of the results of the multi-batch series AMK1 181
3.3.5. Conclusions to multi-batch titrations of Al-ions 184
References 186

CHAPTER IV. Solution speciation studies of hydrolysed zirconium-ions
4.1. Investigation of zirconium speciation at room temperature 189
4.1.1. Single-batch potentiometric titrations of Zr-ion solutions at room temperature 189
4.1.2. Discussion of the single-batch potentiometric titrations of Zr-ion solutions with alkalis at room temperature 194
4.1.3. Conclusions 199

4.2. Multi-batch potentiometric titrations of Zr-ion solutions at high temperature 200
4.2.1. Conventional potentiometric titration curves from the multi-batch experiments 201
4.2.2. Kinetics of pH change in the multi-batch titrations of zirconium-ions 208
4.2.3. Evidence of complexation from pH measurements for the multi-batch series of Zr-ion titrations 210
4.2.4. Discussion of the potentiometric data obtained from multi-batch titrations Zr-ions 212
4.2.5. Conclusions 223
4.3. Application of Xylenol Orange organic reagent assay in the multi-batch titrations of Zr-ions at elevated temperature 224
4.3.1. Choice of organic reagent 225
4.3.2. Evaluation of Xylenol Orange assay for the determination of hydrolysed Zr-ions 225
4.3.3. Results of Xylenol Orange Assay. Graphs 'Absorbance vs. hydrolysis ratio' 228
4.3.4. Kinetics of Zr-ion condensation as observed with Xylenol Orange assay 231
4.3.5. Discussion of the results of Xylenol Orange organic reagent assay 232
4.3.6. Conclusions on the results of the Xylenol Orange organic reagent assay 236
4.4. Results of the dynamic light scattering measurements of the multi-batch titrations of Zr-ions at high temperature 236
References 243

CHAPTER V. Solid-state studies of Al and Zr speciation
5.1. Introduction 245
5.2. Spray-freeze-drying technique for solid-state analysis of solution speciation 246
5.3. Solid-state characterisation of the spray-freeze-dried samples of the series **AMK1** 247
5.3.1. Re-dissolution of the spray-freeze-dried samples of the series **AMK1** and ^{27}Al solution NMR measurements 247
5.3.2. ^{27}Al solid-state NMR characterisation of spray-freeze-dried samples of the series **AMK1** 248
5.3.3. X-ray diffraction studies of the solid samples of the series **AMK1** 249
5.4. Solid-state characterisation of spray-freeze-dried samples of Zr-containing series **ZrOH, ZrHCO3, ZrOHSO4, ZrOHAc, ZrOHGly** 252
5.4.1. PXRD spectra of Zr-containing samples 252
5.4.1.1. XRD spectra of the series **ZrHCO3** 254
5.4.1.2. XRD spectra of the series **ZrOH** 262
5.4.1.3. XRD spectra of the series **ZrOHSO4** 267
5.4.1.4. XRD spectra of the series **ZrOHAc** 272
5.4.1.5. XRD spectra of the series **ZrOHGly** (Zr:Gly=2:1, 1:1, 1:2) 274
5.5. Discussion of SFD and XRD data 281
5.5.1. Spray-freeze-drying 281
5.5.2. Series **AMK1** 282
5.5.3. Advanced treatment of PXRD spectra 284
5.5.4. Discussion of the PXRD spectra from the series of 'pure' hydrolysed Zr-ions (**ZrOH, ZrHCO3**) 285
5.5.5. Effect of anions and glycine on the solid-state speciation of

Zr-containing crystalline phases 288
5.6. Infrared spectra of solid samples produced by spray-freeze-drying (SFD) 295
5.6.1. Infrared spectra of the solid samples from the series **AMK1** 295
5.6.2. Mid-infrared spectra of the series **ZrHCO3** 307
5.6.3. Far-infrared spectra of the solid samples of the series **ZrHCO3** 317
5.6.4. Mid-infrared spectra of the samples of **ZrOH** series 321
5.6.5. Far-infrared spectra of the series **ZrOH** 323
5.6.6. Mid-infrared spectra of the series **ZrOHSO4** 326
5.6.7. Far-infrared spectra of the solid samples of the series **ZrOHSO4** 331
5.6.8. Mid-infrared spectra of the solid samples of **ZrOHAc** series 333
5.6.9. Far-infrared spectra of the solid samples from the series **ZrOHAc** 337
5.6.10. Mid-infrared spectra of the solid samples from the series **ZrOHGly2:1, ZrOHGly1:1 and ZrOHGly1:2** 340
5.6.11. Far-infrared spectra of the series **ZrOHGly1:2, 1:1** and **2:1** 353
References 360

CHAPTER VI Summary
6.1. Aqueous chemistry of aluminium ions 363
6.1.1. Monomeric hydrolysis of Al-ions 364
6.1.2 Formation of large aluminium polycations 364
6.1.3. Kinetics of the formation of large Al polycations 371
6.1.4. Factors affecting speciation of Al-ions 372
6.1.4.1. Effect of temperature 372
6.1.4.2. Effect of ionic strength 373
6.1.4.3. Effect of alkali 374
6.1.4.4. 'Local' alkali-induced perturbations 375
6.1.4.5. Effect of anions 377
6.1.4.6. Formation of colloidal phases. The fate of Al polycations at higher pH 378
6.2. Aqueous chemistry of zirconium ions 382
6.2.1. Hydrolysis of zirconium ions 382
6.2.2. Condensation of zirconium ions 383
6.2.3. Structural features of Zr-ion condensation 384
6.2.4. Effect of pH and temperature 386
6.2.5. Effect of anions 391
6.3. Future work 393
References 395
Appendix 1. Table 4.3. PCM calculations of Zr polycation complexes with glycine
Appendix 2. Powder diffractograms of the series **ZrOH** ar different sampling times
Appendix 3. FT-IR spectra of the series '**ZrOHGly**'

Abstract

Systematic studies of chemical and structural aspects of aqueous chemistry of aluminium and zirconium over a wide range of pH conditions with special emphasis on the formation of large polynuclear hydrolytic species have been performed. Medium-concentrated (0.05-0.25 mol/L) solutions of aluminium and zirconium chloride were used and acid-base titration was chosen as a method for pH variation. The effect of anions (chloride, nitrate, acetate, sulphate and carbonate), temperature (room temperature and 90°C), ionic strength, strength and type of alkali (KOH, $KHCO_3$, NH_4OH) and the presence of selected complexing agents including glycine (for complexation with zirconium only) on hydrolysis-condensation of Al and Zr-ions were investigated.

At high temperature (90 °C) Keggin polycation $Al_{13}O_4(OH)_{24}(H_2O)_{12}^{7+}$ (Al_{13}) dominated in the pH range $4 \leq pH \leq 6$, but was gradually replaced by $Al_{30}O_8(OH)_{56}(H_2O)_{32}^{18+}$ (Al_{30}) polycation after 12 hours of hydrolysis. The kinetic rate of the Al_{30} polycation formation was at least 2 orders of magnitude lower than that of the Al_{13}-mer. The Al_{30}-mer appears to be formed directly from the Al_{13}-mer and monomers. Sulphate-ions totally change the speciation patterns of Al-ions under acidic conditions, prohibiting the formation of Keggin polycations (Al_{13} and Al_{30}).

Spray-freeze-drying of solution samples with $4<pH<6$ ($1.0<h<2.8$) gave largely aluminium polycations (Al_{13} and Al_{30}) in the solid state. The solid samples were mainly amorphous (pseudoboehmite) with minor quantities of gibbsite.

Hydrolysis of zirconium-ions at 90°C led to a mixture of monoclinic zirconia and zirconyl salts with variable hydration at very low pH ($pH<0.6$). At higher pH values amorphous zirconia dominated the equilibrium. At alkaline pH tetragonal zirconia was the major solid phase formed. Particle size of the hydrolytic zirconium polymers varied with pH, being the lowest at pH~0.6 (d~0.2-0.4 nm) and rapidly increasing with pH increase. At alkaline conditions, partial dissolution of hydrous zirconia led to smaller particle sizes, particularly in the presence of carbonate-ions from alkali which formed strong complexes with zirconium.

The effect of sulphate and acetate ions on the speciation of zirconium-ions was pH-dependent. At equimolar ratios of $SO_4^{2-}:Zr^{4+}$, crystalline zirconium sulphate was formed at $pH<0.5$. At $0.5<pH<3.5$ basic zirconium sulphates began to prevail as solid products. At $pH>3.5$ amorphous zirconia dominated. Acetate-ions behaved similarly to sulphate-ions, albeit amorphous zirconia began to form at lower pH. Unidentate, bridging and chelating complexes of sulphate and acetate-ions with zirconium polymers were identified. The reaction of glycine with zirconium was quantitative in acidic conditions and complexes formed were stronger than those with acetate. The presence of glycine hindered condensation of Zr polymers below pH~2.0. Five complexes between zirconium and glycine were identified.

CHAPTER I: Aqueous chemistry of aluminium and zirconium: a literature review and theoretical considerations

1.1. Preamble

The aqueous chemistry of aluminium and zirconium is important to a large number of technological processes and areas of science [1-8]. Due to their extensive hydrolytic and complexation behaviour, these metal ions can be present in aqueous solutions in several forms simultaneously [1]. Equilibrium in metal ion solutions is very complex and highly sensitive to many factors [5]. Along with monomeric Al and Zr ions, several transient polynuclear species of Al and Zr ions have been detected. These metastable species are an intrinsic part of the chemical equilibrium as well as prospective candidates to become truly nano-sized molecular blocks to Al- and Zr-containing materials [4]. Colloidal and solid phases of the corresponding oxides hydroxides of Al and Zr often coexist with solution species at higher concentrations of these metal ions. Therefore, an exhaustive knowledge of chemical speciation of Al and Zr ions must contain colloidal and solid-state transformations in solution as well as the soluble species. On the basis of this we shall use the term "chemical speciation" in its broadest sense as an exhaustive description of the chemical equilibria and dynamics of *all* chemical forms of the elements (e.g. Al or Zr) including phase transformations solution ↔ colloid ↔ solid state.

There are a vast number of scientific areas for which knowledge of aluminium speciation, is important, examples are given in Fig. 1.1.

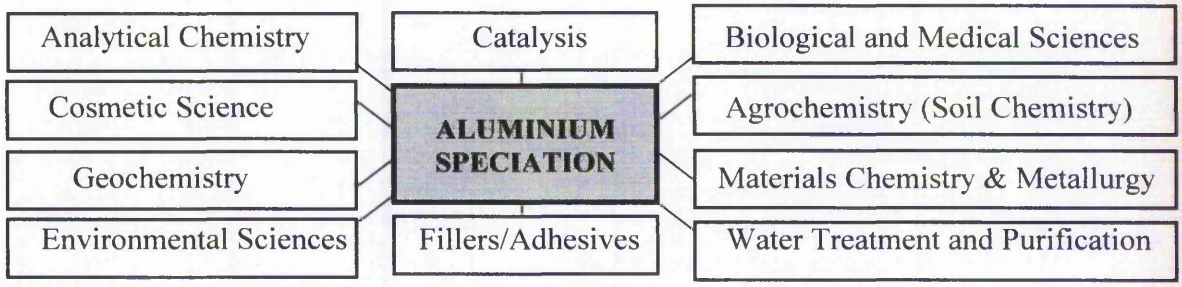


Fig. 1.1. Major research fields requiring the chemical speciation of Al-ions

Many more speciality applications and research areas could be added to the list shown in Fig. 1.1. However, despite a massive research effort spanning more than a century [9], the overall picture of the processes occurring in Al ion solutions is far from complete [4, 5]. The problems which are not fully understood, include kinetic and thermodynamic aspects of the formation of large aluminium polycations and factors affecting the phase transformations of these large polynuclear species into colloidal and solid state materials [4].

The aqueous chemistry of zirconium finds extensive application in modern technologies (Table 1.1), and it has been studied much less than that aluminium. Analysis of the literature indicates that a lack of suitable analytical methodologies is a major problem in the study of zirconium speciation.

Table 1.1. Some examples of application of Zr-containing materials [10]

Application	Purpose and benefits
Alloys	Added strength to lightweight alloys
Antiperspirants	Antiperspirant actives in deodorants
Binders	Silica-free foundry binders
Catalysis	Catalytic systems and supports in general catalysis
Cement additives	Enhanced cement fluidity while pumping
Ceramic colours	Inexpensive colours and glazes of low toxicity
Protective coatings	Wool flame-proofing; waterproof emulsions; paper coatings
Cross-linkers	Printing inks and polymers
Drilling muds	Clay stabilisers for improvement of drilling muds in the oil industry
Electronic ceramics	Dielectrics for use in capacitors, sensors and piezoelectrics
Engineering ceramics	Tough wear-resistant technical ceramics
Gemstones	Zirconia gemstones in high street jewellers
Glass	Glass toughening and optical property control
Ion exchange	Use in kidney dialysis and removal of toxic impurities in water
Clays pillaring	Controlled basal spacings, improved stability and interlayer porosity
Thermal barrier coatings	Improved aircraft fuel consumption
Chromatography	Stationary phases with high chemical resistance

1.2. Aluminium and zirconium: the elements

Aluminium and zirconium show a number of similarities in their elemental properties [5,6]. Both elements possess relatively small atomic radii (0.51 and 0.74 Å for Al and Zr respectively). Their electron configuration is of a high symmetry and low polarisability. Hence, Al and Zr cations are "hard spheres" of the A-type according to the classification by Ahrland et al. [11]. From Pearson's Hard and Soft Acid Theory [12], all A-type metal cations including Al^{3+} and Zr^{4+} are hard acids. Therefore, they possess the following preference for ligand atoms: F > O > P > N = Cl > Br > I > S. The ligand affinity towards A-type metal cations is the following [13]:

$$OH^- > RO^- > RCO_2^- > CO_3^{2-} >> NO_3^-, \quad (1.1)$$

and the preference increases with increase in ligand charge: $PO_4^{3-} >> SO_4^{2-} >> ClO_4^-$. A preference of the OH-ion as a complexing agent is the basis of the extensive hydrolytic ability of Al^{3+} and Zr^{4+} ions. Since this ability determines the aqueous chemistry of these metal ions to a great extent, we shall examine their hydrolytic behaviour further.

1.3. Aqueous chemistry of aluminium and zirconium

The great diversity of applications of Al and Zr aqueous chemistry has resulted in a large number of publications across a broad variety of fields. In this chapter, the essential aspects of Al/Zr speciation such as thermodynamics, kinetics and electronic properties of the major aqueous species will be briefly outlined as well as the major analytical techniques used for the speciation studies of Al and Zr solutions, colloids and solid materials.

1.3.1. Thermodynamic equilibrium constants for aluminium ions

A great amount of effort has been devoted to the determination of the thermodynamic stability constants of hydrolysed Al^{3+} species and their numerous complexes with various ligands. Early extensive reviews on the thermodynamic data of hydrolysis of Al-ions by Baes and Mesmer [5] and by the Russian authors [6] have been updated recently by G. Sposito [14], Fitzgerald [7], Casey et. al [15]. Series of reports by Ohman [16, 17], Wesolowsky and co-authors [18-20], Berthon et. al [21, 22] and other numerous works are dedicated to the determination of hydrolysis constants of Al species and the stability of complexes with ligands of geochemical, biological and analytical importance. A comprehensive review on the stability constants of the Al complexes with various organic ligands can be found in [23]. Smith and Martell [24] have reviewed the available stability constants for a wide range of complexes of Al-ions with inorganic and organic ligands.

Thermodynamic data available for the most established monomeric and oligomeric hydrolysed species found in aqueous solutions of Al-ions with non-complexing anions (chloride, nitrate, perchlorate, etc.) are summarised in Table 1.2.

Table 1.2. Thermodynamic data for the major Al^{3+} hydrolysis species (25 ^{0}C) [5, 14]

Species	h^*	$-\log K_{x,y}$	$\pm\sigma$ $(\log K_{x,y})$**	a***	b***	$\Delta H^0_{x,y}$, kcal	$\Delta S^0_{x,y}$, kcal/K
$Al(OH)^{2+}$	1.00	4.97	0.02	-2.044	0.52	11.9±0.5	17.2±1.7
$Al(OH)_2^+$	2.00	9.30	0.1	-3.066	0.55	-	-
$Al(OH)_3$	3.00	15.00	0.2	-3.066	0.45	-	-
$Al(OH)_4^-$	4.00	23.00	0.3	-2.044	0.36	-	-
$Al_2(OH)_2^{4+}$	1.00	7.70	0.3	-	-	18.7±2	27.5±7
$Al_3(OH)_4^{5+}$	1.33	13.94	0.1	1.022	-	35.4±4	57±13
$Al_{13}O_4(OH)_{24}^{7+}$	2.46	98.73	0.05	-18.40	3.55	278.8±2	457±7
α-$Al(OH)_3$(gibbsite,K_{s0})	3.00	8.50	0.1	3.066	-0.45	-	-

* - hydrolysis ratio $h = [OH^-]/[Al^{3+}]$;
** - - experimental error of the stability constant $K_{x,y}$; $K_{x,y}$ – the stability constant in the notation of Baes and Mesmer [5] which corresponds to hydrolysed species $Al_x(OH)_y^{(3x-y)+}$;
*** - a and b are coefficients of the extended Debye-Davies Equation (1.2) given below.

From the data of Table 1.2 one can see that at least eight Al species can be found at equilibrium conditions at room temperature in Al-ion aqueous solutions: Al monomers with $0 \le h \le 4$, small oligomeric species such as dimers and trimers, large Al isopolycations (Al_{13}-mer) and the solid phase of Al hydroxide. Gibbsite was included in Table 1.2 as an example of a crystalline phase of Al hydroxide. However, depending on the conditions of hydrolysis,

other amorphous or crystalline Al hydroxide phases can be observed at equilibrium conditions (e.g. amorphous pseudoboehmite, boehmite, bayerite, diaspore, norstrandite, tohdite, etc. [25]). These solid phases exhibit dissolution constants $K_{S1,0}$ different from gibbsite and can alter the corresponding speciation patterns significantly.

A large number of other hydrolysed Al species has been detected using various techniques (reviewed by Rosenberg and Fitzgerald in [26]). Up to now, the best agreement between researchers is for the species listed in Table 1.2.

A broad range of techniques is employed for the identification of hydrolysed Al species in aqueous solutions [8, 14, 26]. However, none of the listed techniques are 'universal' and none can detect the whole range of the hydrolysis products in Al-ion solutions [14]. For Zr-ions the situation is even more complicated since the range of the methods applicable for the studies of the speciation of this metal is limited [8]. The choice and features of the techniques applied in the present work for the studies of Al and Zr speciation will be discussed in Chapter 2.

Quantification of the speciation patterns and construction of speciation diagrams of Al-ion hydrolysis over a wide range of pH is an even more complicated task than identification of the hydrolysed species. Potentiometric acid-base titration of Al-ion solutions is the most common technique for this purpose [5]. The majority of the hydrolysis constants listed in Table 1.2 have been determined using this method. However, due to the intrinsic problems of pH measurement using glassy pH-electrodes [27], pH-metric titrations provide the most reliable results only in very dilute Al-ion solutions (preferably, below the solubility limit of the corresponding Al hydroxide, e.g. $[Al]<10^{-5}$ mol/L). At higher concentrations of Al-ions, pH measurements become biased with large errors, especially in the region of pH where Al hydroxide starts to form [5, 13]. From Table 1.2 it can be seen that experimental error $\sigma_{x,y}$ is lowest for the mono-hydrolysed Al-ions and tends to increase with increase of the theoretical (or formal) hydrolysis ratio of the corresponding species. Only for the large tridecameric species (Al_{13}-mers) is the error relatively small. The problem of the reliability of the measurement of thermodynamic parameters is further aggravated by the fact that at Al-ion concentrations higher than the solubility limit of Al hydroxide, the corresponding aqueous solutions are 'supersaturated' in terms of the Al hydroxide phase. This leads to the well-known phenomenon of the formation of colloidal Al hydroxide due to 'local perturbations' caused by alkali addition to Al-ion solutions of relatively high concentration below the pH of bulk Al hydroxide precipitation (pH~7) [4]. The colloidal hydroxide phase having a frustrated pseudoboehmite structure [25] can hinder unambiguous determination of hydrolysis constants of Al species at pH>4 [5]. Attempts to minimise the effect of 'local disturbances' by alkali addition have been undertaken, such as by decrease of alkali concentration, powerful stirring, application of softer alkalis as titrants, modifications to the titration procedure, etc. [28-30].

However, we presume that at conditions of 'supersaturation' (above the solubility limit of Al hydroxides) it is virtually impossible to eliminate completely the abovementioned effect using the conventional procedure for the acid-base titration of Al-ion solutions.

One more obstacle prevents unambiguous determination of hydrolysis constants of Al-ions at higher Al concentrations – variable ionic strength. It is well established that ionic strength is a significant parameter affecting equilibrium in solutions of hydrolysed Al species [5]. Two major schools of thought exist regarding the way to overcome the variation of ionic strength in the course of acid-base titrations of metal ions [31]. The first school led by Sillen has proposed to use a high concentration of electrolyte in solution (usually 1 to 3 mol/L) in order to make ionic strength variations due to titration negligible. The majority of the stability constants of various Al-ion complexes in aqueous solutions have been determined this way. However, at Al-ion concentrations more than 0.1 mol/L the intrinsic ionic strength of these solutions (e.g. for $AlCl_3$ I~0.6 mol/L at [Al]=0.1 mol/L) becomes comparable with the concentration of added electrolyte). This makes the use of ionic strength adjusters (non-complexing electrolytes such as sodium or potassium perchlorate) unreasonable. Another school of thought has proposed the determination of stability constants in aqueous solutions of metal ions without ionic strength adjustments. This type of experimentation has been criticised for obvious bias of the determined thermodynamic values due to the varying effect of ionic strength in titrated solutions [31].

On the basis of the available thermodynamic data and using the following empirical formula known as the extended Debye-Davies equation [5, 13]:

$$LogQ_{xy} = \log K_{xy} + aI^{1/2}/(1+I^{1/2}) + bC_x \qquad \textbf{(1.2)}$$

where $Q_{x,y}$ is a concentration quotient of the corresponding species $Al_x(OH)_y^{(3x-y)+}$; $K_{x,y}$ – thermodynamic stability constant of the corresponding species; a and b – empirical parameters given in Table 1.2, I – the ionic strength of solution, C_x – the concentration of counter-ions,

pH-based speciation diagrams of Al-ion hydrolysis can be readily constructed (Fig. 1.2). The concentration of the counter-ion (C_X) is directly linked to the total concentration of Al^{3+} in solution (Al_T) as follows:

$$C_X = \frac{3Al_T}{z'} \qquad \textbf{(1.3)}$$

where z' – the charge of the counter-anion.

In Fig. 1.2 the effect of Al-ion concentration and ionic strength on speciation diagrams at corresponding conditions is examined (t=25°C). Only the species listed in Table 1.2 are represented in Fig. 1.2. The following formulae were applied in order to calculate the speciation diagrams in Fig. 1.2:

$$\left(\frac{13Al_T^{12}Q_{13,32}}{[H^+]^{32}}\right)\alpha_0^{13}+\left(\frac{3Al_T^{2}Q_{3,4}}{[H^+]^4}\right)\alpha_0^{3}+\left(\frac{2Al_TQ_{2,2}}{[H^+]^2}\right)\alpha_0^{2}+\left(\frac{Q_{1,1}}{[H^+]}+\frac{Q_{1,2}}{[H^+]^2}+\frac{Q_{1,3}}{[H^+]^3}+\frac{Q_{1,4}}{[H^+]^4}+1\right)\alpha_0-1=0$$

$$\alpha_{1,1}=\frac{\alpha_0 Q_{1,1}}{[H^+]} \qquad \alpha_{1,2}=\frac{\alpha_0 Q_{1,2}}{[H^+]^2} \qquad \alpha_{1,3}=\frac{\alpha_0 Q_{1,3}}{[H^+]^3} \qquad \alpha_{1,4}=\frac{\alpha_0 Q_{1,4}}{[H^+]^4} \qquad \textbf{(1.4)}$$

$$\alpha_{2,2}=\frac{\alpha_0^{2} Al_T Q_{2,2}}{[H^+]^2} \qquad \alpha_{3,4}=\frac{\alpha_0^{3} Al_T^{2} Q_{3,4}}{[H^+]^4} \qquad \alpha_{13,32}=\frac{\alpha_0^{13} Al_T^{12} Q_{13,32}}{[H^+]^{32}}$$

where $Q_{x,y}$ - the hydrolysis quotient of the particular hydrolysed species; Al_T - the total concentration of Al^{3+}; α_0 - the fraction of the non-hydrolysed Al^{3+} ion; $\alpha_{x,y}$ - the fractions of the particular hydrolysed species.

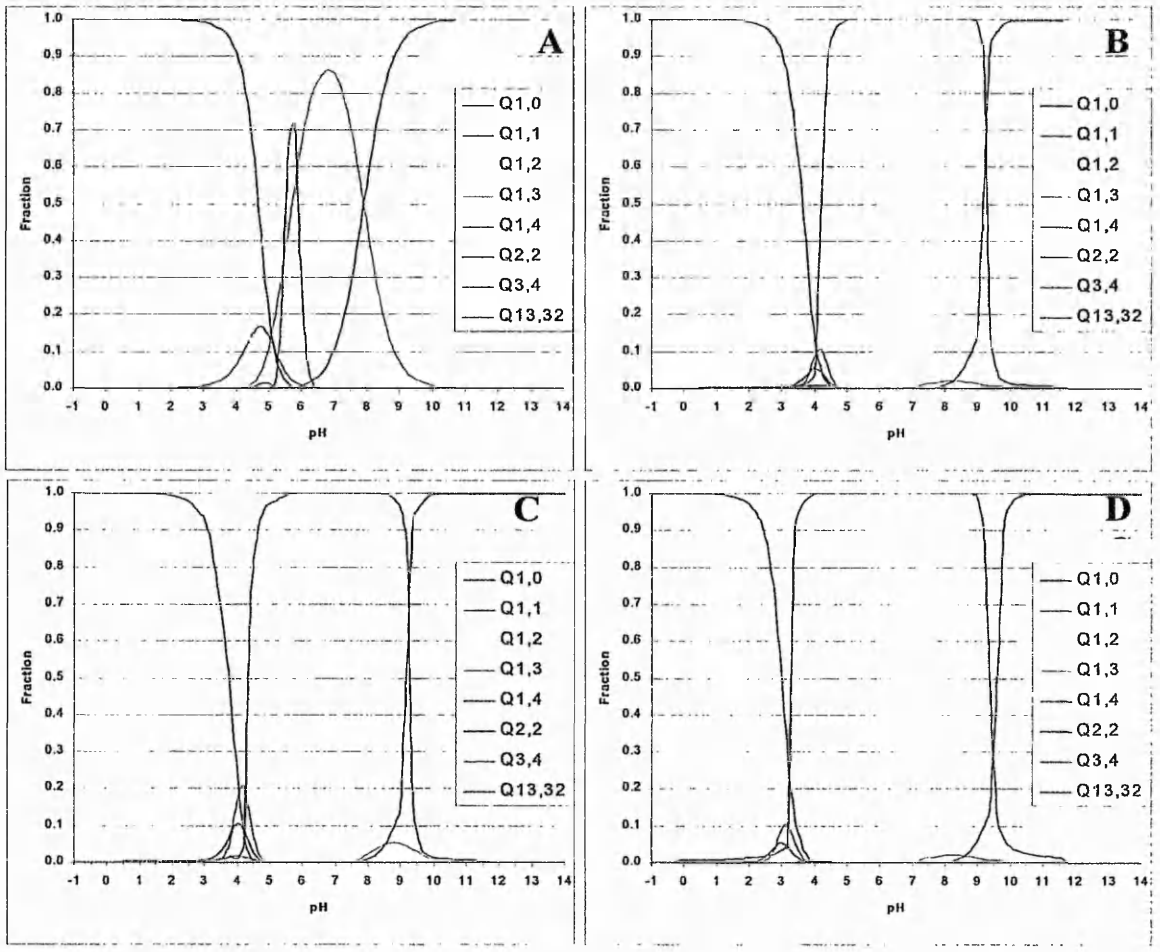


Fig. 1.2. Al^{3+} speciation diagrams at different conditions (temperature in all cases is 25 °C). ***A*** – C(Al)=1*10^{-5} mol/L, I=0.1 mol/L, z'=1; ***B*** - C(Al)=0.1 mol/L, I=0.1 mol/L, z'=1; ***C*** - C(Al)=0.1 mol/L, I=1 mol/L, z'=1; ***D*** - C(Al)=0.1 mol/L, I=0.1 mol/L, z'=2 (non-complexing ligand).

From the data of Fig. 1.2*A* one can find that at low Al-ion concentration (10^{-5} mol/L) the major form of Al-ion are monomers. The degree of hydrolysis (formal hydrolysis ratio) of the monomeric Al species gradually increases with increase of pH. Small oligomeric species constitute only a tiny fraction in the overall species distribution, while Al_{13}-mer species are present in significant amounts only in a very narrow pH range with the maximum at pH~5.8.

At pH~7 when the hydrolysis ratio of the species reaches 3, soluble monomeric $Al(OH)_3$ dominates the solution equilibrium. This species is easily transformed into aluminate-ions $Al(OH)_4^-$ at alkaline conditions (pH>7). Solid phase of Al hydroxide is at a very low level.

The speciation diagram in Fig. 1.2*B* indicates that at considerable Al-ion concentration (0.1 mol/L) monomeric species dominate only at very low and at very high pH values. Small oligomers constitute a significant fraction (~10%) of the species present under these conditions. The Al_{13}-mer species are the dominant species over a wide range of pH from ca. 4 to ca. 6. Precipitation of Al hydroxide becomes a dominant process in the vicinity of the point of electroneutrality at pH~7 [4, 25]. This phase is significantly harder to dissolve in alkaline conditions (pH>7). Monomeric $Al(OH)_3$ species is virtually absent in the calculated equilibrium.

Using the extended Debye-Davies equation (1.2) the effect of ionic strength on the concentration quotients of the hydrolysis products of Al-ions can be examined (Fig. 1.3).

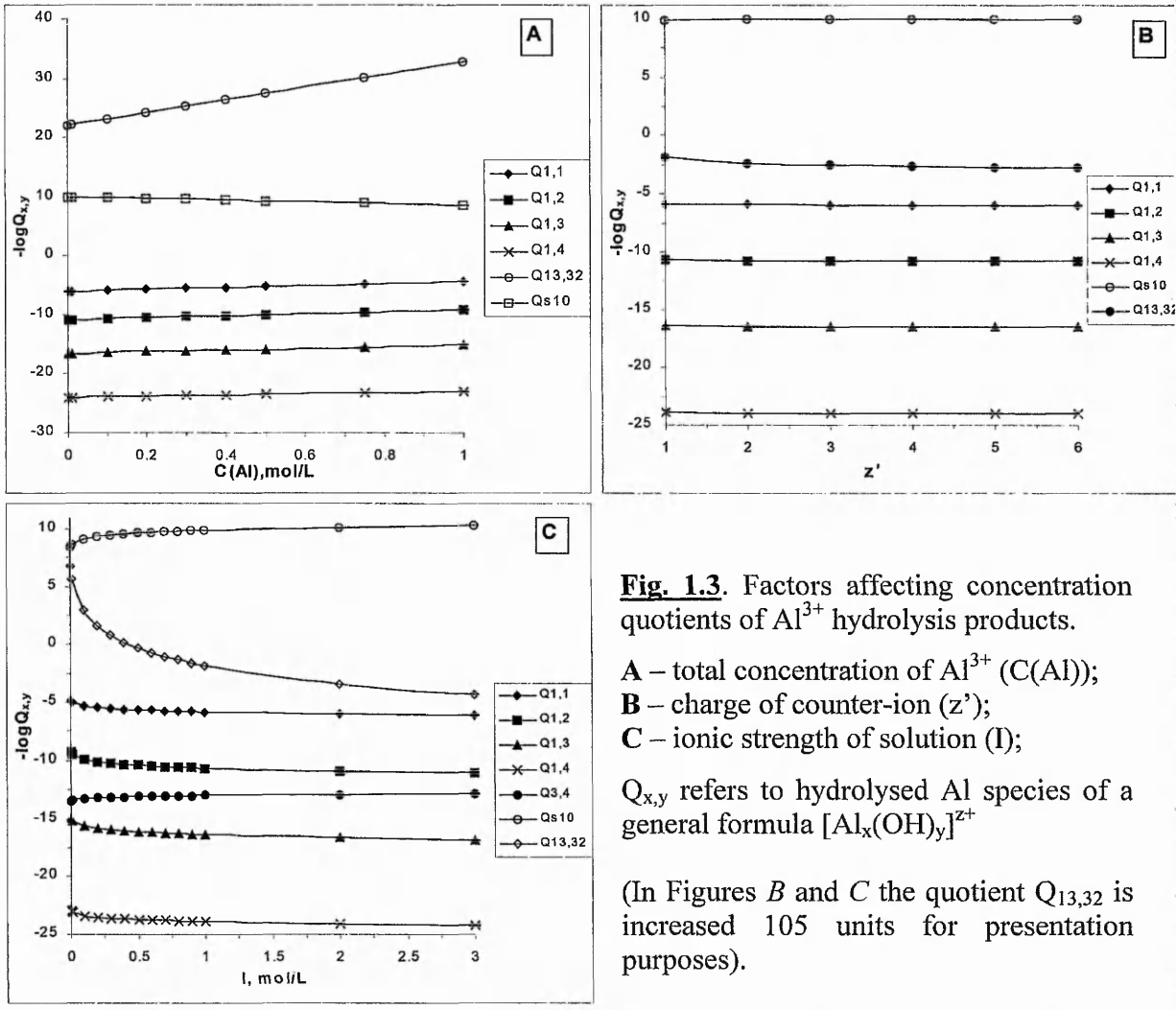


Fig. 1.3. Factors affecting concentration quotients of Al^{3+} hydrolysis products.

A – total concentration of Al^{3+} (C(Al));
B – charge of counter-ion (z');
C – ionic strength of solution (I);

$Q_{x,y}$ refers to hydrolysed Al species of a general formula $[Al_x(OH)_y]^{z+}$

(In Figures *B* and *C* the quotient $Q_{13,32}$ is increased 105 units for presentation purposes).

From the data of Fig. 1.3 one can find that, generally, polymeric species and soluble hydroxide $Al(OH)_3$, due to their metastable nature, are more susceptible to variations of different parameters of solution than monomeric Al species. The most significant factor of

thermodynamic stability of Al species is the total concentration of aluminium (Fig. 1.3*A*). The stability quotients $Q_{x,y}$ of Al species vary linearly with increase of Al concentration in accordance with the term bC_X in Eq. (1.2). The data of Fig. 1.3*A* explain an empirical rule, according to which the extent of hydrolysis usually increases with dilution, while the concentration of polynuclear species tends to decrease [5, 13, 14]. Obviously, the solubility of $Al(OH)_3$ decreases at higher Al^{3+} concentrations [20].

Another important factor in the thermodynamics of Al speciation, as mentioned above, is the ionic strength of solution (Fig. 1.3*B*). The concentration quotient of the Al_{13}-mer varies most notably with increase of ionic strength, while the quotients for monomeric species change only slightly. The relationship between $Q_{x,y}$ and I for the Al_{13}-mer species is close to an exponential decay function in agreement with the term $aI^{1/2}/(1+I^{1/2})$ in Eq. (1.2). This is the reason for the most drastic decrease of $-\log Q_{x,y}$ in the range of ionic strengths 0-1 mol/L.

Finally, the charge of the counter-ion produces a small change in the thermodynamic stability of Al species (Fig. 1.3*C*), noticeable only when one increases z' from 1 to 2.

Along with Al-ion concentration and ionic strength discussed above, several other important parameters affect speciation of Al-ions, particularly temperature. Khodakovskii et al. [32] have calculated the prevalence of the different monomeric hydroxo-aluminium species at various temperatures (Fig. 1.4).

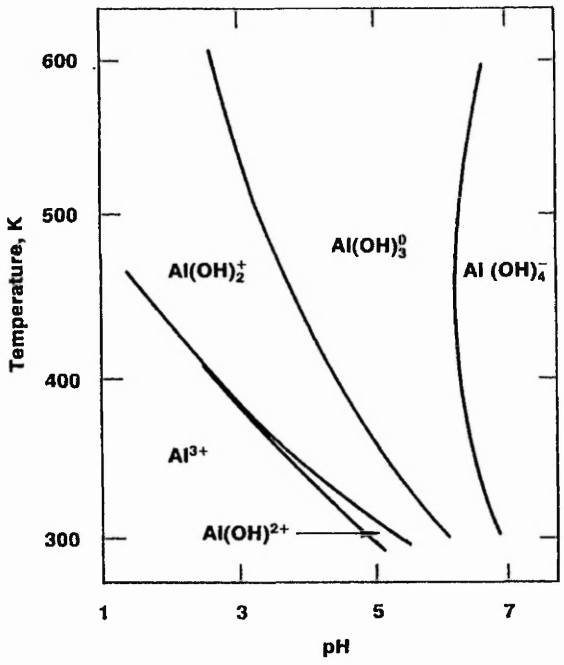


Fig. 1.4. Stability ranges of aluminium monohydroxo-complexes in water

As can be seen in Fig. 1.4, the stability range of the cationic forms of monomeric Al-ions decrease sharply with increasing temperature. The activity of the dissolved neutral hydroxo complex $Al(OH)_3^0$ increases correspondingly. As a result, the solubility of Al hydroxide (and corundum) in acidic solutions decreases with increasing temperature. The

ratio of $Al(OH)_3^0$ to $Al(OH)_4^-$ species is practically independent of temperature [25].

Baes and Mesmer [5] have compiled the data available on the temperature-dependent variation of stability (concentration) quotients of polymeric Al hydrolysis products which can be presented graphically as shown in Fig. 1.5.

The data in Fig. 1.5 indicates that the dependence of concentration quotients of Al dimers and trimers is close to linear. In the case of the Al_{13}-mer species, the relationship of the concentration quotients $Q_{x,y}$ and temperature is more complex. We have arbitrarily chosen the Boltzman function [33] for fitting the data on the Al_{13}-mer.

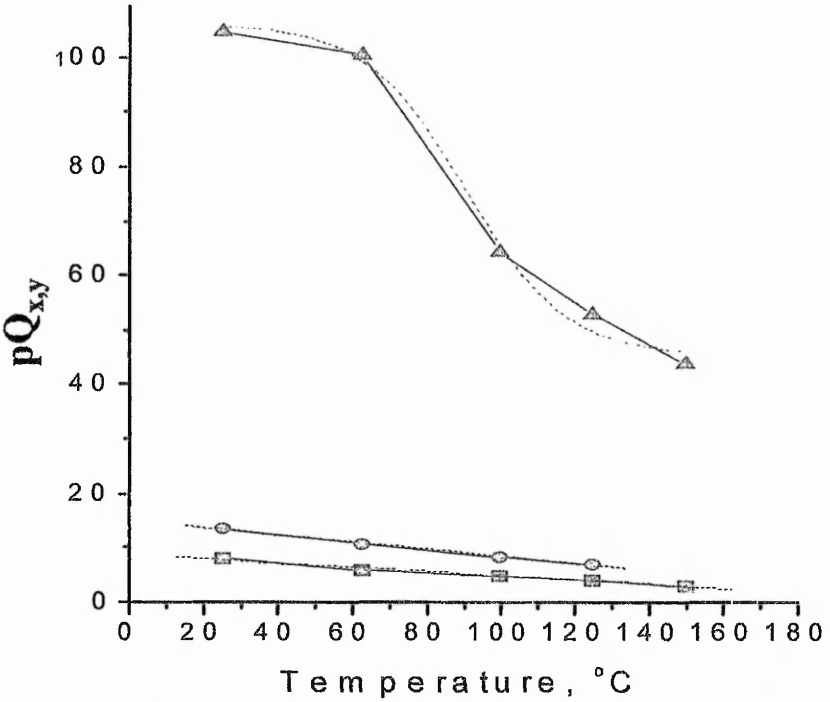


Fig. 1.5. Logarithm of stability quotients $pQ_{x,y}=-\log Q_{x,y}$ for Al^{3+} polynuclear species at different temperatures [5]. Dashed lines represent graphic approximations calculated in this work.

The following formulae were obtained from the non-linear curve-fitting of the data shown in Fig. 1.5:

$$\underline{\text{Al dimer}}: pQ_{x,y} = 8.69691 - 0.03863 \cdot T\ (^0C) \quad (R^2 = 0.992) \qquad \textbf{(1.5)}$$

$$\underline{\text{Al trimer}}: pQ_{x,y} = 14.96865 - 0.06558\ T\ (^0C) \quad (R^2 = 0.997) \qquad \textbf{(1.6)}$$

$$\underline{\text{Al tridecamer}}: \quad pQ_{x,y} = \frac{101.18}{1 + e^{(T-90.26)/13.53}} + 45.34 \quad (R^2 = 0.992) \qquad \textbf{(1.7)}$$

High correlation coefficients (R^2) in Eqs. (1.5-1.7) indicate a good fit of the data in Fig. 1.5 with the chosen functions. In principle, Eqs. (1.5-1.7) enable one to predict the stability quotients of the polynuclear aluminium species as a function of temperature.

As follows from the data of Fig. 1.5, the higher the polymer nuclearity, the stronger

the impact of temperature. For instance, the value of $pQ_{x,y}$=-log$Q_{x,y}$ for the Al_{13}-mer drops from 105 to 45, when heating solutions from 20 to 130 ^{0}C. Another important feature is that the slope of the calculated curve for Al_{13}-mer is steepest in the temperature range 80-100 ^{0}C, a fact that correlates well with literature data [34] on the temperature dependence of the Al_{13}-mer synthesis.

The values of standard thermodynamic potentials ΔH^0 and ΔS^0 for major Al species are listed in Table 1.2. The available values of standard enthalpy (ΔH^0) are positive for all the hydrolysed Al species. This is compensated by high values of standard entropy (ΔS^0). Therefore, the sign and the value of the Gibbs energy ΔG^0 will strongly depend on temperature according to the third law of thermodynamics [13].

Baes and Mesmer [5] have established empirical relationships between the fundamental thermodynamic potentials of the hydrolytic condensation and the charge of a cation z:

$$\Delta H° = 75.2 - 9.5\,z \quad \text{(kJ/mol);} \quad \textbf{(1.8)}$$

$$\Delta S° = -148.4 + 73.1\,z \quad \text{(J/K/mol);} \quad \textbf{(1.9)}$$

$$\Delta G° = 119.5 - 31.35\,z \quad \text{(kJ/mol)} \quad \textbf{(1.10)}$$

The reaction is spontaneous ($\Delta G°<0$) for elements with z equal or greater than 4. It means, that for Al^{3+} the value of $\Delta G°$ becomes negative only at elevated temperatures ($T >$ 298 K). The literature data indicate that at higher temperatures small Al oligomers can occur in quite concentrated Al-ion solutions [35].

1.3.2. Thermodynamic equilibrium constants of zirconium-ions

The chemistry of Zr (IV) in aqueous media is dominated by the complexation of Zr^{4+} with OH^- [5]. Numerous studies have dealt with the formation of zirconium-hydrolysed complexes in aqueous solution albeit many discrepancies exist between authors concerning the major species formed and the values of the corresponding constants of formation [5, 36, 37].

Generally, in the case of tetravalent cations (Zr (IV), Hf (IV), Ti(IV), Th(IV)) hydrolysis reactions occur at low pH values. It has been found [5,6, 37, 38] that hydrolysis starts in very dilute ($<10^{-6}$ M) Zr solutions at pH = 0 and above. The first hydrolysis step (h = 1) leads to the formation of monomeric hydrolyzed species $[Zr(OH)(OH_2)_7]^{3+}$, which undergo further hydrolysis (h = 2) through the olation mechanism in the absence of complexing anions [4,39]:

$$[Zr(OH)(OH_2)_7]^{3+} + H_2O \rightarrow [Zr(OH)_2(OH_2)_6]^{2+} + H_3O^+ \quad \textbf{(1.11)}$$

These partially hydrolyzed species have OH^-groups with a rather high partial charge so

that condensation occurs leading to the formation of the well-known cyclic tetramer $[Zr_4(OH)_8(OH_2)_{16}]^{8+}$ (MW ≈ 788) [37]. Intervals of Zr concentration and pH in which oligomeric species start to form, are still debatable. For instance, authors of the report [38] using potentiometry and highly sensitive radiochemical assay have found that monomeric Zr species exist only at concentrations below 10^{-8} M. Some other studies are consistent with somewhat higher Zr concentrations of monomeric species oligomerisation ($<10^{-6}$ M) [36].

In the case of Zr^{4+}, hydrolysis is a spontaneous reaction according to Eqs. (1.8-1.10). Unlike the Al^{3+}-ion, which gives rise to weakly acidic solutions on dissolution due to auto hydrolysis but does not hydrolyse any further without increasing the temperature or without adding a base, Zr^{4+}-ions acidify solutions when dissolved and hydrolyse spontaneously [37]. The extent of hydrolysis and the species produced depends on the total Zr^{4+} concentration. The level of discrepancy between the values of thermodynamic constants of zirconium hydrolysis from different sources can be evaluated from the data of Table 1.3.

Table 1.3. Zr^{4+} hydrolysis constants from the literature sources [5, 6, 36].

Species	h	$-\log K_{x,y}$[5]	±σ	$-\log K_{x,y}$[6]	±σ	$-\log K_{x,y}$[36]	±σ
$Zr(OH)^{3+}$	1.00	-0.3	0.05	-	-	-0.05	-
$Zr(OH)_2^{2+}$	2.00	(1.7)[1]	-	-	-	0.28	-
$Zr(OH)_3^{+}$	3.00	(5.1)	-	0.52	0.01	0.43	-
$Zr(OH)_4$	4.00	9.7	~1	4.52	0.07	0.80	-
$Zr(OH)_5^{-}$	5.00	16.0	-	-	-	-	-
$Zr_2(OH)_7^{+}$	3.50	-	-	2.22	0.07	-	-
$Zr_3(OH)_4^{8+}$	1.33	0.6[2]	0.1	-	-	-	-
$Zr_3(OH)_5^{7+}$	1.66	3.7[2]	0.1	-	-	-	-
$Zr_4(OH)_8^{8+}$	2.00	6.0	0.1	-	-	-	-
ZrO_2 (c), Q_{s10}	-	1.9	~1	0.74	0.08	-	-

Eq. (1.2) has been proposed for the estimation of stability quotients of Zr^{4+} hydrolysis at different ionic strengths and Zr^{4+} concentrations [5]. We have used the values of the constants estimated by these authors in order to calculate the speciation diagrams for Zr^{4+} at different concentrations (Fig. 1.6).

---

[1] - the values of $Q_{x,y}$ in parentheses have been estimated only.

[2] - these hydrolysis quotients have been calculated with assumption that the only one of the trimer species formed [5].

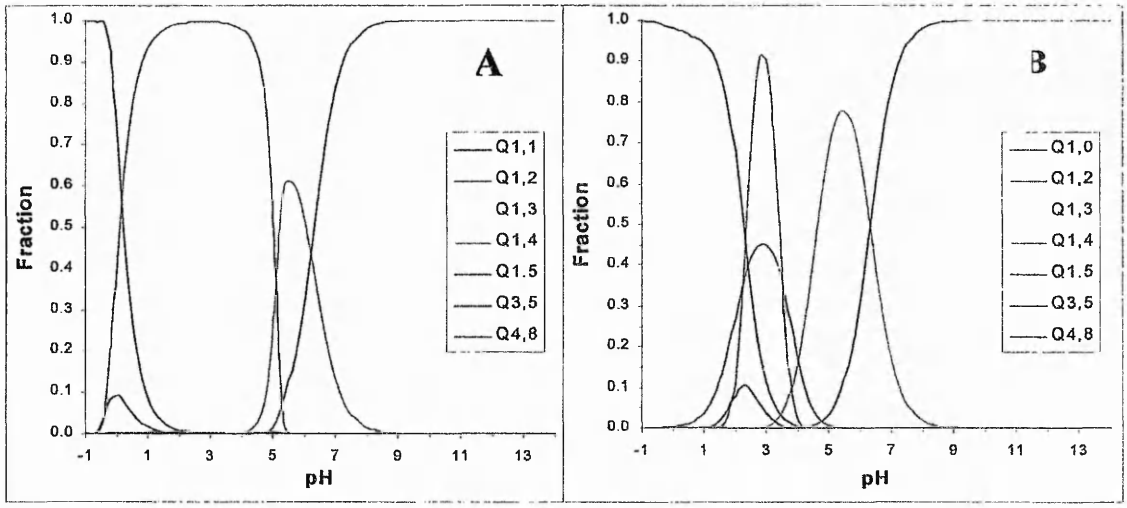


Fig. 1.6. Speciation diagram of zirconium at different Zr^{4+} concentrations. **A** - C(Zr)=0.1 mol/L; **B** – 0.00001 mol/L; t = 25 ^{0}C; ionic strength is negligible. The curves refer to the species of a general formula $[Zr_x(OH)_y]^{z+}$.

Analysing the diagram in Fig. 1.6, one can see, that in the pH range 1-5 tetrameric species dominate at higher concentrations, completely replacing $Zr(OH)^{3+}$ species, although they are important at Zr concentrations as low as 10^{-5} M. As will be shown below, the condensation of these tetrameric species in most cases leads to the formation of different solid products, depending on the conditions under which polymerisation process occurs.

Calculation of the hydrolysis constants from the Eq. (1.2) and (1.3) also shows that the effect of a higher ionic strength on the distribution of the hydrolysed species of zirconium is not as profound as in the case of Al^{3+} ions. However, the tendency to decrease hydrolysis constants for polynuclear species is similar to that for Al^{3+}. Temperature drastically decreases the hydrolysis constant for the Zr tetramer (~ 10-20 %). That is also the case for Al^{3+} speciation.

It is necessary to mention that both for aluminium and zirconium a significant part of the calculated speciation diagrams relates to supersaturated solutions [5, 40]. For aluminium, supersaturation depends on Al concentration and usually begins at pH ca. 4.2, while for zirconium this process occurs as early as at pH ≥ 1. Another feature, which distinguishes zirconium from aluminium, is that the solid phase once formed does not re-dissolve for a long time due to an extremely low rate for the reaction of dissolution. Both the phenomena of supersaturation and the low dissolution rate change the actual picture of Zr speciation at pH > 1. After the formation of the tetramer $Zr_4(OH)_8^{8+}$, a further increase of pH leads to the eventual creation of an insoluble hydrous oxide with the general formula $[Zr(OH)_4]_n$.

1.3.3. The Partial charge model

Description of chemical speciation of metal ions in solutions is usually based on thermodynamic data. However, these data are not always available or reliable, especially for numerous transient species formed in the course of hydrolysis-condensation of metal ions

[5,6]. In order to fill this gap, an empirical theory called the Partial charge model (PCM) developed by J. Livage, M. Henry and co-workers [39, 41] will be used throughout this thesis in order to describe the electronic and acid-base properties of the molecular species of aluminium and zirconium.

The preferential use of the PCM theory is based on the following advantages over other theoretical approaches.

1. The PCM provides computationally inexpensive theoretical means for evaluation of the hydrolysis, condensation and complexation reactions of aluminium and zirconium ions in aqueous solution and allows for the prediction of possible pathways and likely products from these processes.
2. One of the unique features of the PCM is that it relates microscopic quantities such as charge, electronegativity, hardness, softness and partial charges on molecules/ions with macroscopic parameters such as pH and hydrolysis ratio.
3. The PCM enables one to evaluate and to compare acid-base properties of the species in aqueous solutions with regard of the important role which coordination with water and other ligands plays in adjustment of these properties. These estimations do not require preliminary knowledge of thermodynamic parameters. This also provides an opportunity to calculate the electronic properties of the 'virtual' species and to estimate the probability of their occurrence in aqueous medium for given conditions from an electrostatic point of view.

The Partial charge model (PCM) [39] is based on a classical concept of electronegativity proposed by L. Pauling and the principle of electronegativity equalisation suggested by R. Sanderson. This model utilises relatively simple terms such as the mean electronegativity of a molecule χ, Pearson's hardness η and softness σ, and atomic partial charges δ.

By the quantum-mechanical definition the mean electronegativity is the opposite of an electronic potential μ [41]:

$$\chi = -\mu, \tag{1.12}$$

On the other hand, according to Pauling's definition, electronegativity is an average of ionisation potential (I_p) and electron affinity (A):

$$\chi = (I_p + A)/2 \tag{1.13}$$

Equations (1.12) and (1.13) establish a firm theoretical basis for the implementation of the Partial charge model in practice [39].

According to Sanderson's assumption, "when two or more atoms initially different in

electronegativity combine, they adjust to the same intermediate electronegativity in the compound". The resulting electronegativity of the product χ can then be defined as [39]:

$$\chi = \chi_i = \chi_i^0 + \eta_i \delta_i + \sum_j \frac{\delta_j}{R_{ij}} \qquad i(j) = 1, \ldots, n \qquad \textbf{(1.14)}$$

where χ_i – the electronegativity of *i*-th atom; χ_i^0 – the Pauling electronegativity of *i*-th atom; η_i – the hardness of *i*-th atom; δ_i and δ_j – the partial charge on the *i*-th (*j*-th) atom in the resulting compound; R_{ij} – interatomic distances. The summation $\sum_j \frac{\delta_j}{R_{ij}}$ is the perturbative electrostatic potential.

Owing to conservation of electrical charge:

$$\sum_i \delta_i = z \qquad \textbf{(1.15)}$$

where z – the total electrical charge of the resulting compound.

Equations (1.14) and (1.15) allow for the computation of structure-dependent partial charge distributions in molecules, albeit that they require resolution of a linear set of equations [39]. This can be avoided by making an approximation $\sum_j \frac{\delta_j}{R_{ij}} \langle\langle \chi_i^0$ leading to a structure-independent version of the PCM [41]. In this simplified model the major parameters are the mean electronegativity of the molecule and the partial charges on atoms (or groups of atoms) defined as follows:

$$\chi = \frac{\sum_i \sqrt{\chi_i^0} + 1.36z}{\sum_i 1/\sqrt{\chi_i^o}} \qquad \text{and} \qquad \delta_i = \frac{(\chi - \chi_i^0)}{1.36\sqrt{\chi_i^0}} \qquad \textbf{(1.16, 1.17)}$$

where χ - the mean electronegativity of molecule; *z* – the total charge of the molecule,
χ_i^0 – the electronegativity of i-atom in Allred-Rochow scale of electronegativities;
δ_i – the partial charge of each atom in the molecule.

The structure-independent Partial charge model (SI PCM, hereinafter - PCM) has been successfully applied [39, 41-44] for the study of the aqueous chemistry of metal ions. The successful application of a purely electrostatic theory (PCM) to the complicated processes of hydrolysis-condensation and complexation of metal ions indicates the ultimate importance of electrostatic factors in the interactions occurring during these reactions.

The following limitations of the Partial charge model should be considered when implementing it for metal ion speciation studies:

1. The model is structure-independent which implies that 'averaged' values of partial

charges on atoms in the species are calculated. This feature limits PCM calculations to monomeric and relatively small (symmetric) oligomeric species.

2. The purely electrostatic nature of the model is not capable of the evaluation of chelates, complexes with aromatic molecules and other compounds where donor-acceptor interactions with electron transfer or strong structural stabilisation are involved.
3. Presently, there is no direct link established between the electronic parameters calculated using the PCM model and thermodynamic/macroscopic parameters of solution species. The calculations by the PCM model are relevant at 25 °C.

In spite of the limitations listed above, the PCM model is a very useful tool for elucidation and visualisation of the mechanistic patterns in the aqueous chemistry of metal ions.

1.3.4. Hydrolysis of monomeric ions of aluminium and zirconium; Partial charge model considerations

It is well established that the hydrolysis of metal cations results from their solvation by dipolar water molecules and their subsequent deprotonation [4,13]. Solvation leads to the formation of $[M(OH_2)_n]^{z+}$ species. Water behaves as a Lewis base and the M-OH_2 σ-bond involves charge transfer from the bonding $3a_1$ molecular orbital of the water molecule to empty atomic orbitals on the metal cation. This weakens the O-H bond within the water molecule, which becomes more acidic. Depending on the water acidity and, hence, the magnitude of charge transfer, the following equilibria are established [41]:

$$[M(OH_2)_N]^{z+} + h\,H_2O \leftrightarrow [M(OH)_h(OH_2)_{N-h}]^{(z-h)+} + h\,H_3O^+ \leftrightarrow$$
$$\leftrightarrow [MO_{2h}(OH)_{N-2h}]^{(z-2h)} + 2h\,H_3O^+ \leftrightarrow [MO_{2h}]^{(z-2h)-} + 2h\,H_3O^+ \quad \textbf{(1.18)}$$

where M – the metal cation; z – the charge of cation; N – the coordination number of water molecules around M; h – the molar ratio of hydrolysis (the hydrolysis ratio).

In dilute solutions Eq. (1.18) leads to a set of monomeric species with a different extent of protonation ranging from aquo-ions $[M(OH_2)_n]^{z+}$ to aquo-hydroxy species $[M(OH)_h(OH_2)_{n-h}]^{(z-h)+}$, oxo-hydroxy species $[MO_{2h}(OH)_{n-2h}]^{(z-2h)}$ and even fully deprotonated oxo-anions $[MO_{2h}]^{(z-2h)-}$. In Eq. (1.18) equilibria depend on the properties of a metal atom and parameters of solution, such as pH, temperature, ionic strength, presence of anion, different complexing agents, saturation with corresponding solid phase, etc. [4,5,39].

The Partial charge model can be used to calculate the magnitude of charge transfer between oxo-, hydroxo-, or aquo-ligands and metal ion. On the basis of the PCM calculations it is possible to build a "pH-charge" diagram, empirically derived earlier [39] (Fig. 1.7).

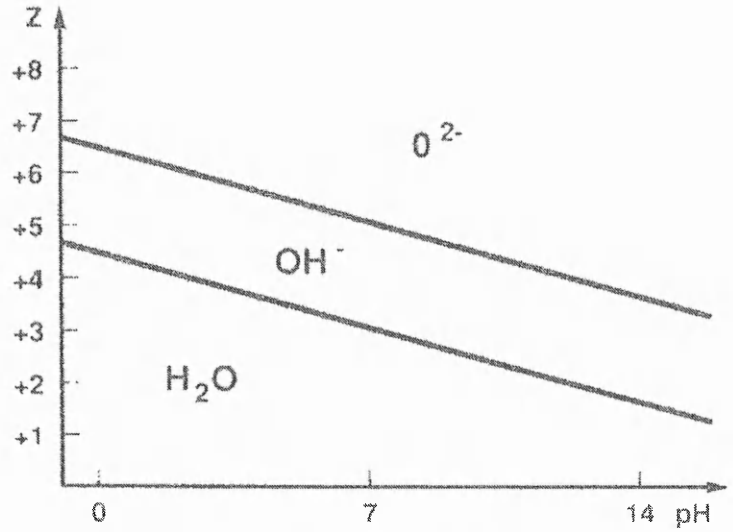


Fig. 1.7. The 'Charge-pH' diagram [39]. Three domains for the hydrolysis ratio h as a function of the metal charge and pH are depicted as OH_2; OH^- and O^{2-} in respect of the favourable ligand for metal complexation.

The lowest of the three domains depicted in the diagram in Fig. 1.7 corresponds to the aquo-species $[M(OH_2)_N]^{z+}$), the upper domain – to the oxo-species $[MO_{2h}]^{(z-2h)-}$, and the intermediate domain – to the hydroxo-species $[M(OH)_h]^{(z-h)+}$. Near the borderlines of these domains (derived at h = 1 and h=2N-1, respectively) the mixed aquo-hydroxy species $[M(OH)_h(OH_2)_{N-h}]^{(z-h)+}$ or oxo-hydroxy species $[MO_{2h}(OH)_{N-2h}]^{(z-2h)}$ can be observed.

In general, two conditions are possible for hydrolysis reaction to occur – **acidic** (without addition of alkali) where hydrolysis of some metal ions can proceed spontaneously ('autohydrolysis') and **basic,** where hydrolysis is 'forced' by the addition of alkali.

Under acidic conditions, autohydrolysis of metal ion with coordination number N and charge z:

$$[MO_NH_{2N}]^{z+} + pH_2O \rightarrow [MO_NH_{2N-p}]^{(z-p)+} + H_3O^+ \qquad \textbf{(1.19)}$$

is limited by the cleavage reaction of the O-H bond of coordination water due to the polarising power of the metal-ion [41]. The reaction proceeds as long as the partial charge on the acquired hydroxyl-groups $\delta(OH)<0$ in the $[MO_NH_{2N-p}]^{(z-p)+}$ precursor. According to the PCM:

$$p = 1.45z - 0.45N - 1.07(2.71-\chi^0_M)/\sqrt{\chi^0_M} \qquad \textbf{(1.20)}$$

indicating that the number of protons removed (p) depends on the charge (z), the coordination number (N) and the atomic electronegativity of the metal (χ^0_M).

Three limiting cases are encountered when applying Eq. (1.20):

1. p**=0**: $[MO_NH_{2N}]^{z+}$ is not deprotonated and autohydrolysis is not possible. Base must be added to cause hydrolysis.
2. p**>2**N **(**p**>0)**: no water molecules are present in the coordination sphere of metal-ion, and the corresponding oxo-ion, $[MO_N]^{(2N-z)-}$ cannot be protonated by H_3O^+.

3. **$0<p<2N$**: autohydrolysis is possible. Under acidic conditions two species corresponding to $h=E(p)$ and $h=E(p+1)$ are in equilibrium ($E(p)$ is an integer part of p, h is the molar hydrolysis ratio determined as $[OH]/[M^{z+}]$).

For Al^{3+} ions with $N=6$ and $\chi^0_M=1.47$ the number of protons removed is $p=0.56$, according to Eq. (1.20). Thus, the autohydrolysis can proceed and two species with $h=0$ and $h=1$ ($[Al(H_2O)_6]^{3+}$ and $[Al(H_2O)_5(OH)]^{2+}$ correspondingly) should be found in solutions of Al-ions, this is supported by numerous experimental results [5, 8, 14]. It is well known that on dissolution of Al salts the pH value is weakly acidic (e.g. pH<3 at [Al]=0.1 mol/L). The value of pH in Al solutions as a function of Al autohydrolysis depends strongly on the concentration of Al-ions and the nature of any counter-ions. The reasons for the latter will be discussed below.

For Zr^{4+} ions with $N=7$ and $\chi^0_M=1.29$ the value of $p=1.31$ (Eq. 1.20) indicates that autohydrolysis is also possible and two species with $h=1$ ($[Zr(H_2O)_7(OH)]^{3+}$) and $h=2$ ($[Zr(H_2O)_6(OH)_2]^{2+}$) must exist in equilibrium. From experimental data it is known [36] that the zirconium-ion is a strong acid and hydrolyses completely when Zr salts with non-complexing anions (chloride, perchlorate) are dissolved in water [41]. The pH value reaches pH≤1 at [Zr]=0.1 mol/L and is also strongly dependent on the concentration of zirconium and the nature of counter-ions present [37, 41].

Under basic conditions, hydrolysis is limited by the cleavage of the M-OH bond due to the low polarising power of the strongly hydrolysed $[[MO_NH_{2N-q}]^{(z-q)+}$ precursor, where $2N-q$ corresponds to the number of protons which cannot be removed from the OH-groups of the precursor even at very high pH. Hence, q is the maximum number of protons which are able to be removed at high pH values. Hydrolysis can proceed until $\delta(OH) = -1$. From the PCM:

$$q = 1 + 1.25z - 0.92(2.49 - \chi^0_M)\sqrt{\chi^0_M}. \qquad \textbf{(1.21)}$$

Two limiting cases are encountered when applying Eq. (1.21):

1. **$q > 2N$**: the most basic form of metal-ion is an oxo-ion $[MO_N]^{(2N-z)-}$.
2. **$0 < q < 2N$**: two species corresponding to $h=E(q)$ and $h=E(q+1)$ are in equilibrium at very high pH ($E(q)$ is an integer part of q).

In the case of aluminium-ions the calculation of q from Eq. (1.21) yields a value of 3.97. Thus, the maximum hydrolysis ratio is equal to 4, which results in the experimentally observed aluminate-ion $Al(OH)_4^-$ [45]. For zirconium-ions, the use of Eq. (1.21) renders $q=5.05$ which corresponds to $h=5$ ($Zr(OH)_5^-$ species) observed in practice [46].

The Partial charge model also allows for the relationship between mean electronegativity of the precursor (microscopic parameter) and the pH of the medium (macroscopic parameter) to be established [39]. According to the PCM, proton exchange between a non-hydrolysed precursor and solution proceeds until the mean electronegativity of the hydrolysed precursor χ_h becomes equal to the mean electronegativity of water χ_w:

$$\chi_h = \chi_w = 2.732 - 0.035\text{pH} \quad \textbf{(1.22)}$$

Eq. (1.22) enables one to calculate the pH conditions for hydrolysed species to exist (see Table 1.4, 1.5, 1.7 below).

It is necessary to stress that along with the value of pH, the hydrolysis ratio is one of the most important macroscopic quantities for hydrolysis and condensation reactions since it is related to the structure and molecular composition of the hydrolysed species. The value of pH frequently serves as a common scale for building speciation diagrams and other speciation-related relationships. This value is both "a reason and a consequence" of the hydrolysis-condensation reactions of metal ions (protons can be consumed or released upon such reactions as autohydrolysis, alkaline or acidic hydrolysis, condensation into polymers, formation of colloidal and solid phases). Moreover, the value of pH is usually derived from the activity of hydrogen-ions determined using a glassy pH-electrode [5, 13]. The value of hydrogen-ion activity varies strongly with temperature, ionic strength, charge and other parameters such as counter-ions and 'spectator' ions including alkaline and alkali earth metal ions, ammonia, various counter-anions, etc. Measurements of pH using a pH-electrode exhibit strong errors in highly concentrated and, therefore, non-ideal solutions of metal ions, and when colloidal or solid phases are present along with soluble species [5]. The value of the hydrolysis ratio is free from these variations and errors. It is determined only by the total concentration of a metal-ion and alkali (or acid) added to a metal-ion solution. Owing to this, we have replaced the value of pH with the value of hydrolysis ratio in the present experimental studies, whenever possible.

The Partial charge model establishes an important relationship between the theoretical hydrolysis ratio of hydrolysed species and microscopic properties such as the charge of the species, the coordination number of the metal and the partial charges of atoms in the hydrolysed precursor. From this model the hydrolysis ratio for aquo-species $[M(OH_2)_N]^{z+}$ is calculated as follows:

$$h = \frac{z - N\delta_O - 2N\delta_H - \delta_M}{1 - \delta_H} \quad \textbf{(1.23)}$$

where δ_O, δ_M and δ_H are the partial charges of oxygen, metal and hydrogen in the precursor, respectively, and can be found from Eqs. (1.16) and (1.17); z – the total charge of the species; N – the coordination number of metal.

Computing partial charges of oxygen and hydrogen in Eq. (1.23) using Eqs. (1.16) and (1.17), we can rewrite Eq. (1.23) as follows:

$$h = \frac{z + 4.94N + 0.74\sqrt{\chi_M^0} - (2.732 - 0.035pH)(1.41N + 0.74/\sqrt{\chi_M^0})}{1.39 + 0.01785pH} \quad \textbf{(1.24)}$$

where χ_M^0 is the electronegativity of a metal atom from the Allred-Rochow scale [39].

The aluminium-ion with a charge of +3 and a coordination number N=6 predominantly exists as the aquo-species $[Al(OH_2)_6]^{3+}$ at pH ≤ 3, according to the 'charge-pH' diagram (Fig. 1.7), consistent with experimental data [3,5,18]. The use of Eq. (1.24) leads to the interval of possible hydrolysis ratios for Al^{3+} ranging from h=0.3 (~0) at pH=0 to h=4.9 (~5) at pH=14. Thus, hydrolysis can proceed stepwise from the aquo-cation $[Al(OH_2)_6]^{3+}$ (h=0) to at least $[Al(OH)_4]^-$ (h=4) as the pH increases. In very dilute solutions (below the "mononuclear wall" or the solubility limit of Al hydroxide ranging from $1*10^{-6}$ and $1*10^{-5}$ mol/L depending on the type and crystallinity of the corresponding hydroxide [25]) the experimental data are consistent with the presence of monomeric species such as $Al(OH)^{2+}$, $Al(OH)_2^+$ and soluble $Al(OH)_3$ [5,6]:

$$\begin{aligned} [Al(H_2O)_6]^{3+} &\leftrightarrow [Al(H_2O)_5OH]^{2+} + H^+ \\ [Al(H_2O)_5OH]^{2+} &\leftrightarrow [Al(H_2O)_4(OH)_2]^+ + H^+ \\ [Al(H_2O)_4(OH)_2]^+ &\leftrightarrow [Al(H_2O)_3(OH)_3]^0 + H^+ \end{aligned} \quad \textbf{(1.25)}$$

Soluble monomeric hydroxide $[Al(H_2O)_3(OH)_3]^0$ can transform under alkaline solutions into aluminate-ions with the Al atom decreasing its coordination number from N=6 to N=4 [4,14]:

$$[Al(H_2O)_3(OH)_3]^0 \leftrightarrow [Al(OH)_4]^- + 3H_2O + H^+ \quad \textbf{(1.26)}$$

In the case of Zr^{4+} (N=8), the diagram in Fig. 1.7 indicates that aquo-species are present only at very acidic conditions. The use of Eq. (1.24) gives h=0.4 at pH=0 and h=5.3 at pH=14. Hence, the hydrolysed monomeric species ranging from the aquo-precursor $[Zr(H_2O)_8]^{4+}$ (h=0) to the hydroxo-species, e.g. $[Zr(OH)_5]^-$ (h=5), are theoretically possible. In practice, two species are detected by potentiometry in extremely dilute Zr-ion solutions ($[Zr]<10^{-6}$ mol/L) [40]:

$$[Zr(OH)(H_2O)_7]^{3+} \leftrightarrow [Zr(OH)_2(H_2O)_6]^{2+}] \quad \textbf{(1.27)}$$

Further extensive hydrolysis leads to the formation of zirconium hydroxide $[Zr(OH)_4]_n$ or, more precisely, hydrous zirconium oxide ZrO_2*2H_2O which is practically insoluble ($K_{s10}(ZrO_2*2H_2O)\sim10^{-14}$) over a wide range of pH values [35]. In highly alkaline solutions, the following reaction is possible [46]:

$$ZrO_2 + 2H_2O + OH^- \leftrightarrow Zr(OH)_5^- \quad \textbf{(1.28)}$$

Summarising the above examples of the use of the PCM for the evaluation of the hydrolysis of metal ions one can see that empirical relationships between pH and the charge of species ('pH-charge' diagram), the charge and the electronegativity of the species ('charge-electronegativity' diagram [41]), the hydrolysis ratio of the hydrolysis products and their electronegativity (Eq. 1.23, 1.24) can all be established allowing us to predict the hydrolytic behaviour of any metal ion without preliminary knowledge of structural and thermodynamic aspects. Excellent correlation of the PCM calculations with available experimental data shows the validity of the described model.

1.3.5. General condensation pathways of hydrolysed metal ions

In order to evaluate relative propensity of metal ions to condense, the electronic properties of molecular precursors (monomeric species) must be considered first. The Partial charge model offers a simple way for such evaluation (Table 1.4).

Table 1.4. The partial charges on atoms and ligands of the hydrolysed monomeric species of aluminium as calculated from the PCM.

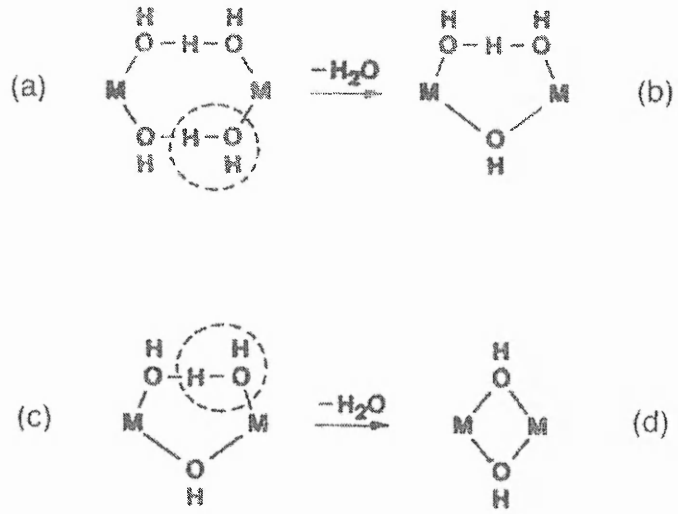
Species	h	z	χ_t	δ(Me)	δ(O)	δ(H)	δ(H_2O)	δ(OH)	$pH_{opt.}$
Al^{3+}									
$[Al(H_2O)_6]^{3+}$	0	3	2.757	0.755	-0.293	0.332	0.372	-	*-0.7*
$[Al(H_2O)_5(OH)]^{2+}$	1	2	2.679	0.708	-0.324	0.292	0.262	-0.015	*1.5*
$[Al(H_2O)_4(OH)_2]^{+}$	2	1	2.591	0.655	-0.359	0.247	0.139	-0.027	*4.0*
$[Al(H_2O)_3(OH)_3]^{0}$	3	0	2.491	0.595	-0.398	0.197	0.000	-0.033	*6.9*
$[Al(OH)_4]^{-}$	4	-1	2.300	0.480	-0.474	0.099	-	-0.046	*12.3*
Zr^{4+}									
$[Zr(H_2O)_8]^{4+}$	0	4	2.761	0.953	-0.290	0.336	0.504	-	-0.8
$[Zr(H_2O)_7(OH)]^{3+}$	1	3	2.703	0.915	-0.313	0.306	0.396	-0.004	0.8
$[Zr(H_2O)_6(OH)_2]^{2+}$	2	2	2.639	0.874	-0.338	0.274	0.277	-0.016	2.6
$[Zr(H_2O)_5(OH)_3]^{+}$	3	1	2.570	0.828	-0.366	0.238	0.147	-0.021	4.6
$[Zr(H_2O)_4(OH)_4]^{0}$	4	0	2.492	0.778	-0.396	0.199	0.003	-0.024	6.8
$[Zr(OH)_5]^{-}$	5	-1	2.407	0.723	-0.430	0.156	-	-0.027	9.3

h – the hydrolysis ratio [Me]/[OH^-]; z – the charge on metal (Me) atom; χ_t – the mean electronegativity of the species; δ(Me), δ(O), δ(H) – the partial charges on Me, O and H atoms correspondingly; δ(OH) and δ(H_2O) - the partial charges on hydroxyl- and aquo-ligands respectively; $pH_{opt.}$ - the pH value calculated from Eq. (1.22), which indicates the minimum pH necessary to enable a positive charge on aquo-ligands (leaving group in hydrolysis/condensation reactions).

The results of the calculations presented in Table 1.4 show the following patterns. The absolute value of the partial charge on hydroxyl-groups δ(OH) for Al and Zr monomeric species increases with increase of the total number of OH-groups. This means that further hydrolysis creates species which are more likely to be involved in condensation reactions due to the higher nucleophilic properties of the OH-ligand. Reciprocally, the positive partial charge on aquo-ligands decreases with higher h and lower z indicating that susceptibility of these ligands towards hydrolytic dissociation in agreement with Eq. (1.19) decreases. The same trend is observed for the partial charge on the metal atom δ(Me) of the monomeric species listed in Table 1.4. A zero-value for neutral precursors. J.-P. Jolivet [47] sets a condition δ(Me) > 0.3 for the possibility of further reaction to proceed. In the case of Al and Zr for all monomeric species, in spite of a gradual decrease with increase of h, this value is

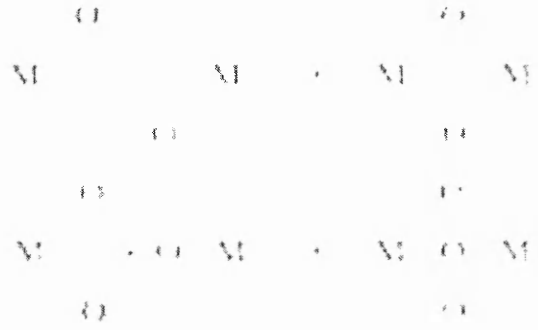
more than 0.3. Thus, there is no limitation for hydrolysis-condensation in terms of the partial charge on the metal atom.

Condensation can be defined as a reaction between hydrolysed ion species with the elimination of one water molecule. According to Brinker and Scherer [4], condensation may occur through nucleophilic substitution (S_N) or nucleophilic addition (A_N) mechanisms. Two main condensation pathways are observed - "olation" and "oxolation". Olation is a condensation process in which an hydroxy bridge (or "ol" bridge) is formed between two metal centres. For coordinatively saturated hydroxo-aquo precursors, olation occurs by an S_N mechanism where the hydroxy group is the nucleophile and H_2O is the leaving group. Olation occurs via a reaction intermediate involving H_3O_2 bridging ligands (structures (*a*) and (*c*) in the scheme below) [4].

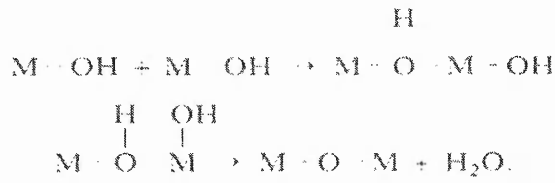


Several OH-bridges can be formed by this type of condensation as shown below in the example of one (*b*) and two (*d*) μ_2-'ol'-bridges. The number of hydroxo-bridges along with the electrostatic boundaries set up by the charge, the coordination number and the electronegativity of the corresponding metal-ion is limited mainly by the coordination geometry of the reacting metal ions as well as steric factors [4].

Oxolation is a condensation reaction in which an oxo bridge (-O-) is formed between two metal centres. When the metal is coordinatively unsaturated, oxolation occurs by nucleophilic addition (A_N) [4] with rapid kinetics ($> 10^5$ $M^{-1}s^{-1}$) leading to edge- or face-shared polyhedra:



Oxolation can also proceed via deprotonation of hydroxo-groups of reacting metal ions:



The thermodynamic data discussed above, despite evaluating the presence of polynuclear species, dose not provide mechanisms for their formation. The Partial charge model offers a general guideline for the prediction of condensation pathways and corresponding products [41] (Fig. 1.8).

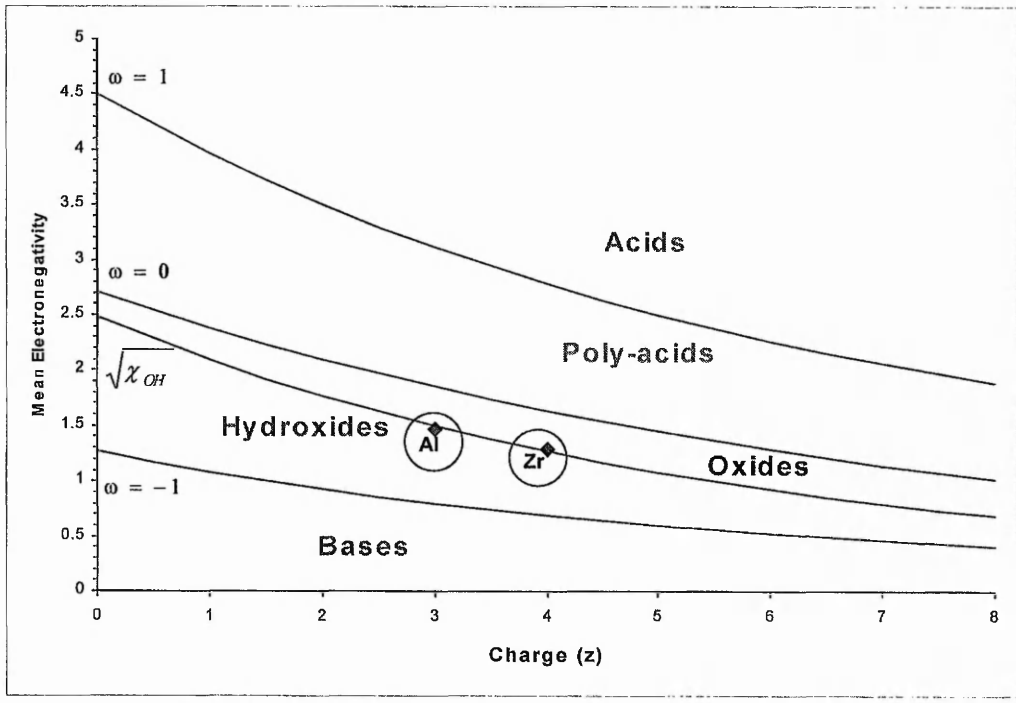
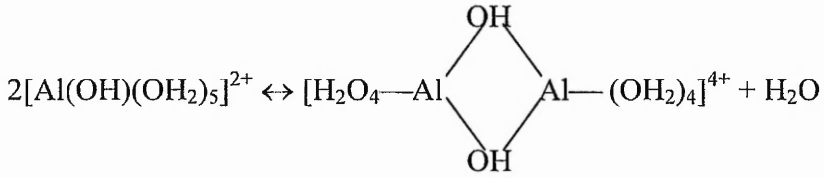


Fig. 1.8. The 'Charge-Electronegativity diagram calculated from the PCM.

The 'Charge-Electronegativity' diagram in Fig. 1.8 describes the behaviour of metal cations as a function of their charge and 'standard' electronegativity. Al^{3+} and Zr^{4+} cations are on the borderline dividing hydroxides and oxides. This means, that both elements can form hydroxides and oxides which is consistent with empirical data [5,25,48]. However, in the case of Al^{3+} the hydroxide is the more stable form of the solid phase, while for Zr^{4+}, the oxide phase is the more stable.

1.3.6. Condensation pathways of aluminium ions

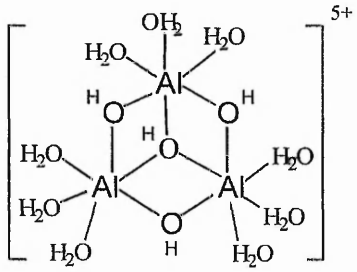
Literature data suggest that for the hydrolysis-condensation of Al-ions olated Al polycations are formed during the first steps of condensation [15, 41]. The first step begins with the hydrolysis ratio $h = 1$ and $[Al(OH_2)_5(OH)]^{2+}$ precursor. It gives rise to edge-sharing dimers as follows:



(1.29)

Such di-μ_2-hydroxocations are formed in trace amounts upon neutralisation [49]. However they have been clearly observed by X-ray diffraction of single crystals of a sulphate salt [50].

A further condensation pathway leads to the formation of trimers (h=1.33) which have not been determined directly by XRD so far [15] and have the following idealised structure:



The transformation of Al dimers into trimers most probably occurs in the narrow range of hydrolysis ratios: $1 \leq h \leq 1.33$. It should also occur in a relatively short time (in few minutes range) [15]. The relative fraction of dimers and trimers at equilibrium conditions (Fig. 1.2) is quite small compared with the tridecameric species and monomers. Thus, equilibrium in the mildly acidic pH range (pH $\geq$ 4) is shifted towards the formation of the well-known tridecameric species discussed below.

Authors of the work [41] suggest that when the trimeric species are formed an electron cloud of oxygen in the trimer $[Al_3(OH)_4]^{5+}$ is strongly polarised towards Al^{3+} making the μ_3-OH bridge highly acidic: This favours hydrolysis reaction of trimers as follows:

$$[Al_3(OH_4)(OH_2)_9]^{5+} + H_2O \rightarrow [Al_3O(OH)_3(OH_2)_9]^{4+} + H_3O^+ \quad \textbf{(1.30)}$$

Owing to this polarisation, water molecules in the trans-position of the trimer become less acidic than water molecules in a cis-position (so called trans-influence). According to the authors of the described mechanism half of these cis-H_2O ligands are hydrolysed upon mild conditions (h < 2.6) leading to:

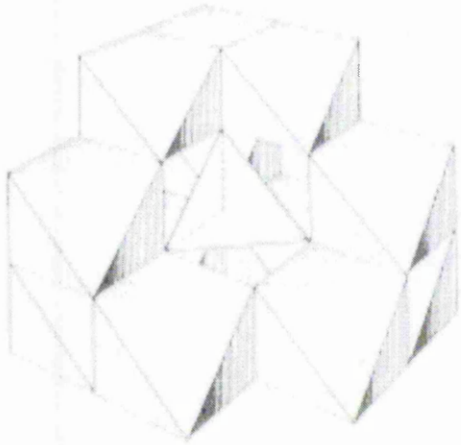
$$[Al_3O(OH)_3(OH_2)_9]^{4+} + 3OH^- \rightarrow [Al_3O(OH)_6(OH_2)_6]^+ + 3H_2O. \quad \textbf{(1.31)}$$

This trimer (h=2.67) has a highly nucleophilic oxygen atom and thus behaves as a ligand for h = 0 precursors ($[Al(OH_2)_6]^{3+}$ species). Such a reaction is limited only by diffusion rates and it should be rather fast. So far, the nucleophilic addition of four deprotonated trimers onto a single aquo-ion leads to the olation reaction with the formation of the well-known Keggin-like

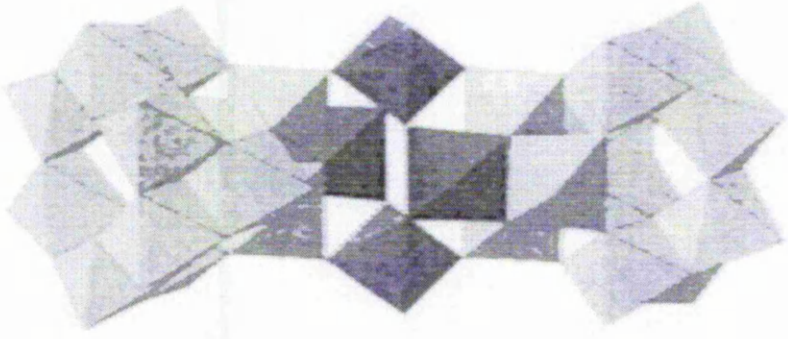
structure of the tridecameric species [5]:

$$[Al(OH_2)_6]^{3+} + 4[Al_3O(OH)_6(OH_2)_6]^{+} \rightarrow [Al\{Al_3O(OH)_6(OH_2)_6\}_4]^{7+} + 6H_2O \quad \textbf{(1.32)}$$

The structure of the tridecameric isopolycation ($[AlO_4Al_{12}(OH)_{24}(H_2O)_{20}]^{7+}$, Al_{13}-mer) is of ε-type where trimeric units of octahedral 'shell' Al-atoms share edges with each other [5,15]:



An important idea follows from the described mechanism that the trimeric species is the direct precursor to the large Al_{13} polycation. According to the data of Table 1.5 below (Species 9), aquo-ligands of the Al_{13}-mer are much less reactive than Al trimers (species 2). The μ_2-OH-groups of the Al_{13}-mer gain some negative partial charge probably due to tensions between the joined trimeric units of the Al_{13} octahedral 'shell' (this is also a good explanation for the broad signal in ^{27}Al NMR spectra of octahedral Al in the Keggin 'shell'). Thus the Al_{13}-mer can act as a nucleophile and attack the h=0 precursors giving rise to the Al_{30}-mer [51,52]:



The Al_{30}-mer molecule consists of two equal δ-forms of the Al_{13}-mer. One of the 'shell' trimers is rotated by 60^0 and two Al_{13}-mers are joined by four monomeric Al species. The Al_{30}-mer molecule crystallised as the sulphate contains also a Na-atom, which end-caps the front trimers [34]. The sodium cap on the Na-δAl_{13} unit has an extremely distorted O_h

coordination of three water molecules and three bridging hydroxides of the cluster, leading to a reduction of the cluster's ideal C_{3v} symmetry in the solid state. Such a strong interaction, as assumed by the authors, plays a role in the ε→δ transformation of the Al_{13} unit [51]. The heteroatom (here – Na) could be inducing isomerisation by stabilising the δ-isomer. Similar data have been obtained in the study [53], where accelerated transformation of the Al_{13}-mer into higher polymers has been observed in the presence of Sn^{2+} ions. The work [54] also reports on the ability of the Al_{13}-mer to adsorb significant amounts of Cu^{2+} ions. It has been shown that complexation of Cu^{2+} ions ($[Cu^{2+}]=4.8*10^{-5}$ mol/L) to aggregated Al_{13} ($[Al_{13}]=4.6*10^{-4}$ mol/L) is characterised by a remarkably steep adsorption curve starting at pH=5.5 and reaching a 95 % value at pH 6.2. The mechanism of adsorption has not been revealed so far. However, one can assume that it is similar to the end-capping mechanism proposed for Na^+ and Sn^{2+} ions.

A probable mechanism of the formation of the Al_{30}-mer has been proposed [51, 52]. During the thermal treatment of ε-Al_{13}-mer suspensions, some of these polycations dissociate into AlO_6 monomers that subsequently add to undissociated ε-Al_{13}. These ε-Al_{13} species with one to three attached AlO_6 units (capped ε-Al_{13+1}, -Al_{13+2}, Al_{13+3}) are prone to isomerise into the respective δ-forms. Once isomerisation is complete, the species may well be sufficiently stable to dimerise to form the Al_{30}-mer molecule. This appears to be the next step of Al hydrolysis after the formation of Al_{13}-mer. It is the first time that the δ-Al_{13} unit has been characterised. The heretofore unassigned (or mistakenly assigned Al_{20} or Al_{24} units [7,55]) ^{27}Al NMR signal at δ=70 and 10 ppm are attributable to the Al_{30} polycation.

The driving force of such a complex transformation: ε-Al_{13}→δ-Al_{13}→Al_{30} is a better 'fit' of tetrahedral AlO_4 unit of the polycation in the case of Al_{30}-mer obtained from the shorter Al-O bond lengths (followed by the shift of peak of tetrahedral Al in ^{27}Al NMR 63.5→64.5→70.0 ppm) [52]. Similar results have been obtained [56] when the tetrahedral 'core' Al-atom has been replaced with Ga^{3+} as has been shown above.

We have calculated the mean electronegativities and the ligand partial charges of some Al polycations on the basis of the PCM (Table 1.5).

As one can see from the data of Table 1.5, in the course of condensation, the mean electronegativity of polycations χ_t generally decreases from dimer to higher polymers. The same goes for the partial charge on aquo-ligands. The value of $pH_{opt.}$, at which aquo-ligands become susceptible to nucleophilic attack, also increases in the same manner, apart from the hexamer $Al_6(OH)_{12}^{6+}$ and the octamer $Al_8(OH)_{20}^{4+}$. Despite a near-zero charge on OH-ligands in dimer molecules, its aquo-ligands are good leaving groups for nucleophilic substitution and can be easily attacked by a nucleophile, e.g. $[Al(OH)_2(H_2O)_4]_{2+}$ forming a trimer.

In the case of the trimer $Al_3(OH)_4^{5+}$ we can observe one of the limitations of the Partial charge model – it cannot distinguish between the different types of hydroxyl-ligands

(here – $3\mu_2$ and $1\mu_3$ OH-bridges). The resulting average partial charge of hydroxyls is about zero in Table 1.5 (species 3). One can assume that the highly negative charge on the μ_3 OH-group, which makes the trimer so reactive [16], is compensated by the positive charges on the μ_2 OH-bridges.

Table 1. 5. Partial charges on atoms and ligands of hydrolysed polynuclear species of aluminium as calculated from the PCM model*.

No	Species	h	z	χ_t	δ(Al)	δ(O)	δ(H)	δ(H_2O)	δ(OH)	pH_{H2O}	MW
1	$Al_2(OH)_2(H_2O)_8^{4+}$	*1.00*	4	**2.716**	*0.730*	*-0.308*	*0.312*	*0.105*	*0.0010*	*0.5*	232.0
2	$Al_3(OH)_3(H_2O)_{10}^{6+}$	*1.00*	6	**2.716**	*0.730*	*-0.308*	*0.312*	*0.105*	*0.0007*	*0.5*	347.9
3	$Al_3(OH)_4(H_2O)_9^{5+}$	*1.33*	5	**2.713**	*0.728*	*-0.309*	*0.311*	*0.103*	*0.0002*	*0.6*	310.9
4	$Al_6(OH)_{12}(H_2O)_{12}^{6+}$	*2.00*	6	**2.645**	*0.687*	*-0.336*	*0.276*	*0.072*	*-0.0025*	*2.5*	581.9
5	$Al_{10}(OH)_{22}(H_2O)_{16}^{8+}$	*2.20*	8	**2.624**	*0.675*	*-0.344*	*0.266*	*0.062*	*-0.0018*	*3.1*	931.8
6	$Al_{24}(OH)_{60}(H_2O)_{24}^{12+}$	*2.50*	12	**2.585**	*0.651*	*-0.360*	*0.246*	*0.044*	*-0.0009*	*4.2*	2099.5
7	$Al_{54}(OH)_{144}(H_2O)_{36}^{18+}$	*2.67*	18	**2.559**	*0.636*	*-0.370*	*0.233*	*0.032*	*-0.0005*	*5.0*	4552.9
8	$Al_{12}O_4(OH)_{24}(H_2O)_6^{4+}$	*2.67*	4	**2.573**	*0.644*	*-0.364*	*0.240*	*0.038*	*-0.0026*	*4.5*	903.8
9	$Al_{13}O_4(OH)_{24}(H_2O)_{12}^{7+}$	*2.46*	7	**2.608**	*0.665*	*-0.351*	*0.258*	*0.055*	*-0.0019*	*3.5*	1038.7
10	$Al_{30}O_8(OH)_{56}(H_2O)_{32}^{18+}$	*2.40*	18	**2.615**	*0.669*	*-0.348*	*0.261*	*0.058*	*-0.0008*	*3.4*	2465.4
11	$Al_{47}O_{12}(OH)_{88}(H_2O)_{52}^{29+}$	*2.38*	29	**2.616**	*0.670*	*-0.347*	*0.262*	*0.058*	*-0.0005*	*3.3*	3892.1
12	$Al_{64}O_{16}(OH)_{120}(H_2O)_{72}^{40+}$	*2.38*	40	**2.617**	*0.671*	*-0.347*	*0.262*	*0.059*	*-0.0003*	*3.3*	5318.7
13	$Al_{24}O_8(OH)_{48}(H_2O)_{12}^{8+}$	*2.67*	8	**2.573**	*0.644*	*-0.364*	*0.240*	*0.038*	*-0.0013*	*4.5*	1807.5
14	$Al_{36}O_{12}(OH)_{72}(H_2O)_{18}^{12+}$	*2.67*	12	**2.573**	*0.644*	*-0.364*	*0.240*	*0.038*	*-0.0009*	*4.5*	2711.3
15	$Al_{48}O_{16}(OH)_{96}(H_2O)_{24}^{16+}$	*2.67*	16	**2.573**	*0.644*	*-0.364*	*0.240*	*0.038*	*-0.0006*	*4.5*	3615.0
16	$Al_{60}O_{20}(OH)_{120}(H_2O)_{30}^{20+}$	*2.67*	20	**2.573**	*0.644*	*-0.364*	*0.240*	*0.038*	*-0.0005*	*4.5*	4518.8
17	$Al_{41}O_{32}(OH)_{48}(H_2O)_{16}^{11+}$	*2.73*	11	**2.577**	*0.646*	*-0.363*	*0.242*	*0.040*	*-0.0013*	*4.4*	2722.2

* - description of the parameters shown in Table 1.5 see in Table 1.4. Species in *italics* have been evaluated in this work.

The electronic properties of the Al_{13}-mer identified by means of the PCM model show that these species are still reactive nucleophiles (the calculated average charge on OH-ligands is negative). Thus, theoretically, they can form large structures, such as the Al_{30}-mer, even though the nucleophilicity of the μ_1-OH-groups of Al_{13}-mer is relatively low (δ(OH) ≈ -0.0016 according to Table 1.5, species 9). Therefore, higher polymers can be theoretically obtained by the application of heating to the Al_{13}-mer solution. The best conditions of heating

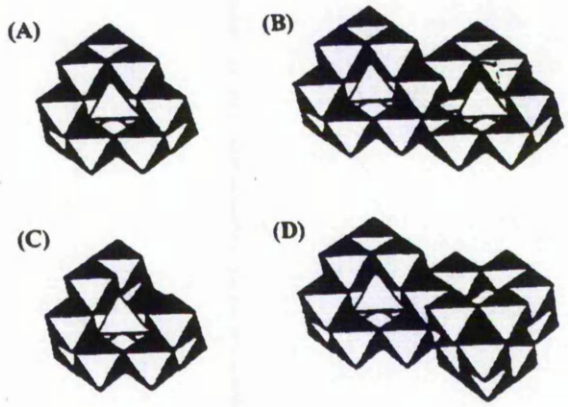
seem to be in the interval of temperatures $80 < T°C < 100$ [7,34].

According to the calculations given in Table 1.5, the transformation of the Al_{13}-mer into the Al_{30}-mer is followed by a slight increase of the mean electronegativity of the polycation (species 10, as well as a considerable reduction of partial charges on aquo- and hydroxo-ligands. It is interesting to note that the formal hydrolysis ratio *h* at which the Al_{30}-mer is formed (h=2.40) is lower than that for Al_{13}-mer (h=2.46), while the value of $pH_{opt.}$ is higher. This probably indicates that the optimum conditions for the formation of higher Al polymers are confined to a very narrow range.

If further condensation by the same mechanism is imagined, one can assume that Al_{47}-mers (AlP_3) and even Al_{64}-mers (AlP_4) can be formed in the same way. The partial charges of the ligands in these virtual polycations are shown in Table 1.5 (Species 11 and 12). The hydrolysis ratio for the formation of the higher polymers is even lower (h=2.38) and further stabilisation occurs as indicated by the constant hydrolysis ratio of the species, ligand partial charges and the total electronegativity. Polymerisation following the described pathway occurs only at higher temperatures owing to the large amount of energy required for the transformation of $\varepsilon \rightarrow \delta$ types of the Al_{13}-mer. The authors of the work [51] suggest that the main driving force of such a complex transformation $\varepsilon\text{-}Al_{13} \rightarrow \delta\text{-}Al_{13} \rightarrow Al_{30}$ is the better 'fit' of tetrahedral AlO_4 unit of the polycation in the case of the Al_{30}-mer (obtained from the shorter Al-O bond lengths (followed by the shift of peak of tetrahedral Al in ^{27}Al NMR $63.5 \rightarrow 64.5 \rightarrow 70.0$ ppm)) as mentioned above. The other driving force for giant polycation formation can be a large entropy gain which for the Al_{13}-mer - $\Delta S^0_{13,32}$=457 kcal/K/mol [5] and could be significantly higher for the Al_{30}-mer molecule. The slow kinetics of reaction can also be explained by the fact that 4 moles of h=0 monomers are required for the formation of 1 mole of Al_{30}-mer, while the concentration of the former is very low at h=2.4.

The possibility of the formation of Al_{64}-mer during the thermohydrolysis of Al chloride or using the 'electrochemical' route (dissolution of Al metal in concentrated HCl or $AlCl_3$) [7] can be supported indirectly by a comparison of the molecular weight of these species (Table 1.5, Species 17) with the large polymers found in ultracentrifugation studies [7]. The molecular weight of the latter is found to be ~5400 Dalton, very close to the MW of the Al_{64}-mer (species 12).

Another polymerisation mechanism described in earlier studies [7,56] includes the formation of 'defective' tridecameric species – the so called Al_{12}-mer. Afterwards, this species reacts with the 'normal' Al_{13}-mer giving rise to the Al_{24}-mer or AlP_2. The structure of the polycations formed is the following [56]:

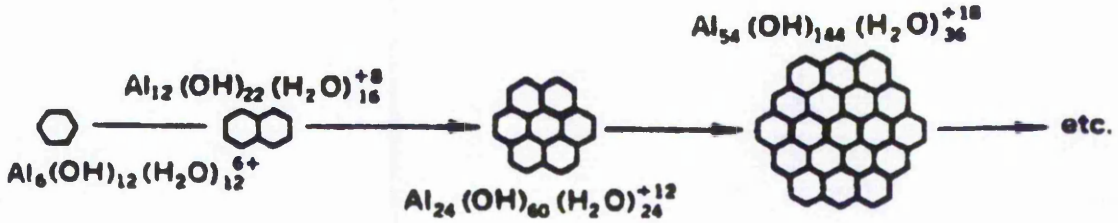


(A) – Al_{13}-mer
(B) – 'unsaturated' structure of Al_{24}-mer (AlP_2)
(C) – 'defective' Al_{12}-mer
(D) – 'saturated' structure of Al_{24}-mer (AlP_2)

The results of calculations by the PCM suggest that the reactive ability of the Al_{12}-mer hydroxyls is higher than those of the Al_{13}-mer (Table 1.5, species 8). The optimal hydrolysis ratio for Al_{12}-mers is h=2.67. Further polymerisation of Al polycations following this pathway does not change the partial charges on its atoms or ligands, as well as the optimal hydrolysis ratio (compare with the hypothetic higher homologous species 13, 14) which is not in agreement with the ^{27}Al NMR data [52].

In the reported work [57] the Al_{41}-mer structure has been described as a possible AlP_3 polymer. As one can see from the data of Table 1.5 (Species 17) this species possesses quite reactive hydroxyl-ligands, which is not favoured in terms of charge minimisation. Another point is that this structure has been elucidated on the basis of indirect measurements of particle size (light scattering and ultracentrifugation) and has not been confirmed by XRD method so far.

Another polymerisation pathway has been proposed in the literature [25] which assumes the formation of Al hexamers $Al_6(OH)_{12}^{6+}$ consisting only of octahedral aluminium. These hexamers polymerise as follows:



The mechanism of $Al_6(OH)_{12}^{6+}$ and hexamer-based species formation would probably include the stepwise olation reactions of Al dimers:

$$3[Al_2(OH)_2(H_2O)_8]^{4+} \leftrightarrow [Al_6(OH)_{12}(H_2O)_{12}]^{6+} + 6H_3O^+ \quad (1.33)$$

$$[Al_6(OH)_{12}(H_2O)_{12}]^{6+} + 2[Al_2(OH)_2(H_2O)_8]^{4+} \leftrightarrow [Al_{10}(OH)_{22}(H_2O)_{16}]^{8+} + 6H_3O^+ \quad (1.34)$$

$$[Al_{10}(OH)_{22}(H_2O)_{16}]^{8+} + 2[Al_2(OH)_2(H_2O)_8]^{4+} \leftrightarrow [Al_{14}(OH)_{32}(H_2O)_{20}]^{10+} + 6H_3O^+ \quad (1.35)$$

* * *

$$[Al_m(OH)_h(H_2O)_n]^{z+} + 2[Al_2(OH)_2(H_2O)_8]^{4+} \leftrightarrow [Al_{m+4}(OH)_{h+10}(H_2O)_{n+4}]^{z+2} + 6H_3O^+ \quad (1.36)$$

The PCM characteristics of the species formed this way have been calculated in this work (Table 1.5). The 'hexamer' structure, which has been proposed as a direct precursor to gibbsite and bayerite structures [25], is a quite reactive polycation both in terms of the nucleophilicity of six μ_1 OH-groups and the positive charge on the aquo-ligands. The μ_2-hydroxyls of hexamer-based species (Table 1.5, Species 4-7) appear to be more reactive than the Al_{13}-mer. The low value of the mean electronegativity of these species could indicate their predominant formation in solution at lower pH values. Also, in the course of the reaction following the pathway described above the negative partial charge on the OH-groups of the larger cyclic hexamer-based species quickly decreases with increase of polycation size. Theoretically, the pathway of Al-ion condensation via hexameric species is allowed, however, it lacks experimental evidence for the existence of any hexamer-based Al species.

The $Al_8(OH)_{20}^{4+}$ species has been identified by indirect potentiometric techniques in one study [58]. The mechanism of formation as well as the structure of this species is quite obscure and has not been explained by the authors who discovered them. The characteristics of these species calculated by the PCM, as well as their hydrolysis ratio and molecular weight, are quite close to those of the Al_{13}-mer. Thus, one can assume that identification of the 'octamer' may have been a result of computational or experimental error.

Experimental results [5] are consistent with the existence of two small polynuclear species at low equivalent additions of base, the dimer $[Al_2(OH)_2(OH_2)_4]^{4+}$ and trimer $[Al_3(OH)_4(OH_2)_9]^{5+}$ and, at higher base additions, one larger polycation – the tridecamer $[AlO_4Al_{12}(OH)_{24}(OH_2)_{12}]^{7+}$. Al_{13} was identified by SAXS and by a narrow ^{27}Al NMR resonance at ca 63.5 ppm (relative to $[Al(H_2O)_6]^{3+}$ with a line at 0.0 ppm) attributed to a single tetrahedrally coordinated aluminium located at the centre of three layers of edge-sharing octahedra. ^{27}Al NMR results by Akitt and Farthing et. al [59, 60] support this mechanism of Al_{13} ion formation. The presented NMR spectra do not show measurable concentrations of the trimer suggesting that these species are converted into the Al_{13}-mer.

We have summarised the main features of the condensation mechanisms from the works [14,15,25] in Table 1.6.

Several additional factors should be mentioned which are important for the process of condensation of metal ions [47]:

1) ***The hydrolysis ratio*** which controls the number of ligands able to form hydroxo- or oxo-bridges and, thus characterizes the structure through the functionality of the cation in the condensation process.
2) ***The geometry of the condensation polyhedron*** (octahedral or tetrahedral structure of Al-ion and square-antiprism structure of Zr-ion);
3) ***The possibility of cyclisation*** which can stabilize μ_2-OH bridges in polycations.

Table 1.6. Mechanisms of condensation of metal ions in aqueous solutions

Mechanism	Nucleophilic Substitution	Nucleophilic Addition
Symbol	S_{N1} or S_{N2}	A_{N1}
Metal ions	Low or intermediate charge ($z \leq 4$)	Intermediate or high charge ($z \geq 3$)
Precursors	Aquo-hydroxo species: $[M(OH)_h(H_2O)_{N-h}]^{(z-h)+}$ Oxo-hydroxo species: $[MO_{N-h}(OH)_h]^{(2N-h-z)-}$	Oxo-species: $[MO_N]^{(2N-z)-}$ Hydroxo-species: $[M(OH)_N]^{(N-h)-}$
Coordination	Saturated (highest)	Saturated or non-saturated
Example	$[Al(OH)(H_2O)_5]^{2+}$ $[Zr(OH)_2(H_2O)_6]^{2+}$	$Al(OH)_4^-$ $Zr(OH)_5^-$
Bridge formation	Hydroxo (ol) bridge (Olation)	Oxo-bridge (Oxolation)
Bridging agent	OH^-; $H_3O_2^-$ (or $H_9O_4^-$, [17])	-
Kinetics	Slow	Fast
Type of precursor connection in solid	Corner- or Edge-sharing	Edge- or Face-sharing
Partial Charge Model requirements	$\delta(OH)<0$; $\delta(M)>0.3$; $\delta(H_2O)>0$	$\delta(O^{2-}) << 0$; $\delta(OH) \geq 0$

1.3.7. Condensation pathways of zirconium ions

In the case of the Zr^{4+} ion, condensation pathways are quite different from those described for Al^{3+} above. Better insight can be obtained from calculations of electronic properties of some virtual or well-established Zr polycations using the PCM, which we have summarised in Table 1.7.

From the data in Table 1.7 it follows that $[Zr_2(OH)_2^{6+}]$ species cannot be formed owing to the positive partial charge on hydroxyl-ions, consistent with literature data [40]. The proposed $Zr_2(OH)_7^+$ species [36] appears to be improbable due to (*a*) a high hydrolysis ratio for these species (h=3.5); (*b*) an abnormally high value of $pH_{opt.}$ = 4.5; and (*c*) a highly negative partial charge on hydroxyl-ligands which would make these species extremely reactive.

The possibility of the formation of Zr trimers is probably limited to very acidic conditions according to the Partial charge model calculations (Table 1.7). Both possible trimers mentioned by Baes and Mesmer [5] (species possess quite high positive charges on the hydroxo-ligands. It is necessary to stress that due to the limitations of the PCM, we cannot distinguish between the different types of OH-groups present in these species, only a calculation of a non-weighed average value is possible [47].

The dimeric species possess relatively high negative partial charge on $2\mu_2$ hydroxo-groups (average $\delta(OH) = -0.0055$), so they can condense further to form the well-established

Table 1.7. The partial charges on atoms and ligands of the hydrolysed monomeric species of aluminium as calculated from the PCM model*.

No	Species**	*h*	z	χ_t	δ(Zr)	δ(O)	δ(H)	δ(H_2O)	δ(OH)	$pH_{opt.}$
1	**$Zr_2(OH)_2(H_2O)_{12}^{6+}$**	*1.00*	**6**	**2.733**	0.934	-0.301	0.321	0.113	0.0049	*0.0*
2	**$Zr_2(OH)_4(H_2O)_{10}^{4+}$**	*2.00*	**4**	**2.662**	0.888	-0.330	0.285	0.080	-0.0055	*2.0*
3	**$Zr_2(OH)_7(H_2O)_6^{+}$**	*3.50*	**1**	**2.566**	0.826	-0.367	0.236	0.035	-0.0093	*4.7*
4	**$Zr_3(OH)_4(H_2O)_{16}^{8+}$**	*1.33*	**8**	**2.742**	0.940	-0.298	0.326	0.117	0.0034	*-0.3*
5	**$Zr_3(OH)_5(H_2O)_{12}^{7+}$**	*1.67*	**7**	**2.758**	0.951	-0.291	0.334	0.125	0.0042	*-0.8*
6	**$Zr_4(OH)_8(H_2O)_{18}^{8+}$ (*linear*)**	*2.00*	**8**	**2.697**	0.911	-0.316	0.303	0.096	-0.0008	*1.0*
7	**$Zr_4(OH)_8(H_2O)_{16}^{8+}$ (*cyclic*)**	*2.00*	**8**	**2.715**	0.923	-0.308	0.312	0.105	0.0002	*0.5*
8	*$Zr_4(OH)_9(H_2O)_{15}^{7+}$*	*2.25*	**7**	**2.693**	0.909	-0.317	0.301	0.094	-0.0009	*1.1*
9	*$Zr_4(OH)_{10}(H_2O)_{14}^{6+}$*	*2.50*	**6**	**2.671**	0.894	-0.326	0.290	0.084	-0.0018	*1.7*
10	**$Zr_8(OH)_{18}(H_2O)_{28}^{14+}$ (sheet-polymer)**	*2.25*	**14**	**2.703**	0.915	-0.313	0.306	0.099	-0.0002	*0.8*
11	**$Zr_8(OH)_{20}(H_2O)_{24}^{12+}$ (stacked polymer)**	*2.50*	**12**	**2.689**	0.906	-0.319	0.299	0.092	-0.0005	*1.2*
12	*$Zr_8(OH)_{21}(H_2O)_{22}^{11+}$*	*2.63*	**11**	**2.681**	0.901	-0.322	0.295	0.089	-0.0006	*1.5*
13	*$Zr_8(OH)_{22}(H_2O)_{20}^{10+}$*	*2.75*	**10**	**2.673**	0.895	-0.325	0.291	0.085	-0.0008	*1.7*
14	***$Zr_{12}(OH)_{28}(H_2O)_{40}^{20+}$***	*2.33*	**20**	**2.698**	0.912	-0.315	0.304	0.097	-0.0002	*1.0*
15	*$Zr_{12}(OH)_{30}(H_2O)_{36}^{18+}$*	*2.50*	**18**	**2.689**	0.906	-0.319	0.299	0.092	-0.0003	*1.2*
16	*$Zr_{12}(OH)_{32}(H_2O)_{36}^{18+}$*	*2.67*	**16**	**2.678**	0.899	-0.323	0.293	0.087	-0.0005	*1.5*
17	*$Zr_{12}(OH)_{33}(H_2O)_{30}^{15+}$*	*2.75*	**15**	**2.673**	0.895	-0.325	0.291	0.085	-0.0005	*1.7*
18	*$Zr_{12}(OH)_{34}(H_2O)_{28}^{14+}$*	*2.83*	**14**	**2.667**	0.891	-0.327	0.288	0.082	-0.0006	*1.9*
19	***$Zr_{16}(OH)_{38}(H_2O)_{52}^{26+}$***	*2.38*	**26**	**2.696**	0.910	-0.316	0.302	0.096	-0.0002	*1.0*
20	*$Zr_{16}(OH)_{40}(H_2O)_{48}^{24+}$*	*2.50*	**24**	**2.689**	0.906	-0.319	0.299	0.092	-0.0002	*1.2*
21	*$Zr_{16}(OH)_{42}(H_2O)_{44}^{22+}$*	*2.63*	**22**	**2.681**	0.901	-0.322	0.295	0.089	-0.0003	*1.5*
22	*$Zr_{16}(OH)_{44}(H_2O)_{40}^{20+}$*	*2.75*	**20**	**2.673**	0.895	-0.325	0.291	0.085	-0.0004	*1.7*
23	*$Zr_{16}(OH)_{45}(H_2O)_{38}^{19+}$*	*2.81*	**19**	**2.668**	0.892	-0.327	0.288	0.083	-0.0004	*1.8*
24	*$Zr_{16}(OH)_{46}(H_2O)_{36}^{18+}$*	*2.88*	**18**	**2.664**	0.889	-0.329	0.286	0.081	-0.0005	*1.9*
25	***$Zr_{20}(OH)_{48}(H_2O)_{64}^{32+}$***	*2.40*	**32**	**2.695**	0.909	-0.317	0.302	0.095	-0.0002	*1.1*
26	*$Zr_{20}(OH)_{50}(H_2O)_{60}^{30+}$*	*2.50*	**30**	**2.689**	0.906	-0.319	0.299	0.092	-0.0002	*1.2*
27	*$Zr_{20}(OH)_{52}(H_2O)_{56}^{28+}$*	*2.60*	**28**	**2.683**	0.902	-0.321	0.296	0.089	-0.0002	*1.4*
28	*$Zr_{20}(OH)_{54}(H_2O)_{52}^{26+}$*	*2.70*	**26**	**2.676**	0.897	-0.324	0.292	0.086	-0.0003	*1.6*
29	*$Zr_{20}(OH)_{56}(H_2O)_{48}^{24+}$*	*2.80*	**24**	**2.669**	0.893	-0.326	0.289	0.083	-0.0003	*1.8*
30	*$Zr_{20}(OH)_{57}(H_2O)_{46}^{23+}$*	*2.85*	**23**	**2.666**	0.891	-0.328	0.287	0.081	-0.0004	*1.9*
31	*$Zr_{20}(OH)_{58}(H_2O)_{44}^{23+}$*	*2.90*	**22**	**2.662**	0.888	-0.329	0.285	0.080	-0.0004	*2.0*

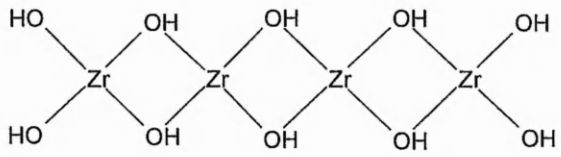
* - the description of the parameters shown in Table 1.7 see in Table 1.5.

** - the species from literature are in **bold**; virtual, although theoretically possible species are in *italics*; purely sheet polymers (starting from Zr octamer) are in ***bold italics***; purely stacked polymers are underlined by a *dotted line*. The transient mixed species containing both stacked and sheet units are listed between sheet polymers and pure stacked polymers.

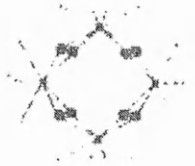
cyclic tetramer [37]:

$$2[Zr_2(OH)_4(H_2O)_{10}]^{4+} = [Zr_4(OH)_8(H_2O)_{16}]^{4+} + 2H_2O \quad \textbf{(1.37)}$$

Theoretically both linear and cyclic structures of tetramer are possible [61]:



Linear tetramer



Cyclic tetramer

The linear polycation possesses a slightly negative charge on the end OH-groups (Table 1.7), so condensation is favoured in both directions along the main axis of the molecule. This polymer can be stabilised by different strongly complexing anions as discussed below.

The cyclic tetrameric species of Zr^{4+} have been identified by X-ray methods (XRD, SAXS) [37,61]. They are direct precursors to the majority of the oxide materials formed from aqueous solutions [62,63].

The ^{91}Zr solution NMR has been tried [64] in order to study zirconium speciation in aqueous solutions, but it was not useful because of the large quadrupolar broadening which takes place in Zr aqueous solutions. The results obtained using ^{17}O and ^{1}H allowed them to suggest the presence of two types of water molecules in zirconium tetrameric species with non-equal acidic properties. On this basis, the formula of the tetramer in aqueous solution has been proposed [64]:

$$[Zr_4(OH)_8(H_2O)_8\boldsymbol{I}(H_2O)_8\boldsymbol{II}]^{8+}, \quad \textbf{(1.38)}$$

This formula indicates the presence of two inert (*I*) and two labile water molecules (*II*) per Zr atom. Up to two of the coordinated water protons can easily dissociate, so that this species constitutes a very strong acid. One of the inert water molecules is replaced with the addition of a monodentate anion (e.g. chloride or nitrate) per Zr atom.

The partial charge of $2\mu_2$ OH-bridges of the cyclic tetramer is close to zero, however condensation does not stop at this stage. Due to the extensive ability of zirconium to hydrolyse spontaneously, as indicated by Eqs. (1.8-1.10), tetrameric species, once formed, hydrolyse further producing species $Zr_4(OH)_9^{7+}$ and even $Zr_4(OH)_{10}^{6+}$. The 'extra' hydroxyl group possesses sufficiently nucleophilic character to attack a highly positive aquo-ligand on the next tetramer.

The authors of the study [61] on the basis of SAXS investigations of the acidified aqueous solutions of $ZrOCl_2$ have derived the possible structures of Zr 'octamers' (Fig. 1.9).

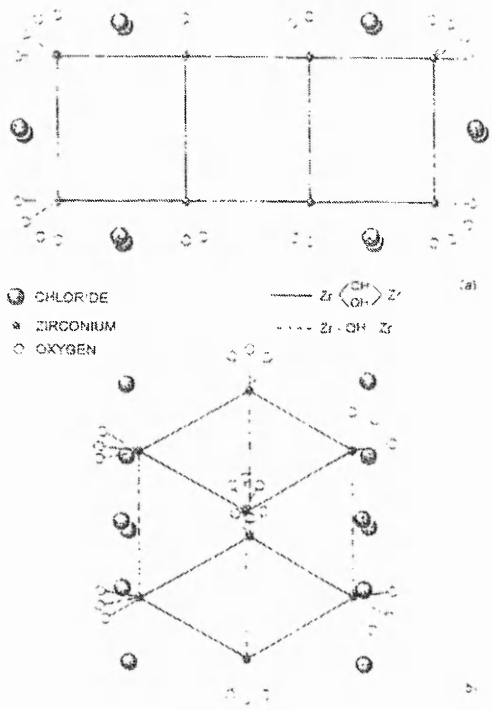


Fig. 1.9. The representation of two Zr octamer configurations: (*a*) – sheet octamer; (*b*) – stacked octamer.

The stacked octamer $Zr_8(OH)_{20}(H_2O)_{24}^{12+}$ (h=2.25) fits the SAXS data better than the sheet octamer $Zr_8(OH)_{18}(H_2O)_{28}^{14+}$ (*h*=2.125) [61]. The authors assume that the octameric unit is formed from tetramers by the following reaction:

$$2[Zr_4(OH)_8(H_2O)_{16}Cl_6]^{2+} \leftrightarrow [Zr_8(OH)_{18}(H_2O)_{24}Cl_{12}] + 4H^+ + 4H_2O \quad \textbf{(1.39)}$$

The chloride-ion, which is included in the formulae of zirconium oligomers in Eq. (26), belongs to the second coordination sphere of zirconium, although it determines the gyration radius of the polycation in SAXS. Below pH ca. 0.65 (or the concentration of added acid <0.6 M) tetrameric species predominate. Starting from pH ca 0.8 octamers are the major zirconium species in 0.2 M solutions of Zr^{4+} [61].

We have estimated the possibility of the formation of Zr octameric species described above by means of the Partial charge model (Table 1.7). The calculation results show that both sheet and stacked structures of Zr octamer can be feasible from the point of view of the PCM if one assumes the preliminary formation of $Zr_4(OH)_9(H_2O)_{15}^{7+}$ (*h*=2.25) or $Zr_4(OH)_{10}(H_2O)_{14}^{6+}$ (*h*=2.50) intermediates. The coincidence of the hydrolysis ratios and the octamers can be additional proof for such a pathway. Another argument is the decrease of the partial charge on OH-groups when switching from the reactive intermediates to octamers. Both the octameric units possess very small negative charges on hydroxyl-ligands, so they will probably condense in a similar fashion to the Zr tetramer, as discussed above. In the case of formation of the octameric intermediates $Zr_8(OH)_{21}(H_2O)_{22}^{11+}$ (*h*=2.63) and

$Zr_8(OH)_{22}(H_2O)_{20}^{10+}$ (h=2.75) the resulting increase in negative charge of OH-ligands is much less than that for the tetramers.

We have verified a further ability of octamers to condense. The comparison of the values supplied by the PCM of the Zr_{12}, Zr_{16}, Zr_{20},... species (Table 1.7) leads to the following conclusions:

1) Further condensation of Zr polymers via olation is possible if the formation of the reactive intermediates at every stage of condensation is assumed to be a result of additional hydrolysis.
2) Condensation of octamers and higher Zr polymers leads to a decrease of total charge z of the polymeric species and the reaction ability of the aquo- and hydroxo-ligands on these polymers.
3) It appears that the polymerisation process in the case of zirconium aqueous precursors does not follow the general empirical rule, according to which large polycations are not the direct precursors for a final solid phase due to their high charge and their polymerisation cannot be infinite. J.-P. Jolivet [47] postulates that only neutral precursors $[M(OH)_h(H_2O)_{N-h}]^0$ are precursors to the corresponding solid hydrous oxide phases. This is the case for Al^{3+} ion as has been shown above. For zirconium the following reaction has been proposed for the formation of an amorphous gel of the oxyhydroxide $ZrO_2{*}xH_2O$ [65]:

$$n[Zr_4(OH)_{16}(H_2O)_8]^0 \rightarrow [Zr_4(OH)_{16}]_n + 8nH_2O \qquad \textbf{(1.40)}$$

SAXS, X-ray and neutron diffraction data are not consistent with the described model [65]. Instead, one can suggest that the further polymerisation of zirconium is based on the direct condensation of the charged zirconium tetrameric species $Zr_4(OH)_{16}^{8+}$. From the data of Table 1.7 it is clear that polymerisation of tetrameric clusters can be infinite. This is indicated by the constancy of the parameters calculated by the PCM and by the very slow increase of the hydrolysis ratio of the growing polymer. Charge neutralisation is partially reached by increase of the hydrolysis ratio of the growing polymers, partially, by the continuous presence of anions in the condensed phase due to the ability of Zr^{4+} to form complexes.
4) The discussion above was based on the assumption that only one type of connection between two tetramers is formed (sheet or stacked polymer). In reality both types can be present in one polymer, as is reflected in Table 1.7 by evaluating of transient species between purely sheet polymers and purely stacked ones. Stacked octameric isomer is more basic (χ_t=2.689) than sheet-isomer (χ_t=2.703), therefore, stacked isomer is preferred in less acidic conditions (cf. $pH_{opt.}$ values in Table 1.7).
5) In practice, thermohydrolysis of acidic solutions of Zr^{4+} always results in a substantial decrease of pH [47, 66]. This is evidence of the continuous hydrolysis of zirconium

polymers simultaneously with their condensation, necessary to produce reactive intermediates.

The described features of the condensation of zirconium oligomers enables us to control the size of the resulting polycations either by the heating of solutions or by adjustment of pH (addition of base or acid). It can also be controlled kinetically applying different ageing times in order to produce polymers of tuneable size.

1.4. Kinetics of hydrolysis and condensation of Al^{3+} and Zr^{4+} aqueous solutions

Since most of the soluble polycations of Al and Zr are thermodynamically unstable, their aqueous chemistry is determined to a great extent by the kinetics of their transformation.

In the case of the Al^{3+} ion, the kinetics of hydrolysis and condensation have been studied extensively. Early work involved potentiometric methods [5, 67], for instance, the application of pH-relaxation curves for the determination of the kinetics of the first hydrolysis steps in very dilute solutions of Al^{3+} [67].

For a long time reagent kinetic assays, especially the 'Ferron' method, has been used as a source of kinetic information on Al^{3+} hydrolysis as well as for the characterisation of polydisperse suspensions of Al condensed species [7,68]. The idea of these methods is a partial replacement or modification of the hydrolysis equilibria by the addition of a marker (usually an organic reagent, e.g. –Ferron), the concentration of which can be monitored with time by measuring some of its properties - most commonly - molecular absorbance in the UV or visible range. The method has allowed three groups of species to be distinguished according to the kinetics of their formation and their average molecular weight. The kinetic curve of the hydrolysis of Al^{3+} as studied by the Ferron method is given in Fig. 1.10 [68]:

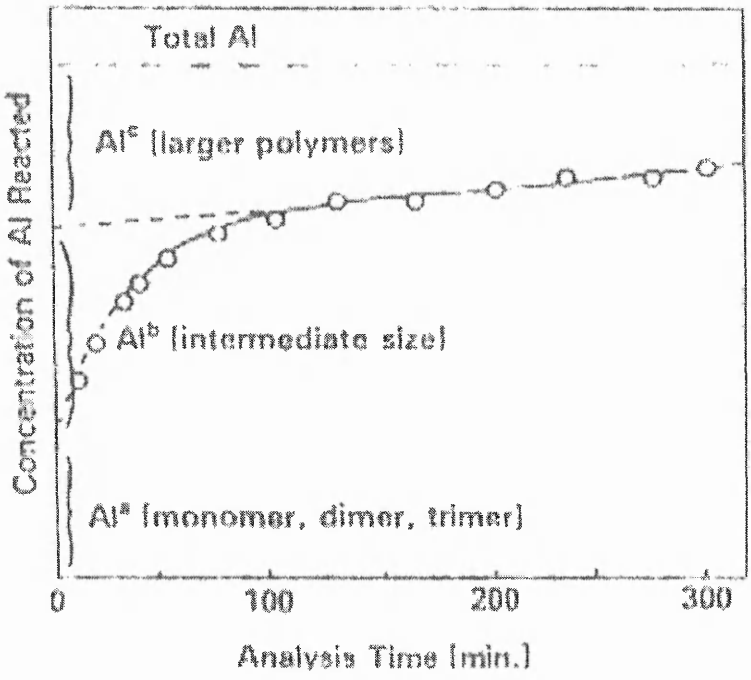


Fig. 1.10. Results of kinetic studies of Al^{3+} hydrolysis as studied by the Ferron method [68].

The information obtained by the Ferron reagent assay is briefly summarised in Table 1.8.

Table 1.8. Summary of Al hydrolysis species on the basis of Ferron reaction assay [7, 68]

Form	Complexes	MW	Relative rate	k_c, min	$t_{1/2}$, min	Total reaction time, min
Al^a	$Al(H_2O)_6^{3+}$ $Al(OH)(H_2O)_5^{2+}$	~130	Fast	2.3	0.3	2
Al^b	$Al_2(OH)_2(H_2O)_8^{4+}$; $Al_3(OH)_4(H_2O_9]^{5+}$ $Al_{13}O_4(OH)_{24}(H_2O)_{12}^{7+}$	~250 – 1000	Slow Pseudo-first order	0.22 $7.5*10^{-2}$	3.0 9.5	14 60
Al^c	High molecular weight soluble polymers (AlP_2; AlP_3;...) Microcrystalline gibbsite	>2000	Very slow	$3.1*10^{-3}$	125	days

A good correlation of the results by the Ferron method with the data of other methods, especially gel-permeation chromatography and multinuclear NMR has been reported [7,68].

Another indirect approach to the studies of Al speciation is an introduction of highly sensitive fluorescent reagents instead of spectrophotometric ones, e.g. 2-hydroxy-1-carbazole carboxylate [69]. The molecular fluorescence method has been used for the determination of hydrolysis constants of aluminium as well as for the detection of tiny amounts of non-hydrolysed Al^{3+}. The method has not found further application, probably, due to high instability of the reagent itself which can lead to poor precision of the data obtained.

Baes and Mesmer have summarised the data on the kinetics of Al hydrolysis [5]:

1. Mononuclear hydrolysis products are formed rapidly and reversibly.
2. Small polynuclear species (dimer and trimer) are formed less rapidly.
3. The Al_{13} ion is formed more slowly still.
4. The precise conditions of hydrolysis (composition and rate of combination of solutions of precursors; type and amount of agitation, temperature) determine the nature and quantity of transient polymeric species, colloidal particles, or amorphous solid phases formed.
5. The rate at which these transient species are converted either to the Al_{13} ion or to crystalline $Al(OH)_3$ depends on temperature, pH, amount of $Al(OH)_3$ present, and on available anions.

From the late 1970s, the multinuclear NMR technique has given a new impetus to studies of Al hydrolysis and condensation [7,9,70]. Modern NMR probes [71] allow fast and high-quality spectral acquisition and the possibility of working at a wide range of

temperatures. Different experimental approaches have been adopted, such as stop-flow kinetics [72], separation techniques (gel-permeation chromatography) [7,73,74] and others in order to study kinetic phenomena during the hydrolysis of different Al-containing aqueous systems. From the investigation of the decomposition of hydrolysed Al^{3+} solutions by the addition of acid [73], the way in which the ion $[AlO_4Al_{12}(OH)_{24}(OH_2)_{12}]^{7+}$ decomposes has been described and a mechanism proposed to explain their observations. According to this study, the decomposition is fast and seems to be controlled by the rate of exchange of H_2O ligands on Al^{3+}. The major component of the metal-hydrolysed solution behaves similarly if an excess of acid is added, but if the acid addition is limited, much more complex behaviour has been observed which might indicate the formation and eventual decomposition of different intermediate species. The high-molecular-weight material present decomposed much more slowly and so it was believed to have a different type of structure to that of the above Al_{13} cluster (consistent with the properties of the Al_{30}-mer as shown above).

In the review on aqueous chemistry of aluminium [75] the following empirical rule for the decomposition kinetics of Al_{13}-mer in acidic media has been described:

$$-\frac{d[Al_{13}]}{dt} = k[Al_{13}][H^+]^{1.35} \qquad \textbf{(1.41)}$$

It has been shown that the proton-promoted decomposition of the polycation consists of two parallel reactions, one is first order and the other - second order with respect to the hydrogen ion activity. The rate constants for these reactions have been established at 25 °C and I=0.1 M (k_1=0.0333, k_2=2.59), and it has found that the first path prevails at pH=3, while both decomposition pathways are important at pH=2 [75]. The half-lives of Al_{13} at pH=3 and pH=4 are about 5 and 50 hours respectively. For lower temperature and ionic strength, significantly larger half-lives are expected.

In the case of Zr^{4+} ion hydrolysis, kinetics of the first hydrolysis and condensation steps (up to the formation of tetrameric species) are very high [5, 8]. The further reaction path follows diffusion-controlled aggregation which is different from the usual nucleation-growth of colloidal dispersions observed in the case of Al^{3+} [4,37].

Matsui and Ohgai in a series of studies [76-78] have investigated the crystal structure, the primary particle size, and the formation rate of hydrous-zirconia fine particles produced in thermohydrolysis conditions: various $ZrOCl_2$ concentrations; reaction temperatures; added salts (NaCl, $CalCl_2$ and $AlCl_3$) and concentration of added HCl. The particles synthesised from all of the hydrolysis conditions were similar to those observed in monoclinic crystalline ZrO_2, except that the crystal structure changed with increasing chloride content. The primary particle size of monoclinic hydrous-zirconia particles decreased with increasing $ZrOCl_2$

concentration and was independent of the reaction temperature. The rate constants (k) of hydrous-zirconia particles were determined experimentally by applying Avrami-Erofeev's equation. The determined k-value decreased, as the $ZrOCl_2$ concentration increased and the reaction temperature decreased. The higher ionic strength and chloride content also negatively affected kinetics of nucleation-growth. From the Arrenhius plots of k, the activation energies for hydrous- zirconia particles in the monoclinic phase and containing high chloride content were determined to be $2.5 \cdot 10^2$ - $4.0 \cdot 10^2$ $kJ \cdot mol^{-1}$, respectively.

1.5. Colloidal and solid phases formed by hydrolysis of Al^{3+} and Zr^{4+}

Formation of colloidal and solid phases in the course of hydrolysis of metal ions can result in (*1*) gelation polymerisation (polycondensation) reaction; (*2*) stable colloidal suspension formation; (*3*) precipitation of the solid phase.

By analogy to the organic polymerisation processes several steps in the process of hydrolysis-condensation-precipitation of metal ions in aqueous solutions have been identified [47]:

a) **Initiation** – first steps of hydrolysis leading to formation of reactive hydrolysed monomers or oligomers;
b) **Propagation** – condensation of hydrolysed species. The condensation reactions (via olation or oxolation) result in polynuclear (hydro)oxides, which can be stable indefinitely, but which are in fact metastable with respect to the precipitation of the solid phase [14].
c) **Termination** – spontaneous interruption of the growth of condensed species. Chemical principles of the termination are described well by the Partial charge model and are briefly summarised in Table 1.6.

The mechanisms of hydrolysis and polycondensation reactions for Al^{3+} and Zr^{4+} ions in aqueous solutions have been discussed in this report in Sections 1.3-5.

From the physicochemical point of view, the formation of metal hydroxides, oxyhydroxides or hydrated oxides is a colloidal process of the transformation of condensed phases into solid precipitate. The precipitation of solids involves four main kinetic steps [41,47]:

1) **Formation of a zero-charge precursor $[M(OH)_h(H_2O)_{N-h}]^0$**, which is able to condense infinitely and form a solid phase.
2) **Creation of nuclei** through the condensation of zero-charge precursors. Most of the metal isopolycations are not the primary nuclei for the solid owing to their high charge. Thus, before precipitation occurs, these species must transform into zero-charged nuclei. Nucleation is an abrupt kinetic phenomenon. It occurs after the critical concentration of

the precursor is reached.

3) **Growth of critical-size nuclei** occurs due to their unstable nature and continues until the primary particle stage. This step follows the same chemical mechanisms as nucleation: olation or oxolation. If the concentration of the precursor is close to critical, the nucleation rate is very small and precursors condense preferentially on existing nuclei. There are two main types of particle growth – diffusion-limited and surface-limited [17]. Homogeneous growth of monodisperse particles can appear only in the case where the nucleation and growth stages can be separated.
4) **Ageing of particles in suspension** leads to various modifications of the primary particles after their growth, e.g. increase of the particle size ('Ostwald ripening'), changes in crystal type and particle morphology.

As has been shown for aluminium and zirconium, the condensation of aquo-hydroxo cationic complexes $[M(OH)_h(H_2O)_{N-z}]^{(z-h)+}$ ($h<z$) at room temperature is always limited. It stops when a finite degree of condensation is reached [47]. The condensed species remain soluble as polycations (e.g. Al tridecamer, Zr tetramer) and are entities of a molecular size.

The further fate of these soluble isopolycations in the case of Al^{3+} and Zr^{4+} is different. For Al^{3+} during the slow alkalinisation of solution, when conditions are met for the formation of the hydroxide, the structure of the transient polycations changes so there is usually no structural relationship between polycations and the resulting solid. Stable polycations such as Al_{13}-mer do not maintain their structure during charge cancellation by alkalinisation and they flocculate as disorganised solids. These condensed, aggregated entities in the metastable amorphous phases formed under kinetic control during rapid precipitation may reorganise during ageing, causing crystallisation of the solid [4,5,15,79,80].

In the case of Zr^{4+}, tetrameric units can condense further if base is added or heating is applied. In this case polycations are direct precursors both to the amorphous oxyhydroxide and crystalline hydrous oxide. The form of Zr solid phase depends on the reaction conditions [4,37].

If one stops the process of solid formation at the stage of stable polycations, the resulting solids (obtained by spray-drying or freeze-drying, or any other chemical or physical reaction-quenching technique) are called 'basic salts' of the general formula $M_x(OH)_yAn_{z-y}$ ($y < z$; An - anion). These salts are known both for aluminium and zirconium and constitute a very important class of materials extensively used as antiperspirant actives [7,8], flocculants [81-83] (water treatment and purification), clay pillaring agents [84-87], etc. Basic salts in the solid state maintain practically the same structure as the polycations from which they are formed [7, 8].

Condensation of neutral precursors $[M(OH)_z(OH)_{2N-z}]^0$ (h=z) is not limited. Formation of colloids in this case is followed by an increase in average electronegativity of the growing species due to dehydration (according to the data of Table 1.5 and 1.7), aquo-ligands in the species $Al(OH)_3(H_2O)_3^0$ and $Zr(OH)_4(H_2O)_4^0$ bear near-zero partial charge and are not present in the inner coordination sphere of the metal). This increase is never sufficient for hydroxo ligands to loose their nucleophilic character. As a result a solid phase precipitates, usually hydroxide $M(OH)_z$. Stability of this hydroxide towards spontaneous dehydration (internal oxolation reaction) depends on a particular metal, as will be shown below.

Before a brief review of the solid phases formed as a result of hydrolysis of Al and Zr ions we should consider three major routes to these phases [4,47]:

1) **Addition of base or acid** – the most common way to neutralise acidic solutions of Al and Zr ions in order to cause rapid precipitation. This route to solid phases has been criticised [4] owing to local perturbations and pH gradients occurring when adding base to the precursor solution. These perturbations cause the uncontrolled formation of the metastable amorphous phase of a poorly defined structure, which subsequently redissolves very slowly to form solute species again. Addition of acid to the anionic species of Al^{3+} and Zr^{4+} also leads to the formation of solid phases, although other precursors involved in this route and the solid phases formed can differ in their structures from those obtained by base neutralisation.
2) **Thermohydrolysis** is one of the best ways to obtain an homogeneous solution during the whole process of the molecular precursor neutralisation. It is based on the heating the precursor solution up to 50-100 °C. This route allows controlled synthesis of materials from aqueous solutions and is especially useful for the hydrolysis of trivalent elements (e.g. Al^{3+}), which cannot be hydrolysed at room temperature without base addition.
3) **Hydrothermal synthesis** also leads to the formation of very homogeneous materials. The synthesis is conducted at high pressure and temperature. Due to dramatic changes of the properties of water as solvent, the materials obtained this way possess quite different structure and properties than the ones synthesised at atmospheric pressure.

Despite its shortcomings, addition of base is one of the oldest and most commonly used methods in Al speciation studies as well as for precipitation of Al hydroxide [5,6]. Alkalinisation of $Al(NO_3)_3$ solution using sodium hydroxide or ammonia to pH ca. 6-7 at room temperature leads to the formation of the translucent amorphous gel [39]. This unstable gel crystallises relatively rapidly and forms different phases depending on the acidity of the medium [88]. It is suggested [4] that the gel formed is unstable due to aggregation of intermediate and inert species such as the Al_{13} polycation. During the evolution of the gel at

room temperature the ^{27}Al NMR peak characteristic of tetrahedral Al atom of Al_{13} disappears as crystallisation takes place. As a result of transformation of amorphous particles into crystalline ones, the lattice energy is released and the free enthalpy of the system decreases.

The other possible reason for the formation of the translucent gel under the conditions of Al nitrate/chloride alkalinisation [39] is the minimum solubility of aluminium species in the pH range 6-8. Thus, mass transfer, that is required to transform Al_{13} entities into crystalline particles, is difficult in solution and is better accomplished within a solid. The transformation involves partial dehydration and leads to γ-AlO(OH) boehmite. Although the boehmite formation is not favoured thermodynamically, it can be stabilised kinetically [4, 25].

At conditions far from the zero charge point (pH < 6 and pH > 8), the solubility of hydrolysed aluminium species is much higher. Crystalline hydroxide, $Al(OH)_3$ (gibbsite or bayerite) is a result of the slow process in this case. In acidic conditions this favors transformation of the soluble species into the neutral precursor $[Al(OH)_3(H_2O)_3]^0$ with the creation of gibbsite (cubic packing) or bayerite (hexagonal packing). At pH >8 $[Al(OH)_3(H_2O)]^0$ tetrahedral species are suggested [4,39] as precursors to the hydroxide phase. Information available on the formation of Al (oxy)hydroxides is summarised in Table 1.9.

Table 1.9. Comparison of the conditions of aluminium (oxy)hydroxide formation at room temperature [4, 25, 39, 47].

Solid phase	**Boehmite**	**Gibbsite**	**Bayerite**
Formula	γ-AlO(OH)	$Al(OH)_3$	$Al(OH)_3$
Type	Oxyhydroxide	Hydroxide	Hydroxide
Form	Crystalline	Highly crystalline	Highly crystalline
Direct precursor	Tetramer $[Al_4O(OH)_{10}(H_2O)_5]^0$	Hexamer $[Al_6(OH)_{18}(H_2O)_{18}]^0$	Hexamer $[Al_6(OH)_{18}(H_2O)_{18}]^0$
pH range	6 – 8	> 8	< 6
Stability	Metastable	Stable	Stable
Kinetics	Fast	Slow	Slow
$\Delta G°_{f298}$,kJ/mol	-436	-546	-548.5
Packing	Tetragonal	Cubic	Hexagonal
Structure	Corrugated sheets	Planar sheets	Planar sheets
$pK_{s1,4}$	-12.45	-14.57	-13.84
$pK_{s0,1}$	-	-33.5	-

The authors of the reviews [39,41] have distinguished between two temperature intervals leading to the formation of different types of Al hydrous oxides. At temperatures below 80 ^{0}C crystalline hydroxides, $Al(OH)_3$ precipitate from aqueous solutions either by increasing the pH of $Al(NO_3)_3$ or upon acidification of sodium aluminate solutions. These hydroxides exhibit lamellar structures based on hexagonal rings linked through μ_2-OH bridges. Formation of planar two-dimensional sheets from aqueous precursors can be described as follows [41]:

1) When a base is added to an Al^{3+} aqueous solution, the octahedral $[Al(OH)_3(OH_2)_3]^0$ neutral precursor is involved. Condensation of these monomers or aggregation of hexameric units then leads to solid particles.
2) The second pathway occurs upon acidification of an aluminate solution. Tetrahedral $[Al(OH)_3(OH_2)]^0$ neutral precursors are formed from $[Al(OH)_4]^-$. Owing to the low coordination number of $[Al(OH)_3(OH_2)]^0$, it can undergo very fast addition reactions leading to octahedral oligomers such as trimers, tetramers, or hexamers. These oligomers form critical nuclei for the oxy-hydroxide phases.

Thermohydrolysis and hydrothermal synthesis can significantly alter the structure of the solid phase formed [71,72]. Higher temperature favours the formation of boehmite γ-AlO(OH). Diaspore α-AlO(OH) can be obtained via hydrothermal synthesis. Crystalline hydroxides $Al(OH)_3$ readily transform into oxy-hydroxides at elevated temperature (T> 80°C).

Authors of the work [39] postulate that the key point for boehmite structure formation is the presence of a highly nucleophilic μ_3-OH bridge whose deprotonation orients nucleation towards a skewed tetramer. From such tetramers the corrugated structure of boehmite sheets is easily derived. This is supported by work [88] where boehmite peptization using ^{27}Al NMR has been surveyed. No evidence for Al_{13} presence in the peptized sol has been found.

A. Clearfield [37] has proposed a mechanism of formation of hydrous zirconia from the tetrameric species. It involves progressive olation leading to the formation of two-dimensional $[Zr(OH)_4]_n$ sheets while the original square antiprism coordination of zirconium atoms is changed to cubic coordination. $[Zr(OH)_4]_n$ layers then aggregate into a three-dimensional fluorite structure via oxolation reactions. Depending on the conditions applied, different oxide phases can be obtained, as shown in Fig. 1.11.

As one can see in Fig. 1.11, subsequent olation of the Zr tetramer induces the reticulation of such units and the frustrated structure of the resulting gels. Heating (Δ) promotes crystallisation into three main polymorphs (monoclinic, tetragonal and cubic) with a high degree of crystallinity of the resulting solid phase.

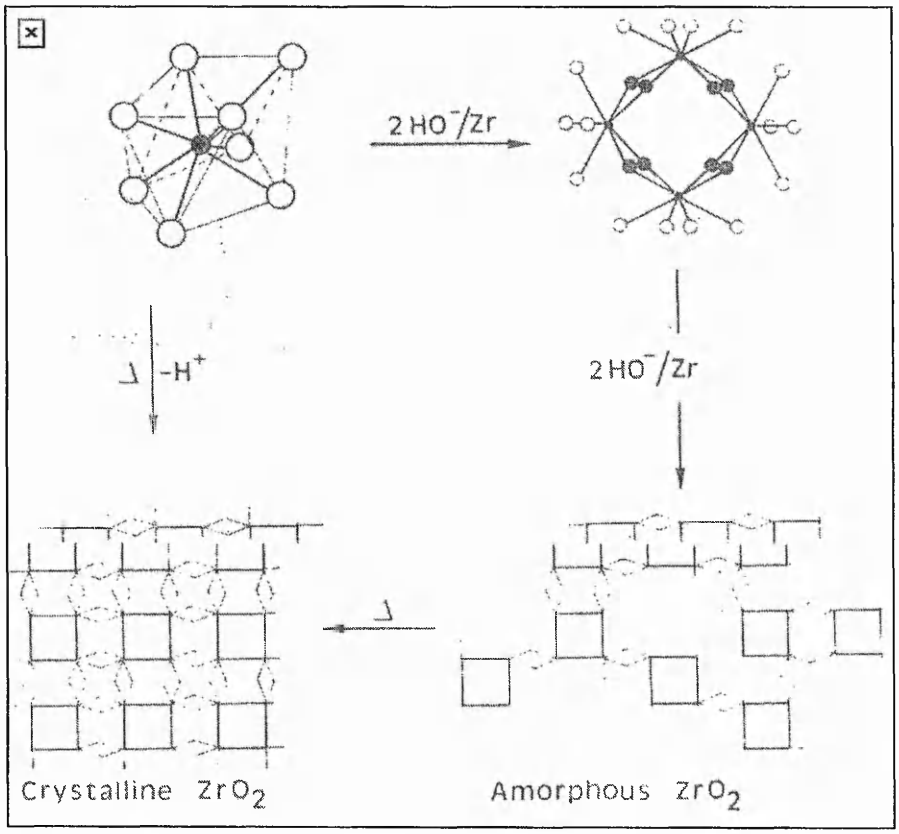


Fig. 1.11. The structural changes and the order of the resulting solid phases of zirconium oxides produced by aqueous route [37, 39].

A brief summary of the crystalline phases of zirconia is given in Table 1.10.

Table 1.10. Precursors and properties of the zirconia crystalline phases [4,37,41,47].

Phase	Tetragonal	Monoclinic	Cubic
Stability	Metastable	Stable	Stable
Precursor	$Zr_4(OH)_8^{8+}$	$Zr_4(OH)_8^{8+}$	$Zr_4(OH)_8^{8+}$
Zr coordination number in solid	8	7	8
Synthesis Route	Hydrothermal (T>100°C; P>1 atm.)	Thermohydrolysis (80<T°C<100, 1atm.)	Calcination of monoclinic phase
Interval of temperature stability	400-950	950-2360	2360-2730

The possibility of orthorhombic crystalline phase formation during the prolonged boiling of zirconia in alkaline media has also been reported [4].

Bleier and Cannon [89] observed that ageing zirconyl salt solutions at 90 and 98 ^{0}C produced quite uniform monoclinic ZrO_2. They have proposed that tetramers aggregate to produce nuclei (comprising 12-24 tetramers), and further ageing results in 3-nm crystallites. A

secondary controlled aggregation process involving these crystallites produces 80 nm particles that exhibited an unusually high degree of crystallographic alignment of the primary crystallites, presumably due to anisotropy in the surrounding double layers.

In recent studies [61,90] a systematic investigation of the nucleation/growth mechanisms involving Zr tetrameric species during thermohydrolysis at low pH has been undertaken involving SAXS analysis. The following general features were observed:

1) During the initial stages of polymerisation no small scattering species were observed indicating that the majority of tetramer precursors transformed into larger particles.
2) The primary species formed are of a one-dimensional rod-like shape with a cross-section radius of gyration of 4.2-4.4 Å which is close to the gyration radius of $Zr_4(OH)_8^{8+}$ ion (~4 Å). Thus the starting polymeric species are chains of tetrameric units, consistent with the discussion of the data of Table 1.7 above. This is in contrast with the two-dimensional model of hydrous zirconia formation proposed by A. Clearfield [43].
3) The growth rate of the initial rod-like species was very slow at lower temperatures (T<90°C). The temperature of 90°C appears to be critical in terms of a drastic increase of the growth rate. Further increase of temperature gradually decreased the growth rate of the initial polymers.
4) The growth mechanism involved aggregation of linear clusters, which form large particulates while retaining their original structure. These three-dimensional aggregates were similar in structure to mass fractals rather than to surface fractals [47]. On ageing, aggregates grew and restructured to form dense particles.
5) At some stage during growth, linear clusters consisting of tetramer chains started to ramify eventually forming fern-like primary particles. The degree of branching of growing polymers as well as the size of the resulting dense particles was strongly dependent on pH. At pH 1.2 only rod-like clusters of hydrous zirconia were present, while at pH 1.7 they were generally branched. Increase of pH also promoted formation of larger dense particles.
6) Once primary particles formed, they coalesced to form large aggregates. Aggregation could occur between two stable particles, between one stable particle and a pre-formed aggregate, or between two aggregates. The SAXS data could not distinguish between these three mechanisms because, apart from the growth of aggregates, restructuring was also occurring.
7) According to the restructuring mechanism proposed [47] primary particles of simple shape would restructure at a faster rate than those with complex shape. Therefore, it is possible that the restructuring of aggregates at higher pH into three-dimensional particles

would be a slower process than the restructuring of aggregates at pH 1.2 that consist of rod-shaped primary particles. This might be the reason for the slower densification rate of aggregates formed at pH 1.7 compared with those formed at pH 1.2. A typical growth process for a solution of pH 1.2 is depicted schematically in Fig. 1.12, to summarise the overall growth process of three-dimensional particles.

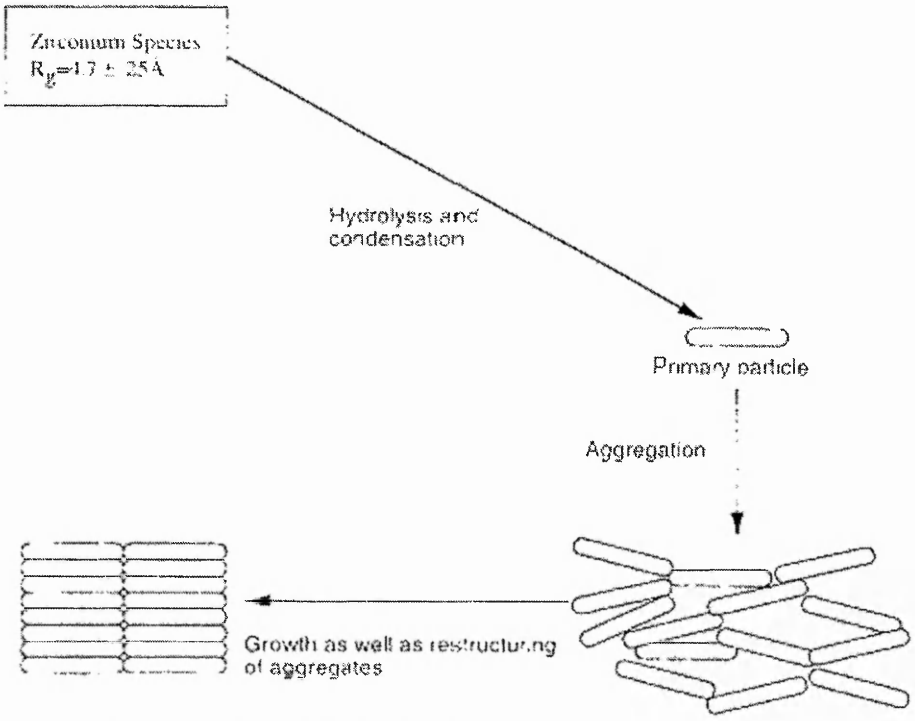


Fig. 1.12. Schematic representation of the hydrous zirconia growth process when rod-like species are present in solution (pH=1.2, T=92°C), [61].

8) The data [61, 90] also supported the possible dehydration of the secondary hydrous zirconia particles with the formation of the final $[ZrO_2]_n$ phase where hydroxyl ions had been replaced by O^{2-} by the internal oxolation reaction [39]. The distance between neighbouring Zr atoms was found to shorten profoundly at this stage.

1.6. Effect of anions on the properties of molecular precursors and the resulting Al- and Zr-containing solid phases

The features of hydrolysis/condensation of Al^{3+} and Zr^{4+} described above considered mainly the presence of non-complexing monodentate ligands such as chloride, chlorate, or nitrate. However, it is well known that the presence of anions can dramatically change the properties of the molecular precursors in the aqueous synthesis of inorganic materials and, as a result, alter the mechanisms of the solid phase formation, as well as composition, structural and chemical properties of the obtained solid phases [41, 47].

The Partial charge model is an excellent and relatively simple tool for the evaluation

of the effect of anions on the molecular precursors in hydrolysis/condensation reactions [39,41]. We have calculated 'Electronegativity-pH' diagrams for a range of Al^{3+} and Zr^{4+} in order to predict their complexation with some common inorganic anions. The calculations are based on the theory provided elsewhere [4,39,41]. The general formula for the calculation of the pH interval of complexation is the following:

$$2.731 - 0.035pH_q^* = \frac{\chi_q(\Delta + 5.732\alpha + 2.064q) - 4.071(3.507\alpha + 2.064q))}{\Delta + (1.408\alpha + 0.507q)\chi_q - (3.507\alpha + 2.064q)} \quad \textbf{(1.42)}$$

where pH^*_q is the pH value of acidic/basic dissociation of complex; χ_q – the mean electronegativity of the ligand; q – the degree of protonation; α - the number of aquo-ligands replaced by ligand.

The value of Δ is calculated from the following expression:

$$\Delta = z - (2.225N) - \left[(4.071 - \chi_m^0)/(1.36\sqrt{\chi_m^0})\right] \quad \textbf{(1.43)}$$

where z – the charge of species; N – the coordination number of metal; χ^0_m – electronegativity of a given metal in Allred-Rochow scale.

The results of the calculations in this work have been compared with the data of previous studies [15-17,20,40] and are summarised in Tables 1.11 and 1.12.

From the wide range of anions listed in Table 1.11, chlorate- and nitrate-ion can be considered as non-complexing counter-ions remaining in the second coordination sphere of aluminium. Behaviour of the chloride-ion is better described when assuming its solvation by 6 water molecules [39]. The resulting value of the mean electronegativity of this ligand is $\chi(Cl(H_2O)_6^-)$ =2.395. From the calculation by the PCM one can see that this anion can form complexes with Al^{3+} only at pH conditions close to neutral. This could explain the fact, that the chloride ion does not influence hydrolysis equilibria in the range of hydrolysis ratios $0<h<2.5$, while a certain amount of Cl^- remains in the solid after precipitation at $h\geq 2.5$ [7] probably due to relatively weak outer-sphere complexation [41].

Authors of the work [41] suggest that owing to the smaller size of the fluoride ion relative to the chloride ion, its solvation number is four. Consequently, the mean electronegativity of the species involved in complexation should be $\chi(F(H_2O)_4^-)$ =2.422. From the PCM calculations (Table 1.11) for such a solvated form of fluoride ions it follows that complex formation is favoured in quite acidic medium. The upper limit (pH_{max}) for complexation with Al^{3+} is 8.4 which supposes very easy replacement of fluoride-ion with hydroxyls. This is not the case in reality. The fluoride ion is a very strong complexing agent, preferably reacting with Al^{3+} over the whole pH range. Experimental data [14,41,91] show the presence of soluble complexes of the general formula $AlF_n^{(3-n)+}$ (n=6) in a wide pH range without any noticeable competition from OH^--ions. We assume that the real electronegativity of the fluoride-ion lies between its fully solvated form and bare F^- (Table 1.11).

Table 1.11. The pH ranges of complexation of anions with Al^{3+} as calculated from the PCM

Anion*	pH range						Complexation behaviour
	Inner-sphere complex****			Outer-sphere complex****			
	pH_{min}	pH_{max}	pH_{opt}	pH_{min}	pH_{max}	pH_{opt}	
ClO_4^-	-7.4	0.3	-3.6	-11.6	-3.6	-7.6	No complexation, behaves as a counter-ion
NO_3^-	-6.8	1.7	-2.5	-11.0	-0.9	-5.9	No complexation, behaves as a counter-ion
$Cl^-(aq.)^{**}$	4.4	8.6	6.5	4.6	9.6	7.1	Complexation is possible in quasi-neutral conditions which are not obtainable in reality
$HCOO^-$	0.3	12.0	5.9	-0.4	13.4	6.5	Complexation occurs in a wide pH range
CH_3COO^-	4.0	11.0	7.5	4.0	11.7	7.9	$Al^{3+}/CH_3COO^- >> 1.5$ – outer-sphere complex; $Al^{3+}/CH_3COO^- \leq 1.5$ – inner-sphere complex
$CH_3COO^-(\alpha=2)$	1.5	10.5	6.0	6.8	12.9	9.9	Can act as a bridging ligand as well*****
$F^-(aq.)^{**}$	-3.8	8.4	2.3	-7.3	8.9	0.8	will complex Al^{3+} whatever coordination mode
F^-	-5.7	30.3	12.3	-4.0	39.6	17.8	-"-
CrO_4^{2-}	-1.6	13.9	6.2	-3.2	19.3	8.1	Complexation occurs in a wide pH range
$HCrO_4^-$	5.1	16.5	10.8	8.1	19.3	13.7	-"-
SO_4^{2-}	-4.5	10.4	2.9	-7.3	12.7	2.7	-"-
HSO_4^-	0.9	11.5	6.2	3.3	12.7	8.0	-"-
SeO_4^{2-***}	-4.6	10.3	2.9	-7.4	12.6	2.6	-"-
$HSeO_4^-$	0.8	11.4	6.1	3.2	12.6	7.9	-"-
$C_2O_4^{2-***}$	-3.0	9.6	3.3	-5.3	11.5	3.1	-"-
$HC_2O_4^-$	1.3	10.6	5.9	3.8	11.5	7.6	-"-
CO_3^{2-}	-3.1	14.7	5.8	-5.3	20.9	7.8	Theoretically a very strong complexing agent for Al^{3+}, for details see text below
HCO_3^-	4.1	17.6	10.8	6.9	20.9	13.9	-"-
PO_4^{3-}	-0.9	14.5	6.8	-3.5	28.9	12.7	Complexation over the whole pH range (inner-sphere complex only)
HPO_4^{2-}	5.5	18.6	12.0	12.1	28.9	20.5	Strong complexing agent
$H_2PO_4^-$	4.0	23.3	13.7	6.9	28.9	17.9	-"-
SiO_4^{4-}	-3.1	12.8	4.8	6.2	44.9	25.5	Complexation over the whole pH range (inner-sphere complex only)
$HSiO_4^{3-}$	4.4	18.2	11.3	14.5	44.9	29.7	Strong complexing agent
$H_2SiO_4^{2-}$	6.4	25.0	15.7	13.3	44.9	29.1	-"-
$H_3SiO_4^-$	6.4	33.6	20.0	9.5	44.9	27.2	-"-

* - anions for which the complexation range has been calculated in this work, are shown **in bold;**

** - aquo-form of anion has been considered; α - the number of water molecules replaced by anion.

*** - for the multidentate anions the values of pH_{min} corresponding to the lower protonation limit have been calculated for all protonated forms;

**** - the values of pH_{min} and pH_{max} for outer- and inner-sphere complexation correspond to the lower and higher limits of the complexation range of a given anion. The value of pH_{opt} has been determined by the formula: $pH_{opt}=(pH_{min}+pH_{max})/2$ and roughly indicates the optimum pH for complex formation with a given anion.

Complexation of Al^{3+} with acetate-ion is expected in weakly acidic or basic conditions according to the data of Table 1.11. The concentration ratio of Al^{3+} and acetate plays an important role in the process [92-94]. In excess of Al^{3+} ions (acid conditions), protonation of the acetate ion occurs which prevents complexation through hydrolysis and induces dimerisation of the resulting h=1 precursors shown in Eq. (1.29). If the Al^{3+}/CH_3COO^- ratio is

higher than 1.5, the pH increases and an inner-sphere complex is formed [93]. Such a complex can act as a precursor for the precipitation of basic salt of approximate formula $Al_2(OH)_2(CH_3COO)_4$. Multinuclear NMR data are consistent with the presence of dimeric $(H_2O)_3Al(OH)Al(H_2O)_3$ units with bridging acetate groups [93]. The PCM calculations support the possibility of acetate-ions interact with Al^{3+} at α=2 (Table 1.11). The formate-ion ($CHCOO^-$) appears to be a much stronger complexing agent for Al^{3+} ions in comparison with the acetate-ion and is able to form complexes over a wide range of pH.

The carbonate-ion appears to be a strong complexing agent for Al^{3+} ions according to the data of Table 1.11. However, it must be appreciated that the protonated form, HCO_3^- is the dominant species at the acidic range of pH according to the following equilibrium [13]:

$$CO_2(g) + H_2O \leftrightarrow HCO_3^- + H_3O^+ \ (lg(\beta_l) = -12.5 \pm 0.001) \quad \textbf{(1.44)}$$

The HCO_3^- ion forms complexes with Al^{3+} above pH≈4.1 (Table 1.11). In a weakly acidic medium this ion will deprotonate, giving rise to the CO_3^{2-} ion [13]. Carbonate-ion then escapes from the solution as carbon dioxide giving rise to slightly alkaline medium. It must be mentioned that acid-base reactions leading to the deprotonation of HCO_3^- and to the elimination of CO_2 are very fast, so there is no real possibility of forming a complex with Al^{3+} for these anions. Thus, complexation of both the carbonate forms is limited, first, by the very narrow pH interval of complexation, and second, by the kinetic factor.

Ohman and Forsling [95] have studied equilibria between Al^{3+}, carbon dioxide and OH^- at 25 °C and have found that some ternary complexes (including both OH^- and carbonate-ions) may exist in aqueous solution. The authors have proposed tentative structures of the ternary complexes: $Al_2(OH)_2CO_3^{2+}$ and $Al_3(OH)_4HCO_3^{4+}$. The carbonate-ion seems to act as a bridging ligand in the case of the Al dimer. The possibility of complexation between carbonate-ions and Al^{3+} is also supported by the existence of minerals in which these complexes are present (dawsonite and dundasite) [95].

Authors of the study [96] have also found that in the case of hydrolysis of Al^{3+} ion in the presence of even small amounts of CO_2 (as bubbled through the solutions) the equilibrium solutions were not sluggish. A stabilising effect of carbon dioxide on the hydrolysis equilibrium, was assumed which is a consequence of the pH-buffering action of CO_2/HCO_3^- system.

Akitt and Farthing [97] have not found any complex formation between carbonate-ions and Al^{3+} ions when studying the hydrolysis of aluminium solutions with sodium carbonate using the ^{27}Al NMR technique. However, the experiments [97] were carried out at higher temperatures (~80-100 °C), and the shortest time of the hydrolysis reaction achieved was about 20 min. One can suggest that most of carbonate-ions would escape from the reaction medium as carbon dioxide gas. Thus, the adjustment of pH (according to Eq. (30)) or

temperature of the reaction medium could control the extent (and probably mechanism) of complexation of carbonate-ions with Al^{3+}.

Comparison of the complexation properties of SO_4^{2-}, SeO_4^{2-} and CrO_4^{2-} ions having similar structure (Table 1.11) shows that sulphate- and selenate ions do not differ much from each other. In the case of chromate-ions, the pH intervals of complex formation as well as the value of pHopt are shifted towards more alkaline solutions. This indicates that complexes of Al^{3+} with chromate-ions are stronger and can resist hydrolysis-condensation much better than complexes with sulphate- or selenate ions. The results of the PCM calculations for the mentioned anions shown in Table 1.11 are in a good agreement with the electronegativities of their central atoms: $Cr^{6+}<S^{6+}\approx Se^{6+}$; $\chi_0=1.59<2.48\approx 2.5$.

For weak and medium strong ligands such sulphate or acetate the concentration ratio Al^{3+}/anion is very important. The literature data show [98,99] that the lower content of sulphate-ion relative to Al^{3+} concentration ($Al^{3+}/SO_4^{2-} >> 1$) can stabilise higher Al polymers, while the high content of this anion ($Al^{3+}/SO_4^{2-} \leq 1$) indirectly inhibits formation of Al_{13}-mer, promoting formation of insoluble hydroxide.

The oxalate-ion shows not very high complexing ability in comparison with other bidentate ions. It is necessary to evaluate a possible chelate effect for the complexation of oxalate-ions with metals [100,101], which makes complexes between aluminium-ions and oxalate very stable [100]. Ternary complexes $Al_3(OH)_3(C_2O_4)_3$ and $[Al_2(OH)_2(C_2O_4)_4]^{4-}$ have been reported [101]. NMR data also indicate the formation of an $[Al(HC_2O_4)]^{n+}$ species in strongly acidic solutions [41].

According to the general rule, the higher the charge of the anion, the stronger is its complexing ability [47]. Phosphate-ion follows this rule, forming strong inner-sphere complexes with Al^{3+} at practically any solution pH. All forms of phosphates ranging from orthophosphoric acid to fully deprotonated PO_4^{3-} react with Al^{3+} [41]. The PO_4^{3-}-ion forms precipitates $AlPO_4$, while complexes of Al^{3+} with HPO_4^{2-} and $H_2PO_4^-$ remain soluble.

The silicate-ion possesses the highest charge in the range of anions listed in Table 1.11. Its complexes with aluminium are extremely stable over a wide range of pH [41,102]. Due to the low charge on silicate in these complexes they undergo further polycondensation [102] that is in contrast with complexes of Al^{3+} with phosphate ions which remain monomeric [103]. The resulting aluminosilicates (zeolites, clays, etc.) comprise a very important class of materials [4].

In the case of Zr^{4+}, the majority of calculations of complexation by the PCM refer to its tetramer $Zr_4(OH)_8^{8+}$ - the most stable known species in medium and highly concentrated aqueous solutions [5]. We have also calculated the pH ranges of complexation for different anions in respect of this species (Table 1.12).

Table 1.12. pH ranges of complexation of anions with Zr^{4+} as calculated from the PCM*.

Anion	pH range						Complexation Behaviour
	Inner-sphere complex			Outer-sphere complex			
	PH_{min}	pH_{max}	pH_{opt}	pH_{min}	pH_{max}	pH_{opt}	
ClO_4^-	-10.7	-2.0	-6.3	-9.5	-3.6	-6.5	No complexation, behaves as a counter-ion
NO_3^-	-9.1	0.4	-4.3	-7.7	-0.9	-4.3	Complexation is possible in a very acidic medium
Cl^-(aq.)	4.4	9.1	6.7	7.4	9.6	8.5	Complexation is possible in quasi-neutral conditions
$HCOO^-$	0.3	12.0	6.1	2.7	13.4	8.0	Complexation occurs in a wide pH range
CH_3COO^-	3.9	11.6	7.8	6.8	12.9	9.9	Complexation occurs at mild pH
CH_3COO^- (α=2)	1.5	10.5	6.0	6.8	12.9	9.9	Can act as a bridging ligand
F^-(aq.)	-3.8	8.4	2.3	-7.3	8.9	0.8	A strong complexing agent for Zr^{4+}
F^-	-5.7	30.3	12.3	-4.0	39.6	17.8	will complex Zr^{4+} whatever coordination mode
CrO_4^{2-}	-1.7	13.8	6.1	3.0	19.3	11.1	Complexation occurs in a wide pH range
$HCrO_4^-$	5.1	16.5	10.8	8.1	19.3	13.7	-"-
SO_4^{2-}	-4.6	10.2	2.8	-7.3	12.7	2.7	-"-
HSO_4^-	-4.6	10.3	2.9	3.3	12.7	8.0	-"-
SeO_4^{2-}	-4.6	10.3	2.9	-7.4	12.6	2.6	-"-
$HSeO_4^-$	0.8	11.4	6.1	3.2	12.6	7.9	-"-
$C_2O_4^{2-}$	-3.0	9.6	3.3	0.3	11.5	5.9	-"-
$HC_2O_4^-$	1.3	10.6	5.9	3.8	11.5	7.6	-"-
CO_3^{2-}	-3.1	14.7	5.8	-5.3	20.9	7.8	Theoretically a very strong complexing agent.
HCO_3^-	4.1	17.6	10.8	6.9	20.9	13.9	-"-
PO_4^{3-}	-0.9	14.5	6.8	-3.5	28.9	12.7	Complexation over the whole pH range (inner-sphere complex only)
HPO_4^{2-}	5.5	18.6	12.0	12.1	28.9	20.5	Strong complexing agent
$H_2PO_4^-$	4.0	23.3	13.7	6.9	28.9	17.9	-"-
SiO_4^{4-}	-3.1	12.8	4.8	6.2	44.9	25.5	Complexation over the whole pH range (inner-sphere complex only)
$HSiO_4^{3-}$	4.4	18.2	11.3	14.5	44.9	29.7	Strong complexing agent
$H_2SiO_4^{2-}$	6.4	25.0	15.7	13.3	44.9	29.1	-"-
$H_3SiO_4^-$	6.4	33.6	20.0	9.5	44.9	27.2	-"-

* - For the description of the parameters in Table 1.12 see footnotes in Table 1.11.

Comparison of the data in Table 1.11 and Table 1.12 shows in the case of Al^{3+} and Zr^{4+} that the calculated pH ranges for the same anions do not differ much. This indicates that the pH

range of complexation is determined mostly by the properties of anion itself (the charge and the mean electronegativity of the anion) rather than by the properties of a metal ion. The other probable reason for such a similarity is that partially hydrolysed zirconium atoms in the tetramer (h=2) are not so strong electrophiles as the initial Zr^{4+} ion.

It follows from the data of Table 1.11 that the chlorate ion most probably acts as a counter-ion as in the case of Al^{3+}. Despite the possibility of the nitrate-ion to form complexes with Zr tetramer only in highly acidic medium, such complexes have been identified [48, 104]. Nitrate-containing basic salts of zirconium have a structure different from the basic salts produced by thermo-hydrolysis of $ZrOCl_2$. Nitrate-ion can act a bridging bidentate ligand which produces chain polymers $[Zr(OH)_2(H_2O)_2(NO_3)]_n^{n+}$ with terminal (NO_3^-) groups [41].

Complexation behaviour of the bidentate anions such as sulphate, oxalate, selenate, chromate in the case of $Zr_4(OH)_8^{8+}$ is somewhat similar to $Al(H_2O)_6^{3+}$. Formate ion increases complexation ability in the case of zirconium clusters (Table 1.12). Higher charge ligands (phosphate, silicate) retain strong complexation in the case of Zr^{4+} and they cannot be directly replaced by the hydroxyl ion at any pH. The abnormal values of the upper limit of the complexation range of pH for these anions in Table 1.12 does not bear any physical sense, it just indicates the strength of the complexes formed with phosphate, silicate and other similar ligands.

Anions such as CH_3COO^-, HSO_4^-, $H_2PO_4^-$, and $HC_2O_4^-$ are able to complex h = 2 precursors whatever their coordination mode. X-ray diffraction performed on $Zr(OH)_2SO_4$ has shown that sulphate ions behave as bridging ligands [105]. They are able to substitute all water molecules giving rise to a three-dimensional network in which sulphate-ions link $[ZrO_4(OH)_2]_n$ infinite chains. Livage and co-workers [41,107] have also suggested that hence zirconyl acetate, oxalate, or phosphate are generally obtained by mixing aqueous solutions of $ZrOCl_2$ with the corresponding acids, complexation occurs between the corresponding anion and Zr(IV). Some precipitated Zr salts become so insoluble that they remain intact in aqua regia [106].

One more feature should be emphasised when describing the effect of anions on the speciation and final solid phases obtained by the hydrolysis of zirconium ions. Depending on the properties of the anion, condensation of Zr^{4+} can give rise to anionic species (ammonium zirconium carbonate; zirconium orthosulphate), neutral species (Zr acetate) and cationic species (Zr oxychloride or nitrate) [17,82,84] as shown in Fig. 1.13.

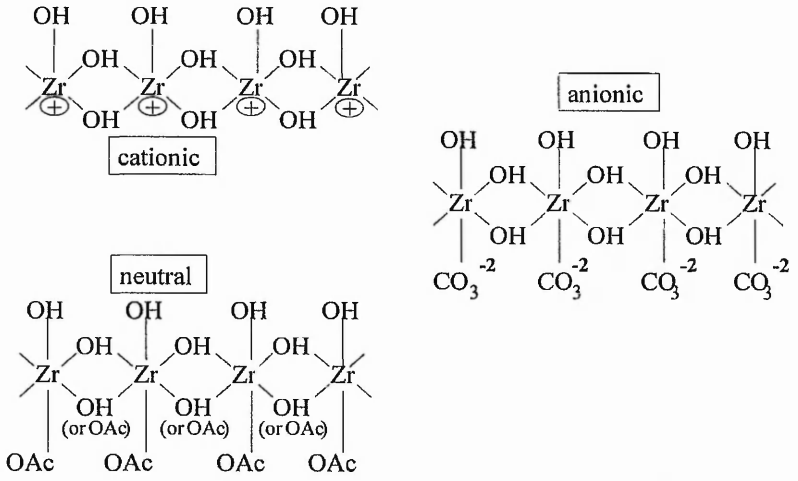


Fig. 1.13. Some examples of Zr-containing polymers with different overall charge.

1.7. Conclusions

On the basis of extensive literature on the subject, one can emphasise the major problems hindering the increase of the understanding of aluminium and zirconium aqueous speciation:

1. High diversity of research efforts in the area of Al and Zr speciation leads to a great dissipation of knowledge and becomes an obstacle for its systematisation and working out universal models describing the behaviour of these metal ions in aqueous solutions and during their transformation into colloidal and solid state materials.
2. The transient species of aluminium and zirconium, which are of major interest in the present study –hydrolytic oligomers (polymers), are lying on the borderline between 'true' solutions and colloidal phases. They possess a 'dual' character as chemical entities with well-defined structure and chemical composition, and as ultrafine colloidal particles having a very high specific surface area and being thermodynamically metastable. These transient species are the foundation for an important class of materials and speciality chemicals – basic aluminium and zirconium salts, and also are important for understanding the speciation of aluminium and zirconium at relatively high concentrations above the solubility limit.
3. The 'dualism' of the properties of aluminium and zirconium polycations makes it difficult to detect and to study them. Traditional analytical techniques for the analysis of metal ions in water may fail since they are designed to deal with 'true' dilute solutions of metal ions. Colloidal techniques are often insufficient to detect and characterise 'true' nano-particulate polycations of Al and Zr of the size around 1-2 nm. Thus, investigation of the metal polycations and their chemistry is a difficult analytical task.
4. There is no 'universal' method for the detection of forms of Al and Zr simultaneously in solution, colloidal and solid state. Thus, an array of diverse analytical techniques must be applied in order to study transformations of these metal ions from solution to solid state. The results of these measurements should then be integrated into one comprehensive

empirical model describing those transformations.

5. Characterisation of Al and Zr speciation in a broad sense (involving chemical and phase transformations) is especially difficult when dealing with their mixtures. As it will be shown below both metals possess a range of similar and dissimilar chemical features which makes it difficult to rationalise and to model them at mutual presence.
6. Aqueous chemistry of aluminium and zirconium is very diverse and complicated owing to the ability of water to act both as a solvent and as a reagent in the complex reactions of hydrolysis-condensation of these metal ions. Water strongly coordinates Al and Zr cations, thus altering their chemical behaviour. The strong complexation ability of both aluminium and zirconium ions with different anions also adds to the complexity and diversity of their aqueous chemistry.
7. Theoretical analysis of Al and Zr speciation using equilibrium thermodynamics is limited mainly to 'true' dilute solutions and when the separation between solution and the solid phase of the corresponding oxide or hydroxide is complete. In the case of the presence of colloidal phases the calculations using equilibrium constants usually fail since colloids are thermodynamically metastable (their occurrence is a purely kinetic phenomenon). Thus, in spite of the fact that for some Al and Zr polycations equilibrium constants have been obtained, their transformation into the colloidal state is impossible to describe in terms of classical thermodynamics.
8. The large number of atoms in the species has hindered theoretical modelling of Al and Zr polycations due to impossibility to apply classical *ab initio* quantum-mechanical methods). Empirical computational models have been able to describe many features of the hydrolytic behaviour of aluminium and zirconium ions. The Partial charge model proposed by Livage and co-workers [41] has been successfully applied for predictions of hydrolysis and condensation conditions of these ions as well as their complexation behaviour with simple inorganic ligands. However, the structural independence of the Partial charge model and other limitations has limited its application in studies of metal ion aqueous chemistry.

On the basis of the above, we have set the following **aims in the present study**:

1. To conduct a range of systematic studies of aluminium and zirconium chemistry in aqueous solutions with special emphasis on the formation of polycations and nano-particulates
2. To develop, improve, implement and integrate existing advanced analytical methodologies for the characterisation of heterogeneous aqueous systems containing Al and Zr polycations and nano-particulates
3. On the basis of existing knowledge and results obtained in this work to attempt to build forecasting qualitative and quantitative theoretical (empirical and thermodynamic) and experimental models of Al and Zr aqueous speciation as a key factor to designed materials.

References

1. Chemical speciation in the environment / Ed. by A.M. Ure, C.M. Davidson (1994) New York, Blackie Academic & Professional. 346 p.
2. Science and technology of zirconia V / Ed. by S.P.S. Badwal, M.J. Bannister, R.H.J. Hannink (1994) Lancaster, Technomic. 862 p.
3. Chemistry of aluminium, gallium, indium and tallium / Ed. by A.J Downs.(1993) London, Chapman and Hall, 526 p.
4. C.J. Brinker, G.W. Scherer. Sol-gel science: the physics and chemistry of sol-gel processing (1990) New York, Academic Press. 908 p.
5. D.F. Baes Jr., R.E. Mesmer. Boron, aluminium and scandium. In: The hydrolysis of cations (1976) New York, Wiley-Interscience, pp.112-123 (Aluminium); pp. 152-158 (Zirconium).
6. V.A. Nazarenko, V.P. Antonovich, N.G. Nevskaya. The hydrolysis of cations in dilute solutions (Russian) (1979) Moscow, Atomizdat, 246 p.
7. J.J. Fitzgerald. Chemistry of aluminium hydrolysis complexes. In: Antiperspirants and Deodorants (1988). New York, Marcel Dekker, 119-296.
8. A.H. Rosenberg, J.J. Fitzgerald. Chemistry of Aluminum-Zirconium-Glycine (AZG) complexes Chlorohydrates. In K. Laden (Ed.) Antiperspirants and Deodorants (1999) New York, Marcel Dekker, 83-136.
9. J.W. Akitt. Prog. Nucl. Mag. Res. Sp. (1989) **21** P. 1-2, 1-149.
10. Website of the MEL Chemicals company (UK): http://www.zrchem.com/
11. S. Ahrland, S.J. Clatt, W.R. Davies (1958) Quart. Rev. (London), **12**, 265.
12. R.G. Pearson. Chemical Hardness (1997) Weinheim-Chichester, Wiley-VCH.
13. W. Stumm, J.J. Morgan. Aquatic Chemistry. An Introduction Emphasizing Chemical Equilibria in Natural Waters. (1981) New York, Wiley and Sons, 780 p.
14. The environmental chemistry of aluminium / Ed. by G. Sposito (1996) Boca Raton, Lewis, 464 p.
15. W. Casey et. al. Aqueous Aluminum Polynuclear Complexes and Nanoclusters: A Review. In: J.F. Banfield, A. Navrotsky (Eds.) Nanoparticles in the Environment. Reviews in Mineralogy & Geochemistry, V. 44. (2001) pp. 167-190.
16. L.-O. Ohman. Chem. Geol. (1998) **151** 41-50.
17. L.-O. Ohman. Acta Chem. Scand. (1991) **45** 258-264.
18. M.K. Ridley et. al. Environ. Sci. Technol. (1997) **31** 1922-1925.
19. D.A. Palmer, D.J. Wesolowski. Geochim. Cosmochim. Acta (1992) **56** 1093-1111.
20. D.A. Palmer, D.J. Wesolowski. Geochim. Cosmochim. Acta (1993) **57** 2929-2938.
21. M. Venturini, G. Berthon. J. Chem. Soc. Dalton (1987) 1145-1148.
22. G. Berthon. Coordin. Chem. Rev. (2002) **228** 319-341.
23. Coordination chemistry of aluminum/Ed. by G.H. Robinson(1993) New York,VCH, 234p.
24. R.M. Smith, A.E. Martell. Critical Stability Constants, Vol. 6, Second supplement (1986)

New York, Plenum Press.

25.K. Wefers, C. Misra. Oxides and Hydroxides of Aluminum. Alcoa Technical Paper No 19, Revised (1987) Alcoa, 92 p.

26. J.J. Fitzgerald, A.H. Rosenberg. Chemistry of Aluminum Chlorohydrate and Activated Aluminum Chlorohydrates. In K. Laden (Ed.) Antiperspirants and Deodorants (1999) New York, Marcel Dekker, 83-136.

27.G. Svehla. Automatic potentiometric titrations (1978) Oxford, Pergamon, 219 p.

28.P. Mishra. Mater. Lett. (2002) **55** 425-429.

29.T. Sugimoto. Monodispersed Particles (2001) Amsterdam, Elsevier, 818 p.

30.F. Salvatore, M. Trifuoggi. Journal of Coordination Chemistry (2000) **51** 271-282.

31.M. Meloun, J. Havel, E. Högfeldt. Computation of solution equilibria: a guide to methods in potentiometry, extraction, and spectrophotometry (1988) Chichester, Ellis Horwood, 297 p.

32. A. Khodakovskii et al. Geokhimiya (1980) 11 1606-1624.

33.Microcal Origin ™ version 6.0 software. Reference Manual.

34.J.T. Kloprogge et. al. J. Non-Cryst. Solids (1992) **142** 87-93.

35.J.W. Akitt et.al. J. Chem. Soc. Dalton (1989) 1889-1895.

36.A. Veyland, L. Dupont, J.C. Pierrard, J. Rimbault, M. Aplincourt. Eur. J. Inorg. Chem. (1998) 1765- 1770.

37.A. Clearfield. Rev. Pure and Appl. Chem. (1964) **14** 91-108.

38.R. Zeuner et. al. Isotopenpraxis (1988) **24** 23-25.

39.J. Livage, M. Henry, C. Sanchez. Sol-Gel Chemistry of Transition Metal Oxides. In Prog. Solid St. Chem. (1988), **18**, 259-341.

40.J.D. Hem, C.E. Roberson. Aluminum Hydrolysis Reactions and Products In Mildly Acidic Aqueous Systems, ACS Symposium Series (1990) **416** 429-446.

41.M. Henry, J.P. Jolivet, J. Livage. Aqueous Chemistry of Metal Cations - Hydrolysis, Condensation and Complexation. Structure And Bonding (1992) **77** 153-206.

42.W. Zhang, F.P. Glasser. J. Eur. Ceram. Soc. (1993) **11** 143-147.

43.J. Livage, M. Chatry, M. Henry, F. Taulelle. Materials Research Society Symposium Proceedings, (1992) **271** (Better Ceramics through Chemistry V) 201-212.

44.S. Giroux et. al. Eur. J. Inorg. Chem. (2002) **5** 1162-1168.

45.H. Watling. Appl. Spectrosc. (1998) **52** 250-258.

46.I.A. Sheka et al. Zhurn. Neorg. Khim. (1987) **32** 1576- 1581.

47.J.-P. Jolivet. Metal Oxide Chemistry and Synthesis. From Solution to Solid State (2000) Chichester, Wiley and Sons, 321 p.

48.I.C. Smith, B.L. Carson. Trace Metals in the Environment. V.3, Zirconium (1978)373-383.

49.J.W. Akitt, N.B. Milic. J. Chem. Soc. Dalton (1984) 981-984.

50.G. Johansson. Acta Chem. Scand. (1962) **16** 403.

51.J. Rowsell, L.F. Nazar. J. Am. Chem. Soc. (2000) **122** 3777-3778.

52.L. Allouche, C. Gerardin, T. Loiseau, G. Ferey, F. Taulelle. Agew. Chem. Int. Edit. (2000) **39** 511-514.

53.B. Lothenbach et.al. Environ. Sci. Technol. (1997) **31** 1452-1462.

54.G. Furrer. Aquat. Sci. (1993) **55** 281-290.

55.G. Fu, L.F. Nazar, A.D. Bain. Chem. Mater. (1991) **3** 602-610.

56.S.M. Bradley, R.A. Kydd, C.A. Fyfe. Inorg. Chem. (1992) **31** 1181-1185.

57.J.J. Fitzgerald. Journal of Magnetic Resonance (1989) **84** 121.

58.M. Venturini, G. Berthon. J. Chem. Soc. Dalton (1987) 1145-1148.

59.J.W. Akitt, A. Farthing. J. Chem. Soc. Dalton (1981) 1617-1623.

60.J.W. Akitt et. al. (1972) J. Chem. Soc. Dalton 604.

61.A. Singhal, L.M. Toth, J.S. Lin, K. Affholter. J. Am. Chem. Soc. (1996) **118** 11529-11534.

62.A.P. Oliveira, M.L. Torem. Powder Technol., 2001, V. 119, 2-3, pp. 181-193.

63.A.N. Sathyagal. J. Colloid Interf. Sci., 1999, V. 219, pp. 20–30.

64.M. Aberg, J. Glaser. Inorg. Chim. Acta (1993) **206** 53-61.

65.J.A. Jutson et. al. Materials Research Society Symposium Proceedings (1990) **180** (Better Ceramics through Chemistry 4) 123-128.

66.K. Matsui, M. Ohgai. J. Ceram. Soc. Jpn. (1998) **106** 1232-1237.

67.L.P. Holmes, D.L. Cole, E.M. Eyring. J. Phys. Chem. (1968) **72** 301-310.

68.P.M. Jardine, L.W. Zelazny. Soil Sci. Soc. Am. J. (1987) **51** 885-889.

69.T.A. Taylor, H.H. Patterson. Analytica Chimica Acta (1993) **278**. 249-257.

70.J.W. Akitt. Aluminium, Gallium, Indium and Thallium. In: Multinuclear NMR / Ed. by J. Mason (1987) New York, Plenum Press, 259-292.

71.J.S. MacFall et. al. Appl. Spectrosc. (1995) **49** 156-162.

72.J.W. Akitt, A. Farthing, O.W. Howarth. J. Chem. Soc. Dalton, (1981) 1609-1614.

73.J.W. Akitt, A. Farthing. J. Chem. Soc. Dalton (1981) 1606-1608.

74.A.H. Rosenberg. In: XIV Congreso Latinoamerica e Iberico De Quimicos cosmeticos and I.F.S.C.C. International Conference, Santiago de Chile 23-26 May, 1999. Conference Proceedings (1999) 25-28.

75.G. Furrer et. al. Geochim. Cosmochim. Acta (1999) **63** 3069-3076.

76.K. Matsui, H. Suzuki, M. Ohgai, P. Arashi. J. Am. Ceram. Soc. (1995) **78** 146-152.

77.K. Matsui, M. Ohgai. J. Ceram. Soc. Jpn. (1998) **106** 1232-1237.

78.K. Matsui, M. Ohgai. J. Ceram. Soc. Jpn. (1999) **107** 643-647.

79.E. Morgado, Y.L. Lam, L.F. Nazar. J. Colloid Interf. Sci. (1997) **188** 257-269.

80.L.F. Nazar et. al. Chem. Comm. (1992) 251-253.

81.J.P. Boisvert, C. Jolicoeur. Colloid. Surface. A (1999) **155** 161-170.

82.R. Bertram et. al. Acta Hydrochim, Hydrobiol. (1994) **22** 265-269.

83.D. Tchoubar, J.Y. Bottero. C. R. Acad. Sci. II A (1996) **322** (7) 523-534.

84.P. Capkova, R.A.J. Driessen, M. Numan, H. Schenk, Z. Weiss, Z. Klika. Clay Clay Miner.,

(1998) **46** 232-239.

85.R.A. Schoonheydt et. al. Clay Clay Miner., (1994) **42** 518-525.

86.A. Sanchez, M. Montes. Micropor. Mesopor. Mat. (1998) **21** 117-125.

87.J.M. Dominguez et. al. Catal. Today (1998) **43** 69-77.

88.E. Morgado, et. al. J. Colloid Interf. Sci., (1995) **176** 432-441.

89.A. Bleier, R.M. Cannon. In: Better Ceramics Through Chemistry II (Mater. Res. Soc. Symp. Proc.)/Ed. by C.J. Brinker, D.E. Clark, D.R. Ulrich, Pittsburgh, Pa. (1986) **73** 71-77.

90.A. Singhal et. al. J. Colloid Interf. Sci. (1997) **194** 470-481.

91.G.S. Townsend, B.W. Bache. Talanta (1992) **39** 1531-1535.

92.J.W. Akitt et. al. J. Chem. Soc. Dalton (1989) 1897-1901.

93.J.W. Akitt, N.B. Milic. J. Chem. Soc. Dalton (1984) 981-984.

94.C.W. Wu, M.K. Wang. Food Sci. Agricul. Chem. (2000) **2** 15-19.

95.L.-O.Ohman, W. Forsling. Acta Chem. Scand. A (1981) **35** 795-802.

96.T. Hedlund, S. Sjoberg, L.O. Ohman. Acta Chem. Scand. A (1987) **41** 197-207.

97.J.W. Akitt, A. Farthing. J. Chem. Soc. Dalton (1981) 1617-1623.

98.G.L. Kerven, P.L. Larsen, F.P.C. Blamey. Soil Sci. Soc. Am. J. (1995) **59** 765-771.

99.A. Benyattou et. al. B. Soc. Chim. Fr. (1995) **132** 1103-1108.

100. L. Ciavatta, M. Iuliano, R. Porto. Ann. Chim.-Rome (1999) **89** 51-61.

101. S. Sjoberg, L.O. Ohman. J. Chem. Soc. Dalton (1985) 2665-2669.

102. F.J. Doucet et. al. Geochim. Cosmochim. Acta (2001) **65** 2461-2467.

103. The environmental chemistry of aluminum / Ed. by D.K. Nordstrom, H.M. May. In G. Sposito (1989) Boca Raton, CRC Press.

104. P.B.Rocherulle et. al. J. Solid State Chem. (1997) **128** 295-304

105. G.M. Muha, P.A. Vaughan. J. Chem. Phys. (1960) **33** 194.

106. M.T. Larrea et. al. J. Anal. Atom. Spectrom. (1997) **12** 1323-1332.

107. J. Livage et. al. Materials Research Society Symposium Proceedings (1992) **271** (Better Ceramics through Chemistry V) 201-212.

CHAPTER II. Materials and Methods

2.1. The choice of model systems

Since the present work is concerned with studies of chemical and structural aspects of aluminium and zirconium speciation in aqueous solutions, it was important to choose a model system for each of these ions and for their mixtures. Aluminium chloride and zirconyl chloride and their aqueous solutions were chosen as molecular precursors to materials and colloidal phases, although other precursors with different anions such as nitrates, sulphates, acetates of aluminium and zirconium were used for comparison. The reason for choosing these precursors is based on the absence of strong interaction of counter-ion (chloride) and metal ion which can otherwise change significantly the pathways of hydrolysis-condensation and related processes in Al and Zr aqueous solutions [1, 2].

Alkaline titration was chosen as a method for pH variation and, consequently, for hydrolysis-condensation reactions of Al and Zr ions. In spite of criticism over this method in literature [3] it has several advantages: (*a*) the method of alkaline titration is fast (hydrolysis-condensation starts to proceed immediately after addition of alkali) that is important for the kinetic studies; (*b*) procedure of alkaline titration is not complicated with many side reactions except for local inhomogeneity which may lead to undesirable early precipitation of metal hydroxide [3] (special care was taken to avert this process as much as possible); (*c*) exact known concentration of alkali allows for quantitative studies of hydrolysis-condensation to be carry out; (*d*) this is a relatively inexpensive method involving commercially available reagents.

The major concentration range of molecular precursors to Al- and Zr-containing hydrolysed colloidal phases and solid materials was within 0.01 and 0.25 mol/L of metal-ions in solution. The chosen medium concentration is high enough for the relationships established to be transferred to colloidal and materials chemistry, while it allows avoiding many problems associated with highly concentrated non-ideal solutions of metal ions [1, 3]. Different experimental strategies were applied in this work to study metal ion hydrolysis - as discussed below in Sections 2.3-2.4.

The temperature was pre-set to ambient (21 ±1°C or 25±0.1 °C) or to higher level (90 °C) in order to study the effect of this important parameter on the hydrolysis-condensation and related processes in Al and Zr solutions. The ionic strength was been also pre-set to 0 (no added electrolyte) or to 1.0 (1 mol/L of NaCl) depending on the experiment. Other variable parameters included application of different anions (nitrate, sulphate, acetate, carbonate) and complexing agents (glycine – for zirconium only).

2.2. The choice of methods

The major problem of speciation studies in medium and highly concentrated metal ion solutions is a choice of relevant analytical methods for providing qualitative and quantitative information on the multifaceted processes occurring upon hydrolysis-condensation reactions

[1, 3]. As mentioned by Blesa in the review on iron speciation in aqueous solutions [4], there is no ultimate or ideal method suitable for the speciation studies and, thus, a number of complimentary techniques should be implemented allowing for characterisation of different sides of speciation process and creating together a consistent picture of the processes in question.

Upon hydrolysis-condensation of Al and Zr aqueous solutions the corresponding precursors transform into highly charged oligomeric species first, these oligomers are then converted at some point of alkali addition into a colloidal phase and, finally, into solid precipitates [1-3]. Therefore, analytical methods allowing for detection of Al and Zr species in the molecular state (including polynuclear species), colloidal state and solid state should be implemented or developed. The choice of complimentary methods applied in the present work is shown. in Fig. 2.1

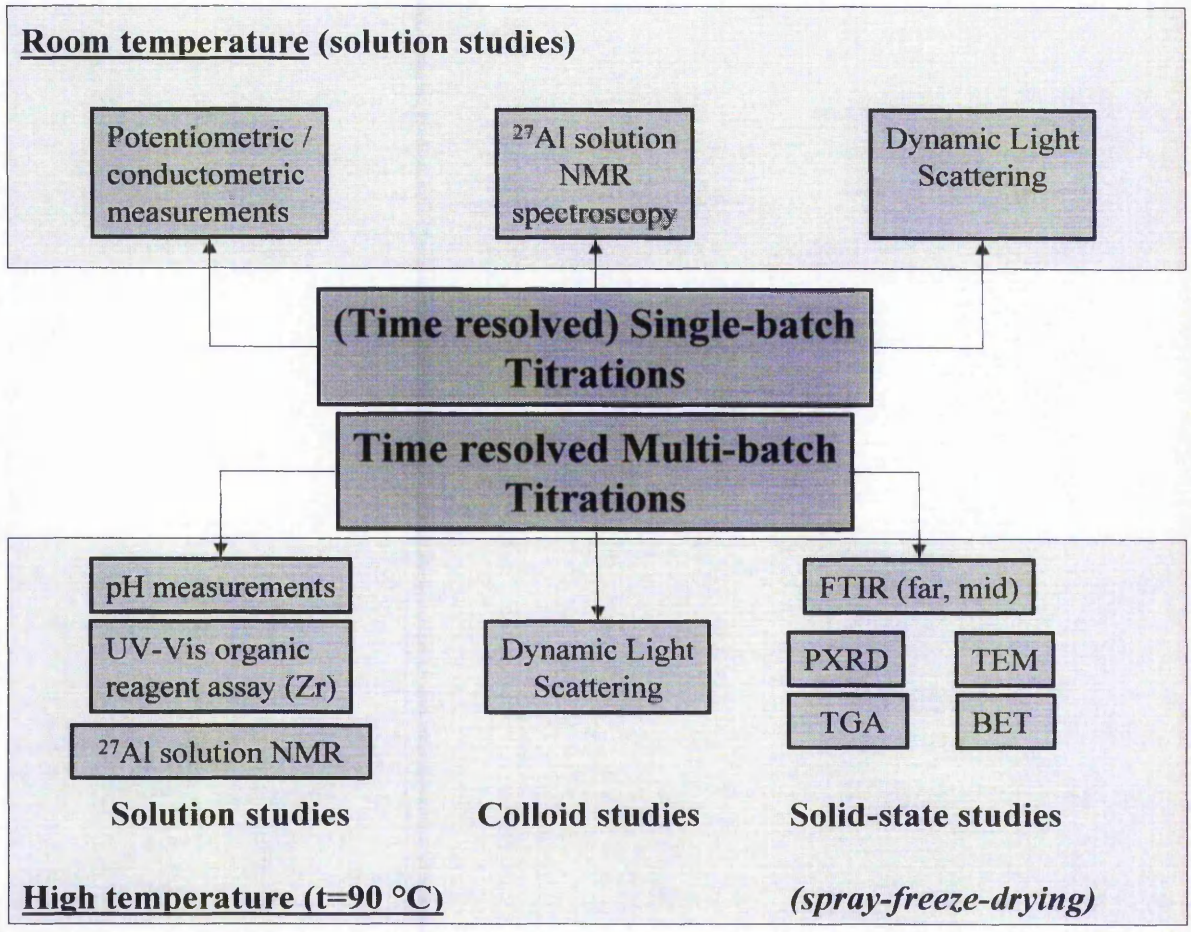


Fig. 2.1. Analytical methods implemented in the present study for different states of Al and Zr species in aqueous solutions (molecular, colloidal, solid state).

The core of the methodology summarised in Fig. 2.1 is application of alkaline titrations for the establishment of the relationships between Al/Zr hydrolysis-condensation pathways and the most significant parameter of these processes – the pH of the solution.

Titrations were carried out in two modes - single-batch and multi-batch, described in

the following sections. Special emphasis was brought to kinetic studies using time-resolved titrations and real-time analysis. The fact that the most of the measurements were conducted from the same sample allowed us to improve greatly consistency of the data between the different methods applied. A number of improvements of analytical methods and procedures was proposed in this work leading to a better detail of the data acquired as well as laying a basis for further experimentation in the field of metal ion speciation. The following sections contain a brief overview of main theoretical principles of the methods applied in this work as well as a description of instrumentation, experimental procedures and data treatment.

2.3. Potentiometry

Potentiometry and potentiometric titrations are the oldest, most established and most widely used methods for speciation studies in metal ion solutions that is indicated by a great number of work done in this field both for aluminium and zirconium [1,5,6]. Potentiometric (pH-metric) measurements performed in this work are concerned with determination of the most important, driving parameter of hydrolysis-condensation of metal ions- pH of solution.

Potentiometry is the application of the Nernst equation to detect unknown concentration of an analyte in solution by measuring the expressed voltage of a redox reaction when it is connected to a half-reaction with known composition (and half-cell potential) [7]. The Nernst equation is written as following [7]:

$$E = E^\circ - (RT/nF)\ln Q \qquad \textbf{(2.1)}$$

At 25°C: $$E = E^\circ - (0.05916/n)\log_{10} Q \qquad \textbf{(2.2)}$$

where E – Nernst potential of half-cell; E° - standard Nernst potential;
R – universal gas constant; n – -number of electrons;
F – Faraday constant; Q – concentration quotient of the components in a half-cell

A potentiometric measurement is based on the principle that if one has a redox reaction:

$$M^{+n} + M'^{+p} \,||\, M^{+n-1} + M'^{+p+1} \qquad \textbf{(2.3)}$$

and the cell voltage is known along with the concentration of three of the reagents, one may determine the concentration of the fourth. The system has two half-cells (one is the reference electrode, the other is the indicator electrode) and a voltmeter to measure the cell potential [8].

The pH-metric method is a variety of potentiometry where the indicator electrode is a glass membrane electrode sensitive to the concentration of H^+, while the reference electrode can be silver-silver halide or saturated calomel electrode [9].

The standard pH electrode is composed of a glass membrane where H^+ can replace Na^+ in the glass structure. This change in ion distribution creates a potential at the membrane surface which can be measured using a voltmeter [8].

2.3.1. Potentiometric titrations. Principles and instrumentation

Titrimetric analysis consists in determining the number of moles of reagent (titrant), required to react quantitatively with the substance being determined (sample). The titrant can be added (*a*) volumetrically, with a glass or automatic burette or with a low flow-rate pump, or (*b*) coulometrically, with an electrochemical generation from a proper electrolyte [8].

Titrimetric methods of analysis have the virtue of being absolute as gravimetric methods, in that the concentration of the substance in question is determined from the basic principles of chemistry and no calibration curves are required [9].

Various methods are available for the end-point determination: spectrophotometry, potentiometry, amperometry, conductometry, etc. [8]. The potentiometric end-point detection is the most widely used method [8].

In modern analytical chemistry automation is of increasing importance [9]. Automation of a point-by-point titration is seldom trivial. Kinetic factors concerning the chemical reaction and the response of the indicating system are of paramount importance. Cell configuration, stirring, positioning of end-point detector and of input of titrant have to be considered to ensure high accuracy.

Equilibrium throughout the titration curve can be attained only when the titrant is dispensed at an infinitely low rate. Two factors determine the rate at which a potentiometric curve approaches the state of equilibrium: the kinetics of the chemical reaction and the kinetics of the electrode process. Both factors are slowest in the vicinity of the equivalent point, the region with utmost importance, from which the end point is determined. At faster titration rates compared to the kinetics of the system, a delayed end point is obtained [9].

The degree of the delay of the end point depends on the concentration of analyte, the composition of the solution, the concentration of titrant and the rate of dispensing. The larger the concentration of the analyte, the smaller the delay. The larger the amount of titrant dispensed at unit of time, the larger the delay.

Several strategies are used to virtually eliminate the delay [10]:

(*a*) Modifying the rate of titrant dispensing, either by reducing it throughout the entire titration curve - the monotonic mode, or by reducing it only along the vicinity of the equivalence point - the dynamic mode. With the dynamic mode, the rate of the titration is inversely proportional to the rate of potential change, $\partial E / \partial \lambda$, where λ is the volume of titrant added [9];

(*b*) Performing a repetitive-monotonic titration. In this mode a series of titrations is performed in a consecutive manner. The measurements are made under non-equilibrium conditions. The titrant is dispensed, or electrochemically generated, at a fast and constant rate. Each titration is discontinued at some time after the end point. A new portion of sample is added to the cell and the titration is resumed at the previous rate. The new aliquot can be added also without suspending the flow of the titrant. The end points of the titrations are usually delayed. Each end point in a series of titrations is delayed only once, by a period of time depending on the specific type of titration. Previous delays are not accumulated. The delay of the previous

titration is always nullified a short time after a new portion of an analyte is added, since the response of the system is slow only around the equivalence point, but not far away from it.

In modern analytical practice automation of titrations is essential for the following reasons: (i) convenience and speed, (ii) performing analysis without supervision, (iii) enable application of elaborate techniques for analyzing the data (with computerised systems) [9].

Several devices for automatic transfer of titrant can be used [9,10]. Piston burettes are highly reliable, do not require calibration, but are expensive. Peristaltic pumps are of relatively low cost and highly versatile. However, they require frequent calibration due to the continual changes in the physical properties of the flexible tubes employed (ID of the tubes is about 0.5 mm). Suction-stroke piston pumps (metering pumps) are as versatile as the peristaltic pumps, but more precise and require less calibration.

There are several methods of automatic end-point determination [9]. In the case of distinct and complete inflexion in the titration curve the end point is determined from the first derivative of the curve. For the indicating system with two identical electrodes, the end point may be determined directly from the titration curve. Incomplete or broad inflexions in the titration curve require different approaches for end-point determination such as Gran's method.

In the present work potentiometric titrations were employed for (*a*) standardisation of the titrant solutions and determination of the concentration of acids or bases involved in the described experiments; (*b*) speciation studies of Al and Zr ions in aqueous solutions using titration as the means of pH variation.

Two general strategies were employed for potentiometric titrations: (*a*) **single-batch mode**, where small repetitive and monotonic additions of the titrant were made into one batch of sample step-wise; (*b*) **multi-batch mode**, where additions of the titrant were made to multiple batches in order to adjust the ratio of titrant (alkali or acid) and metal ion (analyte) to a certain pre-defined level. The single-batch titration mode offers an advantage of being a relatively simple, easily automated way of performing speciation studies in metal ion solutions, while multi-batch mode in spite of being a laborious and more expensive way offers a number of advantages discussed below.

2.3.2. Potentiometric titrations for standardisation of stock solutions of acids and alkalis

Volumetric standard solutions of alkalis and acids supplied commercially were used as titrants in the experiments carried out as well as for standardisation of the stock solutions of different bases and acids prepared from concentrated sources (HCl, H_2SO_4, HNO_3, NH_4OH) and from solid reagents (KOH, $KHCO_3$). In the latter case of 'home-made' stock solutions they were standardised with a volumetric solution of alkali or acid using a standard potentiometric titration procedure [8]. For this purpose a pre-defined aliquot of the stock solution was diluted with deionised water (to make up to 15ml of the sample solution in total)

and titrated with the volumetric standard using the ABU91 autotitrator set in dynamic incremental mode with a 10 or 5 ml high-precision piston pump. The equivalence point was determined from the first derivative of the potentiometric curve and the concentration of the stock solution was calculated. All solutions of KOH were sonicated for 15 min prior to use in standardisation procedures or any other experiments to eliminate the presence of dissolved carbon dioxide.

Standardisation titration procedure. In a 30 ml beaker an aliquot of the sample solution to be standardised and an aliquot of deionised water was added (the volume of aliquot depends on the expected concentration of the sample and titrant) to adjust the total volume of the sample to 15 ml. The prepared solution (in the case of KOH the sample was pre-sonicated for 15 min first) was subjected to the potentiometric titration with a corresponding volumetric standard of acid or base (strong bases were used for strong acids and vice versa) using a Radiometer ABU91 autotitrator. The following setup of the autotitrator was used: 10 ml high-precision piston burette; incremental titration mode; 30 s pre-titration delay; dose dynamics set to 16; minimum dose 1%; maximum dose 5% of the total burette volume; burette speed 80 %; pH variation 0.0005 units of pH; inflexion filter 4; inflexion point rejection slope 30.

The concentration of the sample was determined automatically from the full inflexion point using a first derivative curve and recalculated to the concentration of the sample solution under question. The autotitrator was calibrated every 24 hours with two pH buffer solutions (pH=4.005 and pH=7.001). Temperature was evaluated during the calibration and titrations using a Radiometer thermosensor probe.

2.3.3. Single-batch potentiometric titration setup

Automated single-batch potentiometric titrations were performed using the setup schematically shown in Fig. 2.2.

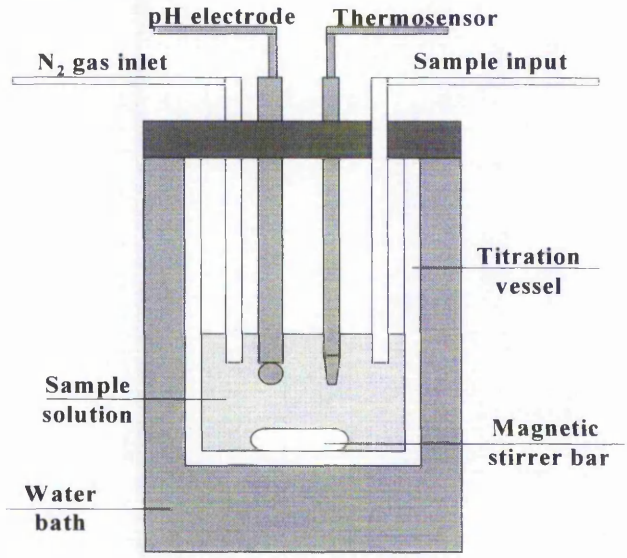


Fig. 2.2. Schematic representation of the setup for automated single-batch potentiometric titrations

The setup included a thermostated titration cell consisting of the titration vessel (glass or polystyrene beaker) immersed in the water bath for temperature control (precision ±0.5 °C). An immersed magnetic stirrer (Stem Ltd.) provided high-speed stirring (300-400 rpm) of the sample inside the titration vessel. Titrants were delivered to the reaction vessel using Radiometer Autotitrator ABU91 with high precision piston pump burette or Eppendorf EDOS5222 liquid handling unit. Additions of titrant with pre-defined volume were made at chosen time intervals (30-180 s for short-term titrations and up to 15 min for long-term titrations). An inert atmosphere was maintained throughout the titration using a steady flow of nitrogen gas. Measurements of pH were conducted at pre-set time intervals (from 1 to 10 s depending on the time span of titration) using a high-precision Radiometer potentiometer PHM240 and Red-Rod combined glass electrode pH240 with internal reference and double junction. Temperature inside the titration vessel was monitored using Radiometer thermosensor T400S. Readings of pH and temperature were recorded in real time by connecting the PHM240 potentiometer to a PC. The radiometer potentiometer PHM240 was calibrated every 24 hours using four pH buffers (pH=1.687, 4.005, 7.000, 10.012).

2.3.4. Time-resolved potentiometric titrations

In the course of potentiometric titrations with discrete titrant additions the system takes some time to stabilise prior next addition of a titrant. This time interval between titrant additions is called 'stabilisation interval', 'delay time' or 'relaxation time' [9] and a time-resolved potentiometric curve during this (short) interval follows several distinct shapes. Time-resolved potentiometric measurements were used for kinetic studies of the first hydrolysis steps in Al^{3+} solutions [11]. The observation of particular shapes of the curves in 'stabilisation intervals' has been reported in the work [4] concerned with the studies of Fe^{3+} aqueous hydrolysis.

It was observed that the shapes of time-resolved (relaxation) curves during potentiometric titrations of Al- or Zr-containing solutions fall into four general shapes, as shown in Fig. 2.3.

The variation of pH values during stabilisation between titrant additions and the occurrence of the relaxation curves shown in Fig 2.3 is a consequence of relatively long times of system equilibration comparing with the time gaps between titrant additions. There may be possible reasons for relaxation curves to occur: (a) insufficient mixing in the titration system; (b) slow equilibration at the working surface of glassy pH-electrode; (c) chemical processes occurring in the system are relatively slow; (d) temperature variations. In the setup of single-batch titrations a thorough temperature control was applied using a thermostat (water bath) with temperature variations not exceeding ±1°C. Powerful stirring was also implemented in order to provide efficient mixing of the components in the titration vessel. The use Radiometer Red Rod combined pH-electrode ensured short response times (less then 1 s in most cases according to manufacturer's data). Therefore, time-resolved curves detected

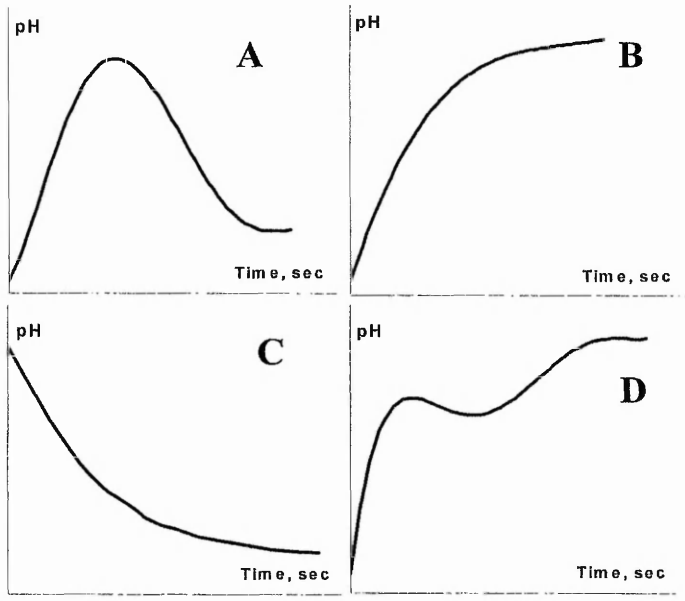


Fig. 2.3. Characteristic shapes of time-resolved 'relaxation' curves observed in potentiometric titrations

between additions of equal amounts -of titrant at equal time intervals are primarily related to the chemical changes occurring in the titration system within these time intervals (ranging from 0.5 to 15 min).

In some cases variations of the pH between titrant additions were as low as ca. 0.005 pH units. High reproducibility of pH readings provided by the combination of PHM240 pH-meter, Red Rod combined pH-electrode (±0.002 units of pH according to manufacturer's data) together with calibration with four high-precision pH standard buffers (±0.001 units of pH) made sure that such small variations are detected reliably.

Another innovation introduced in this work was application of correlation analysis (CA) (principles of CA are described in Section 2.12) for statistical treatment of time-resolved potentiometric curves. The number of these curves corresponds to the number of titrant additions during titration, which in this work varied between 50 and 120 depending on a particular experiment. The use of CA allowed us to automate the treatment of a large number of time-resolved potentiometric curves as well as to extract additional information from potentiometric data as described in Chapter 3.

2.4. Multi-batch titrations

Multi-batch titrations are a useful alternative to single-batch titrations since they allow the detailed study of the processes in question at different conditions for each batch simultaneously and independently. Multi-batch titrations enable kinetic measurements to be made in real-time mode. These features make the multi-batch approach to alkaline titrations of metal ions similar to the principles of dynamic combinatorial chemistry [12]. In the dynamic combinatorial chemistry approach the large number of reactions is conducted

simultaneously at pre-designed conditions which include reagent ratios (hydrolysis ratios in the present case), temperature, ionic strength and any other significant parameters. High throughput of the approach combined with high precision of the tuning of the pre-set conditions makes this approach very attractive for the systematic studies of aluminium and zirconium hydrolysis-condensation reactions which are known for their complexity and the numerous factors affecting the processes (see Chapter 1).

In terms of experimental design a semi-classical block-wise approach was maintained throughout the multi-batch experiments which comprises of several blocks of experiments. Each block of experiments was set at fixed conditions (temperature, ionic strength, concentration of additive, etc.) and contained from 20 to 30 batch samples. The block-wise approach allowed us to study the effect of the experimental conditions other than pH which were set to vary from block to block.

Every sample in the experimental block (or series) was produced at a different hydrolysis ratio ranging from $h = -1.5$ to $h=0.0$ (a corresponding acid was added at $h<0.0$ and no titrant was added at $h=0.0$) or from $h=0.0$ to $h=5.0$ with the addition of the chosen alkali at certain intervals (usually 0.1-0.2 units of hydrolysis ratio). The expression for the 'negative' hydrolysis ratio $h=[H^+]/[Me^{z+}]$ in analogy with the 'positive' hydrolysis ratio $h=[OH^-]/[Me^{z+}]$ was used for presentation purposes only to provide a single scale for acid and alkali additions and does not have any physical meaning. Perhaps, more appropriate would be to derive an 'exact' expression for the 'negative' hydrolysis ratio from the ionic product of water $K_w=[OH^-][H^+]$ and, consequently, $h=K_w/[Me^{z+}][H^+]$. However, primarily due to a low value of K_w (at 25 °C, $K_w=10^{-14}$), the scales of 'positive' and 'negative' hydrolysis ratios would become incompatible and hard to present on a single scale. Another common parameter to use as a scale for the pH-dependent data is ligand number η [1]:

$$\eta = \frac{[H^+] - [OH^-] + m(OH)}{m(Me)} \qquad (2.4)$$

where $[H^+]$ and $[OH^-]$ is 'intrinsic' concentration of acid or alkali before addition of titrant; m(Me) and m(OH) – molar concentrations of metal ion and alkali added.

The parameter η is widely used in the potentiometric and other studies of the thermodynamic stability constants of metal-ion complexes [1]. Preliminary measurements have shown that the calculated value of ligand number is very close to the value of hydrolysis ratio used in this work. The largest difference occurred at values of h and η close to zero (positive values of these parameters were compared) and did not exceed ca. 0.02 units.

2.4.1. Multi-batch titrations of aluminium salt solutions at room temperature

Multi-batch alkaline titrations of Al salt solutions were used for ^{27}Al NMR and dynamic light scattering studies at room temperature. Aliquots of 2.5 or 5 ml (depending on the total volume of the sample) of a chosen stock aluminium solution ($AlCl_3$, $Al(NO_3)_3$, or

$KAl(SO_4)_2$, all 1 mol/L) were placed in the glass conical flasks (100 ml). A calculated volume of deionised water was added to the corresponding flasks in order to adjust the total volume of each sample to 25 or 50 ml to make the final concentration of Al-ions to 0.1 mol/L. Solutions in the flasks were neutralised with calculated aliquots of the desired alkali (KOH, 1.8 mol/L; NH_4OH, 2.0 mol/L; $KHCO_3$ 1.7 mol/L) to give final hydrolysis ratios h (where h=[OH^-]/[Al_{total}]) between 0 and 5. The samples in the flasks were sealed and shaken for 24 hours at 200 rpm in a water bath maintained at 25 ± 0.1 °C.

2.4.2. Multi-batch titrations of aluminium chloride with potassium hydroxide at 90 °C

High temperature and drop-wise addition of alkali were applied in the series **AMK1** of the multi-batch titration of aluminium chloride with potassium hydroxide at elevated temperature in order to increase the homogeneity of hydrolysed aluminium solutions (elimination of local disturbances due to high strength and concentration of alkali which leads to the formation of partly insoluble amorphous aluminium hydroxide even at low pH values).

Preparation of the series AMK1. Aliquots of 24 ml of stock $AlCl_3$ solution in water (1 mol/L) were placed in Erlenmeyer thermo-resistant plastic flasks (150 ml). All aliquots were measured and delivered using a high-precision Eppendorf EDOS 5222 liquid sampling unit. Calculated aliquots of deionised water were added to the aluminium solution in the flasks so to adjust the total volume (including the ongoing alkali addition) to 120 ml. Solutions in the flasks were heated to 90 ^{0}C for 15-30 min and a pre-defined aliquot of alkali was added once for solutions with target hydrolysis ratio $h \leq 1.0$ and intensively stirred. For the pre-heated samples with the target $h > 1.0$, 23.39 ml of KOH (1.026 M) were added immediately with intensive stirring to reach the hydrolysis ratio h=1.0 first. The resulting solution remained clear and free of insoluble matter. After this, another pre-calculated portion of alkali was added drop-wise to each solution with the target $h > 1.0$ (the drop volume - 0.2 ml, the time interval between drops – 5 to 20 s depending on the volume of each aliquot: the smaller the aliquot, the longer the time interval between titrant additions). The time when the last drop of alkali was added was then recorded and used as a start point of the real-time experiment. The Erlenmeyer flasks containing aluminium solutions hydrolysed to different hydrolysis ratios were then placed back in the Grant open-top water bath with a lid and kept at 90 °C during the whole experiment. Shaking of the samples at 200 rpm was also provided.

The aliquots of the reagents and the final hydrolysis ratios of the samples for the series AMK1 of the multi-batch titration of aluminium chloride with potassium hydroxide are listed in Table 2.1. The concentrations of stock solutions were as follows: $AlCl_3$ solution (1.0 mol/L); KOH solution (1.026 mol/L, volumetric standard, as purchased); HCl solution (1.008 mol/L, volumetric standard, as purchased) and distilled, deionised water.

Table 2.1. Preparation of the series AMK1 of multi-batch titration of aluminium chloride with potassium hydroxide at 90 °C

Sample No	V[Al], ml	h=[H^+]/[Al]	V(HCl),ml	V(H_2O), ml
1	24	-1	23.81	72.19
2	24	-0.5	11.90	84.10
3	24	0	0.00	96.00
Sample No	**V[Al], ml**	**h=[OH]/[Al]**	**V(OH), ml**	**V(H_2O), ml**
4	24	0.1	2.34	93.66
5	24	0.25	5.85	90.15
6	24	0.5	11.70	84.30
7	24	0.75	17.54	78.46
8	24	1	23.39	72.61
9	24	1.25	29.24	66.76
10	24	1.5	35.09	60.91
11	24	1.75	40.94	55.06
12	24	2	46.78	49.22
13	24	2.1	49.12	46.88
14	24	2.2	51.46	44.54
15	24	2.3	53.80	42.20
16	24	2.4	56.14	39.86
17	24	2.5	58.48	37.52
18	24	2.6	60.82	35.18
19	24	2.7	63.16	32.84
20	24	2.8	65.50	30.50
21	24	2.9	67.84	28.16
22	24	3	70.18	25.82
23	24	3.5	81.87	14.13
24	24	4	93.57	2.43

In order to conduct real-time experiments, time gaps between samples did not exceed 3 min. Samplings and measurements at specified real-time intervals (0, 3, 6, 12, 24 and 48 hours) were made in such a way so as to maintain the equal time gap between samples. The sampling and measurement at '0' hours was after 5 min of stirring of as-prepared samples.

Sampling and measurements during the real-time multi-batch titration of $AlCl_3$ with KOH at 90 °C (Series AMK1). The described design of the multi-batch titrations enabled the sampling procedures and measurements to be carried out in real-time mode. The list of samplings and measurements in the multi-batch series is presented in Table 2.2.

The value of pH of each sample in the multi-batch series was measured at time intervals of 1-2 s and the results were accumulated during 1.5-2 min until pH equilibration. 10 ml of each sample was then taken for spray-freezing procedure (described below) for instant termination of any solution reactions; 3 or 4 ml of each sample at each sampling time (except for 0 and 1 hours) was taken for centrifugation and further dynamic light scattering measurements (described in Section 2.6); 3 ml was taken from each sample to measure ^{27}Al NMR spectra as described in Section 2.10.

Table 2.2. List of the time-resolved sampling and measurements of the series AMK1

Sampling time, hours	Measurements	Sampling
0	pH, NMR	Spray-freezing
3	pH, NMR, DLS	Spray-freezing
6	pH, NMR, DLS	Spray-freezing
12	pH, DLS	Spray-freezing
24	pH, NMR, DLS	Spray-freezing
36	pH, DLS	Spray-freezing
48	pH, NMR, DLS	Spray-freezing

Possible alterations of the processes in the multiple batches upon decreasing of their volume after samplings were averted using slowing of the shaking rate of the batches in the water bath from 220 rpm down to 200 rpm, 180 rpm etc. by 20 units of shaking rate after each sampling.

2.4.3. Multi-batch titrations of zirconium solutions with different alkalis at 90 °C

In the case of the experiments with zirconium solutions, the procedure used to produce series of multi-batch titrations at high temperature was similar to that described in Section 2.3.3. The list of multi-batch experiments carried out is shown in Table 2.3. The experimental blocks or series listed in Table 2.3 were designed to enable variation in alkali (KOH or $KHCO_3$), or added anion (acetate or sulphate) or complexing agent (glycine) as well the concentration of the added agent (for glycine). All other parameters including temperature, zirconium concentration, ionic strength, type and concentration of alkali were kept the same for all series to enable their comparison.

Table 2.3. The list of multi-batch titrations at high temperature conducted with Zr-ion solutions

Experiment number	[Zr], mol/L	Titrant for h>0	Temperature	Number of samples	h range	Time span, hours	Added reagents
ZHCO3	0.2	$KHCO_3$	90°C	26	-1.5 – 4	48	-
ZOH	0.2	KOH	90°C	21	-1.5 – 4	48	-
ZOHGly1:2	0.2	KOH	90°C	21	-1.5 – 4	48	Glycine, 0.4 mol/L (Zr:Glycine=1:2)
ZOHGly1:1	0.2	KOH	90°C	21	-1.5 – 4	48	Glycine, 0.2 mol/L (Zr:Glycine=1:1)
ZOHGly2:1	0.2	KOH	90°C	21	-1.5 – 4	48	Glycine, 0.1 mol/L (Zr:Glycine=2:1)
ZOHAc	0.2	KOH	90°C	21	-1.5 – 4	48	CH_3COO^- (CH_3COOH or $NaCH_3COO$) Ac^-:Zr=1:1
ZOHSO4c	0.2	KOH	90°C	21	-1.5 – 4	48	(SO_4^{2-}) (H_2SO_4 or K_2SO_4); SO_4^{2-}:Zr=1:1

Preparation of the series ZHCO3. The titrants used in this series were HCl (1.6 M) and $KHCO_3$ (0.8 and 1.6 M). A 1.6 M HCl solution (250 ml) was prepared by diluting an aliquot of 34.33 ml of concentrated HCl (37 wt.%) in deionised water in a 250 volumetric flask. A

500 ml of $KHCO_3$ 1.6 M and 0.8 M solutions were prepared using 80.096 g and 40.048 g of solid $KHCO_3$ correspondingly diluted in deionised water with final volume adjusted in 500 ml volumetric flasks. $ZrOCl_2$ (0.8 M) stock solutions (500 and 250 ml volume) were prepared by weighing of 129 g and 64.5 g of solid $ZrOCl_2*8H_2O$ correspondingly, subsequent dissolution in deionised water and final adjustment of the volume in 500 and 250 ml volumetric flasks.

The list of the samples and their preparation of the series **ZHCO3** is shown in Table 2.4. The total volume of each sample was 100 ml. The final concentration of zirconium in each sample solution was 0.2 mol/L.

Table 2.4. The list of the samples of the series **ZHCO3** and their preparation

Sample No	$V_{aliquot}(Zr)$, ml	Hydrolysis ratio	$V_{aliquot}(HCl)$, ml	C(HCl), mol/L	$V(H_2O)$, ml
1	25	-1.5	18.75	1.6	56.25
2	25	-1	12.50	1.6	62.50
3	25	-0.8	10.00	1.6	65.00
4	25	-0.6	7.50	1.6	67.50
5	25	-0.4	5.00	1.6	70.00
6	25	-0.2	2.50	1.6	72.50
7	25	0	0.00	0.0	75.00
Sample No	**$V_{aliquot}(Zr)$, ml**	**Hydrolysis ratio**	**$V_{aliquot}(KHCO_3)$, ml**	**C($KHCO_3$), mol/L**	**$V(H_2O)$, ml**
8	25	0.112	2.80	0.8	72.20
9	25	0.224	5.60	0.8	69.40
10	25	0.336	8.40	0.8	66.60
11	25	0.448	11.20	0.8	63.80
12	25	0.560	14.00	0.8	61.00
13	25	0.672	16.80	0.8	58.20
14	25	0.784	19.60	0.8	55.40
15	25	0.896	22.40	0.8	52.60
16	25	1.008	25.20	0.8	49.80
17	25	1.120	28.00	0.8	47.00
18	25	1.200	30.00	0.8	45.00
19	25	1.400	35.00	0.8	40.00
20	25	1.679	41.98	0.8	33.02
21	25	1.800	45.00	0.8	30.00
22	25	2.000	50.00	0.8	72.20
23	25	2.239	27.99	1.6	47.01
24	25	2.500	31.25	1.6	43.75
25	25	3.000	37.50	1.6	37.50
26	25	4.000	50.00	1.6	25.00

Stock solution concentrations: [$ZrOCl_2$]=0.8 mol/L; [HCl]=1.6 mol/L; [$KHCO_3$]=0.8 and 1.6 mol/L.

For the preparation of batch samples, 26 aliquots of 25 ml of the stock solution of zirconyl chloride (0.8 M) were dispensed in plastic Erlenmeyer labelled flasks (150 ml). Calculated

amounts of deionised water were added to each flask in order to obtain a final solution volume (including the ongoing addition of titrant) of 100 ml. The content of the flasks was stirred after the addition of titrant using a vortex stirrer in order to obtain homogeneous solutions. Then a stirrer bar was added and pH values were measured until stabilisation (1-2 min) stirring the solution with a magnetic stirrer before putting each flask into a 90°C covered water bath (Grant water bath) where they were shaken with a rate of 200 rpm during the 48 hours of experiment.

Preparation of the series ZOH. The series **ZOH** of multi-batch titrations of Zr-ions with KOH (1.6 M) ('positive' hydrolysis ratios) and HCl (1.6 M) ('negative' hydrolysis ratios) were carried out similarly to the series **ZHCO3**. The total volume of each sample was 100 ml. The list of the samples is given in Table 2.5.

Table 2.5. The list of the samples of the series **ZOH** and their preparation

Sample No	$V_{aliquot}$(Zr), ml	Hydrolysis ratio	$V_{aliquot}$(HCl), ml	V(H_2O), ml
1	25	-1.5	18.75	56.25
2	25	-1	12.50	62.50
3	25	-0.8	10.00	65.00
4	25	-0.6	7.50	67.50
5	25	-0.4	5.00	70.00
6	25	-0.2	2.50	72.50
7	25	0	0.00	75.00
Sample No	**$V_{aliquot}$(Zr), ml**	**Hydrolysis ratio**	**$V_{aliquot}$($KHCO_3$), ml**	**V(H_2O), ml**
8	25	0.2	2.50	72.50
9	25	0.4	5.00	70.00
10	25	0.6	7.50	67.50
11	25	0.8	10.00	65.00
12	25	1	12.50	62.50
13	25	1.2	15.00	60.00
14	25	1.4	17.50	57.50
15	25	1.6	20.00	55.00
16	25	1.8	22.50	52.50
17	25	2	25.00	50.00
18	25	2.5	31.25	43.75
19	25	3	37.50	37.50
20	25	4	50.00	25.00

Stock solution concentrations: [$ZrOCl_2$]=0.8 mol/L; [HCl]=1.6 mol/L; [KOH]=1.6 mol/L

Preparation of the series ZOHGly1:2, ZOHGly1:1, ZOHGly2:1. The series **ZOHGly** are the blocks of experiment where the ratio of zirconium-ions and glycine was varied from Zr:Gly=1:2 for **ZOHGly1:2**; Zr:Gly=1:1 for **ZOHGly1:1** to Zr:Gly=2:1 for **ZOHGly2:1**. The stock solutions of zirconium-ions and glycine for these series containing 0.8 mol/L of zirconium and a concentration of glycine corresponding to each series ratio (1.6 mol/L; 0.8

mol/L; 0.4 mol/L for **ZOHGly1:2**, **ZOHGly1:1, ZOHGly2:1** accordingly) were prepared.

Potassium hydroxide (1.6 M) and hydrochloric acid (1.6 M) solutions were used as a titrant for the multi-batch series **ZOHGly**. The procedure of the multi-batch titrations was similar to that described for the series **ZHCO3** and **ZOH** except for the addition of glycine solution. The order of the addition was the following: Zr solution; glycine solution; deionised water; titrant (KOH or HCl). The samples in the series **ZOHGly** are listed in Table 2.6.

Table 2.6. The list of the samples and the preparation in the series **ZOHGly1:2; 1:1; 2:1**5

Sample No	V(Zr), ml	Hydrolysis ratio	V(HCl), ml	V(Glycine), ml	$V(H_2O)$, ml
1	25	-1.5	19.87	25	30.13
2	25	-1	13.25	25	36.75
3	25	-0.8	10.60	25	39.40
4	25	-0.6	7.95	25	42.05
5	25	-0.4	5.30	25	44.70
6	25	-0.2	2.65	25	47.35
7	25	0	0.00	25	50.00
Sample No	**V(Zr), ml**	**Hydrolysis ratio**	**V(KOH), ml**	**V(Glycine), ml**	**$V(H_2O)$, ml**
8	25	0.2	2.50	25	47.50
9	25	0.4	5.00	25	45.00
10	25	0.6	7.50	25	42.50
11	25	0.8	10.00	25	40.00
12	25	1	12.50	25	37.50
13	25	1.2	15.00	25	35.00
14	25	1.4	17.50	25	32.50
15	25	1.6	20.00	25	30.00
16	25	1.8	22.50	25	27.50
17	25	2	25.00	25	25.00
18	25	2.5	31.25	25	18.75
19	25	3	37.50	25	12.50
20	25	4	50	25	50

Stock solution concentrations: $[ZrOCl_2]$=0.8 mol/L; [HCl]=1.6 mol/L; [KOH]=1.6 mol/L; [Glycine]=0.4 mol/L (**ZOHGly2:1**); 0.8 mol/L (**ZOHGly1:1**) and 1.6 mol/L (**ZOHGly1:2**).

Preparation of the series ZOHSO4. For the series **ZOHSO4** of multi-batch titrations of Zr-ions with KOH at the presence of sulphate-ions ($Zr:SO_4^{2-}$=1:2) 500ml of 0.64 M K_2SO_4 solution was prepared heating gently on a hotplate (40-50 ^{0}C) 55.76 g of solid K_2SO_4 added to ca. 350 ml of deionised water. The volume was then made up to 500 ml after transfer of the cooled down solution into a 500 ml volumetric flask and volume adjustment with deionised water. In order to prepare the stock solution of H_2SO_4 (3.2 M), a standardised 5.144 M H_2SO_4 solution was first prepared, mixing gently 125 ml of concentrated H_2SO_4 (98 wt%) and 275 ml of deionised water in a 500 ml glass beaker cooled with an ice bath. The volume of the solution cooled down was then made up to 500 ml with deionised water in a 500 ml volumetric flask and the initial solution obtained was titrated with a 0.502 M NH_4OH volumetric standard solution. 500 ml of 3.2 M H_2SO_4 stock solution was then prepared by

diluting an aliquot of 155.5 ml of the standardised initial solution (5.144 M) in deionised water.

In order to avoid early precipitation of insoluble zirconium sulphate the following procedure was used. In the 150 ml Erlenmeyer plastic flasks No 1-6 the aliquots of K_2SO_4 (1.6 M), HCl (1.6 M) and water were added. In the flask of the sample No 7 (no titrant) only an aliquot of K_2SO_4 was added as shown in Table 2.7. In the flasks No 8-20 aliquots of H_2SO_4 and water aliquots were added. The excess of H_2SO_4 in the samples No 8-20 was then compensated with the calculated amount of KOH (on top of

Table 2.7. The list of the samples and their preparation in the series **ZOHSO4**

Sample No	V(Zr), ml	Hydrolysis ratio	V(HCl), ml	$V(K_2SO_4)$, ml	$V(H_2O)$, ml
1	12.5	-1.5	18.75	62.5	6.25
2	12.5	-1	12.50	62.5	12.50
3	12.5	-0.8	10.00	62.5	15.00
4	12.5	-0.6	7.50	62.5	17.50
5	12.5	-0.4	5.00	62.5	20.00
6	12.5	-0.2	2.50	62.5	22.50
7	12.5	0	0.00	62.5	25.00
Sample No	**V(Zr), ml**	**Hydrolysis ratio**	**V(KOH), ml**	**$V(H_2SO_4)$, ml**	**$V(H_2O)$, ml**
8	12.5	0.2	21.00	12.5	54.00
9	12.5	0.4	22.00	12.5	53.00
10	12.5	0.6	23.00	12.5	52.00
11	12.5	0.8	24.00	12.5	51.00
12	12.5	1	25.00	12.5	50.00
13	12.5	1.2	26.00	12.5	49.00
14	12.5	1.4	27.00	12.5	48.00
15	12.5	1.6	28.00	12.5	47.00
16	12.5	1.8	29.00	12.5	46.00
17	12.5	2	30.00	12.5	45.00
18	12.5	2.5	32.50	12.5	42.50
19	12.5	3	35.00	12.5	40.00
20	12.5	4	40.00	12.5	35.00

Stock solution concentrations: $[ZrOCl_2]$=0.8 mol/L; [HCl]=1.6 mol/L; [KOH]=1.6 mol/L; $[K_2SO_4]$=0.64 mol/L; $[H_2SO_4]$=3.2 mol/L

the amount required for the hydrolysis reaction to proceed). The flasks were then heated up in the 90°C water bath for 10 minutes before adding the aliquots of the titrants. $ZrOCl_2$ solution aliquots were then added to the flasks 1 to 7, and $ZrOCl_2$ and KOH aliquots were added quickly to the flasks 8 to 20 and the total volume of each sample was made up with deionised water to 100 ml.

Preparation of the series ZOHAc. For this series of experiments the same titrants were used as for **ZOH, ZrHCO3, ZrOHGly and ZrOHSO4**. A 1 M CH_3COONa solution (250 ml) was

prepared using 34.02 g of dry salt diluted into deionised water. A 3.67 M CH_3COOH solution (500 ml) was prepared using a 100 ml aliquot of concentrated CH_3COOH (>99 wt%) diluted in deionised water. The stock solution of CH_3COOH was then standardised similarly to H_2SO_4 stock solution in the series **ZOHSO4**. A 3.2 M CH_3COOH solution (500) was then prepared using a 436 ml aliquot of the standardised solution. The procedure used to prepare the samples of the series **ZOHAc** was the same as that for **ZOHSO4** except for using sodium acetate instead of potassium sulphate and acetic acid instead of sulphuric acid. The list of the samples of the series ZrOHAc is shown in Table 2.8.

Table 2.8. The list of the samples and the preparation of the series **ZOHAc**.

Sample No	V(Zr), ml	Hydrolysis ratio	V(HCl), ml	V(CH_3COONa), ml	V(H_2O), ml
1	25	-1.5	18.75	20	36.25
2	25	-1	12.50	20	42.50
3	25	-0.8	10.00	20	45.00
4	25	-0.6	7.50	20	47.50
5	25	-0.4	5.00	20	50.00
6	25	-0.2	2.50	20	52.50
7	25	0	0.00	20	55.00
Sample No	**V(Zr), ml**	**Hydrolysis ratio**	**V(KOH), ml**	**V(CH_3COOH), ml**	**V(H_2O), ml**
8	25	0.2	7.50	10	57.50
9	25	0.4	8.75	10	56.25
10	25	0.6	10.00	10	55.00
11	25	0.8	11.25	10	53.75
12	25	1	12.50	10	52.50
13	25	1.2	13.75	10	51.25
14	25	1.4	15.00	10	50.00
15	25	1.6	16.25	10	48.75
16	25	1.8	17.50	10	47.50
17	25	2	18.75	10	46.25
18	25	2.5	21.88	10	43.12
19	25	3	25.00	10	40.00
20	25	4	31.25	10	33.75

Stock solution concentrations: [$ZrOCl_2$]=0.8 mol/L; [HCl]=1.6 mol/L; [KOH]=1.6 mol/L; [CH_3COONa]=1.0 mol/L; [CH_3COOH]=3.2 mol/L

Sampling in the series with Zr-ions. For all of the series with Zr-ions sampling took place at the following times: 3, 6, 12, 24 and 48 hours after initiation of reaction (except for pH measurements which were also done at '0' hours at the start of experiment). For each of those samplings two aliquots of 10 ml were taken from each flask: 10 ml for solution characterisation, and 10 ml for spray-freeze-drying (for the description of the technique see Section 2.8). The timing and the list of performed samplings and measurements are given in Table 2.9.

Table 2.9. Sampling and measurements performed in all the series with Zr-ions

Sampling time, hours	Measurements	Sampling
0	pH	-
3	pH, DLS, XO assay*	Spray-freezing
6	pH, DLS, XO assay*	Spray-freezing
12	pH, DLS, XO assay*	Spray-freezing
24	pH, DLS, XO assay*	Spray-freezing
48	pH, DLS, XO assay*	Spray-freezing

* - Xylenol Orange (XO) assay and DLS measurements for the series **ZOHGly1:2** and **ZOHSO4c** were performed only at 24 and 48 hours samplings.

The pH of each sample was measured each time after sampling in 25 ml labelled plastic beakers. The pH measurements were conducted at 2 s time intervals until equilibration. After each sampling the samples for DLS and UV-Vis measurements (Xylenol Orange assay) were prepared (as described in Sections 2.15 and 2.16).

2.5. UV-Vis spectroscopy

UV-Vis spectroscopy along with potentiometry is one of the earliest and most frequently used methods for speciation studies of metal ions and their complexes [1].

2.5.1. Principles and instrumentation of UV-Vis spectroscopy

Spectroscopy is the measurement and analysis of electromagnetic radiation absorbed, scattered, or emitted by atoms, molecules, or other chemical species. The absorption and emission of electromagnetic radiation is associated with changes in energy states of the species. UV-Vis spectrophotometry uses ultraviolet and visible electromagnetic radiation in the range from ca. 200 nm to 800 nm to energetically promote valence electrons in a molecule to an excited energy state. The UV-Vis spectrophotometer measures the absorption of energy by promoted electrons at a specific wavelength or over a range of wavelengths [7].

The absorbance of a solution increases as attenuation of the beam increases. Absorbance A is directly proportional to the path length, b, and the concentration, c, of the absorbing species. Beer's Law states that:

$$A = \varepsilon bc \qquad \textbf{(2.5)}$$

where ε is a constant of proportionality, called the molar absorptivity (or extinction coefficient).

Only chemical species having chromophore groups (functional groups which are responsible for the absorption of light in the UV-Vis region, examples include aromatics,

compounds with multiple bonds, heterocycles and coordination compounds) can be analysed using UV-Vis spectroscopy. This implies that in order to analyse UV-Vis transparent substances, they need to be 'derivatised' with reagents containing chromophore groups. One of the largest families of analytical methods is based on the formation of complexes between metal ions and organic chromophores (organic reagents) that enables quantification of metal ions using UV-Vis spectroscopy [7]. A large number of organic reagents has been proposed [13] which allow for determination of practically all metal ions and metalloids in the Periodic Table.

Advantages of spectrophotometric methods of metal ion determination are: (*1*) it is rapid in comparison with volumetric and gravimetric methods; (*2*) minimum sample preparation is required; (*3*) small amount of sample; (*4*) medium sensitivity; (*5*) relatively high precision and accuracy; (*6*) simplicity of analytical procedure and ease of use of equipment.

Disadvantages include possible interferences from foreign metal ions and anions and chromophores other than organic reagents.

The reactions used in the spectrophotometric analysis in the UV-Vis region require that absorbing species should be stable for sufficient time to permit accurate measurement to be made. Colloidal and insoluble material also must not develop due to side reactions like hydrolysis and complexation with anions.

The general arrangement of the components of a single-beam UV-Vis spectrometer (most typical setup) is shown in Fig. 2.4. The setup consists of radiation source, monochromator, sample cell compartment, detector and output device.

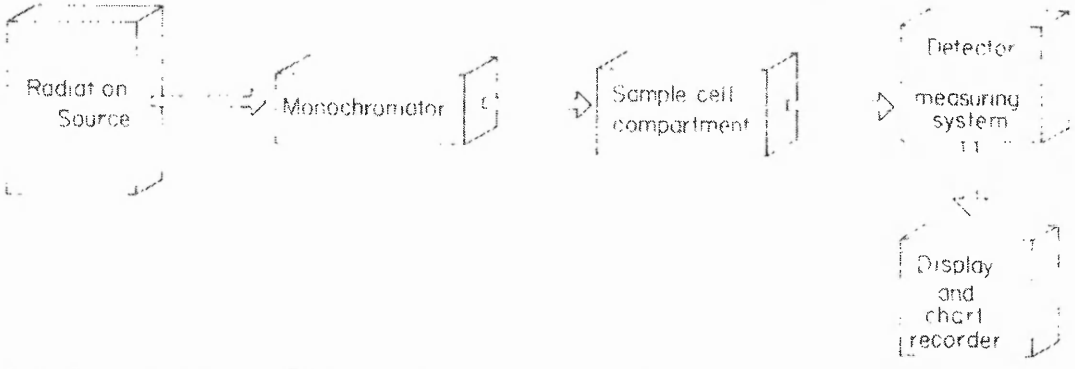


Fig. 2.4. General scheme of the UV-Vis spectrophotometer

In this work a UNICAM UV-Vis single-beam spectrophotometer with a beam split by a cross-section mirror was used. Two sources are supplied with the spectrophotometer: deuterium arc source for UV-range 200-325 nm and tungsten-halogen lamp for measurements in the 325-800 nm wavelengths. The spectrophotometer contains a diffraction grating as a monochromator, double cell compartment with reference and sample cell positions, photomultiplier detector and is connected to a PC with Vision32 UV-Vis software. The

spectrophotometer allows for both spectrum scanning and fixed wavelength measurements. Zeroing and baseline correction of the blank sample was carried out for each sample. Plastic UV-Vis transparent cuvettes with 1 cm path length were used throughout UV-Vis experiments.

2.5.2. Organic reagent assays for speciation studies of aluminium and zirconium

Literature analysis suggests two major trends in the application of UV-Vis spectrophotometry for the studies of Al and Zr speciation. Both employ an application of complexation of these metal ions with organic reagents. The first approach utilises ligand exchange where organic reagent is replaced by hydroxyl-ions in hydrolysis-condensation reactions or other ligands of interest. Examples include UV-Vis studies of Al complexation with Eriochrome Black S [14], Chrome Azurol S [15], Pyrocatechol Violet [16], and several other ligands [13,17]. Examples with Zr include a work with Xylenol Orange as an organic reagent and some other reagents [18]. A recent paper [19] reports successful implementation of a very sensitive fluorescent probe (pyrenecarboxylic acid) for the studies of hydrolytic polymerisation in aqueous solutions of zirconium ions.

The primary limitation of the method described above is that it is confined to monomeric species mostly. Complexation of organic reagents with polynuclear Al and Zr species is very complicated due to a number of species present simultaneously and due to competition from hydrolysis-condensation reactions and other processes (e.g. dissolution of polynuclear species). Another limitation is a possibility of colloidal phase formation with the increase of pH that makes UV-Vis measurements unreliable and at times impossible.

The second approach to the studies of hydrolysis-condensation products of Al and Zr ions is based on kinetic measurements. In this approach hydrolysis-condensation of metal ion is conducted first and then a buffer containing a suitable organic reagent is added. Kinetic curve of the formation of a complex 'metal ion – organic reagent' is recorded. On the basis of the kinetic analysis it is possible to distinguish between monomeric, small oligomeric and larger polymeric hydrolysed metal ions. This method was successfully applied in so called 'Ferron' method [20]. However, there are very few examples of utilisation of this approach in the studies of aluminium speciation. The high stability of the hydroxyl-bridges in zirconium polycations makes it virtually impossible to break these bonds even with quite strong chelators [6]. To author's knowledge, no kinetic-based organic reagent assay has been reported for zirconium polycations so far.

The kinetic-based organic reagent assays have been criticised for several reasons. These methods do not provide direct information on the formation of polynuclear products of metal ion hydrolysis, conclusions being made on the basis of indirect kinetic measurements. Thus, it is hard to discern between species of different nuclearities simultaneously present in solution that is the case for many metal ions including aluminium and zirconium [20]. The

method provides only qualitative and at times very tentative information on the distribution of the species in solutions of hydrolysed metal ions.

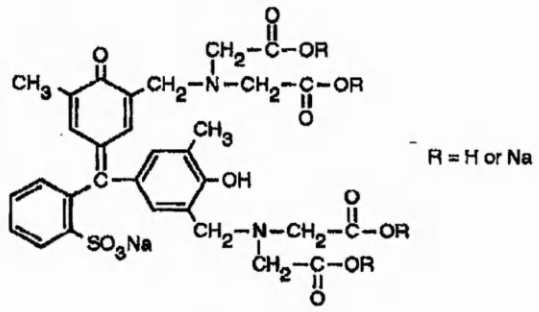
2.5.3. Xylenol Orange organic reagent assay for zirconium-ions

In this workit was intended to employ high stability of nano-sized zirconium polycations (light scattering in the visible region of spectrum is insignificant for such species) for the development of a new UV-Vis organic reagent assay aimed to simultaneous studies of zirconium polymerisation through quantitative complexation with the organic reagent and kinetic investigations involving multi-batch experiments.

The choice of reagent. According to literature [13] there are several rules to be followed when choosing an organic reagent for quantitative assays in UV-Vis spectroscopy: (*1*) high molar absorptivity (ε) for the reaction of organic reagent and analyte; (*2*) high contrast (a difference between maximum wavelength of reagent absorption and reagent-analyte absorption) of the reaction; (*3*) exactly known stoichiometry of the reaction with analyte; (*4*) chemical stability of organic reagent in solution; (*5*) rapid and reproducible reaction; (*6*) selectivity or specificity of the reagent-analyte reaction; (*7*) solvent compatibility of reagent and reagent-analyte complex; (*8*) linearity of the calibration.

In addition to the listed rules of choice of organic reagent, it was attempted to find an organic reagent which reacts with zirconium at the ratio Zr:organic reagent 1:1. This is an important requirement when working with zirconium polymers, since higher stoichiometric ratios of the complex would be hardly achieved due to steric effects. A reagent with polar non-complexing functional groups was sought to ensure solubility of the complex with Zr polymers in aqueous medium. It was important to find a reagent with well-established properties and known complexation with Zr-ions able to form complexes at very low pH.

One of the reagents satisfying all the requirements listed above is Xylenol Orange 3,3'-Bis[N,N-bis(carboxymethyl)aminomethyl]-o-cresolsulfonphthalein, disodium salt. The formula of the reagent is following (R=Na) [13, 18]:



This is a strong chelating organic reagent with highly polar non-complexing sulphonic group. The reaction of Xylenol Orange (XO) with zirconium-ions in dilute solutions is well established [18] and highly recommended for the analytical use. For instance, this reagent has

been proposed in the work [21] as a reference method for quantitative determination of Zr-ions in rocks after autoclave acidic digestion. The analytical reaction of XO with Zr-ions is characterised by high contrast (λ(XO)=455 nm; λ(XO:Zr)=550 nm), high sensitivity (LOD=10^{-7} mol/L), high stability of the soluble stoichiometric Zr:XO=1:1 complex and rapid equilibration of the system (in all cases less then 15 min is required for full colour development). XO forms complex with zirconium monomeric ions in the range of pH from 0 to 10 with optimum at acidic conditions (pH=1-2). The calibration graph is linear in the range of two orders of magnitude.

Electronic absorption spectra of Xylenol Orange solutions were acquired using a UNICAM UV-Vis spectrometer and the Vision32 software in the range of wavelengths 400-700 nm with a scan speed of 120nm/min, a bandwidth of 2.0 nm and a data interval of 0.5 nm. Baseline correction was made with a blank solution of deionised water with pH corresponding to each sample solution in question.

Spectra of pure Xylenol Orange solutions at different pH were studied as following. All solutions were prepared with the same concentration of Xylenol Orange ($1*10^{-4}$ M) at different pH by diluting 2.5 ml of $1*10^{-3}$ M Xylenol Orange stock solution (stock solution was prepared by dissolution of 0.1956 g of the reagent in deionised water and the final volume adjusted to 100 ml in the volumetric flask) with solutions of known pH up to a volume of 20 ml in a 25 ml plastic beakers using a magnetic stirrer and measuring the pH in order to adjust it to a chosen value in the range pH=0-7. After transferring the solutions to 25 ml volumetric flasks, the volume was made up to 25 ml with the buffer solution of the same pH (pH of each 'buffer' solution was preliminary adjusted with HCl, KOH and deionised water). A blank solution was prepared without addition of Zr solution at the conditions identical to the described above.

In order to obtain a calibration curve for quantitative determination of zirconium-ions with Xylenol Orange, 6 standard solutions of zirconium were prepared ($5*10^{-6}$; $1*10^{-5}$; $2*10^{-5}$; $3*10^{-5}$; $4*10^{-5}$ and $5*10^{-5}$ mol/L) from a stock reference solution of zirconium (Aldrich, $1*10^{-3}$ mol/L in 2M HCl). Corresponding aliquots of the stock solution of zirconium were added into 25 ml beakers, 0.25 ml of the stock solution of Xylenol Orange ($1*10^{-3}$ mol/L) and 10 ml of preliminary prepared HCl solution with pH=1.0 were added to each beaker. The pH value in each beaker was measured with pH-meter and adjusted to pH=1.0 with solutions of HCl and KOH. Solutions containing a complex of zirconium and Xylenol Orange at pH=1.0 were transferred into 25 ml volumetric flasks and the final volume of each solution was adjusted with solution of HCl (pH=1.0). Prepared solutions were left for 15 min in order to evolve the colour in the system. The electron spectra of the standard solutions of zirconium and Xylenol Orange were acquired under the conditions described above. For the calibration curve the values of absorbance at λ=560 nm were used, the chosen wavelength corresponds to

the maximum of the spectra of zirconium-Xylenol Orange standard solutions.

The following procedure was used for the obtaining of UV-Vis spectra of zirconium-Xylenol Orange in the systems containing hydrolysed zirconium-ions. For each sample of zirconium two preliminary solutions were prepared (Solutions A and B). For the Solution (A) a 0.1ml aliquot of the sample was taken diluted it with 9.9 ml HCl solution (pH=1.0). For the Solution (B) a 0.25 ml aliquot of each Solution (A) of dilute zirconium sample was taken into a separate 25 ml plastic beaker and mixed up with 1 ml of $1*10^{-3}$ M Xylenol Orange stock solution before adding 8.75 ml of HCl solution (pH=1.0) giving total volume of solution 10 ml. The final set of Solutions (B) for each zirconium sample was stirred on the magnetic stirrer for 3-5 min and electron spectra of the solutions were acquired 10 min after their preparation under the conditions identical to the described above for pure Xylenol Orange solutions. As a blank solution, $1*10^{-4}$ M Xylenol Orange solution with pH=1.0 was used.

2.6. Dynamic light scattering

A number of methods are available for particle size determination in polymer and colloidal systems among which several groups can be distinguished on the basis of the main principle of measurement. These groups include most powerful subatomic particle scattering methods (small angle X-ray and neutron scattering), light scattering methods in the UV-Vis spectral region (photon correlation spectroscopy, laser diffraction, turbidimetry), centrifugation methods (ultracentrifugation) and chromatographic methods (size exclusion chromatography, field flow fractionation) [22-25]. Due to ease of operation, relatively high speed and low cost per analysis light scattering methods are preferable. Photon correlation spectroscopy (alternatively, dynamic light scattering, or quasi-elastic light scattering) is one of the most sensitive methods in terms of lowest and widest particle sizes detected with this method. This method was chosen for particle characterisation of aqueous solutions of hydrolysed Al and Zr ions in the present work.

2.6.1. Principles and instrumentation of dynamic light scattering

Dynamic light scattering (DLS) method determines particle size by measuring the rate of diffusion of particles through a fluid [26]. The rate of diffusion depends on three factors: temperature, viscosity of fluid and particle size. If temperature and viscosity are known, the particle size as well as molecular weight of scattering species can be determined.

Diffusion of the particulate matter in fluid is caused by Brownian motion which arises from random collisions of particles due to thermal agitation. For a solution of a given viscosity and at a constant temperature the rate of diffusion described by diffusion coefficient D is inversely related to a particle size according to Stokes-Einstein equation [26]:

$$D = \frac{k_B T}{3\pi\eta d} \qquad \textbf{(2.6)}$$

where: k_B - Boltzmann constant (erg/°K)
T – temperature (°K)
η - diluent viscosity (poise)
d – equivalent particle diameter (cm)

DLS measurements are based on detecting scattered-light fluctuations in the interference pattern formed by laser light scattering from randomly moving particles and detected by a photomultiplier. DLS characterises particles by measuring the exact time scale of the random scattered light intensity fluctuations. In order to calculate the diffusion coefficient and, therefore the particle size (Eq. 2.5) the changing light intensity signal must be mathematically transformed using an autocorrelation function (ACF) which is defined as:

$$G(\tau) = < I(t) \times I(t+\tau) > \quad \textbf{(2.7)}$$

where $G(\tau)$ – an autocorrelation function
$I(t)$ – intensity detected at time t
$I(t+\tau)$ – intensity detected at time $t+\tau$
τ - delay time
$< >$ - quantity enclosed is a time average

If the molecules or particles in solution are the same size (monodisperse) and shape, the ACF of the scattered-light intensity is a single decaying potential:

$$G(\tau) \propto e^{-2\Gamma\tau} \quad \textbf{(2.8)}$$

The decay constant of the exponential is Γ which is equal to DK^2, where D – the diffusion coefficient and K:

$$K = \frac{4\pi n}{\lambda} \sin\left(\frac{\theta}{2}\right) \quad \textbf{(2.9)}$$

where n – refractive index of the solvent
λ - laser wavelength in vacuo (m)
θ - angle of scattering intensity measurement

For polydisperse samples the ACF is the sum of the exponentials for each component:

$$G(\tau) \propto \sum a_i e^{-2\Gamma_i(d_i)\tau} \quad \textbf{(2.10)}$$

where a_i – the contribution to the total scattered-light intensity of particles of size d_i.

For the determination of the ACF the N4Plus Coulter meter utilises 80 non-equally (logarithmically) spaced channels at each measurement angle for the detection of scattered-light intensity which maximise the information provided in the measurement. The resulting ACF is shown in Fig. 2.5 [27].

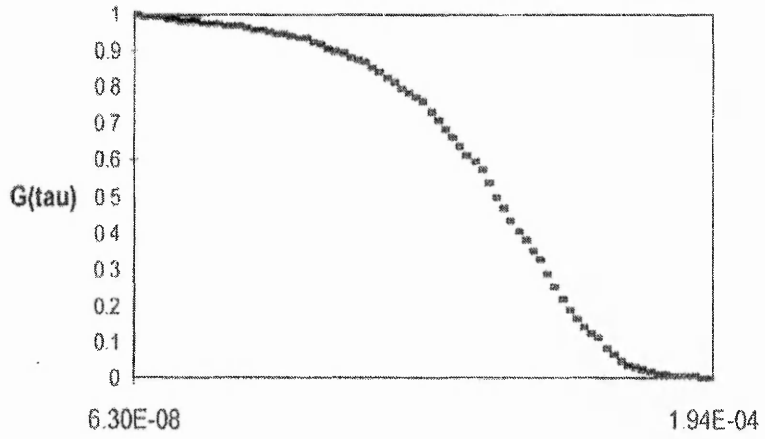


Fig. 2.5. The autocorrelation function (logarithmically spaced channels)

The block diagram of the N4Plus Coulter particle size meter is shown in Fig. 2.6.

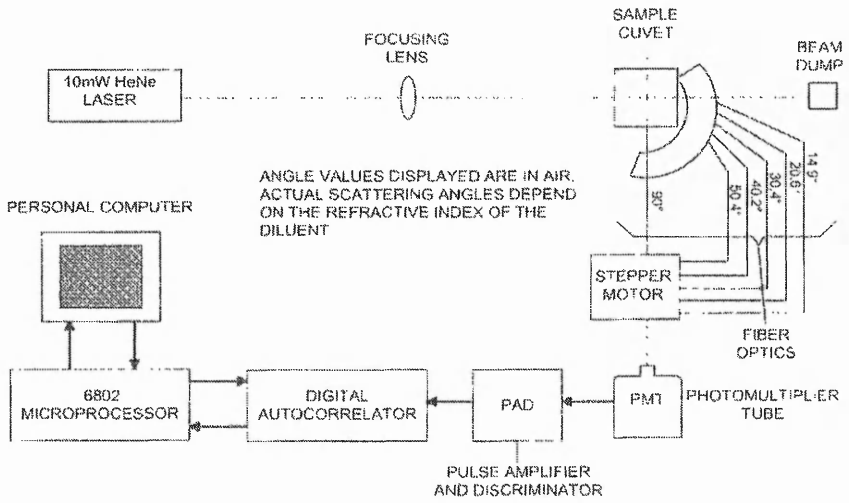


Fig. 2.6. Functional block diagram of the N4Plus DLS instrument [27].

In this instrument the light from He-Ne laser passes through a cuvette containing sample solution. Six fibre-optic receptors (corresponding to measurement angles of 11.1, 15.7, 23.0, 30.2, 62.5 and 90.0 degrees), stepper motor and photomultiplier define the angle of scattered light detection. Digital autocorrelator computes the ACF of the current pulses obtained from photomultiplier. In order to avoid missing a statistically significant number of pulses, the average counts per second detected from sample should be kept between $5*10^4$ and $1.5*10^6$. The resulting ACF is sent to the computer for further analysis and particle size distribution calculation using a Fortran program CONTIN. Analysis of the ACF also contains subtraction of the baseline from the sample data and calculation of the baseline error.

The program CONTIN allows for *unimodal* (single peak in particle size distribution) and *multimodal* distribution of particles in solution to be calculated. Unimodal analysis is a faster but less accurate method. It provides only a measure of the mean size of particles in the sample. Multimodal analysis allows for the extremely polydisperse systems to be characterised.

The CONTIN program that is also called a 'size distribution processor' (SDP) sorts the data from autocorrelator into separate bins (17 to 31 bins are possible) from which a particle size histogram is calculated. There is also one more bin specially assigned to the detection of dust presence in the sample. Standard deviation of the mean particle size in the unimodal analysis and of the particle sizes in the multimodal analysis is calculated as following [27]:

$$SD(d) = \left[\frac{\sum_i a_i (d_i - \bar{d})^2}{\sum a_i} \right]^{\frac{1}{2}} \qquad \textbf{(2.11)}$$

where $\bar{d}$ - the mean diameter of the particle distribution

d_i – the diameter corresponding to the ith bin.

a_i – the contribution to the total scattered-light intensity of particles of size d_i.

Standard deviation provides a good qualitative indication of the polydispersity of the sample, though it may be not strictly accurate for extremely polydisperse systems. The SDP analysis is not able to discern between peaks of particle distributions closer than factor of two of diameter ratio. In order to reach maximum reproducibility and correctness of particle size measurements, an adjustment of the measurement time at each angle is important. It is recommended to use longer measurement times at larger angles. It was found that the use of 240 s measurement time for scattering angle 30.2 degrees, 120 s for 62.5 degrees and 60 s for 90.0 degrees provides optimum of reproducibility and precision of measurements in highly polydisperse aqueous solutions of Al and Zr hydrolysed ions.

DLS measurements after analysis with the SDP program CONTIN can be displayed as intensity size distributions where the magnitude of each histogram bin's content is proportional to the percent of the total scattered intensity due to particles of the corresponding bin size. Another representation of size distribution diagram as 'weight distribution' (based on relative weight of particles of each size in a sample) is more useful than the intensity distribution. Weight distribution provides more correct representation of polydisperse systems due to a fact that scattering intensity is stronger from larger particles [26,27]. This may strongly skew intensity-based representation. Weight distribution is also independent from scattering angle.

The SDP program uses the Mie theory [26] to convert from intensity to weight distributions. In order to obtain exact solution of Mie equation [27], knowledge of the refractive index (a complex number) of particles is required along with the refractive index of solvent. For dielectric (transparent) particles, the imaginary part of the particle refractive index is zero and need not to be entered. If the refractive index of particles is unknown, the SPD program uses an approximate solution of the Mie equation that holds well over a wide variety of refractive indices [27]. Another limitation of Mie theory is that it cannot calculate strongly non-spherical particles. However, information about the shape of particles and its

deviation from spherical can be derived from the comparison of size distributions obtained at different scattering angles.

The measurement cell in the N4Plus is thermostated (temperature range 0 – 90 ± 0.1 °C). It is strongly recommended that longer equilibration times be used prior to measurement of particle size distributions in order to achieve better temperature equilibration throughout the sample in the cuvette and consequently more reproducible readings of the ACF and baseline. 10-30 min equilibration times were used depending on the type of experiment.

Since dust may have a strongly adverse effect on the results of DLS measurements, special care was taken in this work in order to eliminate dust particles from samples using high-speed centrifugation and nano-filtration of deionised water (solvent) with peristaltic pump and Whatman cellulose nano-filters (d_{pores}=200 nm).

The default range of the N4Plus Coulter submicron particle size meter is from 3 to 3000 nm. However, using a complex of appropriate measures, lower particle sizes were observed in the range down to 0.2-0.4 nm.

2.6.2. Dynamic light scattering. Experimental procedure

For strongly opaque (highly hydrolysed) samples of aqueous solutions of hydrolysed Al and Zr ions an aliquot 0.25 – 1.00 ml was added in the centrifuge tube of 5 ml and the total volume was adjusted to 5 ml with pH buffer (pH buffer here is an aqueous solution with pH value adjusted to a certain pH using dilute HCl and NaOH). The pH buffers were chosen to have the closest integer value to that of the sample in question (e.g. for solution with pH=1.25 pH buffer with pH=1.0 was used). All dilute opaque samples were centrifuged for 15 minutes at 4000 rpm in the microcentrifuge to settle down very large particles and dust. Centrifuged samples were then ultrasonicated for 6 minutes to eliminate possible loose aggregates and dissolved gases. Prepared samples were kept closed with caps in order to avoid contamination with gases and dust from atmosphere. The treated samples were transferred into 1 cm PMMA cuvettes washed with dust-free deionised water and capped.

DLS measurements were acquired in triplicates at measuring angles 30.2, 62.5 and 90.0 degrees and run times 240, 120 and 60 s respectively, temperature 20 ^{0}C, equilibration time 10-30 min. The size distribution analysis was performed from the autocorrelation function and the Coulter CONTIN program for size distribution analysis using 31 data bins and the particle size range of 0.01-3000 nm.

Transparent or slightly turbid samples of hydrolysed Al or Zr solutions were measured without dilution. The samples were sonicated for 5-6 min and centrifuged in the microcentrifuge at 12000 rpm for 15 min. Measurements of these samples were performed similarly to highly turbid (opaque) samples as described above except for longer measurement times: 360, 240 and 180 seconds for 30.2, 62.5 and 90.0° respectively. The size distribution analysis was performed using 31 data bins from the autocorrelation function using the Coulter CONTIN program for size distribution analysis in the particle size range 0.1-1000 nm.

Multimodal 'weight' distributions of particle sizes were acquired and analysed throughout the DLS measurements.

2.7. Solution NMR spectroscopy

NMR spectroscopy is one of the most powerful tool for elucidation of Al speciation, coordination chemistry of Al-ions and their hydrolysis-condensation reactions [28]. Numerous works has been done in the field which have led to elucidation of pathways and kinetic features of Al hydrolysis as well as interactions of this ion with different ligands [5, 28]. ^{27}Al NMR spectroscopy was applied for characterisation of soluble fractions of the hydrolysed solutions of Al-ions, as well as for the investigation of kinetics of speciation of medium-concentrated Al-solutions containing large Al polycations.

2.7.1. Theory and instrumentation of NMR spectroscopy

Nuclear magnetic resonance spectroscopy is based on the measurement of absorption of electromagnetic radiation in the radiofrequency region between approx. 4 to 600 MHz. Under magnetic field atomic nuclei develop the energy states required for the absorption to occur [29].

The fundamental property of the atomic nucleus involved in NMR is the nuclear spin (I) which has values 0, 1/2, 1, 1 1/2, etc. in units of $h/2\pi$ where h is Planck's constant. The actual value of the spin of any given nucleus depends on the mass number and the atomic number. Only atomic nuclei with odd numbers (^{1}H, ^{13}C, ^{27}Al, etc.) can give rise to non-zero spin and therefore, can be detected with NMR (exception – ^{14}N nucleus) [18]. The nuclear magnetic moment μ is directly proportional to spin:

$$\mu = \frac{\gamma I h}{2\pi} \tag{2.12}$$

where the constant γ is known as the magnetogyric ratio and is constant for a particular nucleus.

In a magnetic field, the nuclear moments orient themselves with only certain allowed orientations. A nucleus of spin I has $2I+1$ possible orientations, which are given by the value of the magnetic quantum number m_I. m_I has values of $-I$; $-I+1$, …, $I-1$, I. Thus, for a nucleus of spin 3/2 m_I has values –3/2, -1/2, 1/2, 3/2. The energy of interaction is proportional to the nuclear moment and the applied field. Using Eq. (2.11) one may write:

$$E = \frac{-\gamma h m_I B}{2\pi} \tag{2.13}$$

where B is the applied field.

The selection rule for NMR transition is that m_I can only change by one unit, i.e. $\Delta m_I = \pm 1$. Thus the transition energy is given by:

$$\Delta E = \frac{\gamma h B}{2\pi} \tag{2.14}$$

For the detection of the transition energy, radiation given by $\Delta E = h\nu$ must be applied and combining this with Eq. (2.14) gives the fundamental resonance conditions for all NMR experiments:

$$\nu = \frac{\gamma B}{2\pi} \tag{2.15}$$

I.e. when a nucleus of magnetogyric ratio γ id placed in a magnetic field B, the resonant condition is satisfied when the frequency of the applied radiation ν is given by Eq. 2.14. The relationship between field (B) and frequency (ν) provides a basis for NMR spectroscopy. Either the field or the frequency may be varied in NMR experiments.

For a nucleus of spin I=1/2 there are two possible orientations of the nuclear spin, given by m_I=±1/2. The lower-energy α-state is at m_I=+1/2 and the upper β-state has m_I= -1/2. Therefore, there are two allowed transitions: α→β (corresponds to absorption of energy) and β→α (corresponds to emission of energy). The latter transition is observed by NMR spectroscopy. Schematic diagram of the spin splitting for I=1/2 nucleus is shown in Fig. 2.7.

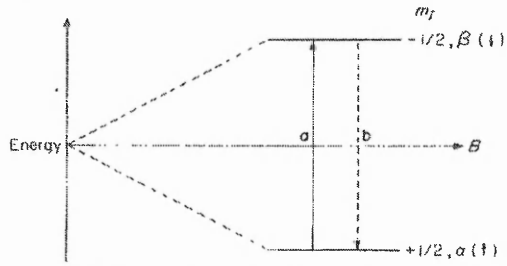


Fig. 2.7. Energy levels and possible transitions for the nucleus of I=1/2 spin

At thermal equilibrium the Boltzmann distribution of energies is maintained:

$$\frac{N_\alpha}{N_\beta} = e^{\frac{-h\nu}{kT}} \tag{2.16}$$

When $N_\alpha < N_\beta$, a net absorption of energy takes place, hence, an NMR signal is observed. Equation 2.11 also emphasises the importance of temperature in measurements of NMR signals.

Magnetic susceptibility is another important parameter of atomic nuclei in NMR measurements. This parameter differs for the same nuclei in different chemical (coordination) environments. Chemical shift of the peak of the NMR signal (the shift of the signal from the peak of an arbitrarily chosen standard) observed in different chemical environments (surrounding atoms and functional groups) provides important chemical and structural information on the nuclei in chemical species [29].

Other effects observed in NMR spectra include spin coupling and decoupling which arises from spin interactions of adjacent atoms. Quadruple broadening is an effect of NMR peak widening due to saturation of quadrupolar nuclei [28]. Such effects may significantly complicate observed NMR spectra and make quantification of the peaks more difficult.

Quantification of the NMR peaks is usually done by integration of peak areas which, in ideal conditions, should be proportional to (*a*) concentration of resonating nuclei, (*b*) the number of nuclei in the species.

NMR spectrometers basically consist of radiofrequency (RF) source and a magnet for induction of magnetic field. The scheme of the NMR spectrometer is shown in Fig. 2.8. The sample is placed in a probe which is positioned between the poles of magnet. The RF radiation is transmitted by a coil on the probe and detected by either the same coil (single-coil spectrometer) or another coil (cross-coil spectrometer). Either magnetic field or RF is slowly varied, and when the resonance condition (Eq. 2.14) is satisfied for the nuclei under observation, the sample absorbs energy from the RF radiation and the resulting signal is detected on the receiver coils, amplified and recorded.

In modern NMR spectroscopy Fourier-transform (FT) spectrometers are commonly used which efficiently decrease the time required for a number of sample scans to be performed over a large range of frequencies [29, 30]. These spectrometers employ accumulation of the signal data in time-domain. Then these data are mathematically transformed into frequency-domain using fast Fourier-transform technique [30]. Time-domain data are pre-treated in order to increase signal-to-noise ratio using a procedure called 'apodisation'. After transformation into frequency-domain the data are phased, calibrated and analysed using specialised software.

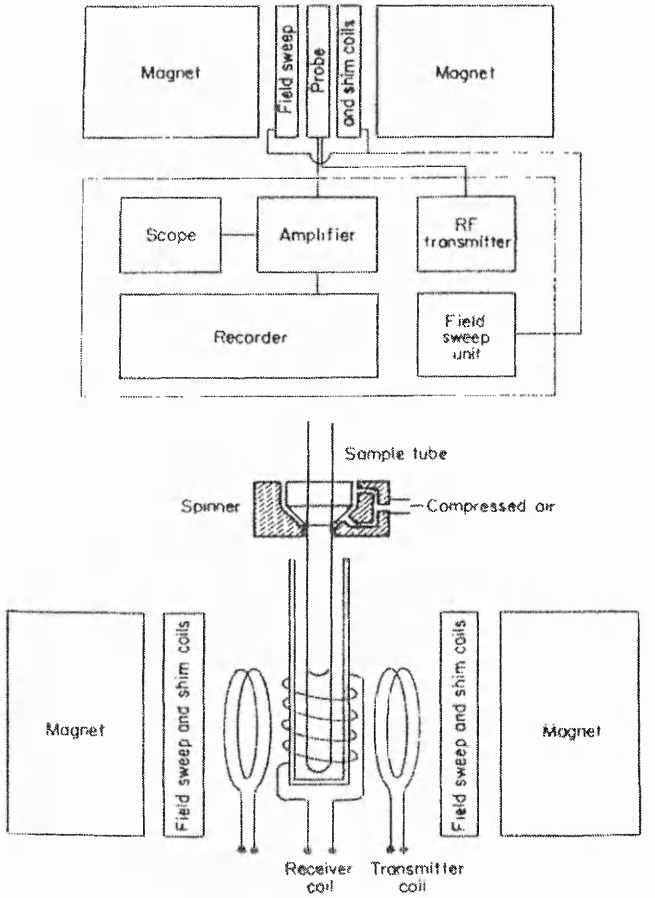


Fig. 2.8. General scheme of the NMR spectrometer

2.7.2. Features of ^{27}Al NMR spectroscopy

The element aluminium-27 (spin I=5/2) 0ccurs at 100% natural abundance and its nucleus has a good receptivity, though its quadruple moment means that its resonances are broadened relative to those of spin-1/2 nuclei [28]. However, this amounts to only a few hertz in many cases. Advances in high-resolution NMR spectroscopy made it possible to obtain rich information from ^{27}Al NMR spectra concerning the structure and pathways of its interactions with solvents (hydrolysis in the case of water) and numerous ligands [5,28].

There are several problems associated with acquisition of ^{27}Al NMR spectra [28]. First, the longest relaxation time to be encountered in the spectra is of the order of 160 ns that makes FT mode of data collection preferable. The FT mode, however, limits the width of the widest line that can be observed by given equipment. The solution is to use higher field spectrometers. Observation of several Al species with shifted resonances of wide range of linewidths also limits the number of species resolved by a given spectrometer. Another danger is that despite the short relaxation times, it is possible to pulse too rapidly and partially saturate the narrower resonances that hinder quantification of ^{27}Al NMR spectra. One more obstacle for quantification is a range of problems related to serendipity of phase correction of ^{27}Al NMR spectra, especially when broad lines are present and 'baseline rolling' occurs [28]. Though methods for reducing a problem of baseline roll have been proposed [28], suitable conditions vary from case to case and are to be found empirically. Sensitivity of ^{27}Al NMR measurement is also somewhat limited, the lowest concentration of 0.0001 mol/L in aluminium sulphate being detected using a 400 MHz spectrometer operating at 104.2 MHz.

The relatively sharp resonance of hexa-aquo Al cation is easily accessible and is a common reference for calculation of chemical shifts in ^{27}Al NMR spectra [19]. Another species used as a reference is aluminate-anion $Al(OH)_4^-$, but this species are far less soluble and resonance peak is slightly broader than that of $Al(H_2O)_6^{3+}$. However, the use of the peak of Al hexa-aquo cation is somewhat serendipitous since the peak is known to broaden and to change its position slightly depending on the conditions of experiment. Another complication arises from the fact that other species (hydrolysed Al monomers or small oligomers) can resonate at similar frequencies [30].

Strong interactions of Al-ions with solvents and any molecule with donor-atom lead to profound chemical shifts observed in NMR spectra. J.W. Akitt [30] derives three general regions of chemical shifts: (*a*) alkylaluminium compounds have shifts of 150 ppm and more to low field of the reference ($[Al(H_2O)_6]^{3+}$); (*b*) tetrahedrally coordinated aluminium with δ between 140 and 40 ppm (exception – AlI_4^- with resonance at –26.7 ppm); (*c*) octahedrally coordinated aluminium between 40 and –46 ppm. Al species with coordination number 5 have been reported and their NMR resonances at ca.30-40 ppm fit well into this classification. The linewidths of aluminium peaks are a function of temperature and pH and become narrower when the temperature is increased [30].

2.7.3. ^{27}Al NMR spectra of the Al-containing samples prepared at room temperature

^{27}Al solution NMR spectra were acquired using a Jeol JNM-EX270 FT NMR-spectrometer operating at 104.2 MHz, field strength of 6.35 Tesla with a D_2O lock, single pulse method, X-pulse of 10 μs, 256 scans, relaxation delay 0.1 s, temperature 21.8 °C using a 5 mm probe with a coaxial insert containing a known concentration of $NaAlO_2$ (99.9 %, Fisher Scientific) in D_2O (99.8%, BDH) as a secondary standard that had been filtered (Whatman filter with < 200 nm diameter pores) prior to use. Solutions of a known concentration of $Al(NO_3)_3$ (99,95 %, Aldrich) in distilled, deionised water were used as a primary standard. The ^{27}Al NMR spectra were processed using Fast Fourier Transformation (Galactic GRAMS/32 Version 5.1 program), using second order zero-filling, apodisation using an exponential function and line broadening of 10 Hz.

Quantification of the ^{27}Al NMR spectra obtained from the samples of Al solutions hydrolysed to a different extent at room temperature (21-22 °C) was carried out using a local integration of the peak areas by means of GRAMS/32 NMR program (an integral part of GRAMS/32 Ver.3.1 software package). The spectra were baselined first using multi-point non-linear baseline correction and then the areas of target peaks were integrated using a common procedure [31].

2.7.4. ^{27}Al NMR spectra of the Al-containing samples prepared at high temperature

Instrumental setting for the recording of the ^{27}Al NMR spectra of the samples prepared at elevated temperature (preparation of the samples is described in Section 2.4.2) were the same as for the measurements at room temperature (see previous Section) except the temperature was set at 90°C, 2.5 ml of the sample were transferred into 10 mm NMR tube, the reference solution of $NaAlO_2$ was introduced in 5 mm NMR tube inside 10 mm sample tube. 256 scans were acquired for each sample in the series.

The portions samples from the series **AMK1** (see Section 2.4.2) which undergone spray-freeze-drying procedure described below in Section 2.10 were also measured by ^{27}Al NMR spectroscopy. For this purpose ca. 0.1 g of the solid post-spray-frozen samples were re-dissolved in deionised water. After measuring pH value of each re-dissolved sample they were subjected to measurement by ^{27}Al NMR spectroscopy at the conditions identical to initial samples described above.

2.7.5. *In-situ* ^{27}Al NMR kinetic measurements of Al hydrolysis at 90°C

The instrumental setup was the same as for ^{27}Al NMR measurements at room temperature (see above) except for usage of 10 mm NMR sample tubes and 5 mm reference inserts. Another change was making a primary standard with the same concentration of $Al(NO_3)_3$ and with HNO_3 of 0.1 mol/L (a corresponding aliquot of 10 ml of 1.00 M volumetric standard of HNO_3 was added to $Al(NO_3)_3$ solution) in order to make the signal at 0.0 ppm of the standard sharper and easier to quantify. The secondary reference solution of

$NaAlO_2$ (prepared the same way as in Section 2.9.4) was been sonicated for 30 min instead of filtering out insoluble matter that also led to the improvement of signal from the secondary reference at 80.0 ppm.

Experimental procedure. A 5 ml aliquot of 1 M $AlCl_3$ solution was placed in the glass volumetric flask (100 ml). A calculated amount of deionised water was added to the flask in order to make up the total volume of the sample of 50 ml. The flask with the sample was closed with stopper (not tightly) and placed into water bath with 90±0.2 °C. After reaching of the temperature 90 °C (at least 5-10 min) the sample was titrated with 1.026 M KOH (volumetric standard solution) in order to reach a desirable hydrolysis ratio. The list of the samples and their hydrolysis ratios is given in Table 2.10. The order of titrant additions was kept in all the performed experiments on *in-situ* ^{27}Al NMR kinetic studies at high temperature similarly to the multi-batch titrations of Al-solutions at high temperature described in the procedure in Section 2.4.5 in order to minimise the insoluble matter formation during alkali additions. After completion of alkali additions the samples were heated for 5 min in the water bath at 90 °C under intensive shaking (220 rpm) and then an aliquot of 2.5 ml of the sample was transferred into 10 mm NMR tube. After ca. 15-20 min the in-situ measurements of ^{27}Al NMR spectra started. The total time between the completion of alkali additions and the start of NMR measurements did not exceed 25 min and was recorded for each sample in question.

Table 2.10. List of the samples and their hydrolysis ratios for conducting in-situ real time ^{27}Al NMR measurements (total volume of the sample 50 ml; $AlCl_3$ solution aliquot – 5 ml)

Sample No	$C(Al)_{final}$, mol/L	$V_{aliquot}(KOH)$, mol/L	Hydrolysis ratio	Duration of experiment, hours
1	0.1	13.92	1.00	48
2	0.1	18.23	1.25	48
3	0.1	19.74	1.50	48
4	0.1	21.93	1.75	48
5	0.1	22.21	2.00	48
6	0.1	22.41	2.10	48
7	0.1	22.61	2.20	48
8	0.1	22.81	2.30	48
9	0.1	23.01	2.40	48
10	0.1	23.21	2.50	48
11	0.1	23.41	2.60	48
12	0.1	23.61	2.70	48

Measurements of ^{27}Al NMR spectra were conducted in kinetic mode at 90°C. For this purpose every sample in question (2.5 ml) located in the 10 mm Al-free NMR tube (Wilmad) with 5 mm reference insert containing 0.7 ml of the reference solution prepared as in Section 2.9.3. was placed in the NMR machine and run a number of consecutive scans during 48 hours. For the first four hours from the start the spectra were acquired every 5 min (48 spectra in total) with 256 scans for each spectrum. During the next 44 hours the spectra were recorded every 30 min (88 spectra in total), 1024 scans for each spectrum. The choice of the number of scans for the spectra in both (4 and 44 hours) parts of each experiment were a result of compromise between the time gap of the measurements (5 and 30 min for 4 and 44 hours correspondingly) and the time required for a certain number of scans to be accumulated (ca. 1.5 min for 256 scans and ca. 6 min for 1024 scans) in order to avoid extensive averaging of the kinetic data over longer time intervals.

2.8. Spray-freeze-drying

NMR spectroscopy of solutions provide valuable data on structural, chemical and kinetic aspects of aluminium speciation [5, 28]. However, for elements like zirconium having a large quadruple broadening effect in the ^{91}Zr NMR spectra this method fails to provide any useful information [32]. Thus, in order to characterise zirconium species obtained upon hydrolysis using solid-state characterisation techniques a certain method for liquid-solid transformation should be applied. Several techniques have been applied for such liquid-solid transformation so far, namely, freeze-drying, spray-drying and spray-freeze-drying (or spray-freezing) [33-38]. An ideal method for liquid-solid transformation of solution species should satisfy following requirements: (*a*) the method should be non-destructive in terms of preservation of species chemical entity, structure and relative distribution; (*b*) the method should quench effectively all reactions in solution that would enable kinetic studies of the speciation patterns to be carried out; (*c*) the method should be fast, reproducible and universal (i.e. applied to a large variety of species ranging from ionic monomers to amorphous colloidal phases).

The method of freeze-drying is based on freezing of solution using different freezing techniques (e.g. freezing on a coldplate; immersing into liquid nitrogen). The frozen sample is then put into a freeze-dryer and dried under low temperature and low pressure. Freezing of significant amounts of solution is not instant. This leads to a gradient of temperatures upon freezing and induces inhomogeneity of the sample. Moreover, conventional freeze-drying has been criticised for strong alteration of speciation patterns of solutes during freezing of solutions [36]. The advantage of the method is gentle removal of solvent by its sublimation at low temperature and pressure. However, the method is also very slow.

Another conventional method used to obtain solid powders from solutions is spray-drying [34]. A general scheme of the method is shown in Fig. 2.9. Spray-drying is based on

spraying of solution with a spray-gun by supplying an inert gas under pressure into a nozzle that produces pressure gradient and entrains sample through the tubing into the nozzle of spray-gun where it is sprayed and converted into aerosol. The aerosol of solution is sprayed into a hot large chamber with counter-flow of a hot gas (e.g. dry air). High temperature and small size of aerosol droplets causes fast evaporation of liquid from the sample and the sample dries as a fine powder. The speed and high productivity of the method is an obvious advantage along with well-defined spherical shape of the particles produced [34]. However, high temperature may induce alterations in speciation patterns of the sample (e.g. species are sensitive to high temperatures) or lead to agglomeration of the particulates [36].

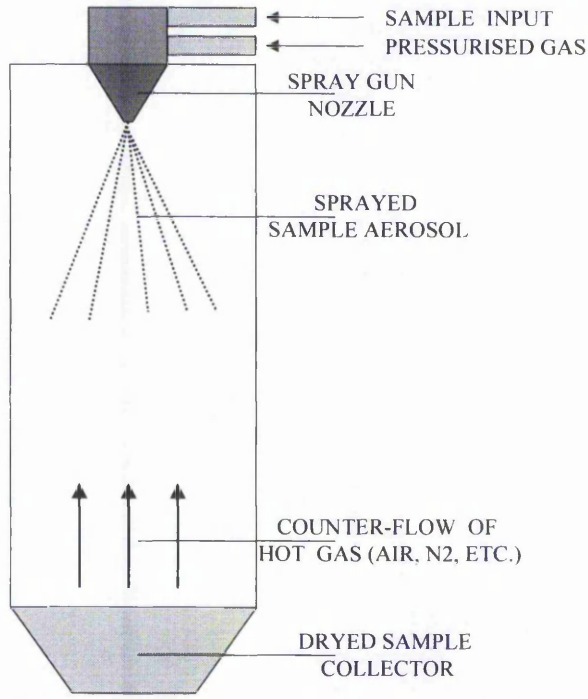


Fig. 2.9. Schematic presentation of the spray-drying method

Spray-freeze-drying (or spray-freezing, in short) is a hybrid method which combines spraying of aerosol and gentle freeze-drying for solvent removal. It is based on spraying of a fine aerosol into a coolant (e.g. liquid nitrogen) for freezing solution and subsequent drying of the frozen solution in the freeze-drier. The advantages of the method include highly effective freezing of solution as a very fine aerosol and gentle removal of solvent in the freeze-drier. The only minor disadvantage of the method is a lengthy period of freeze-drying. Another drawback which is common to all the described methods for liquid-solid transformation of solution species – that **all** components are present in a dry solid sample including target species, electrolytes, ions and any other species formed in solution at the moment of reaction quenching by spray-freeze-drying.

The setup of spray-freeze-drying technique is quite simple, as shown in Fig. 2.10.

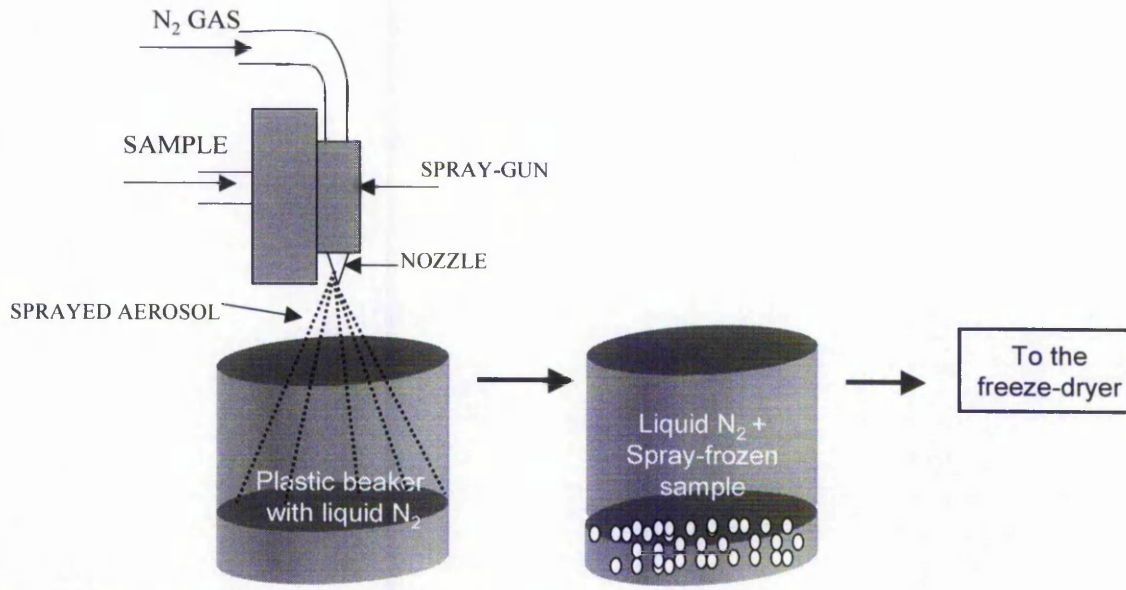


Fig. 2.10. The procedure of spray-freeze-drying.

The method of spray-freeze-drying was first introduced for biological studies [38]. Only one group has applied the method for obtaining of solid materials (perovskites) [35]. However, the mentioned group used spray-freeze-drying for materials synthesis rather than for characterisation of species present in solution. The present study is apparently the first investigation into the possibility of application of spray-freeze-drying for the speciation studies of metal ions in aqueous solutions.

The volume of solution taken for spray-freezing in this work was dependent on the total concentration of metal ion in solution: 10 ml of 0.2 M metal ion solution and 20 ml of 0.1 M solution were taken for spray-freeze-drying. The full procedure of liquid-solid transformation resulted in approx. 0.25-0.3 g of solid product which is believed to be a 'fingerprint' of the major species present in each solution before spray-freezing. Solid samples were characterised using several techniques, including FT-IR spectroscopy, X-ray diffraction.

2.9. FT-IR spectroscopy

Infrared (IR) spectroscopy is one of the most widespread methods for qualitative and quantitative analysis. This method plays important role in the characterisation of inorganic solids and, rarer, inorganic liquids including aqueous solutions [39, 40]. There are several techniques of obtaining infrared spectra which include conventional transmission mode, attenuated total reflection (ATR) mode; diffuse reflection mode (DRIFTS) [41]. It is hard to obtain IR-spectra of aqueous solutions in transmission mode due to extensive absorption bands of water. IR-spectra of solid samples mixed with IR-transparent material (KBr for mid-IR region 4000-400 cm^{-1} and CsI for far-IR region 700-100 cm^{-1}) are usually obtained using transmission mode [39]. It is possible to obtain ATR-IR spectra of aqueous solutions of inorganic species, however, the technique suffers from quite low sensitivity and from

limitation of spectral window determined by ATR crystal material [42]. DRIFTS is suitable for surface characterisation of solid samples [43]. IR-spectroscopy in transmission mode was applied to obtain spectra of solid samples produced by spray-freezing of sample solutions of hydrolysed Al and Zr solutions in mid- and far-IR spectral regions.

2.9.1. Principles and instrumentation of FT-IR spectroscopy

Infrared spectroscopy is based on measurement of absorption of infrared radiation by chemical substances at different wavelengths in the infrared region. The infrared region is arbitrarily divided into near-infrared (28000-4000 cm^{-1}), mid-infrared (4000-400 cm^{-1}) and far infrared (400-10 cm^{-1}) [40]. Absorption of infrared region is confined largely to molecular species for which small energy differences exist between various vibrational and rotational states. In order to absorb infrared radiation a molecule must undergo a net change of dipole moment as a consequence of its vibrational or rotational motion. Only under these circumstances may the alternating electric field of radiation interact with the molecule and cause changes in the amplitude of one of its motions. The dipole moment is determined by the magnitude of the charge difference and the distance between the two centres of charge. If the frequency of radiation exactly matches the natural vibrational frequency of the molecule, a net transfer of energy takes place which results in a change in the amplitude of the molecular vibration and absorption of radiation. Similarly, the rotation of asymmetric molecules around their centres of mass result in a periodic dipole fluctuation which is able to interact with radiative energy [39].

Molecular vibrations fall into three basic categories: (*a*) stretching vibrations; (*b*) torsion vibrations; (*c*) bending vibrations. A stretching vibration involves a continuous change in the interatomic distance along the axis of the bond between the two atoms. These vibrations may be either symmetric or asymmetric depending on the direction of stretching (opposing or same direction). Bending angle deformation vibrations are characterised by a change in the angle between two bonds and consist of four types: (*a*) scissoring; (*b*) rocking; (*c*) wagging; (*d*) twisting. Torsion vibrations do not involve bending or stretching modes of molecules [39].

An anharmonic oscillator model is a good approximation for vibrational modes of molecule [39]. Vibrational energy levels in this model are given as follows:

$$E=(v+1/2)hc\bar{\nu}-(v+1/2)2hc\bar{\nu}x \qquad \textbf{(2.17)}$$

where E – potential energy; v - vibrational quantum number; h - Planck's constant; c – velocity of light; x – anharmonicity constant

The frequency of vibration of the anharmonic oscillator is in wave numbers is given by:

$$\bar{\nu}=\frac{1}{2\pi c}\sqrt{\frac{f}{\mu}} \qquad \textbf{(2.18)}$$

where f – force field constant; μ - reduced mass.

A direct result of anharmonicity of molecular vibrations is that transitions between

more than one energy level are allowed, and hence overtone absorption bands occur in IR-spectra. Since the anharmonicity constant x is always positive, the vibration energy levels slowly converge with increasing vibrational quantum number [39]. Therefore, overtones do not occur at precisely two or three times the fundamental frequency, but differ slightly, according to the anharmonicity constant. The general formula for the separation of energy levels ν and ν-1 is defined as:

$$\Delta E = E_{\nu} - E_{\nu-1} = (1-2\nu x)h\nu \qquad \textbf{(2.19)}$$

Practical use of IR-spectroscopy is based on the following three types of IR instruments: dispersive (or spectrophotometers); Fourier-transform (FT) spectrometers and filter photometers [41]. The advantages of high sensitivity, resolution and speed of data acquisition is offered by Fourier-transform spectrometers. FT-spectrometers are non-dispersive in the sense that they do not require a grating or prism to disperse radiation into its component wavelengths. All wavelengths are detected and measured simultaneously. The source signal is modulated using Michelson interferometer in such a way that it may be decoded by a Fourier transformation. This is done mathematically using a personal computer and specialised software.

2.9.2. FT-IR spectra of solid samples

FT-IR spectra were obtained using Nicolet Magna-750 FT-IR spectrometer in the mid-IR frequency range (4000 - 400 cm^{-1}) and far-IR range (700-100 cm^{-1}) with preliminary background correction. The spectrometer was fitted with DTGS detector and KBr beamsplitter for mid-IR region (7400-350 cm^{-1}) or polyethylene Solid-Substrate beamsplitter for far-IR region (700-50 cm^{-1}). Experimental setup included 96 to 128 spectrum scans, resolution was set to 2 cm^{-1} for mid-IR and to 2-4 cm^{-1} for far-IR region, with automatic sample gain set at 8. Baseline was automatically corrected using the OMNIC 5.0 program. Spectral bands were identified using OMNIC 5.0 automatic detection program with the assistance of the first derivative of spectral curves and Fourier self-deconvolution curves [41]. Samples after spray-freeze-drying were analysed as KBr (mid-IR) or CsI discs (far-IR). KBr discs were prepared using 2 or 3 mg of a sample finely ground with agate mortar and 198 or 197 mg of spectroscopic grade KBr (making discs 200 mg in total) by a standard procedure [41] compressing discs using a hydraulic press at 10 psi. CsI discs were prepared using 4 or 5 mg of a finely ground sample and 246 or 245 mg of spectroscopic grade CsI (making discs 250 mg in total) by compressing the discs twice in a stainless steel die at 12 psi.

2.10. Powder X-ray diffraction measurements

Solid samples produced by spray-freezing technique also underwent structural analysis by powder X-ray diffraction (PXRD). Since the structure of the species of spray-freeze-dried solutions is believed to maintain in the solid state, it was expected to retrieve structural data of the solution species using this powerful technique.

2.10.1. Principles and instrumentation of PXRD

Interaction of the electric vector of X-ray radiation and the electrons of the matter through which it passes, results in scattering [44]. When X-rays are scattered by ordered environment in a crystal, both constructive and destructive interference occurs among the scattered rays because the distance between scattering centres is of the same order of magnitude as the wavelength of radiation.

When an X-ray beam strikes a crystal surface at angle θ, a portion of the beam is scattered by the layer of atoms at the surface. The unscattered portion of the beam penetrates to the second layer of atoms where again a fraction is scattered and so on. The cumulative effect of this scattering from the regularly spaced centres of the crystal is known as diffraction of the beam. The requirements of X-ray diffraction are: (a) spacing between layers of atoms must be roughly the same as the wavelength of the radiation; (b) scattering centres must be spatially distributed in a highly regular way.

The condition for constructive interference of the beam at angle θ is given by Bragg equation:

$$n\lambda = 2d\sin\theta \qquad \textbf{(2.20)}$$

where n – integer; λ - wavelength of X-rays; d – interplanar distance in the crystal; θ - incident angle of X-ray radiation

X-rays are reflected from crystal only if the angle of incidence satisfies the condition that:

$$\sin\theta = \frac{n\lambda}{2d} \qquad \textbf{(2.21)}$$

At all other angles destructive interference takes place.

In a powder X-ray experiment, the data are collected as a powder pattern. This is essentially a plot of diffracted beam against twice the incident angle (2θ). Hence, a diffraction pattern describes a series of peaks corresponding to coherent reflections for a given crystal. The positions of these reflections along the 2θ-axis clearly depend on the value of d which is dependant on the dimensions of the unit cell of the crystal [44].

From the powder diffraction data it is possible also to generate values for the mean crystallite size (d) from the observed half height line width (B_b) of the X-ray diffraction peaks. This may be performed using the Scherer equation:

$$d = \frac{k\lambda}{\beta\cos\vartheta} \qquad \textbf{(2.22)}$$

$$\beta = B_b - B_x \qquad \textbf{(2.23)}$$

where d – average particle size; β - peak width (radians); λ - wavelength of incident radiation (usually CuKα, λ=1.5418 Å); θ - Bragg diffraction angle; k – instrument constant (taken as 0.9); B_x – instrument broadening.

In practice for a value of θ in degrees (°), Equation 2.26 becomes:

$$d = 57.3\frac{k\lambda}{\beta\cos\theta} \qquad \textbf{(2.24)}$$

with dimensions of d equivalent to the dimensions of λ (Å). Due to various problems associated with determining mean particle sizes form PXRD data the Scherer's formula is used mainly for rough estimations [44]. If the average crystal size is less than 2000 Å than peak broadening may occur and readily measured using Scherer's equation (2.22-2.24). The lower limit of detection occurs when the peaks become so broad that they disappear into the background radiation. For very small particle sizes it is best to use low angle peaks if possible since, for a given crystal thickness, the broadening increases with angle.

2.10.2. Preparation and measurement of the solid samples for PXRD

An agate mortar was used to finely grind a sample to a powder. In most cases a powder of α-Al_2O_3 (corundum) was added to the powder of the sample as an internal standard in the ratios sample:α-Al_2O_3=50:50 % by weight. The powder was then packed into the hollow of a cavity holder, and smoothed off by sliding a flat glass slide over the surface. In this work, routine powder X-ray diffraction analysis was conducted using the Philips X-Pert system fitted with a PW Diffractometer control unit operated at 42.5kV/18mA with a copper source CuKα, λ=1.5418 Å. Scans were generally performed in step mode with 0.02° step size and 0.2 to 0.4 second dwell time using 1° divergence slit and 0.1 mm receiving slit. Data were recorded over 2θ range 3-80°.

The powder X-ray diffraction method is useful in qualitative phase analysis because every crystalline material has its own characteristic powder pattern. The resulting powder patterns have two characteristic features: (*a*) the d-spacings of the lines; (*b*) the relative intensities of the lines (I/I_x). Diffraction patterns were analysed using HBX software. Data handling was carried out using Traces PXRD software, version 3.1. This program was used for background correction, spectral smoothing, determination of peak positions, peak widths, intensities, and crystallite size calculations. Comparisons of the collected data were made in conjunction with the JCPDS (Joint Committee on Powder Diffraction Standards) powder diffraction database [45], which consists offsets of cards containing X-ray data for most known crystalline phases.

2.11. Generalised two-dimensional correlation analysis

Generalised two-dimensional (2D) optical spectroscopy has been originally developed in the works [45, 46] by I. Noda and Y. Ozaki. Two-dimensional correlation spectroscopy (2D-COS) has recently received keen interest in analytical chemistry because of the following advantages [46]: (i) simplification of complex spectra consisting of many overlapped peaks and enhancement of spectral resolution by spreading peaks over the second dimension; ii)

establishment of unambiguous assignments through correlation analysis of bands; (iii) probing the specific order of the spectral intensity changes taking place during the measurement or the value of controlling the variable affecting the spectrum; iv) investigations of correlation between bands in two different types of spectroscopy (heterospectral correlation).

2.11.1. Theory of two-dimensional correlation spectroscopy

2D-correlation spectroscopy (2D-COS) is a technique where the spectral intensity is plotted as a function of two independent spectral variables, e.g., wavelength, frequency, or wavenumber [46]. The two orthogonal axes of independent spectral variables define the 2D spectral plane, and the spectral intensity may be plotted along the third axis. Figure 2.11 shows an example of a two-dimensional infrared (2D-IR) spectrum of a dynamically strained polystyrene (PS) film.

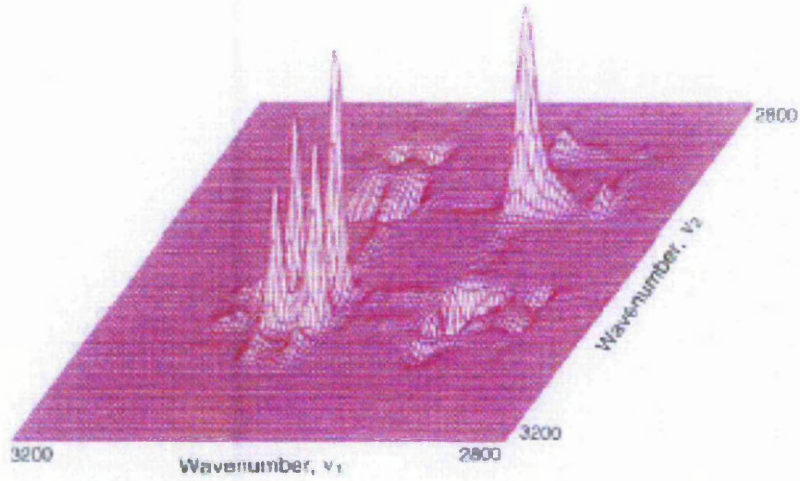


Fig. 2.11. Fishnet representation of a synchronous 2D-IR correlation spectrum of a polystyrene film (from [47]).

One can often obtain additional useful information, which is not readily available from the conventional one-dimensional spectrum, and sort out complex or overlapped spectral features by spreading peaks along the second dimension. For example, the 2D spectrum in Fig. 2.11 indicates clear differentiation between the origins of IR spectral signals, i.e., those from the molecular vibrations of the side group phenyl and main-chain backbone methylene groups of polysterene film.

The basic concept of 2D spectroscopy was originally developed in the field of nuclear magnetic resonance spectroscopy almost three decades ago [46]. The broad range of applications for various types of 2D NMR techniques has been very successful [48]. However, penetration of the ideas of 2D technique into other spectroscopic methods has started in the works of I. Noda and Y. Ozaki [46,47].

A 2D experiment in optical spectroscopy can be carried out with a conventional spectrometer by introducing a relatively slow external perturbation applied to the system of interest. As long as the transient phenomenon to be investigated by the experiment is not the

optical excitation process itself, the perturbation need not be a set of ultra-short optical pulses, as initially thought [47].

Figure 2.12 shows the basic scheme for a 2D correlation spectroscopy experiment based on external perturbation.

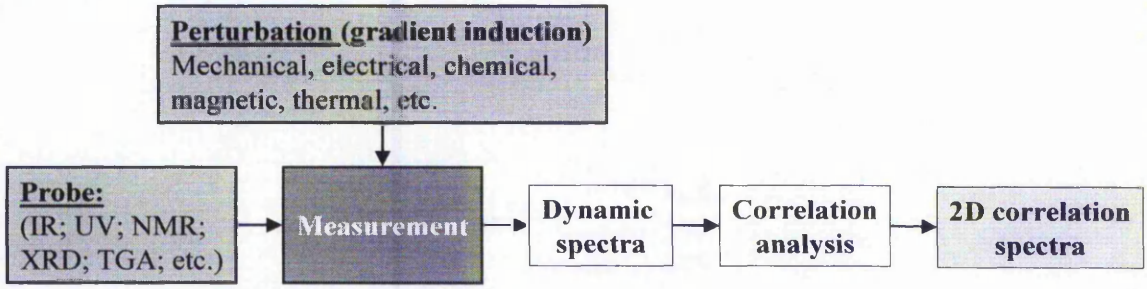


Fig. 2.12. General scheme for obtaining 2D correlation spectra.

In a typical spectroscopic measurement carried out in traditional (i.e., one-dimensional) spectroscopy, a selected electromagnetic probe is used by itself to study the system of interest. Characteristic interactions between the probe and constituents of the system are then analysed in the form of a spectrum to elucidate detailed information about the system. On the other hand, 2D correlation spectroscopy utilises an additional external perturbation applied during the spectroscopic measurement to stimulate the system of interest. The response of the system to the applied perturbation often manifests itself as characteristic variations in the optical spectrum, sometimes known as a dynamic spectrum. In a typical 2D experiment, a series of perturbation-induced dynamic spectra are collected in some sequential order. Such a set of spectra may be readily manipulated mathematically, with the use of a simple scheme of correlation analysis, to yield desired 2D correlation spectra. In many cases, dynamic spectra may be detected as a straightforward transient function of time. It is also very common to collect dynamic spectra as a direct function of the quantitative measure of the imposed physical effect itself, such as temperature, pressure, concentration, stress, electrical field, etc. The conceptual scheme to induce dynamic spectra described in Fig. 2.13 obviously is a very general one. It does not even specify the physical nature or mechanisms with which the applied perturbation affects the system. There are, of course, numerous different types of external perturbations which could be used to stimulate a system of interest. Each perturbation affects the system in a unique and selective way, governed by the specific interaction mechanisms relating the macroscopic stimulus and microscopic or molecular level responses of individual system constituents. The type of physical information contained in a dynamic spectrum, therefore, is determined by the selection of perturbation method and electromagnetic probe. The waveform of the applied perturbation, likewise, can be considerably varied. Thus, a simple sinusoid or sequences of pulses can be applied as a perturbation, as well as random noise or even a static or constant state of a physical variable, like temperature.

Mathematical derivation of the correlation function is provided in the original work

[46, 47]. Below synchronous and asynchronous spectra calculated by the 2D-COS method will be considered and schematically presented in Fig. 2.13.

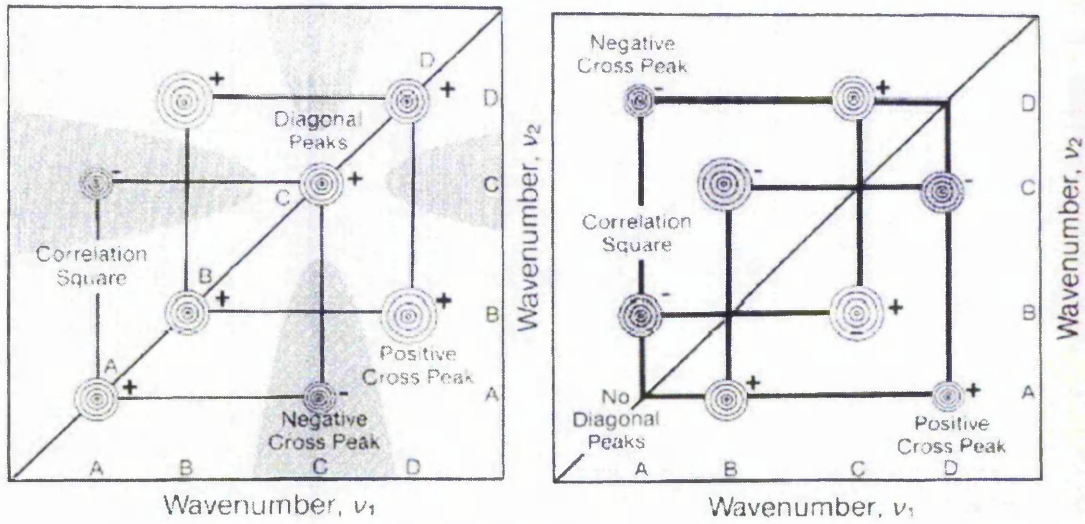


Fig. 2.13. Schematic presentation of synchronous correlation spectrum (left) and asynchronous correlation spectrum (right) [47].

Synchronous spectrum. The intensity of a synchronous 2D correlation spectrum shown in the left part of Fig. 2.13 spectrum $\Phi(\nu_1, \nu_2)$ represents the simultaneous or coincidental changes of spectral intensity variations measured at ν_1 and ν_2 during the interval between T_{min} and T_{max} of the externally defined variable t. The synchronous spectrum is a symmetric spectrum with respect to a diagonal line corresponding to coordinates ν_1 and ν_2. Correlation peaks appear at both diagonal and off-diagonal positions. The intensity of the peaks located at diagonal positions corresponds mathematically to the autocorrelation function of spectral intensity variations observed during an interval between T_{min} and T_{max}. The diagonal peaks are therefore referred to as autopeaks. In the example spectrum shown in Fig. 2.13, there are four distinct autopeaks located at the spectral coordinates *A*, *B*, *C*, and *D*. The magnitude of an autopeak intensity, which is always positive, represents the overall extent of spectral intensity variation observed at the specific spectral variable n during the observation interval between T_{min} and T_{max}. Thus, any regions of a spectrum which change intensity to a great extent under a given perturbation, will show strong autopeaks, while those remaining near constant develop few or no autopeaks. An autopeak represents the overall susceptibility of the corresponding spectral region to change in spectral intensity as an external perturbation is applied to the system. Cross peaks located at the off-diagonal positions of a synchronous 2D spectrum represent simultaneous or coincidental changes of spectral intensities observed at two different spectral variables, ν_1 and ν_2. Such a synchronised change, in turn, suggests the possible existence of a coupled or related origin of the spectral intensity variations. It is often useful to construct a correlation square joining the pair of cross peaks located at opposite sides of a diagonal line drawn through the corresponding autopeaks to show the existence of

coherent variation of spectral intensities at these spectral variables. In the example spectrum, bands *A* and *C* are synchronously correlated, as well as bands *B* and *D*. Two separate synchronous correlation squares, therefore, could be drawn. While the sign of autopeaks is always positive, the sign of cross peaks can be either positive or negative. The sign of synchronous cross peaks becomes positive if the spectral intensities at the two spectral variables corresponding to the coordinates of the cross peak are either increasing or decreasing together as functions of the external variable t during the observation interval. On the other hand, a negative sign of cross peaks indicates that one of the spectral intensities is increasing while the other is decreasing. In the example spectrum (Fig. 2.13, left), the sign of cross peaks at the spectral coordinates *A* and *C* is negative, indicating that intensity at one band is increasing while the other is decreasing. The cross peak sign at the coordinates *B* and *D*, on the other hand, is positive, indicating that both bands decrease (or increase) together.

Asynchronous Spectrum. Figure 2.13 (right) shows an example of an asynchronous 2D correlation spectrum. The intensity of an asynchronous spectrum represents sequential, or successive, changes of spectral intensities measured at ν_1 and ν_2. Unlike a synchronous spectrum, an asynchronous spectrum is antisymmetric with respect to the diagonal line. The asynchronous spectrum has no autopeaks, consisting exclusively of cross peaks located at off-diagonal positions. By extending lines from the spectral coordinates of cross peaks to corresponding diagonal positions, one can construct asynchronous correlation squares. In Fig. 2.13, asynchronous correlation is observed for band pairs *A* and *B*, *A* and *D*, and *B* and *C*, as well as *C* and *D*. From the cross peaks, it is possible to draw four asynchronous correlation squares. An asynchronous cross peak develops only if the intensities of two spectral features change out of phase (i.e., delayed or accelerated) with each other. This feature is especially useful in differentiating overlapped bands arising from spectral signals of different origins. For example, different spectral intensity contributions from individual components of a complex mixture, chemical functional groups experiencing different effects from some external field, or inhomogeneous materials comprised of multiple phases may all be effectively discriminated. Even if bands are located close to each other, as long as the signatures or the pattern of sequential variations of spectral intensities are substantially different, asynchronous cross peaks will develop between their spectral coordinates. The sign of asynchronous cross peaks can be either negative or positive. The sign of an asynchronous cross peak becomes positive if the intensity change at ν_1 occurs predominantly before ν_2 in the sequential order of *t*. It becomes negative, on the other hand, if the change occurs after ν_2. This rule, however, is reversed if $\Psi(\nu_1, \nu_2)<0$. The example in Fig. 2.13 (right) indicates that the intensity changes (either increase or decrease) at bands *A* and *C* occur after the changes at *B* and *D*.

2.11.2. A new method for correlation analysis of the dynamic spectra

The computational procedure described in previous section has several drawbacks: (*a*) the Fast Fourier Transform technique as the basis of the Noda's algorithm is a complicated mathematical procedure, hence a specialised software is needed in order to implement it; (*b*) the Noda's algorithm requires a 'reference' spectrum to be assigned which is arbitrarily chosen from the set of dynamic spectra acquired; (*c*) the limits of 'intensities' in the 2D-correlation spectra calculated using FFT technique vary in accordance with the chosen 'reference' spectrum and the variation in the dynamic spectra; (d) 2D-correlation maps obtained by the 2D-COS method may contain a large number of somewhat cumbersome, feature, which are difficult to comprehend visually; (e) the method definitely lacks an additional algorithm for classification of the identified spectral features into groups according to their chemical origin.

Development of an additional algorithm was attempted in order to overcome some of the drawbacks of the 2D-COS method using a simpler and more illustrative algorithm.

The basic idea of the algorithm is to introduce another correlation function for the statistical description of variations in dynamic spectral sets obtained by external perturbation. The simplest and the most common measure of correlation between two sets of data is a correlation coefficient r [31]: $r=\langle x, y\rangle$, where x and y are two independent sets of data. The correlation coefficient is defined in statistics as:

$$r(x,y)=\frac{\frac{1}{n}\sum_{i=1}^{n}(x_i-\mu_x)(y_i-\mu_y)}{\sigma_x\sigma_y} \qquad \textbf{(2.25)}$$

where n –the number of data points in the data sets x and y;
μ_x and μ_y - mean values of the data sets x and y;
σ_x and σ_y- standard deviations of the data sets x and y.

The value of r varies within 1 and –1. The highest r=1 indicates full correlation, e.g. complete coincidence of variations in the data sets x and y, while r=-1 indicates that the data sets are superimposed or 'anti-correlated' [31].

The value of r is easily calculated in any electronic spreadsheet program, e.g. Microsoft Excel. Correlation coefficients were applied for the construction of square correlation matrix (Fig. 2.14). The correlation matrix (or 2D-correlation spectrum) contains both synchronous and asynchronous modes of the spectral features.

	ν_1	ν_2	ν_3	...	ν_n
ν_1	$r_{1,1}$	$r_{1,2}$	$R_{1,3}$	...	$r_{1,n}$
ν_2	$r_{2,1}$	$r_{2,2}$	$R_{2,3}$	...	$r_{2,n}$
ν_3	$r_{3,1}$	$r_{3,2}$	$R_{3,3}$	...	$r_{3,n}$
...	...	...	...	...	...
ν_n	$r_{n,1}$	$r_{n,2}$	$r_{n,3}$	...	$r_{n,n}$

Fig. 2.14. Schematic representation of a 'correlation sum'

It was also found empirically that the sums of correlation coefficients in the columns (or rows) of the correlation matrix (S) can retrieve rich information about the dynamic systems in question:

$$S_i = \sum_1^n (r_{1,1} + r_{i,2} + ... + r_{i,n}) = \sum_1^n r_{i,n} \qquad \textbf{(2.26)}$$

The 'correlation sum' parameter appears to be unique for each dynamic data set and helps to identify similar/dissimilar data sets. The fact that the plot of correlation sums against a variable parameter (in most cases – the hydrolysis ratio in solution of metal-ion) resembles the original dynamic curves or spectra, while revealing much more information than the original curves and being sharper and more illustrative has been found very encouraging. The 'correlation sum graph' which is plotted against a dynamic variable or on a spectral scale, reveals similarities-dissimilarities between the data sets versus varied parameter. On the basis of this analysis it was possible to establish groups of similar data sets and proceed with CA of the groups which provided more detailed information than the CA of the whole range of data.

The developed procedure was applied for treatment of time-resolved potentiometric data, FT-IR spectra and XRD patterns. The results of the method of correlation sums are presented and discussed in the following experimental chapters.

2.12. List of reagents and materials

1. Aluminium nitrate nonahydrate, $Al(NO_3)_3*9H_2O$, dry salt, >99.5 % wt, Aldrich
2. $Al(NO_3)_3*9H_2O$, dry salt, extra pure, >99.95 % wt, Aldrich
3. Aluminium chloride hexahydrate, $AlCl_3*6H_2O$, dry salt, > 99 %, Riedel-de-Haen
4. Potassium aluminium sulphate dodecahydrate, $KAl(SO_4)_2*12H_2O$, dry salt, > 99 wt. %, Fluka
5. Zirconyl choride octahydrate, $ZrOCl_2*8H_2O$, dry salt, >98 % wt., Acros Organics
6. Al standard solution, 1mg/L (1 M HCl medium), Aldrich

7. Zr standard solution, 1010μg/l of Zr in 5wt % HCl, Aldrich
8. Potassium hydroxide, KOH, 45-47 wt. % aqueous solution, Aldrich
9. KOH, ca. 1 mol/L (exact value on the bottle), volumetric standard solution, Riedel
10. KOH, dry, >98 wt. %, Fluka
11. Potassium hydrogen carbonate, $KHCO_3$, dry salt,>97-103 wt. %, Acros Organics
12. Sodium hydrogen carbonate, $NaHCO_3$, dry salt, >98 wt. %, Fluka
13. 0Ammonium hydroxide, NH_4OH, ca. 1-5 mol/L (exact value on each bottle), aqueous solution, volumetric standard, Riedel-de-Haen
14. NH_4OH, concentrated aqueous solution (37 wt. %), Sigma
15. Hydrochloric acid, HCl, 37 wt. %, concentrated aqueous solution, Fisher Chemicals
16. HCl, ca. 1 mol/L (exact value on each bottle), aqueous solution, volumetric standard, Riedel-de-Haen
17. Nitric acid, HNO_3 ca. 1 mol/L, (exact value on each bottle), aqueous solution, volumetric standard, Riedel-de-Haen
18. Acetic acid, CH_3COOH, glaceous, >98 wt. %, concentrated aqueous solution, Fisher Chemicals
19. Sulphuric acid, H_2SO_4, >98 wt. %, concentrated aqueous solution, Fisher Chemicals
20. Sulphuric acid, H_2SO_4, ca. 1 mol/L, (exact value on each bottle), aqueous solution, volumetric standard, Riedel-de-Haen
21. Glycine, $C_2H_6N_2O_2$, >99 %, dry, Fluka
22. Alumina, α-Al_2O_3, dry, (PXRD standard), BDH
23. Potassium bromide, KBr, pure for IR-spectroscopy (>99.5 %), Fisher Chemicals
24. Cesium iodide, CsI, pure for IR-spectroscopy (>99%), Fluka
25. Xylenol orange (sodium salt), $C_{31}H_{27}N_2Na_5O_{13}S$, dry salt, >72 %, Aldrich
26. Al metal, fine powder, 200 mesh, ~100 %, Aldrich
27. Potassium chloride, KCl, dry salt, >99 wt. %, Aldrich, Fluka
28. Sodium chloride, NaCl, dry salt, >99 wt. %, Fluka
29. Sodium aluminate, $NaAlO_2$, >98%, Riedel-de-Haen
30. Potassium sulphate, K_2SO_4, dry salt, >98 wt. %, Analar
31. Sodium acetate, $NaCH_3COO$, dry salt, >99 wt. %, Fisons
32. Deuterium oxide, >99.5 %, Aldrich
33. Distilled, deionised water
34. A set of pH-buffers: pH=1.687; 4.005; 7.000; 10.012 (Riedel-de-Haen, Fluka, Fisher Chem.)

References:

1. D.F. Baes Jr., R.E. Mesmer. Boron, aluminium and scandium. In: The hydrolysis of cations. (1976) New York: Wiley-Interscience, pp.112-123; 152-158.
2. M. Henry, J.P. Jolivet, J. Livage. Aqueous Chemistry of Metal Cations - Hydrolysis, Condensation and Complexation. (1992) Structure and Bonding **77**, 153-206.
3. C.J. Brinker, G.W. Scherer. Sol-gel science: the physics and chemistry of sol-gel processing (1990) Academic Press. 908 p.
4. M.A. Blesa, E. Matijevic. Adv. Colloid Interfac. Sci. (1989) **29** 173-221.
5. Chemistry of aluminium, gallium, indium and tallium / Ed. by A.J Downs (1993) London, Chapman and Hall, 526 p.
6. A. Clearfield. (1964) Rev. Pure and Appl. Chem. **14** 91-108.
7. D. A. Skoog, J.J. Leary. Principles of Instrumental Analysis (1992) Fort Worth, Saunders.
8. E.A.M.F. Dahmen. Electroanalysis: theory and applications in aqueous and non-aqueous media and in automated chemical control (1986) Amsterdam, Elsevier, 383 p.
9. G. Svehla. Automatic potentiometric titrations ((1978) Oxford, Pergamon, 219 p.
10. C.M.A. Brett, A.M. Oliveira Brett. Electroanalysis (1998) Oxford, Oxford Universisty Press.
11. L.P. Holmes, D.L. Cole, E.M. Eyring. J. Phys. Chem. (1968) **72** 301-310.
12. H. Koinuma, H.N. Aiyer, Y. Matsumoto. Sci. Technol. Adv. Mater. (2000) **1**, 1-10.
13. K. Burger. Organic reagents in metal analysis (1973) Oxford, Pergamon, 266 p.
14. N.I. Ershova, V.M. Ivanov. Anal. Chim. Acta, (2000) **408** 145-151.
15. D.J. Hawke, K.J. Powell, S. Sjoberg. Polyhedron, (1995) **14** 377-385.
16. S.L. Simpson et. al. Anal. Chim. Acta (1998) **359** 329-340.
17. Z. Holzbecher. Handbook of organic reagents in inorganic analysis (1976) Chichester, Ellis Horwood, 734 p.
18. A.R. Coscione et. al. Anal. Chim. Acta (2000) **423,** 31-40.
19. J.J. Tulock, G.J. Blanchard. J. Phys. Chem. B (2002) **106** 3568-3575.
20. P.M. Jardine, L.W. Zelazny. Soil Sci. Soc. Am. J. (1986) **50** 895-900.
21. T. Okai. Geostandards Newsletter (1997) **21** 97-99.
22. A.H. Rosenberg. In: XIV Congreso Latinoamerica e Iberico De Quimicos cosmeticos and I.F.S.C.C. International Conference, Santiago de Chile 23-26 May, 1999. Conference Proceedings (1999) 25-28.
23. A.H. Rosenberg, J.J. Fitzgerald. Chemistry of Aluminum-Zirconium-Glycine (AZG) complexes Chlorohydrates. In: Antiperspirants and Deodorants / Ed. by K. Laden (1999) New York, Marcel Dekker, 83-136.
24. M.L. Magnuson et. al. Anal. Chem. (2001) **73** 4815-4820.
25. Modern Methods of Particle Size Analysis / Ed. by H.G. Barth (1984) Wiley-Interscience, 320 p.
26. B.Chu. Laser light scattering: basic principles and practice (1991) London, Academic Press, 343 p.

27. N4Plus Coulter Particle Sizer. Instruction Manual, (2001).
28. J.W. Akitt. Prog. Nucl. Mag. Res. Sp. (1989) **21** P. 1-2, 1-149.
29. W. Kemp. NMR in chemistry: a multinuclear introduction (1986) London, Macmillan, 240 p.
30. J.W. Akitt. Aluminium, Gallium, Indium and Thallium. In: Multinuclear NMR / Ed. by J. Mason (1987). New York, Plenum Press 259-292.
31. M.J. Adams. Chemometrics in Analytical Spectroscopy (1995) London, RSC, 216 p.
32. M. Aberg, J. Glaser. Inorg. Chim. Acta (1993) **206** 53-61.
33. E. Ponthieu et. al. Journal of Sol-Gel Science and Technology (1997) **8** 201-206.
34. M. Balasubramanian, S.K. Malhotra, C.Y. Gokularathnam. Transact. Indian Institute of Metals (1995) **48** 259-262.
35. J. Kirchnerova et. al. Catal. Lett. (1993) **21** 77-87.
36. K. Matsui, M. Ohgai, H. Arashi. J. Ceram. Soc. Jpn., (1995) **103**. 593-597.
37. S.V. Kalinin et. al. J. Sol-Gel Sci.Technol. (1995) **4** 31-35.
38. S.D. Fields, G.W. Strout, S.D. Russell. Microsc. Res. Techn. (1997) **38** 315-328.
39. K. Nakamoto. Infrared and Raman spectra of inorganic and coordination compounds, Part B (1997) New York, John Wiley.
40. S.D. Ross. Inorganic infrared and Raman spectra (1972) Maidenhead, McGraw-Hill, 414p.
41. The infrared spectra handbook of inorganic compounds (1984) Philadelphia, Sadtler Research Laboratories.
42. J. Degenhardt, A.J. McQuillan. Langmuir (1999) **15** 4595-4602
43. H. Wijnja, C.P. Schulthess. Spectrochim. Acta A (1999) **55** 861-872.
44. H.P. Klug, L.E. Alexander. X-ray diffraction procedures: for polycrystalline and amorphous materials (1974) New York-Chichester, Wiley.
45. JCPDS Powder Diffraction computer file (1999).
46. I. Noda. J. Am. Chem. Soc. (1989) **111** 8116-8118.
47. I. Noda et. al. Appl. Spectrosc. (2000) **54** 236A-248A.
48. J. Schraml, J.M. Bellama. 2D NMR. (1988) New York, Wiley and Sons, 220 p.

CHAPTER III. Solution speciation studies of hydrolysed aluminium ions

A study of aluminium-ion speciation in aqueous solutions is described in the following chapter. The aim of the study was to apply an integrated physicochemical and analytical approach to the investigation of the speciation patterns of Al-ions which would provide: (*a*) full speciation patterns in Al-containing aqueous systems from molecular precursors to condensed Al polymers, colloidal phases, solid phases and products of their dissolution over a wide pH range; (*b*) development, improvement and implementation of methods providing reliable and comprehensive information on Al speciation; (*c*) retrieval of maximum chemical and structural information on species present in hydrolysed solutions of Al-ions using advanced data treatment algorithms.

The study was divided into two parts according to the temperature conditions at which hydrolysis-condensation of Al-ions was characterised: room temperature studies (20 to 25 °C) and high-temperature studies (90 °C). The major interest of the present work was in the Al_{13}-mer and especially in the larger Al_{30}-mer species which are favoured at higher temperatures [1,2]. The choice of room temperature conditions for comparison was made because of the abundance of previous work at these particular conditions [3-5] and the relative ease of temperature control at ambient conditions. The large difference of temperatures studied dictated some difference in experimental design, however, the major approach to aluminium speciation based on alkaline titrations and implementation of the hydrolysis ratio as a fundamental parameter of metal-ion speciation was maintained irrespective of the temperature conditions chosen.

3.1. Solution studies of aluminium speciation at room temperature

The aim of the room-temperature study was to investigate the speciation of Al-ions and in medium concentrated solutions (0.01-0.2 M) during neutralisation of inorganic salt solutions (aluminium nitrate, chloride and sulphate) at 25 ± 1 °C with alkalis of different strength (KOH, NH_4OH, $KHCO_3$) and concentration (0.45–2.0 M). The effect of ionic strength on the speciation of Al-ions is also investigated.

3.1.1. Potentiometric titrations of aluminium solutions at room temperature

As mentioned above, potentiometric titration is one of the oldest and most widely used methods for the studies of metal hydrolysis-condensation. This method was chosen for the systematic study of aluminium and zirconium speciation in solutions. Several improvements to the conventional titration routine were introduced including a new time-resolved methodology in conjunction with general correlation analysis.

The first improvement is an introduction of the formal hydrolysis ratio value (h) as an x-axis for the presentation of titration curves instead of the frequently used titrant volume [6]. In order to do so, the original values of titrant volume (V(KOH), ml) were re-calculated to give values of the hydrolysis ratio h=[OH^-]/[Al_{total}] and used for the x-axis. It is then possible for an assignment of the inflexions observed in titration curves to the particular species on the basis of the theoretical hydrolysis ratios of the species as described in Chapter 1. We call this approach a 'phenomenological' analysis of the potentiometric titration curves similar to the assignment of spectral signals in spectroscopy [7] in contrast with conventional analytical volumetric approach [8] or more comprehensive thermodynamic approach based on calculation of equilibrium constants from the potentiometric data [9,10]

Another improvement is an introduction of first derivative curves ($\Delta pH/\Delta h$ vs. h) instead of conventional integral curves (pH vs. h) as shown in Fig. 3.1. Derivatisation allows for a sharper presentation of the observed inflexions and for more exact determination of the inflexion points. The first derivative presentation of the potentiometric curves has been made preferential throughout this study. Moreover, the first derivative curve of a potentiometric titration enables one to perform peak-fitting procedure as shown in Fig. 3.1 for further refining of the inflexion point positions in terms of hydrolysis ratios and resolving of close (overlapping) inflexion points.

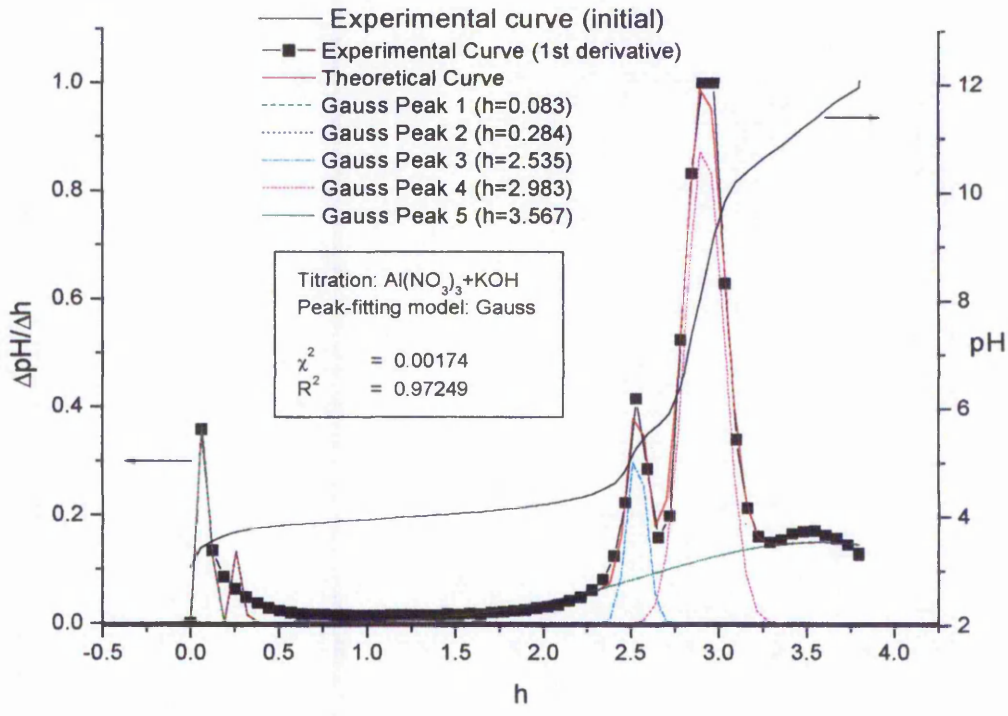


Fig. 3.1. Potentiometric titration curve obtained from the titration of $Al(NO_3)_3$ (0.1M) aqueous solution with KOH (1.6 M) at 25°C.

Fitting of the inflexion peaks observed in the first derivative potentiometric titration curve shown in Fig 3.1 using Microcal Origin 6.1 peak-fitting module enabled identification of five major inflexions at h=0.083, h=0.284, h=2.572, h=2.983 and h=3.506 related to different stages of the hydrolysis-condensation of Al-ions and other processes occurring in the Al solution during the alkaline titration. Assignments of the inflexions are given in Table 3.1.

Table 3.1. Assignments of the inflexion points observed in the potentiometric titration of $Al(NO_3)_3$ (0.1M) aqueous solution with KOH (1.6 M) at 25°C

Peak No	Inflexion peak assignment	Peak centre	pH
1	Early stages of Al hydrolysis: monomeric species $[Al(OH)(H_2O)_5]^{2+}$; $[Al(OH)_2(H_2O)_4]^{+}$	h = 0.083	3.65
2	Tentatively, oligomeric species - dimer $[Al_2(OH)_2(H_2O)_4]^{4+}$ and trimer $[Al_3(OH)_4(H_2O)_9]^{5+}$	h = 0.284	4.11
3	Tridecameric Al species	h = 2.572	5.69
4	Bulk precipitation of amorphous aluminium hydroxide	h = 2.983	7.38
5	Dissolution of aluminium hydroxide	h = 3.506	11.12

The high-quality fitting of results was indicated by a high correlation coefficient value (R^2=0.97249) and non-parametric coefficient (χ^2=0.00174) as well as excellent coincidence of the experimental and theoretical curves obtained from the peak-fitting procedure. Peak-fitting allowed resolution of two adjacent peaks at h=0.083 and h=0.284 that otherwise would have remained unresolved even in the first derivative curve of the performed titration.

Shape and symmetry of the inflexion peaks can also be revealed by the application of the peak-fitting procedure. Inflexion in an ideal titration curve leads to a highly symmetric peak in the first derivative curve following a certain classical (e.g. Gaussian) distribution [11]. Most of the peaks observed in the titration of aluminium nitrate with potassium hydroxide given in Fig.3.1 also have a Gaussian shape. The peak-fitting procedure enabled a better location of the peak maxima in some cases where the number of experimental points is insufficient to produce a perfect symmetric peak. It also enabled quantification of the parameters of the fitted inflexion peaks such as height, half-width and peak area making it possible to compare more quantitatively titration curves obtained at different conditions.

The advanced 'phenomenological' treatment of the curves obtained from titrations of aluminium salt solutions with alkalis enabled identification of most of the Al species present in solution over a wide pH range which fitted well with literature data [5,12,13] and allowed investigation of detailed Al speciation in relation to several important parameters such as the effect of counter-ions; ionic strength, strength and concentration of alkali as well as concentration of aluminium-ions.

3.1.1.1. Effect of aluminium and alkali concentration on the speciation of Al-ions

The effect of the concentration of aluminium-ions and alkali on speciation was investigated. An illustrative example, the titration of aluminium nitrate with KOH is presented in Fig. 3.2.

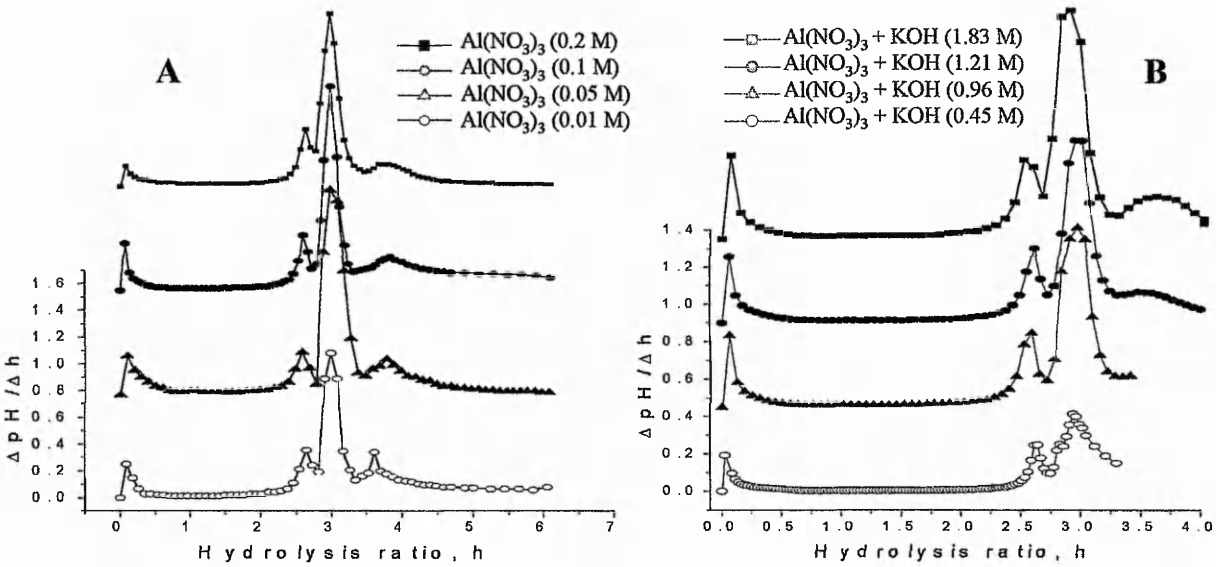


Fig. 3.2. First derivative curves of potentiometric titrations of $Al(NO_3)_3$ of different concentrations (***A, left***) with KOH of different concentrations (***B, right***). Y-offset: ***A*** - 130%; ***B*** - 90%. ([KOH]=1.83 M in graph *A*; [$Al(NO_3)_3$]=0.1 M in graph *B*).

Below *h*~3.0 the overall shape of the first derivative curve of the potentiometric titrations of $Al(NO_3)_3$ with KOH at different concentrations of Al-ions show only minor changes in speciation patterns of hydrolysed Al solutions (Fig. 3.2*A*). Peak positions at *h*~0.08; *h*~0.3; *h*~2.5-2.6 and *h*~3.0 remain practically the same for all four titration curves shown in Fig. 3.2*A*. The inflexion peak at *h*>3.0 corresponding to the dissolution of the Al hydroxide precipitate (Table 3.1) becomes sharper and shifts to lower hydrolysis ratios indicating earlier dissolution with the formation of monomeric aluminate-ions.

Experiments to investigate the effect of aluminium-ion concentration on the shape of the titration curves (Fig. 3.2*B*) indicated that for the concentrations used (0.01 – 0.2 M) no significant differences were observed below *h* = 3.0, Fig. 3.2*B*. For the inflexion point at *h*~3.5 arising from the dissolution process a peak sharpening and a shift of the peak maximum position occurred indicating more intensive dissolution of aluminium hydroxide with the formation of monomeric aluminate-ions.

3.1.1.2. Effect of anions and alkali strength

The strength of alkali may impose variations in the potentiometric titration curves of aqueous aluminium solutions [14,15] and, consequently in the speciation patterns of hydrolysed Al-ions. Potassium hydroxide, ammonia and potassium bicarbonate were chosen for the studies of the alkali effect on the titrations. Aluminium nitrate, chloride and sulphate were chosen as sources of Al-ions. The results are presented in Fig. 3.3 and 3.4.

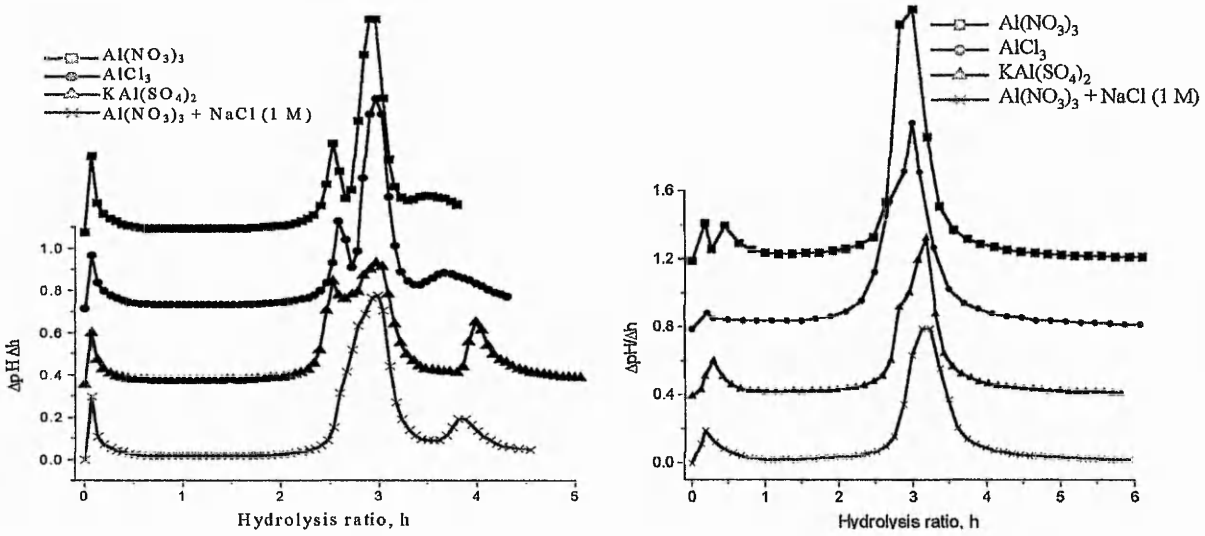


Fig. 3.3. First derivative curves of potentiometric titrations of Al salt solutions (0.1 M) with (***A***) KOH (1.8 M) and (***B***) NH_4OH (1.95 M). T=25 ± 1 °C. (***A***) Y-offset 90%; Y-offset 70%.

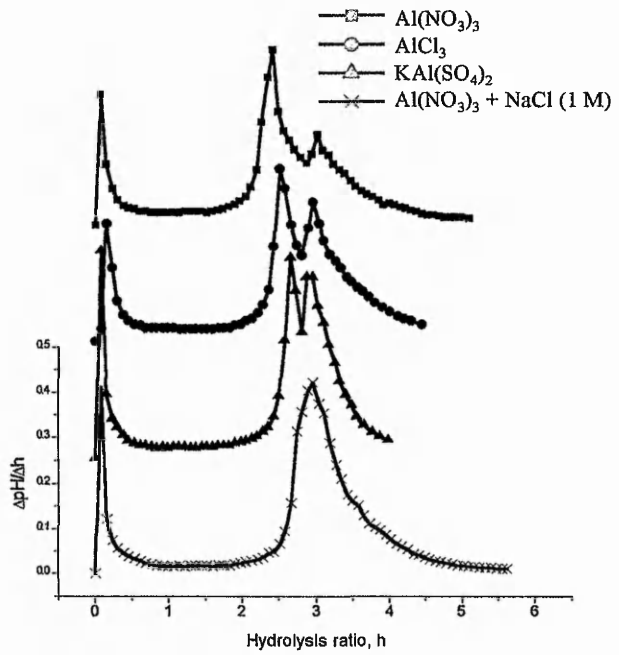


Fig. 3.4. First derivative curves of potentiometric titrations of aluminium salt solutions (0.1 M) with $KHCO_3$ (1.75 M). T=25 ± 1 °C. Y-offset 140%.

Fig. 3.3*A* shows the potentiometric behaviour of the three salts when titrated with potassium hydroxide and the effect of the addition of sodium chloride. The first derivative curves for the nitrate and chloride salts are quite similar and show four major peaks (the fifth peak at $h \sim 0.3$ is not resolved) that correspond to speciation features described above (Table 3.1) in the literature [12,13,16]. The peak at $h < 0.05$ relates to the hydrolysis of Al ions on first additions of alkali to yield dimers and trimers. The peak at $h \sim 2.5$-2.6 reflects the formation of large Al polycations, mainly the tridecameric species $[AlO_4Al_{12}(OH)_{24}(H_2O)_{20}]^{7+}$ or (Al_{13}-mer) [13]. The unresolved peak at $h \sim 3.0$ indicates the complete precipitation of

amorphous aluminium hydroxide [12,13,16]. The fourth peak (h > 3.5) indicates the dissolution of the precipitate in an alkaline medium [13].

In the titration of $KAl(SO_4)_2$ with KOH (Fig. 3.3*A*), all four peaks are present but the peak indicating the formation of large polymers is shifted to h=2.34 and it is poorly resolved from the peak at h ~ 3.0. The peak indicating the dissolution of the precipitate is sharper and is shifted to a higher hydrolysis ratio compared to solutions containing the nitrate and chloride salts of aluminium. When the electrolyte concentration is increased by addition of sodium chloride, the peak at h~2.5 indicating the appearance of polymeric species disappears or is unresolved from the peak at h~3.0.

Peak-fitting of the first derivative curves of potentiometric titrations enabled us to obtain exact values of inflexion points in the first derivative titration curves of Al salts with KOH. The results of peak-fitting analysis performed using Peak-Solve software (a part of Galactic GRAMS/32 version 5.1 software) are given in Table 3.2. For the identification of the peaks in Table 3.2 see data of Table 3.1.

From the data of Table 3.2 one can find that all five peaks in titrations 1-3 and 5 described in Table 3.1 are resolved using the peak-fitting software and their positions are detected quite precisely (the standard error of positioning the peaks as well as for determination of peak heights and widths does not exceed ca. 1 %, the standard error for peak areas lies within 10 %). The peak-fitting procedure is characterised by relatively high accuracy as follows from the comparison of titrations 2 and 3 conducted on the same systems at the same conditions (70 points on the titration curve, time interval between additions 104 s). In the case of the forth titration of potassium aluminium sulphate two more peaks are revealed by the peak-fitting procedure, at h=3.442 and h=4.343. From the data of Table 3.2 it follows that peaks 1 and 2, relating to the hydrolysis of monomers and the formation of small oligomers (as in Table 3.1), remain practically at the same position at h=0.08±0.006 and h=0.2±0.02. The peak No 3 in the titrations of non-complexing Al salts (chloride and nitrate) is located at h=2.6±0.05 while for the titrations of $KAl(SO_4)_2$ its position is at ca. 2.38±0.04. This peak is also shifted to h=2.7±0.4 in the titrations of $Al(NO_3)_3$ at high ionic strength (1 M NaCl).

The peak of precipitation of aluminium hydroxide (peak 4, Table 3.2) is close to the theoretical value for $Al(OH)_3$ h=3±0.04 in the titrations of non-complexing Al salts. For $KAl(SO_4)_2$ it is shifted to h=2.8±0.04 and at high ionic strength to 2.9±0.05. Finally, peak 5 (Table 3.2) relating to dissolution of the precipitate is located at almost the same position (h=3.5±0.2) for non-complexing Al salts regardless of the ionic strength. Dissolution of the precipitate is more complicated for $KAl(SO_4)_2$ where up to four peaks relating to different (competing) processes can be detected the using peak-fitting procedure.

Table 3.2. Results of the peak-fitting of the first derivative curves of potentiometric titrations of aluminium salts with potassium hydroxide at 25°C

Titration No	Sample	Titrant	Peak No	Peak position (*h*)	Peak height	Peak width	Peak area
1	$Al(NO_3)_3$ (0.1 M)	KOH (1.83 M)	1	0.087	0.235	0.097	0.023
			2	0.181	0.097	0.497	0.041
			3	2.580	0.384	0.169	0.069
			4	2.991	0.988	0.283	0.298
			5	3.495	0.169	0.579	0.081
2	$AlCl_3$ (0.1 M)	KOH (1.83 M)	1	0.078	0.216	0.061	0.014
			2	0.195	0.047	0.244	0.052
			3	2.605	0.342	0.141	0.051
			4	3.025	0.878	0.284	0.265
			5	3.582	0.373	3.415	0.107
3	$AlCl_3$ (0.1 M)	KOH (1.83 M)	1	0.075	0.213	0.070	0.019
			2	0.202	0.045	0.557	0.012
			3	2.598	0.365	0.163	0.063
			4	2.991	0.909	0.268	0.277
			5	3.605	0.330	0.867	0.109
4	$KAl(SO_4)_2$ (0.1 M)	KOH (1.83 M)	1	0.075	0.235	0.073	0.018
			2	0.205	0.034	0.161	0.006
			3	2.414	0.379	0.257	0.104
			4	2.814	0.554	0.430	0.254
			5	3.442	0.039	0.522	0.022
			6	4.063	0.262	0.184	0.051
			7	4.343	0.058	0.504	0.031
5	$AlCl_3$ (0.1 M) + NaCl (1 M)	KOH (1.83 M)	1	0.084	0.389	0.060	0.024
			2	0.271	0.066	0.537	0.033
			3	2.68	0.335	0.265	0.095
			4	2.905	0.923	0.390	0.383
			5	3.521	0.161	0.695	0.115

Titration with NH_4OH at a concentration similar to the systems 'Al salt solution – KOH' described above gives first derivative curves that are markedly different (Fig. 3.3*B*). The peak at h~0.3 prevails over the peak at h<0.1 unlike in the titrations with KOH (Fig.3.3*A*). The peak corresponding to the formation of large polymers is located at h≥2.7 and is only present as a shoulder on the main peak at h~3.0. The peak at h>3.5 disappears from all titration curves conducted with NH_4OH (Fig. 3.3*B*). The addition of NaCl to the reaction medium had much less effect on the shape of the derivative curve produced with NH_4OH than for addition of electrolyte prior to titration with KOH.

Titration with $KHCO_3$ yielded different first derivative curves again (Fig. 3.4). For titration of the nitrate and chloride salts, the peak at h~2.6 is the dominant feature but its position shifts to higher hydrolysis ratio as the aluminium salt used was changed from nitrate to chloride to sulphate. There is also a concomitant shift to lower hydrolysis ratio for the peak corresponding to the precipitation of amorphous aluminium hydroxide species at h~3.0. At high ionic strength the peak at h~2.6 disappears, probably merging with the peak at h~3.0. It

was not possible for any sample to see a peak corresponding to the dissolution of the sample to give aluminate ions.

3.1.1.3. Time-resolved potentiometric titrations of Al solutions

During potentiometric titrations of Al solutions described above which have been performed at fixed time intervals between titrant additions and with the measurement of pH values every 2-5s it has been noticed that time-resolved pH profiles between the additions fall into certain characteristic shapes as described in Section 2.3.4. An attempt was made in the present study to implement these pH-profiles for the investigation of Al speciation.

Time-resolved pH-profiles for the titration of $Al(NO_3)_3$ solution (0.1 M) with KOH (1.8 M) as an illustrative example are shown in Fig. 3.5.

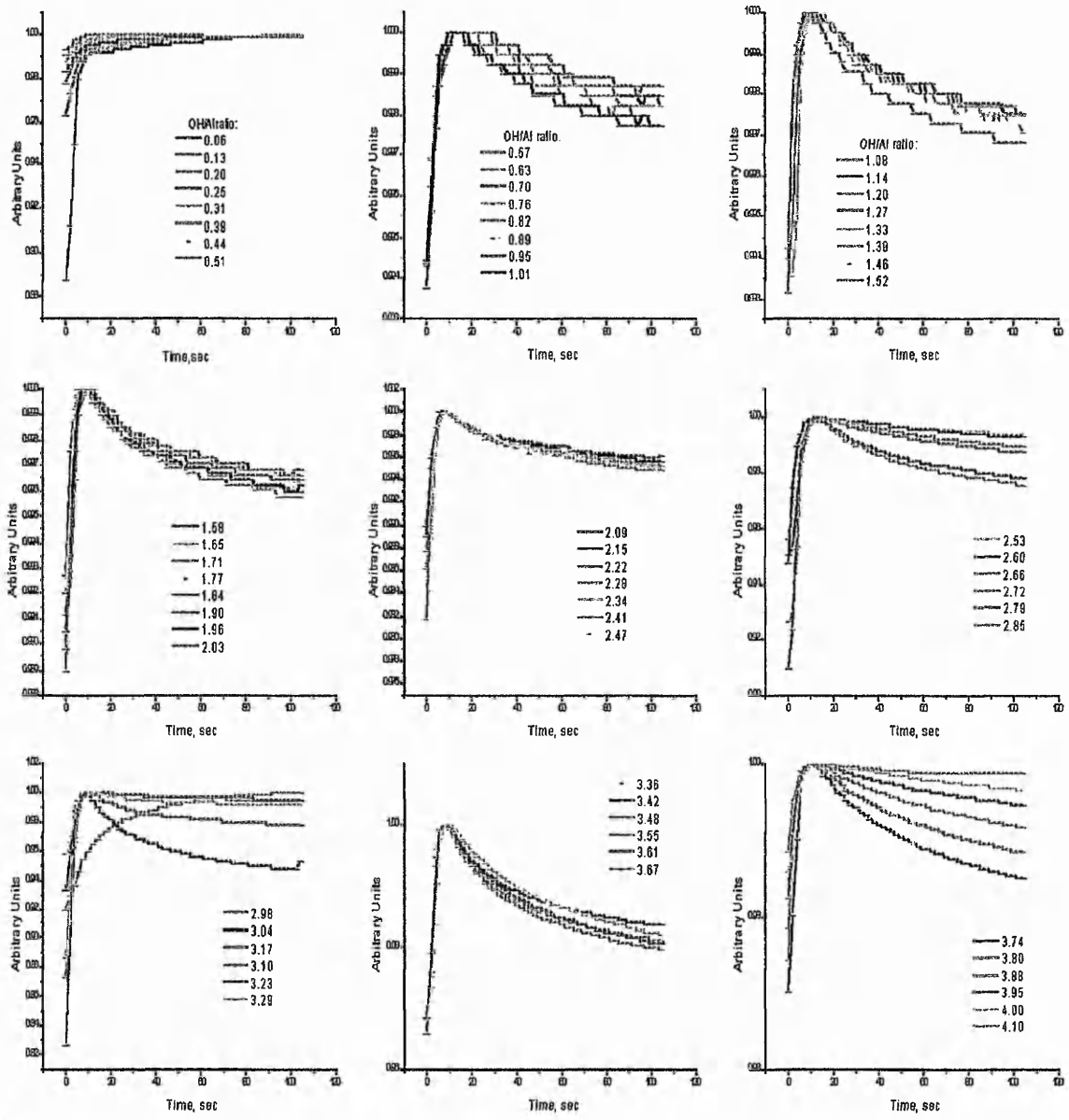


Fig. 3.5. Time-resolved pH-profiles obtained from the potentiometric titration of 0.1 M $Al(NO_3)_3$ solution with 1.8 M KOH. T=25 °C (Curves are normalised to unity for presentation purposes).

From the data of Fig. 3.5 one can see that the shape of the time-resolved pH-profiles strongly depends on the hydrolysis ratio at each titration point. Thus, these time-resolved curves may provide additional information on the hydrolysis-condensation of Al-ions during alkaline titrations.

The shape of the time-resolved pH-profiles in the early stages of aluminium hydrolysis (h<0.51) are of type *B* according to the classification presented in Section 2.3.4 (Fig. 2.3). The shape indicates the absence of complications in aluminium hydrolysis followed by a fast consumption of OH^- by Al-ions. At higher hydrolysis ratios ($0.57 \leq h \leq 2.95$) type *A* relaxation curves occur. The decay of the time-resolved pH-curves probably arises from the dissolution of the aluminium hydroxide phase formed due to local disturbances produced by additions of strong alkali. A large depth of dissolution decay shows that the colloidal phase of amorphous hydroxide is very unstable at acidic conditions and quickly disappears within 2 min between titrant additions. Visual observations support this assumption – after each addition of strong concentrated alkali in the mentioned hydrolysis ratio range the sample solution became slightly turbid and then cleared. The decay in time-resolved pH-profiles reaches a minimum at h~2.53 (compare this to the inflexion at h=2.57 in the 'normal' titration curve shown in Fig. 3.1). Then the decay deepens at $2.61 \leq h \leq 2.79$. The most drastic change in time-resolved pH-curves occurs in the hydrolysis ratio range $2.98 \leq h \leq 3.29$ where the time-resolved curves change their shape twice at h=2.98 (*B* type) and h<2.98 (*A* type) (compare this to the inflexion at h~3.0 in the titration curves Fig. 3.1, 3.2). The type *A* curves are observed at alkaline conditions (h>2.98) and the curve decay reaches a maximum at h~3.5 (compare this to the inflexion at h=3.5 in Fig. 3.1). There is an obvious similarity between the patterns in the shapes of time-resolved pH-profiles (Fig. 3.5) and conventional titration curve of the same system (Fig. 3.1).

The shape patterns of time-resolved pH-profiles are very sensitive to the conditions under which a titration is conducted. For instance, when changing the system from non-complexing aluminium salt (chloride or nitrate) to aluminium sulphate, the shape patterns become completely different (the full set of time-resolved pH-profiles of the titration of $KAl(SO_4)_2$ with KOH is omitted for the sake of brevity). Significant changes in time-resolved pH-curves also occur when the ionic strength of solution is increased.

In order to automate the shape classification procedure of numerous time-resolved profiles accumulated in the potentiometric titrations (the number ranged from 50 to 120 corresponding to the number of points in a potentiometric titration) we have applied Correlation Analysis (CA) described in Chapter 2, Section 2.11. The general treatment procedure of the time-resolved potentiometric curves is shown in Fig. 3.6.

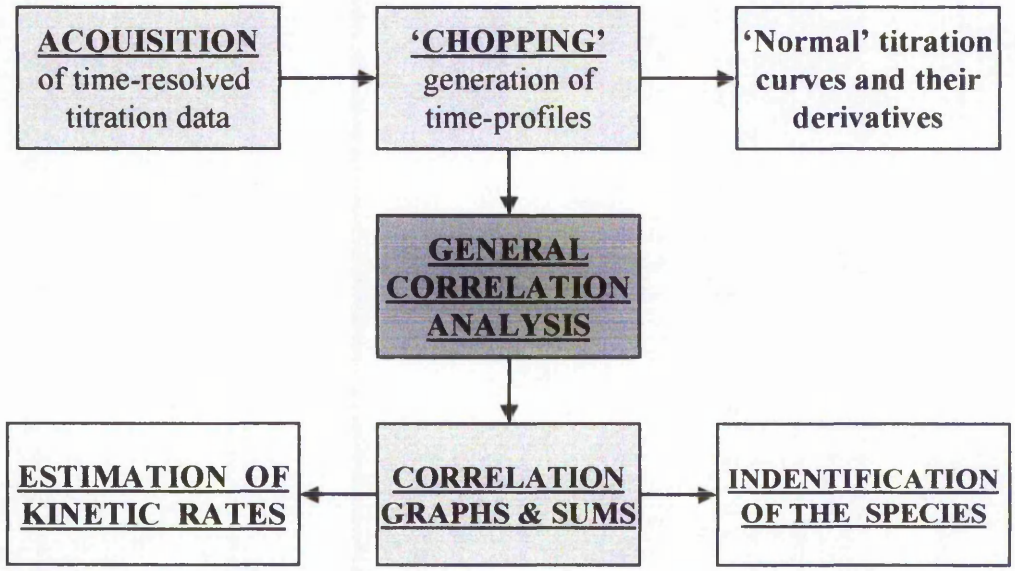


Fig. 3.6. The general procedure of treatment of time-resolved potentiometric titrations

From the scheme presented in Fig. 3.6 one can see that along with reconstruction of 'normal' titration curves and their following derivatisation and peak-fitting analysis, one may also conduct a correlation analysis of the time-resolved pH-profiles. From the contour 3D correlation maps [17] or correlation sums introduced in this work one may then identify the species detected in the potentiometric titration by the phenomenological analysis of the hydrolysis ratios at particular inflexion points. Moreover, kinetic rate constants of the pH relaxation process can be extracted from the time-resolved measurements. These constants do not reflect the real kinetics of aluminium hydrolysis-condensation, nevertheless, they can be used as a quantitative measure of the relaxation processes during titration and related to particular changes in speciation patterns observed during the alkaline hydrolysis of metal ions. This approach has been implemented in multi-batch titrations of aqueous zirconium solutions and will be discussed in Chapter 4.

On the basis of the modified procedure of CA proposed in this work and described in Section 2.11.2 one can also build a 'titration curve' in the coordinates 'correlation sum *vs.* hydrolysis ratio' and apply this curve for the identification of the major Al species present in solution. The results of the application of the CA to the data of the potentiometric titration are presented in Fig. 3.7 in comparison with conventional titration curve and its first derivative.

The resulting 'correlation sum' curve has several positive and negative peaks (Fig. 3.7). The positive peak at h~0.08 (hydrolysis of Al monomers, Table 3.1) coincides with the peak of the first derivative curve. The next peak in the correlation sum curve is negative with the maximum at h~0.3. The presence of this peak indicates drastic changes occurring with the shape of the time-resolved pH-profiles in the range of $0.1 \leq h \leq 0.5$. This peak is unresolved

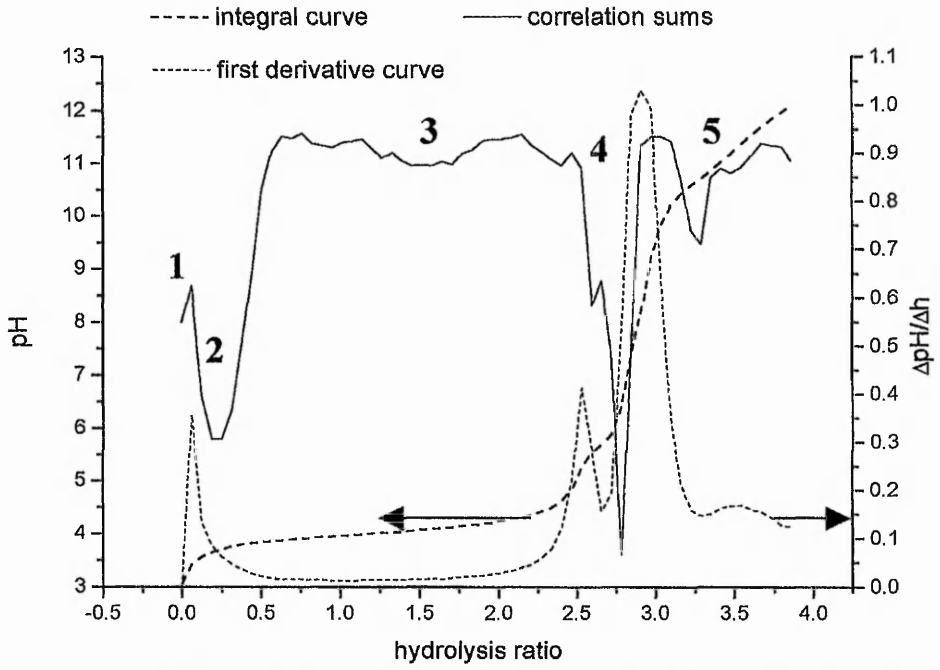


Fig. 3.47. Comparison of the results of the CA of the time-resolved pH-profiles with the first derivative curve of the potentiometric titration of 0.1 M $Al(NO_3)_3$ solution with 1.8 M KOH.

in the first derivative curve of the titration unless the peak-fitting procedure is applied (see Fig. 3.1 and Table 3.2). The negative peak at h~0.3 in the correlation sum curve is followed by a quite steady plateau ($0.6 \leq h \leq 2.46$) indicating that the shape of time-resolved pH-profiles changes only slightly. The next negative peak at h=2.61 in the correlation sum curve is slightly shifted to the right compared with a similar peak at h=2.53 in the first derivative curve. Another negative correlation sum peak at h=2.78 is in between peaks at h=2.53 and h=2.96 of the first derivative. The correlation sum curve then reaches another maximum at $3.01 \leq h \leq 3.09$ before the final negative peak at h=3.26 which is followed by another plateau at $h \leq 3.61$. It is necessary to stress that the observed correlation sum curve was reproduced in a series of three titrations of the same system '$Al(NO_3)_3$-KOH', and is statistically reliable (standard deviation at each curve point did not exceed ca. 5 %).

In terms of the particular shapes of the time-resolved pH-profiles we have discerned the following intervals in the correlation sum curve as shown in Fig. 3.7: ***1*** – curves of type *A* shape prevail (see Fig. 2.3 in Chapter 2 for classification); ***2*** – time-resolved pH-profiles are of *B*-shape; ***3*** – curves are again type *A* with the decay reaching a maximum at h~1.4-1.6 (corresponds to a local minimum or 'negative peak' in the correlation sum curve); ***4*** – several changes occur in this short interval of hydrolysis ratios where the time-profiles change their shape from *A* to *B* and back twice; ***5*** – time-profiles change to a profound *A*-type after which only *B*-type curves occur at higher hydrolysis ratios.

One may see that the correlation sum curve shown in Fig. 3.7 actually represents a quantitative measure of the changes in the time-resolved pH-profiles discussed above for Fig. 3.5. The results of correlation analysis for the system $AlCl_3$-KOH are shown in Fig. 3.8.

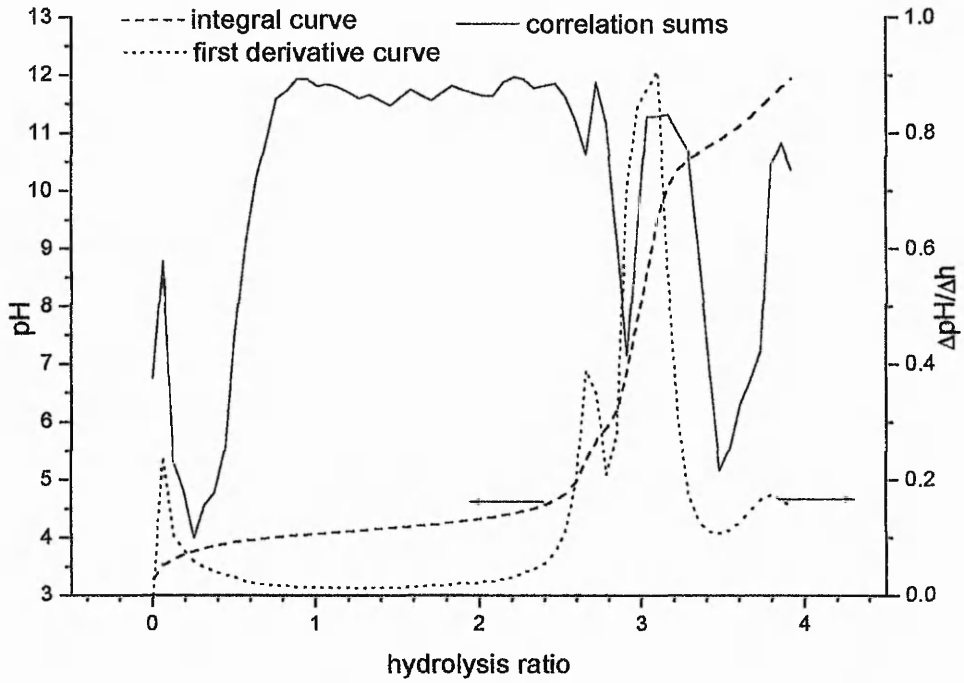


Fig. 3.8. Comparison of the results of the CA with the first derivative curve of the potentiometric titration of 0.1 M $AlCl_3$ solution with 1.8 M KOH. T=25 °C.

One can see from Fig. 3.8 that the correlation sum curve from the potentiometric titration of $AlCl_3$ with KOH obtained by the modified CA procedure proposed in the present work is very similar to that of the system '$Al(NO_3)_3$-KOH' (Fig. 3.7). The only minor difference is the magnitude of the time-profile shape change indicated by the height of the positive and negative peaks observed during titration of $AlCl_3$ with KOH. The negative peak at h=2.63 of the correlation sum curve is only slightly shifted to the right compared with the analogous peak at h=2.60 of the first derivative curve. The rest of the features of the correlation sum curve shown in Fig. 3.8 practically coincide with the description of the same curve in Fig. 3.7.

In the case of '$KAl(SO_4)_2$ – KOH' system one would expect a different shape of the correlation sum curve on the basis of the shapes of the time-resolved profiles obtained from the titration (Appendix A) and the first derivative curve (Fig. 3.3). The results of the CA performed on the titration of aluminium sulphate with KOH are shown in Fig. 3.9.

From the data of Fig. 3.9 one can see that the shape of the correlation sum curve is significantly different from the curves shown in Fig. 3.7 and 3.8. In the presence of sulphate, the negative peaks at h~0.24, h~2.60 and h~2.98 are much shallower in the corresponding correlation sum curve. The plateau at low hydrolysis ratios ranges from h=0.4 to h=2.2 in the correlation sum curve in Fig. 3.9. Yet again the negative peaks at h=2.60 and h=2.98 are located at higher hydrolysis ratios than the corresponding peaks in the first derivative curve of the titration of $KAl(SO_4)_2$ with KOH. There are two new negative peaks in the correlation sum curve at h~3.45 and h~4.22 (compare this with the data of Table 3.2, titration 4).

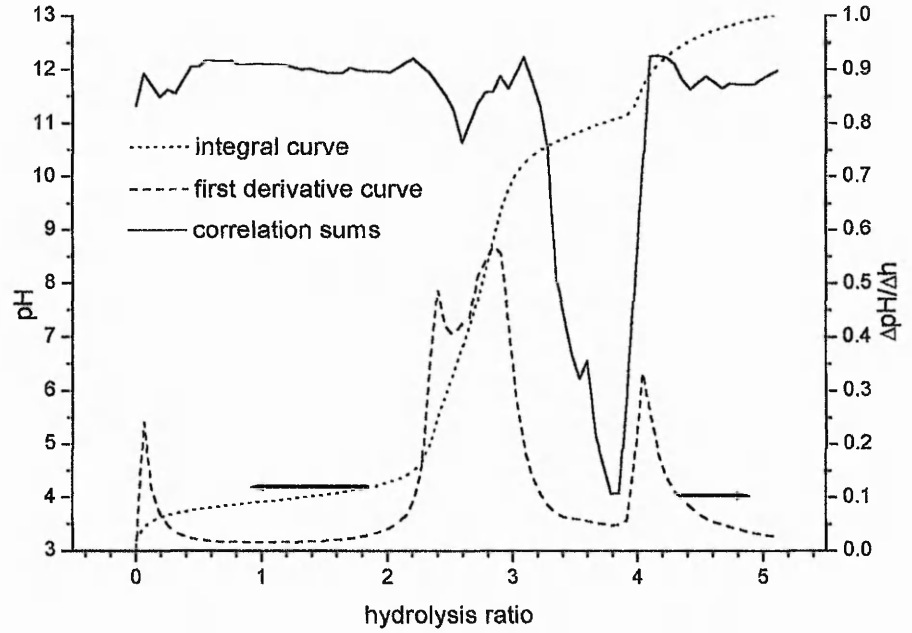


Fig. 3.9. Comparison of the results of the CA with the first derivative curve of the potentiometric titration of 0.1 M $KAl(SO_4)_2$ solution with 1.8 M KOH. T=25 °C.

The effect of high ionic strength on the correlation sum curve is shown in Fig. 3.10.

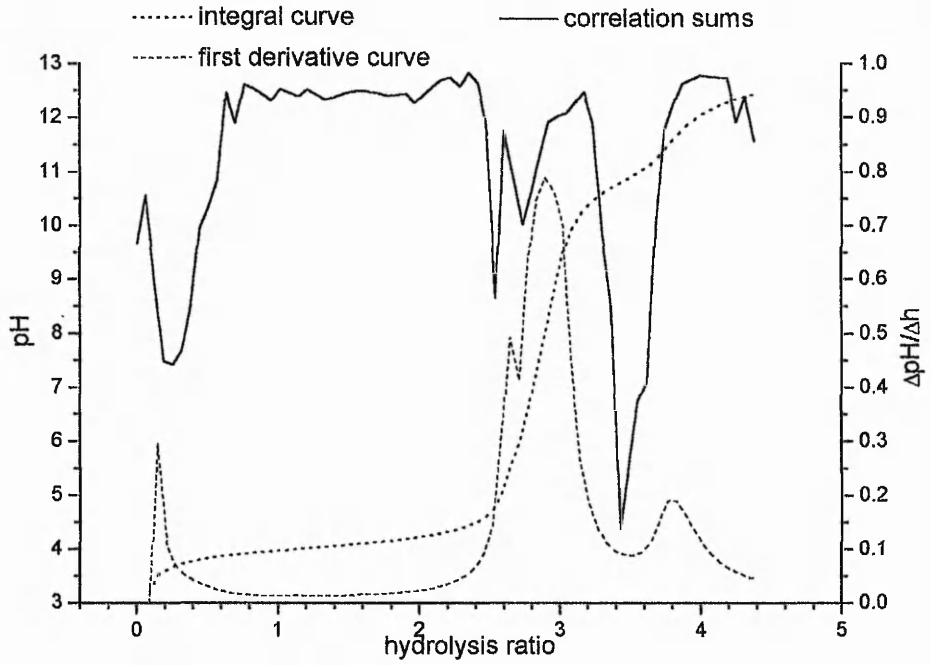


Fig. 3.10. Comparison of the results of the CA with the first derivative curve of the potentiometric titration of 0.1 M $Al(NO_3)_3$ solution with 1.8 M KOH at the presence of 1 M NaCl. T=25 °C.

The correlation sum curve observed in the titration of $Al(NO_3)_3$ with KOH at high ionic strength is very similar to the analogous curve for pure aluminium nitrate solution (Fig. 3.7). The only slight difference is in the position of the negative peaks at h=2.49 and h=2.69 in the correlation sum curve in Fig. 3.10 comparing to h=2.53 and h=2.78 in Fig. 3.8. These

peaks are also much better resolved in Fig. 3.10 at high ionic strength comparing to pure aluminium nitrate titration (Fig. 3.7), unlike the analogous peaks at h=2.59 and h=2.83 in the first derivative titration curve at the same conditions (Fig. 3.10).

Generalising the above one may see that the peaks observed in the correlation sum curve in some cases do not coincide with the similar peaks in the first derivative curves. This indicates that the chemical origin of the peaks in the correlation sum curve can be different from that of the first derivative curve.

The utilisation of the Correlation Analysis (CA) described above is based on the analysis of correlations in the 'volumetric domain' expressed by the hydrolysis ratio which means that each time-resolved set of pH-profiles has been correlated with another according to their hydrolysis ratio. We propose another application of the CA in time-resolved potentiometric titrations with a correlation in the time domain, where the sets of data contain pH-measurements at every time the measurement was made (e.g. 0, 2, 4,6, ...s after each addition of titrant). The results of CA in the time domain expressed as correlation sum curves for the titrations of different Al salts with KOH as an illustrative example are shown in Fig. 3.11.

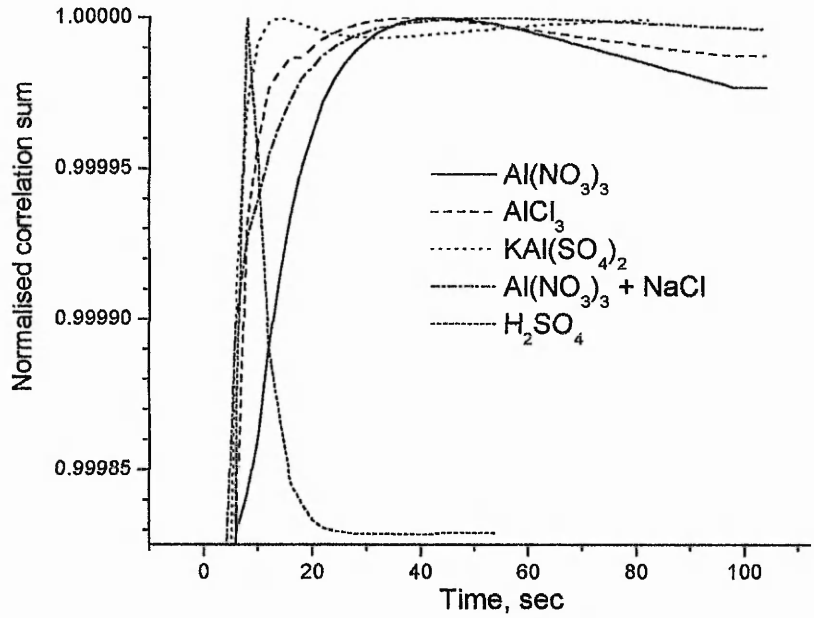


Fig. 3.11. Time-domain correlation sum curves from the titrations of (0.1 M) Al salt solutions with KOH (1.8 M). The correlation sum curves are normalised to unity and truncated (the lower part) for presentation purposes

From Fig. 3.11 it follows that the value of the correlation sum in the presented time-domain curves quickly rises and reaches a maximum after the first few seconds. The range of the maximum in the curves is quite wide: ca. 11s for H_2SO_4; 38 s for $Al(NO_3)_3$ and $Al(NO_3)_3$+NaCl; 33 s for $AlCl_3$; and 14 s for $KAl(SO_4)_2$ (the first maximum on the curve). The curve for the strongest acid studied - H_2SO_4 is the fastest to reach the maximum value, albeit the order of the rate of reaching the curve maximum for aluminium salt precursors is

the reverse of that for their complexation constants K_1 ($K_1(Al_2(SO_4)_3)$=2.57> $pK_1(AlCl_3)$=0.08 > $pK_1(Al(NO_3)_3)$=-0.05 at 20-25°C [18,19]). The strength of complexation of Al-ions with counter-ions can affect their first hydrolysis constant $K_{1,0}$ [18,19] which according to the literature is as follows: $pK_{1,0}(Al_2(SO_4)_3)$=5.23 > $pK_{1,0}(AlCl_3)$=4.97 > $pK_{1,0}(Al(NO_3)_3)$= 4.93 [5,18-21]. It must be noted that the stability constants are given for aluminium sulphate instead of alum ($KAl(SO_4)_2$), and we assume that the constants of these sulphate-containing salts will be similar at least in the first approximation. Therefore, the rate of reaching the curve maximum correlates (reciprocally) with the hydrolysis constants of Al salts which, in turn, depend on the strength of complexation of Al-ions with inorganic counter-ions. Interestingly, at high ionic strength (1M NaCl) the rate of reaching the curve maximum for $Al(NO_3)_3$ is lower than for the pure salt (Fig. 3.11). On the basis of the correlation with thermodynamic data derived above, it appears that the acidity of aluminium nitrate as well as the value of K_1 and $K_{1,0}$ decreases at high electrolyte concentration in agreement with literature data [18,19,22].

The second part of the correlation sum curves in the time-domain shown in Fig. 3.11 is a decay for H_2SO_4, $AlCl_3$ $Al(NO_3)_3$ and $Al(NO_3)_3$+NaCl, while for $KAl(SO_4)_2$ this part of the curve goes through a minimum and then starts to increase again. The decay period in the curves indicates relaxation or stabilisation of the system in question and, that along with the short-time equilibration (first, rising part of the curves) there are other processes occurring on a longer time scale, and that these processes take much longer to reach equilibrium than the time between the titrant additions. The depth of the decaying part of the correlation sum curve shows the significance of the changes on a longer time scale. This parameter does follow the order of increasing acidity of the precursors described. In spite of being only a small fraction of the overall normalised correlation sums, the decay appears to be statistically significant (the probability α>0.1) due to a large number of components (correlation coefficients) accumulated in the correlation sums obtained in the time domain (the number of correlation coefficients is equal to a total number of points in the titrations which in the present study ranged from 60 to 120).

Summarising the above, one can find that application of time-domain correlation analysis for time-resolved potentiometric titrations can yield valuable information on the time interval required for the system to reach equilibrium, on the kinetic data at the very short (scale in seconds) time range and some correlations with thermodynamic equilibria in the titration systems in question.

3.1.2. Results from ^{27}Al NMR spectroscopy

The single-batch titration setup was impossible to implement with standard NMR spectroscopy equipment. Thus, NMR studies of Al hydrolysed solutions was performed by a multi-batch approach.

Samples of hydrolysed Al solutions produced by multi-batch titrations at room temperature as described in Section 2.3 were characterised by ^{27}Al NMR spectroscopy after 24 hours of hydrolysis. The effect of base strength and counter-ion identity (chloride, nitrate and sulphate) on the hydrolysis of Al species has been explored. ^{27}Al NMR spectra of hydrolysed solutions of aluminium nitrate and chloride, as expected, were similar, with spectra collected over the hydrolysis range h = 0 - 5 being shown in Fig. 3.12*A* for aluminium chloride. NMR spectra of the hydrolysed and aged samples of $AlCl_3$ at h=0.5 and h=2.3 are shown separately in Fig. 3.13*A* and 3.13*B*.

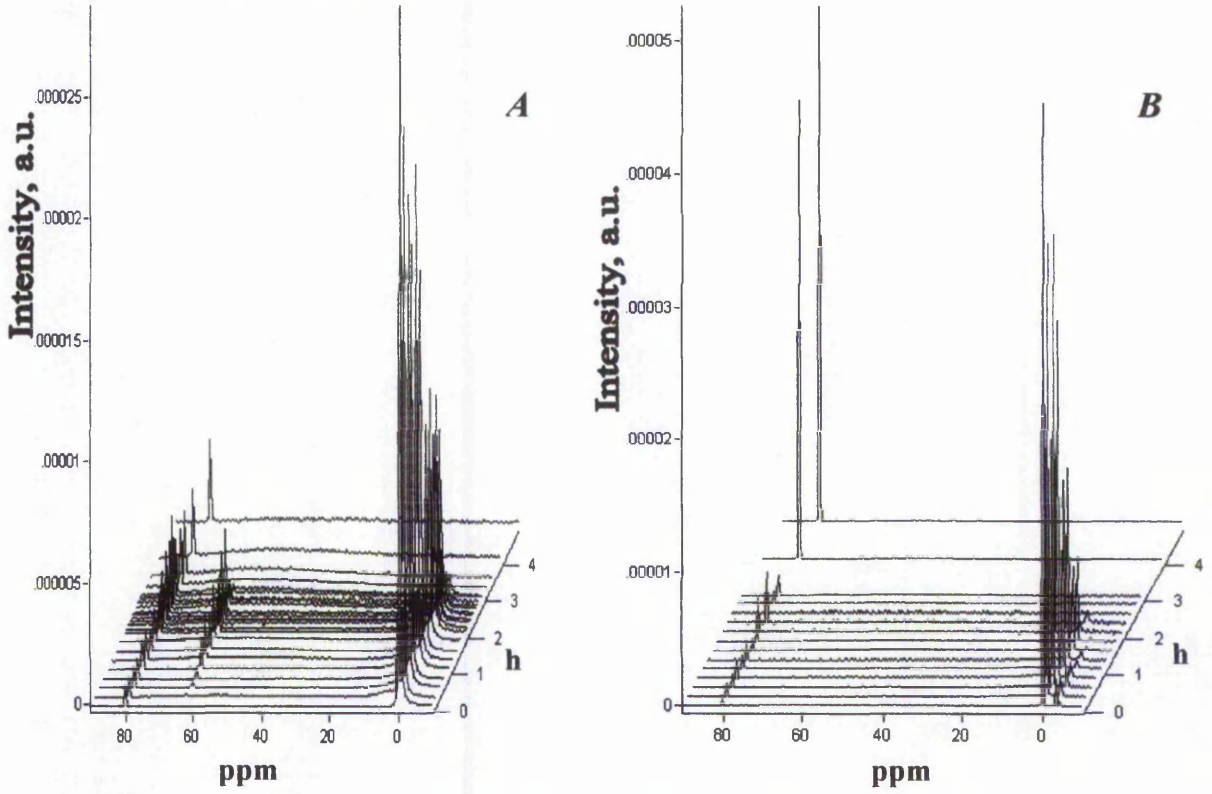


Fig. 3.12. ^{27}Al NMR spectra of aluminium-ion solutions (0.1 M) hydrolysed for 24 *h* with KOH (2.0 M). (***A***) – $AlCl_3$; (***B***) – $KAl(SO_4)_2$. The *z*-axis is the hydrolysis ratio *h*.

The spectra of $AlCl_3$ solutions in Fig. 3.12*A* and Fig.3.13*A* and *B* exhibit several major peaks most of which have been described in the literature [5,23-27]. The peak at ~0.0 ppm corresponds to the monomeric non-hydrolysed aquo-cation $Al(H_2O)_6^{3+}$; the tiny peak at ~0.34 ppm most probably derives from the monohydrolysed species $[Al(OH)(H_2O)_5]^{2+}$; the peaks at δ~0.77 and δ~4.3 ppm from small oligomeric polynuclear species, dimer $[Al_2(OH)_2(H_2O)_8]^{4+}$ and trimer $[Al_3(OH)_4(H_2O)_9]^{5+}$ respectively, the broad peak at 40-50 ppm is assigned to octahedral aluminium in the Al_{13}-mer 'shell', the peak at 63.5 ppm to tetrahedral aluminium of the Al_{13}-mer 'core' and the peak at 80.0 ppm to tetrahedral aluminium ($Al(OH)_4^-$) present in the solution of the reference NMR insert as well as produced in sample solutions under conditions of high alkalinity.

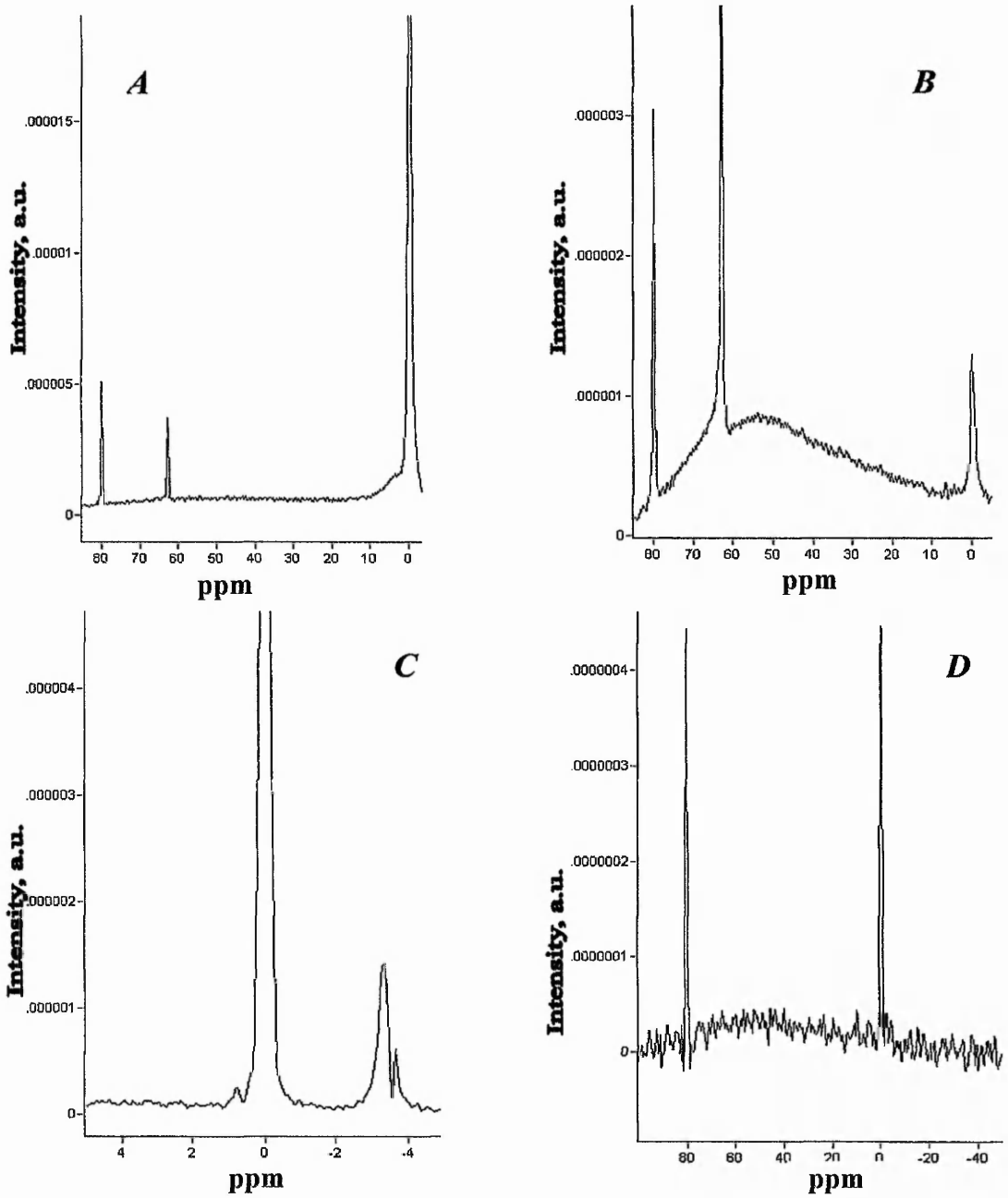


Fig. 3.13. Individual ^{27}Al NMR spectra of (0.1 M) solutions of $AlCl_3$ (***A*** and ***B***) and $KAl(SO_4)_2$ (***C*** and ***D***) hydrolysed for 24 *h* at hydrolysis ratios (***A***) h=0.5; (***B***) h=2.3; (***C***) h=0.5 and (***D***) h=2.25. Some peaks have been truncated for presentation purposes.

As follows from Fig. 3.12*A* and Fig. 3.13*A*, at low hydrolysis ratios ($0 \leq h \leq 0.5$) the solutions initially contain only the unhydrolysed aquo-cation (~0.0 ppm) and tiny concentrations of hydrolysed monomer as indicated by the small peaks at 0.34 and 0.77 ppm (at higher hydrolysis ratios these appear as a shoulder on the peak at ~0.0 ppm). Increase of the hydrolysis ratio leads to the appearance of a broad peak at ~4.3 ppm ($h \geq$ 0.75-1.0), that eventually overlaps the peak at 0.77 ppm, and to a decrease in intensity of the peak at ~0.0 ppm. The peak at ~0.0 ppm completely disappears by h~2.8-3.0, while the peak at 4.3 ppm related to Al small oligomers merges with the increasing broad peak at δ~40 ppm at h>2.0. A

peak at 63.5 ppm appears in the spectra at *h* as low as 0.5 for most of the experiments.

^{27}Al NMR spectra of solutions of aluminium sulphate (alum) show different patterns (Fig. 3.12*B*). The spectrum of low-hydrolysed alum (Fig. 3.13*C*) contains four sharp peaks at -3.68; -3.32; 0.0 and 0.77 ppm with peaks at δ~0.0 and δ~-3.32 ppm showing the largest areas. The peak at δ~ -3.3 ppm has been assigned to the complex of sulphate-ion with monomeric non-hydrolysed Al-ions [28]. There is, probably, another complex of minor importance present in solution that is indicated by the peak at δ~ -3.68 ppm. The small peak at *h*~0.77 cannot be distinguished from the peak at δ~ 4.3 ppm which appears in the hydrolysed solutions of alum at $h \geq 0.75$ (Fig. 3.13*D*). The peak at 63.5 ppm does not appear in the spectra for the whole range of hydrolysis ratios studied (Fig. 3.12*B*). The peak at ca. 4.3 ppm (dimers and/or trimers) remains virtually unchanged in intensity over a wide range of hydrolysis ratios (*h*~0.75-2.0) as does the broad peak of octahedral aluminium at δ~ 40-50 ppm ($h \geq 1.0$). At higher hydrolysis ratio ($h \geq 2.0$) the peak at 30-50 ppm completely overlaps the peak at 4.3 ppm. The intensity of the peak at 80.0 ppm also starts to increase rapidly above *h*~ 3.0 in the NMR spectra of alum solutions.

We have compared the ratios of the areas of the major peaks in the ^{27}Al NMR spectra, Fig. 3.14. Results of $AlCl_3$ multi-batch titrations with different alkalis monitored by NMR are shown in Fig. 3.14*A*-*C* and data for titration of $KAl(SO_4)_2$ with KOH in Fig. 3.14*D*.

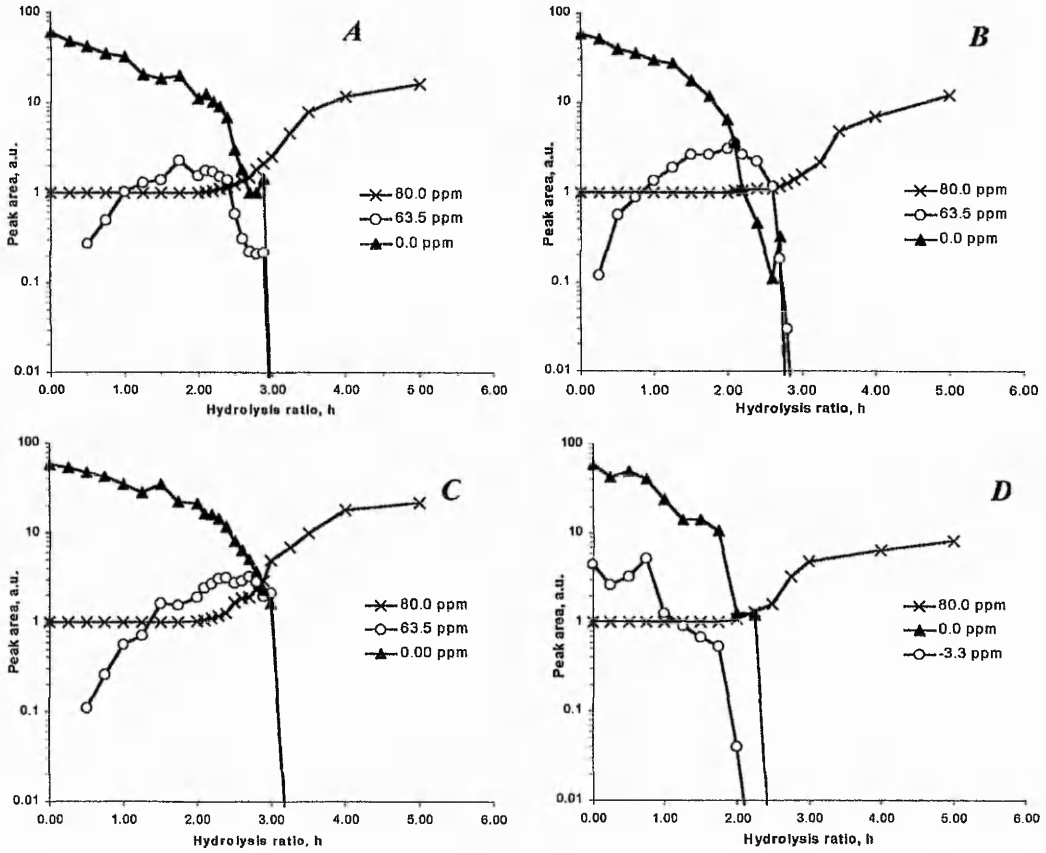


Fig. 3.14. Peak areas (*10^6) from ^{27}Al NMR spectra of (0.1 M) aluminium-containing solutions hydrolysed with alkali. (***A***) $AlCl_3$ with $KHCO_3$ (2.0 M); (***B***) $AlCl_3$ with NH_4OH (2.0 M); (C) $AlCl_3$ with KOH (2.0 M) and (***D***) $KAl(SO_4)_2$ with KOH (2.0 M).

The area of the peak at δ~ 0.0 ppm decreases with increase of hydrolysis ratio for all the observed systems, abruptly reaching zero at *h*~ 3.0 - 3.25 for $AlCl_3$ (irrespective of the alkali used) and at *h*~ 2.4 for alum titrated with KOH. The area of the other important sharp peak at 63.5 ppm from the Al_{13}-mer (only in spectra from the chloride) reaches considerable levels at *h* ~ 1 - 1.5 that remain up to *h*~ 2.3 - 2.5 when the peak area arising from the tridecameric species starts to decrease rapidly, completely disappearing at almost the same hydrolysis ratio as for loss of the monomeric species. The peak area at 80.0 ppm starts to increase exponentially above *h*=2.0 and above *h*>3.0-3.5, aluminate-ions are the only species present in completely neutralised aluminium solutions with a large excess of alkali, regardless of the alkali or counter-ion present. In the case of the NMR spectra of alum it was possible also to calculate areas of the peak at -3.3 ppm arising from the monomeric aluminium complex with sulphate, Fig. 3.14*D*. The decrease of peak area generally correlated with the behaviour of the peak at ~0.0 ppm, with both completely disappearing at $h \geq 2.0$.

We also monitored a position of the peak at ca. 0.0 ppm corresponding to the monomeric non-hydrolysed aquo-cation $Al(H_2O)_6^{3+}$ against the value of hydrolysis ratio of Al solutions as shown in Fig.3.15.

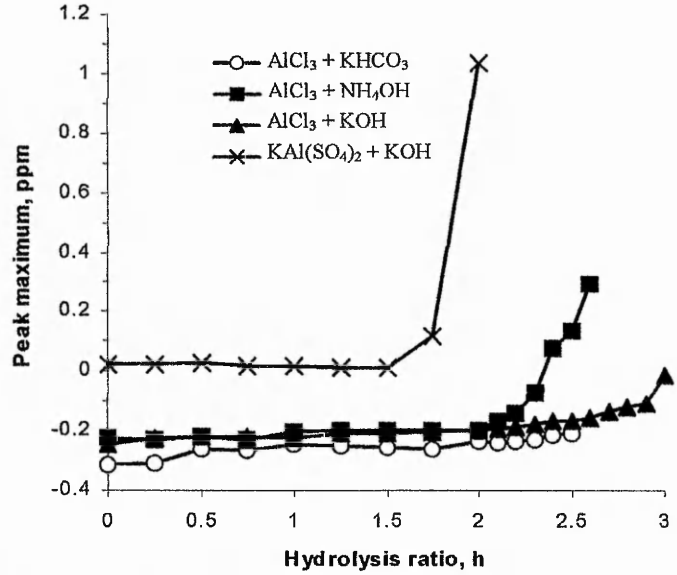


Fig. 3.15. The chemical shift (ppm) of the peak arising from $[Al(H_2O)_6]^{3+}$ ion *vs.* hydrolysis ratio (*h*) from the ^{27}Al NMR data.

From the data of Fig. 3.15 one may see that the increase of hydrolysis ratio of Al-solutions results in the constant drift of the large and sharp peak at δ=0.0 ppm. At hydrolysis ratios below 2, for titration of the chloride salt with KOH and NH_4OH the chemical shift position measured (relative to the aluminate ion at 80.0 ppm) was about -0.2 ppm, and for titration with $KHCO_3$ the chemical shift position was -0.3 ppm. At hydrolysis ratios above this there was a slight shift towards zero for titrations with all three alkalis before the species disappeared from the NMR spectra. For titrations of alum with KOH, at hydrolysis ratios below 1.5 the chemical shift measured was 0.0 ppm and for hydrolysis ratios between 1.5 and

2.0 increased to 1.0 ppm. Similar results have been reported by J.W. Akitt in [25] who described the difference between the position of the unhydrolysed monomer peak in $AlCl_3$ and $Al_2(SO_4)_3$ solutions as being about 0.2 ppm.

3.1.3. Results from dynamic light scattering

Along with ^{27}Al NMR spectroscopy characterisation of the multi-batch samples of Al salt solutions hydrolysed with different alkalis we have conducted dynamic light scattering measurements of the particle sizes in the colloidal Al-containing systems produced by alkaline hydrolysis. Dynamic light scattering measurements were made on aged solutions (24 hours) of aluminium chloride and alum (0.2 M) hydrolysed with KOH (2.0 M). The results of DLS measurements at the scattering angle of 90 degrees and at h values from 1 to 3 are reported in Table 3.3. At least 0.2 M solutions were required in order to detect a signal from solutions where the presence of Al_{13} species had been identified by ^{27}Al NMR spectroscopy.

Table 3.3. Results of particle size analysis by dynamic light scattering of aluminium-containing solutions (0.2 M) hydrolysed for 24 *h* with KOH (2.0 M)

Hydrolysis ratio, *h*	**Maximum of the particle distribution peak ***	
	$AlCl_3$	**$KAl(SO_4)_2$**
1.00	-	-
1.25	-	-
1.50	-	-
1.75	-	-
2.00	1 ± 0.3	-
2.25	1 ± 0.3	-
2.50	1 ± 0.3	Larger particles
2.75	Polydisperse**	Larger particles
3.00	Larger particles***	Larger particles

* - as determined at 90° measuring angle;
** - more then one maximum in the particle size distribution diagram.
*** - by larger particles we mean d>20 nm.

From the data of Table 3.3 it follows that no scattering was observed for the sulphate-containing solutions for hydrolysis ratios below h=2.5. At hydrolysis ratios above this, a floccular precipitate was observed with a wide range of particle sizes 20-2000 nm. For solutions of aluminium chloride of the same concentration at hydrolysis ratios between 2.0 and 2.5 particles of $d \sim 1 \pm 0.3$ nm were detected. At higher hydrolysis ratios much larger particles of amorphous hydroxide were observed both in solutions of aluminium chloride and sulphate with d>20 nm.

Multi-angle dynamic light scattering also was applied for the characterisation of particulates in Al-containing hydrolysed solutions in the range of hydrolysis ratios $2.0 \leq h \leq 2.5$ (Fig. 3.16).

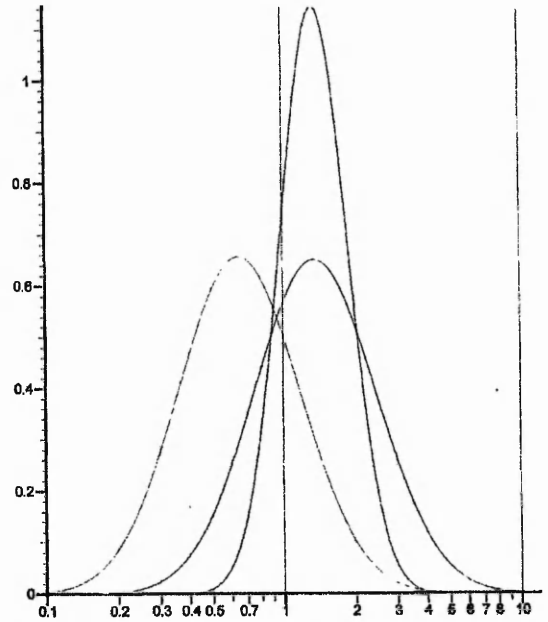


Fig. 3.16. Size distribution diagram from multi-angle DLS measurements of Al-containing solution hydrolysed with KOH (2.0) for 24 hours to h=2.25 (25°C). *Green line* – a measurement at 30 degrees scattering angle; *red line* –62.5 degrees; *blue line* –90 degrees.

The maxima of the particle size distributions in Fig. 3.16 obtained at different scattering angles are quite close (0.7 nm at 30 degrees, 1.1 nm at 62.5 degrees and 1.3 nm at 90 degrees). The distributions are quite narrow, therefore the Al nano-particles present in solution are uniformly sized and of spherical shape that corresponds well to the Al_{13}-mer species [29].

3.1.4. Discussion

Conversion of the conventional titration curves obtained from the automated potentiometric titrations of Al-ion solutions with alkalis into the first derivative curves brings the benefit of better inflexion point resolution, more exact determination of the inflexion point positions as well as better visualisation of the inflexion points as distinct peaks. Further improvement of the resolution between overlapped peaks can be achieved by implementation of the peak-fitting procedure described in Section 3.1.1 of the present chapter. Moreover, in some cases (see Table 3.2, titration 4) peak fitting reveals new inflexions otherwise undetectable in a conventional titration curve. In addition to the advanced treatment of the potentiometric titrations proposed in this work, an introduction of the hydrolysis ratio as a x-axis for the titration graphs enabled us to carry out a 'phenomenological' analysis of Al speciation based on the identification of the inflexion points and subsequent relation of them to particular Al species by comparison of the hydrolysis ratio at which an inflexion point occurs and a theoretical hydrolysis ratio of a given Al species.

The analysis of the first derivative curves of potentiometric titrations of Al-ion solutions with alkalis at room temperature shows the following inflexions:

1) ***h*** **~ 0.08 ± 0.004** - the inflexion is related to the hydrolysis of monomeric Al species and remains practically unchanged at all the experimental conditions studied in this work. The theoretical hydrolysis ratio of Al monomers is h=1.0 for $[Al(OH)(H_2O)_5]^{2+}$ species and h=2.0 for $[Al(OH)(H_2O)_5]^{2+}$. Thus, only a small fraction of the hydrolysed monomeric species is formed during the titration, and the process switches to condensation early in the medium range of Al-ion concentrations in good accordance with literature data [19,25].
2) ***h*** **~ 0.20 ± 0.03** – the inflexion corresponds to the formation of small oligomers (dimers or trimers). Again, there is a mismatch between the observed inflexion point and the theoretical hydrolysis ratios for dimer $[Al_2(OH)_2(H_2O)_4]^{4+}$ (h=1.0) and trimer $[Al_3(OH)_5(H_2O)_9]^{5+}$ (h=1.33). The same assumption can be made in that the conversion of Al monomers into small oligomers is far from complete when condensation to give larger Al polycations becomes the dominant process.
3) ***h*** **~ 2.6 ± 0.09** - at higher hydrolysis ratios the inflexion related to the Al_{13}-mer ($[AlO_4Al_{12}(OH)_{24}(H_2O)_{12}]^{7+}$) occurs [5,23]. The observed inflexion is shifted towards higher hydrolysis ratios comparing to the theoretical h=2.462 for Al_{13}-mer. We assume that the potentiometric titration reflects not the formation of Al_{13}-mer, but its abrupt conversion into colloidal phase containing only octahedral Al atoms as supported by the results of ^{27}Al NMR spectroscopy. Generally, the narrower the peak at h~2.6 the narrower the distribution of the polymerised Al-ions (at room conditions it would be limited mostly to Al_{13}-mer). Broadening of the peak probably indicates complications of the process arising from the presence of colloidal aluminium hydroxide along with Al polycations. The shift of the peak position to higher hydrolysis ratios and overlapping with the peak at h~ 2.9 (total precipitation) probably indicates an increasing proportion of the colloidal aluminium hydroxide formed along with polycations. At some conditions the amount of the colloidal phase is much higher than the amount of Al polycations (mostly Al_{13}-mer) and the peak at h~ 2.6 is completely overlapped by the peak at h~ 2.9. Finally, the ratio of the areas of the peaks at h~ 2.6 and 2.9 (total precipitation) also indicates a relative amount of Al polycations formed during the titration.
4) ***h*** **~ 2.9 ± 0.12** – the peak related to the total precipitation of aluminium hydroxide. The position of the peak also depends on the ratio of the Al polycations and colloidal aluminium hydroxide. In general, the higher the amount of colloids – the lower the hydrolysis ratio at which the inflexion peak occurs.
5) ***h*** **≥ 3.45** – the last inflexion observed in potentiometric titrations of Al-ion solutions arises mainly from dissolution of an amorphous precipitate of aluminium hydroxide (presumably, pseudo-boehmite [30]). Along with the parameters of titration, the peak position, height and breadth depends on the nature and particle size distribution of the

aluminium hydroxide precipitate. Obviously, the more amorphous and less dense the precipitate, the easier it is dissolved in alkaline conditions resulting in a more distinct shape of the peak at $h \geq 3.5$. The larger the particles of the precipitated hydroxide, the faster the dissolution process and the lower the position of the discussed inflexion peak.

Positions of the first two inflexion peaks ($h \sim 0.08$ and $h \sim 0.20$) in the potentiometric titrations of Al-ions with alkalis remain practically unchanged regardless of the conditions of the titration. The positions of the last three peaks depend on both chemical conditions and the titration setup. Chemical conditions include the factors studied: alkali strength and concentration; Al concentration; ionic strength of solution; the presence of different inorganic anions. Titration conditions include stirring rate, volume of sample, concentrations of sample and titrant, interval between titrant additions, volume of titrant additions. Two key processes affected by the chemical and titration conditions are the formation of Al polycations and its transformation into aluminium hydroxide through structural reorganisation as discussed in chapter 1, and the formation of colloidal precipitate due to local disturbances in equilibrium produced by the addition of highly concentrated alkalis. These two competitive processes will determine the shape of the titration curve and its first derivative. The formation of a metastable colloidal phase also means that the observed differences in speciation behaviour on the short time scale related to aluminium containing solutions supersaturated with amorphous aluminium hydroxide rather than to the equilibrium of soluble species only [31].

If the titration conditions listed above are kept constant, then it is possible to elucidate the effects of chemical parameters on the shape of the titration curves and, consequently on the speciation of Al-ions.

Results of potentiometric titrations have shown that the chemical identity of the alkali used and ionic strength both affect the shape of the titration curves. The occurrence of large polynuclear species (mainly Al_{13}-mers), indicated by the inflexion in the titration curves at $h \sim 2.5$-2.6, decreases in the order: $KHCO_3 > KOH >> NH_4OH$, which is not correlated with the strength of the alkali. The reason for such an order can be derived from the effect of the chosen alkalis on the competitive process occurring alongside the formation of Al polycations – the formation of metastable colloidal phase due to local disturbances produced by alkali as mentioned above. Ammonium-ions are known as strong 'structure-breakers' (induce breakage of water structure) [32], therefore ammonia is a strong flocculating agent [33,34]. These properties result in production of large visible snowflake-like particles formed during titration of Al-ion solutions starting as early as from $h \geq 0.08$. Potassium hydroxide produces strong local disturbances, however, the colloidal phase is very unstable and dissolves quickly (as was observed visually) between the titrant additions, especially at lower hydrolysis ratios ($h < 2.0$). Additions of potassium hydrogen carbonate did not produce any visual turbidity up to relatively high hydrolysis ratios ($h \leq 1.0$).

The alkali identity also causes variations in the position of the inflexion peak at $h \sim 2.9$.

In the case of KOH and non-complexing Al-salts the peak is closer to the theoretical hydrolysis ratio of the formation of $Al(OH)_3$ (h=3.0). In the case of ammonia the peak is shifted to slightly lower hydrolysis ratios at h ca. 2.9±0.3 and for $KHCO_3$ the peak is further shifted to h~2.8±0.3 and strongly diminished in size compared to the peak at h~2.6.

The last inflexion observed in the titrations of Al-containing non-complexing salts is also affected by alkali identity since the latter determines the size, concentration and the solubility of the amorphous particles produced by precipitation at h~3.0. In fact, the position and the shape of the peak at highly alkaline conditions can serve as an indirect qualitative measure of the properties of the aluminium hydroxide precipitate.

The identity of the counter-ion also modified the speciation of aluminium in the course of alkaline titration. The largest effects were observed for sulphate ions where the peak related to the polymerisation process is shifted to lower hydrolysis ratios (h~2.34) and is less separated from the peak at h~2.84 arising from the bulk precipitation of amorphous hydroxide. Sulphate ions also affect dissolution of the precipitate as shown by a shift in the peak corresponding to this process at higher hydrolysis ratio (h~4.1). This feature indicates that the hydroxide solid phase formed in the presence of sulphate is more stable towards alkaline dissolution than in the case of aluminium chloride or nitrate. Thus, significant change in the structure and ordering of the precipitate should be expected for the 'aluminium sulphate' system. We assume that the prevailing form of the precipitate in this case is crystalline $Al(OH)_3$, which is supported by literature data [35]. However, additional peaks revealed by the peak-fitting procedure (Table 3.2, titration 4) may indicate that some minor part of aluminium hydroxide is still amorphous (again, due to local disturbances produced by alkali additions) and dissolves at h~3.44 while another minor part is even more stable (h~4.34) than the bulk of the precipitate relating to the dissolution inflexion at h~4.1. Obviously, these findings need further examination by direct structural methods.

Increase in ionic strength of solutions led in most cases to a virtual absence of the inflexion peak at h~2.5-2.6 or its strong overlapping with the peak at h~2.9 suggesting that the formation of the Al_{13}-mer and larger polymeric species was suppressed and increased flocculation led to a direct formation of aluminium hydroxide precipitate.

The shape of pH profiles obtained from the time-resolved potentiometric titrations can provide valuable additional information from the potentiometric titrations, since this parameter is very sensitive to the transformations between Al aqueous species and phases reflected in the short-time kinetics of pH-profiles between titrant additions. Correlation analysis has proved to be a useful tool for the analysis of the time-resolved titration curve shapes. There are several important features revealed from the graphs of correlation sum curves *vs.* hydrolysis ratio (Fig. 3.7 –3.10):

a) It is possible to detect the inflexion point at h~0.20 (formation of small Al oligomers) using correlation analysis in the 'volumetric' domain, which replaces the peak-fitting

procedure of the first-derivative titration curves;

b) The constant value of correlation sums as a consequence of the unchanged shape of time-resolved pH-profiles in the range of hydrolysis ratios $0.6 \leq h \leq 2.46$ indicates that only one species prevails in this region, namely Al_{13}-mers. This fact coincides well with thermodynamic speciation diagrams for medium Al-ion solutions discussed in chapter 1 as well as with the ^{27}Al NMR data described below. The upper limit of the mentioned range (h=2.46) coincides with the theoretical hydrolysis ratio of Al_{13}-mer and indicates that this is a critical limit for these species to exist.

c) Negative peaks in the correlation sum curves in the range of h>2.5 indicate drastic changes occurring in the time-resolved pH-profiles when Al polycations are transformed into the colloidal state (peak at h~2.6-2.7) and into a final aluminium hydroxide precipitate (peak at h~2.8-2.9). Interestingly, the change in the shape of the time-resolved pH-profiles indicated by the decreasing correlation sum always precedes the corresponding maximum in the first derivative curve of titration.

Summarising the above one can find that correlation analysis in the 'volumetric' domain can reveal features uncovered by the derivatisation of the titration curve, as well as serving as a very informative complimentary treatment method of the potentiometric titration curves along with their derivatisation and subsequent peak-fitting.

The potentiometric titrations carried out in the present study provide information on aluminium speciation on a relatively short time scale within 2-3 hours. According to literature data [36,37] this time is sufficient for the hydrolysis of monomeric species and the condensation of hydrolysed aluminium monomers into small oligomers (dimers and trimers) and larger polycations such as the Al_{13}-mer (Table 1.8 in Chapter 1). The longest time taken for the latter to reach its maximum concentration is about 60 min at room temperature [36,37]. It should be noted that the time scale and temperature conditions used for the titrations at room temperature was not sufficient to transform Al_{13}-mers completely into larger polymers, or for crystalline aluminium hydroxide to be formed [36].

Correlation analysis conducted in time-domain also allows one to emphasise the impact of very short time scales between titrant additions ranging between 1 and 3 minutes for the majority of the titrations carried out. There are two time domains observed with correlation sums in the 'time' domain (Fig. 3.11). The first stage (within 10-40 s) is related to extremely rapid processes such as neutralisation of the free protons at acidic conditions, hydrolysis of Al monomers and, probably, partial dissolution of the least stable part of the colloidal phase produced by local disturbances due to concentrated alkali addition. The second stage at τ>40 s corresponds to slower processes such as the formation of larger Al polycations (mainly Al_{13}-mer at room temperature), continuing dissolution of the more stable part of the colloidal phase and other slow processes. The incompleteness of the second part within 2 min between titrant additions indicates that much longer times are required to reach equilibrium at each point of the titration, which is especially true at higher hydrolysis ratios

where such slow processes as precipitation and dissolution of Al hydroxide prevail. However, one must stress that the time scale of the titrations conducted in the present study is a compromise between equilibration in aqueous solutions of strongly hydrolysed Al-ions and a total throughput of titration analysis reflected by the number of the titrations conducted.

Generally, after ageing hydrolysed solutions for 24 hours, equilibrium is considered to be established [5,36,37]. In the multi-batch experiments reported here, visible solid material was only present in samples containing aluminium chloride and nitrate within the narrow range $2.6 \leq h \leq 3.0$ irrespective of the alkali used for neutralisation. Below h~3.0 the material was in a relatively stable colloidal phase while at $h \geq 3.0$ only a more dense precipitate was present. In the case of alum, fine turbidity was observed visually in the range $2.0 \leq h \leq 3.0$. Literature data suggest that well-defined crystalline aluminium hydroxide could be formed in the presence of sulphate-ions on such a long time scale [38,39].

^{27}Al NMR measurements of the solutions aged for 24 hours have shown that in the case of aluminium nitrate and chloride, the hydrolysis-condensation reaction goes through the formation of Al_{13}-mer indicated by a peak at 63.5 ppm (Fig. 3.12*A*, 3.13*A,B*). This species is appreciable in $AlCl_3$ and $Al(NO_3)_3$ solutions in the range $1 \leq h \leq 2.5$ (Fig 3.14*A-C*). The concentration of oligomers indicated by the peak at 4.3 ppm remains relatively small but steady in the broad range of hydrolysis ratios $0.25 \leq h \leq 2.0$. Above this range the tracing of oligomers in NMR spectra becomes impossible at room temperature owing to overlap of the peak with the increasing broad peak at δ~40-50 ppm arising from the octahedral 'shell' of the Al_{13}-mer. The observed features can be explained considering the assumption that small oligomeric species are 'synthons' for the formation of the tridecamer. Thus, continuous consumption of the oligomeric species to make larger oligomers keeps their overall concentration relatively small, a feature that is confirmed by speciation diagrams derived from thermodynamic stability constants of the hydrolysed aluminium species [19] (Fig. 1.5).

It is necessary to stress that the estimated area of the peak at δ~0.0 ppm relates to both $[Al(H_2O)_6]^{3+}$ (δ~0.0 ppm), $[Al(OH)(H_2O)_5]^{2+}$ (δ~0.34 ppm) and $[Al(OH)_2(H_2O)_4]^{+}$ (δ~0.77 ppm, assignment in the present study) species which were impossible to separate in most of the NMR spectra acquired for hydrolysed aluminium solutions. Nevertheless it is possible to monitor a constant 'drift' of the large peak at ~0.0 with increase of hydrolysis ratio (Fig. 3.15).

When sulphate ions are present in the aluminium solution, the general pattern of the ^{27}Al NMR spectra obtained is substantially different. Four peaks with chemical shifts of approx. –3.68, -3.32, 0.0 and 0.77 ppm are observed in the spectrum of unhydrolysed alum, with the high intensity peak at -3.3 ppm being ascribed to the species $[Al(OH)(SO_4)(H_2O)_4]^{+}$ [8]. The other peak at -3.68 ppm probably arises from another complex of monomeric aluminium with sulphate, e.g. $[Al(H_2O)_4(SO_4)_2]^{-}$. Such complexes of monomeric aluminium-ions with sulphate are known and their stability constants have been determined [18,40].

The absence of the peak at 63.5 ppm in the NMR spectra of aluminium sulphate solutions (Fig. 3.12*B*, *3.13C*, *D*) indicates that the Al_{13}-mer is not formed and the condensation reaction follows another pathway. It is likely that the observed alteration is based on the stabilisation of the small oligomeric species such as dimer as the peak ~4.3 ppm is observed in the spectra obtained from solutions containing sulphate ions. These species gradually transfer into higher polymeric species containing octahedral aluminium only as indicated by increases in the intensity of the broad peak at ~40 ppm. Formation of the higher polymers is also supported by the decrease in concentration of both complexed (with sulphate) and non-complexed forms of the aluminium monomer (Fig. 3.14*D*).

According to the mechanism of the formation of Al_{13}-mer proposed by Henry et. al [41] and described in detail in chapter 1, Al trimers $[Al_3(OH)_4(H_2O)_9]^{5+}$ undergo further hydrolysis to form reactive species $[Al_3O(OH)_6(OH_2)_6]^{+}$. These species then act as nucleophilic agents for h=0 precursors $[Al(H_2O)_6]^{3+}$ to produce Al_{13}-mer species. Henry et al [41] through use of the Partial charge model have also shown that sulphate ions are able to form both inner and outer sphere complexes with Al^{3+} ions over a wide range of pH conditions. One can assume that the detrimental effect of the presence of sulphate-ion on the formation of large Keggin polycations (Al_{13}-mer) occurs at early hydrolysis stages preceding formation of the Keggin-ions in one of three possible ways such as: a) decreasing the susceptibility of the monomer towards nucleophilic attack of hydrolysed species; b) decreasing the probability of the formation of the above mentioned reactive Al trimer by stabilising $[Al_3(OH)_4(H_2O)_9]^{5+}$ species; c) stabilisation of Al dimers and complete prevention of Al trimer formation. Dimeric species containing aluminium ions and sulphate have been isolated and characterised by X-ray diffraction [42] and therefore their involvement in the condensation pathway cannot be ruled out. Certainly the hypothesis needs further experimental investigation.

In an attempt to verify the hypotheses mentioned above we have estimated the electronic parameters of monomeric and polymeric Al-ion containing different numbers of sulphate-ions as ligands using PCM calculations. The results of some calculations of Al monomers containing sulphate-ions are shown in Table 3.4.

Several conclusions can be derived from the data of Table 3.4:

1) Al non-hydrolysed monomers containing sulphate-ions in the inner coordination sphere are quite stable species (compare electronegativities and partial charges on aquo ligands of species 1-6, Table 3.4). Both unidentate (α=1, where α is the denticity of the ligand) and bidentate (α=2) sulphate ligands are feasible. Bidentate sulphate coordination is more likely in acidic conditions judging by the increased partial charge of remaining aquo ligands $\delta(H_2O)$ and the decreased value of pH_{H2O} determining the lower limit of the species to exist (compare species 2 and 3, 4 and 5). Up to three sulphate ligands can be theoretically present in the coordination sphere of monomeric Al-ions. However, with the increase in the number of sulphate ligands coordinated with an Al-ion, the minimum pH

Table 3.4. Results of the PCM calculations of different Al monomeric species containing sulphate-ions in the inner coordination sphere

No	Species*	h	α	χ_t	δ(Al)	δ(O)	δ(H)	δ(S)	$\delta(H_2O)$	$\delta(OH^-)$	$\delta(SO_4^{2-})$	pH_{H2O}
1	$\mathbf{Al(H_2O)_6^{3+}}$	0	-	**2.757**	*0.754*	*-0.292*	*0.333*	*0.129*	**0.124**	-	-	*-0.7*
2	$Al(H_2O)_5(SO_4)^+$	0	1	**2.686**	*0.712*	*-0.320*	*0.297*	*0.096*	**0.091**	-	**0.1947**	*1.3*
3	$Al(H_2O)_4(SO_4)^+$	0	2	**2.719**	*0.732*	*-0.307*	*0.314*	*0.112*	**0.106**	-	**0.2108**	*0.4*
4	$Al(H_2O)_3(SO_4)_2^-$	0	1	**2.645**	*0.687*	*-0.336*	*0.277*	*0.077*	**0.072**	-	**0.0874**	*2.5*
5	$Al(H_2O)_2(SO_4)_2^-$	0	2	**2.674**	*0.705*	*-0.325*	*0.291*	*0.091*	**0.085**	-	**0.0944**	*1.7*
6	$Al(SO_4)_3^{3-}$	0	2	**2.619**	*0.672*	*-0.346*	*0.263*	*0.065*	-	-	**0.0540**	*3.2*
7	$\mathbf{Al(OH)(H_2O)_5^{2+}}$	1	-	**2.679**	*0.708*	*-0.323*	*0.294*	*0.093*	**0.087**	**-0.0145**	-	*1.5*
8	$Al(OH)(H_2O)_3(SO_4)^0$	1	1	**2.609**	*0.666*	*-0.350*	*0.258*	*0.060*	**0.055**	**-0.0454**	**0.1575**	*3.5*
9	$Al(OH)(H_2O)_2(SO_4)^0$	1	2	**2.631**	*0.679*	*-0.342*	*0.269*	*0.070*	**0.065**	**-0.0358**	**0.1680**	*2.9*
10	$Al(OH)(H_2O)(SO_4)_2^-$	1	2	**2.573**	*0.644*	*-0.364*	*0.240*	*0.043*	**0.038**	**-0.0617**	**0.0699**	*4.5*
11	$\mathbf{Al(OH)_2(H_2O)_4^+}$	2	-	**2.591**	*0.655*	*-0.357*	*0.249*	*0.052*	**0.047**	**-0.0269**	-	*4.0*
12	$Al(OH)_2(H_2O)_2(SO_4)^-$	2	2	**2.530**	*0.619*	*-0.381*	*0.218*	*0.024*	**0.018**	**-0.0403**	**0.1191**	*5.8*
13	$Al(OH)_2(SO_4)_2^{3-}$	2	2	**2.456**	*0.574*	*-0.410*	*0.181*	-	**-0.016**	**-0.0569**	**0.0415**	*7.9*
14	$\mathbf{Al(OH)_3(H_2O)_3^0}$	3	-	**2.491**	*0.595*	*-0.397*	*0.198*	*0.005*	**0.000**	**-0.0328**	-	*6.9*
15	$Al(OH)_3(H_2O)(SO_4)^{2-}$	3	2	**2.415**	*0.549*	*-0.426*	*0.160*	-	**-0.035**	**-0.0441**	**0.0630**	*9.1*

*-species not containing SO_4^{2-}-ions are taken from Table 1.2; α - the denticity of SO_4^{2-}-ligand.

of the aquo ligand elimination (pH_{H2O}) also increases. Thus, a lower number of sulphate ligands is favoured in more acidic conditions and vice versa. The partial charge on sulphate-ions in the coordination sphere also indicates relative stability of the electrostatic complex. A monosulphate complex (species 2 and 3) shows $\delta(SO_4^{2-})$ higher than the initial value of $\delta(H_2O)$ of aquo ligands (species 1). Thus, these species are less stable than the non-hydrolysed $[Al(H_2O)_6]^{3+}$. Increase in the number of sulphate ligands in the coordination sphere of aluminium leads to decrease of $\delta(H_2O)$ and $\delta(SO_4^{2-})$ indicating that species 4-6 are theoretically more stable than initial $[Al(H_2O)_6]^{3+}$.

2) The ability of the Al monomer to hydrolyse is decreased by the presence of sulphate ligands, as indicated by the decreased partial charges on protons of coordinated water, δ(H), and increased values of δ(O). This is in a good agreement with higher pH values of solutions of alum comparing to $Al(NO_3)_3$ or $AlCl_3$ observed experimentally in this work and other studies [43] and with their hydrolysis constants [18,19] discussed above.

3) Coordinated sulphate ligands have a higher partial charge than aquo ligands in species 2 – 6, making them a better leaving group than aquo ligands. Thus, sulphate ligands are going to be replaced first by nucleophilic attack (e.g. by hydroxo ligands, or by hydrolysed Al monomers). However, the increasing number of sulphate ligands in the coordination sphere of aluminium diminishes the absolute values as well as the differences between

$\delta(H_2O)$ and $\delta(SO_4^{2-})$.

4) After hydrolysis has started, the hydrolysed Al monomers do not accept sulphate-ions as easily as non-hydrolysed species, as indicated by the increased negative partial charge on OH-ligands in the sulphate-containing hydrolysed Al species, e.g. No 8-10, etc. At the same time the decreased value of $\delta(H_2O)$ for sulphate-containing hydrolysed Al species indicates that they would undergo further hydrolysis reactions less readily then the pure hydrolysed monomers.

The results of the PCM calculations of polymeric Al species containing sulphate-ions are shown in Table 3.5. We have examined the most thermodynamically established polynuclear cations such as Al dimer, Al trimer and Al_{13}-mer. For the dimer we have analysed the possibility of the formation of the OH-bridged complexes (Table 3.5, Species 1-5), mixed (OH^-, SO_4^{2-})-bridged complexes (Species 6-10) and sulphate-only-bridged complexes (Species 11-14). Some examples of possible complexes of the sulphate ligands with Al trimer (Species 15-29) and Al tridecamer (Species 30-44) are also included.

One can see from the data of Table 3.5 that introduction of SO_4^{2-}-ions into the inner coordination sphere of aluminium polynuclear species induces the following effects:

1) Increase of the $\delta(OH)$ in sulphate-containing species comparing to the non-complexed ones (for instance, species 2-6 in comparison with species 1) indicates that complexation of polynuclear Al ions with sulphate is not favourable in most cases. There are few exceptions – the minimum alteration of the $\delta(OH)$ is observed in the case of the complex $Al_2(OH)_2(H_2O)_6SO_4^{2+}$ (species 2), and for the complex $Al_2(OH)(H_2O)_8(SO_4)^{4+}$ (species 6) with one bridging sulphate instead of hydroxyl ligand. Thus, in the case of Al dimer, only one sulphate ligand would be allowed in the inner coordination of Al atoms. The sulphate-ion in Al dimers can be either unidentate or bridging bidentate. The structural data of Johansson [42] on aluminium hydroxide sulphate hydrate indicate the formula $[Al_2(OH)_2(H_2O)_{10}(SO_4)_2]$ of neutral charge, with two sulphate ligands per each Al dimer. However, the actual ratio between aquo ligands in the coordination sphere and water in the crystallohydrate is unclear.
2) In the case of Al trimeric cation the complexation with sulphate is even less favourable than for dimer (species 15-29). The only species marginally feasible on the basis of their electronic parameters {χ_t, $\delta(OH)$ and $\delta(H_2O)$} is the species $Al_3(OH)_4(H_2O)_7(SO_4)^{3+}$ with a single bidentate chelating sulphate. The increase of the number and denticity of sulphate ligands up to 3 (species 18-29 in Table 3.5) further decreases the value of $\delta(OH)$, making such complexation more unlikely.
3) The μ_1-ligand replaces 1 aquo ligand, and μ_2–ligand replaces two aquo ligands, making feasible both unidentate and bidentate complexes with sulphate-ion with the total number of SO_4^{2-} up to four (species 30-43). However, the solid-state product containing a Al_{13}-mer complex with sulphate, characterised structurally by Johansson [43], has a total formula

Table 3.5. Results of PCM calculations of known Al polynuclear sulphate-containing species

No	Species	h*	α**	μ	χ_t	$\delta(H_2O)$	$\delta(OH^-)$	$\delta(SO_4^{2-})$	pH_{H_2O}
1	**$Al_2(OH)_2(H_2O)_8^{4+}$**	*1.00*	-	-	**2.716**	*0.105*	*0.0010*	-	*0.5*
2	$Al_2(OH)_2(H_2O)_6(SO_4)^{2+}$	*1.00*	1	1	**2.690**	*0.093*	*-0.0046*	*0.1968*	*1.2*
3	$Al_2(OH)_2(H_2O)_4(SO_4)_2^{0}$	*1.00*	1	1	**2.662**	*0.080*	*-0.0110*	*0.0915*	*2.0*
4	$Al_2(OH)_2(H_2O)_2(SO_4)_3^{-2}$	*1.00*	1	1	**2.630**	*0.065*	*-0.0181*	*0.0558*	*2.9*
5	$Al_2(OH)_2(SO_4)_4^{-4}$	*1.00*	1	1	**2.594**	*0.048*	*-0.0263*	*0.0374*	*4.0*
6	$Al_2(OH)(H_2O)_8(SO_4)^{3+}$	*0.50*	2	2	**2.717**	*0.106*	*0.0029*	*0.2101*	*0.4*
7	$Al_2(OH)(H_2O)_6(SO_4)_2^{1+}$	*0.50*	2	2	**2.694**	*0.095*	*-0.0076*	*0.0994*	*1.1*
8	$Al_2(OH)(H_2O)_4(SO_4)_3^{-}$	*0.50*	2	2	**2.668**	*0.083*	*-0.0191*	*0.0621*	*1.8*
9	$Al_2(OH)(H_2O)_8(SO_4)^{3+}$	*0.50*	2	1	**2.699**	*0.097*	*-0.0056*	*0.2008*	*1.0*
10	$Al_2(OH)(H_2O)_7(SO_4)_2^{-}$	*0.50*	2	1	**2.676**	*0.086*	*-0.0155*	*0.0950*	*1.6*
11	$Al_2(OH)_2(H_2O)_6(SO_4)^{2+}$	*1.00*	2	1	**2.656**	*0.077*	*-0.0123*	*0.1801*	*2.2*
12	$Al_2(OH)_2(H_2O)_6(SO_4)_2^{0}$	*1.00*	2	2	**2.631**	*0.065*	*-0.0179*	*0.0840*	*2.9*
13	$Al_2(OH)_2(H_2O)_6(SO_4)_3^{2+}$	*1.00*	2	2	**2.671**	*0.084*	*-0.0089*	*0.1877*	*1.7*
14	$Al_2(OH)_2(H_2O)_6(SO_4)_2^{0}$	*1.00*	2	2	**2.645**	*0.072*	*-0.0148*	*0.0874*	*2.5*
15	**$Al_3(OH)_4(H_2O)_9^{5+}$**	*1.33*	-	-	**2.713**	*0.103*	*0.0002*	-	*0.6*
16	$Al_3(OH)_4(H_2O)_8(SO_4)^{3+}$	*1.33*	1	1	**2.678**	*0.087*	*-0.0037*	*0.1906*	*1.6*
17	$Al_3(OH)_4(H_2O)_7(SO_4)^{3+}$	*1.33*	2	1	**2.693**	*0.094*	*-0.0021*	*0.1980*	*1.1*
18	$Al_3(OH)_4(H_2O)_7(SO_4)_2^{+}$	*1.33*	1	1	**2.645**	*0.072*	*-0.0074*	*0.0873*	*2.5*
19	$Al_3(OH)_4(H_2O)_6(SO_4)_2^{+}$	*1.33*	2	1	**2.657**	*0.077*	*-0.0061*	*0.0903*	*2.1*
20	$Al_3(OH)_4(H_2O)_5(SO_4)_2^{+}$	*1.33*	2	1	**2.671**	*0.084*	*-0.0045*	*0.0937*	*1.7*
21	$Al_3(OH)_4(H_2O)_6(SO_4)_3^{-}$	*1.33*	1	1	**2.614**	*0.057*	*-0.0108*	*0.0533*	*3.4*
22	$Al_3(OH)_4(H_2O)_5(SO_4)_3^{-}$	*1.33*	1,2	1	**2.623**	*0.062*	*-0.0098*	*0.0548*	*3.1*
23	$Al_3(OH)_4(H_2O)_4(SO_4)_3^{-}$	*1.33*	1,2	1	**2.634**	*0.067*	*-0.0086*	*0.0565*	*2.8*
24	$Al_3(OH)_4(H_2O)_3(SO_4)_3^{-}$	*1.33*	2	1	**2.647**	*0.073*	*-0.0071*	*0.0586*	*2.4*
25	$Al_3(OH)_4(H_2O)_5(SO_4)_4^{-3}$	*1.33*	1	1	**2.585**	*0.044*	*-0.0140*	*0.0365*	*4.2*
26	$Al_3(OH)_4(H_2O)_4(SO_4)_4^{-3}$	*1.33*	1,2	1	**2.592**	*0.047*	*-0.0133*	*0.0373*	*4.0*
27	$Al_3(OH)_4(H_2O)_3(SO_4)_4^{-3}$	*1.33*	1,2	1	**2.600**	*0.051*	*-0.0124*	*0.0383*	*3.8*
28	$Al_3(OH)_4(H_2O)_2(SO_4)_4^{-3}$	*1.33*	1,2	1	**2.610**	*0.055*	*-0.0113*	*0.0394*	*3.5*
29	$Al_3(OH)_4(H_2O)(SO_4)_4^{-3}$	*1.33*	2	1	**2.621**	*0.061*	*-0.0101*	*0.0408*	*3.2*
30	**$Al_{13}O_4(OH)_{24}(H_2O)_{20}^{7+}$**	*2.46*	-	-	**2.586**	*0.044*	*-0.0023*	-	*4.2*
31	$Al_{13}O_4(OH)_{24}(H_2O)_{19}(SO_4)^{5+}$	*2.46*	1	1	**2.576**	*0.040*	*-0.0025*	*0.1413*	*4.5*
32	$Al_{13}O_4(OH)_{24}(H_2O)_{18}(SO_4)^{5+}$	*2.46*	2	1	**2.578**	*0.041*	*-0.0025*	*0.1423*	*4.4*
33	$Al_{13}O_4(OH)_{24}(H_2O)_{18}(SO_4)_2^{3+}$	*2.46*	1	1	**2.567**	*0.035*	*-0.0027*	*0.0684*	*4.7*
34	$Al_{13}O_4(OH)_{24}(H_2O)_{17}(SO_4)_2^{3+}$	*2.46*	1,2	1	**2.569**	*0.036*	*-0.0027*	*0.0688*	*4.7*
35	$Al_{13}O_4(OH)_{24}(H_2O)_{16}(SO_4)_2^{3+}$	*2.46*	2	1	**2.570**	*0.037*	*-0.0026*	*0.0693*	*4.6*
36	$Al_{13}O_4(OH)_{24}(H_2O)_{17}(SO_4)_3^{+}$	*2.46*	1	1	**2.558**	*0.031*	*-0.0029*	*0.0441*	*5.0*
37	$Al_{13}O_4(OH)_{24}(H_2O)_{16}(SO_4)_3^{+}$	*2.46*	1,2	1	**2.559**	*0.032*	*-0.0028*	*0.0443*	*4.9*
38	$Al_{13}O_4(OH)_{24}(H_2O)_{15}(SO_4)_3^{+}$	*2.46*	1,2	1	**2.561**	*0.033*	*-0.0028*	*0.0446*	*4.9*
39	$Al_{13}O_4(OH)_{24}(H_2O)_{14}(SO_4)_3^{+}$	*2.46*	1,2	1	**2.562**	*0.033*	*-0.0028*	*0.0449*	*4.8*
40	$Al_{13}O_4(OH)_{24}(H_2O)_{16}(SO_4)_4^{-}$	*2.46*	1	1	**2.548**	*0.027*	*-0.0030*	*0.0320*	*5.2*
41	$Al_{13}O_4(OH)_{24}(H_2O)_{15}(SO_4)_4^{-}$	*2.46*	1,2	1	**2.550**	*0.027*	*-0.0030*	*0.0321*	*5.2*
42	$Al_{13}O_4(OH)_{24}(H_2O)_{14}(SO_4)_4^{-}$	*2.46*	1,2	1	**2.551**	*0.028*	*-0.0030*	*0.0323*	*5.2*
43	$Al_{13}O_4(OH)_{24}(H_2O)_{13}(SO_4)_4^{-}$	*2.46*	1,2	1	**2.553**	*0.029*	*-0.0029*	*0.0325*	*5.1*

* - for the description of the parameters given in Table 3.4, 3.5 see footnotes of Table 1.2.

** -α - the denticity of SO_4^{2-} -ligand (α=1,2 – both unidentate and bidentate ligands are present) , μ - the bridging effect (1 – non-bridging, 2 – bridging, 1,2 – both μ=1 and μ=2).

$Na[AlO_4Al_{12}(OH)_{24}(H_2O)_{12}](SO_4)_2 \cdot 10H_2O$ which is clear evidence that sulphate ligands do not enter the inner coordination sphere of Al-atoms of Al_{13}-mer remaining charge-compensating counter-ions in the crystal structure.

Summarising the results of the PCM calculations of Al monomeric and polymeric cations with sulphate one can find that the role of sulphate-ions is limited to the charge-compensating counter-ion in the external coordination sphere of Al polycations (dimer, trimer and Al_{13}-mer). This is supported by the literature data based on the extensive ^{27}Al NMR and molar volume studies [44, 45]. These studies indicate that Al-ions and sulphate ions are closely associated in the second coordination sphere, there being no free Al^{3+}, and only a small portion of the anions enters the first sphere of Al-ions.

Only in the case of non-hydrolysed Al monomer can sulphate-ions enter the inner coordination sphere of the metal. In spite of a relatively weak complexation of sulphate with Al-ions its high negative charge can stabilise Al-ions both in the monomeric and in the dimeric form and, as was shown in the potentiometric, DLS and ^{27}Al NMR experiments above, this influence is enough to completely change the pathway of Al-ion condensation in aqueous solutions.

On the basis of the extensive potentiometric titrations, dynamic light scattering measurements, ^{27}Al NMR studies and calculations by the Partial charge model carried out in the present study one may suggest the following flow-chart for speciation of Al-ions at medium concentrations in a wide range of pH and hydrolysis ratios (Fig. 3.17).

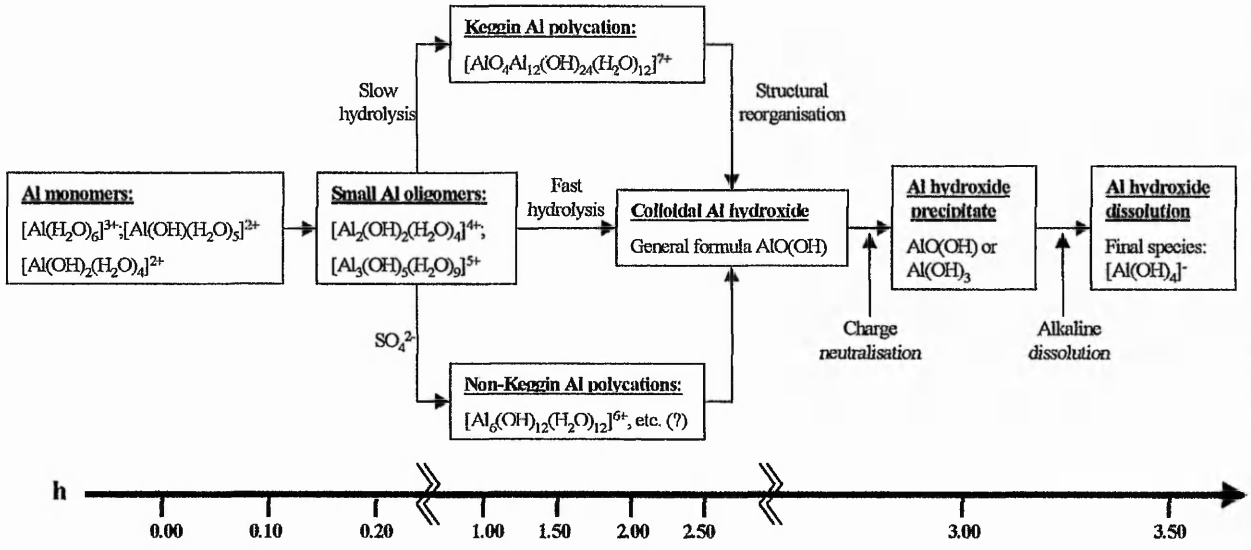


Fig. 3.17. The flowchart of the aluminium ion speciation

As follows from the chart in Fig. 3.17 the crucial step determining the outcome and the final products of the hydrolysis-condensation reaction by forced hydrolysis with alkali is the step of transformation of small oligomeric Al-ions into larger species. Depending on the conditions of the hydrolysis one can produce a straightforward colloidal phase formation with the precipitation of amorphous hydroxide without passing through the stage of distinct

polycation formation (the pathway shown in the middle line of the flow-chart). Such conditions for 'fast precipitation' are high ionic strength, use of coagulation agents (e.g. ammonia) or fast addition of strong alkali. Slow hydrolysis may also have different outcomes depending on the identity of the counter-ion. Non-complexing counter-ions (chloride, nitrate) lead to the formation of Keggin-ions (Al_{13}-mer at room temperature) which need some structural rearrangement in order to transform into a colloidal phase (gel or sol with large particles) and the final precipitate [31]. This transformation certainly goes through the conversion of the 'core' tetrahedral AlO_4 unit of the Keggin-ion into octahedral aluminium as revealed by the ^{27}Al NMR data. However, the exact mechanism of such a transformation is still a point at issue [31,41]. In the presence of sulphate-ions, the Keggin structures are not formed. Instead, large polynuclear species of octahedral aluminium undergo further condensation and eventually transform into colloid and precipitate. Interestingly, the absence of tetrahedral AlO_4 unit in the polycationic structures catalysed by sulphate and their structural isomorphism to the final gibbsite or bayerite structure [31,45] does not lead to a seamless transformation of presumably hexamer-based polycations to final hydroxide phase. Still, when some critical point is reached, the octahedral Al polycations have to undergo some sort of transformation before the formation of the colloidal phase and the final hydroxide precipitate. This process is manifested by the inflexion point at h~2.38 in the potentiometric titrations described above. The 'critical point' at h~2.38 can be attributed either to charge neutralisation of hexamer-based Al polycations, or to their structural transformations.

Literature data indicate that the size of Al_{13}-mer has been estimated to be within the limits $d \sim 0.86$ - 1.2 nm [29], which is lower than the practical limit of the Coulter N4 Plus particle size range (3-3000 nm) [46]. As a consequence, the observed particle size distribution peak at d~1 ± 0.3 nm (which was detected at all measurement angles) has only been detected at relatively high concentrations of aluminium chloride solutions (0.1-0.2 mol/L) and in a narrow range of hydrolysis ratios ($2.0 \leq h \leq 2.5$). Out of this range the concentration of the Al_{13}-mer was perhaps too low to be detected by the particle size meter with an acceptable degree of accuracy. Nevertheless, good accordance of the Al_{13}-mer size detected by DLS in this work with literature data [29] shows that it is possible to detect such small particulates using the DLS technique. Moreover, the appropriate spherical shape of Al_{13}-mer was detected using multiple angle scattering corresponding well with the structure of this Keggin-ion.

The complete absence of the particle size distribution peak at ca. 1 nm in the case of aluminium sulphate solutions in the same hydrolysis ratio range $h = 1 - 3$ provides additional evidence for the lack of formation of Al_{13}-mer species, which is supported by results obtained by automated potentiometric titrations and ^{27}Al NMR measurements.

3.1.5. Conclusions

The use of automated potentiometric titrations, ^{27}Al NMR spectroscopy and dynamic light scattering has enabled us to investigate systematically the speciation of aluminium-ions in the course of forced hydrolysis (alkaline neutralisation) on a relatively short time (0-3 hours) and on a long (24 hours) time scale. Studies of the effect of alkali identity, strength and counter-ion identity on the formation of aluminium polymeric species have shown that for the preparation of solutions containing Al_{13}-mer species and higher polymers on a short time scale, aluminium chloride and nitrate should be used as starting materials. KOH and $KHCO_3$ should be used as the alkalis and experiments conducted at low ionic strength. For aged solutions, there is a considerable hydrolysis window ($2.0<h<2.6$) that can be used to generate significant quantities of the Al_{13}-mer, varying slightly with the alkali used. Al_{13}-mer species are not generated from alum as the precursor. The presence of sulphate ions alters the pathway of aluminium polymerisation to form polymeric and solid materials. The detrimental role of sulphate ions in the formation of the Al_{13}-mer may result from the stabilisation of monomeric aluminium species by complexation with SO_4^{2-}-ions and/or a decrease of the nucleophilic properties of dimers/ trimers in the formation of Al_{13}-mer by electrostatic charge-neutralisation effect.

Advanced methods of treatment of potentiometric titration curves have been introduced including derivatisation of the curves, application of peak-fitting analysis for the identification of the inflexion points and implementation of the correlation analysis in 'volumetric' and 'time' domains which provide additional information on Al speciation and kinetics of the system equilibration.

The possibility of using dynamic light scattering for monitoring the formation of large aluminium polycations has been shown and limitations of the measurements of the subnano- and nano-size aluminium polymers have been discussed.

3.2. Solution studies of aluminium speciation at high temperature

As has been shown in chapter 1, large aluminium polycations such as Al_{13}-mer and Al_{30}-mer are thermodynamically metastable and kinetics of their formation and breakage is of utmost importance for understanding Al speciation patterns. Few studies are available on the kinetics of Al_{13}-mer formation/dissolution at room temperature [1,5,36,37]. To our knowledge there are no published reports on the kinetics of reactions involving large polycations at high temperatures and especially there is a lack of kinetic data on the Al_{30}-mer.

3.2.1. Hydrolysis at elevated temperature as monitored by ^{27}Al NMR spectroscopy

The aim of the present part of the study is to establish speciation patterns of hydrolysed Al ions at medium concentrations (0.1 mol/L) and elevated temperatures (90 °C) using ^{27}Al solution NMR spectroscopy with special emphasis on the kinetics of formation of large Al polycations (the Al_{13}-mer and the Al_{30}-mer) and their kinetic stability. The studies of aluminium hydrolysis were carried out in the interval of hydrolysis ratios which corresponds to the optimum conditions of the formation of large Al polycations [1,5] and which were close to the theoretical hydrolysis ratios of these polycations (h=2.462 for Al_{13}-mer and h=2.40 for Al_{30}-mer).

Experimental conditions of the kinetic experiments on Al-ion hydrolysis at medium concentration (0.1 M) and high temperature (90°C) are given in Section 2.7.6 of Chapter 2. Assignments of the peaks observed in ^{27}Al NMR spectra of the hydrolysed Al-ion solutions are shown in Table 3.6.

Table 3.6. Assignment of the peaks observed in ^{27}Al NMR spectra of the samples containing Al-ions hydrolysed at 90°C for up to 48 hours

Peak position	Relative broadness	Assignment	Ref.
80 ppm	Sharp	Reference peak of tetrahedral Al of the secondary standard of $NaAlO_2$ in D_2O	[5,24]
70 ppm	Broad	Tetrahedral AlO_4 units of the Al_{30}-mer	[5,47]
63 ppm	Sharp	The tetrahedral AlO_4 unit of the Al_{13}-mer	[5,23]
~10 ppm	Very broad	Octahedral Al 'shell' of Al_{13}-mers and Al_{30}-mers	[5,23]
0 ppm	Sharp	Octahedral Al signal of the monomeric species, mainly $[Al(H_2O)_6]^{3+}$	[5,23]

From the Table 3.6 one can see that five major peaks were observed in the dynamic ^{27}Al NMR spectra of hydrolysed solutions of Al-ions. Four of them arise from the species present in sample solutions, the fifth peak at 80 ppm relates to the reference solution in the insert tube. We also observed the peak at 4 ppm from the small Al oligomeric ions (dimers). However, it was impossible to quantify this peak due to strong overlap with the broad peak at 10 ppm and the peak of Al monomers at 0.0 ppm.

Examples of the spectra obtained during in-situ kinetic monitoring of Al hydrolysis with ^{27}Al NMR spectroscopy are shown in Fig. 3.18.

From the data of Fig. 3.18 it follows that while positions of all the peaks listed in Table 3.6 remain constant, their areas undergo significant changes during alkaline hydrolysis of Al-ion solutions (except for the peak at 80 ppm related to the signal of internal reference solution). We attempted to quantify these changes using several approaches described in the next section.

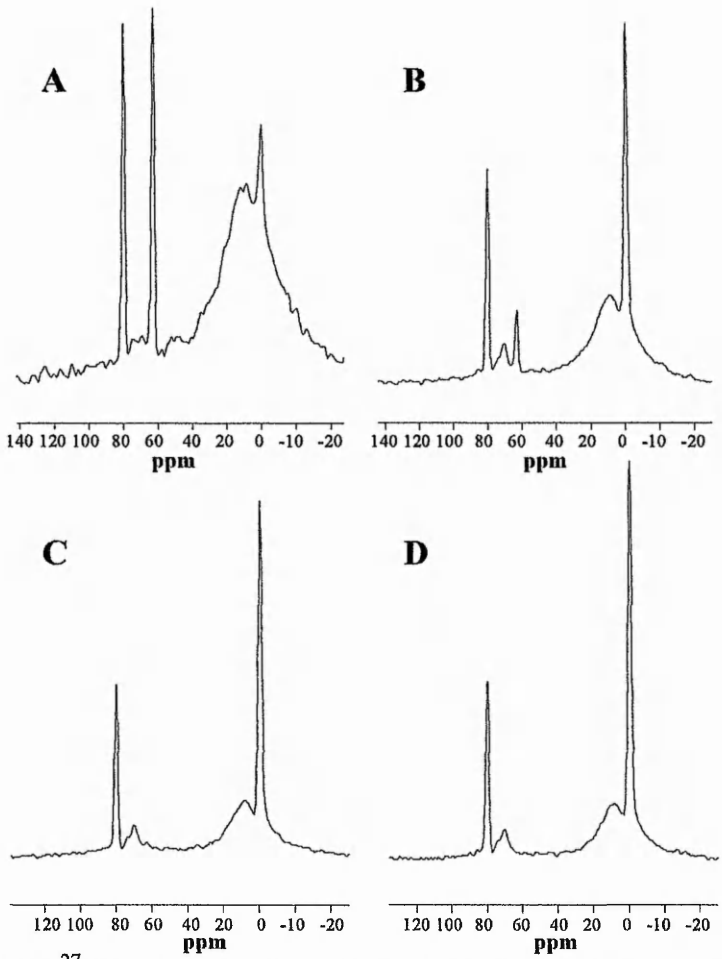


Fig. 3.18. Individual ^{27}Al NMR spectra of the hydrolysed Al-ion solutions obtained at h=2.40, T=90°C. Reaction time: (***A***) - 1 hour; (***B***) – 12 hours; (***C***) – 24 hours; (***D***) – 48 hours.

3.2.2. Quantification of the ^{27}Al NMR spectra

Quantitative data acquisition from the ^{27}Al NMR data is quite problematic when broad signals are present in the spectrum and there may be strong overlaps between adjacent peaks [48]. In addition, there are problems related to the 'rolling' of the baseline and corresponding phase correction, which also hinder the gain of quantitative information. In spite of the efforts to overcome the abovementioned problems both at an instrumental level [23,48] and at the level of data treatment [49], the choice of spectral measurement and data treatment for quantitative analysis remains somewhat serendipitous [23]. We attempted to overcome some of the problems of ^{27}Al NMR spectral quantification by comparison of different data treatment techniques and by development of a consistent algorithm of quantification, which at least would provide an insight into relative changes observed in the kinetics of Al hydrolysis and, hopefully, would enable us to quantify fractions of different Al species in solutions.

The algorithms chosen for comparison included non-linear curve-fitting with subsequent peak integration [50]; direct local integration [49]; total integration with height calculation [51]; and computational algorithm developed in the present study. The flowchart of the compared algorithms is shown in Fig. 3.19.

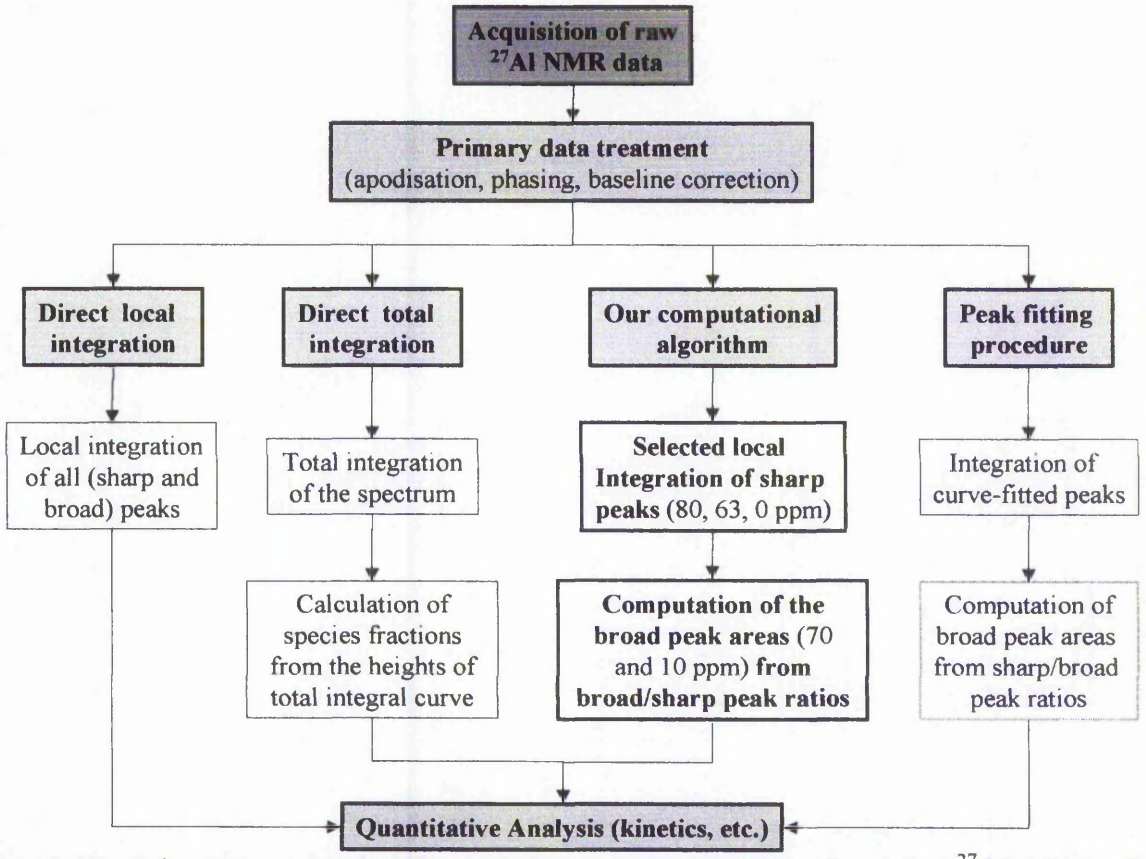


Fig. 3.19. Schematic representation of the quantitative algorithms for ^{27}Al NMR data treatment

1. Direct local integration quantification algorithm. Quantification of the peaks in ^{27}Al NMR spectra using local integration was carried out following a standard procedure: the peaks were baselined locally (in addition to total baseline correction) and integrals were taken of each peak present in the spectrum within integration limits dictated by the widest peak linewidth (the peak at 10 ppm) as shown in Fig. 3.20.

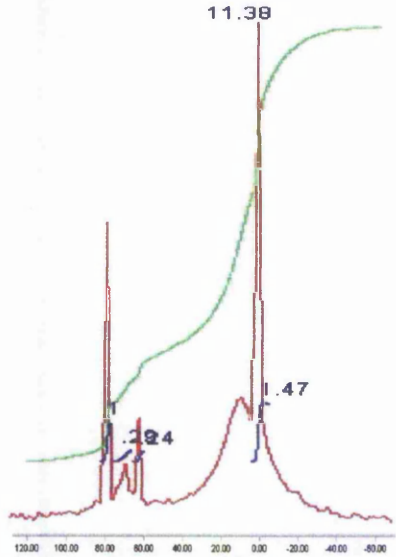


Fig. 3.20. An example of local integration procedure for quantification of ^{27}Al NMR spectra. The ^{27}Al NMR spectrum obtained from the sample at h=2.40, 12 hours of hydrolysis at 90°C.

The integration curve corresponding to the total area of the spectrum peaks is coloured green in Fig. 3.19. The areas of relatively sharp peaks at 80, 70, 63 and 0 ppm were obtained from direct local integration (blue curves in Fig. 3.19). The area of the broader peak at ca. 10 ppm (Table 3.6) was obtained by subtraction of the areas of the sharper peaks within their integration limits as follows:

$$S_{10}^{o} = S_{total} - S_{80}^{t} - S_{70}^{t} - S_{63}^{t} - S_{0}^{o} \qquad \textbf{(3.37)}$$

where S_{10}^{o} - the area of the peak at 10 ppm (symbol "o" is for octahedral Al coordination)

S_{total} - the total peak area in the spectrum ; S_{80}^{t}, S_{70}^{t}, S_{63}^{t}, S_{0}^{o} - the areas of the peaks at 80, 70, 63 and 0 ppm correspondingly (the symbol "t" is for tetrahedral Al).

Integration limits for the calculation of peak areas were as follows: S_{total} (120 to -70 ppm); S_{80}^{t} (81.2 – 78.8 ppm), S_{70}^{t}(78.8 – 64.3 ppm), S_{63}^{t}(64.3 – 62.7 ppm), S_{0}^{o}(3.0 - -1.5 ppm).

2. Direct total integration. The computational algorithm developed in the report [51] is based on the calibration of the secondary reference solution of sodium aluminate in D_2O with a solution of extra pure aluminium nitrate as a primary standard (same method of calibration of the reference was used in the present work). The concentration of the secondary standard $C(Al_{std})$ is calculated as following:

$$C(Al_{std}) = \frac{S_{0}^{o} M}{S_{80}^{t} 375} \qquad \textbf{(3.38)}$$

where M is the weight of $NaAlO_2$ used to prepare the secondary standard solution;
375 – molecular weight of $Al(NO_3)_3$*$9H_2O$.

The total concentration of aluminium detectable in ^{27}Al NMR spectra $C(Al_{detected})$ is calculated using the formula:

$$C(Al_{detected}) = (S_{total} - S_{80}^{t}) * C(Al_{std}) \qquad \textbf{(3.39)}$$

From $C(Al_{detected})$ the percentage of the recovery of the solution species is given as:

$$\%_{recovery}(\text{all species}) = \frac{C(Al_{detected})100 \cdot 27}{M \cdot \%Al} \qquad \textbf{(3.40)}$$

where M is the weight of Al salt in solution, $\%Al$ – the concentration of Al-ions in %wt.

The number of moles of Al monomers $\nu(Al^{3+})$ and Al_{13}-mers $\nu(Al_{13})$ are calculated as follows:

$$\nu(Al^{3+}) = \frac{S_{0}^{o}}{S_{80}^{t}} C(Al_{std}) \qquad and \qquad \nu(Al_{13}) = \frac{S_{63}^{t}}{S_{80}^{t}} C(Al_{std}) \cdot 13 \qquad \textbf{(3.41)}$$

where the factor 13 accounts for the fact that there are 13 Al atoms in the Al_{13}-mer.

The number of moles of the species AlP_2 (currently known as Al_{30}-mer) is calculated using the formula:

$$\nu(Al_{30}) = (S_{total} - J - \left(\frac{J \cdot S_{63}^{t}}{S_{80}^{t}}\right)) \cdot 14 \cdot C(Al_{std}) / J \qquad (3.42)$$

where $J = S_{80}^{t} + S_{70}^{t} + S_{63}^{t}$; the factor 14 reflects the ratio of tetrahedral and octahedral Al atoms in the Al_{30}-mer.

Finally, the percentage of recovery of all known Al species (Al monomers, Al_{13}-mers and Al_{30}-mers) can be calculated according to the report [51] as follows:

$$\%_{recovery}(\text{known species}) = \frac{(\nu(Al^{3+}) + \nu(Al_{13}) + \nu(Al_{30})) \cdot 100 \cdot 27}{M \cdot \%Al} \qquad (3.43)$$

where M is the weight of Al salt in solution, $\%Al$ – the concentration of Al-ions in %wt.

3. Selective local integration (the approach developed in the present work). The ideas behind this approach are the following: (*a*) direct local integration described above produces most reliable results when sharp peaks are integrated (e.g. peaks at 80, 63 and 0 ppm) while broad peaks are not reliably estimated by this method [49]; (*b*) the ratio of the peak at 63 ppm and 10 ppm in the absence of other large polycations (e.g. Al_{30}) is exactly 12 according to several sources [52,53], and this number reflects the ratio between tetrahedral and octahedral Al-atoms in Al_{13}-mer. Thus, it would be logical to assume that this ratio is 14 for Al_{30}-mer (mirroring the ratio of octahedral and tetrahedral Al-atoms in these species). Numerical expression for these ratios is following:

$$S_{63}^{o} = 12 S_{63}^{t} \quad and \quad S_{70}^{o} = 14 S_{70}^{t} \qquad (3.44)$$

Therefore, the peak area at 10 ppm (S_{total}^{o}) represents a sum of the octahedral parts of Al_{13}-mer and Al_{30}-mer when both species are present in solution:

$$S_{total}^{o} = S_{63}^{o} + S_{70}^{o} \qquad (3.45)$$

On the basis of Equations (3.44) and (3.45) one can derive that the area corresponding to the peak of tetrahedral Al units of Al_{30}-mer is:

$$S_{70}^{t} = \frac{S_{total}^{o} - 12 S_{63}^{t}}{14} \qquad (3.46)$$

Another parameter easily obtained from the ^{27}Al NMR spectra is the total peak area S_{total} which is the sum of all detectable species:

$$S_{total} = S_{80}^{t} + S_{70}^{t} + S_{63}^{t} + S_{total}^{o} + S_{0}^{o} \qquad (3.47)$$

Therefore:

$$S_{total}^{o} = S_{total} - S_{80}^{t} - S_{70}^{t} - S_{60}^{t} - S_{0}^{o} \qquad (3.48)$$

Combining Equations (3.47) and (3.48) one may obtain the formula for the calculation of the octahedral component of Keggin-polycations using all known parameters:

$$S^{o}_{total} = \frac{S_{total} - S^{t}_{80} - S^{o}_{0} - 1.857143 S^{t}_{63}}{1.071429} \qquad \textbf{(3.49)}$$

The formulae (3.46) and (3.49) allow for computation of the areas of broad overlapping peaks at 10 and 70 ppm which are otherwise determined with great error as will be shown below. An improvement was made in order to increase the accuracy of calculated sharp peak areas. Using the same integration limits as for standard local integration described above, twelve readings of each peak integral were made by tiny variation of the integration limits (about 0.01 parts of ppm) and subsequent averaging which produced the peak area values practically free from background effects or spectral noise. The same procedure was used for the calculation of the total peak area in each spectrum, but the variation was larger (about 10 ppm, starting from the edges of spectrum). The total peak area being the largest value in the integration procedure, dictates to a great extent an overall consistency and reproducibility of the quantification of NMR spectra.

Another improvement was a calculation of the area of the peak at 70 ppm partially overlapped with the peaks at 80 and 63 ppm from the following formula:

$$S^{t}_{70} = S_{tetrahedral} - S^{t}_{80} - S^{t}_{63} \qquad \textbf{(3.50)}$$

where $S_{tetrahedral}$ is the total integral over the region containing all three tetrahedral signals (80, 70 and 63 ppm) with integration limits from 100 to 55-60 ppm.

Peak-fitting for peak area calculation is the last, fourth method of computation of peak areas implemented for quantification of the ^{27}Al NMR spectra. A standard peak-fitting procedure was carried out using Peak Solve software (an integral part of Galactic GRAMS/32 program, version 5.1). An example of the peak-fitting treatment of a typical NMR spectrum obtained from the hydrolysed Al-ion solution is shown in Fig. 3.21.

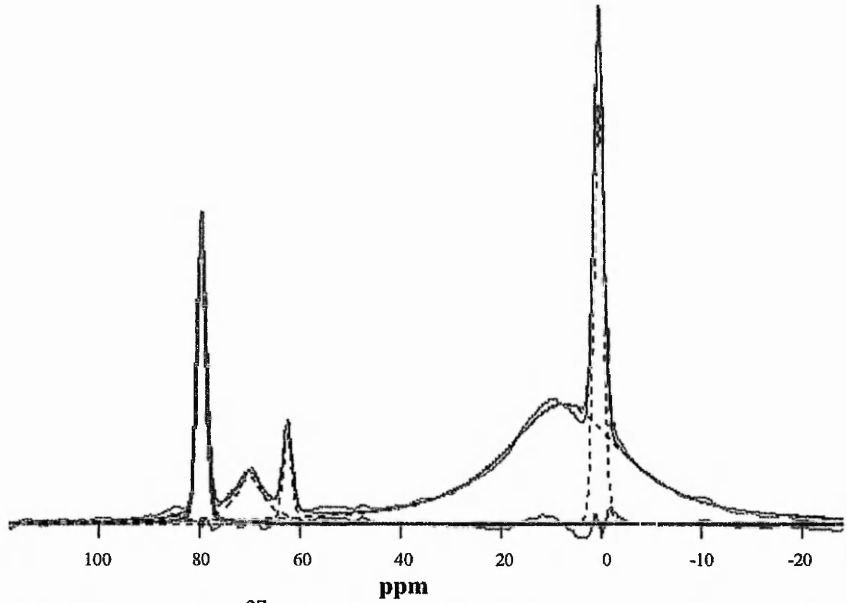


Fig. 3.21. Peak-fitting of the ^{27}Al NMR spectrum obtained from the Al-containing sample hydrolysed to h=2.4 after 12 hours of hydrolysis at 90°C.

From Fig. 3.21 one can find that the peak-fitting procedure yields good fit of the calculated spectrum (blue line) and experimental spectrum (red line) with correlation coefficient R^2=0.9954 ; χ^2=0.02608391 and RMS noise = $4.3*10^{-8}$. The fitting residuals curve (green line) is quite close to the baseline. The standard error for the peak areas did not exceed 5 % in most cases. The peaks (dashed lines) were fitted with a mixed Gaussian-Lorentzian function. The percentage of the Lorentzian component was found for the peak at 80 ppm <25%; the peak at 70 ppm ~100%; the peak at 63 ppm <25%; peak at 10 ppm <80%; peak at 0 ppm <5%.

Described methods of quantification of the peak areas of ^{27}Al NMR spectra were compared using the same spectrum of the sample hydrolysed to h=2.4 for 12 hours at 90°C (cf. Fig. 3.21), where the signals of all species in question are present. The results of comparison are given in Table 3.7.

Table 3.7. Results of the peak area calculations from the same ^{27}Al NMR spectrum by different methods*

Computational method	Peak position, ppm	Peak area, $*10^6$	% reference **	% recovery (known species)***
Local integration	Total area	17.13	79.77	115.2
	79.99	1.28	101.99	
	70.26	0.81	101.08	
	62.88	0.39	102.77	
	9.23	12.8	78.08	
	0.07	1.79	99.98	
Total integration	Total area	15.10	70.22	107.9
	79.99	1.25	99.64	
	70.26	0.57	66.18	
	62.88	0.36	98.85	
	9.23	11.45	70.09	
	0.07	1.81	101.21	
Selected local integration (this work)	Total area	21.48	100.00	93.7
	79.99	1.26	100.00	
	70.26	0.86	100.00	
	62.88	0.37	100.00	
	9.23	16.34	100.00	
	0.07	1.79	100.00	
Peak-fitting	Total area	20.53	95.61	94.6
	80.01	1.28	101.99	
	70.59	0.87	101.08	
	62.90	0.39	105.83	
	7.21	16.18	99.02	
	0.01	1.82	101.59	

* - the sample in question was hydrolysed to h=2.4 for 12 hours at 90°C

** - %refererence is the parameter comparing the value of peak area calculated by selective integration method with other methods;

*** - %recovery (known species) is calculated from Equation (3.43).

From the data of Table 3.7 one can see that the best coincidence is between the areas of sharp peaks at 80, 63 and 0 ppm calculated by all methods implemented. The calculation of broad peaks (70 and 10 ppm) in the case of the local integration method and the total integration method provides strongly underestimated values. The peak fitting and the selective integration method cope with broader peaks much better. A good testing value to evaluate the accuracy of the calculated areas of broad peaks is the ratio between the area of the peak at ca. 10 ppm (S_{10}^{o}) and the sum of peaks related to tetrahedral Al-atoms of Keggin-ions at 70 ppm and 63 ppm (parameter R_{Keggin}):

$$R_{Keggin} = \frac{S_{10}^{o}}{S_{70}^{t} + S_{63}^{t}} \qquad \textbf{(3.51)}$$

Since the theoretical ratio of octahedral and tetrahedral Al-atoms for Al_{13}-mer and Al_{30}-mer is 12 and 14 respectively, then the ratio of areas for the mixture of these species must always be within the interval $12 \leq R_{\text{Keggin}} \leq 14$.

As can be calculated from the data of Table 3.7, the value of R_{Keggin} obtained from the standard local integration method is 10.27, which is below the acceptable limit of the parameter (R_{Keggin}=12). This is due to erroneous computation of the broad peak areas. In the case of the method of total integration the value of R_{Keggin} is 10.77 that is also unacceptable. For the method of selective integration R_{Keggin} = 13.14, while for the peak-fitting method R_{Keggin} = 12.98. The values are comparable and indicate the accuracy of the calculations.

3.2.3. Discussion of the methods for quantification of ^{27}Al NMR spectra

The method for quantification of ^{27}Al NMR spectra proposed in this work appears to produce most reliable and reproducible data comparing to the other methods. This method, in fact, is a hybrid containing the best features of the available methods. Combination of more precise measurements of sharp peak areas with computation of the broad peak areas from known values produces a desirable effect. The results of calculations by proposed selective integration methods are in a good agreement with the data of independent calculation method-the peak-fitting. The method of selective local integration can fail for the spectra where only broad peaks are present (e.g. the peak at 70 and 10 ppm). In this case the use of the peak-fitting method is the only choice for the adequate quantification of the NMR data.

The percentage of recovery of known species in the ^{27}Al NMR spectra using selective integration and peak-fitting procedure are usually lower than 100 %. This fact indicates that some undetectable species are present in the samples, such as colloidal particles or small oligomeric ions (dimers and trimers).

The method of total integration provides useful estimation of concentrations of known Al species as well as of the recovery of total soluble Al species detectable with ^{27}Al solution NMR (formula 3.40) and known Al species (formula 3.43).

3.2.4. Kinetic studies of aluminium-ion hydrolysis at elevated temperature using *in-situ* ^{27}Al NMR monitoring

The experimental conditions of Al hydrolysis and *in-situ* monitoring using ^{27}Al NMR spectroscopy are described in Section 2.7.6. The list of experiments performed can be found in Table 2.15 (Chapter 2).

An example of a three-dimensional view of the sets of time-resolved ^{27}Al NMR spectra obtained at high temperature is given in Fig. 3.22.

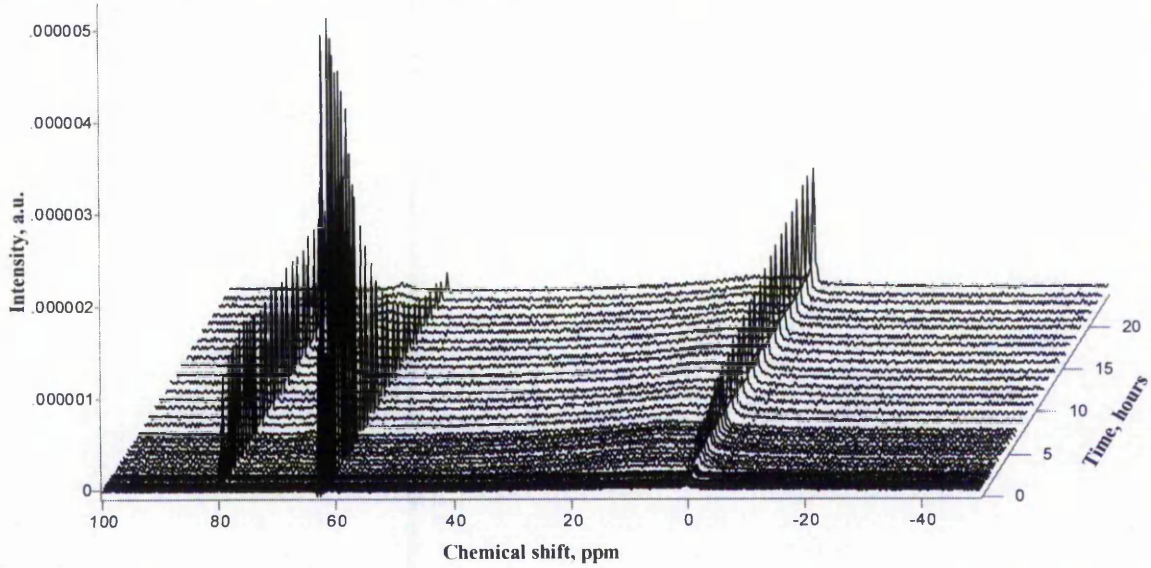


Fig. 3.22. ^{27}Al NMR spectra of solution of Al-ions hydrolysed at h=2.40 and T=90°C during 48 hours (spectra for the first 24 hours of hydrolysis are shown).

From Fig. 3.22 one may find that the heights and consequently the areas of the sharp peaks at 0 and 63 ppm are subject to constant change during the time scale investigated. However, the peak at 80 ppm remains practically unchanged during the experiments, making it a good reference for estimation of peak positions as well as for the quantitative assessment of the spectra. It is necessary to stress that the positions of the peaks at 80, 70 and 63 ppm also remained constant, while chemical shifts of the peaks at 10 and 0 ppm changed only slightly (within 1-2 ppm) throughout the NMR experiments.

The areas of the peaks present in the ^{27}Al NMR spectra of solutions of hydrolysed Al-ions were calculated using the selective integration algorithm proposed in this work and described previously. For some of the spectra the peak-fitting procedure for estimation of peak areas was also used. The spectra were also cross-normalised between the series using the peak area at 80 ppm of the reference solution of sodium aluminate in D_2O of known concentration. The reference peak of the series at h=1.0 was chosen arbitrarily as a reference for cross-normalisation and the formula for adjusting the peak areas to the reference value was the following:

$$S^t_{80}(new) = \frac{S^t_{80}(h)C_{ref}(h)}{S^t_{80}(h=1)C_{ref}(h=1)} \qquad and \qquad S_x(new) = \frac{S^r_{80}(new)S_x}{S^t_{80}} \tag{3.52}$$

where $S^{t}_{80}(new)$ - the cross-normalised value of the area of the peak at 80 ppm for a given spectrum; $S^{t}_{80}(h)$ - the actual area of the peak at 80 ppm for a given spectrum; $S^{t}_{80}(h=1)$ - the average peak area at 80 ppm for the series at h=1.0 used as a reference; $C_{ref}(h)$ – the known concentration of the reference solution of $NaAlO_2$ in D_2O (within 0.0011-0.0017 mol/L); $C_{ref}(h=1)$ the concentration of the reference solution of $NaAlO_2$ used in the series at h=1.0; $S_x(new)$ – the value of cross-normalised peak area at the chemical shift x ppm; S_x – initial area of the peak at chemical shift of x ppm

The cross-normalised areas of the reference peak at 80 ppm are shown in Fig. 3.23.

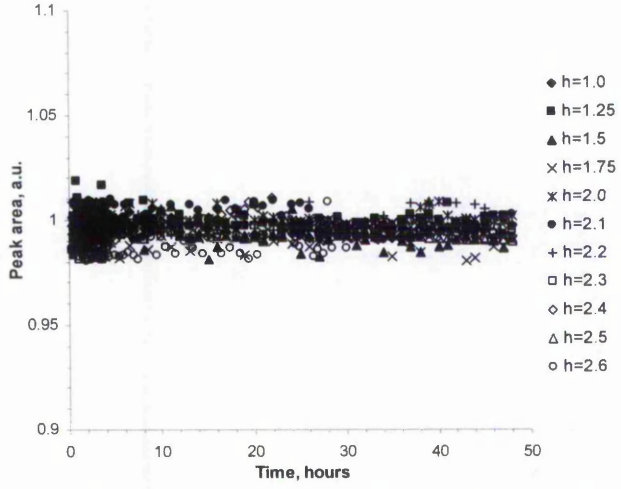


Fig. 3.23. Cross-normalised areas of the reference peak at 80 ppm in the time-resolved *in-situ* ^{27}Al NMR spectra versus time.

The data of Fig. 3.23 indicates that the variation of the areas of the reference peak at 80 ppm in the ^{27}Al NMR spectra is very small (maximum standard deviation <2% and 0.2% in average) and does not vary between the experiments. Thus, the reference peak area is suitable for cross-normalisation of time-resolved ^{27}Al NMR spectra of the hydrolysed Al-ion samples.

The cross-normalised areas of the peak at 63 ppm *vs.* measurement time for eleven solutions of Al-ions (0.1 mol/L) hydrolysed with 1.026 M solutions of KOH at 90°C in the hydrolysis ratio range from 1.0 to 2.6 are presented in Fig. 3.24.

From Fig. 3.24 one can find that the areas of the peak at 63 ppm reflecting the concentration of Al_{13}-mer species rapidly increase within a relatively short time of experiment (in less then 2 hours from start). After reaching a brief maximum, the time-resolved peak area curves show exponential decay behaviour due to the disappearance of the Al_{13}-mer at prolonged hydrolysis times. The general shape of the curves shown in Fig. 3.24 remains practically unchanged in the range of hydrolysis ratios at which the experiments were performed. Nevertheless, features of the curves such as initial slope, depth and the rate of the decay show strong dependence on the hydrolysis ratio.

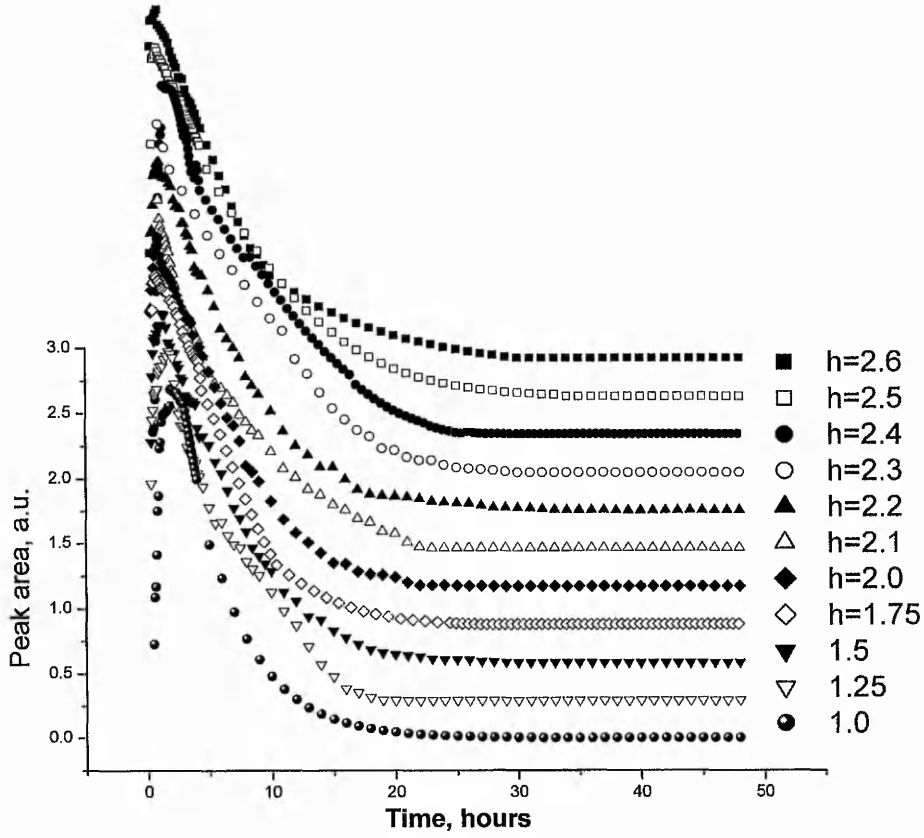


Fig. 3.24. Areas of the peak at 63 ppm in the *in-situ* time-resolved ^{27}Al NMR spectra vs. time. Y-axis offset 90% between the curves. Hydrolysis ratios (*h*) are indicated in the legend.

The calculated areas of the peak at 0.0 ppm *vs.* measurement time in the same *in-situ* time-resolved NMR experiments as above are presented in Fig. 3.25.

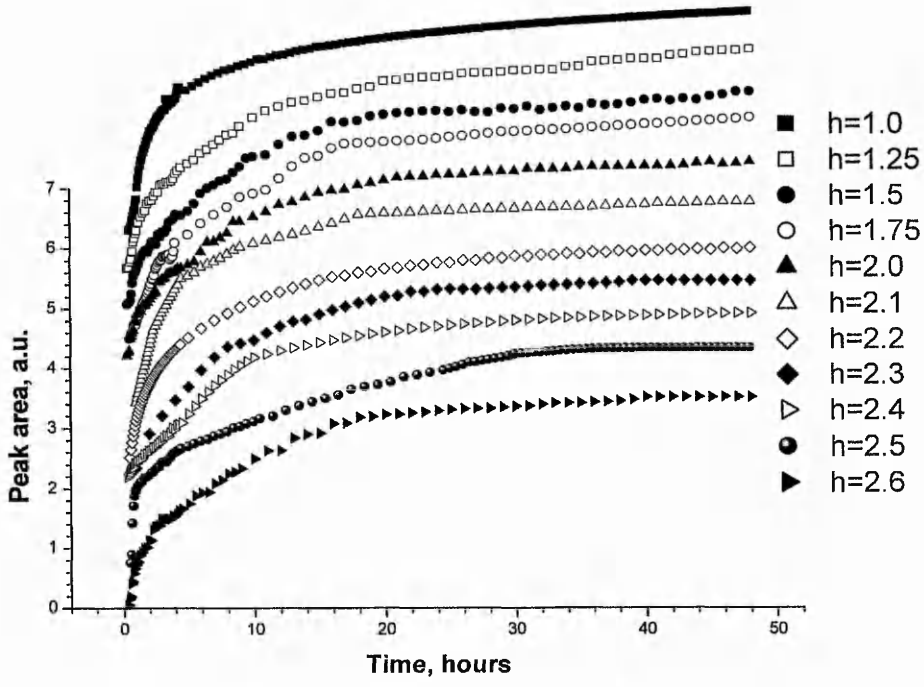


Fig.3.25. Areas of the peak at 0 ppm in the time-resolved ^{27}Al NMR spectra vs. time. Y-axis offset between the curves - 90%.

Evolution of Al monomer species in time (peak at 0 ppm) follows a completely different pattern compared to the signal at 63 ppm (Al_{13}-mer) as seen from the data of Fig. 3.24. Areas of the NMR peak at 0.0 ppm are close to zero at the beginning of the experiments and start to increase rapidly in short time range (within 2 to 4 hours). The increasing fraction of monomeric species reflected by the NMR peak at 0 ppm slows down gradually at prolonged hydrolysis times. The logarithmic-like shape of the time-resolved peak area curves is similar regardless of the hydrolysis ratio at which each experiment was conducted. The maximum height of the cross-normalised peak area curves varies within ca. 20% of the highest value between the series. The maximum variation in the curves appears at the initial slope, at the point of reaching a plateau and at the end of the curves. At low hydrolysis ratios the initial slope is high indicating a high rate of Al monomer evolution, the point of reaching a plateau is located at earlier times and the slope of the curve at the end of a 48 hour experiment is steeper than for higher hydrolysis ratios.

The dependence of the peak areas at 70 ppm in the ^{27}Al NMR spectra on hydrolysis time is presented in Fig. 3.26. From the data of Fig. 3.26 one can find that the time-resolved peak area curves for the peak at 70 ppm related to Al_{30}-mer species consist of three major domains. The first domain is a rapid decay of initially quite high value of the calculated peak area within 0.75-1.5 hours. The next domain is a growth of the peak area at 70 ppm until it reaches a plateau. In the third domain after a plateau the peak area at 70 ppm starts to diminish, although only a fractional decrease was observed on the time scale of 48 hours.

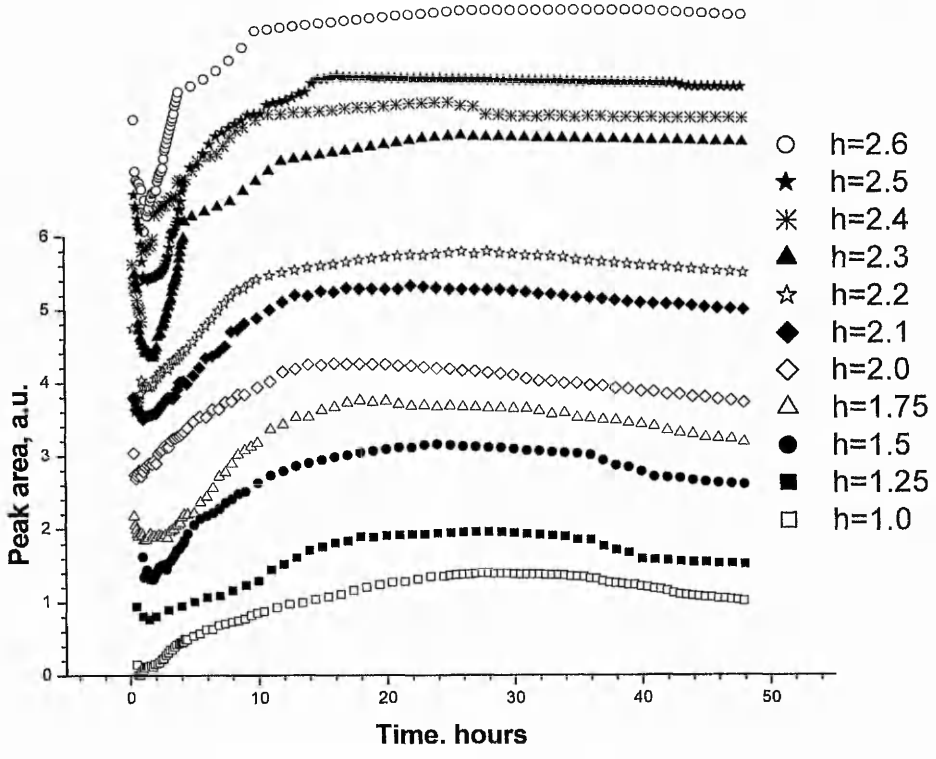


Fig.3.26. Areas of the peak at 70 ppm in the time-resolved *in-situ* ^{27}Al NMR spectra *vs.* time. Y-axis offset 100%.

Although the shape of the curves shown in Fig. 3.26 follow a similar pattern regardless of experimental conditions, the features of the curves in all three described domains were strongly affected by the hydrolysis ratio at which Al-ion solutions were prepared. The relative height of the curves increases with the increase of h and reaches a maximum at h=2.4. Moreover, the initial slope of the growth domain of the curves reflecting the formation of Al_{30}-mers becomes steeper with an increase of the hydrolysis ratio. The depth of the initial abrupt drop of the peak area value at the start of the curves also increases at higher h. The decay of the curve at prolonged hydrolysis time decreases in depth and starts later with the increase of h.

The dependence of the areas of the broad peak at 10 ppm (octahedral Al of Al polycation shell) on hydrolysis time is shown in Fig. 3.27.

The peak area curves of the broadest and largest peak in the acquired time-resolved ^{27}Al NMR spectra at 10 ppm contain a rapidly increasing initial part which, after reaching a maximum within ca. 1 hour is followed by a steady decay at longer hydrolysis time. The decay is not monotonic, especially for samples at lower hydrolysis ratios. The relative height of the curves shown in Fig 3.27 decreases with increase of the hydrolysis ratio of the samples. The depth of decay follows the same pattern. The overall behaviour of the peak at 10 ppm in the time domain reflects evolution of Keggin polycations – Al_{13}-mer and Al_{30}-mer.

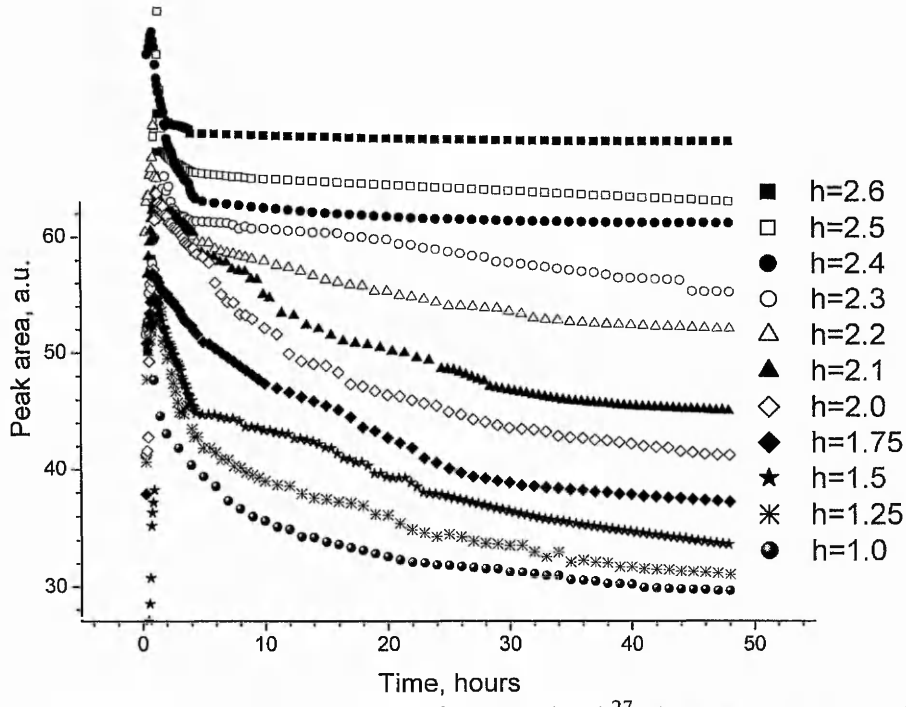


Fig. 3.27. Areas of the peak at 10 ppm in the time-resolved ^{27}Al NMR spectra vs. time. Y-axis offset 50%.

The areas of the peak at 10 ppm contribute more than 80% of the total peak area extractable from the acquired time-resolved NMR spectra. Distributions of the peak areas expressed as a percentage of the total peak area of the NMR spectra is given in Fig. 3.28.

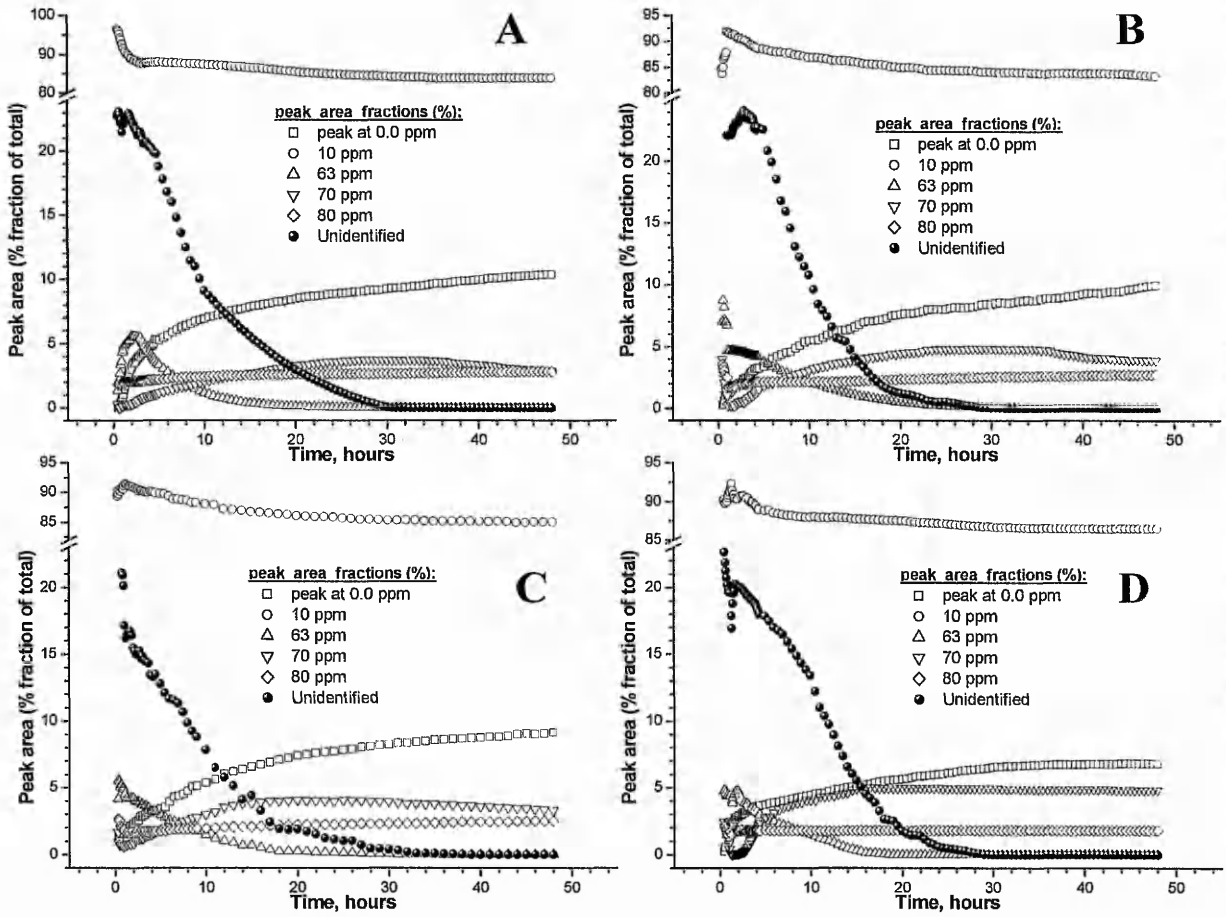


Fig. 3.28. Distribution of the peak area fractions in time-resolved *in-situ* ^{27}Al NMR spectra of the samples of hydrolysed Al-ions *vs.* time. ***A*** – h=1.0; ***B*** – h=1.5; ***C*** – h=2.0; ***D*** – h=2.5. Y-axis breaks from ca. 23-25% to 80-85 %.

From the data of Fig. 3.28 follows that the patterns of the percentage distributions of the peak areas at hydrolysis ratios 1.0, 1.5, 2.0 and 2.5 presented as an illustrative example are close to the absolute (cross-normalised) peak area values shown in Fig. 3.23 – Fig. 3.27. The overall peak area in the spectra are mainly dictated by the area of the large peak at 10 ppm tends to decrease with hydrolysis time. We have also estimated the percentage of the 'unidentified' part of the total peak area in the NMR spectra indicated as a curve '% unidentified' in Fig. 3.29 using the following formula:

$$S_{unidentified} = S_{total} - S_{80}^{r} - S_{70}^{t} - S_{63}^{t} - S_{10}^{o} - S_{0}^{o} \qquad \textbf{(3.53)}$$

This value represents 'unaccountable' area of the spectrum, which most probably arises from the presence of species other than those evaluated in the present *in-situ* kinetic NMR assay. It shows that at the beginning of the experiment the percentage of the unaccounted area is as high as 25-30% of the total area in the ^{27}Al NMR spectra and decreases with hydrolysis time reaching near-zero values after ca. 25-30 hours of hydrolysis for the samples prepared at different hydrolysis ratios. The curve of the unidentified peak area is superimposed to the curve of the peak at 63 ppm (Al_{13}-mer).

Only eleven out of twelve series of kinetic studies of Al hydrolysis using ^{27}Al NMR spectroscopy are discussed above. The twelfth series at h=2.7 are not considered for the discussion due to complete transformation of Al-ions into colloidal state which is hard to detect with the current (solution) setup of NMR. Two examples of the spectra of the series at h=2.7 at the beginning and at the end of the experiment are shown in Fig. 3.29.

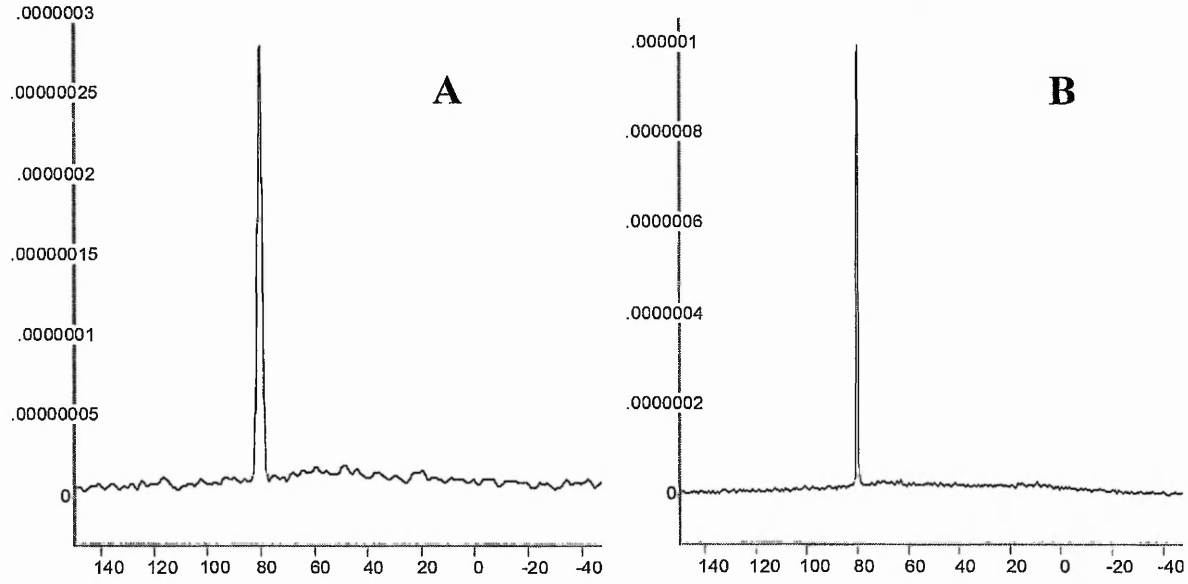


Fig. 3.29. Individual ^{27}Al NMR spectra of the sample solution of Al-ions produced at h=2.7 and 90 ^{0}C. ***A*** – at 0.5 hours after start; ***B*** – at 48 hours after start of the experiment.

From Fig. 3.29 one can find that both at the beginning and at the end of the experiment at h=2.7 only two peaks are present in the corresponding NMR spectra –at 80 ppm (reference) and at ca. 50 ppm. The latter peak is probably related to octahedral Al atoms of the colloidal phase. The peak at 50 ppm is very broad and decreases in area after 48 hours of experiment.

Along with the qualitative analysis of the time-resolved data from the acquired ^{27}Al NMR spectra, we also attempted to quantify the kinetics of the formation and breakage of the species present in the system. Elucidation of exact kinetic rates is a problematic issue since one needs to know the exact concentrations of each species involved in equilibrium at each time of kinetic measurements [54] as well as the mechanism of the formation/breakage of the species which, for large Keggin ions (Al_{13} and Al_{30}) is still largely unknown [31]. However, on the basis of the time-resolved NMR data is still possible to provide estimates of the process kinetics by curve-fitting of the obtained kinetic curves (Fig. 3.24-3.28) with an appropriate exponential function.

We have chosen a first-order exponential decay function ('ExpDec1' pre-set function in Microcal Origin software) and a first-order reverse exponential function ('MnMolecular1' function in the Origin software) which provide relatively simple means for estimation of the rate of exponentially decaying or growing experimental curves. The equations of the

mentioned functions are the following:

'ExpDec1' function $$y = y_0 + Ae^{-x/t} \quad (3.54)$$

'MnMolecular1' function $$y = A_1 - A_2 e^{-kx} \quad (3.55)$$

Functions (3.54) and (3.55) are very similar and can be easily substituted with each other considering the following relationships: $y_0 = A_1$; $A = -A_2$ and $k = 1/t$. The variable y in these equations represents peak areas, and variable x represents time (hours). The choice of the abovementioned exponential functions for the kinetic NMR analysis is based on their similarity to the equation for the kinetic rate of a pseudo-first order reaction [54,55]:

$$A_\infty - A_t = (A_\infty - A_o)e^{kt} \quad (3.56)$$

where A_0, A_t, A_∞, – are analytical signals at the start of reaction, at a given time t, and at equilibrium correspondingly; k – is a kinetic rate constant.

Considering that in an ideal situation the areas of ^{27}Al NMR peaks are proportional to the concentration of the corresponding Al species [48], one can easily estimate kinetic rates for the formation/dissolution reactions of the species on the basis of the value of the exponential parameters t or k. Pre-exponential parameters y_0, A, A_1 and A_2 relate to the current conditions of the process such as total Al concentration, relative fractions of the species, presence of colloidal phases and other parameters, while the parameters k and t are estimates of the kinetic rate constant.

The estimated results of kinetic rates of formation/dissolution of Al_{13}-mer from the curve-fitting of the experimental time-resolved data obtained from ^{27}Al NMR spectra of hydrolysed solutions of Al-ions is given for the peak areas at 63 ppm (Fig. 3.24) in Table 3.8 (formation of Al_{13}-mer) and Table 3.9 (dissolution of Al_{13}-mer).

The data of Table 3.8 and 3.9 indicate that the results of the curve-fitting using the functions from Eq. 3.54 and 3.55 is statistically sound as supported by high values of the correlation coefficient R^2 as well as low values of the parameter χ^2. Standard deviation (*SD*) of the calculated parameters of the fitted functions is reasonably low. In the case of the initial incline in the time-resolved NMR peak area curves (Table 3.8) the 'upper cut' time which reflects the slope of the initial cut of the curves grows in agreement with increasing hydrolysis ratio of the samples. The parameter A_1 of the reverse exponential growth function 'MnMolecular1' (Eq. 3.55) indicating the highest obtainable height (and thus peak area) of the fitted curve also tends to increase at higher h. The second pre-exponential parameter A_2 from Eq. 3.55 (an indicator of the slope of the initial cut of the curves) shows reciprocal behaviour to that of A_1. Finally, the estimate of the kinetic rate constant at each hydrolysis ratio k increases with the growth of h reaching a maximum at h=2.5.

Table 3.8. Results of the curve fitting of the inclining (initial) part of the time-resolved peak area curves at 63 ppm (tetrahedral Al of Al_{13}-mer) with the first-order exponential function (MnMolecular, Eq. 3.55)

h*	Upper cut**	χ^2 ***	R^2	A_1****	SD(A_1)	A_2	SD(A_2)	k	SD(k)
1.0	1.67	0.00831	0.97917	2.5299	0.0473	8.8341	0.2700	2.398	0.2013
1.25	1.58	0.00561	0.963044	2.5383	0.0363	7.8968	0.0515	3.6893	0.1668
1.5	1.25	0.00561	0.973044	2.6007	0.0363	7.8045	0.2791	4.6893	0.2668
1.75	1.08	0.00246	0.97023	2.6598	0.019	7.7627	0.2922	8.0473	0.0836
2.0	1.00	0.00226	0.96471	2.6735	0.047	6.8978	0.1033	14.1473	0.8285
2.1	1.00	0.00078	0.98981	2.6775	0.012	6.2488	0.0510	17.1325	0.668
2.2	1.00	0.00007	0.99723	2.7188	0.0057	5.9488	0.0761	20.6389	0.6333
2.3	0.92	0.00077	0.9984	2.8298	0.011	4.9871	0.0453	24.2638	1.0200
2.4	0.92	0.00601	0.9698	2.9431	0.0431	3.8766	0.0720	25.8964	0.3102
2.5	0.67	0.002613	0.9778	3.2122	0.05569	2.8757	0.0791	32.2239	0.3212
2.6	1.00	0.00078	0.9924	3.859	0.0129	2.2306	0.0713	27.933	0.215

* - h – the value of hydrolysis ratio;
** - 'Upper cut' (hours) shows the upper time limit of the time-resolved data below which the curve-fitting was conducted;
*** - χ^2 is a non-parametric coefficient reflecting goodness of curve-fitting; R^2 – is a correlation coefficient describing a correlation between calculated and experimental curves
**** - A_1, A_2 and k are coefficients of Equation 3.55, k – is an estimate of the kinetic rate constant of a given process. SD is a standard deviation calculated in Origin software for each fitted coefficient of Equations 3.54 or 3.55.

Table 3.9. Results of the curve fitting of decaying part of the time-resolved peak area curves at 63 ppm with the first-order exponential decay function (ExpDec1, Eq. 3.54)

h*	Decay start**	Decay finish	χ^2	R^2	y_0***	SD(y_0)	A	SD(A)	t_1	SD(t_1)	k****
1.0	1.67	22.0	0.01723	0.9876	0	0	4.0948	0.09667	5.3525	0.21549	0.1868
1.25	1.58	26.0	0.00675	0.9922	0	0	3.4862	0.06093	6.1302	0.16249	0.1631
1.5	1.25	28.0	0.00362	0.9962	0	0	3.3678	0.03448	6.4786	0.11191	0.1544
1.75	1.08	29.5	0.00730	0.9925	0	0	3.3246	0.04249	6.7143	0.16482	0.1489
2.0	1.00	30.5	0.01391	0.9875	0	0	3.2904	0.04614	6.8600	0.19020	0.1458
2.1	1.00	31.0	0.00270	0.9971	0	0	3.1962	0.02154	7.5400	0.10400	0.1326
2.2	1.00	32.0	0.00367	0.9964	0	0	2.9306	0.03143	7.6000	0.11717	0.1316
2.3	0.92	37.0	0.00337	0.9965	0	0	3.1929	0.02784	7.8900	0.11223	0.1267
2.4	0.92	39.0	0.00355	0.9969	0	0	3.1054	0.01985	8.5944	0.13522	0.1164
2.5	0.67	42.0	0.01152	0.9822	0	0	3.1239	0.07272	8.6514	0.29086	0.1156
2.6	1.50	40.5	0.00818	0.9920	0	0	3.4455	0.03747	7.3376	0.14380	0.1363

* - for the description of the parameters h, χ^2 and R^2 in Table 3.9 see footnotes of Table 3.8;
** - parameters 'Decay start' and 'Decay finish' indicate approximate time (in hours) of the start and the end of the decaying part of the curves in Fig. 3.24. The 'Decay start' parameter was also used as a lower limit for the curve-fitting procedure.
*** - y_0, A and t_1 are the coefficients in Equation 3.54.
**** - the value of k analogous to the value shown in Table 3.8 was calculated as $k=1/t_1$ and represents an estimate of the kinetic rate constant of a given process.

Results of the curve fitting of the time-resolved NMR data on Al monomer (peak at ca. 0 ppm) in Al-ion solutions hydrolysed to a different extent are shown in Table 3.10. First-order exponential decay function (Eq. 3.54) was applied for the curve fitting of time-resolved data.

Table 3.10. Results of the curve-fitting of the time-resolved peak area curves at 0 ppm

h	Growth slowdown*	χ^2	R^2	A_1	SD(A_1)	A_2	SD(A_2)	k	SD(k)
1.0	**18.0**	0.00831	0.97917	3.8289	0.04685	2.7355	0.04883	0.2718	0.01256
1.25	**19.0**	0.00561	0.963044	3.6874	0.03862	2.8612	0.02106	0.2390	0.00947
1.5	**20.0**	0.00561	0.973044	3.6620	0.01512	3.0058	0.02845	0.1740	0.00404
1.75	**20.5**	0.00246	0.97023	3.6593	0.02112	3.1641	0.03742	0.1472	0.00426
2.0	**23.0**	0.00226	0.96471	3.6013	0.01824	3.3043	0.04584	0.1316	0.00360
2.1	**24.0**	0.00078	0.98981	3.5849	0.02041	3.3326	0.05642	0.1307	0.00525
2.2	**24.5**	0.00007	0.99723	3.5791	0.01259	3.4261	0.03315	0.1288	0.00266
2.3	**25.0**	0.00077	0.9984	3.4968	0.02581	3.5550	0.09032	0.1280	0.00691
2.4	**26.0**	0.00601	0.9698	3.4929	0.02214	3.6095	0.03597	0.1216	0.00431
2.5	**29.0**	0.002613	0.9778	3.4557	0.02958	3.6165	0.03468	0.1165	0.00258
2.6	**30.0**	0.00078	0.9924	3.3924	0.02350	3.8551	0.07946	0.0782	0.00521

* -'Growth slowdown' (hours) is a tentative point (determined from a first or second derivative of the initial curve) where the rate of growth of the curve reaches minimum.

As follows from the data of Table 3.10, the 'growth slowdown' time at which the rate of formation of Al monomers (as indicated by the peak at 0 ppm) becomes steady is dependent on the hydrolysis ratio and increases with increasing *h*. Pre-exponential factors A1 and A_2 are affected by the hydrolysis ratio in the opposite way: The A_1 parameter declines with an increase of *h* and A_2 increases. (Parameters A_1 and A_2 decline and incline respectively with increasing *h*.) The most important parameter determined by the curve-fitting procedure is the exponential coefficient *k*, which is also affected by the hydrolysis ratio. However, the effect of conditions during sample preparation are less significant for the formation of Al monomers as indicated by a steady change of the value of *k* than for the case of Al_{13}-mer (peak at 63 ppm, Table 3.8). The order of magnitude of the parameter *k* is also about three times less for the time-resolved curves of the NMR peak areas at 0 ppm than for the peak at 63 ppm. The minimum rate of Al monomer formation is at h=2.6.

The growing part of the time-resolved NMR curves for the peak at 70 ppm related to tetrahedral Al of Al_{30}-mer (Fig. 3.27) was also subjected to curve-fitting analysis (Table 3.11).

Table 3.11. Results of the curve fitting of the inclining part of the time-resolved peak area curves at 70 ppm

h	Growth start*	Growth slowdown	χ^2	R^2	A_1	SD(A_1)	A_2	SD(A_2)	k	SD(k)
1.0	0.50	16.5	0.00621	0.9871	3.0008	0.1606	2.1968	0.0758	0.0720	0.01090
1.25	0.75	17.0	0.00166	0.9956	2.8170	0.1622	2.5293	0.0457	0.0840	0.00300
1.5	0.92	20.0	0.01846	0.9676	2.7770	0.0628	2.5721	0.0391	0.1070	0.01000
1.75	1.00	23.5	0.00797	0.9881	2.5455	0.0541	2.5936	0.0503	0.1300	0.00590
2.0	1.00	25.0	0.01072	0.9688	2.5336	0.0338	2.6224	0.0277	0.1410	0.00310
2.1	1.08	26.0	0.00375	0.9953	2.5310	0.0913	2.6690	0.0232	0.1430	0.00840
2.2	1.25	28.0	0.00949	0.9871	2.4381	0.0389	2.9910	0.1265	0.1450	0.00650
2.3	1.33	34.0	0.00624	0.9893	2.3462	0.0145	3.1582	0.0844	0.1742	0.01450
2.4	1.50	48.0	0.01836	0.9746	2.3047	0.0324	3.5427	0.0743	0.2861	0.01730
2.5	1.92	46.0	0.00834	0.9860	2.2719	0.0135	3.7560	0.1335	0.2761	0.01090
2.6	2.08	45.0	0.00241	0.9960	2.2296	0.0258	3.7902	0.1112	0.2431	0.01410

* -'growth start' parameter indicates the start of the incline and the lower limit of curve-fitting

Results in Table 3.11 indicate that in the case of peak areas at 70 ppm both the start of inclining part of the time-resolved peak area curves and the point of 'growth slowdown' are increasing in accordance with growing hydrolysis ratios of the samples. The pre-exponential parameters A_1 and A_2 show reciprocal behaviour with variation of h. The value of the kinetic rate constant estimate k increases with the raise of h and reaches a maximum at h=2.4 (the theoretical hydrolysis ratio for Al_{30}-mer formation). Then this parameter tends to decline at higher hydrolysis ratios (h=2.5 and h=2.6).

Estimation results of the kinetic rate constants from the curve-fitted NMR data are summarised in Fig. 3.30. The error bars in Fig. 3.30 indicate the standard deviation of the estimated kinetic rate constant calculated by Origin program from the curve-fitting data.

From the data in Fig. 3.30 it follows that the maximum kinetic rate of the Al_{13}-mer formation at 90 ^{0}C is at hydrolysis ratio ca. 2.5. The rate of formation is slower at lower and higher hydrolysis ratios. The fastest rate of Al_{30}-mer formation appears to be at h=2.4, although the difference between the rate constant estimates at h=2.4 and h=2.5 is statistically unreliable according to a partial overlap of the error bars at the corresponding points of the curve. Outside this narrow interval the formation rate follows the same patterns as for Al_{13}-mer, however, statistical significance of the difference between adjacent points at h=2.0-2.2 is questionable. Evolution of Al monomers follows a reciprocal pattern to those of Al_{13}-mer and Al_{30}-mer. In the range of hydrolysis ratios h>2.0 the rate of formation of Al monomers is the

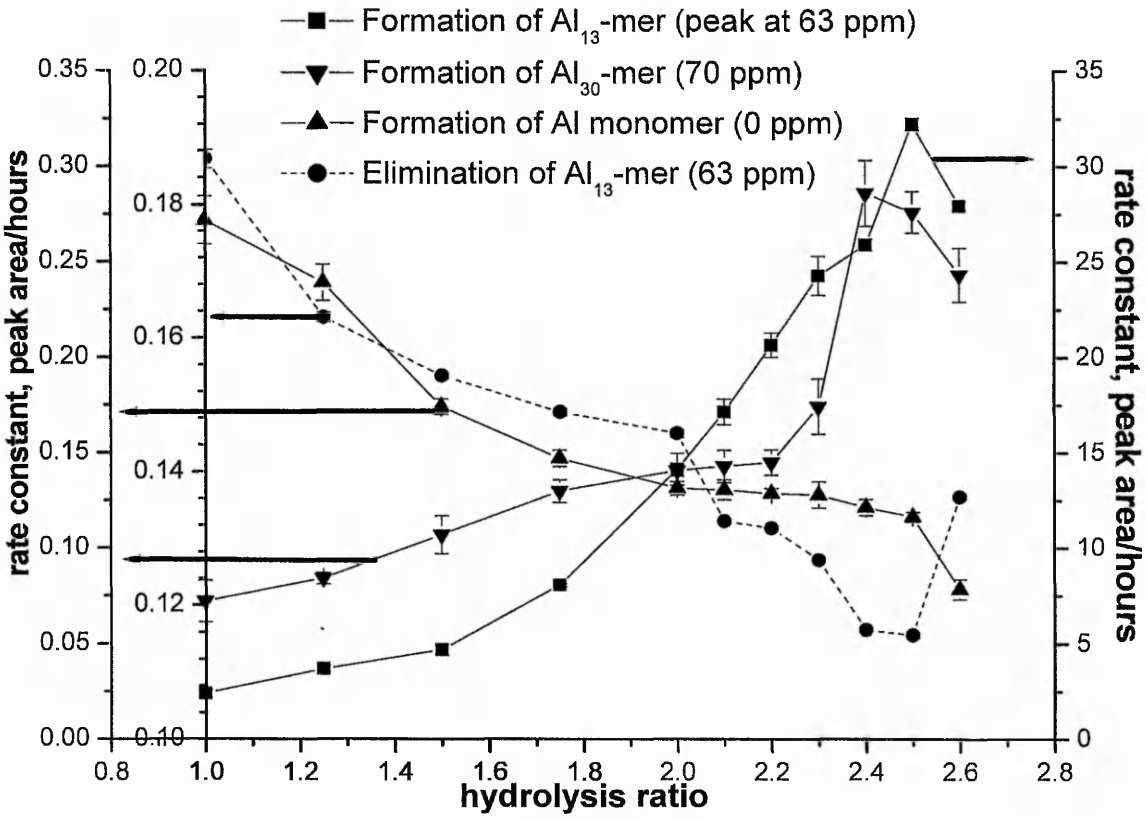


Fig. 3.30. Rate constant estimates for the species observed in time-resolved in-situ ^{27}Al NMR spectra of hydrolysed Al-ion solutions. Y-errors from the curve-fitting results are indicated at each point of the graph. Arrows indicate the Y-axis to which the curves belong.

lowest in the studied range, reaching minimum at h=2.6. With the decrease of h the rate of monomer formation steadily increases. Finally, the kinetic stability of Al_{13}-mers determined from the curve fitting of time-resolved ^{27}Al NMR data is in reverse proportion to the formation rate of this species and reaches minimum in the range of h between 2.4 and 2.5.

Along with the kinetic analysis of the results of time-resolved experiments at high temperature described above, one may also attempt to estimate at first approximation a real concentration distribution of Al species detectable with ^{27}Al NMR spectroscopy. Equations 3.39-3.43 provide a basis for such calculations (Table 3.12).

The values of time and maximum percentage of the species of hydrolysed Al-ions detectable with ^{27}Al NMR spectroscopy that are summarised in Table 3.12 on the basis of time-resolved *in-situ* NMR measurements are a rough estimate due to: (*a*) intensity lost outside the region over which integration was performed; (*b*) difficulty of accurate measurements of the total peak area in the spectra owing to apodisation errors, 'baseline rolling', intrinsic spectral noise and other hindering factors of spectral processing; (*c*) the constant presence of colloidal phase and species not easily identifiable by the ^{27}Al solution NMR technique using current experimental procedure. Nevertheless, these estimated values

Table 3.12. Estimation of maximum concentrations of Al species (percentage of the total concentration of Al-ions of 0.1 mol/L) detected in time-resolved ^{27}Al NMR spectra

h	Al^{3+}		Al_{13}-mer		Al_{30}-mer		%Al(detected)***		Peak area in the NMR spectra assigned to known species				Colloid phase, %	
	Time,* hours	% (Al^{3+})**	Time, hours	% (Al_{13}-mer)	Time, hours	% (Al_{30}-mer)	0 hours	48 hours	Time, hours	Known species, %	Time, hours	Known species, %	0 hours	48 hours
1.0	48	**27.1**	1.67	**68.7**	16.5	**11.9**	**90.2**	**95.1**	0.0	**76.8**	48.0	**94.9**	**9.8**	**5.0**
1.25	48	**27.0**	1.58	**70.2**	17.0	**39.9**	**86.5**	**94.8**	0.0	**79.1**	48.0	**94.7**	**13.6**	**5.2**
1.5	48	**22.4**	1.25	**71.6**	20.0	**61.7**	**82.5**	**94.4**	0.0	**79.5**	48.0	**94.2**	**17.6**	**5.7**
1.75	48	**16.6**	1.08	**78.0**	23.5	**65.0**	**83.7**	**94.1**	0.0	**75.1**	48.0	**93.9**	**16.3**	**6.0**
2.0	48	**14.4**	1.00	**78.7**	25.0	**66.0**	**80.8**	**91.7**	0.0	**74.5**	48.0	**90.8**	**19.2**	**8.4**
2.1	48	**10.8**	1.00	**80.8**	26.0	**75.9**	**77.2**	**90.1**	0.0	**76.3**	48.0	**91.3**	**22.8**	**8.0**
2.2	48	**9.6**	1.00	**81.1**	28.0	**76.9**	**77.8**	**89.4**	0.0	**75.3**	48.0	**88.7**	**22.3**	**10.6**
2.3	48	**3.0**	0.92	**81.6**	34.0	**79.7**	**77.2**	**88.4**	0.0	**75.0**	48.0	**87.3**	**22.9**	**11.7**
2.4	48	**1.9**	0.92	**82.7**	48.0	**82.7**	**76.4**	**89.4**	0.0	**74.8**	48.0	**89.0**	**23.6**	**10.6**
2.5	48	**1.9**	0.67	**82.8**	46.0	**90.2**	**76.3**	**86.9**	0.0	**75.4**	48.0	**86.5**	**23.8**	**13.1**
2.6	48	**0.5**	1.00	**82.8**	45.0	**90.2**	**74.4**	**85.7**	0.0	**75.4**	48.0	**84.9**	**25.7**	**14.3**

* - measurement time at which the maximum concentration of a given species is calculated;

** - *%(species)* - the maximum concentration of a given species (% of the total NMR-detected concentration of Al-ions);

*** - '*%Al(detected)*' is calculated using Eq. 3.39 and indicates the total amount of Al species detected with ^{27}Al solution NMR; '*Known species*' percentage is calculated using Eq. 3.43 (maximum percentage of '*Known species*' is indicated); '*Colloid phase*' percentage was calculated as "*%Al(total) - %(Known)*".

can be used for comparison of fractions of known species as well for the estimation of the total amount of unidentified species and colloidal phase in samples of hydrolysed Al-ions. For instance, the fraction of monomeric Al species (expressed as Al^{3+} in Table 3.12) clearly tends to decrease with increase of the hydrolysis ratio. The fact that the maximum of these species always occurs at the end of an experiment (48 hours) suggests that further progress of the reaction would lead to increasing concentrations of Al monomers. Therefore, at conditions of very high temperature (90 °C) studied in the present work large polycations are kinetically unstable and tend to decrease in concentration at longer reaction times. The maximum concentration of the Al_{13}-mer species is obtained within 1-1.5 hours (depending on hydrolysis ratio) and for a short period of time can reach as high levels as ~83% of the total Al content in solution. Al_{30}-mer species reach a maximum at much longer hydrolysis times than the Al_{13}-mer. At 90 °C it is possible to obtain concentrations of Al_{30}-mer as high as 90 percent of the total Al content. The percentage of known species detectable with ^{27}Al NMR strongly depends on the hydrolysis ratio. The maximum of the Keggin ion percentage can be reached in the vicinity of the hydrolysis ratios corresponding to their theoretical values.

From the data of Table 3.12 also follows that total recovery of Al species detectable with solution NMR (%Al(detectable)) significantly differs at the beginning and at the end of the kinetic experiments performed. Recovery of the Al signal is poorer at the start of hydrolysis than after 48 hours. The highest recovery in both cases is reached at lower hydrolysis ratios, probably due to the lower content of colloidal phase.

The difference between the amount of Al species recovered in NMR spectra and the actual concentration of Al-ions in solution (0.1 mol/L) gives a rough estimation of the amount of colloidal hydroxide phase not detectable with solution NMR. This value ranges from ca. 10 to ca. 25 % in the beginning of the kinetic experiments and tends to increase with the increase of the hydrolysis ratio of the samples in question. At prolonged hydrolysis times (48 hours) the relative fraction of undetectable colloidal phase reduces significantly (Table 3.12).

Known Al species detectable with ^{27}Al NMR are comparable both with identifiable species (%Al(detectable)) and the difference between amount of colloidal phase and the total Al amount (Table 3.12). Therefore, percentage of the detected by the NMR, but unaccounted for, is very low (<5 % of the total Al content). Only at h=1.0 this difference appears to be larger (compare the values of %Al(detectable) and 'Known species, %', Table 3.12).

3.2.5. Discussion

The kinetic experiments with *in-situ* time-resolved ^{27}Al NMR monitoring of Al-ion hydrolysis at medium concentration (0.1 mol/L) and at high temperature (90°C) have enabled us to detect along with Al monomers (peak at 0 ppm), Al_{13}-mers (peaks at 63 ppm and 10 ppm) the new species – Al_{30}-mers, present in significant amounts only at elevated temperatures. The signal of the latter species as measured by the signal from the tetrahedral

Al atom of the Keggin-ion 'core' is located at 70 ppm [47], while the broad signal from octahedral Al 'shell of Al_{30}-mer has the same chemical shift as an analogous signal from Al_{13}-mer – at 10 ppm and these peaks are completely overlapped.

Advanced data treatment of the ^{27}Al NMR data described in section 3.2.2 of this chapter allowed us to extract quantitative data from the time-resolved NMR experiments on Al-ion hydrolysis and to estimate kinetics of the major processes occurring in solution during hydrolysis-condensation reactions at high temperature. However, the approach to curve-fitting applied in this study was rather simplistic and exponential functions of higher order than the ones in Eq. 3.54 and 3.55 gave in many cases even better fit. Nevertheless, the first-order exponential functions of Eq. 3.54 and 3.55 gave curve fits good enough to enable a comparison of the kinetic data obtained at different hydrolysis ratios.

According to the quantitative time-resolved ^{27}Al NMR data there are three major species in Al-ion solution in the range of the hydrolysis ratios studied which appear to be in dynamic equilibrium as schematically presented in Fig. 3.31.

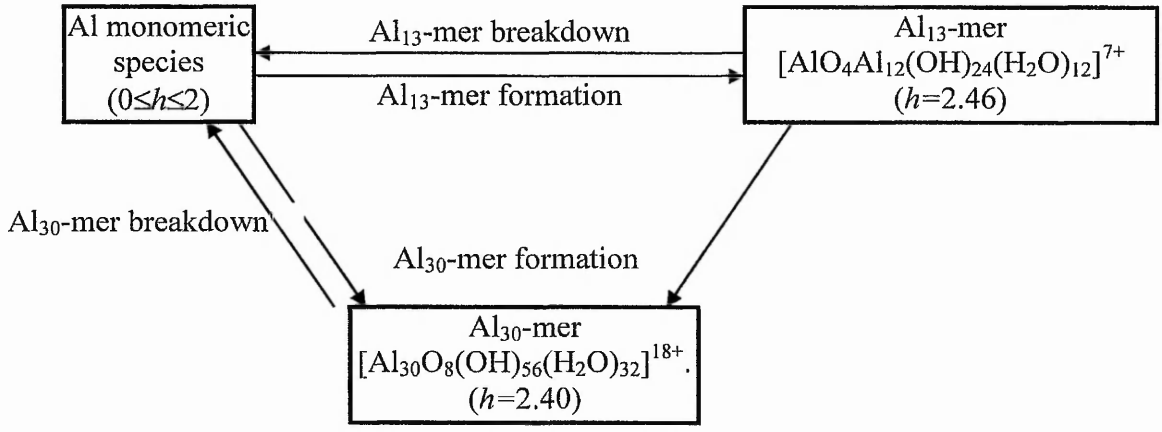


Fig. 3.31. Schematic representation of the equilibrium in hydrolysed solutions of Al-ions at high temperatures

From Fig. 3.31 it follows that the formation of Al_{13}-mer proceeds from hydrolysed Al monomers. This is a reversible process, however, we assume that small oligomeric Al species should precede the formation of large Al_{13}-mer ion from monomers. The kinetic NMR experiments were not able to identify these species directly, although the high probability of their presence is supported by the fact that up to 25 percent of the NMR signal was not assigned to any of the three species shown in Fig. 3.31. These species are abundant at the early stages of hydrolysis (cf. Fig. 3.28 and Table 3.12). The close correlation of the '% unidentified' curve and the curve of the peak at 63 ppm in Fig. 3.28 probably indicates that these species are related (e.g. small oligomers are direct precursors or intermediates in the formation of Al_{13}-mer). The reverse process of Al_{13}-mer breakdown leads to Al monomers and, judging by the data of kinetic NMR experiments (Fig. 3.24 and 3.25), this process occurs without any intermediates detectable by ^{27}Al NMR spectroscopy.

In order to produce Al_{30}-mers, both Al_{13}-mers and Al monomers are required. The dependence of the kinetic rate constant of Al monomers (Fig. 3.30) on the hydrolysis ratio is reciprocal to the analogous curves derived for the Al_{13}-mer and Al_{30}-mer. The overall difference for the formation of Al monomers between h=1.0 and h=2.6 (Δk=0.21) is equal to the maximum difference between the formation rates of Al_{30}-mer at h=1.0 and h=2.5. Thus, the formation of Al monomers is strongly related to the breakdown of the large Keggin-ions.

The kinetics of the formation of Al_{30}-mer is much slower than that of the Al_{13}-mer. While the first is formed after several hours of hydrolysis at 90 °C, the latter starts to form within the first few minutes of the reaction and its formation is complete within 60-90 min depending on the conditions. The kinetic rate constant estimates given in Table 3.8 and 3.11 for the formation of Al_{13}-mer and Al_{30}-mer correspondingly differ about 1000 times for the range of hydrolysis ratios $2.3 \leq h \leq 2.6$. In contrast, the stability of the Al_{30}-mer is much higher at 90 °C than that of the Al_{13}-mer. Estimated kinetic rate constants for the Al_{30}-mer breakdown at low h (the kinetic curves in Fig. 3.26 exhibit a shallow decay only at hydrolysis ratios h<2.0) which is within $0.003 \leq k \leq 0.005$ that is ca.500-700 times less than the corresponding rates for the Al_{13}-mer breakdown shown in Table 3.9 and Fig. 3.30. At hydrolysis ratios h≥2.2 the Al_{30}-mer does not show any significant breakdown detectable with the NMR technique even after 48 hours of hydrolysis at 90°C. With the decrease of hydrolysis ratio the breakdown rate both of Al_{13}-mer and Al_{30}-mer increases, their stability decreases, the decrease being much larger for Al_{13}-mer (the difference of k between h=1.0 and h=2.5 is ~1.6, Fig. 3.30).

Along with soluble Al species detected by solution NMR there is a fraction of colloidal species formed due to local disturbances of equilibrium during strong alkali addition which produces too broad a signal to be detected with the current solution NMR setup [23]. Nevertheless, we assume that these colloidal particles have a broad range and the smallest particles contribute to the detectable broad signal of octahedral Al-atom. This is supported by the spectra of the series at h=2.7 (Fig. 3.29) where no soluble species (monomers, Al_{13}-mers or Al_{30}-mer) are detected while the spectrum of the samples contains only one peak at ca. 50 ppm related to large colloidal Al-species containing octahedral Al-atoms only. The remaining larger colloidal particles are not manifested in the NMR solution spectra and result in a lower percentage of recovery of the NMR signal compared to the total concentration of Al-ions (Fig. 3.28, Table 3.12).

Evaluation of the colloidal phase detectable with the NMR technique (small colloidal particles) and its transformation during Al hydrolysis at high temperature can be done (*a*) from the calculations of the soluble species detectable with ^{27}Al NMR using Eq. 3.40 (cf. Fig. 3.28 and Table 3.12) or (*b*) from the kinetic NMR peak-area curves obtained from the signal of Al_{30}-mer at 70 ppm (Fig. 3.26). At the beginning of the hydrolysis reaction the peak at 70 ppm is not detected by NMR. However, in the curves shown in Fig. 3.26 there is a significant

proportion of species which cannot be assigned either to Al_{13}-mer nor to Al_{30}-mer. As mentioned above, these species most probably are very small colloidal particles, which contribute to the signal of octahedral Al atoms in the NMR spectra. A rapid decay of the initial part of the curves in Fig. 3.26 within the first hour of hydrolysis indicates that colloidal species detected with NMR quickly dissolve to form more soluble ionic species, most probably, Al monomers [56]. Therefore, the kinetics of dissolution of the soluble fraction of colloidal aluminium hydroxide can be detected with the NMR technique. On the other hand, the presence of the colloidal phase may induce alterations in the Al_{13}-mer formation, which remains incomplete until soluble colloid fraction is dissolved.

The kinetics study of the processes involved in speciation of Al-ions at high temperature shows that the hydrolysis ratio is a crucial parameter controlling both relative species distribution and kinetics of their formation/breakdown. In the range of hydrolysis ratios studied ($1.0 \leq h \leq 2.7$) an estimated kinetic rate constant for the Al_{30}-mer formation at h=2.40 is about 1.5 times higher than at h=2.0 (Fig. 3.30). The Al_{13}-mer breakdown indicated by the decay of the peak area at 63 ppm is almost 2 times slower at h=2.50 than at h=1.0.

The formation of Al_{30}-mer requires more acidic conditions than of Al_{13}-mer and this follows from the theoretical hydrolysis ratio (2.40 for Al_{30}-mer against 2.46 for Al_{13}-mer) as well as from the structure of the Al_{30}-mer (chapter 1), which consists of two Al_{13}-mer units and four monomeric Al 'bridges' connecting Al_{13}-mers [47,57]. It is possible that at some point during hydrolysis ($h \geq 2.46$) when all monomeric species are consumed by the formation of Al_{13}-mers, the formation of Al_{30}-mers may become hindered. This is indicated by the lower formation rate constant at h>2.5 (Fig. 3.30). However, the dynamic equilibrium between Al_{13}-mer formation and breakdown provides all necessary synthons for the Al_{30}-mer.

The detailed analysis of the acquired ^{27}Al NMR spectra in real time has allowed us to support indirectly the structure of Al_{30}-mer on the basis of the ratio of tetrahedral (70 ppm) and octahedral (10 ppm) signals close to 14 when only traces of Al_{13}-mer remain in solution and the signal at 10 ppm is largely attributed to the Al_{30}-mer. When Al_{13}-mers are the dominant species in solution – the ratio of the peak areas at 63 ppm (tetrahedral centre) and 10 ppm (octahedral 'shell') is close to 12.

Comparison of the kinetic rate estimates for Al_{13}-mer and Al_{30}-mer calculated in the present study with the literature data at room temperature [5,36,37,58] shows that at 90°C the rate of the Al_{13}-mer formation is ca. 3 times higher and the rate of the Al_{30}-mer formation is one order of magnitude higher than at room temperature. The breakdown rate of Al_{13}-mers at 90°C is 5-7 times higher than the values given in the literature [36].

3.2.6. Conclusions

The kinetic study of Al-ion hydrolysis at medium Al concentration and elevated temperature using ^{27}Al NMR spectroscopy has enabled us to draw the following conclusions:

1. Speciation of Al-ions at high temperature (90°C) is governed by the dynamic equilibrium of three major soluble species: Al monomers, Al_{13}-mers and Al_{30}-mers. Involvement of the Al dimer in equilibrium is of high probability, albeit these species could not be quantified directly from the NMR spectra acquired. The presence of colloidal phase in the samples of hydrolysed Al-ions can be detected and evaluated indirectly from ^{27}Al NMR data and is an important parameter of the equilibrium.
2. Kinetics of the formation of large polycations of Al_{13}-mer and Al_{30}-mer differ about 1000 times, while kinetics of breakdown differ as much as 500-700 times indicating that Al_{13}-mers are far less stable species than Al_{30}-mers. The early stages of hydrolysis (within first 1-2 hours of experiment) are dominated by the Al_{13}-mer species and then Al_{30}-mers become predominant reaching up to ca. 90% of the total amount of aluminium detectable with ^{27}Al NMR spectroscopy after at least 12-16 hours of hydrolysis.
3. Hydrolysis ratio is one of the most crucial parameters of solution governing speciation. In the hydrolysis ratios studied ($1.0 \leq h \leq 2.6$) the highest formation rate of Al_{13}-mer is reached at h=2.5 that is close to the theoretical hydrolysis ratio of the polycation. The difference between the estimated formation rate constants of Al_{13}-mer reaches ca. 10 times between h=1.0 and h=2.5, and for Al_{30}-mer – ca.2 times. Hydrolysis ratios higher than h=2.6 lead to complete disappearance of large Al polycations and monomers from the samples replaced by a practically insoluble colloidal phase.
4. Al monomers are not present in detectable amounts at the early stages of the kinetic experiments. The occurrence of these species is solely a result of breakdown of large polycations – Al_{13}-mer and Al_{30}-mer and evolves with time in the opposite sense to the decaying concentration of the Al_{13}-mer and steady concentration of the Al_{30}-mer.

3.3. Multi-batch titration of Al-ions at high temperature (series AMK1): results of solution studies

Along with room-temperature single-batch titrations of Al-ions discussed in section 3.1 of the present chapter and kinetic studies of high-temperature Al-ion hydrolysis described in section 3.2 out a multi-batch titration experiment at 90°C with Al concentration of 0.2 mol/L over a wide hydrolysis ratio range ($-1.0 \leq h \leq 4.0$) was carried out in order to elucidate speciation patterns of Al-ions at high temperature in greater detail. Special emphasis was made on the hydrolysis ratio range $2 \leq h \leq 3$ (resolution between experimental batches 0.1 units of h) where the optimum conditions of the Keggin ion formation were observed. Solution studies of the batch samples produced in this experiments are discussed below, while solid-state studies of the spray-freeze-dried samples are described in chapter 6 of the thesis. The

experimental procedure for the multi-batch titration of Al-ion solutions with KOH (series **AMK1**) is described in section 2.4.2, chapter 2.

3.3.1. Potentiometric measurements in the series AMK1

The multi-batch titration of Al-ions with KOH at high temperature (series **AMK1**) was designed in such a way to provide data on the effect of hydrolysis ratio on hydrolysed Al-ion speciation, and time-resolved data (experiments were conducted in real time) to provide an insight on the kinetics of Al-ion hydrolysis at high temperature. One of the methods of Al hydrolysis monitoring was pH-metry. The pH-measurements of each batch were performed at 8 different times of experiment: 0, 1, 3, 6, 12, 24, 36 and 48 hours. The pH measurements are presented as titration curves (*h* vs. pH) in Fig. 3.32.

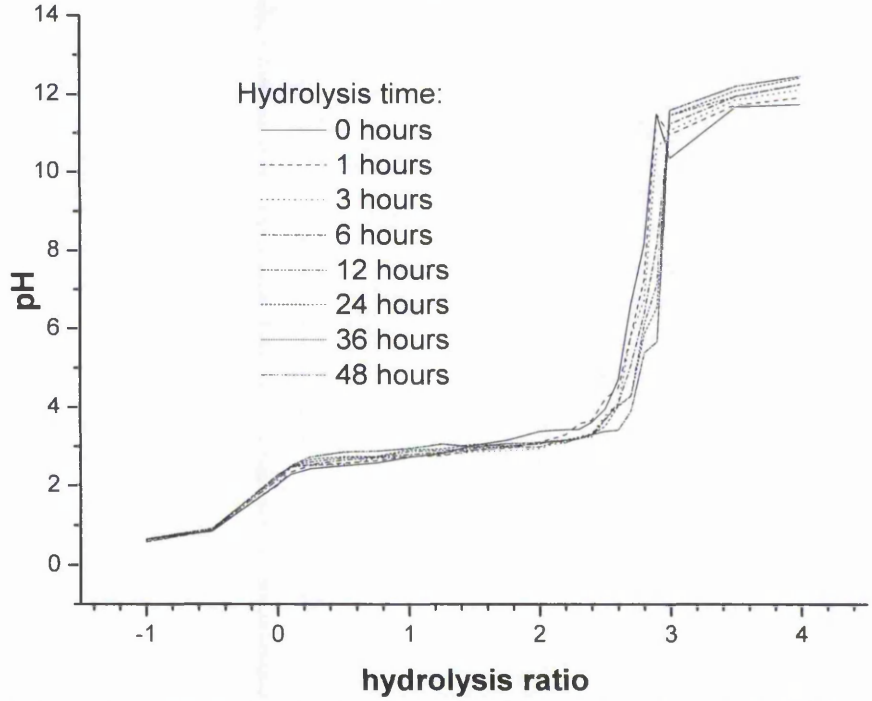


Fig. 3.32. Multi-batch potentiometric titration of $AlCl_3$ (0.2 mol/L) with KOH (1.026 mol/L) at 90°C. The times of pH measurement are indicated in the legend.

The general shape of the curves obtained from the multi-batch potentiometric titration of Al-ion solution with KOH (Fig. 3.32) are very similar to the integral curve from single-batch titrations in Fig. 3.1 except at acidic conditions ('negative values of *h*) which were obtained by the addition of HCl instead of KOH. There are at least three distinct inflexions at h~0.3, h~2.5 and h~2.9 in the curves in Fig. 3.32. Assignment of the inflexions is the same as for single-batch titrations of Al-ions with alkalis (Table 3.1).

From Fig. 3.32 also follows that multi-batch titration curves reconstructed at different measurement times (from the start of experiment at '0' hours to 48 hours) show only minor differences with the most significant being in the range of $2 \leq h \leq 3.5$. The inflexion at h~2.5 related to large Al polycations (Al_{13}-mer and Al_{30}-mer) becomes more profound at longer hydrolysis times (>24 hours). Generally, resolution of the potentiometric measurements

between the observed inflexions in the multi-batch titration is lower than in single-batch titration due to the lower number of experimental points on titration curve (24 in the present multi-batch experiment and between 60 and 120 in a single-batch titration) However this drawback is compensated for by the possibility of a substantially longer time span of kinetic monitoring of every batch achieved by the real-time multi-batch experiment design.

The results of pH measurements in the series **AMK1** as a function of time are shown in Fig. 3.33.

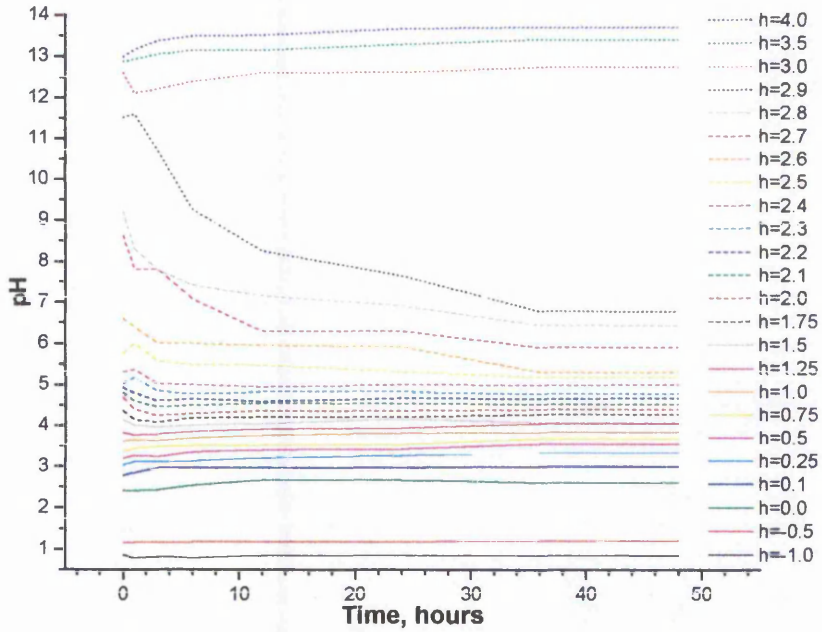


Fig. 3.33. Time-resolved pH-profiles obtained from the multi-batch titration of $AlCl_3$ (0.2 mol/L) with KOH (1.026 mol/L) at 90°C.

The time-resolved pH-curves in Fig. 3.33 show different shapes according to the range of hydrolysis ratios at which the curves are obtained. At very acidic conditions the time-resolved pH curve (h=-1.0) shows a hybrid shape with a decaying part within the first 12 hours of pH monitoring and a steadily growing part at longer hydrolysis times. At higher hydrolysis ratios ($-0.5 \leq h \leq 1.25$) the decaying part of the curves disappears and a steady growth of pH value is observed, being the most pronounced during the first 6 hours of the experiment. At $h \geq 1.5$ the time-resolved pH curves change their shape again, this time to the decaying pattern. The depth of the decay of pH values is the most dramatic at $2.6 \leq h \leq 2.9$ where the transformation of Al polycations into colloidal aluminium hydroxide occurs. The observed kinetic pH behaviour correlates well with the time-resolved data of single-batch titrations at room temperature (section 3.1.1.3). At hydrolysis ratios corresponding to alkaline conditions (h>3) the shape of time-resolved pH-profiles changes into a steady state again.

The comparison of the shapes of time-resolved profiles obtained from single-batch titrations of Al-ions at room temperature (section 3.1.1.3) and from multi-batch titrations at 90°C show that particular shapes of the curves may not coincide exactly at each particular

hydrolysis ratio. This fact is a consequence of completely different time scales involved in the time-resolved pH measurement. The time scale of single-batch titrations is 1-2 min between titrant additions, while in the multi-batch titration it is 48 hours. However, the major changes in the shape of the time-resolved pH-profiles follow similar patterns for both types of titrations.

3.3.2. Dynamic light scattering measurements of the series AMK1

In order to estimate particle sizes in solutions of hydrolysed Al-ions dynamic light scattering has been used as a fast technique requiring minimum sample preparation. The experimental procedure for the DLS is described in section 2.6.2.

The results of DLS measurements after 1, 6, 12 and 24 hours of Al hydrolysis in the series **AMK1** are given in Fig. 3.34. The fraction of the particle size distribution <3 nm is displayed only. Vertical error bars for each measurement represent average values of standard deviations obtained from 3 consecutive measurements of each sample at each scattering angle.

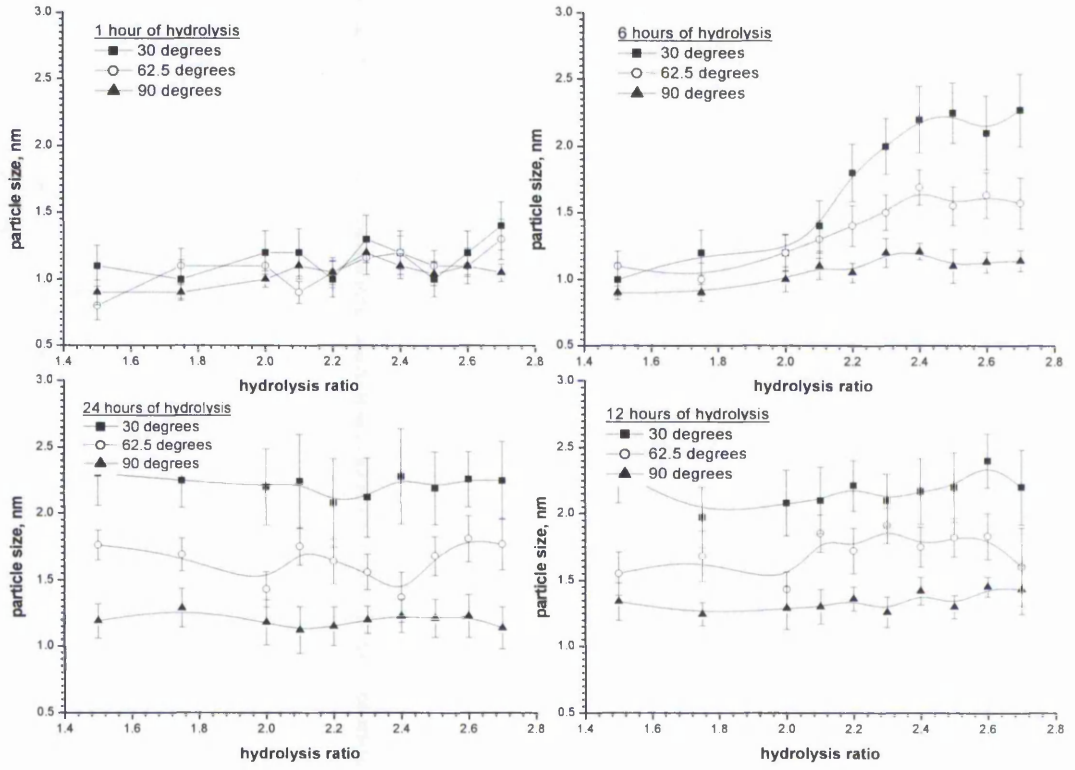


Fig. 3.34. Results of the DLS particle size monitoring of the multi-batch series **AMK1** after 1, 6, 12 and 24 hours of experiment ($N_{measurement}$=3).

At hydrolysis ratios 1.5 – 2.7 very small nanoparticles with mean size 1-2 nm are detected by DLS (Fig. 3.34). At lower hydrolysis ratios (h<1.5) DLS measurements did not detect any particulate matter. At higher hydrolysis ratios (h≥2.7) particles with larger diameter prevail. 20-25 nm and 70-80 nm particles are observed already at h=2.7 contributing to >10% of the total measured particles, the data is not shown in Fig. 3.34 for presentation purposes.

The particles of diameter larger than 1000 nm dominate solutions of hydrolysed Al-ions at h>2.9. The larger particles belong to the colloidal phase of aluminium hydroxide and have very broad distribution and are not shown in Fig 3.34.

The comparison of the mean particle size of weighed distributions at different scattering angles (30, 62.5 and 90 degrees) indicates that at the start of the series **AMK1** only particles of narrow distribution around 1 ± 0.3 nm are present in solutions of hydrolysed Al-ions. As has been mentioned above for the room-temperature studies of Al hydrolysis this particle size is very close to the size of Al_{13}-mers reported in literature [29]. The DLS data is not able to quantify the number of Al_{13}-mers, however, the scattered intensity tends to increase from ca. $4.5*10^4$ counts per second to ca. $1.2*10^6$ counts per second when the hydrolysis ratio of solutions was increased from h=1.5 to h=2.7.

At a longer time of hydrolysis (6 hours) the mean particle size below h=2.1 is practically the same as for 1 hour series (~1 nm). At higher hydrolysis ratios the data at different scattering angles splits (Fig. 3.34). Results of DLS measurement at 30 degrees indicate particle size of 2 ± 0.5 nm, while at 90 degrees the mean size of particles is ca. 1 nm. The DLS data at 62.5 degrees shows intermediate values between the results at 30 and 90 degrees.

Further hydrolysis of Al-ions at 90 °C in the multi-batch series **AMK1** for 12 and 24 hours shows that the mean particle size of the nanoparticles detected at 90 and 30 degrees remains separated (ca. 1 and 2 nm correspondingly), while the measurements at 62.5 degrees show intermediate values between 1 and 2 nm throughout the hydrolysis range shown in Fig. 3.34. The DLS measurements obtained after 36 and 48 hours show very similar patterns to those described for the time series at 24 hours.

3.3.3. Results of ^{27}Al NMR characterization of the series AMK1

The samples obtained from the multi-batch titration of Al-ions with KOH at 90 °C (series **AMK1**) were also characterised using ^{27}Al solution NMR spectroscopy. NMR measurements were carried out at the same temperature as the multi-batch experiment (90 °C) at experimental conditions similar to the kinetic ^{27}Al NMR experiments described in section 3.2 using a fixed number of 256 scans for each spectrum.

An overall representation of the hydrolysis ratio dependent ^{27}Al NMR spectra obtained for the samples of the series **AMK1** during 48 hours of experiment is shown in Fig. 3.35. NMR measurements at 24 hours of experiment are shown as an illustrative example.

The NMR spectra were strongly dependent on the hydrolysis ratio at which each batch was prepared. Along with peaks at 80 ppm, 70, 63, 10 and 0 ppm assigned in Table 3.21 above, we observed several other NMR signals were observed. Selected individual ^{27}Al NMR spectra are given in Fig. 3.36 in order to provide a more detailed insight into the spectral features.

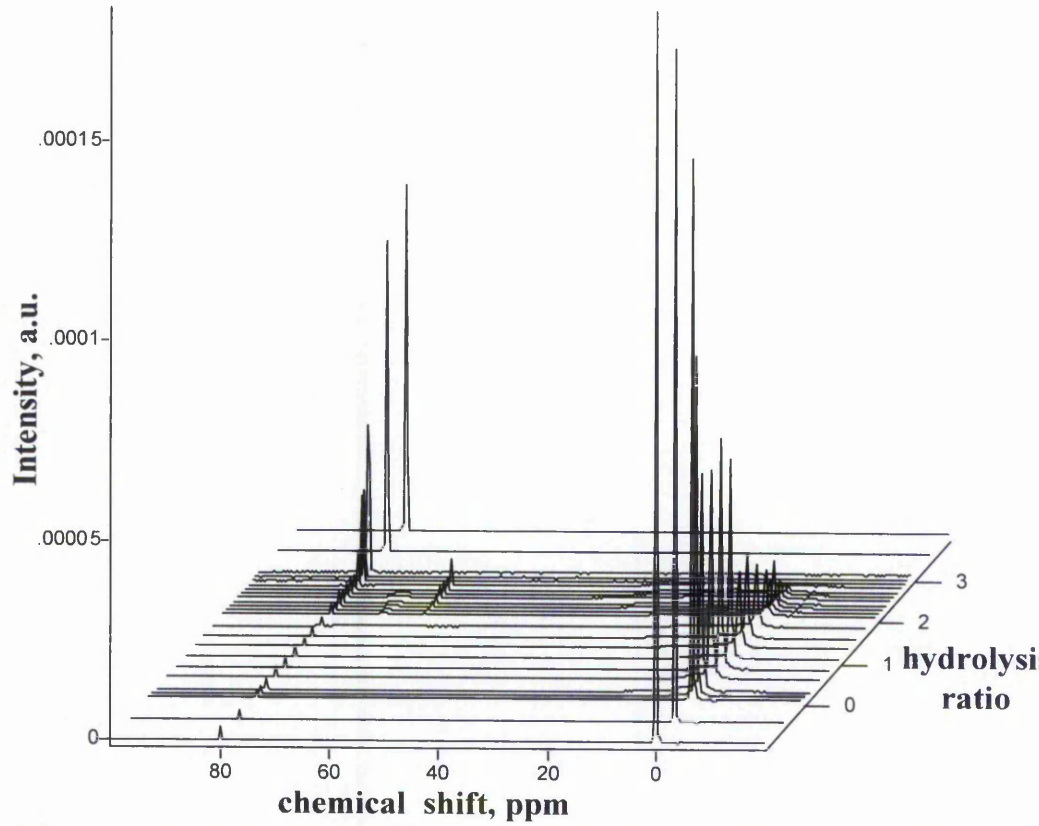


Fig. 3.35. 3D-representation of the ^{27}Al solution NMR spectra of the samples from the series **AMK1** after 24 hours of hydrolysis at 90°C.

Fig. 3.36 shows that in acidic medium (0.2 M HCl, h=-1.0) the only peak observed at ca. 0.0 ppm relating to Al monomers is split into two peaks with δ=-0.51 and δ=-0.18 ppm (Fig. 3.36A). This may indicate either (*a*) weak complexation with chloride-ions at low pH, or (*b*) the presence of non-hydrolysed Al hexaaquocations $[Al(H_2O)_6]^{3+}$ along with monohydroxo complexes $[Al(OH)(H_2O)_5]^{2+}$ in comparable amounts [23,25]. At lower acid concentration (0.1 M HCl, h=-0.5) three peaks are detected in the ^{27}Al NMR spectra of the batch produced (Fig. 3.36*B*), at δ=-0.13; 0.62 and 1.35 ppm. Some authors relate the peak at 1.35 ppm to dihydroxo complexes of monomeric Al-ions $[Al(OH)_2(H_2O)_4]^{2+}$ [27], and some to the dimeric Al polycation $[Al_2(OH)_2(H_2O)_4]^{4+}$ [23].

The original $AlCl_3$ solution (0.2 M) with h=0.0 also shows three NMR signals after 1 hour of hydrolysis at δ=-0.12, 1.35 and 3.12 ppm (Fig. 3.36*C*). There is also an artefact at $\delta \sim -4.2$ ppm of unknown origin which is constantly present in the acquired NMR spectra in the very wide hydrolysis range $-1.0 \le h \le 2.8$.

The peak at ca. 3-4 ppm, which we assign to Al oligomers, is apparent over a broad hydrolysis ratio range $0.0 \le h \le 2.4$. At higher hydrolysis ratios when larger polycations (Al_{13} and Al_{30}) occur in solutions of hydrolysed Al-ions, this peak is located on the top of the broader peak at 10 ppm as shown in Fig. 3.36*D*. The peak at ca. 4 ppm disappears from the spectra at h~2.4. (Fig. 3.36*E*). It is necessary to stress that improved preparation conditions

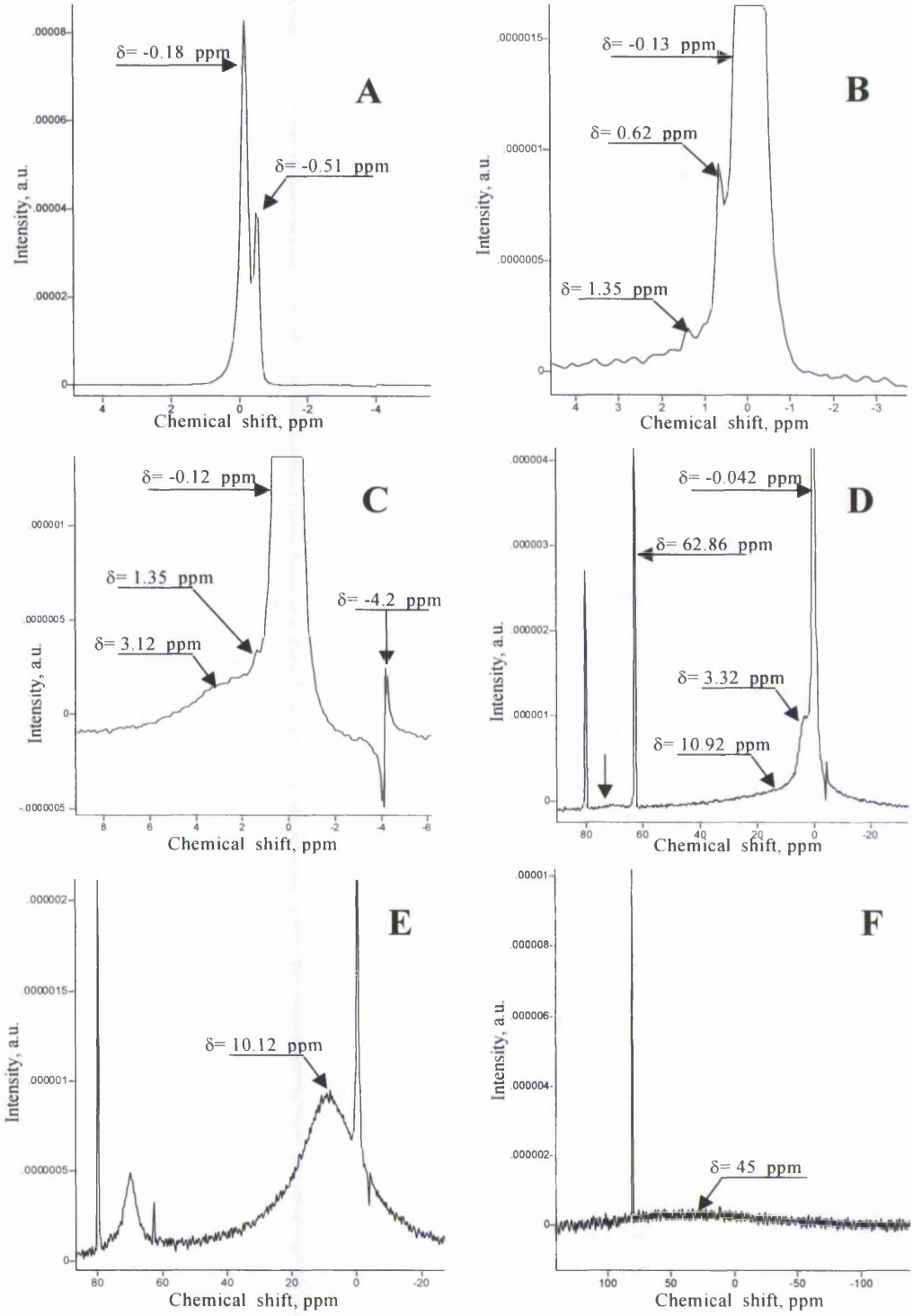


Fig. 3.36. Fragments of individual ^{27}Al NMR spectra obtained from the samples of the series **AMK1**. ***A*** – h=-1.0, hydrolysis time - τ=1 hour; ***B*** – h=-0.5, τ=1 hour; ***C*** – h=0.0, τ=1 hour; ***D*** – h=1.5, τ=3 hours; ***E*** – h=2.4, τ=24 hours; ***F*** – h=2.9, τ=24 hours. The spectral fragments *B*, *C*, *D*, *E* were truncated for presentation purposes.

of the series **AMK1**, namely, pre-heating of the batch samples to 90 °C prior to start of hydrolysis and careful titration-like addition of alkali led to a dramatic improvement in the quality of the ^{27}Al NMR spectra comparing to the kinetic series described in section 3.2. The samples prepared using the improved procedure were visibly clear up to h=2.8 while the

samples in the kinetic series reported above showed slight turbidity as early as at h>2.0. Lower content of colloidal phase explains lower noise level in the spectra obtained and a better separation of the peaks at 4 ppm and at 10 ppm unattainable during kinetic studies which allowed us to quantify them separately as reported below.

The ^{27}Al NMR spectra of the series **AMK1** at h>1.0 are dominated by the Keggin ions which manifest themselves through the sharp peak at 63 ppm (tetrahedral Al of Al_{13}-mer), the broad peak 70 ppm (tetrahedral Al of Al_{30}-mer) and very broad peak at 10 ppm (octahedral Al 'shell' of Al_{13}-mer and Al_{30}-mer) as illustrated by Fig. 3.36*E*. Monomeric Al species (the peak at 0.0 ppm) are still present at hydrolysis ratios up to h<2.7. Only at h=2.7 and h=2.8 the spectra indicate the signals of Keggin ions and no signal of monomeric species.

At h≥2.9 the NMR signals of large Keggin ions disappear from the spectra of the series **AMK1** (Fig. 3.36*F*). Only two peaks at 80 ppm and an extremely broad peak at ca. 40-50 ppm remain in the spectra. The latter peak gradually vanishes from the spectra at h>3.0, while the area of the peak at 80 ppm grows dramatically.

Along with the described signals obtained during ^{27}Al NMR characterization of the samples of the series **AMK1**, we observed another three signals at higher chemical shifts as illustrated by the data of Fig. 3.37.

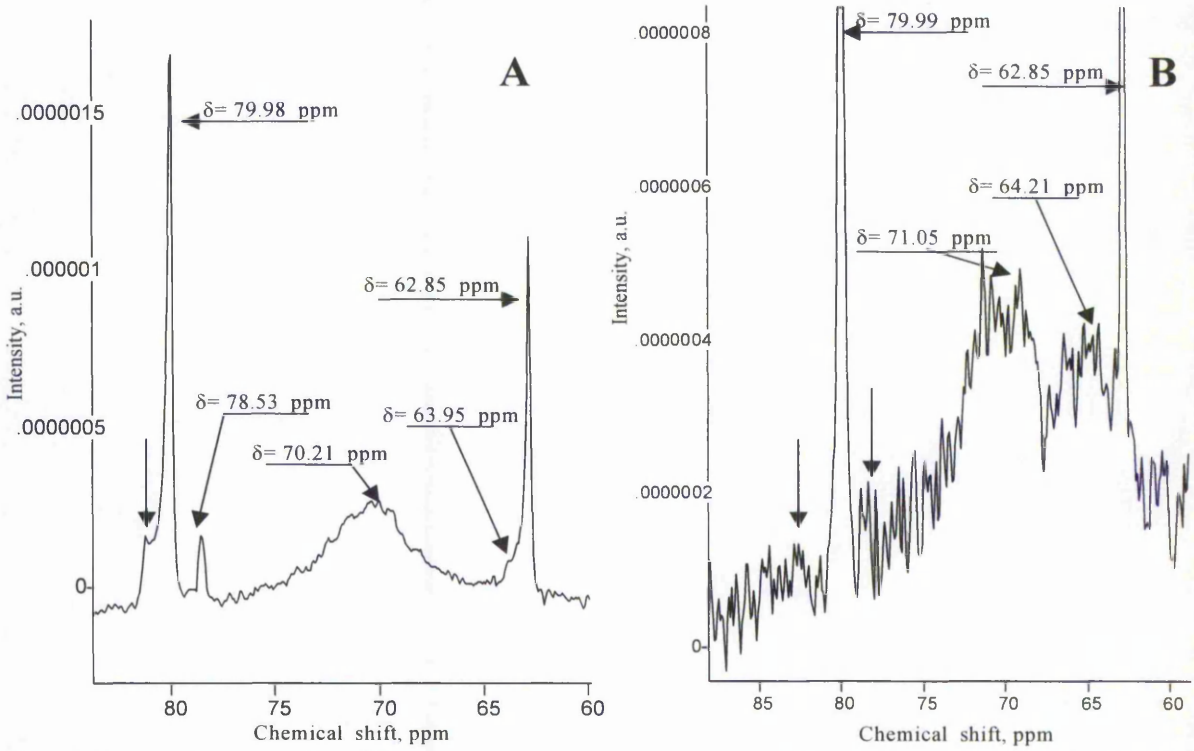


Fig. 3.37. Fragments of the ^{27}Al NMR spectra of the series **AMK1**. ***A*** – h=2.1; τ=6 hours; ***B*** – h=2.7, τ=24 hours. Peaks of the spectral fragment *B* were truncated for presentation purposes.

New peaks at δ=63.9-64.3 ppm, ~78.5 ppm and ~81.1 ppm are shown in Fig. 3.37. The peak at ca. 64 ppm was also detected in the work [47] and was assigned to the δ-structure of Al_{13}-mer as a transient species during the transformation Al_{13}-mer → Al_{30}-mer. This peak

is observed in the relatively narrow hydrolysis ratio range $2.1 \leq h \leq 2.6$. It was difficult to find exact range of h where the peak occurs along with its actual position and area owing to its overlapping with the peak at ca. 63 ppm (Al_{13}-mer) and rising spectral noise at higher h. From the data available it appears that the peak at ca. 64 ppm drifts to higher chemical shifts with increasing hydrolysis ratio. The peak area also changes, which was impossible to quantify under the current experimental conditions due to obstacles mentioned above.

The peak at ca. 78 ppm (Fig. 3.37*A*, *B*) was detected only in a few NMR spectra of the series **AMK1** within hydrolysis times 6-24 hours and hydrolysis ratios $h>2.0$. Some authors attribute this quite sharp peak to the larger Al polycations [1,5], however the assignment was tentative and no additional evidence has been provided. Authors of the reviews [5,23] describe a similar NMR signal at 76 ppm and assign it to the tetrahedral dimer $Al_2O(OH)_6^{2-}$ occurring in alkaline medium. Regardless of the origin, the species contribute only a minor fraction to the overall Al content as indicated by small peak area of the peak at ca. 78 ppm.

The peak at ca. 81 ppm (Fig. 3.37) may arise from the differences in NMR signals between $Al(OH)_4^-$ in D_2O (reference insert) and in aqueous solutions. This peak is encountered in acidic medium where the concentration of $Al(OH)_4^-$ ions is negligibly small [19] and coincides with the large ratio of the peak areas at 80 ppm (reference) and 81 ppm observed in the spectra given in Fig. 3.37. At higher hydrolysis ratios ($h>2.7$) the peaks at 80 and 81 ppm completely overlap.

In order to analyse quantitatively the trends in Al speciation, the peak areas of the obtained ^{27}Al NMR spectra of the series **AMK1** were calculated using a selective local integration algorithm and confirmed in some cases (where the peaks were strongly overlapped or broadened) by peak-fitting. The results of quantification are shown in Fig. 3.38 as graphs of the peak areas versus hydrolysis ratio.

From Fig. 3.38 one can see that the area of the ^{27}Al NMR peak at 80 ppm increases 1.5 times in average across the hydrolysis ratio range $h=-1.0$ to $h=2.4$ (Fig. 3.38*B*). In the narrow range of hydrolysis ratios ($2.4<h\leq3.0$) there is an abrupt dramatic shift of the peak area at 80 ppm (Fig. 3.38*A*) similar to the major inflexion point in the potentiometric titration curves of the same series (Fig. 3.32). During this shift the peak area changes more than 10 times. The growth of the peak area at 80 ppm is slowed down at conditions of high alkalinity ($h>3.0$). The data of Fig. 3.38*A* also indicates that the areas of the peak at 80 ppm tend to decrease slightly at prolonged hydrolysis times in the hydrolysis ratio range $-1.0 \leq h \leq 2.4$, the same effect being more profound under the alkaline conditions ($h>3.0$).

The curves of the peak areas at 70 ppm reflecting the presence of Al_{30}-mer species show that these species start to form as early as at $h=0.5$ (Fig. 3.38*C*). Their concentration increases almost exponentially at $h>0.5$ and reaches a maximum at $h=2.4$ (theoretical hydrolysis ratio of Al_{30}-mer). An abrupt drop of the Al_{30}-mer concentration follows at higher

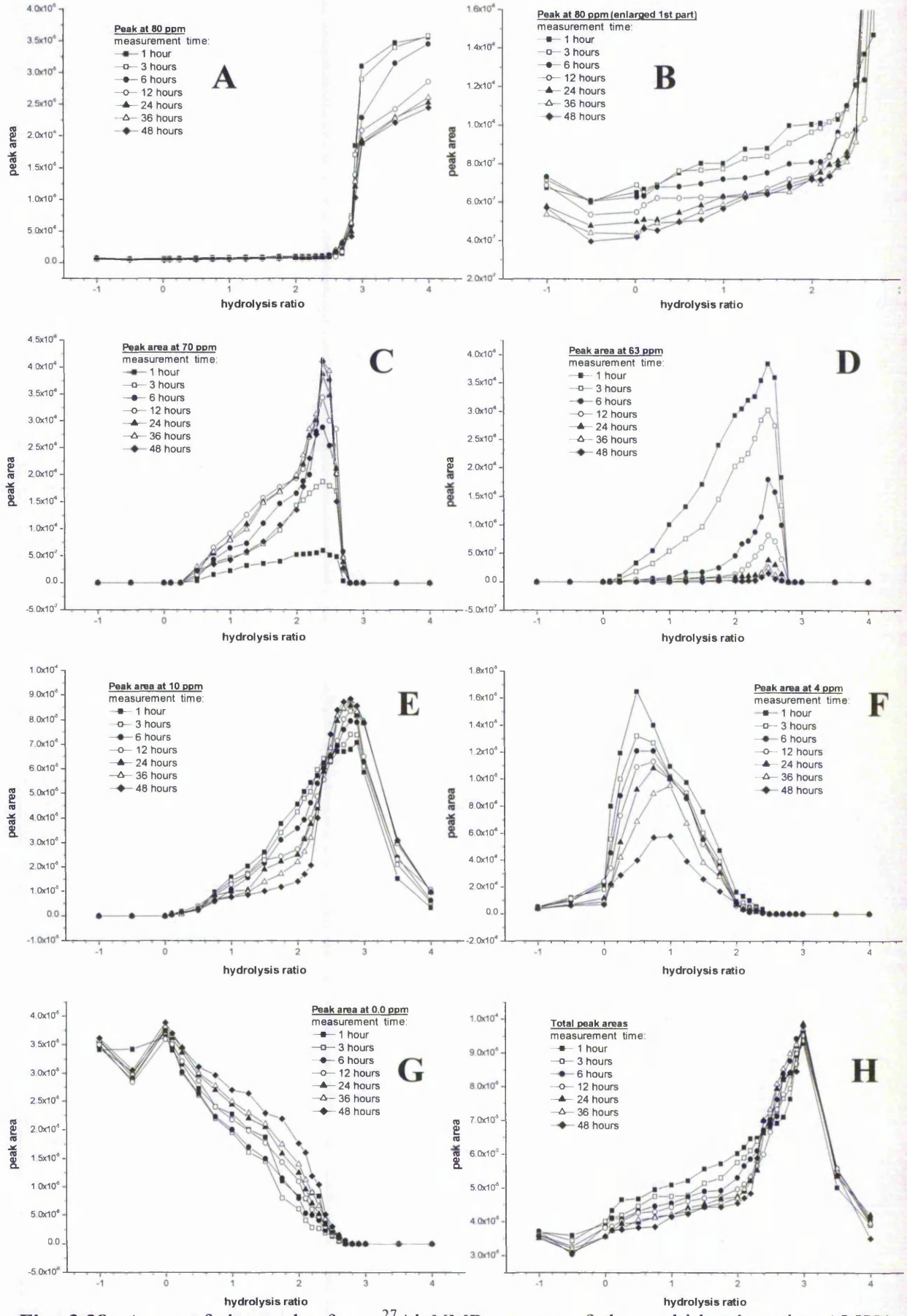


Fig. 3.38. Areas of the peaks from ^{27}Al NMR spectra of the multi-batch series **AMK1** obtained at different NMR measurement times (from 1 to 48 hours).

hydrolysis ratios ($h > 2.4$). The NMR signal at 70 ppm completely disappears from the spectra at $h \geq 2.8$. The time-dependence of the Al_{30}-mer concentration is clearly evidenced by the increasing area of the peak at 70 ppm within the hydrolysis ratio range $0.5 \leq h \leq 2.7$ which reaches maximum after 36 hours of hydrolysis and was lower at 48 hours.

As follows from Fig. 3.38*D*, another Keggin-ion, Al_{13}-mer, also forms as early as at h=0.1. An exponentially increasing peak area reaches a maximum at h=2.5 (theoretical hydrolysis ratio for Al_{13}-mer is h=2.462). The abrupt drop of the Al_{13}-mer concentration follows the maximum in the peak area curve and the species became undetectable at $h \geq 2.9$. The time-dependence of the peak area curves at 63 ppm (Fig. 3.38*D*) is very strong: maximum peak area is observed at 1 hour measurements, while the peak gradually disappears from spectra reaching a minimum after 48 hours of hydrolysis.

The area of the peak at 10 ppm corresponding to the octahedral Al 'shell' of the Keggin ions follows the same general pattern as the peaks at 70 and 63 ppm (Fig. 3.38*E*). However, after close to exponential increase of the peak area at weakly acidic conditions ($0.1 \leq h \leq 2.8$) the peak reaches a maximum at higher hydrolysis ratios ($2.8 \leq h \leq 3.0$) than the corresponding NMR peaks of the tetrahedral Al-atoms of Al Keggin-ions. The peak area at 10 ppm decreases at h>3.0. The lowest peak areas at 10 ppm are obtained at the beginning of the experiment, while the highest values at the same value of the hydrolysis ratio – after 48 hours of hydrolysis.

One of the new important parameters for quantitative estimation of Al speciation introduced in this section is the area of the peak at ca. 4 ppm reflecting small oligomeric Al species such as dimers and trimers (Fig. 3.38*F*). The peak appears at very low pH conditions (pH ca. 1.5-1.6 and h=-0.5) and increases in area more or less exponentially up to $0.75 \leq h \leq 1.0$. At higher hydrolysis ratios it rapidly decreased and completely disappeared from the NMR spectra of the series **AMK1** at h~2.4. The location of the curve maximum and the broadness of the peak at 4 ppm strongly depend on hydrolysis time. The maximum of the oligomer concentration is at h~0.75 and gradually shifts to higher hydrolysis ratios at prolonged hydrolysis times reaching h~1.0 for the measurements at 48 hours. The fact that the peak occurs around hydrolysis ratio $h \rightarrow 1.0$ allows one to suggest that it is related to the dimeric species $[Al_2(OH)_2(H_2O)_4]^{4+}$ and this is in a good agreement with assignments made in literature [23].

The peak area at ca 0.0 ppm indicates the concentration of the monomeric Al species (Fig. 3.38*G*). The first local minimum of the peak area is encountered at h=-0.5, indicative of minor oligomerisation (the peak at ca. 4 ppm of the Al dimer also appears at h=-0.5). The maximum of Al monomers is at h=0.0 in the absence of forced hydrolysis using KOH. With an increasing concentration of added alkali the concentration of monomers gradually decreases. The peak at 0.0 ppm completely disappears from the spectra at h~2.7. Hydrolysis time affects the shape of the decay of monomeric species concentration in the hydrolysis ratio

range $0.0<h<2.7$. At the beginning of the experiment (τ=1 hour) the decay follows a single exponential decay, while with increasing hydrolysis time two subsequent decays can be observed in the peak area curves, the first around $0.0\leq h\leq 1.6$-1.8 and the second at $h>1.6$-1.8.

The final graph (Fig. 3.38*H*) illustrates hydrolysis ratio-dependent behaviour of the total peak areas obtained from the ^{27}Al NMR spectra of the series **AMK1**. The total peak area curves exhibit shapes similar to those of the peak at 10 ppm (Fig. 3.38*E*) that is a consequence of the largest contribution from this peak into the total peak area of the spectra (up to 80-90 percent at $1<h<3.5$). The maximum total area of the spectra is located at h=3.0 regardless of the hydrolysis time and is followed by a decrease at more acidic and more alkaline conditions.

Quantitative time-resolved ^{27}Al NMR data obtained from the multi-batch series **AMK1** enabled us to estimate kinetic rate constants of formation of Al_{13}-mer and Al_{30}-mer using curve-fitting approach similar to that described earlier in the chapter (section 3.2.4). This is a quite rough approximation due to (*a*) relatively small number of experimental points and (*b*) lack of knowledge of exact mechanism of Al Keggin ion formation. Nevertheless it provides a value for comparison of the kinetics of the Keggin ion formation at different hydrolysis ratios. The results of the estimation of kinetic rate constants are shown in Fig. 3.39.

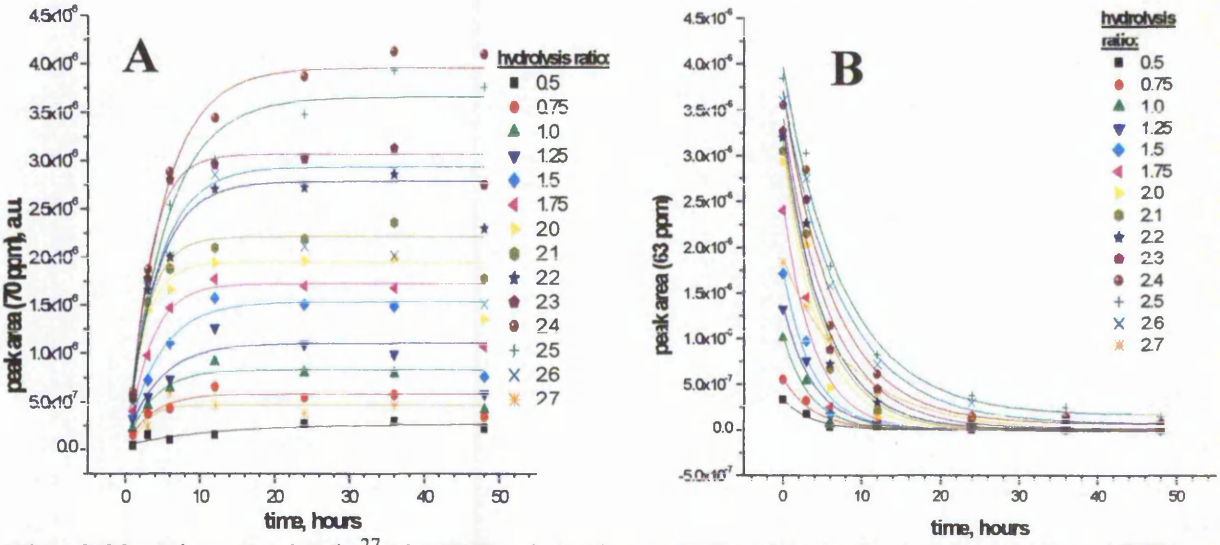


Fig. 3.39. Time-resolved ^{27}Al NMR data from the multi-batch titration series **AMK1**. ***A*** – time-resolved peak area curves at 70 ppm; ***B*** – time-resolved peak area curves at 63 ppm. Colour-coded curves were obtained at the hydrolysis ratios listed in the legend using curve-fitting of the experimental points.

Curve-fitting of the experimental time-resolved NMR data obtained from the series **AMK1** with functions from Eq. 3.54 and 3.55 gives high goodness of fit of the growing areas of the curves in Fig. 3.39*A* and decaying curves in Fig. 3.39*B* with correlation coefficients R^2 within 0.91 and 0.99. Only the growing parts of the peak area curves in Fig. 3.39*A* (up to 36 hours of hydrolysis) were used for the curve-fitting at $h<2.4$. The peak areas at 70 ppm after 48 hours of hydrolysis tend to become lower, the decrease being most profound at lower hydrolysis ratios ($h<2.4$). The data of Fig. 3.39*B* also suggests that the formation of Al_{13}-mers

in the batch solutions of hydrolysed Al-ions is completed before the first NMR measurement has been made (τ=1 hour).

The results of estimation of the kinetic rate constants from the curve-fitted NMR data of the series **AMK1** versus hydrolysis ratio are given in Fig. 3.40. The kinetic data suggests that the rate of elimination of Al_{13}-mer from aqueous solutions of hydrolysed Al-ions due to either breakdown into Al monomers or formation of Al_{30}-mers decreases with increasing hydrolysis ratio in the range of $0.5 \leq h \leq 2.5$ reaching a minimum at h=2.5 close to the theoretical hydrolysis ratio of Al_{13}-mer (h=2.462). At higher values of h (h>2.5) the elimination rate increases. The rate of formation of Al_{30}-mer increases with the increase of h practically exponentially reaching a maximum at h=2.4 (theoretical ratio for Al_{30}-mer). Further increase of the hydrolysis ratio leads to a slowdown of the Al_{30}-mer formation. The NMR data obtained from the multi-batch titrations (series **AMK1**) correlate well with the data of in-situ ^{27}Al NMR kinetic measurements of Al-ion hydrolysis (Section 3.2.4).

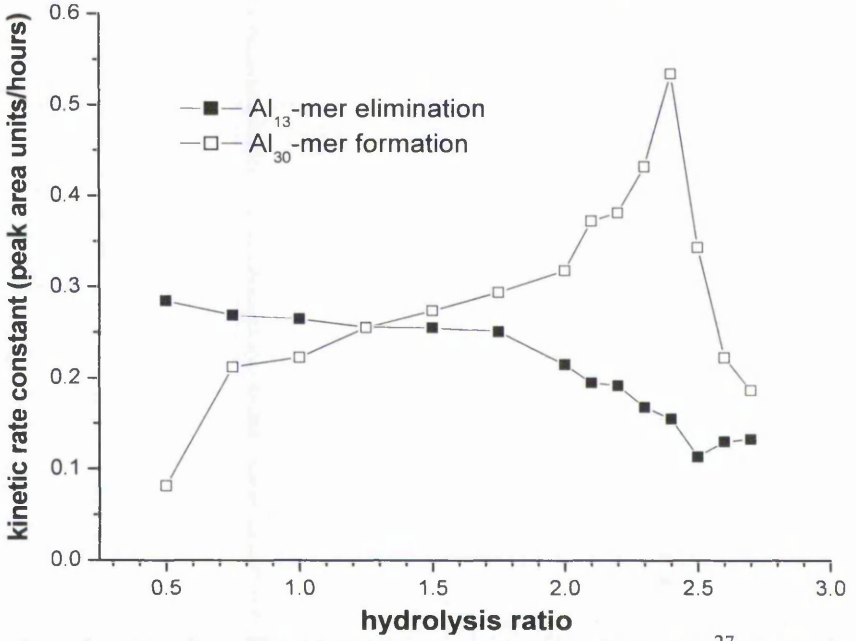


Fig. 3.40. Results of estimation of the kinetic rate constants from the ^{27}Al NMR data obtained from the multi-batch titration series **AMK1**.

The formulae 3.38-3.43 described earlier allow for the quantitative estimation of the relative distribution of Al species at different hydrolysis ratios (speciation diagrams) on the basis of the calculated areas of the corresponding ^{27}Al NMR peaks. Speciation diagrams obtained from the NMR data of the multi-batch titration series **AMK1** are given in Fig. 3.41 for seven different hydrolysis times ranging from 1 hour to 48 hours. At every measurement time two diagrams are presented: species fraction (% of total) against the pH of solution and against the hydrolysis ratio. The latter diagram is important for understanding the relationship between the chemical changes that occur in Al-ion solutions and the structure of the corresponding Al species manifested by the value of the theoretical hydrolysis ratio. An average value of the peak area at 80 ppm within the hydrolysis ratio range $0.0 \leq h \leq 1.0$ was

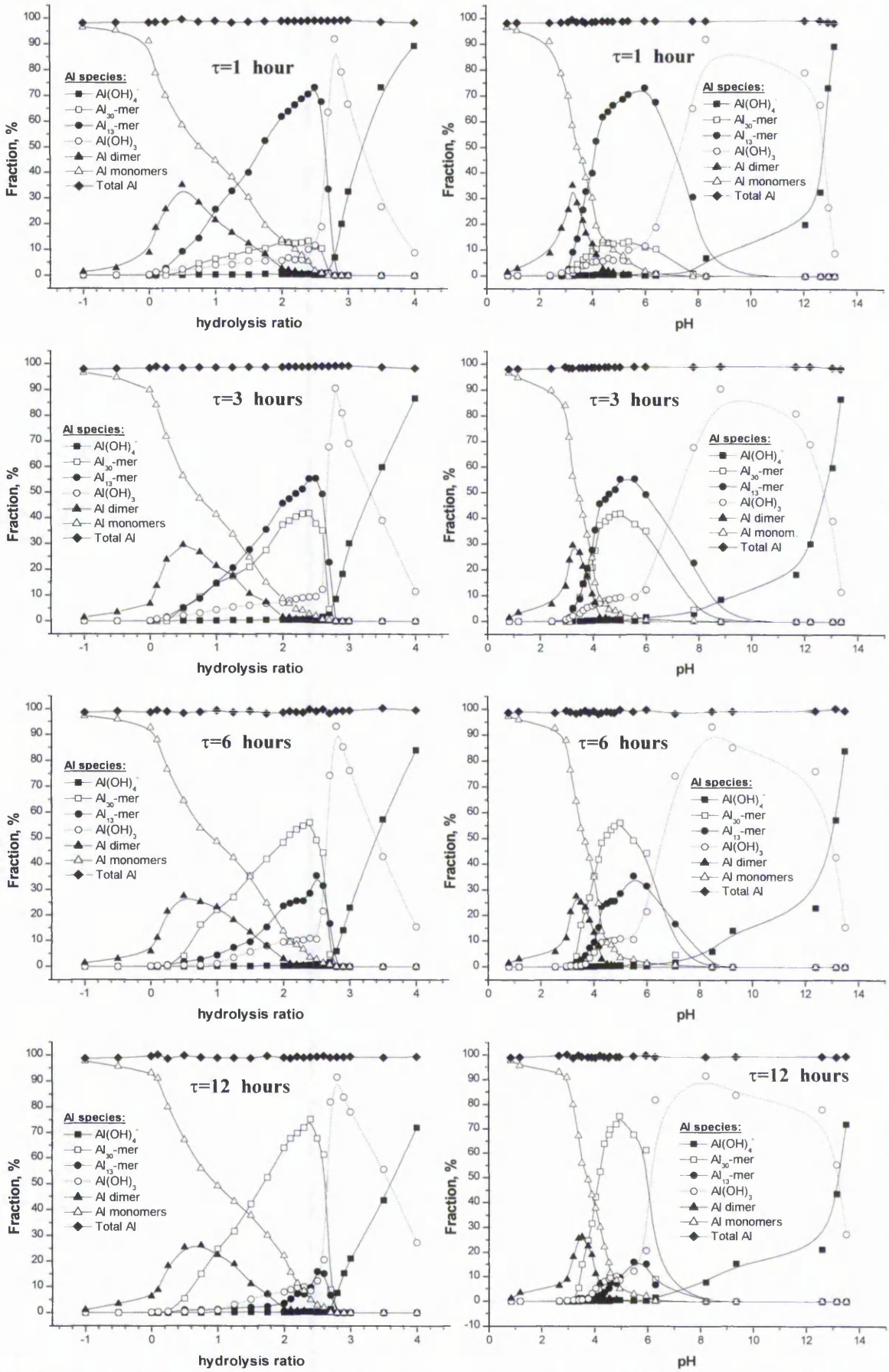


Fig. 3.41. Speciation diagrams of Al-ion hydrolysis at 90 °C at different hydrolysis times on the basis of ^{27}Al NMR measurements of the multi-batch titration **AMK1**. τ - hydrolysis time.

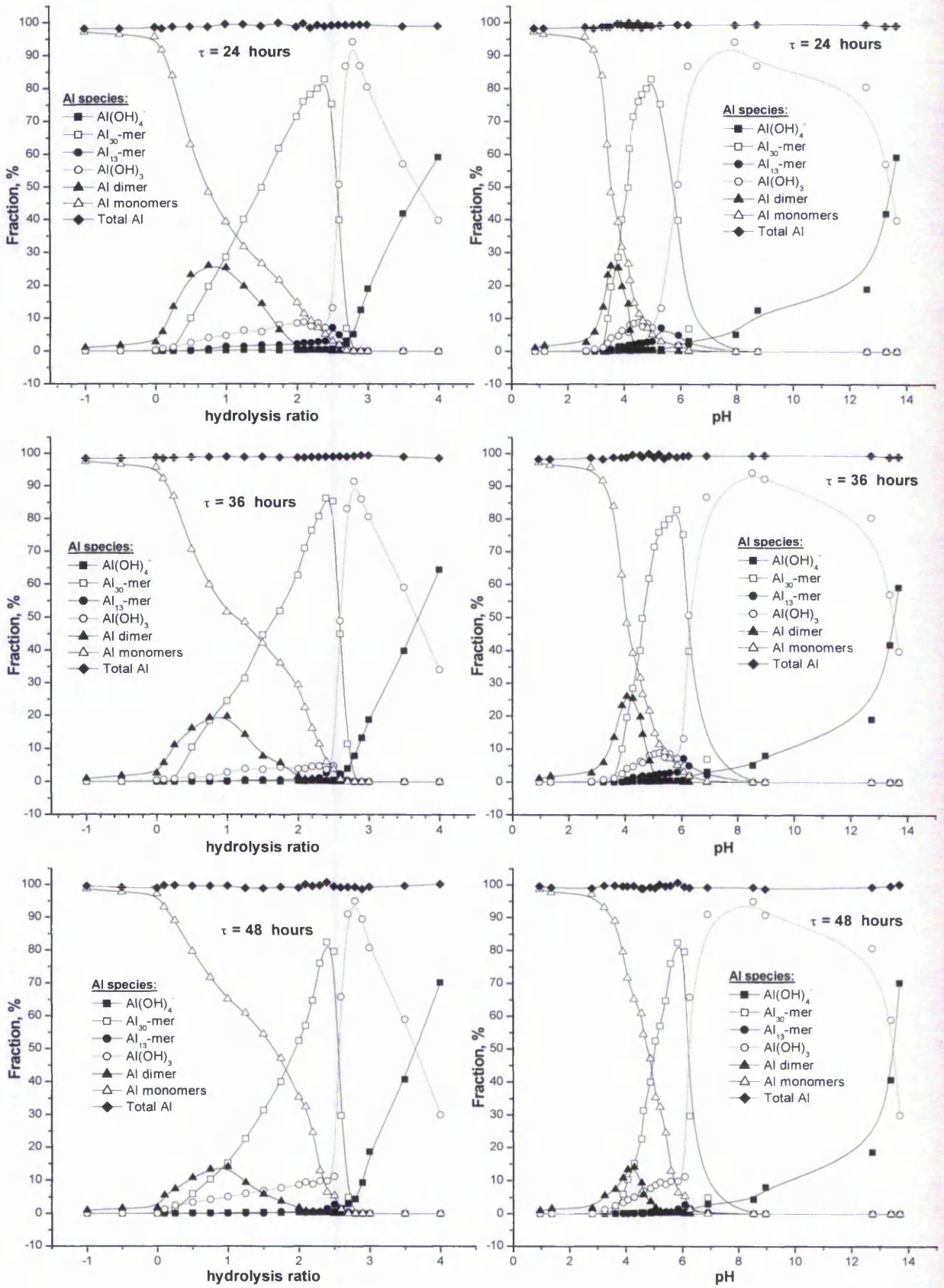


Fig. 3.41 (continues). Speciation diagrams of Al-ion hydrolysis at 90 °C at different hydrolysis times on the basis of ^{27}Al NMR measurements of the multi-batch titration **AMK1**. τ - hydrolysis time.

chosen as a standard S_{80}^{t} required for the calculations using Eq. 3.38-3.43. The curves of the species fractions shown in Fig. 3.41 were smoothed for presentation purposes using a B-spline function of the Microcal Origin program [59].

The data of Fig. 3.41 indicate that the equilibrium of the system containing hydrolysed Al species and aluminium hydroxide phase at 90°C can be described practically in full using the following species all detected with ^{27}Al NMR spectroscopy: the sum of monomeric Al-ions, the Al dimer, the Al_{13}-mer, the Al_{30}-mer, the aluminate-ion and colloidal aluminium hydroxide phase (the latter presumably contains fine colloidal particles in the nanometre range. Sufficiency of the listed species for the complete description of the equilibrium in the system in question is supported by the calculated total detectable Al content close to 100 % and, correspondingly, low percentage (< 2 %) of the unidentified NMR signal most probably arising from undetectable larger colloidal particulates.

As follows from Fig. 3.41, aluminium monomers (NMR peak at 0.0 ppm) prevail at low pH values and corresponding hydrolysis ratios. It is impossible to distinguish between the fractions of non-hydrolysed Al hexaaquo cations, mono- and di-hydrolysed monomeric species solely from the NMR peak at 0.0 ppm. We assume that all three species contribute to the overall fraction of Al monomers shown in Fig. 3.41. Upon the increase of pH (pH>3) and hydrolysis ratio (h>0.0), Al monomers gradually decline being replaced with Al dimers and Al Keggin ions (Al_{13}-mer and Al_{30}-mer).

The maximum of the fraction of Al dimer (20-30 % of the total detectable Al content) is reached within the range 0.7≤h≤1.0 and 3.50≤pH≤3.90 (Fig. 3.41). The concentration of Al dimers was quantified in a way similar to Al monomers and Al_{13}-mers using the following formula analogous to Eq. 3.41:

$$\nu(Al_{dimer}) = \frac{S_4^o}{S_{80}^t} C(Al_{std}) \qquad \textbf{(3.57)}$$

where $\nu(Al_{dimer})$ is the concentration of Al dimer, mol/L, S_4^o - the area of the peak at 4 ppm corresponding to the Al dimeric species, S_{80}^t - the averaged value of the area of reference peak of aluminate-ions at 80 ppm and $C(Al_{std})$ is the concentration of the reference defined by Eq. 3.38.

The Al dimer fraction peak shifts to higher pH and hydrolysis ratios at prolonged time of hydrolysis. Dimeric Al-ions were present at all measurement times and their overall contribution does not change significantly for the 48 hours of hydrolysis at 90 °C.

The fractions of Al Keggin ions dominate over the range of solution acidity 4.0≤pH≤6.5 and the hydrolysis ratio range 1.6 ≤ h ≤ 2.6 (Fig. 3.41). Time of hydrolysis is a crucial parameter defining the ratio of Al_{13}-mer and Al_{30}-mer in solutions of Al-ions hydrolysed at high temperature. At short hydrolysis time (τ=1 hour) Al_{13}-mers prevail while

with the increase of the reaction time the Al_{30}-mer starts to dominate, practically completely replacing the Al_{13}-mer after 36 hours of hydrolysis.

Colloidal aluminium hydroxide phase is also quantifiable in the ^{27}Al NMR spectra of the multi-batch series **AMK1**. The fraction of aluminium hydroxide given in Fig. 3.41 is derived from the peak area of the broad signal of octahedral Al between 10 and 50 ppm using the following formula:

$$S_{Al(OH)3} = S_{10}^{0} - S_{10}^{0}(70) - S_{10}^{o}(63) \qquad \textbf{(3.58)}$$

where $S_{Al(OH)3}$ – the peak area assigned to Al hydroxide, S_{10}^{0} - the overall area of the peak related to octahedral species in the range of chemical shifts 10-50 ppm; $S_{10}^{0}(70)$ and $S_{10}^{0}(63)$ – the calculated peak areas attributable to the octahedral shell of the Al_{30}-mer and Al_{13}-mer correspondingly.

One may assume that the particles of colloidal aluminium hydroxide must be extremely fine in order to produce a measurable signal in the ^{27}Al solution NMR spectra. The fraction of the aluminium hydroxide phase covers a broad pH range 6<pH<14 and hydrolysis ratio range ca. $0.5<h<4.0$. At lower hydrolysis ratios ($0.5 \leq h \leq 2.4$) the fraction of aluminium hydroxide is relatively small (below 10%) At $h>2.4$ it increases rapidly and becomes a dominating fraction at $2.8<h<3.5$. In the progress of the hydrolysis reaction in Al-ion solutions the aluminium hydroxide fraction becomes slightly broader.

At alkaline conditions ($h>3.0$) the aluminate-ion fraction replaces gradually the aluminium hydroxide fraction (Fig. 3.41). The calculation of the of $Al(OH)_4^-$-ion concentration is based on the value of the area of the NMR peak at 80 ppm determined as a difference of the overall peak area at 80 ppm at each titration point and the averaged value of S_{80}^{t} at $0 \leq h \leq 1$ used as a standard for NMR quantification. The interval of the predominance of aluminate-ions in the equilibrium in question lies beyond $h=3.5$ most of which is outside of the range of hydrolysis ratios studied in the multi-batch titrations (series **AMK1**) described in the present study. The occurrence and relative abundance of aluminate-ions also indicates indirectly the small size and colloidal character of the aluminium hydroxide phase which dissolves significantly at high pH values to produce monomeric $Al(OH)_4^-$ species.

3.3.4. Discussion of the results of the multi-batch series AMK1

The results of the multi-batch titration (series **AMK1**) of 0.2 M $AlCl_3$ solution with 1.026 M KOH solution at 90°C and solution characterisation of the multiple batches obtained at different hydrolysis ratios using pH-metry, dynamic light scattering and ^{27}Al solution NMR spectroscopy have established qualitative and quantitative speciation patterns in solution of Al-ions hydrolysed to different extents over a wide range of h and pH. Simultaneous kinetic studies of Al speciation over a time period of 48 hours were also possible due to the real-time

multi-batch experimental design of the series **AMK1**.

As shown in section 3.3.1, pH-metric titrations reconstructed from the multi-batch pH measurements over 48 hours of hydrolysis are similar to those at room temperature (section 3.1.1), albeit of lower resolution owing to a lower number of titration points.

Time-resolved pH measurements at 0, 1, 3, 6, 12, 24, 36 and 48 hours carried out in the series **AMK1** showed only minor changes in pH values (~0.5-5 %) over the hydrolysis ratio range $-1.0 \leq h \leq 2.4$. This is in apparent contrast with the room-temperature time-resolved data (section 3.1.2) showing more pronounced variation in time-resolved pH profiles obtained over a period of time 1-2 min. However, the actual start of pH measurements was at least after 5 min from the beginning of each batch experiment. Considering the very high temperature at which the **AMK1** experiment was carried out, it becomes clear that the kinetics of the fast processes such as hydrolysis of Al monomers and formation of small Al oligomers is mostly finished by that time. The only changes observed by time-resolved pH monitoring of the **AMK1** series were those related to slower condensation processes (formation of large Keggin ions) and yet more slow processes related to the formation and dissolution of the aluminium hydroxide phase. The condensation processes in general are not followed by any significant pH changes as one may find in the protracted plateau of the pH-titration curves (e.g. Fig. 3.1, Fig. 3.32, etc.) within the hydrolysis ratio range $0.5 < h < 2.0$. A steady shape of the time-resolved pH profiles obtained from the series **AMK1** (Fig. 3.32) reflects this. The major changes in the time-resolved pH profiles obtained at high temperature occur in the range $2.5 \leq h \leq 3.0$ where the curves show a prevailing decaying shape. We assume that the shape of the curves is related to the process of rapid formation of colloidal phase of aluminium hydroxide due to additions of strong alkali and its subsequent dissolution into monomers and their hydrolysis followed by a release of protons.

Values of pH for multi-batch titrations at high temperature are somewhat lower than analogous values from single-batch titrations at ambient conditions. This is probably a consequence of (*a*) more profound hydrolysis of Al-ions at high temperature [19,60] and (*b*) changing ionic product of water K_w [61], which becomes about 38 times lower at 90°C compared to 25°C. The change of K_w is followed by the increasing activity of protons and generally, more acidic character of water at pH<7 [61].

Dynamic light scattering measurements of the centrifuged batch samples of the **AMK1** series show the presence of nanosize particles with the mean size between ca. 1 and 2 nm within the hydrolysis ratio range $0.5 \leq h \leq 2.7$. Considering a size of Al_{13}-mer of approx. 1 nm [29] and a possible size of Al_{30}-mer of ca. 1×2 nm since the latter species contain two Al_{13}-mer moieties, one may assign observed results of DLS measurements to these Al polycations. Moreover, it is possible to observe a relative change of the particle size over the time of the experiment (48 hours). From Fig. 3.34 one may find that Al_{13}-mers are the

predominant species at short hydrolysis times, while the larger Al_{30}-mers gradually replace them at prolonged hydrolysis times. As shown with ^{27}Al NMR data discussed below, after 24 hours of hydrolysis the Al_{30}-mer species prevail in Al-ion solutions, however, the DLS results remain split between ca. 1 and 2 nm at different scattering angles. This difference possibly indicates the non-spherical (elongated) shape of the Al_{30}-mer species, which would be in good agreement with its structure.

^{27}Al NMR spectroscopy data on the characterisation of the multi-batch **AMK1** series indicates the presence of the majority of signals described in literature on the subject [1,5,23]. Along with well-established signals related to tetrahedral Al of aluminate-ions in reference solution in D_2O (80 ppm), Al_{30}-mers (70 ppm), Al_{13}-mers (63 ppm), octahedral Al of Keggin-ions (10 ppm), dimers (ca. 4 ppm), and monomers (ca. 0 ppm) it was possible to detect other signals at –0.5 ppm which we assign to non-hydrolysed Al monomers, 0.6 ppm (monohydrolysed Al monomers) 1.3 ppm (dihydroxo Al monomers), ca. 64 ppm (transient Al_{13}-mer-based species, possibly the δ-form of the Al_{13}-mer), 78 ppm (probably, dimeric $AlO(OH)_6^{2-}$ species) [62], 81 ppm – presumably, aluminate-ions in aqueous solutions.

Quantification of the ^{27}Al NMR spectra obtained from Al-ion solutions at different hydrolysis ratios and T=90°C was possible due to (*a*) careful and uniform conducting of apodisation, phasing and baseline correction in the NMR raw data treatment; (*b*) hybrid computational algorithm based on selective integration of sharp peaks and subsequent calculations of the broad peak areas which led to more precise quantification; (*c*) the way the samples were obtained, particularly addition of alkali to hot Al-ion solutions which increased the overall quality of the ^{27}Al NMR spectra dramatically. The latter improvement is mainly due to lower content of insoluble aluminium hydroxide that increased signal-to-noise ratios, decreased 'baseline rolling' effect and made possible the complete assignment of the NMR spectral signal to known Al species.

The major result of the ^{27}Al NMR studies of the samples produced by the multi-batch titrations is the possibility to devise full speciation diagrams shown in Fig. 3.41 for a wide range of hydrolysis ratios and pH. Since Al polycations are metastable species in their nature [19,61], time-resolved speciation diagrams given in Fig. 3.41 provide valuable additional information on the evolution of these species with time.

As follows from the time-resolved speciation diagrams shown in Fig. 3.41, Al_{30}-mers gradually 'replace' Al_{13}-mers in the system equilibrium becoming the dominant species after ca. 36 hours of hydrolysis at 90 °C. The optimum time of 36 hours for the synthesis of Al_{30}-mers correlates well with the literature data [1,5]. The concentration of Al dimer shows a similar kinetic behaviour to that of the Al_{13}-mers, albeit the rate of the species decay is slower than that of the Al_{13}-mers. This apparent discrepancy can be a result of the lower sensitivity of the ^{27}Al NMR measurements to the Al_{13}-mer concentration (measurements of the Al_{13}-mer concentration are based on the peak area of tetrahedral Al atom of the species which

represents only 1/13 part of the overall NMR signal, the rest accounts for the peak at 10 ppm) comparing to that for the Al dimer.

In the range of hydrolysis ratios of ca. 1.6 - 2.6 preferable for the formation of the Al_{13}-mer and the Al_{30}-mer, the concentration of Al monomers changes drastically as a function of *h* or pH that indicates that these species are extensively consumed in the formation of Keggin-ions.

Another important feature of the combination of ^{27}Al NMR studies and multi-batch experiments at high temperature is the possibility to quantify indirectly the amount of the aluminium hydroxide phase as a function of pH, hydrolysis ratio and time. The particles of aluminium hydroxide formed at high temperature are very fine evidenced indirectly by (*a*) the presence of the signal in the ^{27}Al NMR spectra at $h>2.0$ arising from these particles which is usually undetectable with the solution NMR technique [23]; (*b*) quite extensive dissolution of the hydroxide phase at higher pH and *h* that is unusual at relatively high concentrations of Al-ions.

Time-resolved NMR measurements in the multi-batch titration series **AMK1** led to the establishment of the kinetic rate constant estimates which have similar values and hydrolysis ratio-dependent trends compared to the *in-situ* kinetic measurements described in section 3.2.4. However, the different ways of the sample preparation for the *in-situ* kinetic NMR experiments and time-resolved multi-batch titrations led to a different extent of precipitation of aluminium hydroxide at the same hydrolysis ratios. This may account for the slight differences in the kinetic patterns observed in the two types of experiments performed.

Summarising the above, one can see that the combination of quantitative ^{27}Al NMR spectroscopy with multi-batch titrations has made possible the quantitative speciation of Al-ions from molecular ions to colloidal phase and quantification of the kinetics of speciation to be obtained at the same time. We envisage that further improvements of this approach could lead to the establishment of thermodynamic stability constants, kinetics and mechanisms of transformation for all Al species detectable with the NMR technique including the recently discovered Al_{30}-mer. Other factors need to be evaluated in speciation studies including different temperatures of hydrolysis, effect of ionic strength, etc. Advanced chemometric approaches [63] would assist better NMR spectra treatment including increase of spectral resolution, signal-to-noise ratios and sensitivity of the NMR method. Quantification of Al speciation using the NMR technique would strongly benefit from the comparison with the results of other independent methods capable of detection of the majority of Al species present in solution during hydrolysis-condensation.

3.3.5. Conclusions to multi-batch titrations of Al-ions

1. Implementation of the time-resolved multi-batch titration experimental design combined with an integrated analytical approach based on the simultaneous use of

potentiometry, dynamic light scattering and NMR spectroscopy has allowed a systematic and comprehensive quantitative study of aluminium-ion speciation at conditions of medium Al concentration (0.2 mol/L), high temperature (90°C) over a wide range of hydrolysis ratios and pH.

2. The value of hydrolysis ratio is a defining parameter in speciation patterns of Al-ions. The maximum of Al species concentration occurs exactly at a hydrolysis ratio corresponding to the theoretical value of the species. For instance, the formation of small oligomeric species (Al dimer) reaches a maximum at hydrolysis ratio h=1.0 (equal to the theoretical hydrolysis of Al dimer), the maximum of formation of Al_{13}-mers occurs at h~2.5 (the theoretical hydrolysis ratio of this species is 2.462), the maximum of Al_{30}-mer concentration is reached at h=2.4 (coinciding with the theoretical ratio of this species), bulk precipitation of aluminium hydroxide occurs around h=3.0 and the maximum of $Al(OH)_4^-$ concentration is reached at h~4.0. The maximum concentration of Al monomers is observed at $h \leq 0.0$ The pH conditions correlate with the hydrolysis ratio range at which Al species occur: pH<3.0 for Al monomers (all ionic forms), pH=3.5-3.9 for the Al dimer, 4.0<pH≤6.0 for the Al_{13}-mer and 4.0<pH≤5.5 for Al_{30}-mer; 6.0<pH≤8.5 for aluminium hydroxide; pH>9 for $Al(OH)_4^-$.
3. On the basis of the kinetic studies of Al speciation in real-time mode combined with the integrated analytical approach it was established that Al_{13}-mer species dominate the speciation patterns at early stages of hydrolysis – the concentration of these species reaches a maximum after 0.5-1.5 hours of hydrolysis depending on the pH and the hydrolysis ratio of the sample. The formation of Al_{30}-mer is a much slower process, this species starts to dominate Al speciation patterns after ca. 24-36 hours depending on the conditions. Consequently, the kinetic rate of Al_{30}-mer formation is almost 3 orders of magnitude lower than that of the Al_{13}-mer. The Al_{13}-mer species are less kinetically stable than the Al_{30}-mer, the kinetic rate of the Al_{13}-mer breakdown is estimated to be ca. 1000 times lower than that of the Al_{30}-mer.
4. As supported by the *in-situ* kinetic ^{27}Al NMR studies of Al speciation at elevated temperature, the dynamic equilibrium in solutions of hydrolysed Al-ions over the hydrolysis ratio range $0.0<h<2.6$ involves three major species: Al monomers, Al_{13}-mers and Al_{30}-mers. Al dimers were also found to correlate with the dynamics of formation of the Al_{13}-mer. Therefore, this species is also likely to be involved in the formation of the Al_{13}-mer along with monomeric ions. This fact may provide important information concerning the possible mechanism of Al_{13}-mer formation. It is very likely, that the formation of Al_{30}-mer involves mainly Al monomer and Al_{13}-mer species. However, the exact pathway of the formation of large Keggin ions needs further investigation.
5. Above the hydrolysis ratio ca. 2.6 the equilibrium is gradually shifted to the formation of the aluminium hydroxide colloidal phase, which reaches maximum at h ca. 3.0. For

the first time it was found possible to account for this phase from the data of ^{27}Al solution NMR spectroscopy. Special conditions of sample preparation in the multi-batch titration series were worked out in order to prevent undesirable effects of the large aluminium hydroxide particulates on the overall quality of the NMR spectra and the results of speciation quantification. The resulting colloidal phase at h>2.6 presumably contains the nanometre scale fine particles, which can be observed in the solution NMR spectra. Therefore, both the formation of fine colloids of aluminium hydroxide and their eventual dissolution in alkaline conditions can be monitored using NMR spectroscopy.

References

1. A.H. Rosenberg, J.J. Fitzgerald. Chemistry of Aluminum Chlorohydrate and Activated Aluminum Chlorohydrates. In: Antiperspirants and Deodorants / Ed. By K. Laden (1999) New York, Marcel Dekker, 83-136.
2. R.C. Turner. Cnd. J. Chem. (1975) **54** 1528-1536.
3. R.W. Smith. Coordin. Chem. Rev. (1996) **149** 81-93.
4. J.D. Hem, C.E. Roberson. Aluminum Hydrolysis Reactions and Products In Mildly Acidic Aqueous Systems. (1990) ACS Symposium Series **416,** 429-446.
5. J.J. Fitzgerald. Chemistry of aluminium hydrolysis complexes. In: Antiperspirants and Deodorants / Ed. by K. Laden (1988) New York: Marcel Dekker, 119-296.
6. C.M.A. Brett, A.M.Oliveira Brett. Electrochemistry : principles, methods, and applications (1993) Oxford, Oxford University Press.
7. H.H. Perkampus. Encyclopedia of spectroscopy (1994) Weinheim, Cambridge, VCH, 669p.
8. D.A. Skoog, D.M. West. Analytical chemistry. (1980) Philadelphia, Saunders College, 685p.
9. M. Meloun, J. Havel, E. Högfeldt. Computation of solution equilibria : a guide to methods in potentiometry, extraction, and spectrophotometry (1988) Chichester, Ellis Horwood, 297 p.
10. F.J.C. Rossotti, H. Rossotti. The determination of stability constants and other equilibrium constants in solution (1961) New York - London, McGraw-Hill, 425 p.
11. G. Svehla. Automatic potentiometric titrations (1978) Oxford, Pergamon, 219 p.
12. R.E. Mesmer, C.F. Baes Jr. Acidity measurements at elevated temperatures. Inorg. Chem. (1971) **10** 2290.
13. S.M. Bradley, R.A. Kydd, R.F. Howe. J. Colloid Interf. Sci. (1993) **159** 405-412.
14. J. Aveston. J. Chem. Soc.-London (1965) **111** 4438-4443.
15. S. Ramanathan, et. al. Ceram. Internat. (1997) **23** 45-53.
16. A.C. Vermeulen, J.W. Geus, R.J. Stol, P.L. DeBruyn. J. Colloid Interf. Sci. (1975) **51** 449-453.
17. Y. Ozaki, B. Czarnik-Matusewicz, S. Sasic. Analyt. Sci. (2001) **17** 663.
18. L.G. Sillen, A.E. Martell. Stability constants of metal-ion complexes: Section 1: Inorganic

ligands (1964) London, Chemical Society, 754 p.
19. D.F. Baes Jr., R.E. Mesmer. Boron, aluminium and scandium. In: The hydrolysis of cations. (1976) New York, Wiley-Interscience, 112-123.
20. A.K. Alva, G.I. Kerven, D.G. Edwards, C.J. Asher. Soil Sci. (1990) **150** 495-505.
21. J.D. Hem, C.E. Roberson ACS Symposium Series (1990) **416** 429-446.
22. N.B. Milic, Z.D. Bugarcic, S.R. Niketic Gazzetta Chimica Italiana (1991) **121** 45-48.
23. J.W. Akitt, In: Multinuclear NMR / Ed. J. Mason (1987) Plenum Press, New York, 259-292.
24. J.W. Akitt, J.M. Elders. J. Chem. Soc. Dalton (1988) 1347-1355.
25. 27. J.W. Akitt, A. Farthing. J. Chem. Soc. Dalton (1981) 1617-1623.
26. J.W. Akitt, N.N. Grenwood, G.D. Lester (1969) Chem. Comm. 988.
27. L.F. Nazar, S.W. Liblong, X.T. Yin. J. Am. Chem. Soc. (1991) **113** 5889-5890.
28. J.W. Akitt, J.A. Farnsworth, P. Letelier. J. Chem. Soc. Faraday Trans. I (1985) **81** 1930.
29. P. Capkova et. al. Clay Clay Miner. (1998) **46** 232-239.
30. A. Violante, P.M. Huang Clay Clay Miner. (1993) **41** 590-597.
31. J.-P. Jolivet. Metal Oxide Chemistry and Synthesis. From Solution to Solid State. (2000) Chichester, Wiley and Sons, 321 p.
32. J. Burgess. Metal ions in solution (1978) Chichester, Ellis Horwood, 481 p.
33. R.K. Iler. The chemistry of silica: solubility, polymerization, colloid and surface properties, and biochemistry (1979), New York, Wiley, 866 p.
34. H. Ratnaweera, H. Odegaard, J. Fettig Water Sci. Technol. (1992) **26** 1229- 1237.
35. H. Nagai, S. Hokazono, A. Kato. Brit. Ceram. Transact. (1991) **90** 44-48.
36. P.M. Jardine, L.W. Zelazny. Soil Sci. Soc. Am. J. (1986) **50** 895-900.
37. J.W. Akitt, A. Farthing, O.W. Howarth. J. Chem. Soc. Dalton (1981) 1609-1614.
38. C.J. Brinker, G.W. Scherer. Sol-gel science: the physics and chemistry of sol-gel processing (1990) Academic Press. 908 p.
39. E. Morgado, Y.L. Lam, L.F. Nazar. J. Colloid Interf. Sci. (1997) **188** 257-269.
40. M.K. Ridley, D.J. Wesolowski, D.A. Palmer, R.M. Kettler. Geochim. Cosmochim. Acta (1999) **63** 459-472.
41. M. Henry, J.P. Jolivet, J. Livage. Aqueous Chemistry of Metal Cations - Hydrolysis, Condensation and Complexation. (1992) Structure And Bonding **77** 153-206.
42. G. Johansson. Acta Chem. Scand. (1962) **16** 403.
43. G. Johansson. Arkiv for Kemi (1962) **20** 321.
44. M.A. Fedotov, O.P. Krivoruchko, R.A. Buyanov. Izvestiya Akademii Nauk SSSR - Ser. Khim. (1977) **12** 2647-2651.
45. K. Wefers, C. Misra. Oxides and Hydroxides of Aluminum. Alcoa Technical Paper No 19, Revised (1987) Alcoa, 92 p.
46. Coulter N4Plus particle size meter. Instruction manual.
47. L. Allouche, C. Gerardin, T. Loiseau, G. Ferey, F. Taulelle. Agew. Chem. Int. Edit. (2000)

39 511-514.

48. F. Kasler. Quantitative analysis by NMR spectroscopy (1973) London, Acad. Press, 190 p.
49. D.E. Leyden, R.H. Cox. Analytical applications of NMR (1977) New York – London, Wiley, 456 p.
50. F. Rouessac, A. Rouessac. Chemical Analysis: Modern Instrumental Methods and Techniques (2000) New York, Wiley, 300 p.
51. Internal Unilever report on the application of ^{27}Al NMR spectroscopy for quantification of Al species.
52. J.T. Kloprogge, D. Seykens, J.W. Geus, J.B.H. Jansen. J. Non-Cryst. Solids (1992) **142** 87-93.
53. R.J.M.J. Vogels, J. Kloprogge, P.A. Buining, D. Seykens, J.B. Jansen, J.W. Geus. J. Non-Cryst. Solids (1995) **191** 38-44.
54. R.G. Wilkins. Kinetics and mechanism of reactions of transition metal complexes (1991) New York, VCH, 372 p.
55. H.E. Avery. Basic reaction kinetics and mechanisms (1974) Macmillan Education, 174 p.
56. S. Castet, J.I. Dandurand, J. Schott, R. Gout. Geochim. Cosmochim. Acta (1993) **57** 4869- 4884.
57. J. Rowsell, L.F. Nazar. J. Am. Chem. Soc. (2000) **122** 3777-3778.
58. G. Furrer Aquat. Sci. (1993) **55** 281-290.
59. Microcal Origin program (version 6.1). Instruction Manual.
60. J.J.Fitzgerald, L.E.Johnson,J.S. Frye. J. Magn. Reson. (1989) **84** 121-133.
61. W. Stumm, J.J. Morgan. Aquatic Chemistry. An Introduction Emphasizing Chemical Equilibria in Natural Waters. (1981) New York, Wiley and Sons, 780 p.
62. G. Johansson. Acta Chem. Scand. (1966) **20** 505.
63. R.G. Brereton. Chemometrics: applications of mathematics and statistics to laboratory systems (1990) New York – London, Ellis Horwood.

CHAPTER IV. Solution speciation studies of hydrolysed zirconium-ions

The aim of the work presented in Chapter 4 was to investigate speciation patterns in medium-concentrated (0.1-0.2 mol/L) aqueous solutions of zirconium-ions during the process of forced alkaline hydrolysis using solution-based techniques such as potentiometry, UV-Vis spectroscopy (organic reagent assay) and dynamic light scattering. Several important factors of zirconium speciation were studied including the effect of alkali strength and concentration, the effect of strong acid (HCl), the effect of counter-ions (chloride, sulphate, acetate) and the effect of added complexing agent (glycine). As in the case of the aluminium speciation studies described in Chapter 3, two experimental regimes were chosen for comparative investigation of zirconium speciation: room temperature (single-batch titrations) and high temperature (90°C, multi-batch titrations).

4.1. Investigation of zirconium speciation at room temperature

4.1.1. Single-batch potentiometric titrations of Zr-ion solutions at room temperature

Single-batch potentiometric titrations of medium-concentrated zirconyl chloride solutions were conducted using different alkalis (KOH, NH_4OH, $KHCO_3$) of various concentration (0.9-2.1 M). Results of the titrations are presented in Fig. 4.1.

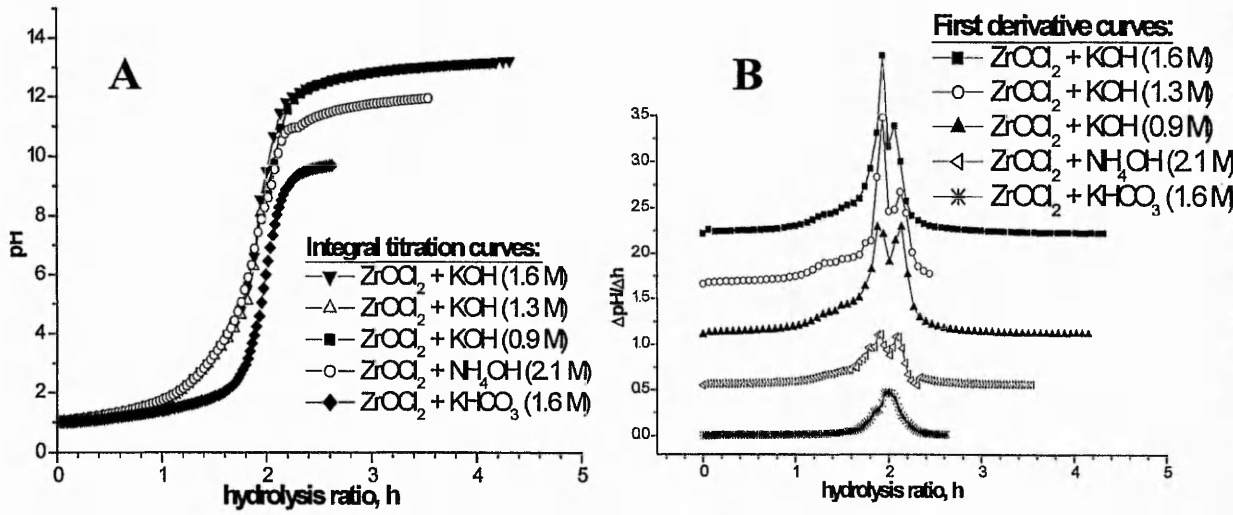


Fig. 4.1. Potentiometric titrations of $ZrOCl_2$ (0.1 M) solutions with different alkalis at 25°C. *A* – integral titration curves; ***B*** – first derivative curves (Y-offset – 80%).

The data of Fig. 4.1*A* indicates similarity of the integral titration curves obtained from single-batch potentiometric titrations of Zr-ion solutions regardless of alkali strength and concentration. The integral curves from titrations of $ZrOCl_2$ solutions with KOH of different concentrations (0.9 – 1.6 M) practically coincide, the curve from the titration with ammonia solution (2.1 M) is almost identical to the curves obtained with KOH, the difference appears only at h>2.0.

First derivative curves of Zr-ion alkaline titrations (Fig.4.1*B*) reveal several inflexions:

1) $\boldsymbol{h \sim 1.23 \pm 0.12}$ – the first broad and poorly resolved inflexion (identified using peak-fitting and higher order derivatisation procedures) corresponds well with the literature data [1] (h~1.3) and relates to the formation of so called 'gel α'. This inflexion points coincides with visual observations of the formation of a visible colloidal phase in Zr-ion solutions at this point of titration.
2) $\boldsymbol{h \sim 1.6 \pm 0.09}$ – the second inflexion point is also broad and poorly resolved. This inflexion is related to further colloidal transformations of Zr-ion solution at higher hydrolysis ratios ('gel β', h~1.7 [1]). The inflexion is followed by a further increase of viscosity of the sample. When titrating with strong alkalis of high concentration, the solution can transform into a hydrogel.
3) $\boldsymbol{h \sim 1.92 \pm 0.07}$ and $\boldsymbol{h \sim 2.07 \pm 0.05}$ – two inflexions in the vicinity of hydrolysis ratio h=2.0 correspond to total precipitation of zirconium hydrous oxide [2]. The splitting of the single inflexion at h=2.0 into two occurs mainly at higher concentrations of alkali and is caused, probably, by the breakdown of the hydrogel structure formed at $h \geq 1.6$ (first inflexion at h~1.92) and final precipitation of the hydrous oxide phase at h~2.07. The absence of the split of inflexion peak into two for the curve at lower KOH concentration (0.9 M, Fig. 4.1*B*) supports this hypothesis.

Single-batch potentiometric titrations described above were also conducted in time-resolved mode. Time-resolved pH-profiles obtained from the time-resolved data and normalised for presentation purposes are given in Fig. 4.2 for the titration of $ZrOCl_2$ (0.1 M) solution with KOH (1.6 M) as an illustrative example. Time-resolved pH-profiles for other titrations of Zr-ion solutions are omitted for the sake of brevity.

From Fig. 4.2 one can see that at the beginning of the titration the shape of the time-resolved pH-profiles is of A-type according to the classification introduced in Chapter 2 (Section 2.3), which remains unchanged over a broad range of hydrolysis ratios $0.06 \leq h \leq 1.13$. At h>1.13 the time-resolved curve shape transforms into a B-type with a decaying part at the end. The depth of the curve decay rapidly becomes more pronounced in the progress of the titration and reaches a maximum at h=1.50. After the critical point at h=1.50 the decay depth of the time-resolved pH-profiles rapidly decreases and in the narrow interval of $1.69 \leq h \leq 1.75$ the curve shape is again of A-type as at the beginning of the titration. Further increase of alkali concentration leads to a hybrid C-type time-resolved pH-profile (h=1.81) prior to converting back to the B-type decay shape at $1.88 \leq h \leq 2.07$ with the most dramatic changes and a deepest decay observed at h=1.88. The decay becomes more shallow at h>1.88 and at h>2.07 the time-resolved curve shape again transforms into the initial A-type which remains until the end of the titration at h=4.38 (concentration of alkali at this point is double the concentration required for precipitation of Zr hydrous oxide).

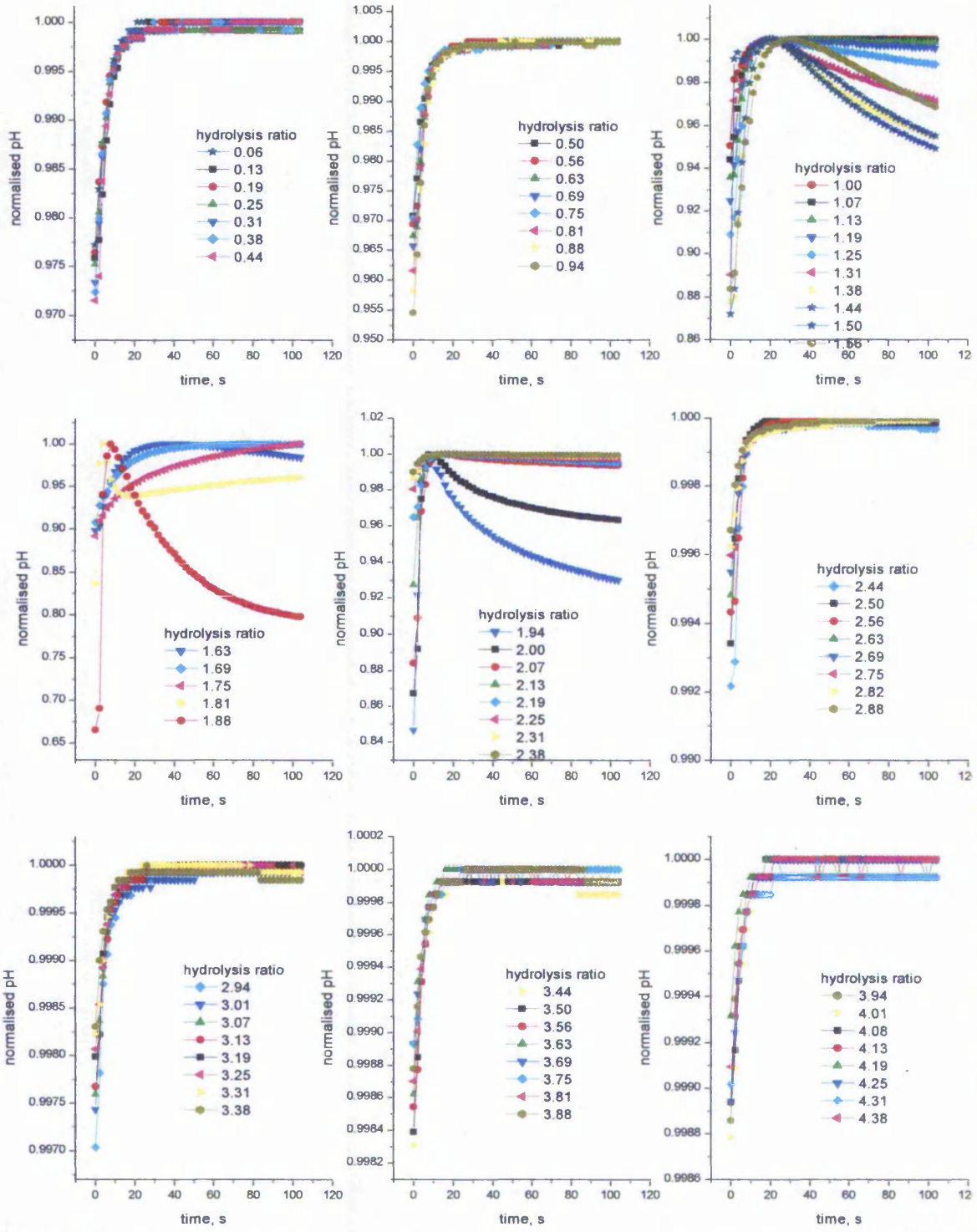


Fig. 4.2. Time-resolved pH-profiles obtained from potentiometric titration of $ZrOCl_2$ (0.1 M) solution with KOH (1.6 M) at 25°C (pH-profiles are normalised to unity for presentation purposes). Hydrolysis ratio is h=OH/Zr.

The transformations of the time-resolved pH-profiles during the titration of Zr-ion solutions with alkalis described above can be summarised using Correlation Analysis in one graph of correlation sums vs. hydrolysis ratios (Fig. 4.3).

The results of the application of the CA to time-resolved curves of potentiometric titrations of Zr-ion solutions with KOH at different concentrations ranging from 0.9 to 1.6 M

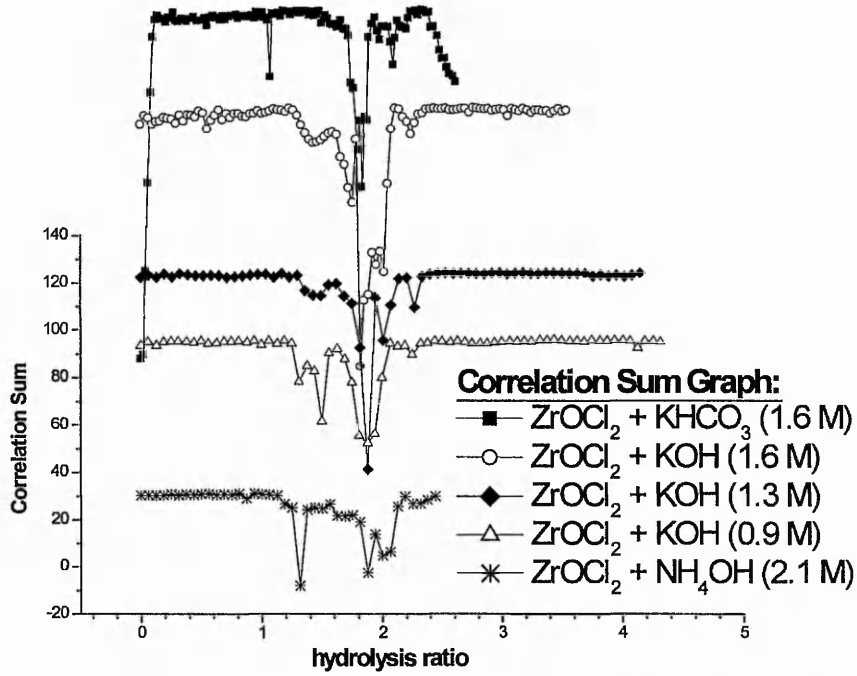


Fig. 4.3. The correlation sum graph in the hydrolysis ratio domain calculated for the time-resolved curves obtained from the potentiometric titrations of $ZrOCl_2$ (0.1 M) solutions with different alkalis (Y-offset – 90 %).

at room temperature reveal the following negative peaks (Fig. 4.3): at h~1.3 (for the titration with 0.9 M KOH this peak splits into two adjacent peaks at h~1.21 and h~1.38); at h~1.6 – poorly resolved peak appearing only at higher concentrations of alkali (1.6 and 1.3 M KOH); at h~1.9 (this peak also splits into two peaks at h~1.81 and h~2.05 for the titrations with 1.6 M and 1.3 M KOH); and at h~2.19. The first four peaks detected in the correlation sum graph can be attributed to the inflexion points observed in the first derivative curves (Fig. 4.1*B*). The peak at h~2.19 may correspond either to partial dissolution of zirconium hydrous oxide or to structural rearrangement of the amorphous precipitate into a more dense phase which can occur in alkaline medium [3,4]. The latter feature is not observed in the conventional titration curves (Fig. 4.1).

Decrease of the KOH concentration leads to two major consequences in the correlation sum graphs (Fig. 4.3). At lower concentration of alkali (0.9 M KOH) the negative peak at h~1.3 spits into two perhaps indicating two different processes occurring at this hydrolysis ratio in hydrolysed Zr-ion solution. However, this hypothesis needs further verification. Another change is the merge of the split peaks at h~1.8 and h~2.0 into one peak at h~1.9 observed at lower alkali concentrations (0.9 M KOH).

The correlation sum graph obtained from the time-resolved titration of $ZrOCl_2$ solution with NH_4OH (2.1 M) has a similar shape to those for the titrations with KOH of different concentrations discussed above (Fig. 4.3). The only major difference is that the

negative peak at h~1.3 is much sharper and higher in the case of the titration with ammonia.

Replacement of KOH with $KHCO_3$ as a titrant leads to dramatic changes in the shape of the correlation sum graph shown in Fig. 4.3. First, low values of the correlation sums in the beginning of the titration with $KHCO_3$ ($h \leq 0.15$) indicate a completely different shape of the time-resolved pH-profiles (B-type with decay at the end). This shape gradually changes to 'normal' A-type as characteristic for the titrations with KOH and NH_4OH. The reason for such a change is unclear, it may be related to the weakness of $KHCO_3$ as alkali or to some other peculiarities. Another change in the titration with $KHCO_3$ is the virtual absence of the peak at h~1.3 and a very low, poorly resolved peak at h~1.5-1.6. The peak at h~1.8 is the major peak in the correlation sum graph of the titration with $KHCO_3$, along with it there is a peak at h~2.1 and an emerging peak at h>2.2. This peak is not present in the correlation sum graphs of the titrations with stronger alkalis and, as will be shown below, indicates the increasing complexation of carbonate-ions with hydrolytic polymerised zirconium species occurring under alkaline conditions.

Along with the correlation analysis of the time-resolved potentiometric data obtained from single-batch titrations of Zr-ion solutions with alkali at room temperature discussed above, it is possible to perform a time-domain correlation analysis as described in Chapter 3 for single-batch alkaline titrations of Al-ion solutions. The results of the time-domain correlation analysis of the data on Zr-ion titrations are summarised in Fig. 4.4.

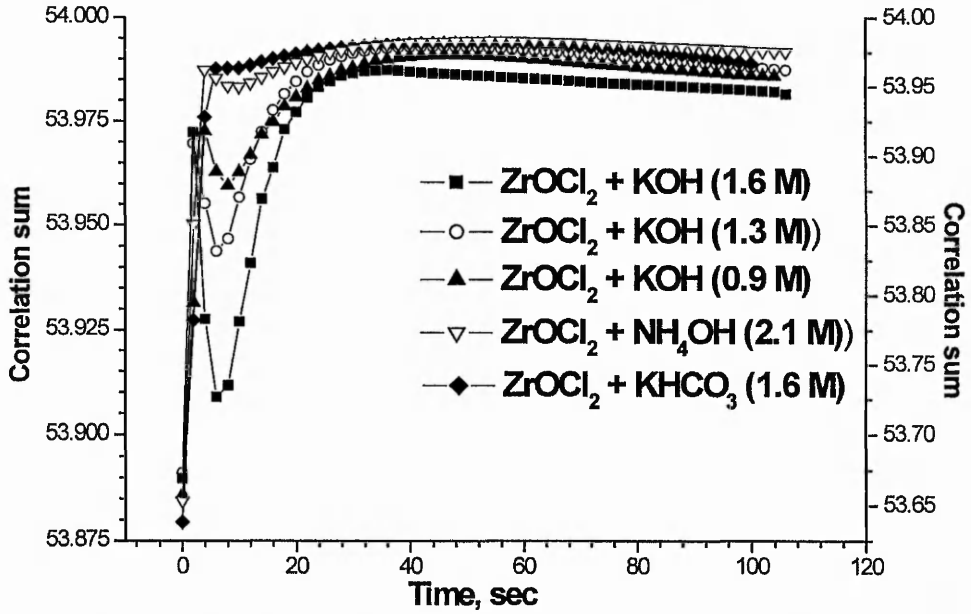


Fig. 4.4. Time-domain correlation sum graph calculated from the single-batch titrations of $ZrOCl_2$ (0.2 M) solutions with different alkalis at room temperature.

Time-domain correlation analysis depicted in Fig. 4.4 shows that during the first 2-4 sec correlation sums obtained from all time-resolved titrations reach nearly a maximum. At longer measurement times (τ>4 sec) for the time-resolved pH-curves obtained from the

titrations of Zr-ions with KOH there is a decay, the depth of which increases with concentration of alkali and the minimum of the decay slightly shifts from τ=8 sec (KOH, 1.6 M) to τ = 12 sec for titration with 0.9 M KOH. Correlation analysis of the titration with ammonia shows little decay in the same region, while the titration with $KHCO_3$ does not produce decay. After this, correlation sums in all curves start to increase. Again, the time point at which the curve reaches the maximum of the correlation sum depends on the concentration and strength of alkali. For the titration with 1.6 M KOH, this point is at τ~26 sec; τ~32 sec for 1.3 M KOH; τ~44 sec for 0.9 M KOH; τ~42 sec for 2.1 M NH_4OH and τ~46 sec for $KHCO_3$. At longer times of pH monitoring the corresponding correlation sums start to decrease again in agreement with the properties of alkali used as a titrant. The deepest decay is observed for the titration with 1.6 M KOH and it decreases in depth at lower KOH concentrations. For NH_4OH and $KHCO_3$ the final decay is very shallow.

4.1.2. Discussion of the single-batch potentiometric titrations of Zr-ion solutions with alkalis at room temperature

Literature data and the analysis with the Partial charge model conducted in Chapter 1 of the present study show that without external perturbations (temperature, alkali, coagulating agents, ligands, etc.) zirconium-ions are present in medium-concentrated solution as well-established tetrameric [5] or octameric species [6] which were shown to prevail in the absence of strong acid at pH<0.65. Results of the single-batch potentiometric titrations of 0.1 M $ZrOCl_2$ solutions with different alkalis indicate that at early stages of forced hydrolysis of zirconium-ions with alkali the reaction occurs as a diffusion-controlled growth of polymer chains [7] most probably consisting of a single stacked array of tetramers [6] as described in Chapter 1 of the thesis. The chain growth occurs in the large hydrolysis ratio interval $0.0 \leq h \leq 1.0$ ($0.9 \leq pH \leq 1.5$) that is indicated by (*a*) clear non-opaque solutions during the early alkali additions and (*b*) steady featureless increase of pH values in the potentiometric titrations without any major inflexions (Fig. 4.1). The time-resolved potentiometric data in the hydrolysis ratio range $0.0 \leq h \leq 1.0$ also does not contain any major features (Fig. 4.2, 4.3) in the case of KOH and NH_4OH and supports the hypothesis of the steady growth of zirconium hydrolytic polymer chains caused by additions of strong alkalis. In these positively-charged polymers with a general formula $[Zr_{8n-4}(OH)_{12n-4}(H_2O)_{8n+8}]^{4n+4}$ (where n is the number of Zr tetramers: for tetramer n=1; for octamer – n=2, etc.) zirconium atoms are connected by hydroxo-bridges only and their growth is limited by the total concentration of Zr-ions and the amount of alkali added.

At hydrolysis ratios $h \geq 1.0$ a colloidal phase of zirconium hydroxide starts to appear. It is assumed that the first inflexion point at h~1.3 which corresponds to the formation of 'gel α', actually occurs (or starts) at h~1.0 and indicates an important transition from large

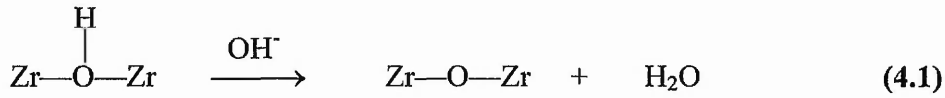
zirconium hydrolytic polymers (at maximum of their possible length and elimination of all small oligomers such as tetramers and octamers) with chain-like 2D-continous structure to 3D-structures where hydroxo-bridges start to form between adjacent chains of Zr polymers. The reason for the occurrence of the transition between chain-like 2D-growth to 3D-growth exactly at h~1.0, possibly, is related to the exhaustion of the possibilities for further chain growth (all tetrameric units are stacked in chains). It should be noted that at the beginning of the titration the actual hydrolysis ratio of the tetrameric units of Zr-ions is already h=2.0 corresponding to the formal h=0.0 at the start of the alkaline titration. The hydrolysis ratio of Zr octamers is h=2.5. As was mentioned in Chapter 1, both Zr tetramers and octamers are stable under acidic conditions and only an external perturbation (alkali addition, temperature, coagulation agent, etc.) can cause them to condense further. Condensation occurs via stacking of the growing polymeric chain with additional tetrameric units. Each event of stacking requires four additional single hydroxo-bridges to be formed between adjacent Zr-atoms of the neighbouring tetramers. The formation of single OH-bridges is unidirectional and leads to the 'needles' of Zr polymer chains [6]. The process can be virtually indefinite and is only limited by the number of free tetramers and, therefore, by the total concentration of Zr-ions. The overall hydrolysis ratio of the growing chains of tetramers interconnected with single OH-bridges is between h=2.5 (octamer) and asymptotically approaches h=3.0 for higher homologues (Chapter 1), that corresponds to h=1.0 in the titration curves of Zr-ion solutions with alkalis. When all opportunities for the formation of the inter-tetramer single OH-bridges are theoretically exhausted and the end of the process is manifested by the slightly delayed inflexion point at h=1.3.

Above the critical point at h~1.0 the abovementioned switch between 2D chain-like growth of Zr hydrolytic polymers and 3D inter-chain growth. This leads to a quick increase of the particle size of growing polymers and visually corresponds to the formation of a colloidal phase described as 'gel α' in the work [1]. Due to the 'forced' nature of alkaline hydrolysis and local perturbations produced by strong alkalis, step-wise inter-chain growth occurs together with aggregation into large colloidal particles. The first 'chemical' process produces ordered 3D-structures of Zr hydroxo-polymers which can further transform into crystalline phase of tetragonal zirconia (at the point of full charge neutralisation). The latter process (aggregation) leads to the formation of a 'loose' frustrated network between the particles and, eventually, to the poorly defined amorphous zirconia phase. The process of charge neutralisation of Zr polymers relates to the thinning of the electric double layer of the particles allowing for the aggregation process to occur [7,8].

If it is assumed that 3D inter-chain growth follows approximately the same mechanism as the 2D chain growth described above (i.e. through the formation of a single additional hydroxo-bridge between adjacent Zr atoms of the polymers), then it can be shown that the maximum theoretical hydrolysis ratio for the 3D growth is h=3.5 which corresponds

to h=1.5 on the titration curves. Therefore, the inflexion point at h~1.7 is a slightly delayed manifestation of the end of the 3D growth of Zr hydroxo-polymers through the formation of additional hydroxo-bridges the possibility of which is completely exhausted by the critical value of hydrolysis ratio h=1.5 on titration curve (corresponding theoretical value is h=3.5).

Above the critical point at h~1.5 another process starts to dominate, namely, deoxolation reaction [9], where existing OH-bridges start to deprotonate during further additions of alkali and to transform into oxo-bridges (Zr-O-Zr) of the future Zr hydrous oxide as schematically shown below:



(4.1)

The corresponding colloidal process observed visually is a transformation of the loose colloidal phase of 'gel α' into a thicker and denser 'gel β' [1]. Physically, densification of the loose aggregates of 'gel α' relates to (*a*) the formation of the larger number of interconnecting bonds between the aggregates [8], (*b*) shortening of the distances between adjacent Zr atoms of the growing Zr polymer due to the shorter bond length of Zr-O-Zr oxo-bridges compared to Z-OH-Zr hydroxo-bridges [8].

One can hypothesise that around the point of h=1.5 on the corresponding titration curves only the least stable hydroxo-bridges undergo oxolation that implies a non-uniformity of the hydroxo-bridges in Zr hydrolytic polymers. As a first approximation, one can divide OH-bridges into 'intrinsic' ones (double OH-bridges of the initial Zr tetramers in non-hydrolysed Zr-ion solutions) and 'extrinsic' ones (single OH-bridges formed during the hydrolysis-condensation). 'Intrinsic' OH-bridges are probably more stable at acidic conditions where original tetramers prevail (h≤0.0, pH<1.0), while 'extrinsic' bridges acquired through hydrolysis seem to be more stable at higher pH and hydrolysis ratios. Moreover, there is certain diversity between 'extrinsic' OH-bridges themselves as they can be divided into (*a*) bridges of the original chains of Zr hydrolytic polymers and (*b*) inter-chain bridges connecting adjacent chains of Zr tetramers. However, it is not clear what type of OH-bridges undergoes oxolation with the formation of Zr-O-Zr bridges first; perhaps it is 'intrinsic' OH-bridges which could be less stable at higher pH and h. The distance between Zr atoms connected by double hydroxo-bridges must be shorter than for single OH-bridge connected atoms. Therefore, the deprotonation and, consequently, the formation of the highly negatively charged oxo-bridges would be favoured structurally (shorter Zr-O distance would make a more covalent bond and electrostatically (better charge compensation on oxo-bridge from closer Zr atoms).

After the second inflexion point in the titration curves at h~1.7 indicating the oxolation stage, further addition of alkali leads to the precipitation of hydrous zirconia at around h~2.0 (theoretical hydrolysis ratio is h=4.0). Chemically, the formation of hydrous

zirconia is most probably a consequence of the completion of oxolation of the second half of OH-bridges of Zr-polymers (probably, 'extrinsic' bridges).

The final process indicated only in the correlation sum graphs obtained from time-resolved potentiometric titrations of $ZrOCl_2$ solutions and not observed in conventional titration curves or their first derivatives is the process at h>2.1 where either structural rearrangement of Zr oxide or its partial dissolution takes place. The solubility limit of hydrous zirconia is very low ($K_{s1,0}$~$10^{-6.8}$ [10]) and its dissolution is only possible if the fresh precipitate has an highly disordered 'loose' structure inherited from the amorphous gel from which it precipitates. Structural rearrangement of hydrous ZrO_2 can lead either to a denser amorphous structure (e.g., due to completion of oxolation reaction), or even to the formation of crystalline tetragonal ZrO_2 [4]. Certainly, these hypotheses need to be investigated further.

The described empirical model of chemical transformations in hydrolytic Zr polymers occurring in medium-concentrated solutions of Zr-ions at room temperature upon forced hydrolysis with alkali can be summarised in a diagram schematically depicted in Fig. 4.5.

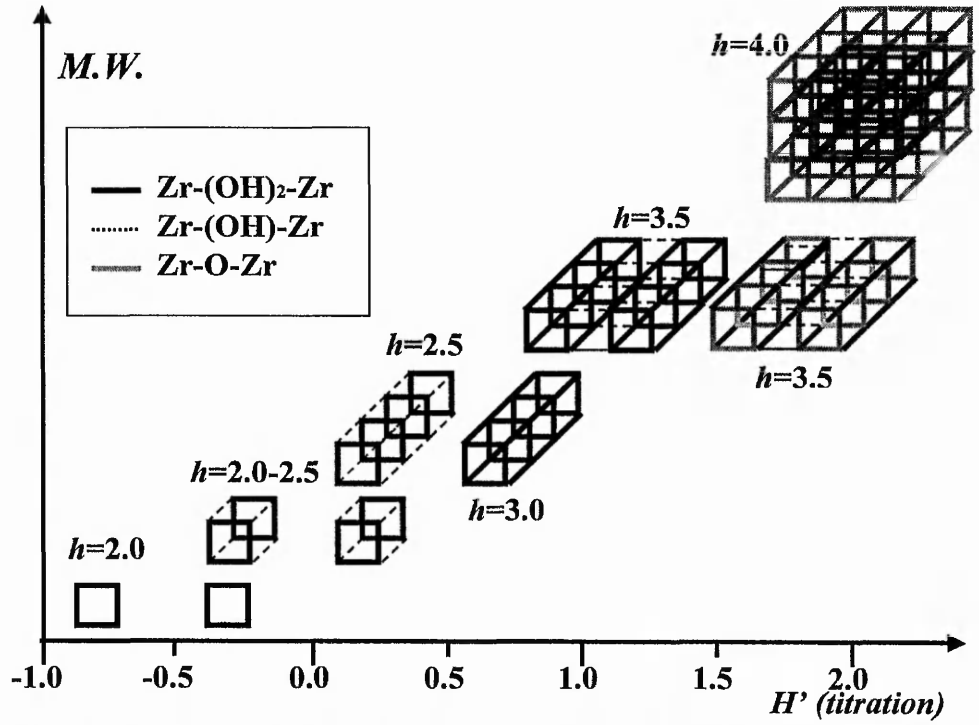


Fig. 4.5. Schematic representation of the transformations in hydrolytic Zr polymers during the hydrolysis-condensation. (Zr-atoms are in the corners of black squares representing Zr tetramer units). *H'* – a formal hydrolysis ratio as a ratio of added alkali and Zr-ion concentrations; *h* – a theoretical hydrolysis ratio of the species; *M.W.* – molecular weight.

The model presented in Fig. 4.5 generally follows Clearfield's model of Zr polymerisation [5] with later corrections and additions [6]. The difference is that the model described in the present work takes into account hydrolysis ratio as a fundamental parameter related to chemical and structural composition of Zr polymers. It is necessary to stress that the drawn model of the step-wise formation of hydrous ZrO_2 from hydrolytic Zr polymers is both idealistic and simplified. In an ideal situation (no local alkali perturbations, perfect stirring,

temperature homogeneity, etc.) the described model could yield a well-ordered phase of (tetragonal) crystalline Zr oxide. In reality, forced alkaline hydrolysis leads to the formation of an amorphous precipitate as will be shown in Chapter 5. One can suggest that chemical transformations of Zr polymers (condensation via olation and oxolation) occur in parallel with colloidal transformations and the final product strongly depends on the prevailing process: either a frustrated colloidal growth-aggregation or a highly ordered chemical growth.

As follows from the potentiometric data of single-batch alkaline titrations of Zr-ion solutions, alkali concentration plays a minor role in the speciation of polymeric zirconium as shown by an example of varying KOH concentration (Fig. 4.1, 4.3). Only the splitting of the peak at h~2.0 is affected by the decreasing of alkali concentration.

The replacement of KOH as a titrant by ammonia does not significantly change speciation patterns observed in the potentiometric titrations. When $KHCO_3$ is used as a titrant, drastic changes are observed in the time-resolved data of potentiometric titrations (Fig. 4.3). These data indicate that the formation of 'gel α' and 'gel β' is less pronounced as follows from the diminished inflexions at h~1.3 and h~1.6, precipitation of hydrous oxide occurs at a lower hydrolysis ratio (h~1.8) and the inflexion at h~2.1 is not observed. Instead, a pronounced change in the shape of the time-resolved pH-profiles occurs at h>2.2, most probably indicating the start of the dissolution of hydrous zirconia due to complexation with carbonate-ions under alkaline conditions [11]. The drastic change of the shape of the time-resolved pH-curves at h<0.1 (Fig. 4.3) can possibly relate to the intensive evaporation of carbon dioxide from $KHCO_3$ which usually happens at very low pH values [12]. The origin of this strong deviation at low h in the case of $KHCO_3$ as a titrant also needs further investigation.

The observed difference of Zr polymer behaviour in the vicinity of the first inflexion point at h~1.3 between stronger alkalis (KOH and NH_4OH) and weak $KHCO_3$ can be explained by the assumption that in the latter case 'forced' character of hydrolysis-condensation reaction is less pronounced. This probably leads to the formation of smaller particles at the stage of 'gel α' which would aggregate stronger at the stage of 'gel β', primarily due to higher surface free energy [7]. This hypothesis will be supported below by the results of organic reagent assay and dynamic light scattering measurements.

The splitting of the peak at h~2.0 in the case of Zr-ion titrations with strong alkalis can be explained from the described model as a consequence of two separate processes: oxolation of 'intrinsic' double hydroxo-bridges of tetrameric structural building blocks and the following oxolation of the rest of hydroxo-bridges which are mainly 'extrinsic' single OH-bridges connecting stacked chains of Zr tetramers or surfaces of aggregated particles.

Correlation analysis of the time-resolved pH-profiles in the time domain (Fig. 4.4) shows that equilibration of the system is a complicated process and strongly depends on the strength and concentration of alkali used as a titrant. There are at least two processes at short

equilibration times (within first ca. 20 sec) and another two time-dependent processes on longer time scales (from ca. 20 to 106 sec). One can assume that processes in the shorter time domain are related to fast acid-base equilibration (e.g. neutralisation of free protons released upon hydrolysis of Zr-ions), while the processes in the longer time domain are induced by the slower processes of condensation of hydrolytic Zr polymers and colloidal processes occurring in medium-concentrated Zr-ion solutions during forced hydrolysis. The incompleteness of the long-time processes shown by the correlation analysis indicates that much longer time is required in the systems to reach equilibrium at each titration point, especially true in the range of hydrolysis ratios $h>1.0$ where the formation of a colloidal phase and precipitation of hydrous zirconia are the dominant processes.

4.1.3. Conclusions

1. Forced hydrolysis of Zr-ions with alkalis at room temperature induces strong perturbations in the system as detected using correlation analysis in the time domain. These perturbations probably lead to early formation of colloidal phase of Zr hydrous oxide which dissolves only partially on the time scale of single-batch titrations (within ca. 3 hours) at low hydrolysis ratios ($h<1.0$). Therefore, the speciation patterns of Zr-ions upon alkaline hydrolysis investigated at room temperature using potentiometric titrations correspond to a state of 'supersaturation of solution' where soluble polymeric species are in equilibrium with amorphous phase of hydrous zirconium hydrous oxide.
2. Variation of alkali concentration as well as the replacement of potassium hydroxide with ammonia as a titrant in the potentiometric titrations of Zr-ion solutions does not produce significant changes in the speciation manifested in conventional or time-resolved single-batch potentiometric titrations. The introduction of $KHCO_3$ as a titrant leads to drastic differences in speciation patterns. These differences cannot be detected in full in the conventional titration curves or their first derivatives, but they are readily detectable in time-resolved potentiometric titrations, especially in combination with the correlation analysis introduced in the present study. The most important differences revealed so far are connected with (*a*) weakness of $KHCO_3$ as alkali which affects the early stages of Zr-ion polymerisation ($h<0.1$), and gelation at $h>1.0$ where no distinct stages at $h\sim1.3$ and $h\sim1.6$ are observed in the corresponding titration curves, unlike in the titrations with stronger alkalis; (*b*) ability of carbonate-ions to complex zirconium in the precipitated hydrous oxide at alkaline conditions.
3. At room temperature (20-25 °C) speciation patterns of Zr-ions in aqueous solutions at conditions of forced alkaline hydrolysis are dominated by the chemical transformations of polynuclear Zr species based on tetramers $[Zr_4(OH)_8(H_2O)_{16}]^{8+}$ and, possibly, analogous octamers $[Zr_8(OH)_{20}(H_2O)_{24}]^{16+}$ which prevail in the medium-concentrated solutions of zirconyl chloride, into zirconium hydrous oxide $ZrO_{2n}*(H_2O)_n$. These transformations can

be divided into the process of chain formation between stacked tetrameric units below hydrolysis ratio h~1.0 involving only hydroxo-bridges (olation reaction), linkage of parallel chains into 3D-structures with hydroxo-bridges (inter-chain olation) below h=1.5; and deprotonation of the acidic hydroxo-bridges of the linked polymers (deoxolation reaction) with the formation of oxo-bridges within at $1.5<h<2.0$ leading to the transformation of gel-like hydroxide phase into hydrous ZrO_2 and its eventual precipitation at h~2.0. Along with chemical transformations described above, a classical diffusion-controlled growth-aggregation of hydrolytic Zr polymers into colloidal particles and gel phase with highly frustrated structure takes place. The structural properties of the final product of the forced alkaline hydrolysis at room temperature – amorphous precipitation of hydrous zirconium oxide are the result of the balance between disordered colloidal processes and the highly ordered chemical process of Zr polymer condensation.

4.2. Multi-batch potentiometric titrations of Zr-ion solutions at high temperature

In order to enable multi-technique studies of zirconium speciation at industrially relevant elevated temperatures, multi-batch titrations of large amounts (100-120 ml for each batch) of $ZrOCl_2$ (0.2 M) solutions were carried out in the present study. The experimental setup and conditions of the titrations at 90°C is described in Chapter 2. As was mentioned in Chapter 2 and Chapter 3, multi-batch titration setup provides the following advantages: (*a*) experiment is conducted on a real-time scale over a long period of time (48 hours) which is especially important for the monitoring of slow polymerisation processes, colloid formation and precipitation in hydrolysed Zr-ion solutions; (*b*) the setup enables one to conduct a multi-technique characterisation of batch-samples both on hydrolysis ratio scale and on time scale; (*c*) the setup allows for carrying out experiments at high temperature with good temperature control using a precision water bath.

According to the literature [13, 14], slow spontaneous condensation of Zr polymers with eventual formation of highly crystalline monoclinic ZrO_2 occurs at temperatures higher than 90 °C. Below this temperature condensation is either impossible or is too slow to be accounted for. Therefore, the choice of temperature 90°C for multi-batch experiments seemed to be appropriate due to (*a*) speeding up condensation process in Zr hydrolytic polymers and (*b*) prevention of spontaneous formation of monoclinic form of hydrous zirconia which contains Zr atoms with coordination number seven (unlike N=8 for the original Zr tetramers) found in stock solutions of zirconyl chloride and probably proceeds via mechanism of thermoinduced deoxolation leading straight to oxide phase rather than alkali-induced condensation via olation or the formation of hydroxo-bridges found at lower temperature. The occurrence of two competitive mechanisms would considerably complicate interpretation of the experimental results obtained from multi-batch titrations.

4.2.1. Conventional potentiometric titration curves from the multi-batch experiments

The following factors were evaluated in the series of multi-batch experiments: the effect of alkali (titration with KOH, 1.6 M in the series **ZrOH**, and titration with $KHCO_3$, 1.6 M in the series **ZrHCO3**); the effect of nature of counter-ions (addition of sulphate-ions to Zr-ion solutions in the series **ZrOHSO4**, $Zr:SO_4^{2-}=1:1$ and of acetate-ions in the series **ZrOHAc**, $Zr:CH_3COO^-=1:1$); the effect of complexing agent (glycine) as well as Zr:glycine ratio on the hydrolysis-condensation of Zr-ions (Zr:Gly=2:1, series **ZrOHGly21**; Zr:Gly=1:1 – series **ZrOHGly11** and Zr:Gly=1:2 in the series **ZrOHGly12**). The pH-metric data presented as titration curves and their first derivatives are given in Figs. 4.6 – 4.12.

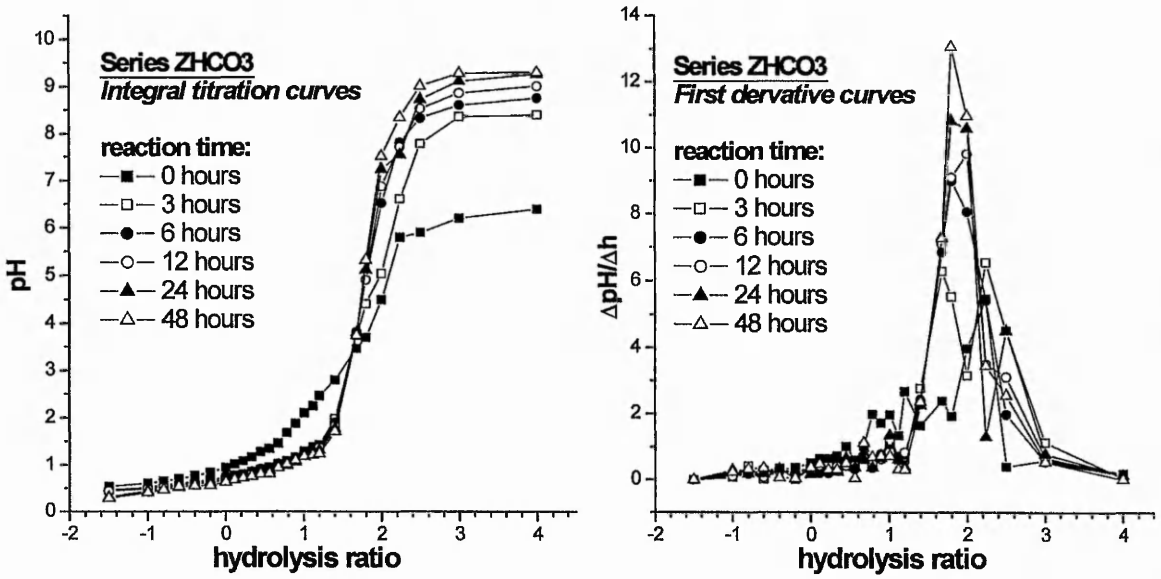


Fig. 4.6. Potentiometric titration curves (integral, *left* and first derivative, *right*) of $ZrOCl_2$ solutions (0.2 M) with $KHCO_3$ (1.6 M) at different measurement times obtained from the multi-batch series **ZrHCO3**. T=90°C.

The data of potentiometric measurements in the multi-batch series **ZrOH** presented in Fig. 4.6 indicate that the shape of the reconstructed titration curves at high temperature is similar to the analogous curves obtained at room temperature (Fig. 4.1). The most significant difference in the integral curve shapes occurs at shorter reaction times ("0" and 3 hours). From the more detailed first derivative curves (Fig. 4.4) one can see that titration of medium-concentrated Zr-ion solutions with $KHCO_3$ leads to the appearance of three major inflexions - at hydrolysis ratios h~1.0, h~2.0 and h~2.5. The first inflexion is probably related to the formation of a metastable amorphous gel of variable composition and is the most pronounced at early hydrolysis times (τ="0" and τ=3 hours). The complete precipitation of hydrated zirconia is indicated by a broad peak at h~2.0 which splits into two peaks (h~1.7 and h~2.2) at early reaction times (τ="0" and τ=3 hours). The inflexion point at h~2.5 most probably arises from the extensive complexation of carbonate-ions which has been shown to take place at pH>6 [15,16]. This process was also detected in the time-resolved single-batch titration curves at room temperature (Fig. 4.3). The colloidal phase resulting from the process is

possibly potassium zirconium carbonate - a mixture of negatively charged polymers which become water-soluble at a certain ratio of carbonate-ions and zirconium [16].

The results of multi-batch titration of Zr-ion solution at high temperature using KOH as alkali (series **ZrOH**) are given in Fig. 4.7.

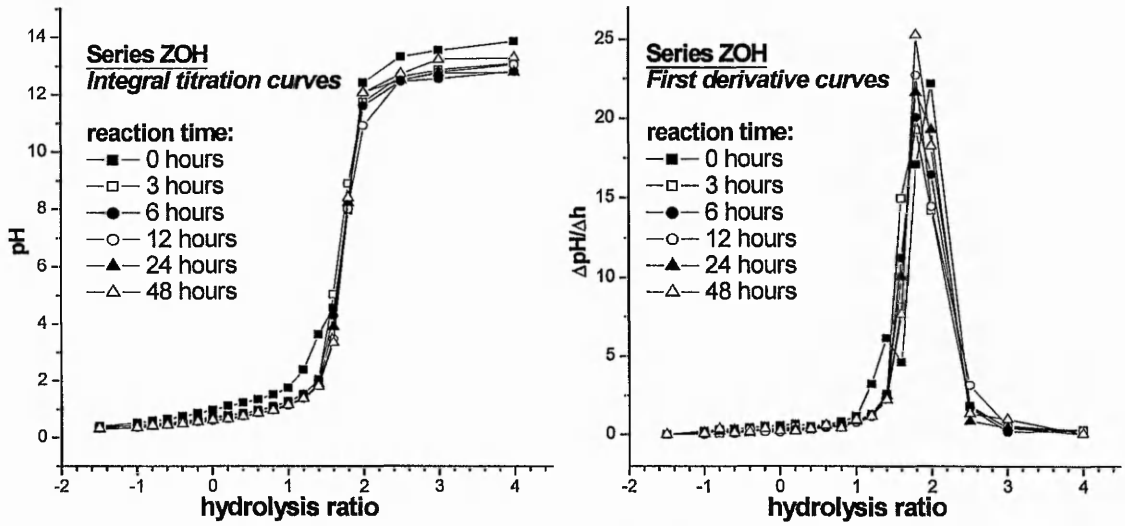


Fig. 4.7. Potentiometric titration curves (integral, *left* and first derivative, *right*) of $ZrOCl_2$ solutions (0.2 M) with KOH (1.6 M) at different measurement times obtained from the multi-batch series **ZrOH**. T=90°C.

From the data of Fig. 4.7 one can find that integral titration curves obtained from the multi-batch series **ZrOH** are very similar except for the curve at τ="0" hours. The first derivative curves indicate that there is only one major broad inflexion point at h~2.0 which probably overlaps the peaks related to colloid formation and gelation of Zr-ion solution at h~1.3 and h~1.7 unlike the analogous titrations at room temperature (Fig. 4.1) in which the latter two inflexions are more distinct. As was discussed above, these inflexions correspond to two distinct stages in the colloid formation (gels α and β [1]) detected in the single-batch titrations of Zr-ion solutions at room temperature (Fig. 4.1). At τ="0" hours the first derivative curve is of a distinct shape: there are two clearly detected peaks at h~1.7 and h~2.1 indicative of the fact that the major variation of pH and, probably, hydrolytic processes taking place in Zr-ion solutions at 90°C and manifested by pH changes, occur within first 1-2 hours of the experiment. At highly alkaline conditions there are no inflexions in the titration curves of the series **ZrOH** which could be related to the process of structural rearrangement or partial dissolution of the amorphous zirconia precipitate that also distinguishes the multi-batch potentiometric titration with KOH (Fig. 4.7) from $KHCO_3$ (Fig. 4.6).

The effect of complexing counter-ions such as sulphate and acetate on the hydrolysis-condensation of medium-concentrated Zr-ion solutions at elevated temperature (90°C) was also investigated in the present study. The potentiometric results of the multi-batch titration of $ZrOCl_2$ with KOH at the presence of sulphate-ions (series **ZrOHSO4**) are shown in Fig. 4.8.

The presence of sulphate-ions in Zr-ion solutions at the ratio $Zr:SO_4^{2-}$ = 1:1 leads to a major inflexion at h~1.2-1.4 with other poorly resolved inflexions at h~0.2-0.4 and h~0.6-0.8

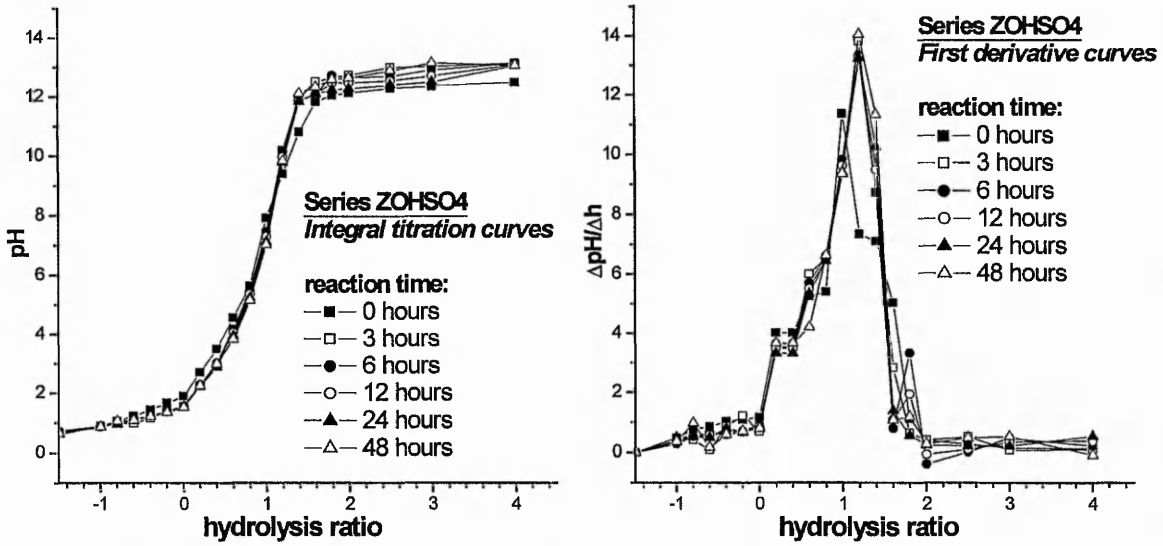


Fig. 4.8. Potentiometric titration curves (integral, *left* and first derivative, *right*) of $ZrOCl_2$ solutions (0.2 M) with KOH (1.6 M) at the presence of sulphate-ions (0.2 M) at different measurement times obtained from the multi-batch series **ZrOHSO4**. T=90°C.

(identifiable only by the peak-fitting procedure or in higher derivative curves). Unlike the series **ZrHCO3** and **ZrOH** produced without sulphate-ion addition where the major inflexion in the titration curve is observed at h~2.0, for the reaction at the presence of sulphate-ions the process of precipitation is practically complete at this hydrolysis ratio (no significant pH variations at $h \geq 2.0$).

The processes occurring at $h<1.5$ most probably lead to precipitation of a mixture of basic zirconium sulphates [5, 16, 17]. The fact that the major inflexion point is at h~1.2-1.4 indicates that the most significant product of the precipitation has an approximate formula $Zr(OH)_x(SO_4)(H_2O)_z$ with $3.2 \leq x \leq 3.4$ (where x is an equivalent of the 'basicity' of zirconium sulphate) and $0<z\leq 4.8$ (the value of z is derived from $z = N - x - 1$, where $N = 8$ is the coordination number of Zr, and n is the number of aquo-ligands remaining in the coordination sphere of Zr atoms). Some amount of zirconium-ions precipitates at earlier hydrolysis ratios h~0.3 and h~0.7 and the 'basicity' of the Zr sulphate precipitate indicated by the ratio of OH-ligands per Zr atom decreases correspondingly to an average Zr:OH=1:2.3 and Zr:OH=1:2.7.

It is not clear from the potentiometric data whether the precipitation of basic Zr sulphates completely removes all Zr-based hydrolytic polymers from solution. There is another poorly resolved minor inflexion observed in the titration curves of the series **ZrOHSO4** at h~1.8. This inflexion is most distinct at τ=6 hours and it probably indicates that either the removal of Zr-ions by neutralisation with sulphate-ions and precipitation is not complete, or some basic Zr sulphate precipitate is still able to transform into hydrous zirconia (the maximum of the formation at h~2.0).

Visual observation suggests that stirring of suspensions of basic Zr sulphates in the range of hydrolysis ratios $h \geq 0.0$ is stopped, phase separation occurs relatively quickly (within 5 min), especially at $h>1.0$ possibly indicating that neutralised basic Zr sulphates appear to be

a precipitate rather than a colloidal phase. However, these data alone are not sufficient for the exact determination of phase composition, structure as well as crystallinity of the solid phases formed in the series **ZrOHSO4** at $h \geq 0.0$.

Time of the reaction for the series **ZrOHSO4** plays a significant role in the early stages of the experiment. From Fig. 4.8 one can see that at the beginning of pH monitoring (τ = "0" hours) the major inflexion point is at h~1.0 and prevails over inflexion at h~1.4. At $\tau \geq$ 3 hours the inflexion at h~1.4 dominates the titration curves. At longer reaction times the shape of the integral and first derivative curves remains very similar, possibly indicating that the major processes of interaction with sulphate-ions and hydroxyls of alkali is complete by the time $\tau \geq 3$ hours.

The effect of acetate-ions on the hydrolysis-condensation of zirconium at elevated temperature was investigated, the series **ZrOHAc**. Results of potentiometric measurements at different times of experiments reconstructed as titration curves and their first derivatives are shown in Fig. 4.9.

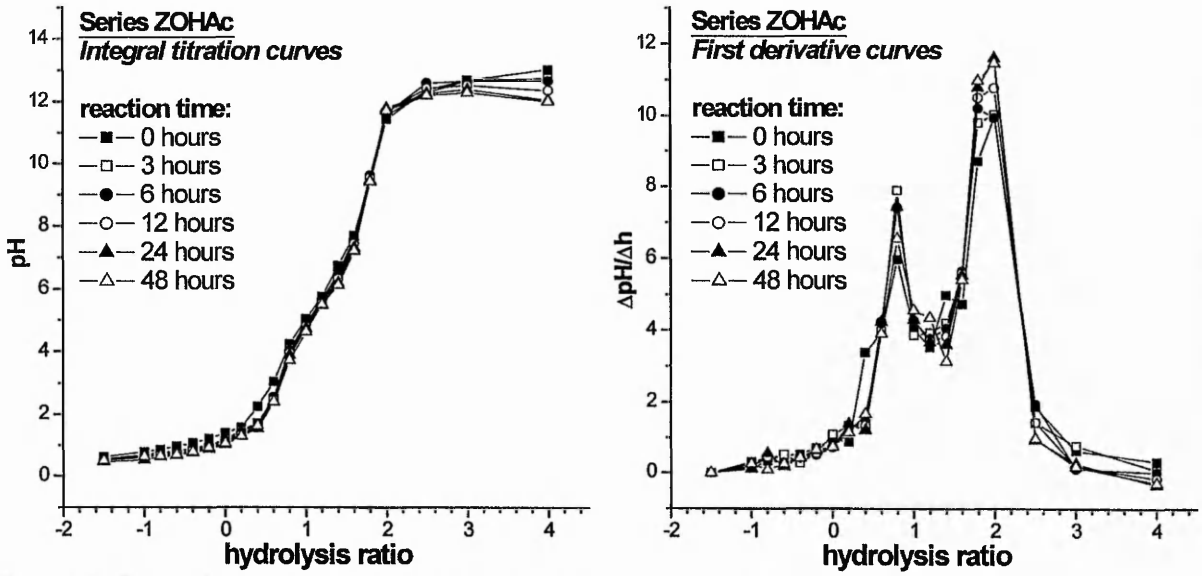


Fig. 4.9. Potentiometric titration curves (integral, *left* and first derivative, *right*) of $ZrOCl_2$ solutions (0.2 M) with KOH (1.6 M) at the presence of acetate-ions (0.2 M) at different measurement times obtained from the multi-batch series **ZrOHAc**. T=90°C.

From Fig. 4.9 one can see that the shapes of the integral titration curves in the series **ZrOHAc** are very similar to each other regardless of the time at which potentiometric measurements were made. The first derivative curves show the occurrence of two significant inflexion points h~0.8 and h~2.0. The latter major inflexion is probably indicative of the bulk precipitation of hydrous zirconia, while the inflexion at h~0.8 possibly indicates the formation of zirconium basic acetates with an average formula $Zr(OH)_{2.8\text{-}3.0}(H_2O)_m(CH_3COO)_x$, where $0<x<N$- n(OH)-m(H_2O) ($N = 8$ – the coordination number of Zr).

Complexing ability of acetate-ions towards Zr-ions appears to be lower than that of sulphate-ions [17]. Due to lower negative charge and complexing ability acetate-ions do not

precipitate Zr-containing hydrolytic polymers at low pH and hydrolysis ratios (pH<1.0, h<0.0), unlike sulphate-ions, as was observed visually in the series **ZrOHAc**. At relatively low hydrolysis ratios (0.0<h≤0.4) acetate ions can possibly act as bridging ligands to form neutral zirconium basic acetate polymers of various composition [18-20] similar to the materials prepared in the presence of sulphate-ions discussed above (series **ZrOHSO4**). However, the lower stability of Zr-acetate complexes and lower charge compensation leads to (*a*) formation of colloidal phase (visually stable in the absence of stirring) rather than a precipitate and (*b*) at increasing concentrations of hydroxyl-ions (h≥1.2), acetate ions are gradually eliminated from the coordination sphere of Zr-ions probably yielding relatively pure hydrous zirconia at h~2.0. The time of reaction induces only minor changes in the shape of potentiometric titration curves obtained from the series **ZrOHAc** at the beginning of the experiment (τ="0" hours).

Hydrolysis of Zr-ions at the presence of glycine over a wide range of hydrolysis ratios was investigated in the multi-batch series **ZrOHGly12**, **ZrOHGly11** and **ZrOHGly21** with different ratios of Zr:Glycine – 2:1; 1:1 and 1:2 correspondingly. Results of potentiometric measurements for the series **ZrOHGly12** are given in Fig. 4.10.

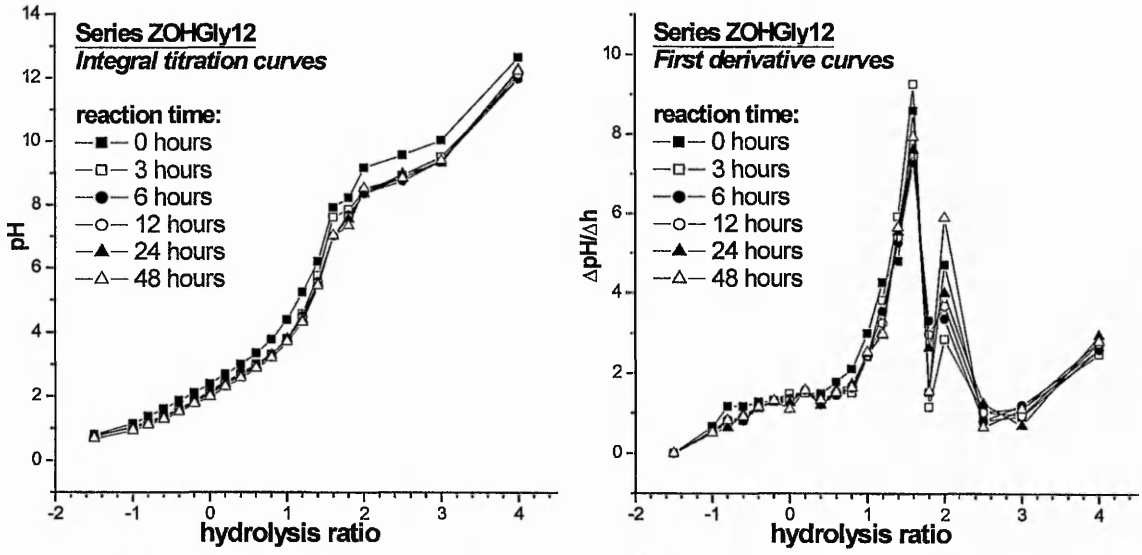


Fig. 4.10. Potentiometric titration curves (integral, *left* and first derivative, *right*) of $ZrOCl_2$ solutions (0.2 M) with KOH (1.6 M) at the presence of glycine (0.4 M) at different measurement times obtained from the multi-batch series **ZrOHGly12**. T=90°C.

The data in Fig. 4.10 shows that there are two major inflexions in the first derivative titration curves obtained from the series **ZrOHGly12**: at h~1.6 and h~2.0. There is an indication of another unaccomplished inflexion at h≥4.0. Application of peak-fitting and higher derivatisation of the titration curves indicates the presence of a fourth poorly resolved inflexion at h~1.0-1.2. The first two inflexions at h~1.0-1.2 and h~1.6 can be related to the formation of a colloidal phase of basic zirconium glycinate of various composition, similar to that observed for the other carboxyl-containing ligand – acetate (series **ZrOHAc**). The carboxylic group of glycine has pK_a=2.3, while for acetic acid pK_a=4.78 [21]. Thus, glycine

contains a more acidic carboxylic group than acetic acid and one can assume the formation of a stronger complex between zirconium and glycine than between acetate-ions and Zr-ions. Therefore, more alkali (KOH) is required in order to replace glycine in the coordination sphere of zirconium. This is supported by the location of the corresponding inflexion in the series **ZrOHGly12** at higher hydrolysis ratio (h~1.6) compared to a similar major inflexion in the series **ZrOHAc** (h~0.8-1.0). However, unlike the series **ZrOHSO4**, after most glycine has been replaced by hydroxyl-ions, reaction at higher hydrolysis ratios proceeds via 'normal' precipitation of hydrous zirconia. Similarity of the hydrolytic behaviour of Zr-ions in the presence of acetate-ions (series **ZrOHAc**) and glycine (series **ZrOHGly12**) lies in the formation of a colloidal phase rather than a precipitate at h>0.0.

The emerging inflexion peak at h~4.0 is of unclear origin, it could be either dissolution of hydrous zirconia (unlike series **ZrOH** with pure Zr-ion solutions hydrolysed using KOH), or another process, e.g. deprotonation of amino-groups of glycine occurring in alkaline medium (pK_a(glycine, NH_2)=9.6 [21]).

As follows from Fig. 4.10, kinetics is an important factor in the series **ZrOHGly12** conducted with a two-fold molar excess of glycine to Zr-ions. The major inflexion at h~1.6 reaches a maximum at τ = 3 hours and then tends to decrease at longer reaction times. The inflexion at h~2.0 shows opposite kinetic behaviour, after reaching a minimum at τ = 3 hours it increases in the progress of the experiment and reaches a maximum at τ = 48 hours.

Results of the series **ZrOHGly11** where hydrolysis of Zr-ions at 90°C was conducted at the presence of equimolar ratio of glycine to Zr-ions are shown in Fig. 4.11.

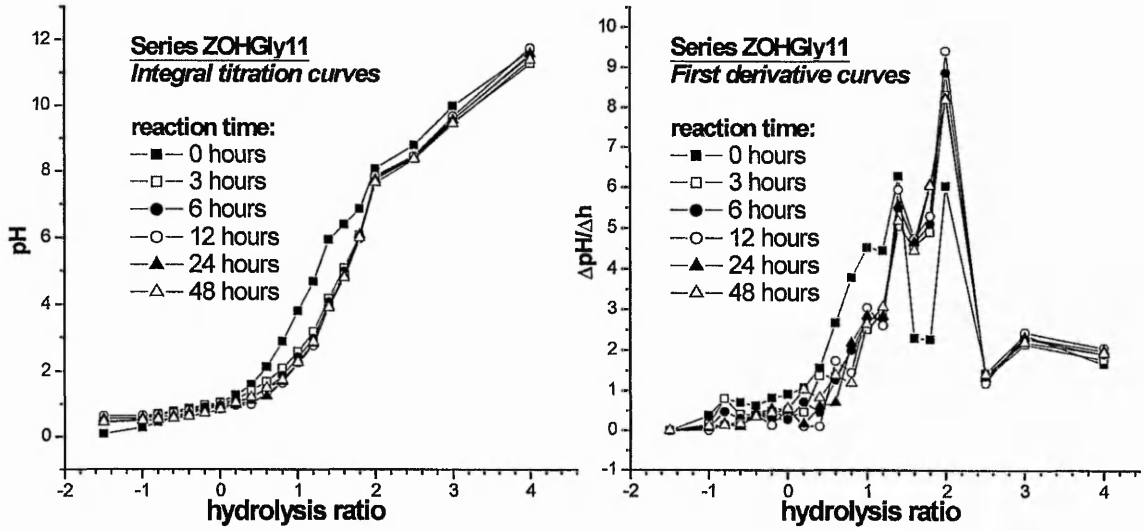


Fig. 4.11. Potentiometric titration curves (integral, *left* and first derivative, *right*) of $ZrOCl_2$ solutions (0.2 M) with KOH (1.6 M) at the presence of glycine (0.2 M) at different measurement times obtained from the multi-batch series **ZrOHGly11**. T=90°C.

As follows from Fig. 4.11, at equimolar quantities of glycine and Zr-ions (series **ZrOHGly11**) the inflexion at h~2.0 (bulk precipitation of hydrous zirconia) becomes dominant compared to the series **ZrOHGly12** (Zr:Glycine=1:2) discussed above. The

inflexion at h~1.4 is less resolved from the inflexion at h~2.0 for the series **ZrOHGly11**, while the inflexion at h~1.0-1.2 grows in significance and becomes more distinct than for the series **ZrOHGly12**. The inflexion at alkaline conditions shifts from $h \geq 4.0$ (**ZrOHGly12**) to h~3.0-3.5 (**ZrOHGly11**). The changes in the potentiometric titration curves can be probably ascribed to the decrease of overall concentration of glycine.

In terms of kinetics, there is an obvious difference of the titration curve at the beginning of the series **ZrOHGly11** (τ = "0" hours, Fig. 4.11). This curve has a closer shape to that for the series **ZrOHGly12**. The rest of the curves in the series **ZrOHGly11** obtained at longer reaction times ($\tau \geq 3$ hours) the shape changes observed are of minor importance both in the integral and derivative curves.

The multi-batch series **ZrOHGly21** were obtained with the excess of zirconium (the ratio Glycine:Zr=1:2). Results of the potentiometric measurements in the series **ZrOHGly21** are given in Fig. 4.12.

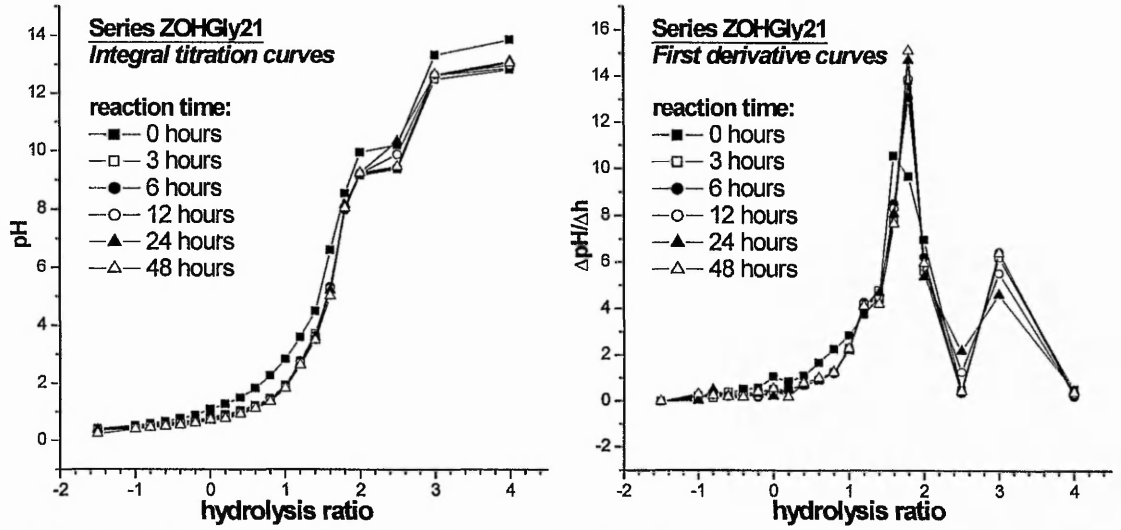


Fig. 4.12. Potentiometric titration curves (integral, *left* and first derivative, *right*) of $ZrOCl_2$ solutions (0.2 M) with KOH (1.6 M) at the presence of glycine (0.1 M) at different measurement times obtained from the multi-batch series **ZrOHGly21**. T=90°C.

From Fig. 4.12 one can see that the shapes of the potentiometric curves of the series **ZrOHGly21** generally follow the trend described above when comparing the series **ZrOHGly12** and **ZrOHGly11**. Predominance of the inflexion at h~2.0 becomes yet more obvious, while only a poorly resolved inflexion at h~1.2 corresponds to the formation of the colloidal phase of zirconium polymers in the series **ZrOHGly21** in the presence of minor quantities of glycine.

Time of reaction is more important in the beginning of the series **ZrOHGly21** (τ=0 hours, Fig. 4.12). The inflexion peak at h~2.0 increases its in height with the progress of the reaction and reaches a maximum at the end of experiment (τ=48 hours). The inflexion observed at alkaline conditions appears to shift its maximum in Fig. 4.12 further to lower h (series **ZrOHGly21**) compared to the series **ZrOHGly12** and **ZrOHGly11**. The highest point of this inflexion reaches a minimum after 24 hours of the reaction.

4.2.2. Kinetics of pH change in the multi-batch titrations of zirconium-ions

As was mentioned above, multi-batch design of the experiments used for the study of the aqueous chemistry of zirconium-ions at medium concentration (0.2 M) and elevated temperature (90°C) enabled us to conduct time-resolved measurements including potentiometric monitoring of the processes occurring in solutions of hydrolysed Zr-ions. The number of measurements (6 points) was not enough to perform quantitative kinetic analysis of the potentiometric data, however, extraction of additional information from time-resolved pH data concerning speciation patterns of hydrolysed Zr-ions in the course of alkaline hydrolysis at different conditions was attempted.

Time-resolved potentiometric curves obtained from all seven multi-batch series are shown in Fig. 4.13. One can find that the shape of the curves strongly depends on the hydrolysis ratio of each batch in the experiment.

For the series **ZrHCO3**, at lower hydrolysis ratios (h<1.7) the shape of the time-resolved pH-profiles is of an exponential decay type (Fig. 4.14). The decay is nearly over at the reaction time τ=3 hours. The depth of the decay increases with the increase of hydrolysis ratio. The major decay occurs at $\tau \leq 6$ hours (except h=-1.5, for which the decay is complete after ca. 24 hours). At h~1.7 the shape of the pH-curves of the series **ZrHCO3** changes to a power-law (logarithm-like) shape which pertains at the alkaline conditions (up to h=4.0). At high hydrolysis ratios (h>1.7) the change of pH value during the 48 hours of the experiment (**ZrHCO3**) is the most significant (ΔpH varies from 0.4 at h=1.7 to ca. 2.9 at h=4.0).

In the series **ZrOH** (titration of pure $ZrOCl_2$ solution with KOH) the time-resolved profiles observed at h<1.6 are generally of a decay shape with the hydrolysis ratio-dependent patterns very similar to the series **ZrHCO3** described above. The only major difference between the series **ZrHCO3** and **ZrOH** is that in the latter case the decay is apparently completed at longer times of experiments (τ=12 hours). At h~1.6 to h~1.8 the curve changes to a more complex shape with initial increase of pH in the first 3 hours and a further decay of pH value at longer reaction times. At $h \geq 2.0$ the time-resolved pH-profiles of the series **ZrOH** again have a shallow decay shape gradually decreasing in depth with the growth of h. The maximum variation of pH in the series **ZrOH** is ca. 1.5 units of pH at h=2.0.

The presence of sulphate-ions in the series **ZrOHSO4** leads to a composite shape of the time-resolved pH-profile at h=-1.5 with gradual increase of pH until τ=6 hours and further shallow decay on the curve at longer times of experiment (Fig. 4.14). At higher hydrolysis ratios ($-1.0 \leq h \leq 1.0$) the time-resolved pH curves are prevailingly of a decay shape. The decay depth and the time the decay is complete increase in agreement with the increasing hydrolysis ratios, reaching a maximum at h~1.0 (τ_{decay}=12 hours, ΔpH between 0 and 48 hours is ca. 0.9). Starting from h=1.2 the curve shape changes to a more complicated shape with initial growth of pH until τ= 3 hours with further decay of pH value at longer reaction times. This shape is

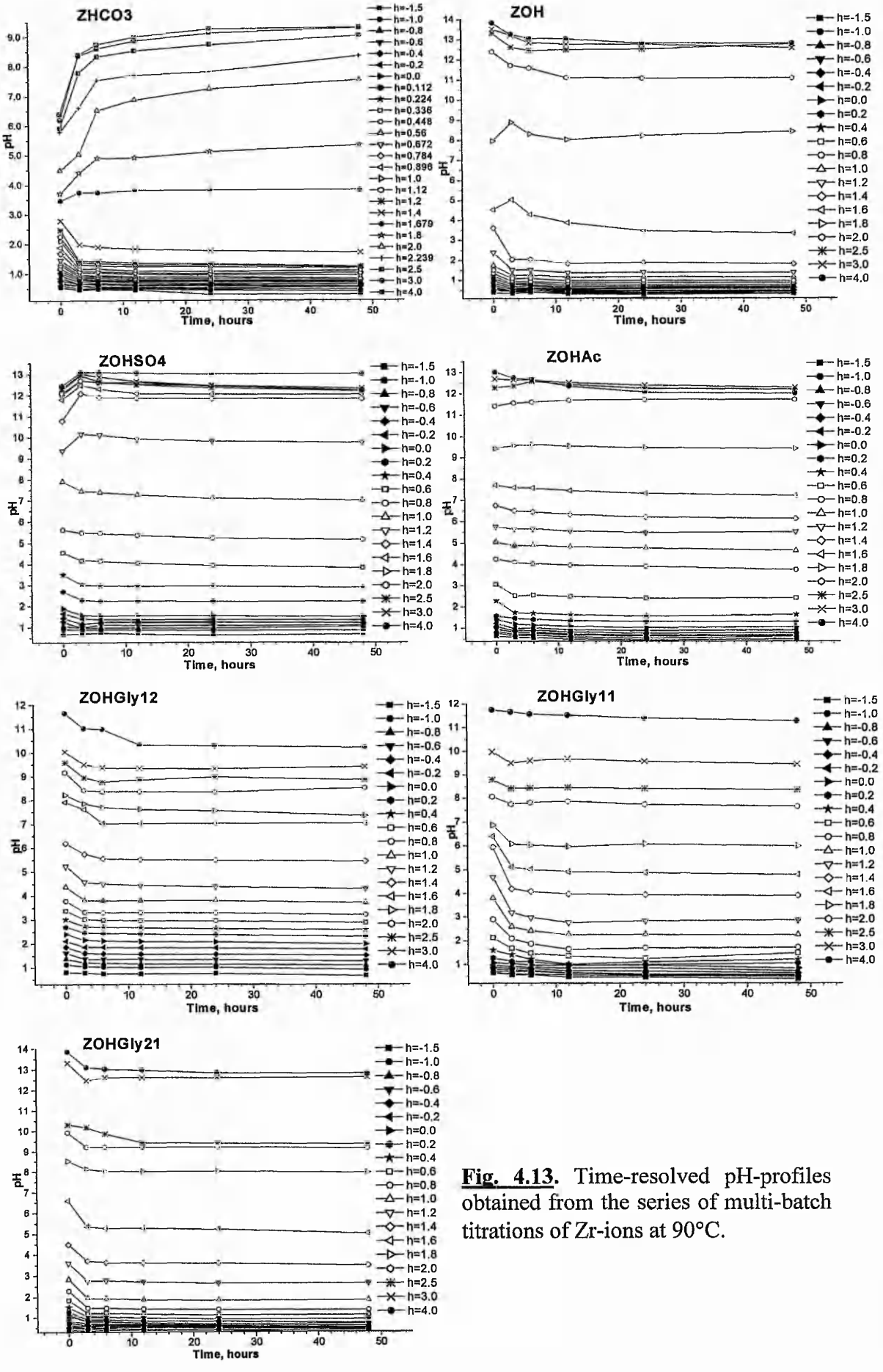


Fig. 4.13. Time-resolved pH-profiles obtained from the series of multi-batch titrations of Zr-ions at 90°C.

maintained up to h=4.0 where it changes to a 'power-law growth type. The variation of pH values within 48 hours of experiments is much smaller for the series **ZrOHSO4** than for the series **ZrHCO3** and **ZrOH** with the highest value of ΔpH=1.2 (between 0 and 3 h) at h=1.4.

In the series **ZrOHAc** (presence of acetate-ions) the shape of time-resolved pH-profiles at low hydrolysis ratios (h≤1.6) is very similar to those of the series **ZrOHSO4** (Fig. 4.14). The decay is very shallow and pH values decrease for much longer times compared with the data obtained from the series **ZrHCO3**, **ZrOH** and **ZrOHSO4** (some curves show decreasing pH values until τ = 48 hours). At h=1.8 the time-resolved pH curve shows a composite shape with initial growth until τ~6 hours and further slight decay of pH values. At h=2.0 the curve indicates constant growth of pH. At h=2.5 the curves are again of a hybrid shape with pH growth at the beginning (until τ=6 hours) and further decay at longer reaction times. Finally, at h≥3.0 the curves are again of a decay shape.

The series **ZrOHGly12**, **ZrOHGly11** and **ZrOHGly21** with different amounts of glycine present along with Zr-ions show strong similarity of the time-resolved pH-profiles (Fig. 4.13). All profiles are of an exponential decay type. The difference between the curves within each series and between the series is the time of the decay completion and the overall pH variation within 48 hours of experiment. One can see from Fig. 4.14 that the longest decay time is at 1.8≤h≤2.0 for all three series with glycine. The highest pH variation is usually observed within 0.8≤h≤1.6. The maximum value of ΔpH (between 0 and 48 hours) apparently does not follow the same order in the series **ZrOHGly12**, **ZrOHGly11**, **ZrOHGly21** as the ratio Zr:Gly, the highest value is reached in the series **ZrOHGly11** (ΔpH=1.9 at h=1.4) with the ratio Zr:Gly=1:1. Comparison of the series **ZrOHGly12**, **ZrOHGly11**, **ZrOHGly21** with glycine and the series **ZrOH** carried out with pure $ZrOCl_2$ indicate that the presence of glycine alters the shape and shape distribution patterns in the range of hydrolysis ratios studied.

Concluding the description of the results of time-resolved data from the multi-batch series of titrations of Zr-ions at elevated temperature, one can find that the overall time of the processes manifested by pH changes is in most cases within 6-12 hours, and the fastest pH change is observed during first 3 hours of experiments. The shape of the time-resolved pH curves is sensitive to the variation of hydrolysis ratio and conditions of experiment (strength of alkali, presence of foreign anions and different amounts of glycine), especially at higher hydrolysis ratios 0.0<h<2.0 where the most drastic pH changes over time occur.

4.2.3. Evidence of complexation from pH measurements for the multi-batch series of Zr-ion titrations

Along with the analysis of the titration curves reconstructed from the multi-batch potentiometric measurements and kinetic analysis of pH variations during 48 hours of the multi-batch experiments involving forced hydrolysis of Zr-ions with alkali at high

temperature discussed above, one can also analyse 'intrinsic' pH values of Zr-ion solutions without addition of alkali or acid (h=0.0) in order to elucidate the impact of the ligand alone on the changes in Zr-ion solutions. A summary of the pH values of all seven multi-batch series at h=0.0 is presented in Table 4.1.

Table 4.1. Values of pH of zirconium-ion solutions at the presence of various complexing agents at h=0.0 (without addition of alkali or acid)

Series	Agent	pH value					
		0 hours	3 hours	6 hours	12 hours	24 hours	48 hours
ZrHCO3	-	0.946	0.730	0.750	0.687	0.663	0.621
ZrOH	-	0.941	0.737	0.752	0.692	0.666	0.619
ZrOHSO4	SO_4^{2-}:Zr=1:1	1.895	1.550	1.568	1.558	1.547	1.509
ZrOHAc	CH_3COO^-:Zr=1:1	1.408	1.207	1.150	1.091	1.031	1.071
ZrOHGly12	Glycine:Zr=2:1	2.402	2.162	2.127	2.100	2.074	1.988
ZrOHGly11	Glycine:Zr=1:1	1.764	1.620	1.147	1.416	1.403	1.401
ZrOHGly21	Glycine:Zr=1:2	1.094	0.802	0.798	0.7425	0.687	0.713

One can see from the data of Table 4.1 that depending on the initial conditions of the hydrolysis the pH value of the Zr-ion solution without base addition depends on the strength and concentration of the complexing ion. The lowest values of pH are obtained from pure solutions (0.2 M) of zirconyl chloride (series **ZrHCO3** and **ZrOH**). The highest pH value is obtained for the complex Gly:Zr=2:1 (**ZrOHGly12**). The acidity of solutions Gly:Zr=1:1 (**ZrOHGly11**) and Gly:Zr=1:2 (**ZrOHGly21**) decreases as a concentration of glycine is decreased. The next highest pH value is obtained for Zr solutions in the presence of sulphate-ions (**ZrOHSO4**), the acidity of acetate-Zr solution is lower (pH=1.408 at the beginning of monitoring), albeit still ~ 1.5 times higher than of the pure Zr-ion solution.

Since crystalline zirconyl chloride presumably consists of Zr tetramers [5], upon dissolution of this salt the tetramers are extensively hydrolysed as indicated by very low pH values of 0.2 M solutions shown in Table 4.1 (series **ZrHCO3**, **ZrOH**). One can assume that the most of the tetramers ($[Zr_4(OH)_8(H_2O)_{16}]^{8+}$) condense into octamers $[Zr_8(OH_{20})(H_2O)_{24}]^{12+}$ which presumably contain four additional OH-bridges between two tetramers constituting the octamer [6]. Suggesting the complete transformation of Zr tetramers into octamers, one can easily derive that the concentration of the former would be 0.05 M (0.2 M initial Zr concentration divide to four) and of the latter - 0.025 M. The concentration of protons released from the hydrolysis-condensation would be 0.05*2=0.1 M (in order to form four OH-bridges in octamers) and the pH value would be 1.0. This value is close to the pH values at the beginning of the reaction monitoring (τ="0" hours) of the series **ZrHCO3** and **ZrOH** (pH0=0.946 and pH=0.941 correspondingly, Table 4.1). It is known from the literature that such polymerisation can occur upon thermoinduced hydrolysis of zirconium-ions [6,21].

Accepting the latter hypothesis, one can derive that in order to produce, for instance, Zr_{12}-mers, 0.2 M of protons should be released that leads to pH=0.699 which is very close to the values of $pH_{12hours}$=0.687 (**ZrHCO3**) and $pH_{12hours}$=0.692 (**ZrOH**). Further hydrolysis is indicated by lower pH values at τ=24 hours to τ=48 hours (Table 4.1). However, due to the small value of ΔpH ca. 0.066 to 0.073 (from τ=12 hours to τ=48 hours), condensation could only lead to a fractional increase of higher Zr polymers (e.g. Zr 16-mer) up to approx. 15-20% of the total Zr-ion concentration in solutions. Summarising the above one can find that thermoinduced hydrolysis is likely to occur at 90°C and can lead to condensation of all Zr tetramers into higher (mainly 12-mer) Zr hydroxopolymers.

The considerations discussed above also help to explain the data of the time-resolved potentiometric measurements in the multi-batch titrations **ZrHCO3** and **ZrOH** (with pure Zr-ion solutions) which indicate that in the absence of any complexing agent the value of pH is very low (pH≤0.2) at h=-1.5 (which can stabilise smaller Zr polymers, e.g. tetramers), and Zr tetramers prevail in strongly acidic conditions (pH<0.65 according to [5]) are unable to hydrolyse and, consequently, to condense into larger polymers. This is supported by steady pH values at low hydrolysis ratios (h<-1.0, Fig. 4.4).

The high value of pH=2.402 for zirconium solution containing 2-times excess of glycine (**ZrOHGly12**) is most likely related to (*a*) prevention of hydrolysis-condensation of Zr-tetramers due to complexation with glycine, and (*b*) the buffering effect of the amphoteric molecule of glycine due to protonation of both carboxylic and amino-groups. Therefore, the high value of pH at h=0.0 in the series **ZrOHGly12** and **ZrOHGly11** may not be fully related to the strength of this complexing agent towards zirconium-ions. However, for sulphate and acetate-ions, pH values at the beginning of hydrolysis are more correlated with their relative complexing strength with Zr-ions and can serve as an additional evidence for such complexation taking place.

4.2.4. Discussion of the potentiometric data obtained from multi-batch titrations of Zr-ions

Comparison of the single-batch potentiometric titrations of Zr-ions with alkalis described in Section 4.1 and multi-batch titrations of similar systems discussed above reveals some substantial differences due to following reasons: (*a*) different kinetics of hydrolysis-condensation of Zr-ion solutions at ambient (20-25°C) and elevated (90°C) temperatures; (*b*) different time scales of single-batch and multi-batch experiments - reactions in the single-batch titration mode are mostly completed within 3 hours, while multi-batch experiments were carried out during 48 hours; (*c*) different resolution of the titration modes – 60-120 points for single-batch titrations vs. 20-26 points for multi-batch titrations. However, there are also fundamental similarities between these two modes of titration including the fact that the absence of complexing agent (sulphate, acetate, or glycine) the major pathway of hydrolysis-

condensation of Zr-ions under forced alkaline hydrolysis remains unchanged regardless of the titration mode and temperature.

The effect of alkali strength on the hydrolysis of Zr-ions was examined in the series **ZrHCO3** and **ZrOH** carried out with 1.6 M $KHCO_3$ and 1.6 M KOH correspondingly. The comparison has shown that the hydrolysis of Zr-ions using weaker base ($KHCO_3$) is more time-dependent and leads to dramatic changes in the relative importance of the different steps of hydrolysis-condensation, albeit not changing the general reaction pathway as manifested in the shape of the potentiometric titration curves obtained (Fig. 4.6). Early stages of hydrolysis-condensation (h<0.1) become more important when titrating with $KHCO_3$, while colloid formation stages are less distinct than for the titration with KOH. Finally, due to presence of carbonate-ions, dissolution of hydrous zirconia in alkaline medium is activated and leads to Zr polymers with complexing carbonate-ions [15,16].

The most important feature revealed in the multi-batch titrations is the effect of complexing agents on the forced hydrolysis-condensation of Zr-ions at high temperature. Although detected only indirectly in the potentiometric titrations, the effect of addition of complexing agents on the shape of the multi-batch titration curves is dramatic (Figs. 4.6-4.10). In order to explain the experimental results, theoretical analysis using the Partial charge model was implemented in the present study. The analysis was conducted in the form of a 'virtual titration' where calculations were conducted for one given Zr polycation and a varying number of ligands. The theoretical analysis using PCM was based on the following assumptions: (*a*) the nature of interaction between complexing agents in question (sulphate, acetate and glycine) is mainly electrostatic; (*b*) complexes of the mentioned ligands with several polynuclear hydroxo-bridged Zr-ions ($4 \leq n(Zr) \leq 16$) are chosen to represent a broad range of polymers dominating the speciation patterns of Zr in aqueous solutions over a wide range of hydrolysis ratios (h<2.0 on the titration curves); (*c*) both protonated and fully-deprotonated forms of the chosen ligands can theoretically form complexes with Zr-ions; (*d*) the chosen ligands cannot replace dihydroxo-bridges of Zr polycations; (*e*) partially protonated ligands cannot be bidentate. The results of the PCM calculations of the complexes of polymeric Zr-ions with sulphate-ions are given in Table 4.2, results with acetate-ions are shown in Table 4.3, the calculations in the system zirconium-glycine are summarised in Table 4.4 of APPENDIX 1.

Sulphate-ions are known to form complexes with zirconium under a broad range of pH values [16,17], they can form both inner-sphere and outer-sphere complexes with Zr-ions [18]. In general, sulphate-ions quickly neutralise highly electropositive polymeric zirconium-ions and precipitate them in the form of various neutral or negatively charged sulphate-bridged polymers [23,24], although other structures of Zr-sulphate complex (with unidentate or bidentate chelating sulphate) are also possible [16-18,24]. The solubility of such basic zirconium sulphates is very low [16] and further transformation into hydrous zirconia is quite unlikely. This fact is supported by the data of the study [26] where monoclinic zirconia has

Table 4.2. PCM calculations of Zr polycation complexes with sulphate-ions

No	Species	h*	Ligand**	z	χ_t	$\delta(H_2O)$	$\delta(OH)$	$\delta_{sulphate}$	$pH_{opt.}$
	Zr tetramers								
1	$Zr_4(OH)_8(H_2O)_{16}$	*2.00*	$SO_4^{2-}(\mu_1)$	8	**2.6913**	0.093	-0.0011	-	*1.16*
2	$Zr_4(OH)_8(H_2O)_{15}(SO_4)$	*2.00*	$SO_4^{2-}(\mu_1)$	6	**2.6717**	0.084	-0.0022	0.1878	*1.72*
3	$Zr_4(OH)_8(H_2O)_{14}(SO_4)_2$	*2.00*	$SO_4^{2-}(\mu_1)$	4	**2.6530**	0.076	-0.0032	0.0893	*2.26*
4	$Zr_4(OH)_8(H_2O)_{13}(SO_4)_3$	*2.00*	$SO_4^{2-}(\mu_1)$	2	**2.6349**	0.067	-0.0043	0.0566	*2.77*
5	$Zr_4(OH)_8(H_2O)_{12}(SO_4)_4$	*2.00*	$SO_4^{2-}(\mu_1)$	0	**2.6175**	0.059	-0.0052	0.0404	*3.27*
6	$Zr_4(OH)_8(H_2O)_{10}(SO_4)_6$	*2.00*	$SO_4^{2-}(\mu_1)$	-4	**2.5846**	0.044	-0.0071	0.0242	*4.21*
7	$Zr_4(OH)_8(H_2O)_8(SO_4)_8$	*2.00*	$SO_4^{2-}(\mu_1)$	-8	**2.5540**	0.029	-0.0088	0.0163	*5.09*
8	$Zr_4(OH)_8(H_2O)_6(SO_4)_{10}$	*2.00*	$SO_4^{2-}(\mu_1)$	-12	**2.5255**	0.016	-0.0104	0.0117	*5.90*
9	$Zr_4(OH)_8(H_2O)_4(SO_4)_{12}$	*2.00*	$SO_4^{2-}(\mu_1)$	-16	**2.4987**	0.004	-0.0119	0.0086	*6.66*
10	$Zr_4(OH)_8(H_2O)_2(SO_4)_{14}$	*2.00*	$SO_4^{2-}(\mu_1)$	-20	**2.4737**	-0.008	-0.0133	0.0065	*7.38*
11	$Zr_4(OH)_8(SO_4)_{16}$	*2.00*	$SO_4^{2-}(\mu_1)$	-24	**2.4502**	-0.019	-0.0146	0.0050	*8.05*
12	$Zr_4(OH)_8(H_2O)_{15}(HSO_4)$	*2.00*	$HSO_4^{-}(\mu_1)$	7	**2.6929**	0.094	-0.0010	0.0234	*1.12*
13	$Zr_4(OH)_8(H_2O)_{14}(HSO_4)_2$	*2.00*	$HSO_4^{-}(\mu_1)$	6	**2.6945**	0.095	-0.0009	0.0120	*1.07*
14	$Zr_4(OH)_8(H_2O)_{13}(HSO_4)_3$	*2.00*	$HSO_4^{-}(\mu_1)$	5	**2.6960**	0.096	-0.0008	0.0082	*1.03*
15	$Zr_4(OH)_8(H_2O)_{12}(HSO_4)_4$	*2.00*	$HSO_4^{-}(\mu_1)$	4	**2.6973**	0.096	-0.0008	0.0063	*0.99*
16	$Zr_4(OH)_8(H_2O)_{10}(HSO_4)_6$	*2.00*	$HSO_4^{-}(\mu_1)$	2	**2.6999**	0.097	-0.0006	0.0044	*0.92*
17	$Zr_4(OH)_8(H_2O)_8(HSO_4)_8$	*2.00*	$HSO_4^{-}(\mu_1)$	0	**2.7021**	0.098	-0.0005	0.0034	*0.85*
18	$Zr_4(OH)_8(H_2O)_6(HSO_4)_{10}$	*2.00*	$HSO_4^{-}(\mu_1)$	-2	**2.7041**	0.099	-0.0004	0.0028	*0.80*
19	$Zr_4(OH)_8(H_2O)_4(HSO_4)_{12}$	*2.00*	$HSO_4^{-}(\mu_1)$	-4	**2.7059**	0.100	-0.0003	0.0024	*0.75*
20	$Zr_4(OH)_8(H_2O)_2(HSO_4)_{14}$	*2.00*	$HSO_4^{-}(\mu_1)$	-6	**2.7075**	0.101	-0.0002	0.0021	*0.70*
21	$Zr_4(OH)_8(HSO_4)_{16}$	*2.00*	$HSO_4^{-}(\mu_1)$	-8	**2.7090**	0.102	-0.0001	0.0019	*0.66*
22	$Zr_4(OH)_8(H_2O)_{14}(SO_4)$	*2.00*	$SO_4^{2-}(\mu_2)$	6	**2.6798**	0.088	-0.0017	0.1917	*1.49*
23	$Zr_4(OH)_8(H_2O)_{12}(SO_4)_2$	*2.00*	$SO_4^{2-}(\mu_2)$	4	**2.6678**	0.082	-0.0024	0.0929	*1.83*
24	$Zr_4(OH)_8(H_2O)_{10}(SO_4)_3$	*2.00*	$SO_4^{2-}(\mu_2)$	2	**2.6552**	0.077	-0.0031	0.0599	*2.20*
25	$Zr_4(OH)_8(H_2O)_8(SO_4)_4$	*2.00*	$SO_4^{2-}(\mu_2)$	0	**2.6419**	0.070	-0.0039	0.0433	*2.58*
26	$Zr_4(OH)_8(H_2O)_6(SO_4)_5$	*2.00*	$SO_4^{2-}(\mu_2)$	-2	**2.6279**	0.064	-0.0046	0.0333	*2.97*
27	$Zr_4(OH)_8(H_2O)_4(SO_4)_6$	*2.00*	$SO_4^{2-}(\mu_2)$	-4	**2.6131**	0.057	-0.0055	0.0266	*3.40*
28	$Zr_4(OH)_8(H_2O)_2(SO_4)_7$	*2.00*	$SO_4^{2-}(\mu_2)$	-6	**2.5976**	0.050	-0.0063	0.0217	*3.84*
29	$Zr_4(OH)_8(SO_4)_8$	*2.00*	$SO_4^{2-}(\mu_2)$	-8	**2.5811**	0.042	-0.0073	0.0180	*4.31*
	Zr octamers								
30	$Zr_8(OH)_{20}(H_2O)_{24}$	*2.50*	-	12	**2.6619**	0.080	-0.0011	-	*2.00*
31	$Zr_8(OH)_{20}(H_2O)_{23}(SO_4)$	*2.50*	$SO_4^{2-}(\mu_1)$	10	**2.6511**	0.075	-0.0013	0.1778	*2.31*
32	$Zr_8(OH)_{20}(H_2O)_{22}(SO_4)_2$	*2.50*	$SO_4^{2-}(\mu_1)$	8	**2.6405**	0.070	-0.0016	0.0863	*2.61*
33	$Zr_8(OH)_{20}(H_2O)_{20}(SO_4)_4$	*2.50*	$SO_4^{2-}(\mu_1)$	4	**2.6200**	0.060	-0.0020	0.0407	*3.20*
34	$Zr_8(OH)_{20}(H_2O)_{18}(SO_4)_6$	*2.50*	$SO_4^{2-}(\mu_1)$	0	**2.6004**	0.051	-0.0025	0.0255	*3.76*
35	$Zr_8(OH)_{20}(H_2O)_{16}(SO_4)_8$	*2.50*	$SO_4^{2-}(\mu_1)$	-4	**2.5816**	0.042	-0.0029	0.0180	*4.30*
36	$Zr_8(OH)_{20}(H_2O)_{23}(HSO_4)$	*2.50*	$HSO_4^{-}(\mu_1)$	11	**2.6635**	0.080	-0.0011	0.0100	*1.96*
37	$Zr_8(OH)_{20}(H_2O)_{22}(HSO_4)_2$	*2.50*	$HSO_4^{-}(\mu_1)$	10	**2.6650**	0.081	-0.0010	0.0054	*1.92*
38	$Zr_8(OH)_{20}(H_2O)_{20}(SO_4)_4$	*2.50*	$HSO_4^{-}(\mu_1)$	8	**2.6678**	0.082	-0.0010	0.0030	*1.83*
39	$Zr_8(OH)_{20}(H_2O)_{18}(SO_4)_6$	*2.50*	$HSO_4^{-}(\mu_1)$	6	**2.6704**	0.084	-0.0009	0.0022	*1.76*
40	$Zr_8(OH)_{20}(H_2O)_{16}(SO_4)_8$	*2.50*	$HSO_4^{-}(\mu_1)$	4	**2.6728**	0.085	-0.0009	0.0018	*1.69*
41	$Zr_8(OH)_{20}(H_2O)_{22}(SO_4)$	*2.50*	$SO_4^{2-}(\mu_2)$	10	**2.6551**	0.077	-0.0013	0.1797	*2.20*
42	$Zr_8(OH)_{20}(H_2O)_{20}(SO_4)_2$	*2.50*	$SO_4^{2-}(\mu_2)$	8	**2.6481**	0.073	-0.0014	0.0882	*2.40*
43	$Zr_8(OH)_{20}(H_2O)_{16}(SO_4)_4$	*2.50*	$SO_4^{2-}(\mu_2)$	4	**2.6335**	0.066	-0.0017	0.0423	*2.82*
44	$Zr_8(OH)_{20}(H_2O)_{12}(SO_4)_6$	*2.50*	$SO_4^{2-}(\mu_2)$	0	**2.6180**	0.059	-0.0021	0.0269	*3.26*
45	$Zr_8(OH)_{20}(H_2O)_8(SO_4)_8$	*2.50*	$SO_4^{2-}(\mu_2)$	-4	**2.6016**	0.052	-0.0024	0.0192	*3.73*
	Zr octamer with sulphate-bridges								
46	$Zr_8(OH)_{19}(H_2O)_{24}(SO_4)$	*2.38*	$SO_4^{2-}(\mu_2)$	11	**2.6635**	0.080	-0.0011	0.1838	*1.96*
47	$Zr_8(OH)_{18}(H_2O)_{24}(SO_4)_2$	*2.25*	$SO_4^{2-}(\mu_2)$	10	**2.6650**	0.081	-0.0011	0.0923	*1.92*
48	$Zr_8(OH)_{16}(H_2O)_{24}(SO_4)_4$	*2.00*	$SO_4^{2-}(\mu_2)$	8	**2.6678**	0.082	-0.0012	0.0465	*1.83*
49	$Zr_8(OH)_{16}(H_2O)_{20}(SO_4)_6$	*2.00*	$SO_4^{2-}(\mu_2)$	4	**2.6552**	0.077	-0.0016	0.0300	*2.20*
50	$Zr_8(OH)_{16}(H_2O)_{24}(SO_4)_8$	*2.00*	$SO_4^{2-}(\mu_2)$	0	**2.6419**	0.070	-0.0019	0.0217	*2.58*

Table 4.2 (continues)

No	Species	h	Ligand*	z	χ_t	$\delta(H_2O)$	$\delta(OH)$	$\delta_{sulphate}$	$pH_{opt.}$
			Zr 12-mers						
51	$Zr_{12}(OH)_{32}(H_2O)_{32}$	*2.67*	-	**16**	**2.6503**	0.074	-0.0008	-	*2.33*
52	$Zr_{12}(OH)_{32}(H_2O)_{31}(SO_4)$	*2.67*	$SO_4^{2-}(\mu_1)$	**14**	**2.6428**	0.071	-0.0010	0.1737	*2.55*
53	$Zr_{12}(OH)_{32}(H_2O)_{30}(SO_4)_2$	*2.67*	$SO_4^{2-}(\mu_1)$	**12**	**2.6354**	0.067	-0.0011	0.0851	*2.76*
54	$Zr_{12}(OH)_{32}(H_2O)_{28}(SO_4)_4$	*2.67*	$SO_4^{2-}(\mu_1)$	**8**	**2.6210**	0.061	-0.0013	0.0408	*3.17*
55	$Zr_{12}(OH)_{32}(H_2O)_{26}(SO_4)_6$	*2.67*	$SO_4^{2-}(\mu_1)$	**4**	**2.6070**	0.054	-0.0015	0.0261	*3.57*
56	$Zr_{12}(OH)_{32}(H_2O)_{24}(SO_4)_8$	*2.67*	$SO_4^{2-}(\mu_1)$	**0**	**2.5935**	0.048	-0.0016	0.0187	*3.96*
57	$Zr_{12}(OH)_{32}(H_2O)_{22}(SO_4)_{10}$	*2.67*	$SO_4^{2-}(\mu_1)$	**-4**	**2.5803**	0.042	-0.0018	0.0143	*4.33*
58	$Zr_{12}(OH)_{32}(H_2O)_{20}(SO_4)_{12}$	*2.67*	$SO_4^{2-}(\mu_1)$	**-8**	**2.5675**	0.036	-0.0020	0.0114	*4.70*
59	$Zr_{12}(OH)_{32}(H_2O)_{31}(HSO_4)$	*2.67*	$HSO_4^{-}(\mu_1)$	**15**	**2.6516**	0.075	-0.0008	0.0046	*2.30*
60	$Zr_{12}(OH)_{32}(H_2O)_{30}(HSO_4)_2$	*2.67*	$HSO_4^{-}(\mu_1)$	**14**	**2.6528**	0.075	-0.0008	0.0026	*2.26*
61	$Zr_{12}(OH)_{32}(H_2O)_{28}(HSO_4)_4$	*2.67*	$HSO_4^{-}(\mu_1)$	**12**	**2.6551**	0.077	-0.0008	0.0016	*2.20*
62	$Zr_{12}(OH)_{32}(H_2O)_{26}(HSO_4)_6$	*2.67*	$HSO_4^{-}(\mu_1)$	**10**	**2.6573**	0.078	-0.0008	0.0012	*2.13*
63	$Zr_{12}(OH)_{32}(H_2O)_{24}(HSO_4)_8$	*2.67*	$HSO_4^{-}(\mu_1)$	**8**	**2.6594**	0.079	-0.0007	0.0010	*2.07*
64	$Zr_{12}(OH)_{32}(H_2O)_{22}(HSO_4)_{10}$	*2.67*	$HSO_4^{-}(\mu_1)$	**6**	**2.6614**	0.079	-0.0007	0.0009	*2.02*
65	$Zr_{12}(OH)_{32}(H_2O)_{20}(HSO_4)_{12}$	*2.67*	$HSO_4^{-}(\mu_1)$	**4**	**2.6633**	0.080	-0.0007	0.0008	*1.96*
66	$Zr_{12}(OH)_{32}(H_2O)_{30}(SO_4)$	*2.67*	$SO_4^{2-}(\mu_2)$	**14**	**2.6454**	0.072	-0.0009	0.1750	*2.47*
67	$Zr_{12}(OH)_{32}(H_2O)_{28}(SO_4)_2$	*2.67*	$SO_4^{2-}(\mu_2)$	**12**	**2.6405**	0.070	-0.0010	0.0863	*2.61*
68	$Zr_{12}(OH)_{32}(H_2O)_{24}(SO_4)_4$	*2.67*	$SO_4^{2-}(\mu_2)$	**8**	**2.6303**	0.065	-0.0011	0.0419	*2.90*
69	$Zr_{12}(OH)_{32}(H_2O)_{20}(SO_4)_6$	*2.67*	$SO_4^{2-}(\mu_2)$	**4**	**2.6197**	0.060	-0.0013	0.0271	*3.21*
70	$Zr_{12}(OH)_{32}(H_2O)_{16}(SO_4)_8$	*2.67*	$SO_4^{2-}(\mu_2)$	**0**	**2.6087**	0.055	-0.0014	0.0196	*3.52*
71	$Zr_{12}(OH)_{32}(H_2O)_{12}(SO_4)_{10}$	*2.67*	$SO_4^{2-}(\mu_2)$	**-4**	**2.5973**	0.050	-0.0016	0.0152	*3.85*
72	$Zr_{12}(OH)_{32}(H_2O)_8(SO_4)_{12}$	*2.67*	$SO_4^{2-}(\mu_2)$	**-8**	**2.5854**	0.044	-0.0018	0.0122	*4.19*
			Zr 16-mers						
73	$Zr_{16}(OH)_{44}(H_2O)_{40}$	*2.75*	-	**20**	**2.6441**	0.071	-0.0007	-	*2.51*
74	$Zr_{16}(OH)_{44}(H_2O)_{39}(SO_4)$	*2.75*	$SO_4^{2-}(\mu_1)$	**18**	**2.6383**	0.069	-0.0007	0.1716	*2.68*
75	$Zr_{16}(OH)_{44}(H_2O)_{38}(SO_4)_2$	*2.75*	$SO_4^{2-}(\mu_1)$	**16**	**2.6327**	0.066	-0.0008	0.0844	*2.84*
76	$Zr_{16}(OH)_{44}(H_2O)_{36}(SO_4)_4$	*2.75*	$SO_4^{2-}(\mu_1)$	**12**	**2.6216**	0.061	-0.0009	0.0409	*3.16*
77	$Zr_{16}(OH)_{44}(H_2O)_{34}(SO_4)_6$	*2.75*	$SO_4^{2-}(\mu_1)$	**8**	**2.6107**	0.056	-0.0010	0.0264	*3.47*
78	$Zr_{16}(OH)_{44}(H_2O)_{32}(SO_4)_8$	*2.75*	$SO_4^{2-}(\mu_1)$	**4**	**2.6001**	0.051	-0.0011	0.0191	*3.77*
79	$Zr_{16}(OH)_{44}(H_2O)_{30}(SO_4)_{10}$	*2.75*	$SO_4^{2-}(\mu_1)$	**0**	**2.5897**	0.046	-0.0012	0.0148	*4.06*
80	$Zr_{16}(OH)_{44}(H_2O)_{28}(SO_4)_{12}$	*2.75*	$SO_4^{2-}(\mu_1)$	**-4**	**2.5796**	0.041	-0.0013	0.0119	*4.35*
81	$Zr_{16}(OH)_{44}(H_2O)_{26}(SO_4)_{14}$	*2.75*	$SO_4^{2-}(\mu_1)$	**-8**	**2.5697**	0.037	-0.0014	0.0099	*4.64*
82	$Zr_{16}(OH)_{44}(H_2O)_{24}(SO_4)_{16}$	*2.75*	$SO_4^{2-}(\mu_1)$	**-12**	**2.5600**	0.032	-0.0015	0.0083	*4.91*
83	$Zr_{16}(OH)_{44}(H_2O)_{39}(HSO_4)$	*2.75*	$HSO_4^{-}(\mu_1)$	**19**	**2.6451**	0.072	-0.0007	0.1749	*2.48*
84	$Zr_{16}(OH)_{44}(H_2O)_{38}(HSO_4)_2$	*2.75*	$HSO_4^{-}(\mu_1)$	**18**	**2.6461**	0.072	-0.0007	0.0877	*2.45*
85	$Zr_{16}(OH)_{44}(H_2O)_{36}(HSO_4)_4$	*2.75*	$HSO_4^{-}(\mu_1)$	**16**	**2.6481**	0.073	-0.0006	0.0441	*2.40*
86	$Zr_{16}(OH)_{44}(H_2O)_{34}(HSO_4)_6$	*2.75*	$HSO_4^{-}(\mu_1)$	**14**	**2.6500**	0.074	-0.0006	0.0295	*2.34*
87	$Zr_{16}(OH)_{44}(H_2O)_{32}(HSO_4)_8$	*2.75*	$HSO_4^{-}(\mu_1)$	**12**	**2.6518**	0.075	-0.0006	0.0223	*2.29*
88	$Zr_{16}(OH)_{44}(H_2O)_{30}(HSO_4)_{10}$	*2.75*	$HSO_4^{-}(\mu_1)$	**10**	**2.6535**	0.076	-0.0006	0.0179	*2.24*
89	$Zr_{16}(OH)_{44}(H_2O)_{28}(HSO_4)_{12}$	*2.75*	$HSO_4^{-}(\mu_1)$	**8**	**2.6552**	0.077	-0.0006	0.0150	*2.20*
90	$Zr_{16}(OH)_{44}(H_2O)_{26}(HSO_4)_{14}$	*2.75*	$HSO_4^{-}(\mu_1)$	**6**	**2.6568**	0.077	-0.0006	0.0129	*2.15*
91	$Zr_{16}(OH)_{44}(H_2O)_{24}(HSO_4)_{16}$	*2.75*	$HSO_4^{-}(\mu_1)$	**4**	**2.6583**	0.078	-0.0005	0.0113	*2.11*
92	$Zr_{16}(OH)_{44}(H_2O)_{38}(SO_4)$	*2.75*	$SO_4^{2-}(\mu_2)$	**18**	**2.6403**	0.070	-0.0007	0.1725	*2.62*
93	$Zr_{16}(OH)_{44}(H_2O)_{36}(SO_4)_2$	*2.75*	$SO_4^{2-}(\mu_2)$	**16**	**2.6365**	0.068	-0.0008	0.0853	*2.73*
94	$Zr_{16}(OH)_{44}(H_2O)_{32}(SO_4)_4$	*2.75*	$SO_4^{2-}(\mu_2)$	**12**	**2.6287**	0.064	-0.0008	0.0417	*2.95*
95	$Zr_{16}(OH)_{44}(H_2O)_{30}(SO_4)_6$	*2.75*	$SO_4^{2-}(\mu_2)$	**8**	**2.6206**	0.060	-0.0009	0.0272	*3.18*
96	$Zr_{16}(OH)_{44}(H_2O)_{28}(SO_4)_8$	*2.75*	$SO_4^{2-}(\mu_2)$	**4**	**2.6124**	0.057	-0.0010	0.0199	*3.42*
97	$Zr_{16}(OH)_{44}(H_2O)_{26}(SO_4)_{10}$	*2.75*	$SO_4^{2-}(\mu_2)$	**0**	**2.6038**	0.053	-0.0011	0.0155	*3.66*
98	$Zr_{16}(OH)_{44}(H_2O)_{24}(SO_4)_{12}$	*2.75*	$SO_4^{2-}(\mu_2)$	**-4**	**2.5950**	0.049	-0.0012	0.0125	*3.91*
99	$Zr_{16}(OH)_{44}(H_2O)_{22}(SO_4)_{14}$	*2.75*	$SO_4^{2-}(\mu_2)$	**-8**	**2.5860**	0.044	-0.0013	0.0104	*4.17*
100	$Zr_{16}(OH)_{44}(H_2O)_{20}(SO_4)_{16}$	*2.75*	$SO_4^{2-}(\mu_2)$	**-12**	**2.5766**	0.040	-0.0014	0.0088	*4.44*

* - h –hydrolysis ratio of Zr species (n(OH)/n(Zr); z – overall charge; χ_t – mean elecronegativity; δ – partial charge; $pH_{opt.}$ –lower pH limit of the corresponding species.

been obtained from Zr basic sulphate only after prolonged hot water annealing at very high temperature. Sulphate-ions can cause precipitation in Zr-containing solutions even at very acidic conditions (negative values of h, pH<0.6) that was visually observed in the series **ZrOHSO4**. Correlation analysis of the time-resolved potentiometric data (Fig. 4.5) also suggests that in the hydrolysis ratio range $-0.8 \leq h \leq 0.8$ drastic changes in the time-resolved pH-profiles obtained from the multi-batch series **ZrOHSO4** are indicative of the significant interaction of sulphate-ions with Zr polymers. However, polymeric forms of zirconium basic sulphates stay soluble longer in strongly acidic conditions than under forced alkaline hydrolysis (h>0.0) that is supported by the visual absence of noticeable precipitation during the early stages of process (τ<1 hour) at h<0.0.

As follows from Table 4.2, three forms of sulphate-ions were examined for a potential to form complexes with polynuclear Zr species: the fully deprotonated SO_4^{2-} form acting as a μ_1 unidentate ligand; the unidentate partially protonated HSO_4^- ligand and the deprotonated μ_2 SO_4^{2-} as a bidentate ligand. The electronic parameters obtained from the PCM analysis were mean electronegativity χ_t, partial charges on the ligands in the coordination sphere of Zr – δ(OH), $\delta(H_2O)$, δ(ligand) and $pH_{opt.}$ (lower pH limit of the species formation calculated from Eq. 1.5, Chapter 1). The calculated parameters were compared with the analogous values for non-complexed Zr-species.

The results in Table 4.2 (species 2-11) indicate that up to 12 of μ_1 SO_4^{2-} unidentate ligands can theoretically complex Zr atoms of Zr tetramer. At a higher number of μ_1 sulphate-ligands ($n(SO_4^{2-})$>12) the value of $\delta(H_2O)$ becomes negative thus making the corresponding complexes (species 10 and 11) theoretically impossible. In general, introduction of larger numbers of μ_1 SO_4^{2-} ligands ($n(SO_4^{2-})$<12) leads to a substantial decrease of $\delta(H_2O)$ which results in the reduced propensity of aquo-ligands to hydrolyse [7,18]. The negative partial charge increases in absolute value making the complex of this polycation with μ_1 SO_4^{2-} unfavourable compared to the initial tetrameric species 1. However, the quickly diminishing value of $\delta_{sulphate}$ can probably make up for the increasing δ(OH). The value of pH_{opt} which reversibly depends on χ_t (Eq. 1.5), shifts to less acidic pH with the increase of the number of μ_1 SO_4^{2-} ligands. However, at the increasing pH these ligands would face a stiff competition from hydroxyl-ions of alkali.

Partially protonated μ_1 sulphate-ligands (species 12-21 in Table 4.2) show an opposite trend to that of the μ_1 SO_4^{2-}ligands. The mean electronegativity of these complexes decreases with increase of the number of ligands in the coordination sphere of Zr atoms of the tetramer, decreasing pH_{opt} values. This is in line with the high value of $pK_a(HSO_4^-)$=1.92. Therefore, HSO_4^- will prevail at the same highly acidic conditions as Zr tetramers (pH<1.0). The value of δ(OH) is less than for initial Zr tetramer (species 1) and also decreases with the increasing number of HSO_4^-. The described features make complexes of Zr tetramers with μ_1 HSO_4^- ligands highly feasible in acidic conditions.

The third form of sulphate-ligand is bidentate μ_2 SO_4^{2-}. Complexes of μ_2 SO_4^{2-} ligands with Zr tetramers (species 22-29) generally follow the same pattern as the μ_1 SO_4^{2-} ligand. However, the increase of δ(OH) and pH_{opt} is much slower in this case, while electrostatic stabilisation of μ_2 SO_4^{2-} ligands is much higher than for the μ_1 analogue (lower values of $\delta_{sulphate}$). Therefore, μ_2 SO_4^{2-} can form complexes with Zr tetramers at lower pH than μ_1 SO_4^{2-}. The acidity of aquo-ligands indicated by the value of $\delta(H_2O)$ also decreases suggesting that the complex of Zr tetramer with μ_2 SO_4^{2-} ligands is less susceptible to hydrolysis than the initial (non-complexed) tetramer.

On the basis of the discussed complexation of sulphate-ions with Zr tetramers one can make the conclusion that sulphate-ions can form complexes with Zr tetramers over a very wide range of pH ($0<pH<10$ according to the PCM calculations in Chapter 1 and in the work [18]). At lower pH values the dominating form is unidentate partially protonated HSO_4^- form of sulphate-ions and at higher pH the complex with μ_2 SO_4^{2-} should dominate speciation patterns of hydrolysed Zr ions in the presence of sulphate.

The effect of increase of the nuclearity of Zr polycations on complexation with sulphate-ions was also investigated in the present study. The data of Table 4.2 show that the increasing size of Zr polymers from Zr tetramers (species 1-29) to octamers (species 30-45), 12-mers (species 51-72) and 16-mers (species 73-100) coinciding with the increase of the corresponding theoretical hydrolysis ratios of the species gives rise to similar patterns as described above for the Zr tetramer. However, μ_2 (SO_4^{2-}) form of sulphate-ions becomes more feasible for complexation with the increase of n(Zr) and h as indicated with very low increase of absolute value of δ(OH) of the corresponding complexes with μ_2 SO_4^{2-} as well as low positive values of $\delta(H_2O)$ and $\delta_{sulphate}$. In fact, the increasing size and hydrolysis ratio of Zr hydroxopolymers makes all three forms of sulphate-ions more similar in terms of their complexation ability as supported by similar parameters of χ_t, δ(OH), $\delta(H_2O)$, δ(sulphate) and pH_{opt}. All three forms of sulphate-ions are able to complex Zr polynuclear species in the medium to mildly acidic environment that coincides with conditions of the formation of Zr hydroxopolymers. However, one should bear in mind that due to the low value of $pK_a(HSO_4^-)$ complexation with the HSO_4^- ligand will always be limited to lower pH values, than complexation with SO_4^{2-} as the ligand.

Precipitation of basic Zr sulphates probably occurs upon charge neutralisation of Zr hydroxo-polymers with sulphate-ions. From Table 4.2 one can see that for the neutralisation of Zr tetramers four SO_4^{2-} ligands are required (n(Zr):$n(SO_4^{2-})$=1:1) regardless of their denticity (μ_1 or μ_2), while eight HSO_4^- ligands are required for the same Zr species neutralisation (Zr:HSO_4^-=1:2). Therefore, under the conditions of the multi-batch experiment (series **ZrOHSO4**) the amount of sulphate-ions (Zr:sulphate=1:1) is sufficient to fully neutralise Zr tetramers.

With the increase of the size of Zr hydroxopolymers and, consequently, their

theoretical hydrolysis ratio from h=2.0 (Zr tetramer) to h=2.75 (Zr 16-mer) the actual amount of sulphate-ions required for the neutralisation decreases: $n(SO_4^{2-})$=10, Zr: SO_4^{2-}=1.6:10, and $n(HSO_4^-)$=20, Zr:HSO_4^-=0.8:1. Hence, upon forced alkaline hydrolysis the probability of precipitation of basic zirconium sulphate increases. This can explain the results of potentiometric measurements for the series **ZrOHSO4**, where basic Zr sulphate formation is observed as early as at h=0.2-0.4, but reaches a maximum at h~1.2 where the maximum of polymerisation (exhaustion of possibilities for further olation / OH-bridge formation) occurs.

Finally, the possibility of the formation of sulphate-bridged instead of hydroxo-bridged zirconium polymers was investigated in the present study examples being given in Table 4.2, species 46-50. The analysis of PCM calculations shows that one sulphate-bridge cannot be formed between two tetramers due to the very high partial charge of sulphate-ions in the resulting polycation (species 46). Higher numbers of bridging sulphate-ions connecting two adjacent Zr tetramers becomes feasible at $n(SO_4^{2-})\geq 4$ (species 48-50), where the partial charges of all ligands in the coordination sphere of Zr atoms including δ(OH), δ(H_2O) and δ(sulphate) are close to a minimum and are comparable or better than hydroxo-bridged zirconium octamers (species 46). Formation of single SO_4^{2-}-bridges between two Zr atoms (species 48, n(Zr):$n(SO_4^{2-})$=1:1) are more probable than double sulphate-bridges (species 49 and 50). Therefore, the possibility of the formation of a sulphate-bridged basic zirconium sulphate cannot be excluded, albeit this hypothesis needs further investigation.

Acetate-ions are also known to form complexes with zirconium-ions both in unidentate and bidentate mode [18-20]. Sol-gel synthesised zirconium-acetate materials were amorphous and contained bridged acetate groups as shown by infrared analysis [27]. Using PCM calculations it was found that preferable pH conditions for complexation of acetate-ions with zirconium in aqueous solutions are in the mildly acidic medium (pH~6.4) [18]. The range for complexation was indicated to be within 1.5≤pH≤10.0 for the unidentate acetate-ligand and 2.5≤pH≤9.5 for a bidentate ligand.

Results of the detailed theoretical analysis of the complexation of Zr hydroxopolymers with acetate ions using the Partial charge model are shown in Table 4.3. In a similar manner to sulphate, three forms of acetate ligands were included: unidentate deprotonated acetate AcO^- (μ_1), bidentate chelating (or bridging) AcO^- (μ_2). From Table 4.3 the complexation of μ_1 CH_3COO^- ligands with Zr tetramers (species 2-10) leads to a significant increase of δ(OH) compared to the initial Zr tetramer (species 1). Moreover, as follows from the partial charge on the aquo ligands δ(H_2O) which is restricted to non-negative values [7] , only eight μ_1 AcO^- ligands are theoretically allowed to complex one Zr tetramer (comparing to 12 μ_1 SO_4^{2-} ligands). At the ratio n(Zr):$n(AcO^-)$=8 the partial charge on δ(H_2O) reaches a minimum value of 0.001 which means that it is practically impossible for the remaining aquo-ligands to hydrolyse further. The value of pH_{opt} increases more abruptly than the same value of the complex Zr-SO_4^{2-} (μ_1), becoming nearly neutral at the ratio of Zr:AcO^- (μ_1)=1:2. Interestingly,

Table 4.3. PCM calculations of Zr polycation complexes with acetate-ions

No	Species	*h*	Ligand*	z	χ_t	δ(H_2O)	δ(OH)	δ(Ac)	$pH_{opt.}$
	Zr tetramers								
1	$Zr_4(OH)_8(H_2O)_{16}$	*2.00*	-	**8**	**2.6913**	0.093	-0.0011	-	*1.16*
2	$Zr_4(OH)_8(H_2O)_{15}(CH_3COO)$	*2.00*	$AcO^-(\mu_1)$	**7**	**2.6573**	0.078	-0.0030	0.1837	*2.13*
3	$Zr_4(OH)_8(H_2O)_{14}(CH_3COO)_2$	*2.00*	$AcO^-(\mu_1)$	**6**	**2.6268**	0.063	-0.0047	0.0844	*3.01*
4	$Zr_4(OH)_8(H_2O)_{12}(CH_3COO)_4$	*2.00*	$AcO^-(\mu_1)$	**4**	**2.5742**	0.039	-0.0076	0.0358	*4.51*
5	$Zr_4(OH)_8(H_2O)_{10}(CH_3COO)_6$	*2.00*	$AcO^-(\mu_1)$	**2**	**2.5305**	0.018	-0.0101	0.0203	*5.76*
6	$Zr_4(OH)_8(H_2O)_8(CH_3COO)_8$	*2.00*	$AcO^-(\mu_1)$	**0**	**2.4936**	0.001	-0.0121	0.0130	*6.81*
7	$Zr_4(OH)_8(H_2O)_6(CH_3COO)_{10}$	*2.00*	$AcO^-(\mu_1)$	**-2**	**2.4621**	-0.013	-0.0139	0.0089	*7.71*
8	$Zr_4(OH)_8(H_2O)_4(CH_3COO)_{12}$	*2.00*	$AcO^-(\mu_1)$	**-4**	**2.4348**	-0.026	-0.0154	0.0063	*8.49*
9	$Zr_4(OH)_8(H_2O)_2(CH_3COO)_{14}$	*2.00*	$AcO^-(\mu_1)$	**-6**	**2.4110**	-0.037	-0.0168	0.0046	*9.17*
10	$Zr_4(OH)_8(CH_3COO)_{16}$	*2.00*	$AcO^-(\mu_1)$	**-8**	**2.3900**	-0.047	-0.0179	0.0033	*9.77*
11	$Zr_4(OH)_8(H_2O)_{14}(CH_3COO)$	*2.00*	$AcO^-(\mu_2)$	**7**	**2.6644**	0.0809	-0.0026	0.1872	*1.93*
12	$Zr_4(OH)_8(H_2O)_{12}(CH_3COO)_2$	*2.00*	$AcO^-(\mu_2)$	**6**	**2.6383**	0.0690	-0.0041	0.0872	*2.68*
13	$Zr_4(OH)_8(H_2O)_8(CH_3COO)_4$	*2.00*	$AcO^-(\mu_2)$	**4**	**2.5880**	0.0453	-0.0069	0.0375	*4.11*
14	$Zr_4(OH)_8(H_2O)_4(CH_3COO)_6$	*2.00*	$AcO^-(\mu_2)$	**2**	**2.5401**	0.0229	-0.0095	0.0211	*5.48*
15	$Zr_4(OH)_8(CH_3COO)_8$	*2.00*	$AcO^-(\mu_2)$	**0**	**2.4945**	0.0017	-0.0121	0.0131	*6.78*
	Zr octamers								
16	$Zr_8(OH)_{20}(H_2O)_{24}$	*2.50*	-	**12**	**2.6619**	0.080	-0.0011	-	*2.00*
17	$Zr_8(OH)_{20}(H_2O)_{23}(CH_3COO)$	*2.50*	$AcO^-(\mu_1)$	**11**	**2.6431**	0.071	-0.0015	0.1768	*2.54*
18	$Zr_8(OH)_{20}(H_2O)_{22}(CH_3COO)_2$	*2.50*	$AcO^-(\mu_1)$	**10**	**2.6254**	0.063	-0.0019	0.0841	*3.04*
19	$Zr_8(OH)_{20}(H_2O)_{20}(CH_3COO)_4$	*2.50*	$AcO^-(\mu_1)$	**8**	**2.5931**	0.048	-0.0026	0.0381	*3.97*
20	$Zr_8(OH)_{20}(H_2O)_{18}(CH_3COO)_6$	*2.50*	$AcO^-(\mu_1)$	**6**	**2.5642**	0.034	-0.0033	0.0231	*4.79*
21	$Zr_8(OH)_{20}(H_2O)_{16}(CH_3COO)_8$	*2.50*	$AcO^-(\mu_1)$	**4**	**2.5383**	0.022	-0.0039	0.0157	*5.53*
22	$Zr_8(OH)_{20}(H_2O)_{22}(CH_3COO)$	*2.50*	$AcO^-(\mu_2)$	**11**	**2.6468**	0.073	-0.0014	0.1786	*2.43*
23	$Zr_8(OH)_{20}(H_2O)_{20}(CH_3COO)_2$	*2.50*	$AcO^-(\mu_2)$	**10**	**2.6320**	0.066	-0.0018	0.0857	*2.86*
24	$Zr_8(OH)_{20}(H_2O)_{16}(CH_3COO)_4$	*2.50*	$AcO^-(\mu_2)$	**8**	**2.6029**	0.052	-0.0024	0.0393	*3.69*
25	$Zr_8(OH)_{20}(H_2O)_{12}(CH_3COO)_6$	*2.50*	$AcO^-(\mu_2)$	**6**	**2.5747**	0.039	-0.0030	0.0239	*4.50*
26	$Zr_8(OH)_{20}(H_2O)_8(CH_3COO)_8$	*2.50*	$AcO^-(\mu_2)$	**4**	**2.5472**	0.026	-0.0037	0.0163	*5.28*
	Zr octamers with CH_3COO-bridges								
27	$Zr_8(OH)_{19}(H_2O)_{24}(CH_3COO)$	*2.38*	$AcO^-(\mu_2)$	**12**	**2.6553**	0.077	-0.0013	0.1828	*2.19*
28	$Zr_8(OH)_{18}(H_2O)_{24}(CH_3COO)_2$	*2.25*	$AcO^-(\mu_2)$	**12**	**2.6492**	0.074	-0.0015	0.0899	*2.37*
29	$Zr_8(OH)_{16}(H_2O)_{24}(CH_3COO)_4$	*2.00*	$AcO^-(\mu_2)$	**12**	**2.6383**	0.069	-0.0020	0.0436	*2.68*
30	$Zr_8(OH)_{16}(H_2O)_{20}(CH_3COO)_6$	*2.00*	$AcO^-(\mu_2)$	**10**	**2.6128**	0.057	-0.0027	0.0270	*3.40*
31	$Zr_8(OH)_{16}(H_2O)_{16}(CH_3COO)_8$	*2.00*	$AcO^-(\mu_2)$	**8**	**2.5880**	0.045	-0.0034	0.0187	*4.11*
	Zr 12-mers								
32	$Zr_{12}(OH)_{32}(H_2O)_{32}$	*2.67*	-	**16**	**2.6503**	0.074	-0.0008	-	*2.33*
33	$Zr_{12}(OH)_{32}(H_2O)_{31}(CH_3COO)$	*2.67*	$AcO^-(\mu_1)$	**15**	**2.6373**	0.068	-0.0010	0.1740	*2.71*
34	$Zr_{12}(OH)_{32}(H_2O)_{30}(CH_3COO)_2$	*2.67*	$AcO^-(\mu_1)$	**14**	**2.6249**	*0.062*	*-0.0012*	*0.0840*	*3.06*
35	$Zr_{12}(OH)_{32}(H_2O)_{28}(CH_3COO)_4$	*2.67*	$AcO^-(\mu_1)$	**12**	**2.6015**	*0.052*	*-0.0015*	*0.0391*	*3.73*
36	$Zr_{12}(OH)_{32}(H_2O)_{26}(CH_3COO)_6$	*2.67*	$AcO^-(\mu_1)$	**10**	**2.5800**	*0.042*	*-0.0018*	*0.0243*	*4.34*
37	$Zr_{12}(OH)_{32}(H_2O)_{24}(CH_3COO)_8$	*2.67*	$AcO^-(\mu_1)$	**8**	**2.5601**	*0.032*	*-0.0021*	*0.0171*	*4.91*
38	$Zr_{12}(OH)_{32}(H_2O)_{22}(CH_3COO)_{10}$	*2.67*	$AcO^-(\mu_1)$	**6**	**2.5417**	*0.024*	*-0.0024*	*0.0127*	*5.44*
39	$Zr_{12}(OH)_{32}(H_2O)_{20}(CH_3COO)_{12}$	*2.67*	$AcO^-(\mu_1)$	**4**	**2.5246**	*0.016*	*-0.0026*	*0.0099*	*5.93*
40	$Zr_{12}(OH)_{32}(H_2O)_{30}(CH_3COO)$	*2.67*	$AcO^-(\mu_2)$	**15**	**2.6398**	*0.069*	*-0.0010*	*0.1752*	*2.63*
41	$Zr_{12}(OH)_{32}(H_2O)_{28}(CH_3COO)_2$	*2.67*	$AcO^-(\mu_2)$	**14**	**2.6294**	*0.065*	*-0.0011*	*0.0851*	*2.93*
42	$Zr_{12}(OH)_{32}(H_2O)_{24}(CH_3COO)_4$	*2.67*	$AcO^-(\mu_2)$	**12**	**2.6090**	*0.055*	*-0.0014*	*0.0401*	*3.51*
43	$Zr_{12}(OH)_{32}(H_2O)_{20}(CH_3COO)_6$	*2.67*	$AcO^-(\mu_2)$	**10**	**2.5890**	*0.046*	*-0.0017*	*0.0251*	*4.09*
44	$Zr_{12}(OH)_{32}(H_2O)_{16}(CH_3COO)_8$	*2.67*	$AcO^-(\mu_2)$	**8**	**2.5693**	*0.037*	*-0.0020*	*0.0176*	*4.65*
45	$Zr_{12}(OH)_{32}(H_2O)_{12}(CH_3COO)_{10}$	*2.67*	$AcO^-(\mu_2)$	**6**	**2.5501**	*0.028*	*-0.0022*	*0.0132*	*5.20*
46	$Zr_{12}(OH)_{32}(H_2O)_8(CH_3COO)_{12}$	*2.67*	$AcO^-(\mu_2)$	**4**	**2.5312**	*0.019*	*-0.0025*	*0.0102*	*5.74*

No	Species	h	Ligand	z	χ_t	$\delta(H_2O)$	$\delta(OH)$	$\delta(Ac)$	$pH_{opt.}$
	Zr 16-mers								
47	$Zr_{16}(OH)_{44}(H_2O)_{40}$	*2.75*	-	**20**	**2.6441**	*0.071*	*-0.0007*	-	*2.51*
48	$Zr_{16}(OH)_{44}(H_2O)_{39}(CH_3COO)$	*2.75*	$AcO^-(\mu_1)$	**19**	**2.6341**	*0.067*	*-0.0008*	*0.1725*	*2.80*
49	$Zr_{16}(OH)_{44}(H_2O)_{38}(CH_3COO)_2$	*2.75*	$AcO^-(\mu_1)$	**18**	**2.6245**	*0.062*	*-0.0009*	*0.0839*	*3.07*
50	$Zr_{16}(OH)_{44}(H_2O)_{36}(CH_3COO)_4$	*2.75*	$AcO^-(\mu_1)$	**16**	**2.6063**	*0.054*	*-0.0011*	*0.0397*	*3.59*
51	$Zr_{16}(OH)_{44}(H_2O)_{34}(CH_3COO)_6$	*2.75*	$AcO^-(\mu_1)$	**14**	**2.5891**	*0.046*	*-0.0012*	*0.0251*	*4.08*
52	$Zr_{16}(OH)_{44}(H_2O)_{32}(CH_3COO)_8$	*2.75*	$AcO^-(\mu_1)$	**12**	**2.5731**	*0.038*	*-0.0014*	*0.0178*	*4.54*
53	$Zr_{16}(OH)_{44}(H_2O)_{30}(CH_3COO)_{10}$	*2.75*	$AcO^-(\mu_1)$	**10**	**2.5579**	*0.031*	*-0.0016*	*0.0135*	*4.97*
54	$Zr_{16}(OH)_{44}(H_2O)_{28}(CH_3COO)_{12}$	*2.75*	$AcO^-(\mu_1)$	**8**	**2.5436**	*0.025*	*-0.0017*	*0.0107*	*5.38*
55	$Zr_{16}(OH)_{44}(H_2O)_{26}(CH_3COO)_{14}$	*2.75*	$AcO^-(\mu_1)$	**6**	**2.5301**	*0.018*	*-0.0018*	*0.0087*	*5.77*
56	$Zr_{16}(OH)_{44}(H_2O)_{24}(CH_3COO)_{16}$	*2.75*	$AcO^-(\mu_1)$	**4**	**2.5174**	*0.012*	*-0.0020*	*0.0072*	*6.13*
57	$Zr_{16}(OH)_{44}(H_2O)_{38}(CH_3COO)$	*2.75*	$AcO^-(\mu_2)$	**19**	**2.6360**	*0.068*	*-0.0008*	*0.1734*	*2.74*
58	$Zr_{16}(OH)_{44}(H_2O)_{36}(CH_3COO)_2$	*2.75*	$AcO^-(\mu_2)$	**18**	**2.6281**	*0.064*	*-0.0008*	*0.0847*	*2.97*
59	$Zr_{16}(OH)_{44}(H_2O)_{32}(CH_3COO)_4$	*2.75*	$AcO^-(\mu_2)$	**16**	**2.6123**	*0.057*	*-0.0010*	*0.0405*	*3.42*
60	$Zr_{16}(OH)_{44}(H_2O)_{28}(CH_3COO)_6$	*2.75*	$AcO^-(\mu_2)$	**14**	**2.5968**	*0.049*	*-0.0012*	*0.0257*	*3.86*
61	$Zr_{16}(OH)_{44}(H_2O)_{24}(CH_3COO)_8$	*2.75*	$AcO^-(\mu_2)$	**12**	**2.5815**	*0.042*	*-0.0013*	*0.0184*	*4.30*
62	$Zr_{16}(OH)_{44}(H_2O)_{20}(CH_3COO)_{10}$	*2.75*	$AcO^-(\mu_2)$	**10**	**2.5664**	*0.035*	*-0.0015*	*0.0139*	*4.73*
63	$Zr_{16}(OH)_{44}(H_2O)_{16}(CH_3COO)_{12}$	*2.75*	$AcO^-(\mu_2)$	**8**	**2.5516**	*0.028*	*-0.0016*	*0.0110*	*5.15*
64	$Zr_{16}(OH)_{44}(H_2O)_{12}(CH_3COO)_{14}$	*2.75*	$AcO^-(\mu_2)$	**6**	**2.5370**	*0.022*	*-0.0018*	*0.0089*	*5.57*
65	$Zr_{16}(OH)_{44}(H_2O)_8(CH_3COO)_{16}$	*2.75*	$AcO^-(\mu_2)$	**4**	**2.5227**	*0.015*	*-0.0019*	*0.0074*	*5.98*

* - $AcO^-(\mu_1)$ – monodentate acetate-ions; $AcO^-(\mu_2)$ – bidentate bridging / chelating ions.

there is only a minor difference between the complexation patterns of bidentate AcO^- ligands (species 11-15) and their unidentate analogue (species 2-10). Therefore, acetate-ligands can form both unidentate and bidentate complexes with Zr tetramers without a significant variation in reaction conditions. The maximum likelihood of complexation of both ligand types is in mildly acidic conditions (pH<7) that agree well with the literature data [18,19].

Theoretically, acetate-ions can also form bridges between adjacent Zr atoms of hydroxo-polymers. This possibility was investigated in the present study using Zr octamers as an example (Table 4.3, species 27-31). The Partial charge model calculations indicate that a single acetate-bridge is unlikely to form (high value of $\delta(Ac)$ for the species No 27), while the most feasible acetate-bridged species 29 forms with four acetate-bridges instead of four hydroxo-bridges. Acetate-bridged Zr polymers can form in acidic conditions and are still reactive species as indicated by the quite substantial values of $\delta(H_2O)$ and $\delta(OH)$.

Acetate-ions are weaker bases than sulphate-ions due to their lower polarisation and lower charge (-1). The ratio of Zr:Ac required for the complete neutralisation of Zr polymers is 1:2 which was unattainable under the conditions of the multi-batch experiment **ZrOHAc** carried out in the present study (Zr:Ac=1:1). However, upon increase of the size of Zr hydroxo-polymers from tetramers discussed above to octamers (Table 4.3, species 16-26), 12-mers (species 32-46) and 16-mers (species 47-65) the number of acetate-ions required for effective neutralisation of charge on Zr polymers decreases due to the increase of the theoretical hydrolysis ratio of the larger polymers. This can help to explain the observed inflexion point at h=0.8-1.0 in the potentiometric curves obtained for the multi-batch series **ZrOHAc** in the presence of acetate-ions. This point corresponds to a theoretical hydrolysis

ratio h=3.0 of zirconium polymers where all possibilities for hydroxyl-bridging are exhausted and the rest of the net charge is balanced by AcO^- ions under mildly acidic pH conditions. This leads to the early appearance of a colloidal phase which is most probably zirconium basic acetate. However, the strength of complexation of acetate-ions with Zr hydroxo-polymers is possibly not as high as for sulphate-ions thus leading to the formation of colloids rather then bulk precipitates. The results of correlation analysis of time-resolved pH-profiles of the series **ZrOHAc** (Fig. 4.5) also indicate that replacement of acetate-ions and subsequent colloid formation are not followed by any significant change in the pH-profile shape (and correlation sum correspondingly). Therefore, one can suggest that both processes proceed simultaneously and without drastic changes in pH on the time scale studied.

It is necessary to stress that increase of the size and hydrolysis ratio of Zr hydroxo-polymers (Table 4.3) leads to equal opportunities for complexation by all three forms of acetate-ligands. However, the PCM analysis suggests that unidentate μ_1 AcO^- ligands would prevail in moderately acidic pH conditions (pH<4.0) while at higher pH the bidentate (either chelating or bridging) form of AcO^- would dominate (the structure-independent PCM does not allow for distinction of the bridging and bidentate mode to be made). The maximum possible pH for the complexation of acetate-ions with Zr polymers is estimated below ca. pH<9. The complexation of Zr polymers with acetate-ions in strongly acidic medium (pH<1.0) is quite unlikely.

Results of the PCM analysis of Zr hydroxo-polymer complexation with glycine are shown in Table 4.3 of Appendix 1. Five forms of glycine-ligand were examined: unidentate (μ_1) Gly^+-form with protonated amino-group and carboxylic group (H_3N^+-CH_2-COOH); unidentate (μ_1) Z-Gly zwitter-ion form (H_3N^+-CH_2-COO^-); bidentate chelating (μ_2) Z-Gly zwitter-ion form; unidentate (μ_1) Gly^- form with neutral amino- and deprotonated carboxylic group (H_3N^+-CH_2-COO^-); and bidentate chelating (μ_2) Gly^- form. Preliminary check has revealed that complexation of Zr polymers with amino-group of glycine is unlikely due to mismatch of the strongly acidic pH range for such complexation and alkaline conditions for the neutral amino-group existence (protonated NH_3^+-group is likely to be repelled by positively-charged Zr hydroxopolymers).

Zirconium hydroxo-bridged tetramers $[Zr_4(OH)_8]^{8+}$ can theoretically form complexes with positive glycinate-ion (Gly^+) only under highly acidic conditions (Table 4.3, species 2-11). Moreover, the increasing number of Gly^+ (μ_1) ligands corresponds to the decreasing value of pH_{opt}. Substantial positive partial charge on hydroxyl-ligands of the Zr tetramer indicate that complexes with $n(Gly^+(\mu_1))>1$ are practically impossible to form. Partial charges $\delta(H_2O)$ on aquo-ligands Zr atoms are also increasing with the increasing number of μ_1 Gly^+ ligands making them more susceptible to hydrolysis.

The situation with complexation of μ_1 and μ_2 zwitter-ion of glycine (Z-Gly) and Zr tetramer (Table 4.3, species 12-21 and 22-27 correspondingly) is similar to the ligand μ_1-Gly^+. Only one zwitter-ion is allowed in the coordination sphere of Zr atoms of tetramer.

Increasing partial charges δ(OH) on hydroxyl-ions make complexes with higher number of μ_1 Z-Gly or μ_2 Z-Gly ligands unfeasible.

In terms of complexing ability towards Zr polymers, the form Gly^- with neutral amino-group and deprotonated carboxylic group seems the strongest ligand. Both μ_1 Gly^- (species 28-37) and μ_2 Gly^- (species 38-43) can form complexes with Zr tetramers (up to 16 μ_1 Gly^- ligands and up to 8 μ_2 Gly- can be present theoretically). The stability of the former indicated by the δ(OH) is somewhat lower than that of the μ_2 ligand. However, susceptibility of aquo-ligands indicated by positive value of $\delta(H_2O)$ is slightly higher for the μ_2 Gly^- ligand. The pH conditions are acidic for complexation of both μ_1 and μ_2 forms of Gly^- with Zr tetramers, albeit the latter is formed under more acidic conditions than the μ_1 Gly^- form. However, there is a clear mismatch between acidic conditions of Gly^- complexation (both μ_1 and μ_2) with Zr tetramers and alkaline conditions of the existence of Gly^- form.

Glycine-bridged forms of Zr hydroxopolymers were also examined. The results of analysis indicate (species 86-95) that among possible μ_2 glycine-bridged octamers only the species with four μ_2 Gly^- bridges are most theoretically feasible due to low value of δ(OH), $\delta(H_2O)$ and relatively low δ(glycine). However, the mismatch between the pH_{opt} of the species No 93 (pH_{opt}=0.98) and the conditions of Gly^- form existence determined by $pK_a(NH_2)$=9.25 possibly suggests that the formation of glycine-bridges at least on the level of the octamer formation is quite unlikely.

The increase of the size of Zr hydroxopolymers from n(Zr)=4 to n(Zr)=8 (Table 4.3, Appendix 1, species 44-85), n(Zr)=12 (species 96-131) and n(Zr)=16 (species 132-187) leads to similar patterns discussed for the complexation with acetate- and sulphate-ligands above. Generally, four forms of glycine including μ_1 and μ_2 Z-Gly zwitter-ionic form as well as μ_1 and μ_2 Gly^- anionic form ligand become feasible ligands with the increase of n(Zr) and hydrolysis ratio. The PCM analysis shows that in the acidic medium zwitter-ionic form would dominate complexation equilibrium, while μ_1 and μ_2 anionic forms would become dominant in the mildly acidic to neutral pH conditions. It appears that the increase of pH to quasi-neutral values would favour bidentate ligands rather than monodentate ones.

The positive charge on amino-group of zwitter-ionic form would prevent precipitation of Zr-glycine polymeric complexes. This helps to explain a visually observed delay of the colloid formation in the series **ZrOHGly12** and **ZrOHGly11** with Zr:Gly ratios 1:2 and 1:1 correspondingly to h>1.2, while with the deficit of glycine compared to Zr-ions (series **ZrOHGly21**, Zr:Gly=2:1) the colloid formation proceeds similarly to the series **ZrHCO3** and **ZrOH** at $h \geq 0.6$. Another experimental feature observed in the potentiometric measurements of the series **ZrOHGly12**, **ZrOHGly11**, **ZrOHGly21** is the presence of inflexion point at h~1.6 in all titration curves at the presence of glycine. The hypothesis is that below this hydrolysis ratio and corresponding pH range (3≤pH≤4) glycine can stabilise Zr hydroxo-

polymers and prevent inter-chain bridging of the polymers leading to the formation of amorphous colloidal particles at the point h>1.0 where further chain growth becomes impossible.

Summarising the above theoretical considerations, one can see that the Partial charge model can be a useful tool in the elucidation of speciation patterns in the complicated systems of Zr hydroxo-polymers and non-chelating complexing ligands such as sulphate, acetate-ions and glycine with good predicting ability. Certainly, the structure-independent model can provide only qualitative trends in speciation of metal-ions based on prevailing electrostatic component in their interactions with water, anions and non-chelating complexing agents (e.g. glycine). Nevertheless, the PCM calculations helped us to reveal possible pathways of both complexation and hydrolytic polymerisation of Zr-ions and to correlate the theoretical findings with the extensive potentiometric data described in the present study.

4.2.5. Conclusions

1. Speciation patterns of Zr-ion aqueous solutions of medium concentrations (0.1-0.2 M) were studied in detail in a wide range of hydrolysis ratios and pH, including hydrolysis, polymerisation, hydrous ZrO_2 formation, its structural rearrangement and partial dissolution. The potentiometric titration curves obtained from the multi-batch alkaline titrations (with no complexing agent added) generally follow the same patterns as analogous conventional single-batch titrations discussed in Section 4.1 of the present study. However, the conducted multi-batch titrations are characterised by lower resolution than their single-batch counter-parts owing to the lower number of measured points on the curves. The effect of temperature on the speciation of aqueous Zr-ions was investigated using comparison of room temperature and elevated temperature (90°C) potentiometric titrations. It was found that the temperature effect is mainly of a kinetic nature and leads to thermo-induced polymerisation of zirconium-ions at higher temperature.
2. Effect of non-chelating complexing ligands was investigated experimentally at elevated temperature using multi-batch titration experimental setup. It was found that all three examined ligands – sulphate-, acetate-ions and glycine can induce substantial alteration in the pathways of Zr-ion polymerisation, colloid formation and precipitation. Sulphate-ions, due to strong complexing ability towards zirconium and high negative charge are capable of precipitation of basic zirconium sulphates at Zr:sulphate ratio 1:1 starting from very low pH and hydrolysis ratios around h~0.8 and pH<2.0. The process is virtually complete by the hydrolysis ratio h~1.5 and pH~4.6. Acetate ligands are softer complexing agents than sulphate-ions and at the ratio Zr:Ac=1:1 lead to the formation of colloids presumably consisting of basic zirconium acetates at h>0.0. The process reaches maximum point at h~1.0 and further increase of hydrolysis ratio probably leads to gradual replacement of acetate-ions with hydroxyls of alkali. Precipitation occurs at 'normal' hydrolysis ratio of

h~2.0 and is resulted in the formation of virtually acetate-free hydrous zirconia. Finally, glycine can induce significant alteration in the polymerisation of Zr-ions due to its zwitter-ionic character and formation of a stronger complex than with acetate-ions. The complex Zr-glycine, however, most probably breaks down at h>1.6 and again relatively pure hydrous zirconia is formed.

3. Time-resolved potentiometric measurement in Zr-ion solutions under forced alkaline hydrolysis combined with correlation analysis of obtained time-resolved pH-profiles enabled us to reveal and to support a number of additional features of zirconium speciation undetectable with conventional potentiometric method. These features in hydrolysis ratio domain include suppressed polymerisation and complexation of Zr-ions at very low (negative) hydrolysis ratios, complexation of carbonate-ions of $KHCO_3$ with zirconia in alkaline medium and several others. In the time-domain the findings using correlation analysis include revealing of two different time scales in the time-resolved titrations corresponding to fast hydrolysis and slower condensation reactions and the effect of alkali on the kinetics of stabilisation of the potentiometric signal.
4. Theoretical analysis of Zr-ion complexation with non-chelating ligands (sulphate, acetate and glycine) has proved useful for elucidation of possible mechanisms of complexation, most probable compositions of the complexes and the effect of complexing agents on the hydrolysis-condensation pathways in the hydrolysed Zr-ion solutions. These findings were correlated with the results of potentiometric in order to enable better understanding of the non-chelating complexation with Zr-ions.

4.3. Application of Xylenol Orange organic reagent assay in the multi-batch titrations of Zr-ions at elevated temperature

There are a number of spectrophotometric methods available for the studies of the speciation of metal ions [28]. A good example of successful implementation of a spectrophotometric method for the studies of metal hydrolysis is so called 'Ferron method' utilised for the evaluation of the kinetics of Al-ion hydrolysis [29]. As was mentioned in the Chapter 1, using this method workers have been able to distinguish between at least three kinetically separate phases of Al-ion hydrolysis/condensation and corresponding species [29].

Numerous requirements are to be fulfilled in order to create and apply such a method including thorough choice of organic reagent, good analytical properties of the corresponding analytical reaction with the target metal ion, etc. [30]. To our knowledge only few spectrophotometric methods involving organic reagent assays have been proposed in the literature so far for the studies of Zr-ion hydrolysis. However, such method, although indirect, would be useful for the studies in Zr-on aqueous chemistry in the absence of more powerful techniques (e.g. ^{27}Al NMR spectroscopy as for Al-ions).

4.3.1. Choice of organic reagent

A great number of organic reagents is able to form strong complexes with zirconium-ions [30,31]. Xylenol Orange was chosen due to following advantages of this reagent:

1. Xylenol Orange (XO) forms strong and intensively coloured complexes with zirconium-ions over a wide range of pH [30]. Also it is important that XO is able to form complexes with Zr-ions at very low pH (down to pH=0) that is relevant to our studies where high concentrations of Zr-ion are used and highly acidic solutions are produced as a result.
2. Xylenol Orange forms complexes with zirconium of the composition 1:1 [32]. This is crucial for the metal speciation studies, since many organic reagents form complexes of different stoichiometric ratios with metal ions which can absorb light at different wavelengths that makes evaluation of the speciation more complicated.
3. Due to a number of hydrophilic groups of the XO molecule the complex with Zr-ions remains soluble over a wide range of XO and Zr-ion concentrations [32].
4. Kinetics of the complex formation of XO with zirconium is quite fast - the equilibrium in the system is usually established within minutes [30].
5. The maximum of absorbance of Zr:XO complex is located at λ~550 nm (for monomeric zirconium ions) which is important in terms of minimisation of Raleigh scattering from Zr hydrolytic polymers which decreases with the increase of wavelength [32].
6. XO is commercially available reagent, the complexation of which with monomeric Zr-ions and the spectrophotometric properties of the complexes are well established.

4.3.2. Evaluation of Xylenol Orange assay for the determination of hydrolysed Zr-ions

Prior to evaluation of analytical (spectrophotometric) reaction of Xylenol Organge with hydrolysed Zr-ions the reagent itself was evaluated using UV-Vis spectroscopy. The spectra of Xylenol Orange ($1*10^{-4}$ mol/L) solutions at different pH conditions were acquired in a preliminary evaluation (Fig. 4.13).

From the data of Fig. 4.13 one can see that there are two major bands observed in the electron spectra of Xylenol Orange solution at different pH conditions with maxima at λ=435 nm and λ=557 nm. The first band (λ=435 nm) is related to the protonated (neutral) form of the reagent and prevails in acidic medium (pH < 7), while the second band at λ=557 nm is related to the deprotonated (carboxyl-anion) form of the reagent and dominates at neutral and basic conditions (pH≥7) [32]. There is a third band indicated in XO spectra at pH=0.0 and pH=0.5 with λ_{max}~522 nm, which is probably related to protonation of carboxylic groups or sulphonic group of the reagent.

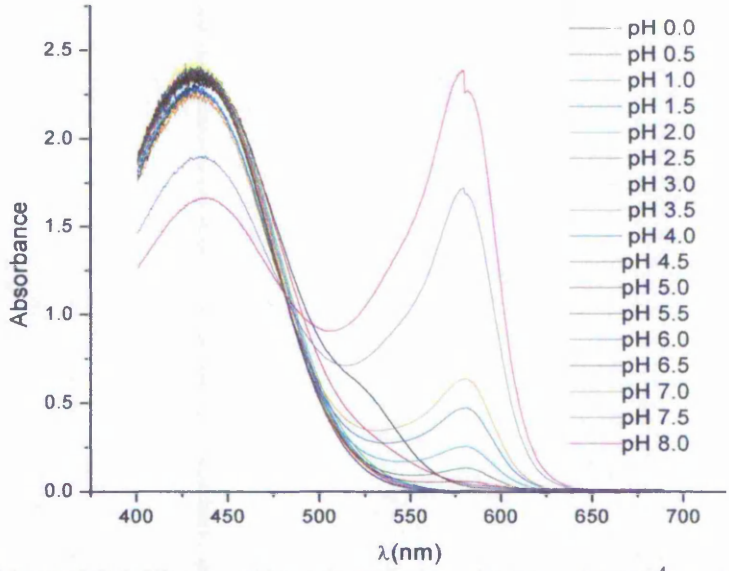


Fig. 4.13. Electronic spectra of pure Xylenol Orange solutions ($1*10^{-4}$ mol/L) at different pH values.

The first step of the experimental evaluation of Xylenol Orange assay was to verify the optimum conditions of the complex formation between Zr-ions and XO using a standard solution of Zr-ions (initial concentration 1000 μg/ml in 2 M HCl) which contains only monomeric form of Zr-ions. The procedure for obtaining the calibration curve is described in the Section 2.4. The spectra of the complex XO:Zr (monomeric) and a corresponding calibration graph are shown in Fig. 4.14.

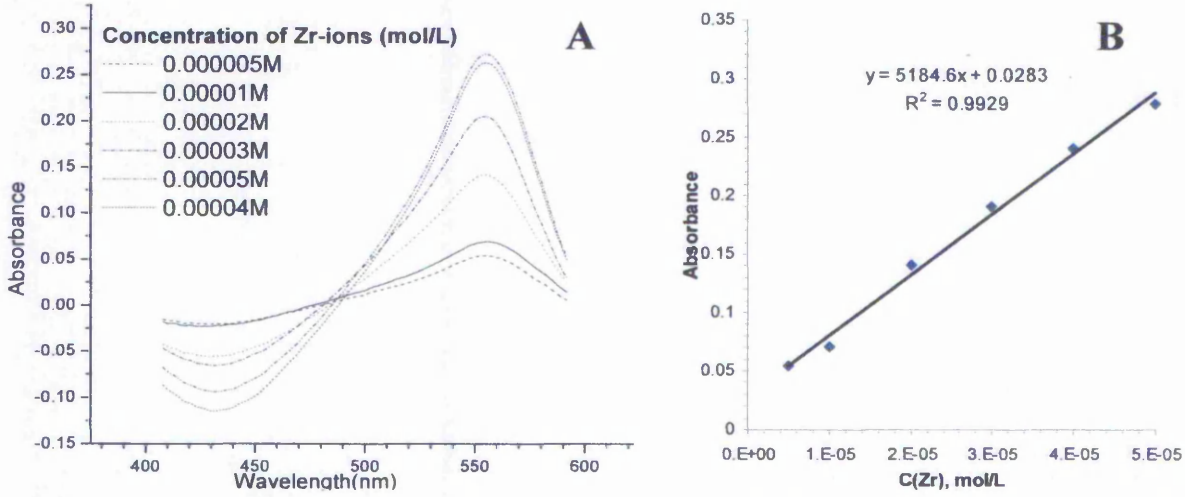


Fig. 4.14. Differential UV-Vis spectra (*A*) and the calibration graph at λ=555 nm (*B*) for the evaluation of Xylenol Orange assay with zirconium-ions.

The spectra of XO:Zr(monomeric) shown in Fig. 4.14*A* indicate a single maximum at λ_{max}=555 nm with absorbance intensity increasing with the increasing concentration of Zr-ions. The calibration graph built from absorbance values at λ_{max}=555 nm (Fig. 4.14*B*) indicates a linear relationship between the absorbance of the complex XO:Zr and concentration of zirconium. High linearity of the graph is supported by the correlation

coefficient (R^2) close to 1. The background signal indicated by the second coefficient of the linear equation presented in Fig. 4.14*B* (*b*=0.0283) is quite close to zero indicating the absence of strong background signal. Thus, Xylenol Orange assay is suitable for determination of monomeric zirconium in the range of concentrations $5*10^{-6}$-$5*10^{-5}$ mol/L.

The next step of the evaluation of Xylenol Orange assay was to verify the method with the samples produced by multi-batch titrations of fairly concentrated (0.2 M) solutions of zirconyl chloride. Conditions of the analytical determination of Zr-ion hydrolysed complexes with XO, such as sample dilution, pH order of reagent addition, Zr:XO ratio, were first optimised (cf. Section 2.4, Chapter 2) in order to obtain statistically consistent data from the UV-Vis measurements of the XO:Zr (polymeric) complex. The established conditions for XO:Zr(polymeric) complex formation are following: pH=1.0; minimum XO:Zr=2:1; reagent addition order: 0.1 M HCl; XO ($C(XO)_{final}=1*10^{-4}$ mol/L); 0.5 ml aliquot of Zr-ion sample solution diluted 4000 times ($C(Zr)_{final}=5*10^{-5}$ mol/L); complex was stirred at room temperature for 15 min to develop an intensive colour (dark orange to red-brown) and measured in 1 cm PMMA cuvette against blank solution of XO prepared at identical conditions without zirconium-ions.

The differential electronic spectra of the complexes of XO with zirconium polymers (solutions of $ZrOCl_2$ hydrolysed to a different extent with KOH, series **ZrOH**) have shown two peaks with maxima at 510 and 575 nm (Fig. 4.15). The maxima of the complexes were confirmed using a mathematical deconvolution with assistance of the Microcal Origin 6.0 software peak-fitting module.

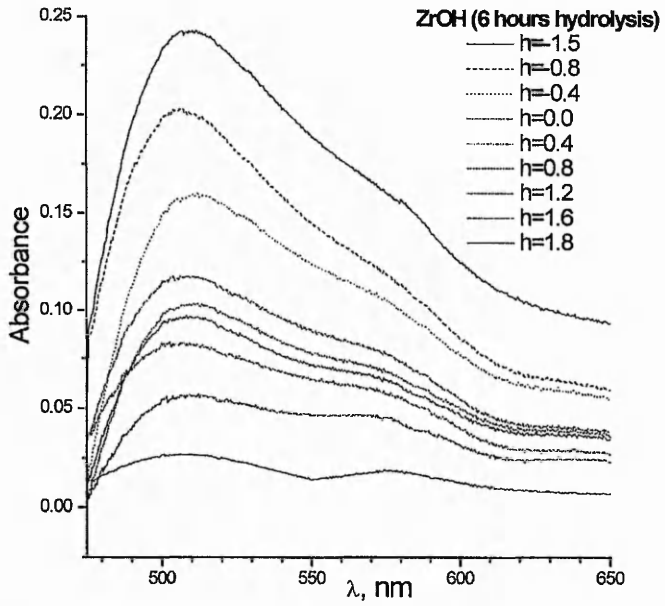


Fig. 4.15. Differential electronic spectra of the samples **ZrOH** at 6 hours of hydrolysis treated with Xylenol Orange at pH=1.0.

One can see from the spectra in Fig. 4.15 that their shape and the maximum positions of two spectral bands (λ=510 nm and λ=575 nm) remain almost unchanged in the hydrolysis

ratio range $-1.5 \leq h \leq 1.8$. Moreover, the absorbance ratio between these two maxima is maintained practically constant: I_{510}/I_{575}=1.5-1.6. Thus, both electronic bands observed in the UV-Vis spectra of hydrolysed zirconium-ions at the presence of Xylenol Orange presumably belong to the same complex. At hydrolysis ratios $h \geq 2.0$ there is practically no UV-Vis signal in the differential spectra. In some cases the absorbance value increases at $h \geq 2.5$, however, the ratio between the maxima at λ=510 nm and λ=575 nm varies significantly indicating that other species than the complex XO:Zr can be present (e.g. free or XO molecules or their deprotonated forms). Therefore, the data at $h \geq 2.0$ (neutral and alkaline solutions of hydrolysed Zr-ions) should be treated with caution.

Additional experiments were also conducted by adding different amounts of zirconium solutions at h=0 and h=0.6 (after 48 hours of hydrolysis at 90 °C) to XO solutions at pH=1.0. It was found that the absorbance intensity of the complexes of XO with corresponding zirconium polymers (λ=510 nm) is linearly proportional to the amount of solution of hydrolysed Zr-ions added and calculated linear correlation coefficients R^2 exceed 0.95 for both zirconium samples at h=0.0 and h=0.6 upon dilution of 0.2 M solution to a different extent ($5*10^{-6} \leq C(Zr)_{final} \leq 5*10^{-5}$ mol/L) at pH=1.0. This indicates that the analytical signal from XO:Zr(polymeric) complex is proportional to the concentration of Zr polymers.

4.3.3. Results of Xylenol Orange Assay. Graphs 'Absorbance vs. hydrolysis ratio'

Results of XO assay application for the multi-batch series of alkaline titrations of Zr-ions are presented in the form of a graph of absorbance value (A) vs. hydrolysis ratio (h). The results for the series **ZrHCO3**, **ZrOH**, **ZrOHSO4**, **ZrOHAc**, **ZrOHGly12** and **ZrOHGly21** are shown in Fig. 4.16. (for some series XO assay was conducted only at 24 and 48 hours hydrolysis time).

The data of Fig. 4.16 show that the maximum absorbance of XO:Zr complex in centrifuged samples is at the most acidic conditions (h=-1.5), regardless of the conditions of experiment (type of alkali, presence of foreign anion or complexing agent - glycine). With the increase of hydrolysis ratio the XO:Zr complex concentration tends to decrease.

The shape of the 'absorbance vs. hydrolysis ratio' curves calculated from the results of XO assay for the series **ZrHCO3** (Fig. 4.16) indicate that the intensity of the complex absorbance and, therefore, the concentration of active sites in zirconium polymers accessible for Xylenol Orange decreases almost exponentially with the increase of the hydrolysis ratio in the range $-1.5 \leq h \leq 4$. The curves from the XO assay obtained at 24 and 48 hours of hydrolysis (series **ZrHCO3**) practically coincide (within <5 of absorbance value in most cases) in the whole hydrolysis ratio range in question that correlates well with kinetic potentiometric data discussed in the previous section. It also appears that there are two consecutive decays in the curves from the series **ZrHCO3**: the first one starts at h=-1.5 and ends at h~1.0, while the second decay of the curve is observed at $h \geq 1.0$. This feature may indicate two different

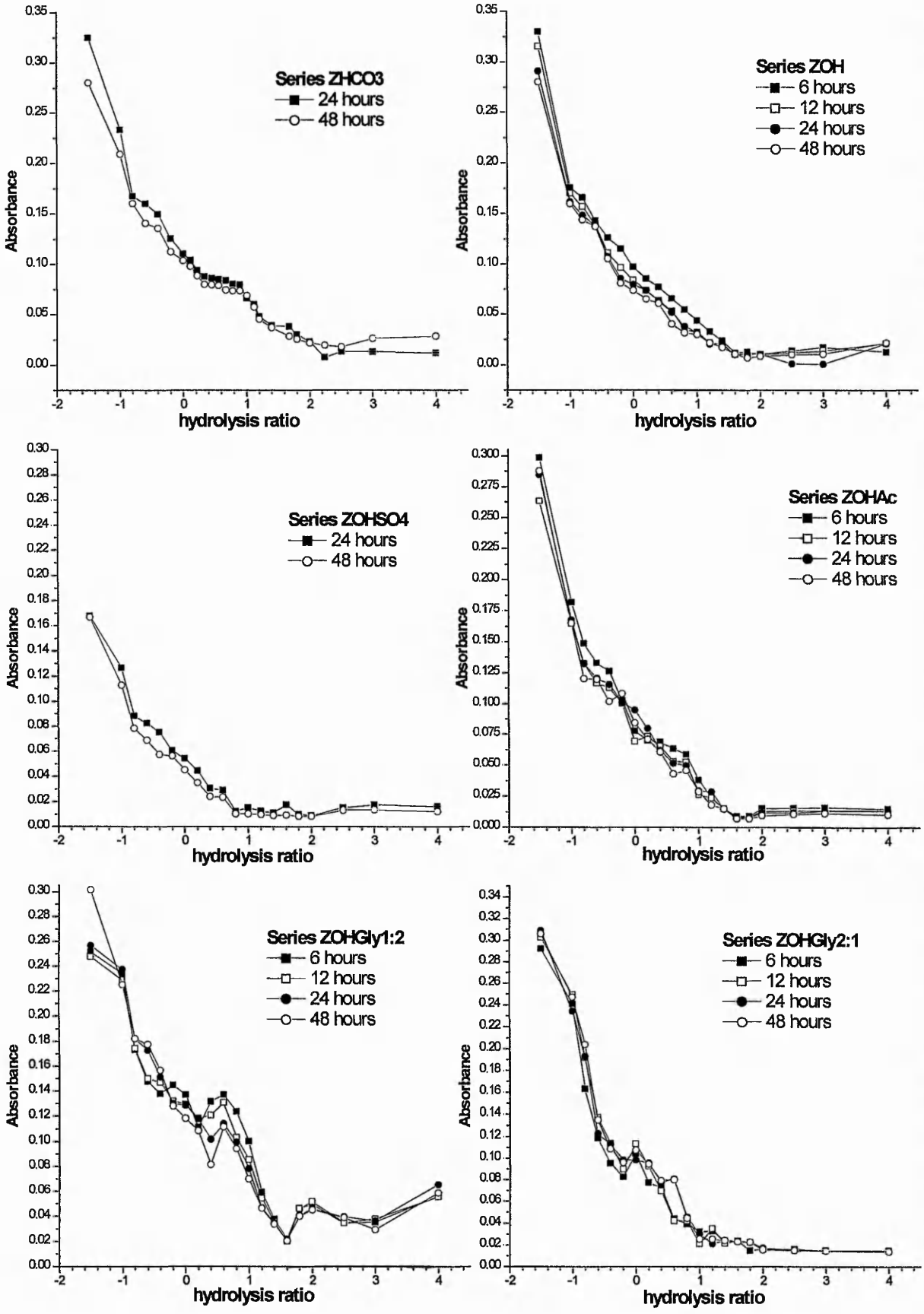


Fig. 4.15. 'Absorbance vs. hydrolysis ratio' graph from Xylenol Orange assay for the series **ZrOH** (λ_{max}=510 nm). The legend indicates time of zirconium solution hydrolysis.

mechanisms prevailing in the mentioned ranges of hydrolysis ratio: chain-like condensation below h=1.0 and 3D inter-chain condensation at h>1.0 which correlates well with the model of Zr-ion polymerisation described in Section 4.1.4.

In the case of the series **ZrOH** the shape of the experimental curves obtained from the XO assay generally follow an exponential decay shape in the hydrolysis ratio range $-1.5 \leq h \leq 4.0$ similar to that of the series **ZrHCO3** (Fig. 4.16). From the comparison of the XO graphs for the series **ZrOH** and **ZrHCO3** one can find that the replacement of weak $KHCO_3$ alkali with much stronger KOH as a titrant in the multi-batch titrations can be traced indirectly using XO assay since the decay of the absorbance value becomes more pronounced in the latter case, and the minimum absorbance at λ=510 nm in the corresponding spectra of **ZrOH** is reached earlier ($h \geq 1.6$) than in the case of **ZrHCO3** ($h \geq 2.0$). Moreover, there is one decay only over the whole range of h for the series **ZrOH**, which is different from two apparent decays observed in the series **ZrHCO3**. Therefore, strength of alkali can alter the degree of polymerisation of Zr-ions, being lower in the case of $KHCO_3$ than for KOH.

The presence of sulphate-ions drastically changes the results of XO assay (Fig. 4.16). Although, the overall shape of the 'A vs. h' curve is similar to the series **ZrOH** and **ZrHCO3**, the intensity of the absorbance from XO:Zr complex is significantly (ca. 3 times) lower even at very acidic conditions (h<0.0). Another feature of the series **ZrOHSO4** is that the decay of the 'A vs. h' curve is practically completed at h~0.8-1.0 that correlates well with the inflexion point observed in the potentiometric titration curves described above. Hence, sulphate-ions substantially reduce the amount of 'soluble' Zr hydrolytic polymers and completely remove Zr-ions from solution at $h \geq 1.0$.

Acetate-ions (series **ZrOHAc**) also change the outcome of XO assay (Fig. 4.16). The curve 'A vs. h' behaves similarly to pure Zr-ion solution titrations (**ZrOH** and **ZrHCO3**) at low hydrolysis ratios h<-0.8. From h~-0.8 acetate-ions start to affect the amount of Zr-ions detectable with XO assay, effectively decreasing the amount of Zr-ions available for UV-Vis detection, albeit to a lower extent than sulphate-ions. This is in line with potentiometric measurements which indicate formation of Zr-Ac complexes within hydrolysis ratio range $-0.8 \leq h \leq 1.0$.

At the presence of the two-fold molar excess of glycine (series **ZrOHGly12**) the results of XO assay indicate that the highest concentration of XO:Zr complex is obtained for the samples at lower hydrolysis ratios, similarly to the series **ZrOH** and **ZrHCO3** (Fig. 4.16). The intensities from XO:Zr complex of the series **ZrOH**Gly1:2 are comparable with those of **ZrOH** and **ZrHCO3** series up to h~0.0-0.2. Starting from h~0.2 the absorbance from XO:Zr complex is higher than that for **ZrOH** and **ZrHCO3** series. However, the measurable amount of XO:Zr complex is observed up to h~1.4-1.6, which is similar to the series **ZrOH** and different from the series **ZrHCO3**. Summarising the above one can assume that in the case of

excess glycine the more 'soluble' form of Zr polymer stays in solution after centrifugation. The latter fact can be a consequence of either (*a*) 'solubilisation' of Zr polymers with glycine ligands, or (*b*) preventive effect of glycine on the hydrolytic condensation of Zr polymers.

In the case of the series **ZrOHGly21** where glycine is in deficit comparing to Zr-ions, the overall '*A* vs. *h*' curve obtained from XO assay is quite similar to that for the series **ZrOH** (Fig. 4.16) except for the region within $-0.2 \leq h \leq 1.0$. At this region absorbance values from the complex XO:Zr are higher for the series **ZrOHGly21** than for the series **ZrOH**. The absorbance approaches minimum at $h \sim 1.4\text{-}1.6$. Therefore, even minor quantities glycine molecules are able to affect the process of polymerisation of Zr-ions, however the effect is much smaller than in the case of the series with the two-fold excess of glycine (**ZrOHGly1:2**) that demonstrates the importance of glycine concentration in the system in question.

4.3.4. Kinetics of Zr-ion condensation as observed with Xylenol Orange assay

Implementation of the multi-batch approach together with Xylenol Orange UV-Vis organic reagent assay proposed in the present study, one could also retrieve additional kinetic information on the processes occurring in Zr-ion solutions upon forced alkaline hydrolysis at elevated temperature. The results of XO assay in the time domain are shown in Fig. 4.17 for the series **ZrOH** as an illustrative example.

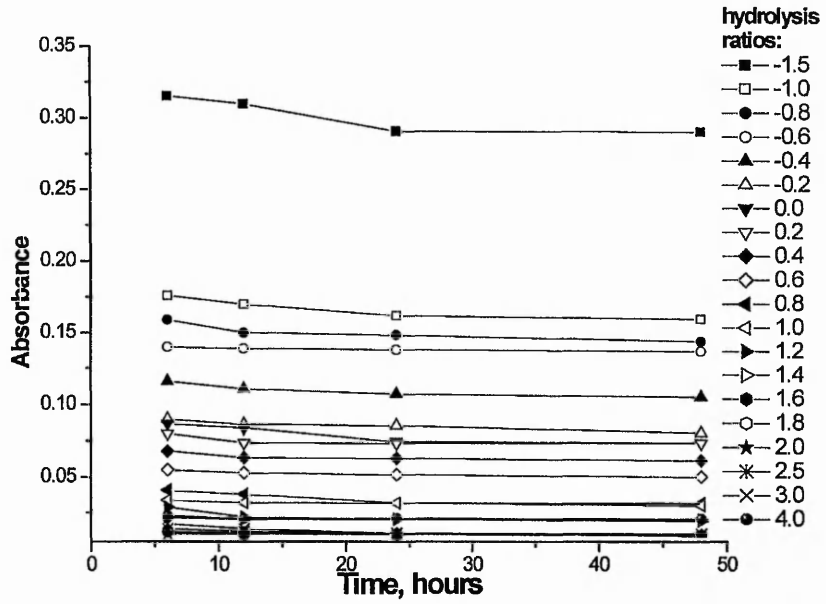


Fig. 4.17. Kinetic curves of XO:Zr complex absorbance at 510 nm against time of reaction. Results from the series **ZrOH**.

As follows from Fig. 4.17, kinetic curves obtained from XO assay of the series **ZrOH** (titration of pure ZrOCl2 solution with KOH) have a slightly decaying shape within the time span studied using this technique (from 6 to 48 hours). Unexpectedly, in apparent contradiction with the potentiometric data discussed in previous section, the most significant

change of absorbance value (~7 % of intensity) and corresponding concentration of XO:Zr complex occurs in highly acidic medium (h=-1.5). This could indicate that in spite of the high concentration of protons, condensation process can still proceed even in such unfavourable conditions due to high temperature of the reaction (90°C). The overall variation of absorption intensity at 510 nm slightly decreases steadily with the increase of hydrolysis ratio, however even at h>1.0 it is still above ca. 5 % of the total intensity. The values of absorbance measured at h>1.0 are less then 0.05 units of absorbance that is close to the noise level of the spectrum (0.01-0.02 absorbance units). Therefore, at higher hydrolysis ratios estimation of the kinetics of condensation becomes unreliable. Another drawback of the kinetic data obtained from XO assay is that due to the real-time organisation of the multi-technique monitoring of the reactions in the multi-batch titrations of Zr-ions carried out in the present study, it was impractical to conduct XO assay at shorter times of reaction (<6 hours). However, from the kinetic data of potentiometry it follows that the major processes occurring in Zr-ion solutions are mainly complete by 6 hours of the reaction. This results in the practically featureless kinetic curves shown in Fig. 4.17. Nevertheless, the proposed UV-Vis assay has a potential to be implemented in the kinetic studies of Zr-ion hydrolysis.

4.3.5. Discussion of the results of Xylenol Orange organic reagent assay

Prior to discussion of the results of XO assay the following preliminary assumptions must be taken into account:

1. By the analogy with complexation of monomeric Zr-ions and XO, the formation of the complex of XO and zirconium atoms of the polynuclear species is assumed to be stoichiometric with the ratio Zr:XO=1:1 regardless of the hydrolysis ratio of Zr-ion samples.
2. The relationship between absorbance intensity and concentration of Zr atoms in the hydrolytic polymers is assumed to be linear over the whole range of the hydrolysis ratios studied.
3. Presumably, the effect of Raleigh scattering from Zr hydrolytic polymers is compensated by the inclusion of the blank spectra of Zr polymers in water produced at the same hydrolysis ratio, centrifugation procedure and following dilution as the samples which underwent XO assay.

The first assumption is supported experimentally from the data of the preliminary investigation of Zr-ion solutions at h=0.0 and h=0.6 with XO assay mentioned above. The results indicate that the intensity of absorbance from XO:Zr complex at 510 nm is linearly proportional to the degree of dilution (and consequently, concentration) of Zr polycations. Certainly, the fact of stoichiometric binding of XO molecules to closely packed Zr hydrolytic polymers as well as the absence of Raleigh scattering effect on the absorption intensity of XO:Zr should be examined further on the basis of chemical, structural and spectroscopic

evidence. However, it would constitute a systematic dedicated work which is out of the scope of the present study. The linearity of the relationship between the intensity of light absorption at 510 nm and the concentration of Zr-atoms available for complexation with XO was implemented in this work as a sufficient prerequisite for carrying out the UV-Vis XO assay.

Comparison of the electronic absorption spectra of the complex of Xylenol Orange with allegedly monomeric Zr-ions of standard Zr-ion solution in concentrated (2 M HCl) (Fig. 4.14) and analogous spectra of XO with polymeric Zr-ions at $-1.5 \leq h \leq 1.8$ shows that in the first case only one maximum at λ_{max}=557 nm is observed, while the spectra with Zr polymers contain two maxima at λ=510 and λ=575 nm (the letter being of lower intensity). The reason for the occurrence of two electronic bands in the spectra of XO:Zr (polymeric) is unclear, however it can be assumed that two types of the complex with XO ligand can arise from (*a*) two distinct binding sites of Zr hydrolytic polymers; (*b*) two different geometries of the complex, or (*c*) the electronic band of the complex is split into two distinct bands. Certainly, these assumptions need further investigation. It has to be taken into account that in the case of monomeric species the complex is four-dentate (it involves all four chelating carboxylic groups of XO) while the polymeric nature of the hydrolysed polynuclear species at higher concentrations of zirconium set some structural constraints on the complexation with the organic reagent in question.

The ratio of the two maxima in electronic spectra of XO:Zr remains practically constant (~1.5-1.6) over the range $-1.5 \leq h \leq 1.8$, thence the choice of the band for quantification of XO molecules bound to Zr polymers does not play important role. The wavelength of 510 nm was chosen which has higher intensity and therefore is more sensitive in he variation of XO:Zr complex concentration.

The results of experimental investigation of the relationship between the extent of complexation of zirconium-ions with XO (represented as absorbance value of the XO:Zr complex at λ=510 nm) and the extent of hydrolysis-condensation in zirconium solutions at the elevated temperature (represented as the hydrolysis ratio of the sample) has shown that the complexation with XO is strongly dependent on the hydrolysis ratio of a particular sample (Fig. 4.16). For pure Zr-ion solutions hydrolysed with KOH (series **ZrOH**) this relationship is close to the exponential decay, where the concentration of the XO:Zr complex decreases with the increase of the hydrolysis ratio. The results of the XO assay show that hydrolysis-condensation processes of Zr-ions in 0.2 M solutions at 90 °C start as early as at h=-1.0, ever increasing with the growth of the value of h.

In the case of the hydrolysis of Zr-ions with weak alkali ($KHCO_3$, series **ZrHCO3**) it was observed that the curve of the graph 'absorbance vs. hydrolysis ratio' obtained from XO assay contains a plateau in the range $0.2 \leq h \leq 1.0$ and the overall shape of the curve can be better described as two consecutive exponential decays: below h=1.0 and above this value.

When increasing the hydrolysis ratio from h=-1.5 to h=-1.0 there is ca. 1.5-1.75 times

decrease in absorbance of the XO:Zr complex in both series **ZrOH** and **ZrHCO3**. This can be a first indirect evidence (apart from SAXS measurements reported in [6]) of the transformation of tetrameric zirconium units prevailing at very acidic conditions into octameric units. A slight trend of the absorbance value growth at high hydrolysis ratios (h>2.5) can be a result of the dissolution of fresh hydrous zirconia precipitate by carbonate-ions with the formation of soluble polymeric units more accessible for XO molecules.

The presence of anions and complexing agents in Zr-ion solutions hydrolysed at high temperature can dramatically change the shape of the curves 'absorbance vs. hydrolysis ratio' derived from the XO assay (Fig. 4.16). In the case of sulphate-ions (series **ZrOHSO4**) the absorption intensity at 510 nm is about three times lower than for the series conducted with pure Zr-ion solutions (**ZrOH** and **ZrHCO3**) even at very low hydrolysis ratio of h=-1.5. Further increase of hydrolysis ratio leads to a quick, close to exponential decrease of the intensity of XO:Zr complex supporting potentiometric and visual observations of the early precipitation of Zr basic sulphates reported above. In good agreement with the potentiometric titrations (Fig. 4.8) of the series **ZrOHSO4**, the absolute minimum of absorbance of XO:Zr complex is reached at h~1.0 indicating that no more Zr-ions accessible for XO ligand remain in solution after centrifugation of the samples with h>1.0 and, therefore, most of Zr polymers are precipitated by sulphate-ions.

In the case of acetate-ions present in hydrolysed Zr-ion solutions (series ZrOHAc) the curves of the graph 'absorbance vs. hydrolysis ratio' obtained from XO assay the intensity of XO:Zr complex at h=-1.5 is the same as of pure Zr-ion solutions (series **ZrOH** and **ZrHCO3**). Starting from h=-1.0 and above the intensity of absorbed light at the presence of acetate is systematically lower than that of pure Zr-ion solutions and reaches minimum values (close to zero) at h~1.6. Therefore, acetate-ions do not precipitate Zr polymers as basic acetates, albeit increase the size of the polymers, probably, by the formation of acetate-bridged larger colloidal species. Significant part of the basic zirconium acetate can react with XO ligand (electrostatically bound acetate-ions should be easily replaced by any strong chelating agent such as XO). The complexation with acetate-ions and, hence, the larger acetate-bridged Zr polymers increase in abundance with the increase of hydrolysis ratio and corresponding pH, due to preferable complexation conditions of acetate and Zr-ions in mildly acidic to neutral conditions [18] as was supported by using Partial charge model calculations described above. The inflexion point in potentiometric titration curves of the series **ZrOHAc** probably corresponding to the replacement of acetate-ions with hydroxyls of alkali is located at h~1.0 (Fig. 4.9). This replacement is not indicated in the curves of XO assay (Fig. 4.16). Therefore, the related chemical reaction is manifested by significant pH change, albeit does not force further substantial increase of particle size of Zr hydrolytic colloids.

The presence of the two-fold excess of glycine (series **ZrOHGly12**) leads to the increase of availability of Zr polymers to complexation with XO reagent (Fig. 4.16) in the hydrolysis ratio range ca. $-0.8 \leq h < 1.6$ in comparison with the series conducted with pure Zr-

ion solutions (**ZrOH** and **ZrHCO3**). Therefore glycine (*a*) complexes Zr-ions starting from very low pH and hydrolysis ratio values and the formed complexes remain in 'soluble' (<100 nm) form over the wide hydrolysis ratio range (up to h~1.6). Unlike for acetate-ions, the replacement of glycine with hydroxyls of alkali occurs at h~1.6 and it is probably followed by drastic decrease of small Zr polymers at $h \geq 1.6$. One can assume that higher solubility and smaller size of the Gly:Zr(polymer) complex is related to (*a*) stabilisation of the complex due to the presence of protonated amino-group of glycine; (*b*) prevention of the condensation of Zr-ions separated by complexed glycine molecules.

In spite of the insufficient number of the measurements on kinetic scale (maximum four), which does not allow a rigorous analysis of the kinetic features of the XO assay in this report, there are several kinetic features which can be outlined. In the case of pure hydrolysed zirconium solutions (series **ZrOH** and **ZrHCO3**) the absorbance value and consequently the concentration of the XO:Zr complex tends to decrease with time as hydrolysis-condensation processes proceed (Fig. 4.17). When a complexing agent (glycine) or complexing anion (sulphate or acetate) is added to zirconium solution prior to hydrolysis, the kinetics of the XO assay change to the reverse: concentration of the XO:Zr complex increases as hydrolysis proceeds. This is an important indication that with time the bonding of glycine, sulphate-ions and acetate-ions becomes weaker due to inevitable transformation of zirconium-ions into polymers, amorphous gels and finally precipitates at high temperature set in the experiment. It is especially clearly observed at acidic and neutral hydrolysis conditions where much longer times are required for the mentioned transformations to take place. Generally, in most cases except in the presence of sulphate-ions, after 24 hours of forced thermohydrolysis of zirconium solutions no further increase of XO:Zr complex concentration is observed indicating that the major processes in the systems in question are accomplished by that time.

For the series **ZrOHGly21** where glycine is in deficit compared to Zr-ion concentration, the corresponding 'A vs. h' curve shown in Fig. 4.16 is very close to the analogous curve for the series **ZrOH** and **ZrHCO3** conducted with pure Zr-ion solutions. Only in the range $-0.2 \leq h \leq 0.8$ the intensity of absorbance and corresponding concentration of XO:Zr(polymeric) complex is higher than that of the series **ZrOH** and **ZrHCO3**. Therefore, even minor quantities of glycine (series **ZrOHGly21**) can force alteration in condensation patterns of Zr polymers, albeit to lower extent than higher glycine concentrations (series **ZrOHGly12**).

On the basis of the discussion above one can summarise that the Xylenol Orange spectrophotometric assay can potentially enable one to study in detail both pH- and time-dependent processes in highly concentrated zirconium solutions providing an important information on the relative size of Zr polymers, reactive ability and extent of complexation in the growing zirconium (oxo)hydroxo-polymer chains. This is a firm basis for further quantitative analytical developments.

4.3.6. Conclusions on the results of the Xylenol Orange organic reagent assay

1. For the first time an organic reagent assay based on the use of UV-Vis measurements and Xylenol Orange as a probe was proposed for the studies of condensation of Zr hydroxo(oxo)polymers in the pH (hydrolysis ratio) domain and in the time domain. The proposed assay was preliminary optimised to provide analytical measure of condensation of Zr-ions in the broad pH and hydrolysis ratio range. Further structural, chemical and spectroscopic studies are required in order to provide an exhaustive picture of complexation of Xylenol Orange with Zr hydrolytic polymers which appears to be more complicated than in the case of well established analytical reactions of Xylenol Orange with monomeric Zr-ions. Further improvements of sensitivity and reproducibility of the proposed procedure of Xylenol Orange assay could be beneficial for the implementation of this new method.
2. The effect of alkali strength and the possibility to detect it was demonstrated on the results of Xylenol Orange assay of the series of multi-batch titrations of zirconyl chloride solutions with KOH and $KHCO_3$ at high temperature. Weaker base ($KHCO_3$) leads to lower degree of condensation and wider distribution of Zr polymers than strong alkali (KOH).
3. Varying hydrolysis ratio was found to be one of the crucial parameters of condensation of Zr-ions under forced alkaline hydrolysis at high temperature. The degree of condensation corresponding to the detectable amount of Zr polymers with Xylenol Orange decreases practically exponentially with the increase of hydrolysis ratio of solution that is in line with previous studies described in the literature [6,33]. The transformation of hydroxo-bridges of Zr hydrolytic polymers into oxo-bridges due to internal deoxolation reaction forced by increasing pH (pH≥3.6) and hydrolysis ratio (h≥1.5) leads to eventual precipitation of hydrous ZrO_2 which becomes inaccessible for Xylenol Orange assay.
4. For the first time since the measurements using small angle X-ray scattering reported in [6], possible transformation of Zr tetramers into more condensed Zr octamers was detected with the help of Xylenol Orange assay.
5. The effect of anions (sulphate and acetate) and complexing agent (glycine) on the condensation patterns of Zr-ions was successfully evaluated using Xylenol Orange assay. The found relationship indicate that sulphate-ions tend to precipitate Zr polymers as basic sulphate, acetate-ions possibly form colloidal forms of basic acetates and glycine can at some stage prevent further condensation of Zr polymers and solubilise them due to zwitter-ionic character of glycine molecule.

4.4. Results of the dynamic light scattering measurements of the multi-batch titrations of Zr-ions at high temperature

Dynamic light scattering measurements of the series of multi-batch titrations of Zr-ions at elevated temperature were carried out according to the procedure described in the

Section 2.5 (Chapter 2). Multi-modal particle size analysis was performed using CONTYN particle size distribution program. Results of the measurements are presented in the weight-based distribution mode which gives more realistic values of the percentage of each fraction of particles since unlike the intensity-based distributions it does not depend on the increase of intensity of the scattered light with the increase of particle size [34]. DLS measurements were conducted at 30, 62.5 and 90 degrees scattering angles. The data at 30 degrees were found to be more useful for particle sizes >100 nm, while measurements at 62.5 and 90 degrees provided better reliability for <100 nm particle size detection. Therefore, the results at <100 nm were averaged for 62.5 and 90 degrees measurements, while for particle sizes >100 nm measurements at 62.5 and 30 degrees were averaged. The calculated standard deviation of the mean particle sizes of the particle fractions can therefore serve as a good indication not only for the broadness of the distribution around mean value, but also provide an indirect insight into the deviations of the particle shapes from spherical (larger values of standard deviation correspond to higher probability of the non-spherical particles).

The DLS data from the series **ZrOH**, **ZrHCO3** and **ZrOHGly12** are summarised in two formats (Figs. 4.18-4.20): the first format reflects a relationship between hydrolysis ratio of the batch samples and a mean particle size of each fraction of particles. The second graph describes a relationship between the percentage of each fraction of particles and hydrolysis ratio in the system in question. Particle fractions (<1 nm; <10 nm; <100 nm; <500 nm; <1000 nm, and ≤5000 nm) were chosen arbitrarily on the basis of preliminary analysis of most frequent particle size populations.

Prior to discussion of the DLS data it must be mentioned that long measurement times were required for accumulation of representative particle size distributions (minimum 15 min period of the system equilibration at 20°C in the thermostat of the Coulter N4Plus instrument and about 10-15 min for the measurement at all three scattering angles made in triplicates). Therefore, only analysis of the particle sizes after 48 hours of hydrolysis was possible.

The results of the particle size analysis in the series **ZrHCO3** are shown in Fig. 4.18. From the data of Fig. 4.18 one can find that there are at least six distinct particle fractions can be elucidated from the multi-modal particle size distributions obtained from the DLS measurements. The first fraction is of sub-nanometre size (0.3 nm≤d≤1 nm) is dominant in the range of low hydrolysis ratios (-1.5≤h≤1.3). The lower size particles around 0.3-0.4 nm prevailing at very high acidities (h=-1.5), correlate with the data of SAXS measurements of similar systems [6] where the particle size of the predominant species –zirconium tetramers has been estimated ca. 0.38 nm. With the increase of hydrolysis ratio the particle size tends to increase that may support the hypothesis of Singhal et al [33] on the formation of Zr octamers even at very low pH values. However, large values of standard deviations of the mean particle sizes (up to 50% of the mean value) arising due to the extremely small size of the measured species (one order below practical limit of the Coulter N4Plus meter [34]) does not allow for precise identification of the size of sub-nanometre Zr species.

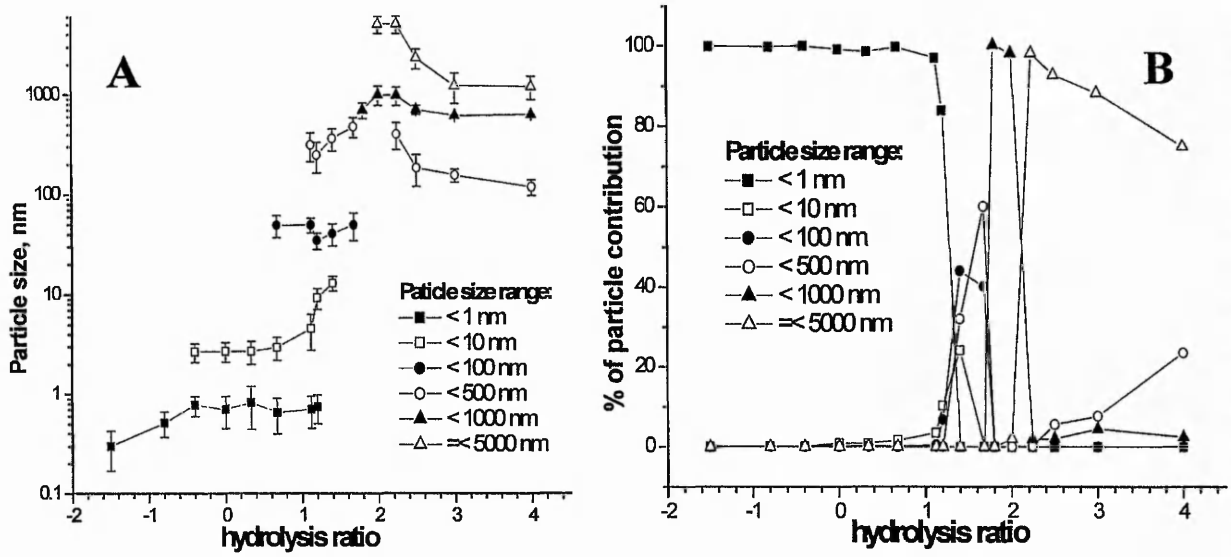


Fig. 4.18. The particle size distribution from the DLS measurements in the series **ZrHCO3**. after 48 hours of hydrolysis at 90 °C. (*A*) Mean particle size of the fractions (listed in the legend) vs. hydrolysis ratio (standard deviation of the mean particle size is indicated as two-side Y-error bars); (***B***) Contribution of the particle fractions (%) in the overall distribution vs. hydrolysis ratio. (Particle sizes are indicated in graph *A* only in the case when a given fraction contributes ≥ 1 % in the overall distribution).

The second fraction of particles with $2 \leq d \leq 10$ nm present in solutions of hydrolysed Zr-ions (series **ZrHCO3**) is located at higher hydrolysis ratios ($-0.4 \leq h \leq 1.4$) than sub-nanometre fraction described above (Fig. 4.18). This fraction probably represents growth of Zr polymers due to chain condensation of sub-nanometre species into larger elongated units. However, the contribution of this fraction into overall number of particles detected (Fig. 4.18B) is below 1 % up to $h \sim 0.8$ and reaches maximum (~20 %) at $h \sim 1.4$. The mean size varies from ca.~2-3 nm at $h < 0.6$ up to ~10 nm at $h = 1.4$.

Larger particles with average size of ca. 40-50 nm are detected in the hydrolysis ratio range $0.6 \leq h \leq 1.6$ (Fig. 4.18). These particles have a relatively narrow distribution of mean values and standard deviations. At higher hydrolysis ratios ($1.0 \leq h \leq 1.8$) significantly larger sub-micron particles ($230 \leq d \leq 370$ nm) appear in solutions of hydrolysed Zr-ions of the series **ZrHCO3**. These particles probably represent first colloidal aggregates of the primary particles. The particle size grows further at higher hydrolysis ratios as indicated by the occurrence of the fraction with $600 < d < 1000$ nm at $1.3 \leq h \leq 2.3$, and even larger particles with $1000 < d < 3000$ nm ($1.0 \leq h \leq 4.0$). The latter large particles of Zr hydrous oxide start to dominate Zr-ion solutions at alkaline conditions ($h > 2.5$).

As follows from Fig. 4.18A, the mean size of large particles of hydrous zirconia decreases significantly at $h > 2.5$ (from $d \sim 2300$ nm to $d \sim 1100$ nm). The fraction of smaller particles with $d \sim 400$-500 nm becomes important (Fig. 4.18*B*) at highly alkaline conditions ($h > 3.0$). These facts can indicate partial dissolution of the oxide particles due to complexation with carbonate-ions in alkaline conditions hypothesised above.

The results of DLS analysis of the series **ZrOH** (after 48 hours of hydrolysis) are given in Fig. 4.19.

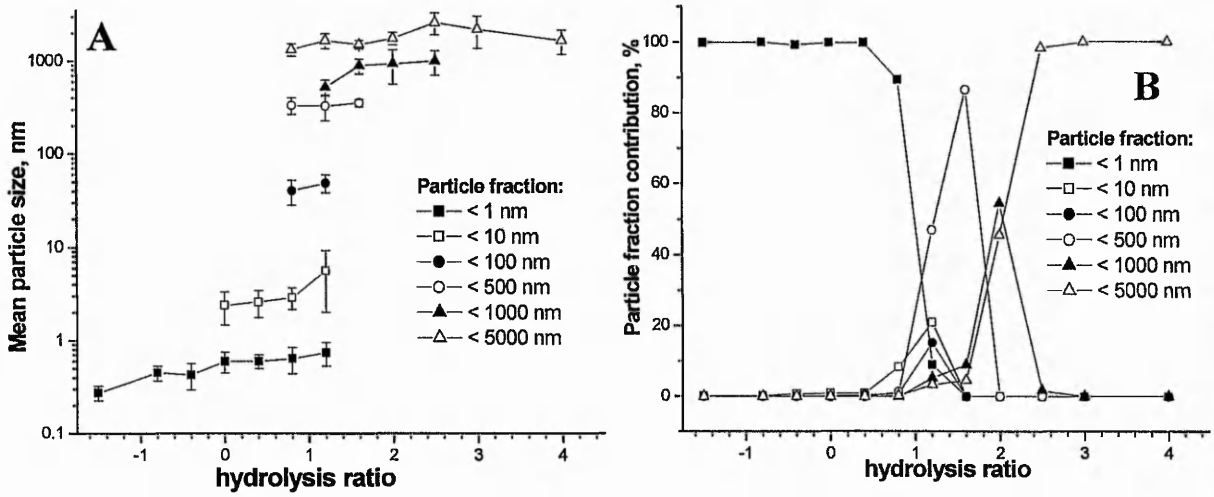


Fig. 4.19. The particle size distribution from the DLS measurements in the series **ZrOH**. (*A*) Mean particle size of the fractions (listed in the legend) vs. hydrolysis ratio (standard deviation is indicated as two-side Y-error bars); (***B***) Contribution of the particle fractions (%) in the overall distribution vs. hydrolysis ratio. (Particle sizes are indicated in graph *A* only if the corresponding fraction contributes ≥ 1 % of the overall distribution).

From the data of Fig. 4.19 follows that similarly to the series **ZrHCO3** there are six fractions of the particles with mean diameters $0.4 \le d \le 1$ nm, $2.0 \le d \le 7.0$ nm, $40 \le d \le 50$ nm, $200 \le d \le 300$ nm, $500 \le d \le 700$ nm and $1000 \le d \le 2000$ nm. The first sub-nanometre fraction dominates Zr-ion solutions at $-1.5 \le h \le 1.2$, identical to the series **ZrHCO3**. The distribution of the particles corresponding to small Zr oligomers (tetramers, octamers, etc.) is relatively narrow in the case of the series **ZrOH** (<20 % of the mean value in most measurements) that possibly indicates absence of chain growth at least at very acidic conditions (h=-1.5). The value of standard deviation indicated as Y-error bars in Fig. 4.19*A* increases with the increase of h that can be a consequence of elongation of the Zr polymer particles due to chain-like growth as discussed above. Apparent particle fraction with $2.0 \le d \le 7.0$ nm is detected in the range $0.0 \le h \le 1.2$ and can be a result of a chain growth, or of appearance of new slightly larger particles in this range of hydrolysis ratios. The particles of average diameter 40-50 nm appear at much narrower range of $0.8 \le h \le 1.2$ comparing to the series **ZrHCO3** and are gradually replaced by still larger colloidal particles with average diameter d~230-240 nm at $h \ge 1.2$. Further increase of hydrolysis ratio leads to the increase of particle sizes to ca. 700-900 nm and ca. 1000-1200 nm. The size of the largest particles of amorphous Zr hydrous oxide dominate in the samples with h>2.5 in the series **ZrOH**.

The comparison of the series **ZrOH** and **ZrHCO3** conducted with alkalis of different

strength indicates that for the series **ZrHCO3** the range of sub-nanometre particles domination is wider due to lower degree of condensation. This fact correlates well with indirect observations of Xylenol Orange described in the previous section. The range of existence of intermediate nanometre-scale colloidal particles with average *d*~45 nm and *d*~235 nm is much narrower for the series **ZrOH** than for **ZrHCO3**. The particles of the final hydrous zirconia precipitate occurring at neutral and alkaline pH conditions are substantially small for the samples hydrolysed with KOH (*d*~1000-1100 nm) than for the samples treated with $KHCO_3$ (*d*~2200-2300 nm). The average size of the particles of hydrous zirconia in the series **ZrOH** remains practically unchanged with the increase of hydrolysis ratio that differs from the data of the series **ZrHCO3**.

The results of the DLS measurements in the series **ZrOHGly12** are shown in Fig. 4.20.

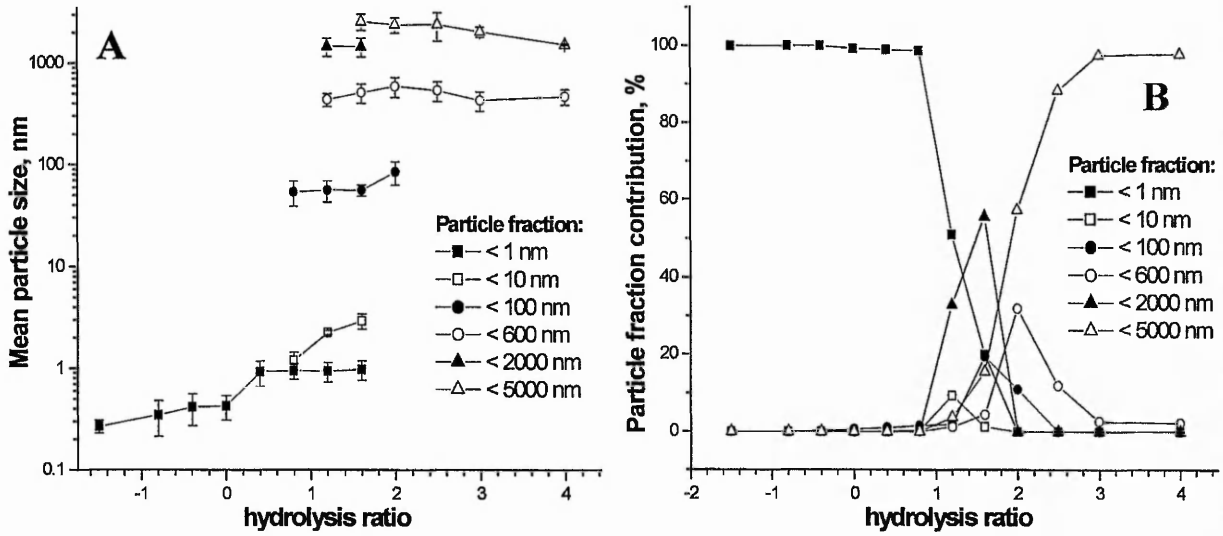


Fig. 4.20. The particle size distribution from the DLS measurements in the series **ZrOHGly12**. (***A***) Mean particle size of the fractions (listed in the legend) vs. hydrolysis ratio (standard deviation is indicated as two-side Y-error bars); (***B***) Contribution of the particle fractions (%) in the overall distribution vs. hydrolysis ratio. (Particle sizes indicated in graph A only if the fraction contributes ≥ 1 % in the overall distribution).

The presence of the two-fold excess of glycine in hydrolysed Zr-ion solutions significantly changes particle size distributions observed in the series **ZrOHGly12** (Fig. 4.20). The sub-nano-metre particles are close to the size of Zr tetramers (*d*~0.38 nm) at highly acidic conditions (*h*=-1.5) similarly to the series with pure Zr-ion solutions (**ZrOH, ZrHCO3**). The mean size of this fraction and broadness of the distribution tends to increase slightly at $-1.0 \le h \le 0$. At $h > 0.2$ a significant jump of the mean size to ca. 0.8-1.0 nm occurs. This particle size is maintained up to *h*~1.6, albeit being gradually replaced by larger particles of Zr polymers with *d*~1-2 nm and eventually d~50-60 nm. The latter fraction is similar to the fraction with *d*~40-50 nm observed in the series **ZrOH** and **ZrHCO3** with slightly larger

apparent particle diameter probably due to complexation with glycine. The nanoparticles of Zr hydroxo-polymers with d~50-60 nm are present in a wide range of hydrolysis ratios ($0.8 \leq h \leq 1.8$) and prevail over other particle fractions at h~1.6 (Fig. 4.20*B*).

Larger colloidal particles of hydrous zirconia with $400 \leq d \leq 500$ nm appear in solutions of hydrolysed Zr-ions as early as at h~1.2. Unlike in the series **ZrOH** and **ZrHCO3**, relatively fine sub-micron colloidal particles are constantly present at different amounts in a very wide range of hydrolysis ratios ($1.2 \leq h \leq 4.0$) and constitute a significant part of the particle distribution at h~2.0 (~35 % of total). The fraction of still larger colloidal particles with d~1100-1500 nm are introduced in a short range of ca. $1.2 \leq h \leq 1.4$. These particles are replaced by the largest particles observable using the DLS measurements with d~2000-2500 nm which appear at small amounts at h~1.6 and start to dominate the particle size distribution at h>2.0. This fraction also decreases its mean particle size with the increase of pH in alkaline conditions (Fig. 4.20*B*).

DLS measurements in the series **ZrOHGly11** with equimolar amount of Zr-ions and glycine produced particle size distributions very similar to the series **ZrOHGly12** that can indicate similarity of effects of two-fold excess of glycine and its equimolar quantities on the process of condensation and colloid formation in the hydrolysed Zr-ion solutions. In the case of the series **ZrOHGly21** with the deficit of glycine in comparison with Zr-ions the results were similar to that of the series **ZrOH** with pure zirconyl chloride solutions indicating that the added amount of glycine (Zr:Gly=2:1, [Zr]=0.2 M) is not sufficient to induce changes observed in the series with higher amount of the aminoacid.

The DLS measurements of the series **ZrOHSO4** and **ZrOHAc** were also conducted but are not presented due to (*a*) large differences between the data at different scattering angles; (*b*) particle sizes with d>5000 nm prevailing over a broad hydrolysis ratio range (h>-0.6 for the series **ZrOHSO4** and h>0.4 for the series **ZrOHAc**). The recommended particle size range for determination with Coulter N4Plus is within 3 - 3000 nm and larger particles become unidentifiable. The presence of such particles also supports the idea of precipitation of Zr hydrolytic polymers with sulphate-ions and the formation of large colloidal acetate-bridged particles in the series **ZrOHAc** discussed above.

Summarising the above, one can see that using multi-batch experimental design of alkaline titrations of Zr-ions it was possible to reveal colloidal transformation occurring in the system upon hydrolysis-condensation at high temperature (90°C) and in the presence of complexing agents (glycine) and anions (sulphate and acetate). The general scheme of colloid formation in hydrolysed solutions of pure $ZrOCl_2$ can be depicted as follows (Fig. 4.21).

From the scheme of Fig. 4.21 it follows that Zr hydroxo-polymers dominate the range of nano- and sub-nanoparticles in the hydrolysis ratio range h<1.0 and particle diameter range d<50 nm. At higher hydrolysis ratios colloid formation occurs primarily due to condensation of primary particles of Zr hydroxo-polymers (d~40-50 nm) into larger colloids, first with d~200-300, then with higher particle sizes. The process of colloid formation is practically

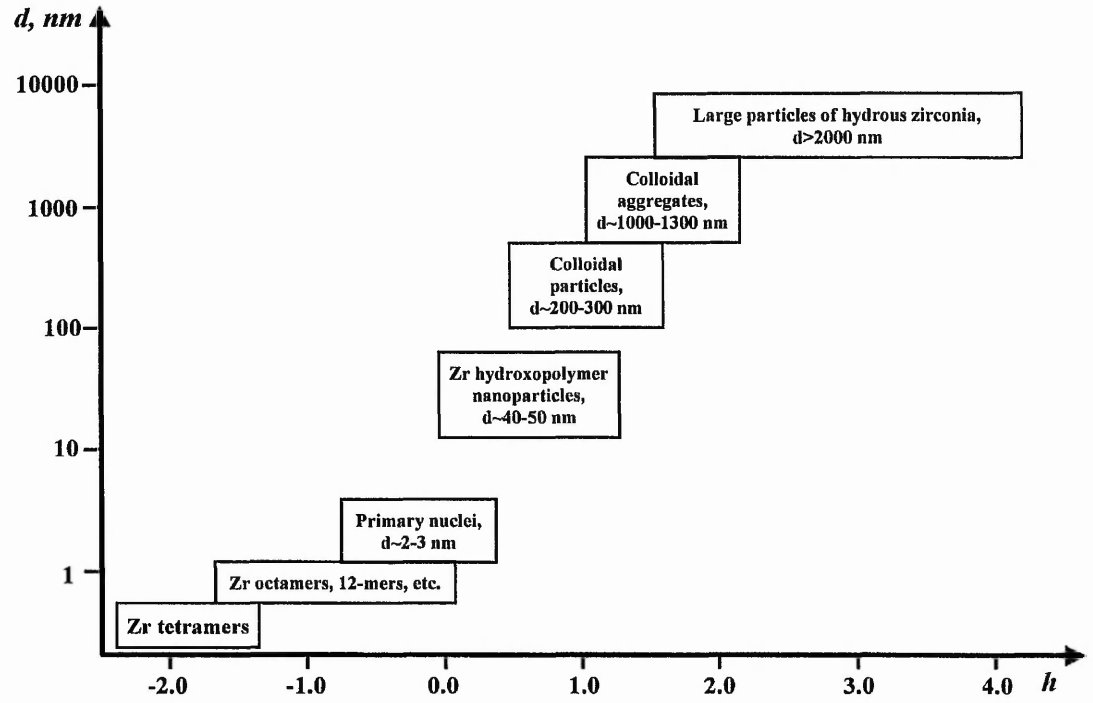


Fig. 4.21. Schematic presentation of the process of colloid formation in hydrolysed Zr-ion solutions under conditions of acidic/alkaline hydrolysis and high temperature (90°C) in coordinates of particle size (d, nm) versus hydrolysis ratio (h).

complete at h~2.0 where large (ca. 2000 nm) particles of hydrous zirconia become dominant. The presented scheme of colloid formation is highly correlated with the proposed pathway of Zr-ion hydrolysis-condensation shown in Fig. 4.5.

The following conclusions can be drawn on the basis of the conducted experiments in solution:

1. The dynamic light scattering method has proved to be useful for the estimation of the particle size distributions in solutions of medium concentrated hydrolysed zirconium-ions. Despite of the extreme difficulty of the systems in question which are highly polydisperse and the lower limit of the measured particle sizes is below 1 nm while the top limit is far above 1000 nm, statistically reasonable and chemically meaningful data were obtained shedding more light on to the complex process of the polymerisation and colloid formation of Zr-ions in aqueous solutions.
2. The predominant species at $h \leq 0$ in the majority of the systems studied are tetrameric zirconium oligomers which have the size of ca. 0.4 nm. It is extremely hard to distinguish these species from slightly larger octamers (d=0.47 nm [6]). However, it is possible to to monitor the tendency of the small oligomers to grow and to reach sizes of ca. 1 nm upon the increase of pH and hydrolysis ratio.
3. When alkaline hydrolysis proceeds, one can find at least five more particulates of different sizes along with tetramers or alike still prevailing at lower hydrolysis ratios ($h \leq 1.2$) in the multi-batch series investigated. The average diameters of these species suggest that they

are primary nuclei (d=2-3 nm), larger particles with d=40-50 nm which result form the growth of the primary particles into colloidal particles with d=200-300 nm as the result of agglomeration of the smaller primary particulates at long times of hydrolysis (48 hours).

4. The effect of alkali strength was elucidated in the DLS measurements. Below h~2.0 weaker alkali ($KHCO_3$) induces formation of smaller particles compared to KOH as a titrant. However, at h~2.0 the resulting particles of hydrous zirconia are larger in the case of $KHCO_3$ as a titrant. Moreover, in alkaline conditions larger particles become a subject to dissolution due to complexation with carbonate-ions and the formation of negatively charged carbonate-containing Zr polymers.
5. Glycine affects strongly the process of Zr-ion condensation and colloid formation. At lower hydrolysis ratios (h<1.0) complexation with glycine reduces the ability of polymeric species to condense further and to aggregate. However, upon the replacement of glycine with hydroxyl-ligands of alkali the aggregation process leads to smaller particle size than in the case of pure Zr-ion solutions. The effect of glycine is two-fold: firstly, it decreases electropositivity of Zr atoms of polymers due to relatively strong complexation; secondly the positively charged amino-group of glycine stabilises Zr polymers in mildly acidic solutions and prevents their aggregation or precipitation as hydrous zirconium oxide.

References

1. J.L. Tosan, et. al. Eur. J. Solid State Inorg. Chem. (1993) **30** 179-193.
2. A. Bleier, R.M. Cannon. In: Better Ceramics Through Chemistry II / Mater. Res. Soc. Symp. Proc. **73** / Ed. by C.J. Brinker, D.E. Clark, D.R. Ulrich (1986) Pittsburgh,Pa.,71-77.
3. G.K. Chuah. Catal. Today (1999) **49** 131-139.
4. H.-J. Noh et. al. Mater. Lett. (2003) **57** 2425-2431.
5. A. Clearfield. Rev. Pure and Appl. Chem. (1964) **14** 91.
6. A. Singhal, L.M. Toth, J.S. Lin, K. Affholter. J. Am. Chem. Soc. (1996) **118** 11529-11534.
7. J.-P. Jolivet. Metal Oxide Chemistry and Synthesis. From Solution to Solid State. (2000) Chichester, Wiley and Sons, 321 p.
8. R.D. Vold, M.J. Vold. Colloid and interface chemistry (1983) Reading, Addison-Wesley.
9. C.J. Brinker, G.W. Scherer. Sol-gel science: the physics and chemistry of sol-gel processing (1990) New York, Academic Press, 908 p.
10. D.F. Baes Jr., R.E. Mesmer. In: The hydrolysis of cations. (1976) New York: Wiley-Interscience, 152-158.
11. K.D. Dobson, A.J.C. McQuillan. Langmuir (1997) **13** 3392-3396.
12. W. Stumm, J.J. Morgan. Aquatic Chemistry. An Introduction Emphasizing Chemical Equilibria in Natural Waters. (1981) New York, Wiley and Sons, 780 p.
13. J.A. Wang et. al. Catal. Today (2001) **68** 21-30.
14. P.D. Southon, et. al. Chem. Mater. (2002) **14** 4313-4319.

15.J.L. Tosan, et. al. Annal. Chim.-Sci. Mater. (1991) **16** 595-606.

16.I.C. Smith, B.L. Carson. Trace Metals in the Environment (1978) V. 3 Zirconium 373-383.

17.G.M. Muha, P.A. Vaughan. J. Chem. Phys. (1960) **33** 194.

18.M. Henry, J.P. Jolivet, J. Livage. Aqueous Chemistry of Metal Cations - Hydrolysis, Condensation and Complexation. (1992) **77** Structure and Bonding, 153-206.

19.S. Hannane et. al. B. Soc. Chim. Fr.. (1994) **131** 262-270.

20.G.O. Noonan, J.S. Ledford. Chem. Mater. (1995) **7** 1117-1123.

21.A.E. Martell. Stability constants of metal-ion complexes. Section 2. Organic ligands. Special Publication No 17 (1964) London, Chemical Society, 758 p.

22.K. Matsui, M. Ohgai. J. Ceram. Soc. Jpn. (1998) **106** 1232-1237.

23.E. Kato et. al. J. Mater. Sci. (1997) **32** 1789-1794.

24.B.I. Nabivanets. Russ. J. Inorg. Chem. (1961) **6** 667.

25.L. Gmelin. Gmelin Handbuch der anorganischen Chemie (1978) Berlin, Springer.

26.A. Nagai et. al. J. Ceram. Soc. Jpn. (1995) **103** 610-615

27.A.C. Geiculescu, H.G. Spencer. J. Sol-Gel Sci. Technol. (2000) **17** 25-35.

28.Element Speciation in Bioinorganic Chemistry / Ed. by S. Caroli (1995) Wiley-Interscience, 474 p.

29.P.M. Jardine, L.W. Zelazny. Soil Sci. Soc. Am. J. (1987) **51** 885-889.

30.Z. Marczenko, M. Balcerzak, E. Kloczko. Separation, Preconcentration and Spectrophotometry in Inorganic Analysis (2000) Amsterdam, Elsevier, 521 p.

31.K. Burger. Organic reagents in metal analysis (1973), Oxford, Pergamon, 266 p.

32.Z. Marczenko. Spectrophotometric determination of elements (1976) New York, Ellis Horwood.

33.A. Singhal et. al. J. Colloid Interf. Sci. (1997) **194** 470-481.

34.N4Plus Coulter Particle Sizer. Instruction Manual (2000).

CHAPTER V. Solid-state studies of Al and Zr speciation

5.1. Introduction

Speciation studies of concentrated metal ion solutions as precursors to materials are mainly limited to "wet" chemical methods due to a tendency to monitor speciation *in-situ* and general inapplicability of the solid-state characterisation techniques for solution chemistry. This significantly limits the arsenal of methods available for speciation studies. An illustrative example is the speciation of Zr-ions and other NMR-inactive metals in aqueous solutions which lack a direct technique for retrieval of structural information concerning solution species. In the literature two main approaches for overcoming the above mentioned limitations can be traced: (*a*) to adapt a solid-state technique for the measurements of speciation in liquid (solution) state; (*b*) to transform solution species into a solid sample and to investigate them using the whole arsenal of solid-state characterisation methods available. The few successful examples of the first approach in the literature include the development of attenuated total reflection spectroscopy for IR measurements of solutes [1,2], adaptation of XRD methods for solution chemistry [3]. This approach appears to be hard to implement, since it requires development and application of dedicated equipment. The second approach mainly includes chemical and physical methods for fast quenching of chemical reactions in solution. For instance, spray-drying is a common method applied to obtain powders of material from solutions [4]. Freeze-drying has been also attempted in order to quench chemical reactions by fast freezing of solutions in a coolant (liquid nitrogen or helium) [5,6]. Both methods have a common drawback of possible severe alteration of the speciation patterns in solution. Spray-drying can easily alter thermosensitive, metastable species, while freeze-drying induces a temperature gradient occurring inevitably when freezing bulk solutions to low temperatures [7]. Some studies on the implementation of 'chemical quenching' exist in the literature where some sort of chemical reagent is introduced into the system to quench the reaction by either (*a*) 'derivatisation' of the species, e.g. complexation, or (*b*) helping the fast removal of the species from solution, e.g. by precipitation. A good example of this technique is stabilisation and precipitation of the crystalline form of Al polycations from solution using sulphate, selenate and other highly charged anions [8, 9]. The problem of 'chemical quenching' is a lack of speed for quenching and possible alterations of speciation patterns of the metal ions caused by strong interaction with quenching agent.

The present Chapter pursues a two-fold task. On one hand, application of the spray-freeze-drying (SFD) method as a new quenching technique for speciation studies is introduced and an attempt is made to validate this method and to show its possibilities and limitations. On the other hand, results of solid-state characterisation of the materials obtained by spray-freeze-drying solutions of hydrolysed Al and Zr ions prepared by the multi-batch titration approach are presented and discussed in an attempt to establish relationships between solid-state and solution data on the speciation of these metal ions.

5.2. Spray-freeze-drying technique for solid-state analysis of solution speciation

The essence of the method of spray-freeze-drying (SFD) has been described in Chapter 2 of this thesis. The introduction of this method in the present work is an attempt to rapidly quench any reactions in solution and to transform solution species intact into a solid state for further characterisation using a number of solid-state techniques, including X-ray diffraction, IR-spectroscopy, thermal analysis, surface area characterisation, etc. It is presumed that effective quenching of all solution reactions is achieved by converting a portion of sample solution into a fine submicron-sized spray using a conventional spray-gun with immediate freezing of the produced aerosol in a large volume of liquid nitrogen. The ultra-small size of solution droplets should reduce the time required for freezing of the solution from seconds (e.g. conventional freeze-drying) to less than microseconds, i.e. at least three orders of magnitude faster. The second part of the method involves normal freeze-drying of the produced frozen 'snow' which is very a gentle, non-destructive technique eliminating the bulk of water from the sample and preserving the major components of the solution intact. Such a combination of very fast freezing and freeze-drying includes the best features of conventional techniques such as spray-drying and freeze-drying, yet allows for elimination of possible alterations of speciation during liquid-solid transformation and for the production of real 'fingerprints' of solution species in the solid state.

To illustrate the appearance and consistency of the materials obtained by SFD a photo of the solid-state samples from the series **ZrOHGly1:2** produced by the hydrolysis of Zr-ion solution with equal amount of glycine at 90 °C for 48 hours is presented (Fig. 5.1).

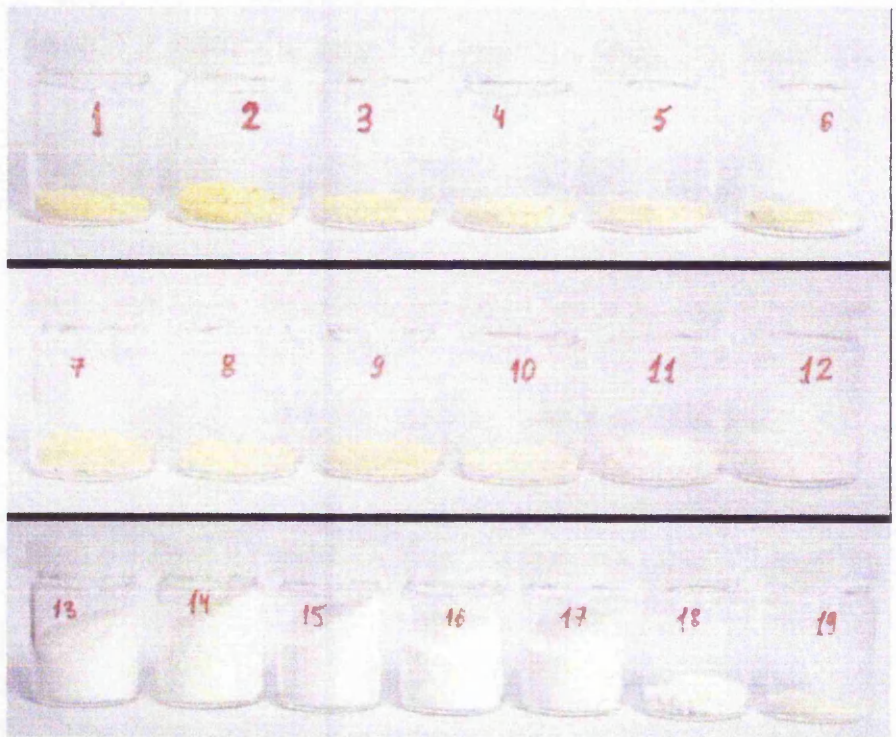


Fig. 5.1. Appearance of the solid samples produced by spray-freeze-drying of multiple batch solutions of the series **ZrOHGly1:1** (48 hours of hydrolysis at 90 °C).

Numbers on the sample vials correspond to the ascending hydrolysis ratios at which the samples were prepared (Table 2.6). One can see from Fig. 5.1 that the appearance and consistency (e.g. the total volume of solid and crystallinity) of the solid materials varies in agreement with the increasing hydrolysis ratio (and increasing sample number). Yellow-coloured (probably crystalline) samples are encountered at h<1.0 (sample numbers 1-10) becoming more pale and then transforming into white amorphous samples at h>1.0 (sample numbers 11-19). The total volume of samples produced by SFD technique increased from lower numbers/hydrolysis ratios to higher numbers/hydrolysis ratios up to h=1.8 (No 17), after which it decreased again. This indicates that even physical characteristics of the samples produced by SFD are determined by the conditions of sample preparation in solution and, therefore, by speciation of Zr-ions.

5.3. Solid-state characterisation of the spray-freeze-dried samples of the series AMK1

Solution studies of the multi-batch series **AMK1** produced at high temperature (90 °C) by alkaline hydrolysis of Al-ions (as 0.2 M $AlCl_3$ solution) have been described in Chapter 3, details of the preparation of the series have been described in Chapter 2 of the thesis. Solid-state characterisation of the SFD samples prepared from this series is reported in this section.

5.3.1. Re-dissolution of the spray-freeze-dried samples of the series AMK1 and ^{27}Al solution NMR measurements

The first step to verify the composition of the solid samples prepared by the SFD technique and its relevance to the initial samples was to compare ^{27}Al solution NMR data of initial and re-dissolved SFD samples. For this purpose, approximately 0.05 g of the solid samples prepared from the series **AMK1** after 6 and 12 hours of experiment were dissolved in 1 ml of distilled water. Freshly prepared solutions of the dissolved SFD samples were measured at room temperature using the NMR setup and the procedure described in Section 2.7.3. Some illustrative examples of the observed ^{27}Al NMR spectra are presented in Fig. 5.2 together with analogous spectra of the corresponding initial samples of the series **AMK1** from Section 3.3.3. The spectra were normalised pair-wise for comparison purposes.

As follows from Fig. 5.2, ^{27}Al NMR spectra of the freshly dissolved SFD samples of the series **AMK1** are quite similar to the initial solution spectra, regardless of the hydrolysis ratio of the sample. All species detected in the initial solutions before application of the spray-freeze-drying are still present in comparable amounts in the spectra of the corresponding dissolved solid samples. The calculated areas of the peaks at 70 ppm (tetrahedral Al of Al_{30}-mer), 63.5 ppm (tetrahedral Al of Al_{13}-mer), 10 ppm (octahedral Al of Al Keggin ions), 4 ppm (Al dimer) and 0 ppm (Al monomers) show t differences in absolute values of less than 15%. Moreover, for the sharp peaks at 63.5 and 0 ppm, the absolute difference in peak areas is always less than 10% and for the peak at 70 ppm of Al_{30}-mer – less than 5% on average.

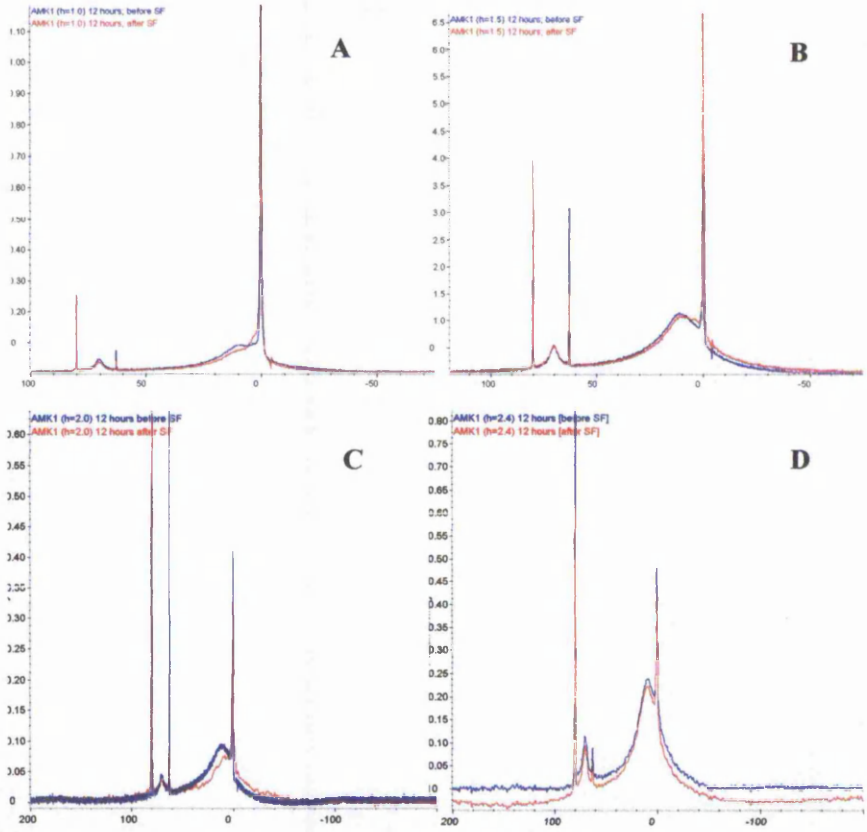


Fig. 5.2. Examples of ^{27}Al solution NMR spectra of the initial samples of the series **AMK1** after 12 hours of hydrolysis (blue), and analogous spectra of the corresponding solid samples prepared by SFD and re-dissolved in water (red). ***A*** – h=1.0; ***B*** – h=1.5; ***C*** – 2.0; ***D*** – h=2.4.

5.3.2. ^{27}Al solid-state NMR characterisation of spray-freeze-dried samples of the series AMK1

Along with re-dissolution experiments described above, solid-state NMR characterisation of selected solid samples from the series **AMK1** was carried out. The spectra were measured by Prof. M. Smith of Warwick University. The results are shown in Fig. 5.3.

Solid-state NMR analysis presented in Fig 5.3 indicates the following signals: broad peak at ca. 68-70 ppm (samples at h = 2.0-2.8) corresponding to the tetrahedral signal from Al_{30}-mer and reaching apparent maximum intensity at h=2.4; sharp peak at ca. 62 ppm (h=2.0-2.6) - tetrahedral Al of the Al_{13}-mer with the maximum intensity at h=2.6 [10]; relatively sharp and intense peak at ca. 9.5-12.5 ppm (h–0.5-2.8) which most probably corresponds to the signal from crystalline gibbsite [11]; the distinct peak 2-3 ppm (h=0.5-2.0) – presumably the signal from Al dimers with intensity maximum at h=1.0; the peak of Al monomers at δ=-1 - -2 ppm (h≤1.0) is the sharp signal from the crystalline aluminium chloride phase [12]. A very broad peak, most likely corresponding to octahedral Al atoms of the Keggin ions is observed at negative chemical shifts (δ_{max}~ -20 ppm), unlike its solution counterpart (δ~10 ppm). The assignment of this peak to Keggin ions (Al_{13}-mer and/or Al_{30}-mer) is based on a correlation of the peak intensity with the peaks at 62 and 70 ppm. There is one more intense peak occurring in the spectra from h=1.5 to h=2.6 at ca. 0-3 ppm. This peak

is initially sharp at h=1.5 and becomes broader at higher hydrolysis ratios. The maximum of the peak shifts constantly with the increase of hydrolysis ratio from ca. –0.5 to ca. 2 ppm and the maximum intensity is reached at h=2.0 and the maximum peak area – at h=2.4. The area of the peak at δ=0-3 is correlated with the signals at δ=62 and δ=70 ppm.

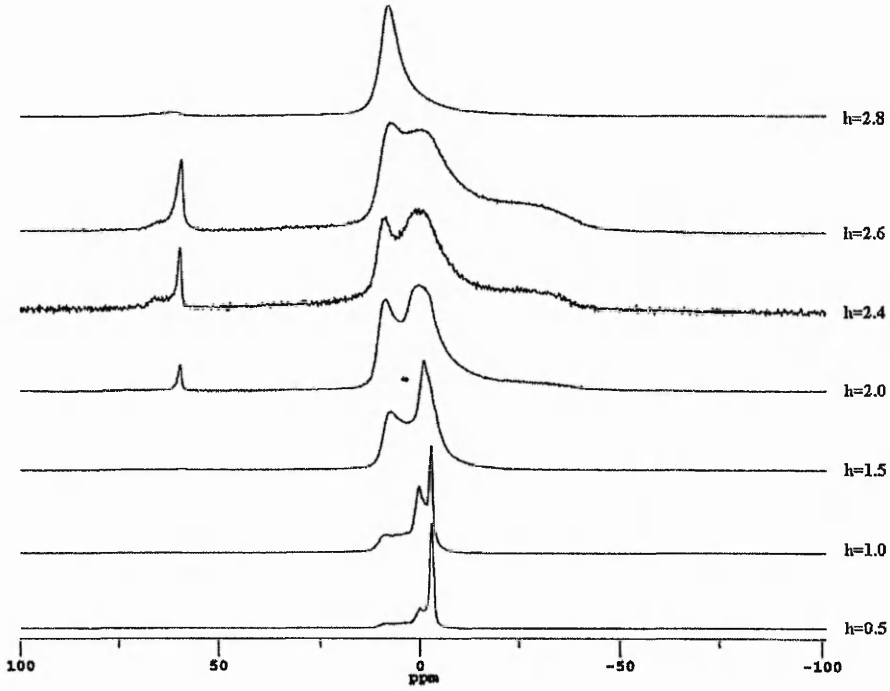


Fig. 5.3. ^{27}Al solid-state NMR spectra of the samples of the series **AMK1** spray-freeze-dried after 6 hours of hydrolysis.

The signals observed in the solid-state NMR spectra are similar to the analogous peaks in the ^{27}Al solution NMR spectra of the initial samples of hydrolysed Al-ions (see Chapter 3) and of the re-dissolved samples (Fig. 5.2). Peak positions in the observed ^{27}Al solid-state NMR spectra are located at 1-3 ppm lower chemical shifts than their solution counterparts. However, peak intensities, areas and their ratios are generally correlated with the analogous values in the solution NMR spectra. Positions of the peaks presumably related to the octahedral Al of Keggin ion are probably differentiated in solid-state NMR spectra of high resolution and are located at different positions than in solution NMR measurements. Perhaps, at lower resolution of the solution NMR spectra these peaks overlap and form a single, very broad peak with the maximum at ca. 10 ppm which includes the signal from Al hydroxide and from the octahedral 'shell' of Keggin ions.

5.3.3. X-ray diffraction studies of the solid samples of the series AMK1

Powder XRD measurements of the spray-freeze-dried samples of the series **AMK1** were acquired as described in Section 2.10.2. Instead of using an internal standard (e.g. corundum) the samples were measured 'as is'. Sample weights in the XRD cell holder were pre-measured and used for the normalisation of the XRD patterns. The measured raw data sets are shown in Fig. 5.4.

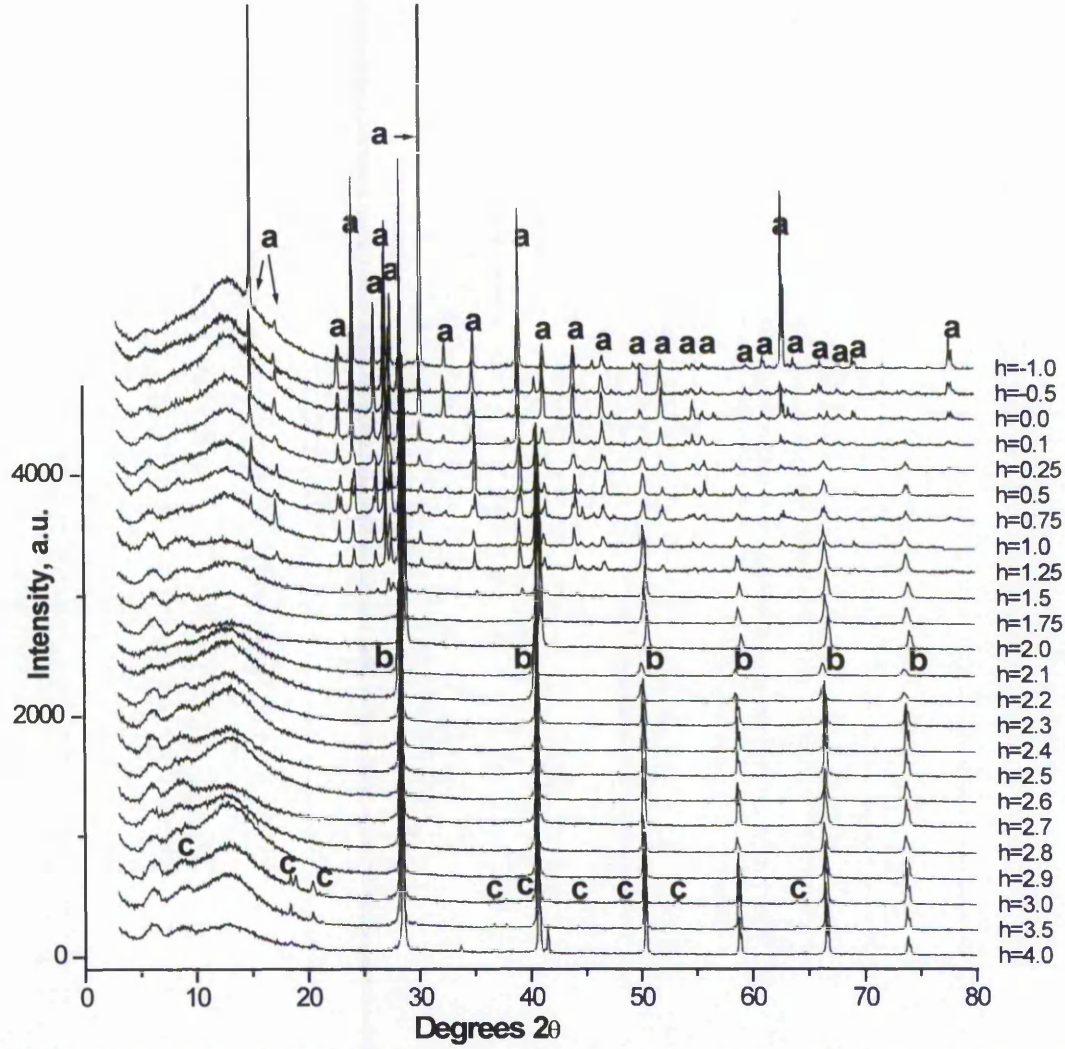


Fig. 5.4. PXRD patterns of the solid SFD samples of the series **AMK1** as a function of the hydrolysis ratio. Y-offset – 100%. Some peaks are truncated for presentation purposes.

Crystalline phase (***a***) in Fig. 5.4 matches very well the reference XRD pattern of the rhombohedral chloraluminite $AlCl_3*6H_2O$ (JCPDS Powder diffraction file card No 8-453). This phase occurs at hydrolysis ratios $h \leq 1.5$ and tends to increase in proportion to the decrease of hydrolysis ratio. Phase (***b***) in Fig. 5.4 detected at hydrolysis ratios $h \geq 0.1$ corresponds to cubic-centred phase of potassium chloride (sylvite, synthetic KCl, JCPDS Powder diffraction file card No 41-1476), which was formed upon addition of KOH to $AlCl_3$ solution during the experiment **AMK1** upon drying. The peak intensity of this phase gradually increases with the increase of hydrolysis ratio and reaches a maximum at h=3.0 after which it slightly falls again. The third weaker pattern (***c***) shown in Fig. 5.4 is detected in the range of hydrolysis ratios $h \geq 2.8$ and corresponds to the monoclinic form of crystalline $Al(OH)_3$ – gibbsite (Powder diffraction file card No 76-1782). This phase has a maximum at h=3.0 and disappears at higher hydrolysis ratios.

Semi-quantitative analysis of the peak areas of the patterns (***a***), (***b***) and (***c***) observed in the PXRD measurements of the series **AMK1** was conducted, the results are shown in Fig.

5.4. The values of the peak areas were preferred to the peak intensities due to varying peak broadening. Peak areas of the most intense peaks in each pattern were measured by direct integration. The relationship between peak areas of the major crystalline phases in the samples **AMK1** and hydrolysis ratio is shown in Fig. 5.5.

The data of Fig. 5.5 show that the chloraluminite phase, after reaching a brief maximum at h=0.0, decreases gradually as the hydrolysis ratio increases and completely disappears at h=1.75. All three major peaks of $AlCl_3*6H_2O$ for which the peak area data are presented in Fig. 5.5 correlate well between themselves.

Sylvite (KCl) phase detected in the XRD data sets of the series **AMK1** shows a pattern opposite to that of crystalline aluminium chloride. It starts to appear at $h \geq 0.1$ where the hydrolysis ratio of the sample was adjusted using KOH solution. The peak areas of KCl pattern increase with the increase of the hydrolysis ratio reaching maximum at h=3.0 for all peaks quantified. At higher hydrolysis ratios this phase rapidly disappears.

The last crystalline phase observed in the XRD patterns of the series **AMK1** is gibbsite. The peak areas of this phase (Fig. 5.5) abruptly increase from h~2.8 to h~3.0. After a maximum at h=3.0 the peaks of gibbsite disappear. The fraction of gibbsite in the material produced by spray-freeze-drying of the series **AMK1** solutions is at least one order of magnitude lower than that of chloroaluminite and sylvite. Therefore the bulk of Al-containing materials in the hydrolysis ratio range $1.0 \leq h \leq 4.0$ are amorphous.

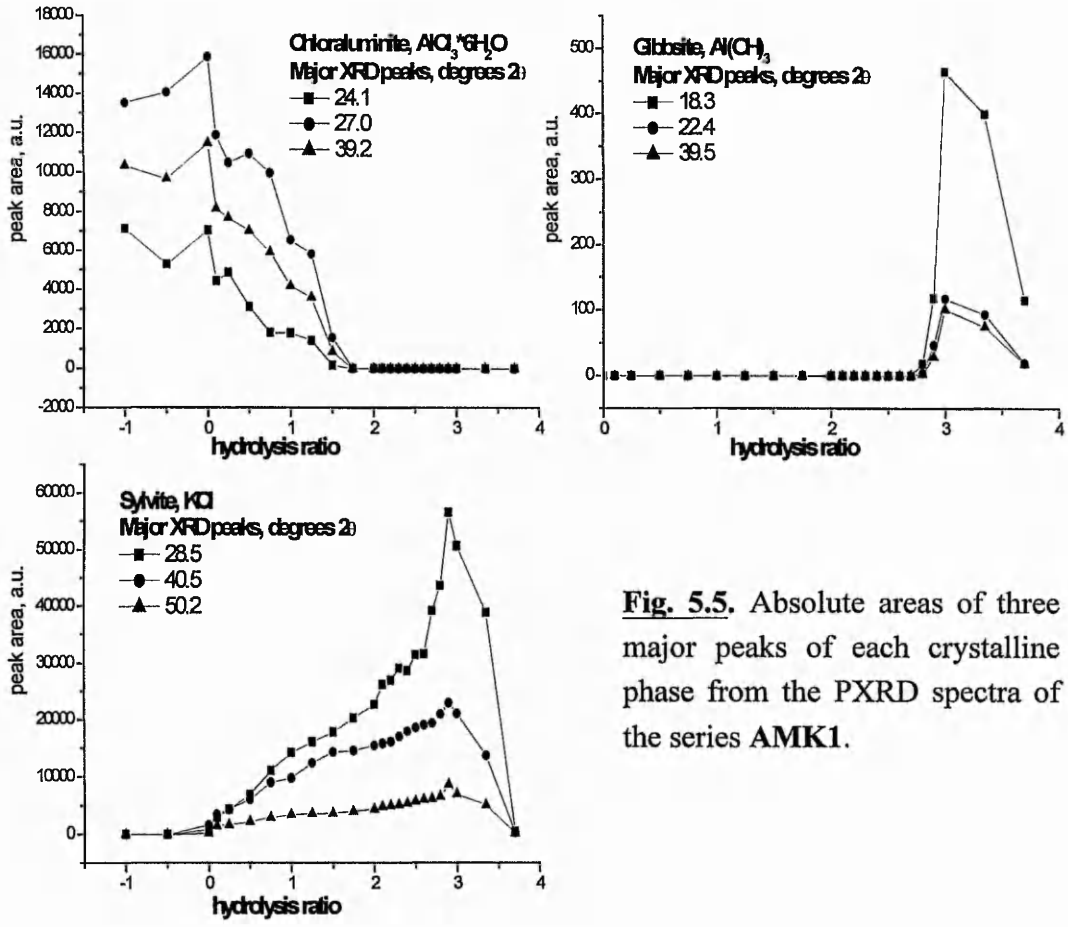


Fig. 5.5. Absolute areas of three major peaks of each crystalline phase from the PXRD spectra of the series **AMK1**.

Along with the areas of the most intense XRD peaks of the major crystalline phases detected in the series **AMK1**, estimated crystallite sizes were estimated using Scherrer's equation as described in Section 2.10.1. The estimates of each crystalline fraction in the XRD patterns were obtained for all detectable non-overlapped peaks and were averaged. The variation of crystallite sizes for each fraction did not exceed 1-2 nm. Results of the crystallite size estimation are presented in Fig. 5.6.

The domain size estimates in Fig. 5.6 of all three major phases follow a pattern similar to that of the peak areas shown in Fig. 5.5. These values also appear to be related to the hydrolysis ratio of the samples of the series **AMK1**. Domain sizes of chloraluminite increase from d=47.8 nm to d=55.2 nm in the hydrolysis ratio range $-1.0 \leq h \leq 0.0$ and then decrease gradually at higher hydrolysis ratios reaching a minimum at h=1.5. Domain sizes of sylvite increase from d=40.3 nm to d=54.5 nm in the hydrolysis ratio range $0.1 \leq h \leq 3.0$ and then decrease slowly at h>3.0. Crystallite sizes of gibbsite are practically in the same range as chloraluminite and sylvite ($40 < d < 56$ nm) and reach maximum size of 54.2 nm at h=3.0.

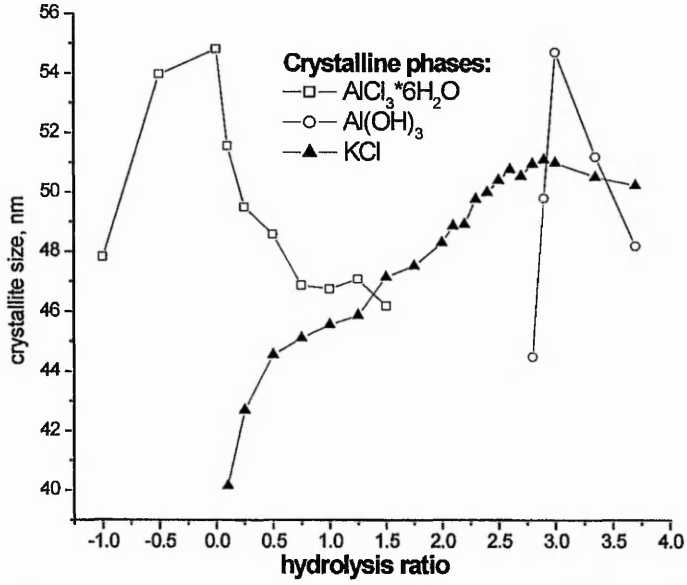


Fig. 5.6. Crystalline domain sizes of the major crystalline phases present in the PXRD patterns of the series **AMK1**.

5.4. Solid-state characterisation of spray-freeze-dried samples of Zr-containing series ZrOH, ZrHCO3, ZrOHSO4, ZrOHAc, ZrOHGly

All samples of the multi-batch series prepared with Zr-ions were subjected to spray-freeze-drying and selected solid samples were analysed using a number of solid-state techniques. The results of the solid-state characterisation are described below.

5.4.1. PXRD measurements of Zr-containing samples

Due to a large number of samples produced by multi-batch titration approach ranging from 120 for the series **ZrOH**, **ZrOHSO4**, **ZrOHAc**, and a set for three series **ZrOHGly**

with different ratios Zr:glycine, to 156 samples for the series **ZrHCO3** (see Section 2.4.3 for details) and due to the relatively long time required for acquisition of the PXRD patterns (3-4 hours per measurement) XRD characterisation was limited by the SFD series produced after 48 hours of hydrolysis (final time point of the experiment).

In the majority of the PXRD measured for the Zr-containing series an internal standard of α-Al_2O_3 (corundum) was used at a fixed ratio sample:standard=4:1. Due to the abundance of diffractive features in most of the XRD measurements, complicated multiphase composition and strong overlap between some of the peaks in the patterns, a more elaborate algorithm was developed in this work in order to identify, classify and quantify PXRD data sets. The scheme of this algorithm shown as flow-chart in Fig. 5.7 employs an approach to the series of XRD measurements as 'dynamic sets' of data according to 2D-correlation analysis (Section 2.13). Hydrolysis ratio was used as a dynamic variable for the correlation analysis of XRD patterns. Both the method of correlation sums developed in this work and a 'classical' 2D-correlation analysis according to [13] were applied for the analysis of XRD patterns.

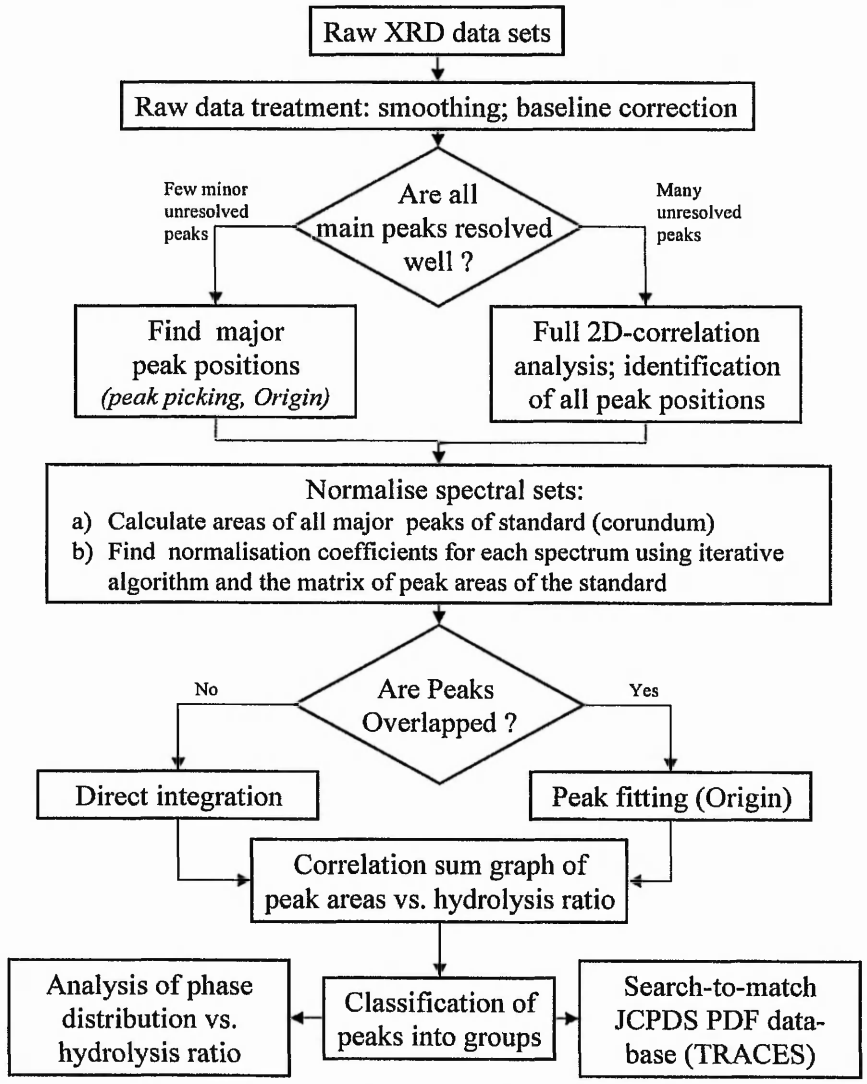


Fig. 5.7. An algorithm of analysis of PXRD data sets including raw data treatment, identification and classification and quantification of the XRD measurements.

5.4.1.1. XRD measurements of the series ZrHCO3

The overall XRD of the series **ZrHCO3** in which Zr-ions were hydrolysed to a different extent (Section 2.4.3) using the soft base $KHCO_3$ are shown in Fig. 5.8.

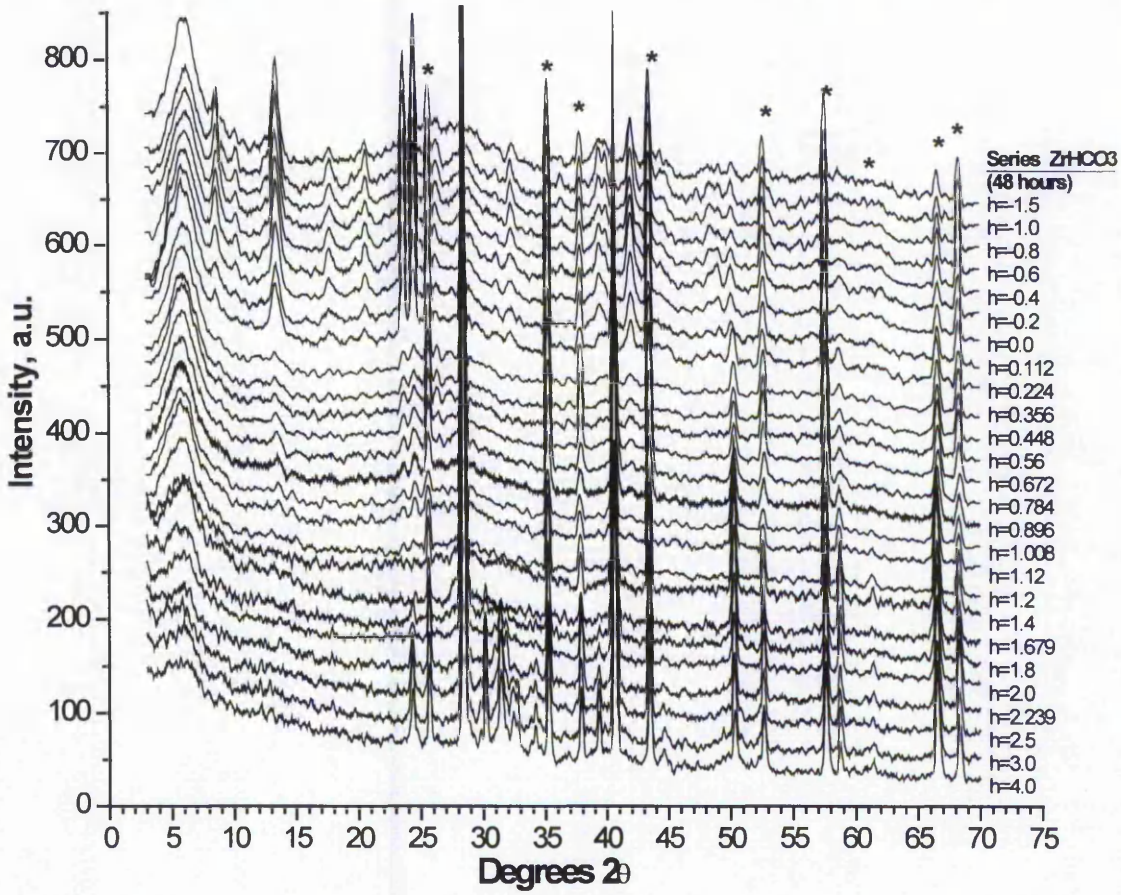


Fig. 5.8. PXRD of the SFD samples prepared from the series **ZrHCO3** after 48 hours of hydrolysis (90°C). Y-offset – 70%. "*"– peaks of the standard α-Al_2O_3 (corundum).

Along with the internal standard peaks of corundum marked with an asterisk (*), a highly crystalline phase was identified in the samples produced at low hydrolysis ratios (h<1.2) containing ca. 218 peaks above RMS limit (see Section 2.10.2). The most intense peaks (I%≥5 %) were compiled in Table 5.1 together with most probable phases matching in part the observed XRD pattern of the first sample in the series **ZrHCO3**.

From Table 5.1 one can see that at least four different crystalline phases partially match the XRD pattern of the solid samples produced at acidic conditions (h<1.2) along with 10 major peaks of alpha-alumina (the standard): tetragonal $ZrOCl_2*8H_2O$ – initial precursor to the produced materials; three partially dehydrated, monoclinic zirconium oxide hydrate phases with overall formulae $ZrOCl_2*6H_2O$, $ZrOCl_2*4H_2O$ and $ZrOCl_2*3H_2O$, as well as monoclinic form of zirconium oxide – baddeleyite. Therefore, more rigorous analysis of the XRD patterns of the series **ZrHCO3** using 2D-correlation analysis is required in order to elucidate complicated phase composition of the samples produced at low hydrolysis ratios.

Prior to subjecting the dynamic set of the XRD spectra in Fig.5.8 to the 2D-correlation

Table 5.1. Possible assignments of crystalline phases in the sample No 1 (h=-1.5), series **ZHCO3**

Sample No 1		$ZOCl_2*8H_2O$*					$ZOCl_2*6H_2O$					$ZOCl_2*4H_2O$**		$ZOCl_2*3H_2O$		m-ZO_2, baddeleyite					α-Al_2O_3 (standard)				
2q	**%I**	**2q**	**%I**	**h**	**k**	**l**	**2q**	**%I**	**h**	**k**	**l**	**2q**	**%I**	**2q**	**%I**	**2q**	**%I**	**h**	**k**	**L**	**2q**	**%I**	**h**	**k**	**l**
7.12	11.32	**7.31**	100	1	1	0	**7.08**	100	1	0	0	**7.35**	45												
8.72	37.14						**8.58**	48	0	2	0	**8.58**	100												
10.20	12.04	**10.35**	7.41	2	0	0																			
11.78	9.12						**11.13**	24	1	2	0			11.71	20										
12.61	19.45	**12.61**	74.6	1	0	1	**12.82**	50	0	1	1	**12.55**	50	12.84	90										
13.34	73.14						**12.99**	46	1	1	1	**12.99**	25												
14.33	6.94	**14.66**	9.81	2	2	0	**14.18**	10	2	0	0														
16.82	7.11	**16.34**	16.4	2	1	1																			
17.72	15.75						**17.21**	13	0	4	0	**17.34**	25			**17.45**	6.91	1	0	0					
20.16	7.80	**20.07**	3.40	3	1	1																			
20.58	17.06																								
21.66	4.13	**21.43**	2.40	4	1	0	**21.47**	15	2	1	1			21.45	20										
23.68	71.67	**23.47**	9.61	4	2	0	**23.41**	24	1	0	2	**23.45**	55	23.39	20	**24.06**	17.92	0	1	1					
24.52	89.64	**24.27**	7.51	1	1	2	**24.79**	39	0	5	1	**24.71**	60	24.99	100	**24.46**	13.71	1	1	0					
25.68	48.30																				**25.39**	75.38	0	1	2
26.26	12.47	**26.03**	15.0	4	2	1						**26.19**	40												
27.52	9.18													27.59	60										
28.44	13.08	**28.57**	18.6	4	3	1	**28.24**	16	4	1	1			28.40	20	**28.19**	100.0	1	1	1					
29.18	12.61																								
29.64	12.32	**29.56**	5.31	4	4	0																			
31.04	9.80	**29.91**	3.64	3	2	2																			
31.48	8.07	**31.39**	4.61	6	0	0										**31.48**	67.47	1	1	1					
32.40	19.61	**32.68**	5.41	5	3	1	**32.84**	11	2	2	2	**32.66**	20	32.90	20										
33.48	7.24						**33.86**	6	4	4	0					**34.17**	20.22	0	0	2					
34.04	6.59															**34.39**	13.21	0	2	0					
35.24	90.49	**35.19**	2.70	6	2	1	**35.23**	5	4	2	1					**35.32**	15.12	2	0	0	**35.58**	100	1	0	4
35.85	12.41	**35.38**	2.60	1	0	3										**35.91**	2.90	1	0	2					
36.26	10.60	**36.70**	3.90	5	2	2	**36.79**	5	0	0	3														
37.34	5.30													37.70	30										
37.86	31.10	**37.86**	2.10	4	4	2															**38.12**	50.35	1	1	0
38.84	8.58	**38.61**	3.70	5	3	2										**38.56**	5.41	0	2	1					
39.46	23.33	**39.35**	2.80	6	0	2																			
39.92	21.94	**39.96**	5.50	3	2	3										**40.74**	12.61	2	1	1					
41.26	6.24	**40.15**	4.00	7	2	1										**41.17**	4.81	1	0	2					
41.96	43.64	**41.15**	2.30	5	4	2						**41.99**	20	41.99	40	**41.39**	5.01	1	2	1	**42.27**	0.20	0	0	6
43.44	100.00	**42.44**	3.60	4	2	3						**43.92**	25	43.65	40						**43.80**	93.69	1	1	3
44.42	22.24	**44.14**	5.91	4	3	3																			
44.94	13.29	**44.25**	8.51	7	1	2								45.45	10	**44.85**	6.51	1	1	2					
45.25	10.85	**45.24**	2.50	7	4	1										**45.54**	6.41	2	1	1	**46.63**	1.70	2	0	2
47.78	12.02	**47.87**	2.20	6	5	2																			
48.30	16.06	**48.02**	2.20	8	4	1																			
48.62	12.73																								
49.14	16.93	**49.12**	4.20	7	6	0										**49.27**	15.82	0	2	2					
50.22	17.24	**50.36**	3.80	8	5	0						**50.08**	15	50.40	3	**50.13**	19.62	2	2	0					
52.08	10.91													51.22	3	**51.21**	5.21	2	2	1					
52.64	43.01																				**53.12**	47.35	0	2	4
53.15	8.90																								
53.28	7.35													53.68	30	**54.12**	10.61	2	0	2					
55.68	6.01	**55.03**	3.40	5	1	4								54.34	10	**55.62**	6.81	1	1	3					
56.30	9.06	**56.29**	2.00	8	1	3										**55.91**	7.21	1	3	0					
56.86	7.17	**56.72**	2.80	4	4	4								56.71	40										
57.58	88.42															**57.19**	7.61	3	1	0	**58.22**	93.59	1	1	6
58.64	13.12	**58.10**	1.30	6	1	4										**57.88**	4.61	3	1	1					
59.78	5.46	**60.38**	1.30	1	0	5										**59.79**	7.51	2	2	2	**60.32**	2.30	2	1	1
61.46	4.18	**61.61**	1.50	7	1	4										**61.39**	4.81	3	0	2	**61.74**	3.50	1	2	2
62.54	7.33	**62.61**	1.20	8	7	2										**62.00**	5.71	1	1	3	**62.18**	6.00	0	1	8
63.10	8.49	**63.65**	1.50	9	6	2								63.88	30	**62.86**	8.41	2	1	3					
64.06	5.83															**64.31**	2.50	3	1	1					
64.82	6.85															**65.39**	2.10	0	3	2					
65.88	8.91															**65.93**	3.60	2	3	1					
66.58	33.63																				**67.24**	35.14	2	1	4
67.36	12.03													65.75	20										
68.34	50.01																				**68.88**	51.45	3	0	0

* - $ZOCl_2*8H_2O$ (tetragonal) – JCPDS PDF card No 74-1615; $ZOCl_2*6H_2O$ (monoclinic) –PDF card No 47-0815; $ZOCl_2*4H_2O$ (monoclinic) – PDF card No 18-1498; $ZOCl_2*3H_2O$ (monoclinic) –PDF card No 15-0337; m-ZrO2 (baddeleyite) -PDF card No 86-1451; α-Al_2O_3, corundum (standard) – PDF card No 43-1484; ** PDF cards of $ZOCl_2*4H_2O$ and $ZOCl_2*3H_2O$ did not provide h, k, l -data.

analysis one needs to classify the XRD data sets into groups according to the similarity of the features observed. A simple way to evaluate similarity of the spectral patterns is to calculate the normal correlation matrix in the hydrolysis ratio domain and to derive the sums of columns (or rows) of the matrix, i.e. correlation sums (Fig. 5.9).

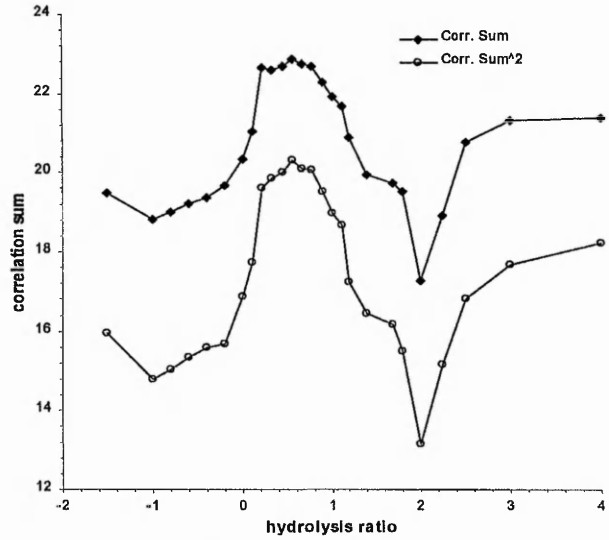


Fig. 5.9. 'Correlation sums vs. hydrolysis ratio' graph calculated from the XRD measurements of the series **ZrHCO3**.

The graph in Fig. 5.9 allows for the following groups to be assigned: **group 1** ($-1.5 \leq h \leq 0.112$) – combines the XRD patterns of the samples produced in the most acidic conditions with the maximum of phases present; **group 2** ($0.112 \leq h \leq 1.2$) – the group with the maximum correlation indicated by high correlation sum values within the dynamic set; **group 3** ($1.2 \leq h \leq 2.0$) – correlation sums of the group are descending gradually towards the minimum at $h=2.0$; **group 4** ($2.0 \leq h \leq 4.0$).

After classification of the XRD patterns of the series **ZrHCO3** into four major groups using the correlation sum analysis, full 2D-correlation analysis was conducted using the 2D-Pocha program by D. Adachi [14]. This program is limited to a 400-column matrix. Due to this, and also for presentation purposes, the data spacing of the XRD patterns in each group was decreased two times, the part of spectra at $2\theta \geq 68$ degrees was cut off to decrease the number of points further (1600 points left) and XRD data sets were divided into four subgroups of 400 points according to four ranges of measurement angles 2θ. The 4x4 correlation matrix was reconstructed from the cross-sections of these groups in the full correlation matrix. 2D-correlation analysis in synchronous and asynchronous modes was conducted only on four diagonal cross-sections of the full correlation matrix as well on 6 non-diagonal cross-sections. The illustrative examples of the analysis of the three first diagonal cross-sections of the correlation matrix are given in Fig. 5.10 as 2D-contour maps both in synchronous (left) and asynchronous (right) modes.

As follows from the data of Fig. 5.10, the 2D-correlation analysis enables one to identify with great detail a large number of the peaks present in XRD patterns of the chosen

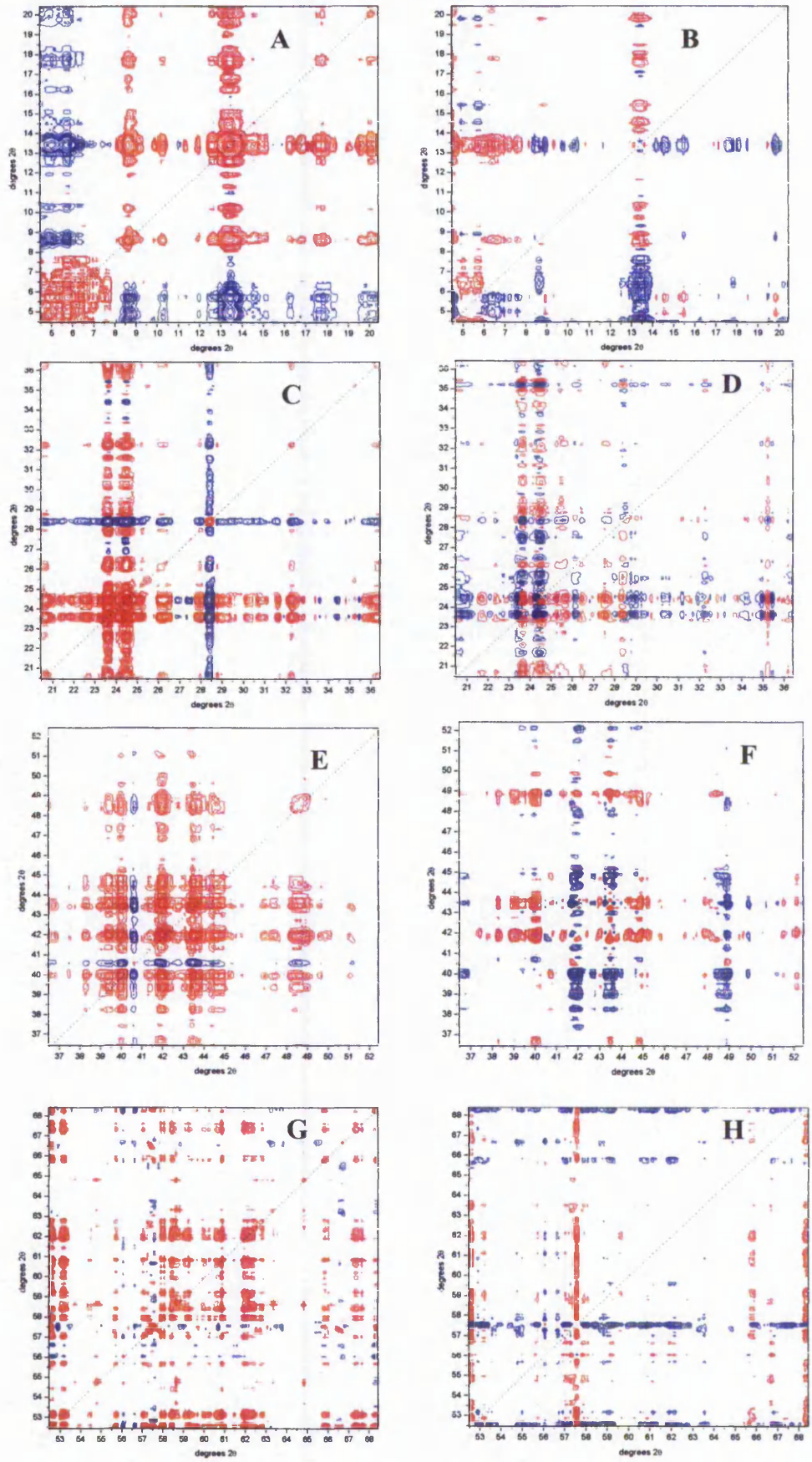


Fig. 5.10. 2D-correlation graphs of the diagonal cross-sections of the full correlation matrix calculated from the XRD patterns of the SFD samples of the series **ZrHCO3**, group 1 ($-1.5 \leq h \leq 0.112$). Syncronous 2D-correlation maps (left side) and asynchronous maps (right side) are shown.

group. The red-coloured peaks on the synchronous maps in Fig. 5.10 indicate the presence of correlated features, blue-coloured – anti-correlated. On the asynchronous maps, the red peaks locate 'out-of-phase' features, and the blue peaks – 'in-phase' features, marking the pairs of peaks with opposite or strongly discriminate correlation behaviour. In the analysis of the diagonal cross-sections all peaks located on the diagonal of the contour map in Fig. 5.10 are considered. The overall number of the peaks identified using full 2D-correlation analysis approaches 260, which is ca. 1.5 times more than visual examination of the XRD patterns. Many of the peaks were either 'buried' in spectral noise, or strongly overlapped by other peaks. The analysis of the non-diagonal cross-sections (not shown for the sake of brevity), where the correlation between different parts of the XRD pattern is investigated, leads to the establishment of the correlation relationships between all major individual peaks.

The individual peaks positions identified using full 2D-correlation analysis of the XRD data sets of the series **ZrHCO3** were subjected to the analysis of correlation sums vs. hydrolysis ratio for the whole series of measurements. The correlation sums of all identified peak positions were sorted in ascending order and the peaks with similar values of correlation sums were put into five major groups. Higher orders of correlation coefficients (up to 5) were used in order to determine the major groups more precisely. Peak areas of the most intense and well-resolved peaks from each group were calculated using either direct integration, or peak-fitting (GRAMS/32 Version 5 software).

Prior to the calculation of the peak areas, all XRD measurements of the series **ZrHCO3** were cross-normalised using the following algorithm. From the nine peaks unambiguously belonging to the corundum phase (internal standard) 4 to 7 peaks were chosen on the basis of the maximum correlation sums for the hydrolysis ratio scale. A few peaks of the standard were discarded from the analysis due to strong overlapping with the peaks of the samples **ZrHCO3**. A rectangular matrix **M** was formed from the values of peak areas of the selected standard peaks where n columns corresponded to the number of peaks chosen, and m rows corresponded to the number of XRD patterns in the series (in the case of **ZrHCO3** series the number m=26). A new rectangular matrix **M'** with the same dimensions as M was calculated as follows:

$$\mathbf{M}*A' = \mathbf{M}' \tag{5.1}$$

$$A \longrightarrow A', \text{ by} \tag{5.2}$$

$$\overset{\text{iteration}}{R \longrightarrow R'}, \text{ where} \tag{5.3}$$

$$\Sigma(\mathbf{R}') \longrightarrow \textbf{minimum} \tag{5.4}$$

where A – the vector of normalisation coefficients (A_j=AVERAGE($\mathbf{M}_{i,j}$), i=const); A' – the new vector of normalisation coefficients obtained by iteration; R, R' – initial and final vector (dimensions of A) of sums of square roots of deviations from mean; $\Sigma(\mathbf{R}')$ – the sum of all deviations R from mean – the criterion for iterative minimisation (MS Excel Solver).

The results of the peak area calculation for three peaks of each identified group of the cross-normalised XRD patterns of the series **ZrHCO3** are shown in Fig. 5.11.

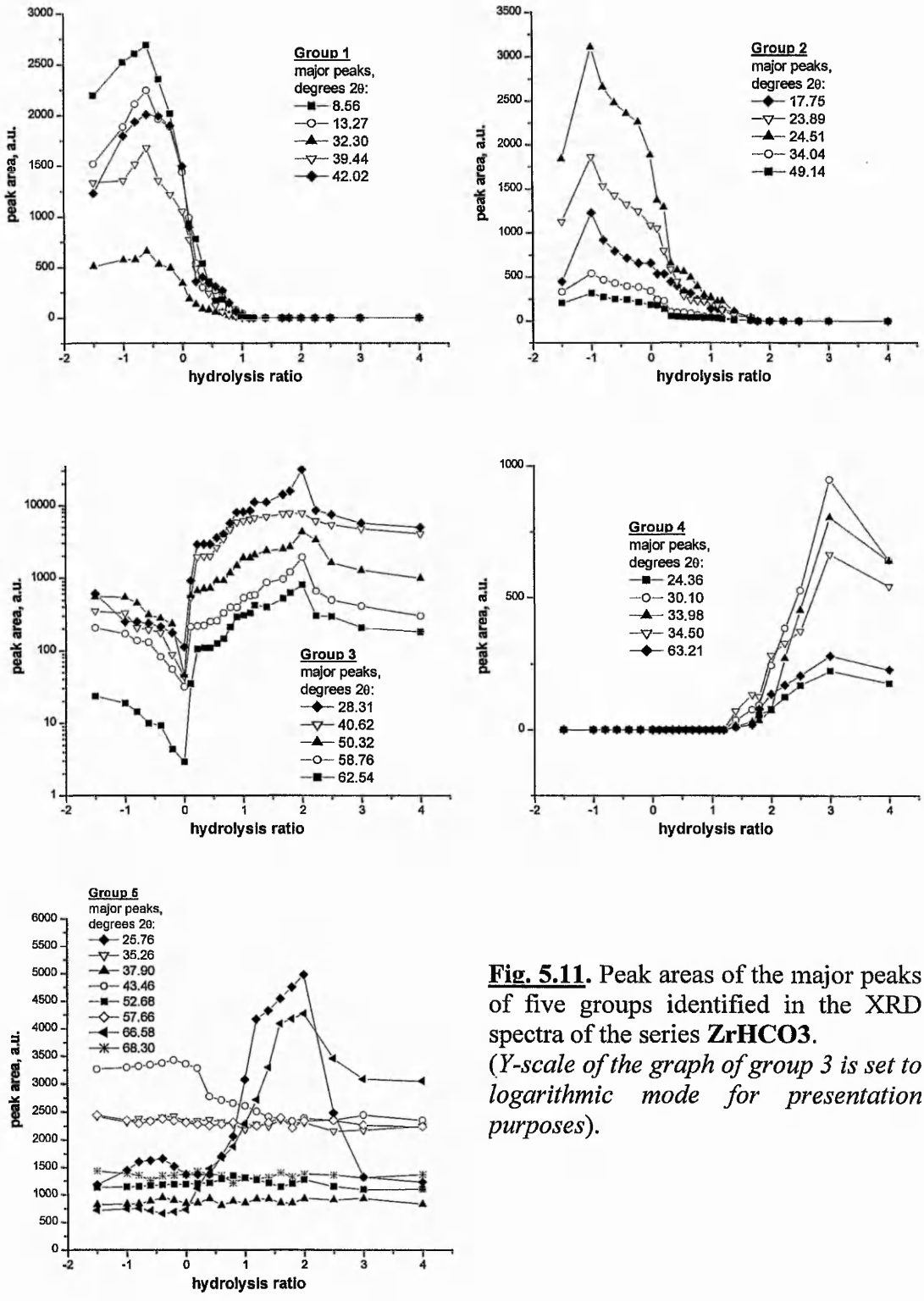


Fig. 5.11. Peak areas of the major peaks of five groups identified in the XRD spectra of the series **ZrHCO3**. (*Y-scale of the graph of group 3 is set to logarithmic mode for presentation purposes*).

As follows from Fig. 5.11, selected peaks of the first group of the XRD peaks of the series possess non-zero peak areas at lower hydrolysis ratios. The areas of all five most intense peaks of the first group increase with the growth of h from –1.5 to –0.6. After the maximum point at h=-0.6 these values gradually fall to zero value at $h \geq 1.2$. This group of peaks is assigned to partially dehydrated monoclinic forms of zirconyl chloride

($ZrOCl_2*8H_2O$), such as $ZrOCl_2*3H_2O$, and especially $ZrOCl_2*4H_2O$ and $ZrOCl_2*6H_2O$. Both latter phases match the peaks of group 1 and have their largest peak (*h-k-l*=0-2-0) at 8.56 °2θ (Table 5.1).

The second group shown in Fig. 5.11 contains XRD peaks highly correlated on the hydrolysis ratio scale. Unlike the peaks of group 1, group 2 peaks show a maximum at h= -1.0 and then gradually fall to zero at the hydrolysis ratio h~1.68. The best match for the group 2 peaks is the crystalline phase of monoclinic zirconia (Table 5.1).

Group 3 of the XRD peaks identified using 2D-correlation analysis shows a more complicated pattern of peak areas vs. hydrolysis ratio. They consist of two distinct regions separated by a minimum at h=0.0. The region at $-1.5 \leq h \leq 0.0$ tends to decrease, while the second large region $0.0 \leq h \leq 4.0$ indicates the increase of peak areas up to h=2 and steadily falling peak areas at h>2.0. On the basis of the fact that the peak positions of this group match major lines of monoclinic ZrO_2 (Table 5.1) as well as the KCl crystalline mineral sylvite (PDF card No 41-1476), one can hypothesise that the shape of the peak area curves against the hydrolysis ratio is caused by both phases. At lower hydrolysis ratios peak areas are related completely to the *m*-ZrO_2 phase, while at h>0.0 these values are attributed to both crystalline phases with the major contribution from sylvite.

Group 4 consists of peaks which appear at high hydrolysis ratios along with sylvite phase which is still present at high intensity in this range of h (cf. Fig. 5.8). Positions of the peaks correspond best to the tetragonal form of zirconium oxide [15]. Peak areas of tetragonal zirconia steadily increase from zero value at h ~ 1.4 to a maximum at h=3.0. At yet higher hydrolysis ratio (h=4.0) the area of the peaks starts to decrease substantially.

The last group of peaks identified in the XRD patterns of the series **ZrHCO3** (Fig. 5.11) consists of the peaks of the internal standard alpha-alumina, or corundum (Table 5.1). Two types of the peaks related to α-Al_2O_3 in Fig. 5.11. The first is pure cross-normalised peaks at 35.26, 37.90, 52.68, 57.66 and 68.30 degrees 2θ which are highly correlated between themselves and give an almost straight line upon the cross-normalisation procedure described above. The second type includes peaks at 25.76, 43.46 and 66.58 ° 2θ and is heavily affected by the adjacent peaks of **ZrHCO3** samples that lead to lower correlation with the rest of the peaks of α-Al_2O_3. The latter type of peaks was excluded from the cross-normalisation procedure.

Along with peak areas of the XRD patterns of the series **ZrHCO3** the crystalline domain sizes were estimated using Scherrer's equation for all five groups of peaks identified above. For each group the crystallite size was evaluated as an average of the measured parameters of at least five of the most intense and well resolved peaks. Results of the calculation are given in Fig. 5.12 as a graph of crystallite size vs. hydrolysis ratio.

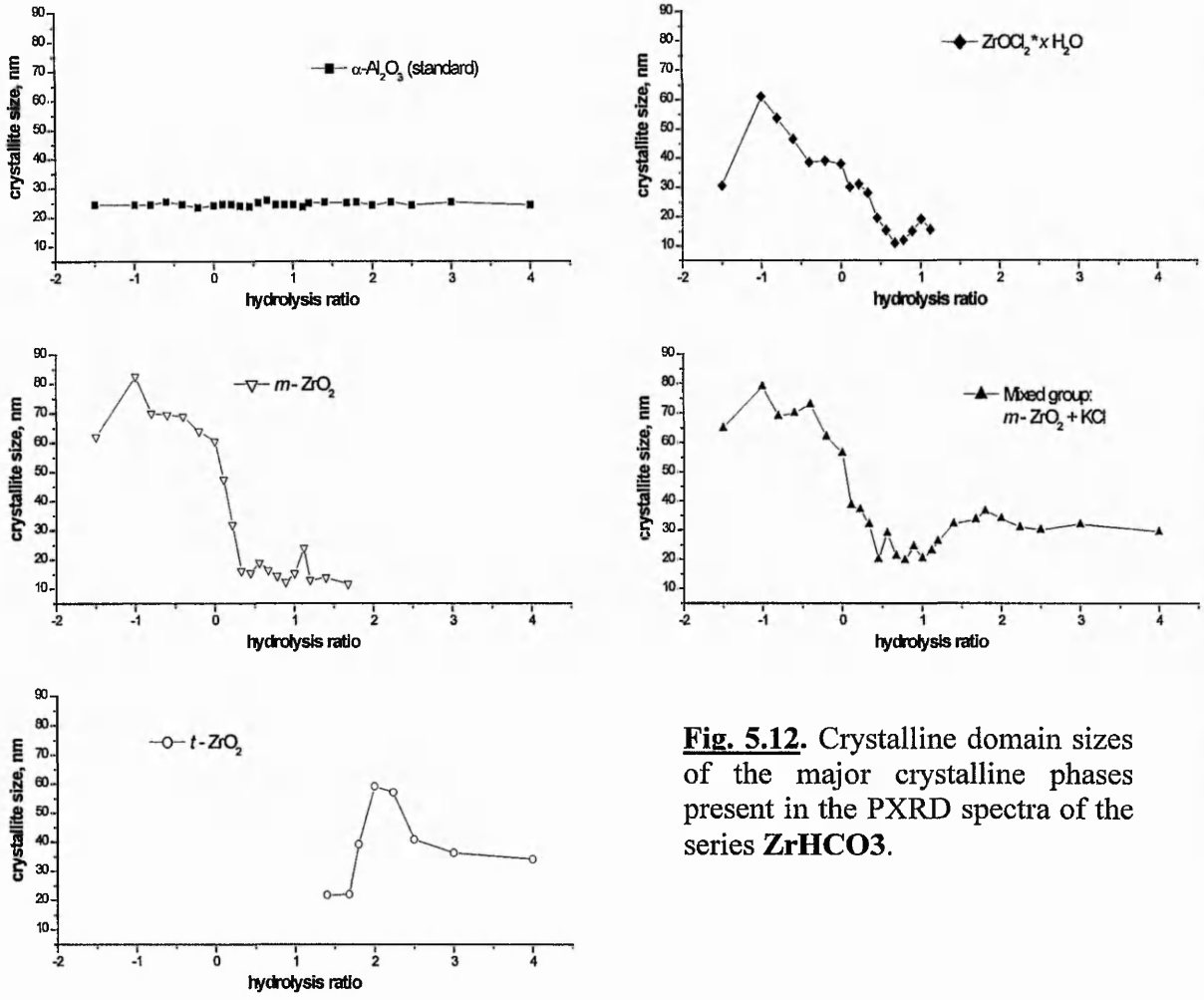


Fig. 5.12. Crystalline domain sizes of the major crystalline phases present in the PXRD spectra of the series **ZrHCO3**.

In Fig. 5.12 an average crystallite size of the internal standard (α-Al_2O_3) remains practically constant (average value 24.54 nm) regardless of the sample measured (similar to the intensity of the corresponding peaks). This indicates that multi-phase composition of the samples does not affect measurements of the peak broadening and crystallite size of the standard and measurements are reproducible (standard error is within ca 5 %). This value was obtained on the basis of 'pure' standard peaks only, the peaks that interfere with the sample signal give significantly lower values of crystallite size.

The crystallite size of the mixture of the partially dehydrated zirconyl chloride phases of the overall formula $ZrOCl_2*xH_2O$ varies strongly with the increase of hydrolysis ratio (Fig. 5.12). After reaching a brief maximum of ca. 62 nm at h=-1.0 the size of crystallites gradually decreases to the values as low as 10 nm at h=0.68. This is in line with the decreasing proportion of $ZrOCl_2*xH_2O$ phase in the samples of hydrolysed Zr-ions (cf. Fig. 5.11).

Monoclinic zirconia produced at very acidic conditions (h<0.0) has larger crystallite sizes than the same phase produced by the addition of $KHCO_3$ to Zr-ion solutions (h>0.0). The maximum size is reached at h=-1.0 (d=82.5 nm) and then decreases to significantly lower average values (d~15 nm) in the range $0.4 \leq h \leq 1.68$ (Fig. 5.12). A very similar pattern is observed in the lower-pH region of the 'mixed' group of XRD peaks in the series ZrKHCO3.

The crystallite size in this case drops from ca. 79 nm to ca. 20 nm in the range $-1.0 \leq h \leq 0.68$. The descending crystallite size again correlates well with peak areas of the *m*-ZrO_2 phase. Increasing concentration of KCl at $h>0.0$ does not affect as substantially the crystallite size of the sylvite phase which varies from d~21 nm within $0.0<h<1.2$ to d~34 nm at h=1.8-2.0. At alkaline conditions $h>2.0$ the size of sylvite crystallites starts to decrease only slightly.

Finally, the size of the tetragonal phase of zirconia emerging at pseudo-neutral and alkaline conditions (Fig. 5.12) exhibits a strong variation with increasing hydrolysis ratio. This variation is almost 3 times that of the crystallite size of *t*-ZrO_2 at h=1.4-1.68 (d=22 nm) with the same value at h=2.0 (d=56.5 nm). After a sharp maximum at h=2.0 the size of *t*-ZrO_2 particles starts to decrease rapidly with the increasing value of h. In the case of *t*-ZrO_2 the crystallite size variation correlates well with the fraction of this phase in the solid sample produced by spray-freeze-drying.

5.4.1.2. XRD measurements of the series ZrOH

In the case of the series **ZrOH** produced by the addition of KOH to Zr-ion solutions at 90°C (Section 2.4.3), diffractograms of the solid samples obtained by SFD after 3, 6, 12, 24 and 48 hours (100 samples in total) were measured. This allowed us to trace time-resolved fluctuations in phase composition and crystallinity of the solid-state fingerprints of Zr-ion solution speciation. The raw data sets obtained from the series **ZrOH** are shown in Figs. 5.13-5.17. (Fig. 5.14-5.17 are in Appendix 2). All spectra were acquired in the presence of α-Al_2O_3 standard (peaks are marked with '*'). Some peaks were truncated for presentation purposes.

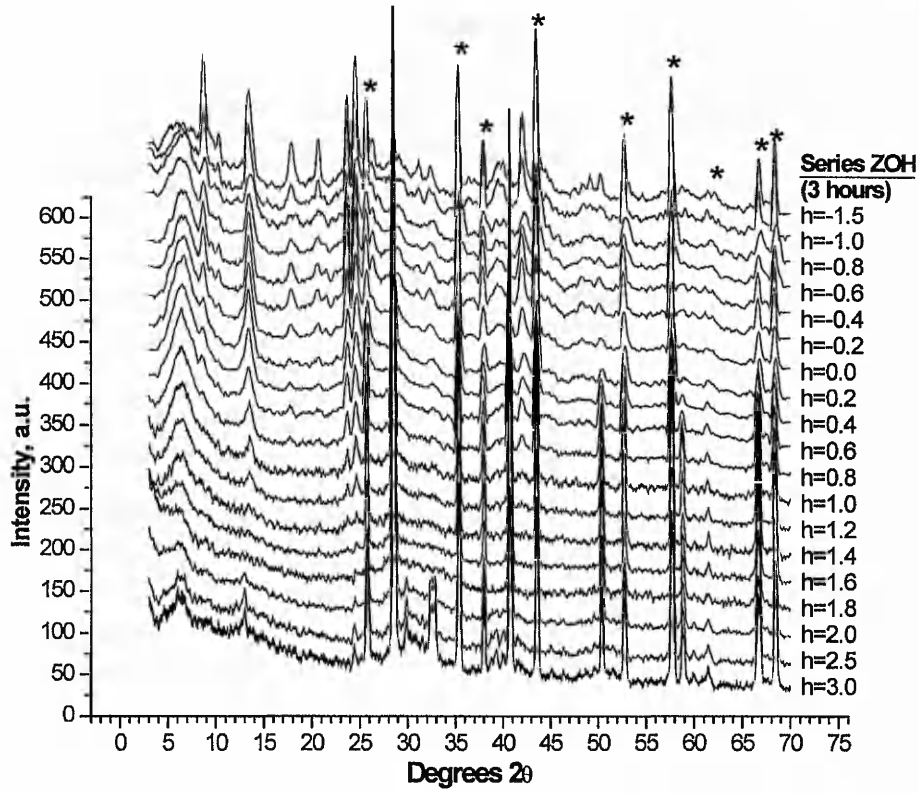


Fig. 5.13. PXRD patterns of the SFD samples prepared from the series **ZrOH** after 3 hours of hydrolysis (90°C). Y-offset – 80 %.

Comparison of the XRD measurements from the series **ZrOH** obtained for the samples at different times of the experiment (Figs. 5.13-5.17) shows general similarity of the diffraction patterns on the hydrolysis ratio scale. As in the case of series **ZHCO3** described above, three major Zr-containing crystalline phases were identified in the x-ray diffractograms: monoclinic and tetragonal zirconia as well as partially dehydrated zirconyl chloride $ZrOCl_2*xH_2O$. Other crystalline phases include corundum and KCl (sylvite).

The distribution of the crystalline phases observed in the **ZrOH** samples can be illustrated on the basis of graphs 'peak area vs. hydrolysis ratio'. Major XRD peaks of the diffractional series shown in Figs. 5.13-5.17 were identified using the same algorithm as for the series **ZrHCO3**. The calculated areas of the most intense peaks of each group identified (except for the peaks of the internal standard of corundum) are given in Fig. 5.18.

For the comparison of the peak areas presented in Fig. 5.18 an additional cross-normalisation procedure had to be conducted in order to normalise peak areas of the standard between the time series. This procedure was carried out in a similar way to the algorithm described by Eqs. 5.1-5.4. The matrix **M** in this case consisted of n columns of the peak areas of the standard of each time series (the total number n=5) and m rows corresponding to m samples in the series. For the sake of clarity, only the most intense peak of each diffraction group was compared in Fig. 5.18 below, both on the time scale and the hydrolysis ratio scale.

The data of Fig. 5.18 indicate that the group 1 of XRD peaks belonging to partially dehydrated $ZrOCl_2*xH_2O$ mixture splits into 2 subgroups (group 1*A* and 1*B*). The difference between these groups is represented by the peak at 8.56 and 13.25 degrees 2θ (group 1*A* and 1*B* correspondingly) as follows: (*a*) the curves of the group 1*A* reach zero value at h=1.0, while the curves of the group 1*B* are extended to h~1.4; (*b*) a local minimum or a plateau in the curves of the group 1*A* occurs at h=-0.8, whereas h=-0.6 for the XRD peaks of the group 1*B*; (*c*) some of the curves of the group 1*B* (at longer times) exhibit a local maximum at h=0.0, while the peaks of the group 1*A* do not; (*d*) the major difference is observed on the time scale, where the variation of peak areas of the group 1*A* is significantly larger than that of the group 1*B*, especially at lower hydrolysis ratios (h<0.0). One can assume that these two subgroups arise from two distinct representatives of the crystalline mixture of $ZrOCl_2$ dehydrated to a different extent. In general, both group 1*A* and 1*B* of the peak area curves of the series **ZrOH** in Fig. 5.18 resemble the analogous curves of the series **ZrHCO3** (Fig. 5.9), especially the curve of the group 1*A* at 48 hours of experiment.

The relationship between peak areas of the group 2 of the XRD peaks of the series **ZrOH** (m-ZrO_2) and hydrolysis ratio of initial sample solution (Fig. 5.18) differs from that of the analogous group 2 in the series **ZrHCO3** (Fig. 5.9). After a gradual fall of the peak areas of the representative peak at 24.51 °2θ, the curves exhibit a local maximum at $1.0 \leq h \leq 1.6$

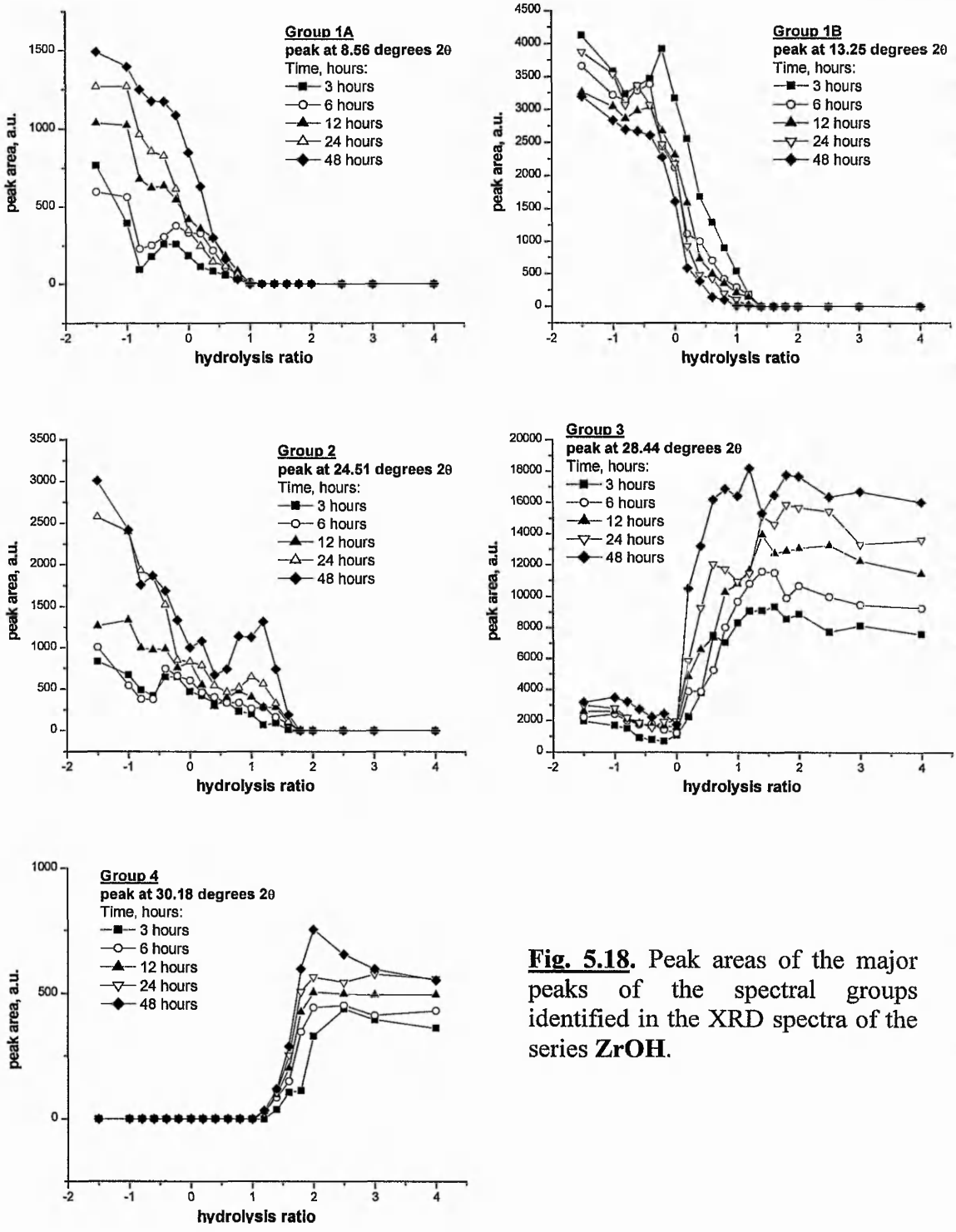


Fig. 5.18. Peak areas of the major peaks of the spectral groups identified in the XRD spectra of the series **ZrOH**.

depending on the time at which the corresponding sampling and spray-freeze-drying of the initial sample solution took place. After the local maximum, most curves of the group 2 reach zero value at h~1.6. The largest variation of areas of the peak at 24.51 degrees 2θ on time scale occurs at very low hydrolysis ratios (h<0.0) and in the range 1.0≤h≤1.6. The trend of variation in time is the growth of the peak areas from short sampling times (3 hours) to longer times (48 hours), which is similar to that of the analogous group 3 of the series **ZrHCO3** (Fig. 5.9) and is opposite to the group 1*A* and 1*B* in Fig. 5.18.

Group 3 in Fig. 5.18 represented by the most intense peak at 28.44 ° 2θ belongs to a 'hybrid' type combining the peaks of monoclinic zirconia and KCl (sylvite). Again, this group of the XRD peaks from the series **ZrOH** resembles closely the analogous group 3 of the series **ZrHCO3**. The initial, lower part of the peak area curves (*m*-ZrO_2) steadily drops to a minimum at h=0.0, where it is overtaken by the second part of the curve arising from sylvite. However, behaviour of the second part of the group 3 curves is not as smooth as for the analogous curves of the series **ZrHCO3** (Fig. 5.9). There are at least two maxima or plateaus observed in this part – the first varies between h=0.8 and h=1.6, while the second maximum occurs around h=1.8-2.0. This deviation from the smooth ascending character of the curves of the previous series (**ZrHCO3**) logically arises from the steadily increasing concentration of added alkali and, correspondingly, KCl, and is probably caused by a strong contribution from the peaks of *m*-ZrO_2 (cf. the group 2 curves in Fig. 5.18). Time order of the peak area curves is similar to the group 2 for the peaks of 'pure' monoclinic ZrO_2, the areas of the XRD peaks increase with increasing reaction time.

The group of the peaks of tetragonal ZrO_2 (representative peak at 30.18 °2θ) emerges at h~1.2 and rapidly increases towards a maximum at h~2.0, after which a quite significant fall of the peak area value takes place. The shape and the order of peak area variation in time is similar to the analogous values of the group 4 of the series **ZrHCO3**, however the t-ZrO2 occurs at lower hydrolysis ratios in the series **ZrOH** comparing to its couterpart in the series **ZrHCO3**. The amount of tetragonal zirconia roughly indicated by the peak area of the group 4 peaks increases with time and reaches a maximum after 48 hours of hydrolysis.

Along with the areas of the XRD peaks, average domain sizes of the major crystalline phases present in the samples of the series **ZrOH** were calculated using Scherrer's formula. Results of the calculation are summarised in Fig. 5.19.

From Fig. 5.19 one can find that crystallite sizes of two subgroups of the group 1 (group 1*A* and 1*B*) behave in an opposite way on the hydrolysis ratio scale. The size of crystallites for group 1*A* is higher at very acidic conditions ($-1.5 \le h \le -1.0$) where this value reaches 40-50 nm. After a local minimum at milder acidity ($-0.8 \le h \le -0.4$) at which the crystallite size is ca. 30±5 nm, this value tends to increase at shorter reaction times (τ=3-12 hours) to d~50-60 nm, while it remains practically the same (d~30-40 nm) at longer reaction times (τ=24-48 hours). At positive values of the hydrolysis ratio the crystallite size of group 1*A* rapidly drops to very small values, ca. 10 nm on average. In contrast, the crystallite size of group 1*B* starts with very small values close to 10-15 nm and gradually increases in the range of hydrolysis ratios $-0.6 \le h \le 0.6$ to the values of $20 \le d \le 30$ nm which remain the same at $h \ge 0.6$. The different behaviour of the crystallite sizes on the hydrolysis ratio scale proves the correctness of the division of group 1 of XRD peaks of the series **ZrOH** into two subgroups (1*A* and 1*B*). The time-dependent variation of the crystallite size of group 1*B* is clearly seen in the part of the curve at $h \ge 0.6$ where the size of crystalline particles increases with the time at

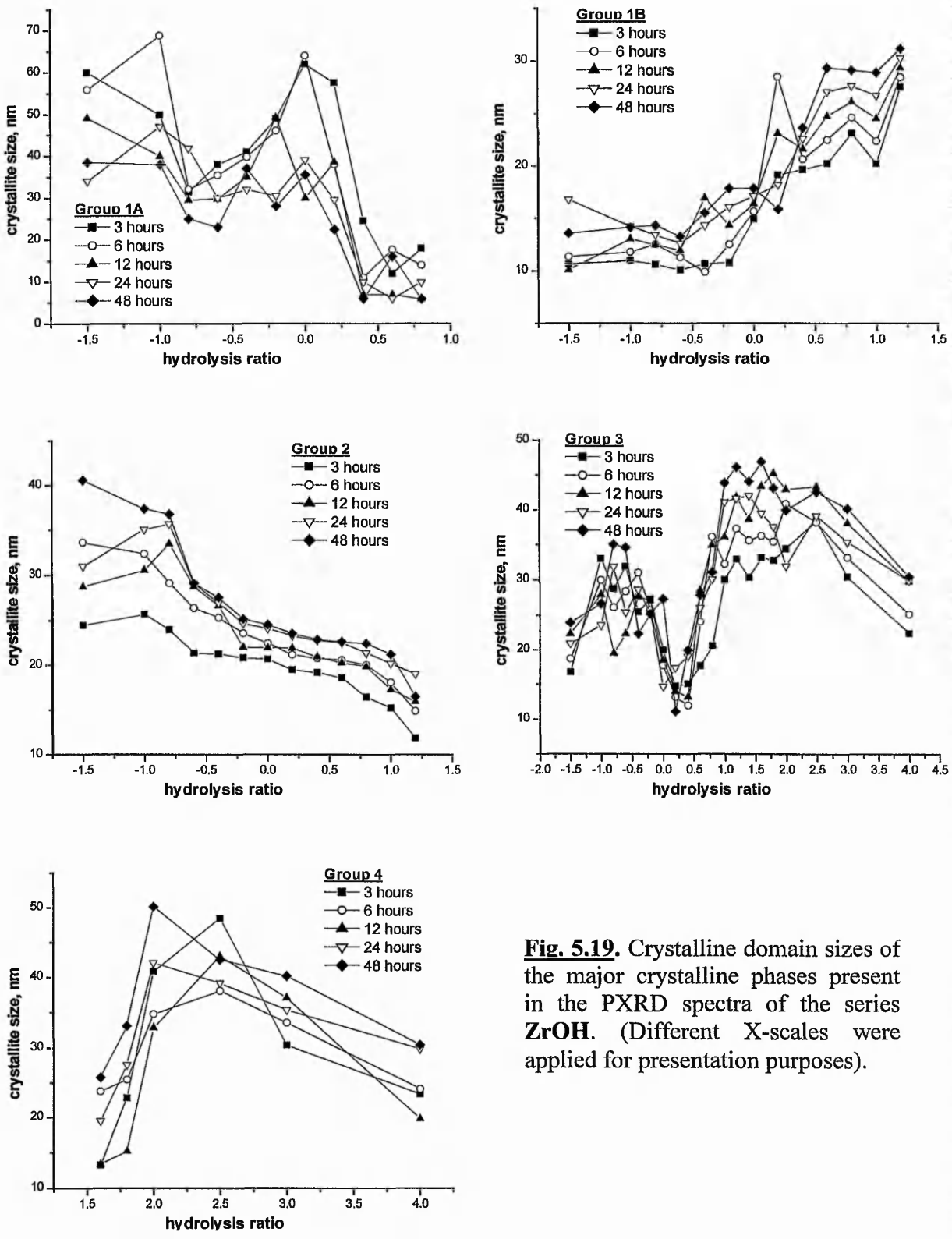


Fig. 5.19. Crystalline domain sizes of the major crystalline phases present in the PXRD spectra of the series **ZrOH**. (Different X-scales were applied for presentation purposes).

which SFD sampling took place.

The value of crystallite size of group 2 relating to monoclinic zirconia (Fig. 5.19) shows a similar trend to that of group 1B. In this case, the size of the *m*-ZrO_2 phase is relatively small at $h<0.0$ and does not exceed ca. 23 nm for all samples. From the hydrolysis ratio $h\geq0.0$ the size of *m*-ZrO_2 crystallites rapidly increases and reaches maximum at h~0.4-

0.6, the exact value being dependent on the time scale (the particle diameter ranges from ca. 26 nm at 3 hours sampling time to ca. 43 nm at 48 hours sampling time). After a brief maximum, the crystallite size of monoclinic zirconium oxide tends to decrease with increase of the hydrolysis ratio.

The crystallite size of the 'mixed' group 3 (*m*-ZrO_2 with KCl) of the XRD peaks of the series **ZrOH** (Fig. 5.19) is similar to that of the group 2 ('pure' *m*-ZrO2 peaks) at negative hydrolysis ratios. The average domain size varies within 10 to 20 nm and does not change profoundly with time. The second part of the crystallite size curve at $h>0.0$ dominated by the peaks of the sylvite phase, increases to its maximum around $h\sim2.0$ in agreement with the growing concentration of potassium-ions introduced into the samples by the titrant (KOH). After the maximum, the crystallite size of KCl starts to decrease again quite rapidly at higher values of the hydrolysis ratio. Time-dependent variation of the crystallite size of the sylvite phase is not significant below $h\sim2.0$.

The tetragonal zirconia phase exhibits a variation of crystallite sizes in agreement with the areas of the XRD peaks corresponding to this fraction. The value of domain size increases dramatically from $h=1.6$ to $h=2.0$ in some cases more than 3 fold. For instance, for $\tau = 3$ hours the particle sizes change from ca. 12 nm to ca. 42 nm. At higher hydrolysis ratios the size of *t*-ZrO_2 crystallites also reduces significantly – 1.5-2 times between the data collected at $h\sim2.0$ and $h\sim4.0$.

5.4.1.3. XRD measurements of the series ZrOHSO4

The series of multi-batch titrations **ZrOHSO4** were conducted in the presence of sulphate-ions in Zr-ion solutions, the ratio of $Zr:SO_4^{2-}$ was fixed at 1:1. Hydrolysis ratio was adjusted with HCl for negative scale and with KOH at positive values of this parameter. The experiment was conducted at 90°C. Details of sample preparation of the series **ZrOHSO4** are described in Section 2.4.3; solution data is given in Chapter 4 of the present work. The raw PXRD measurements of the spray-freeze-dried samples prepared after 48 hours of experiment are shown in Fig. 5.20. One peak at 28.19 °2θ was truncated in Fig. 5.20 for presentation purposes. All diffractograms in Fig. 5.20 were acquired in the presence of the internal standard of α-Al_2O_3 (peaks are marked with asterisk). The ratio of sample to standard was 4:1 for all recorded patterns.

From the set of XRD patterns of the series **ZrOHSO4** in Fig. 5.20 one can see that at low hydrolysis ratios ($-1.5\leq h\leq-0.6$) the diffraction patterns vary constantly. At $-0.6\leq h\leq-0.2$ one specific pattern stabilises, while in the range $0.0\leq h\leq1.8$ the XRD measurements represent another diffraction pattern, different from the ones at lower *h*. The diffraction patterns at $h\geq2.0$ change again and contain fewer peaks than other spectra in the set.

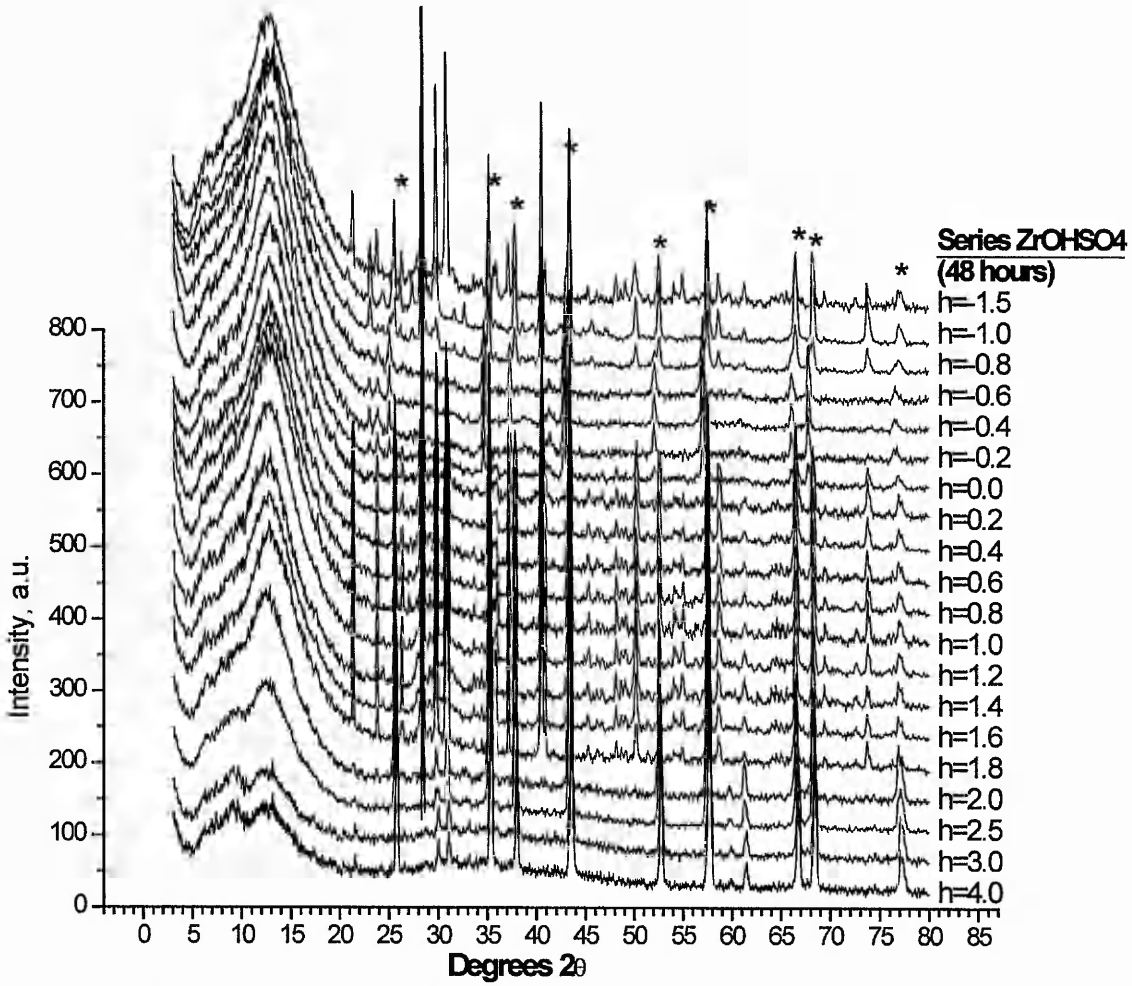


Fig. 5.20. PXRD patterns of the SFD samples prepared from the series **ZrOHSO4** after 48 hours of hydrolysis (90°C). Y-offset – 100%.

Variation in similarity of the XRD data sets of the series **ZrOHSO4** (48 hours) can be illustrated with a correlation sum graph in Fig. 5.21.

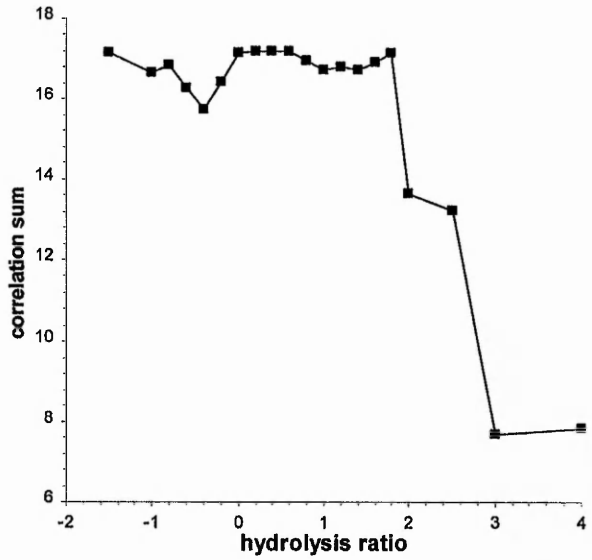


Fig. 5.21. Correlation sums (squares of correlation coefficients) of the XRD data sets from the series **ZOHSO4** vs. hydrolysis ratio.

From Fig. 5.21 the similarity of the diffractograms at $-1.5 \leq h \leq -0.6$; $0.0 \leq h \leq 1.8$ and $h \geq 2.0$ becomes more apparent from the closeness of the correlation sums to each other.

Using 2D-correlation analysis, the majority of the peak positions in the dynamic set of the XRD measurements of the series **ZrOHSO4** were identified. For this purpose the data sets were subdivided into 3 groups according to the correlation sum graph (Fig. 5.21).

Classification of the peaks was performed using the 2D-correlation analysis. Identification of crystalline phases present in the samples of sulphate-containing materials **ZrOHSO4** is not a trivial task due to (*a*) the presence of at least 4 or 5 phases in the dynamic set of XRD patterns; (*b*) abundance of diffraction features in the XRD patterns of **ZrOHSO4** series; (*c*) strong overlap of several peaks which hinders analysis of their dynamic behaviour on the hydrolysis ratio scale; (*d*) a large number of possible Zr sulphate crystalline phases (more than 20 were found in the 1999 version of JCPDS database), several of which fit the diffraction patterns of the series simultaneously, but none of which fits the data perfectly due to strong overlap of some peaks. To illustrate this problem, the list of the most intense peaks (I>4%) of one sample (No 12, h=1.0) is presented in comparison with several phases which partially fit the diffraction pattern (Table 5.2).

As follows from Table 5.2, at least three reference diffractograms partially fit the pattern of sample No 12 from the series **ZrOHSO4** (as well as XRD patterns of other samples within $0.0 \leq h \leq 1.8$): orthorhombic zirconium sulphate hydrate ($Zr(SO_4)_2*4H_2O$), monoclinic zirconia (m-ZrO_2) and zirconium hydroxide sulphate hydrate ($Zr_2(OH)_2(SO_4)_3(H_2O)_4$). The PDF search-to-match function of TRACES v. 3 program gives relatively low figures of merits for all three phases in spite of the fact that 70 to 90 % of the reference peaks match the analysed pattern within <0.6 °2θ. The problem is aggravated by the overlap of some peaks of the mentioned phases with the peaks of KCl and α-Al_2O_3. The situation is more complicated for the samples h<0.0 where the peak positions vary along with the peak intensities.

We assume that a mixture of the identified phases or another phase with very close diffraction features to those in Table 5.2 exists in the samples of the series **ZrOHSO4**. In order to hypothesise on the nature of these phases a classification analysis of the peak areas of the most intense individual peaks was performed using correlation sum graphs as a simple instrument for the group identification. Correlation sums of peak areas of all individual peaks exceeding 3 levels of RMS (107 peaks in total) were obtained in the hydrolysis ratio domain. The correlation sums were sorted in ascending order and qualified into 3 major groups, peak areas of which are shown in Fig. 5.22.

The data of Fig. 5.22 indicate that peak areas of the first, most populated group of XRD peaks in the series **ZrOHSO4** gradually decrease from the XRD pattern at h=-1.5 to the pattern at h=-0.4. After reaching a local minimum at h=-0.4 peak areas of the group 1 peaks starts to build up to an absolute maximum at h=1.2 after which the peak areas rapidly reduce to near zero value at h=2.0 – the point of the formation of final precipitate of hydrated

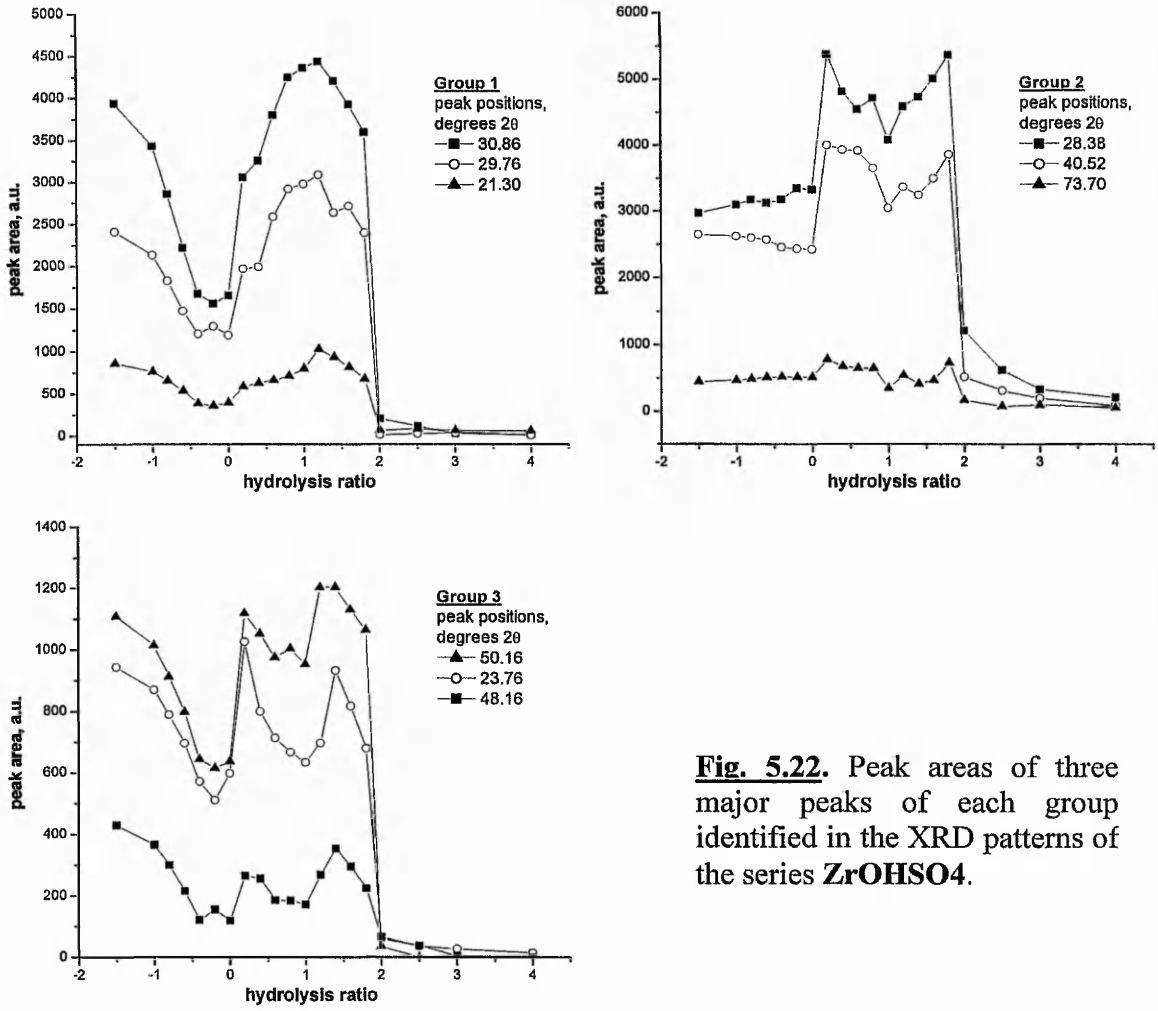


Fig. 5.22. Peak areas of three major peaks of each group identified in the XRD patterns of the series **ZrOHSO4**.

zirconia (Section 4.2). The peak positions of group 1 correspond best to the reference diffractograms of monoclinic zirconia and zirconium sulphate hydrate. As follows from Table 5.2, neither of the phases can be ruled out as well as the possible formation of basic sulphates.

The pH-dependent behaviour of the areas of peaks arising from the KCl phase (group 2) is shown in Fig. 5.22. This group shows a steady behaviour at negative hydrolysis ratios (the peak areas remain practically unchanged). The presence of potassium chloride is caused by conditions of sample preparation of the series **ZrOHSO4** at negative values of h (Section 2.4.3). Equal amounts of potassium sulphate were added to the samples with $h<0.0$ after their hydrolysis ratio was adjusted to the required value with a solution of hydrochloric acid. The fact that the amount of potassium chloride remains constant and quite high (as follows from relatively high peak areas) indicates that probably all chloride ions initially attributed to Zr polymers are replaced by strongly bound sulphate-ions. These freed Cl^--ions crystallise with free K^+-ions to give the sylvite phase upon spray-freeze-drying of the samples.

At $h>0.0$ the amount of crystalline potassium chloride indicated by the areas of the corresponding peaks of group 2 jumps to the highest value and then drops to a local minimum at $h\sim1.0$ (Fig. 5.22). After the local minimum the peak areas increase again up to $h\sim1.8$, above

which these values drop to their lowest values and remain such up to h=4.0. The growth of the peak areas of the KCl phase does not correlate with the increasing concentration of KOH added upon sample preparation, as it did in the series **ZrOH** and **ZrHCO3** (Fig. 5.11 and 5.18). Therefore, some process or species either binds potassium or chloride ions, or hinders the crystallisation of KCl in the solid state. We assume that this could be sulphate-ions, either released upon gradual replacement of them in zirconium hydroxopolymers by the increasing amounts of alkali, or regrouped (e.g. from bidentate to monodentate configuration) in Zr polymers and being able to attach K^+-ions for the charge compensation.

The third group consists of 'hybrid' peaks which show a behaviour, intermediate between group 1 and group 2 (Fig 5.22). We have found that these peaks are often 'twinned', i.e. they result from overlapping of the peaks of the sylvite phase and a zirconium-containing phase. Due to this, peaks of group 3 exhibit the shapes of the peak area curves close to a Zr-containing phase of group 1 at low hydrolysis ratios (h<0.0), while at higher values of h their behaviour resembles the group 3 peaks (KCl).

Results of crystallite size evaluation of all three major groups of XRD peaks of the series **ZrOHSO4** are presented in Fig. 5.23.

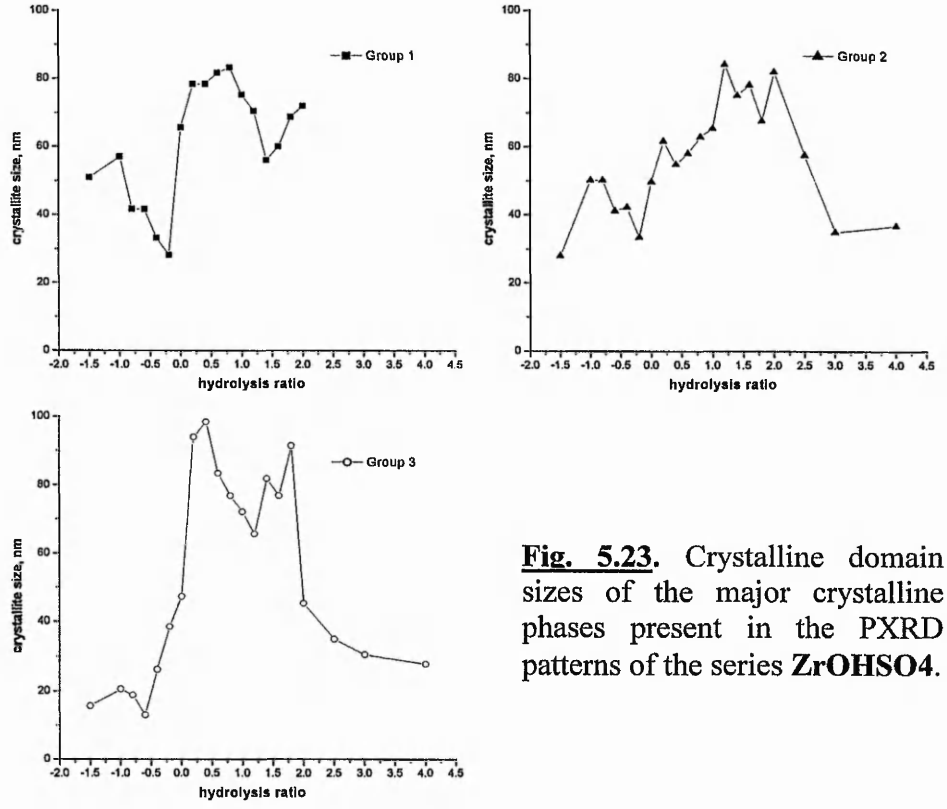


Fig. 5.23. Crystalline domain sizes of the major crystalline phases present in the PXRD patterns of the series **ZrOHSO4**.

From Fig. 5.23 one can see that crystallite sizes of the group 1 XRD peaks of the series **ZrOHSO4** gradually decrease from a local maximum at h=-1.0 (d=58 nm) to ca. 35 nm at h=-0.2. At h>-0.2 the domain size rapidly increases to its highest maximum at h~0.8 (d=84 nm) which is followed shortly by a local minimum at h~1.6 and then the size increases again up to the limit of the phase presence in the samples at h=2.0.

The crystallite size of the group 2 phase tends to increase from ca. 24 to ca. 82 nm along the increase of the hydrolysis ratio from h=-1.5 to h=1.2. There is also a local minimum in this range of h at h~-0.2. Above the range of $1.2 \leq h \leq 1.8$ where crystallite size fluctuates around ca. 70 nm, that is followed by a steep drop at h>1.8. The variation of crystallite sizes of the third 'hybrid' group follows an intermediate path between group 1 and group 3 peaks. The highest crystallite sizes reach as high as d=98 nm at h=0.4. However, the calculated size values from the group 3 peaks are very tentative due to the possible overlapping of at least two peaks belonging to different crystalline phases.

5.4.1.4. XRD spectra of the series ZrOHAc

The multi-batch series **ZrOHAc** were prepared in a similar way to the series **ZrOHSO4** (Section 2.4.3), acetate-ions being introduced instead of SO_4^{2-}-ions at the ratio $Zr:CH_3COO^-$=1:1. Solution measurements of the series **ZrOHAc** are described in Chapter 4. The raw powder XRD measurements of the solid samples of these series prepared by spray-freeze-drying after 48 hours of 'wet' experiment are given in Fig. 5.24. All XRD patterns were acquired at the presence of the internal standard of α-Al_2O_3 (sample:standard=4:1). Two intense peaks at 28.38 and 32.40 °2θ are truncated in Fig. 5.24 for presentation purposes.

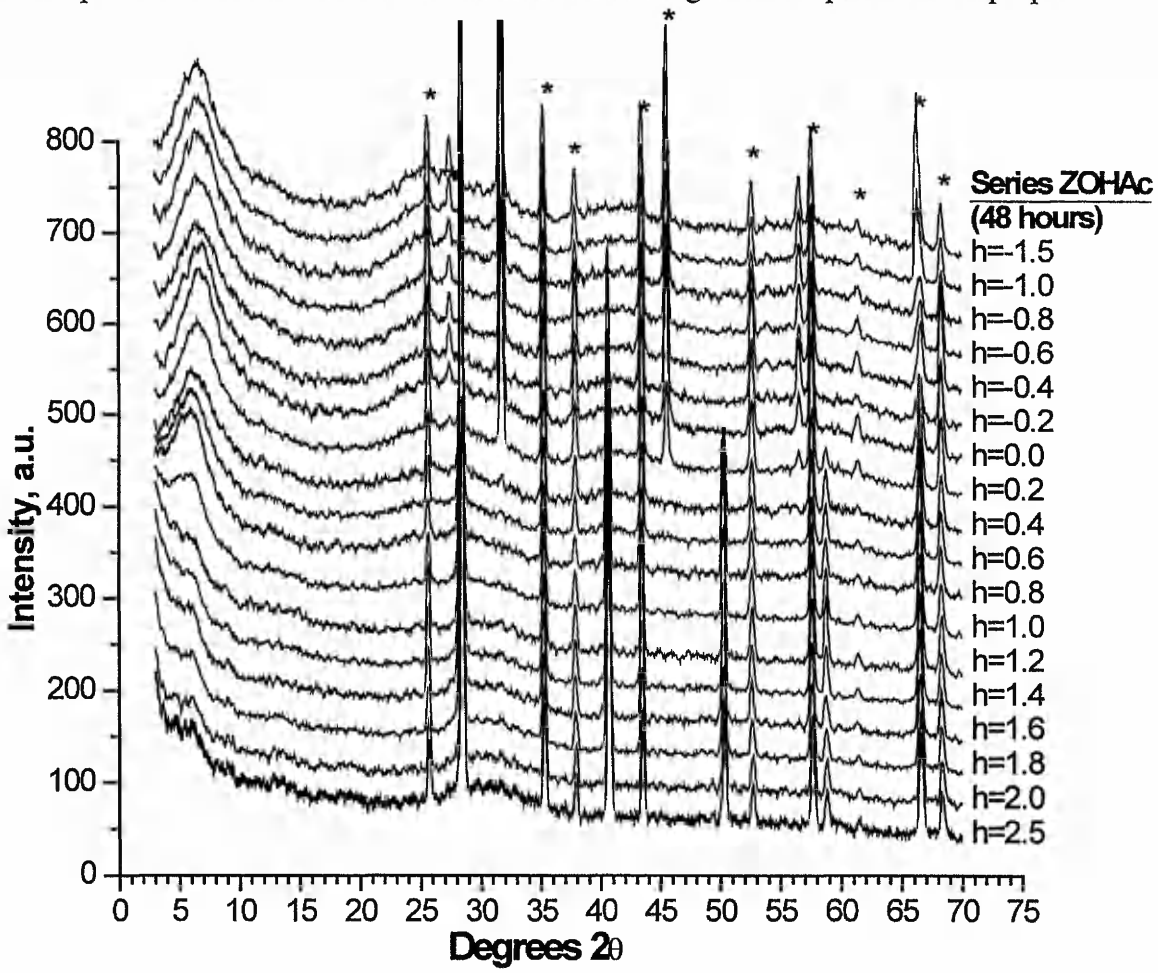


Fig. 5.24. PXRD patterns of the SFD samples prepared from the series **ZrOHAc** after 48 hours of hydrolysis (90°C). Y-offset – 80%.

The data of Fig. 5.24 indicate that XRD patterns of the series **ZrOHAc** have fewer peaks than the series discussed above and can be easily divided into two subsets - below h~0.4 and above this point. The crystalline phase dominating the XRD patterns of **ZrOHAc** series at h<0.4 with four very distinct and intense peaks at 27.46 (5.2 %I), 31.76 (100 %I), 45.54 (25.3 %I) and 56.56 (6.4 %I) could not be identified using JCPDS database (1995, PDF file search using TRACES v. 3 program). There is only one zirconium acetate phase in JCPDS (1999 PDF file, card No 28-1495) which was not matched. The pattern also did not match the XRD pattern of crystalline potassium acetate.

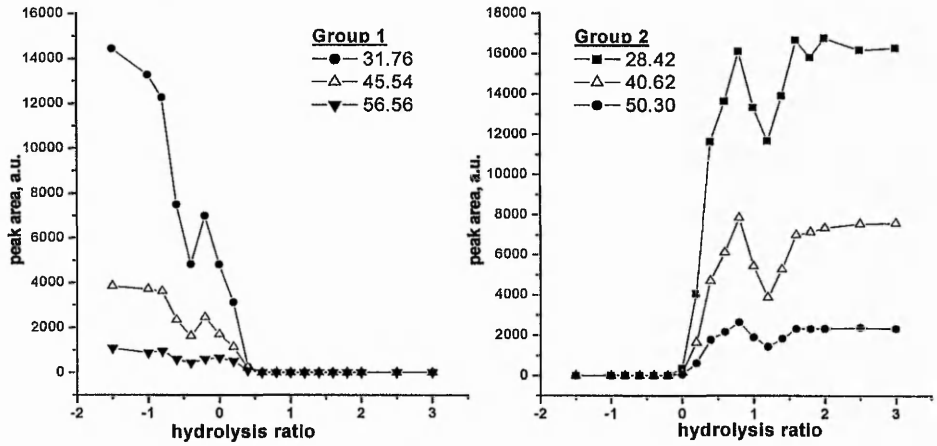


Fig. 5.25. Peak areas of three major peaks of each diffraction group identified in the XRD patterns of the series **ZrOHAc**.

Areas of the most intense peaks of the XRD patterns in Fig. 5.24 were calculated and are shown in Fig. 5.25. Two groups of the peaks can be derived from the peak area curve shapes, which reproduce the division into two groups discussed above (below and above h=0.4). Group 1 in Fig. 5.25 belongs to the unidentified crystalline phase obtained in acidic conditions. The areas of the peaks of this group gradually fall from a maximum at h=-1. There is a local minimum and a maximum of the peak areas at h=-0.4 and h=-0.2 correspondingly, after which peak areas reach zero values at h=0.6. The above-mentioned crystalline phase represented by the group 1 peaks is replaced by the pattern of sylvite (group 2 in Fig. 5.25), the area of which grows steadily from zero at h=0.0 to the maximum at h=0.8 in agreement with the growing concentration of potassium-ions in the initial sample solutions. With the increasing hydrolysis ratio the peak areas of sylvite pattern pass through a local minimum at h~0.4 and then increase again up to the point at h~1.6, after which these values remain practically unchanged up to h=4.0. The amount of sylvite which we assume is proportional to the areas of the corresponding XRD peaks does not follow the concentration profile of free K^+-ions supplied by the increasing additions of alkali at h>0.6. As in the case of the series **ZrOHSO4**, possible reason for this abnormality is either in the release of acetate-ions, which bind K^+ more strongly than Cl^-, or in the charge compensation effect by binding of K^+-ions to the negatively charged sites on the surface of Zr polymers.

The absence of other crystalline patterns at h>0.0 indicates that zirconium-containing

phase is completely amorphous in the presence of acetate-ions that distinguishes the series **ZrOHAc** from the series **ZrOHSO4**.

Crystallite sizes of both group 1 and group 2 XRD patterns have been calculated and the results are presented in Fig. 5.26. The data of Fig. 5.26 show that the domain size of the group 1 phase is at the maximum (d~77 nm) at $h \sim -1.0$ and then reduces gradually to smaller values (d~38 nm) up to h=0.4. The local minimum of the crystallite size curve for the group 1 peaks is observed at h=-0.6. The overall pattern of crystallite sizes of the group 1 phase resembles closely the peak areas curve of the same group shown in Fig. 5.25.

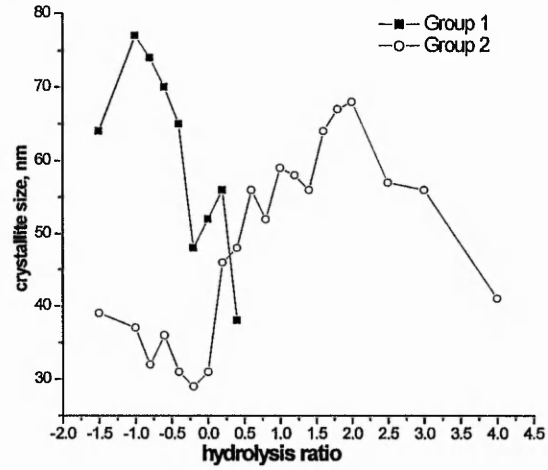


Fig. 5.26. Crystalline domain sizes of the major crystalline phases present in the PXRD patterns of the series **ZrOHAc**.

The domain size of the crystalline phase of sylvite (group 2) shown in Fig. 5.26 is initially lower at $h \leq 0.0$ where it decreases from d~39 (h=-1.5) nm to d~21 nm (h=-0.4). At positive hydrolysis ratios (h>0.0) the size of KCl crystallites increases rapidly up to the maximum d~68 nm at h=2.0 after which it diminishes again to d~41 nm at h=4.0.

5.4.1.5. XRD spectra of the series ZrOHGly (Zr:Gly=2:1, 1:1, 1:2)

Three multi-batch titration series of Zr-ion hydrolysis were conducted in the presence of different amounts of glycine (Zr:Gly=2:1, 1:1, 1:2). PXRD patterns of the solid samples prepared after 48 hours of experiments for these series are shown in Fig. 5.27-5.29. Diffractograms of the series **ZrOHGly1:2** and **ZrOHGly1:1** were acquired in the presence of an α-Al_2O_3 standard. The XRD patterns of the series **ZrOHGly2:1** were measured for the samples 'as is'. The intense peak at 28.38 °2θ was truncated in Fig. 5.27 and 5.28 for presentation purposes.

XRD data of Fig. 5.27 indicate that for series **ZrOHGly1:2** prepared with a two-fold excess of glycine to Zr-ions to (Zr:Gly=1:2) there are significant differences from the diffractograms of the multi-batch series obtained from 'pure' Zr-ion solutions **ZrHCO3** and **ZrOH** (Fig. 5.8, 5.11) The XRD patterns of the series **ZrOHGly1:2** (Fig. 5.27) contain a number of distinct and intense peaks at lower 2θ, such as at 7.18 (I=100%), 8.24 (I=73%) , 9.4 (I=21%), 10.02 ° (28%), etc. These peaks could not be fitted satisfactorily with any of the

Zr-containing phases available in the JCPDS databases (1995, 1999). However, the unknown pattern resembles to

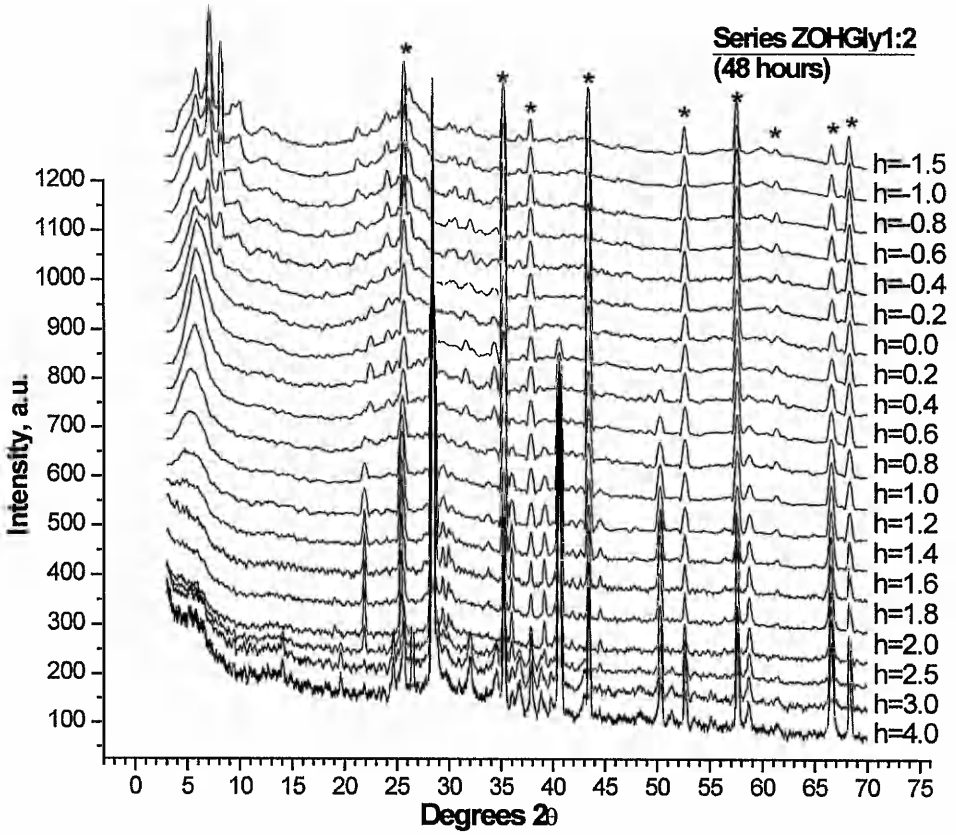


Fig. 5.27. PXRD patterns of the SFD samples prepared from the series **ZrOHGly2:1** after 48 hours of hydrolysis (90°C). Y-offset – 80%. '*' – the peaks of the standard - α-Al_2O_3.

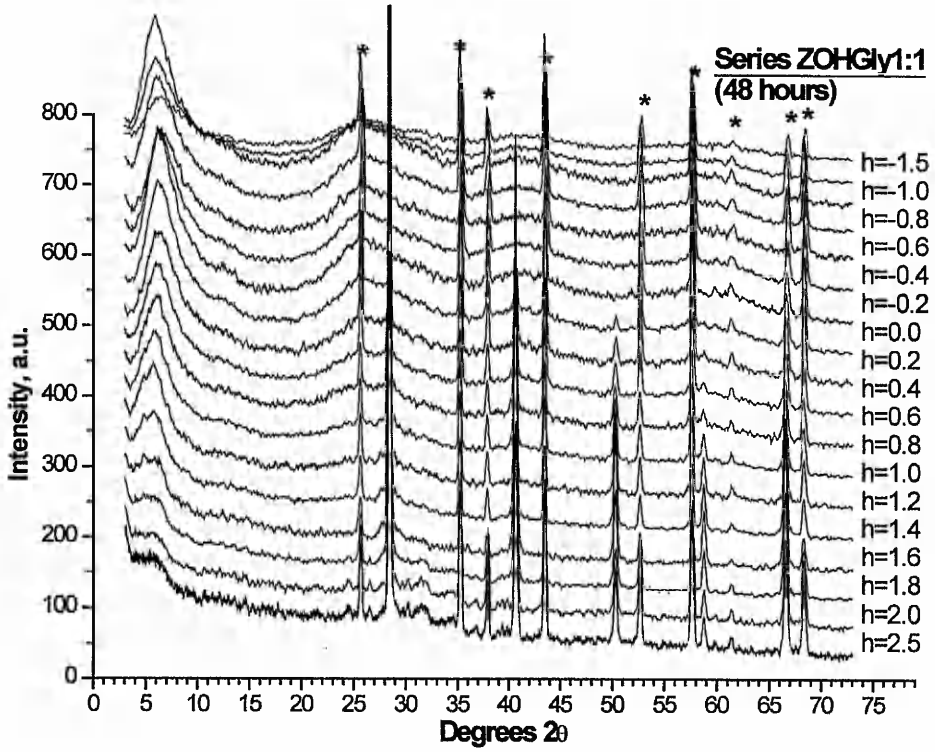


Fig. 5.28. PXRD patterns of the SFD samples prepared from the series **ZrOHGly1:1** after 48 hours of hydrolysis (90°C). Y-offset – 100%. '*' –peaks of the standard - α-Al_2O_3.

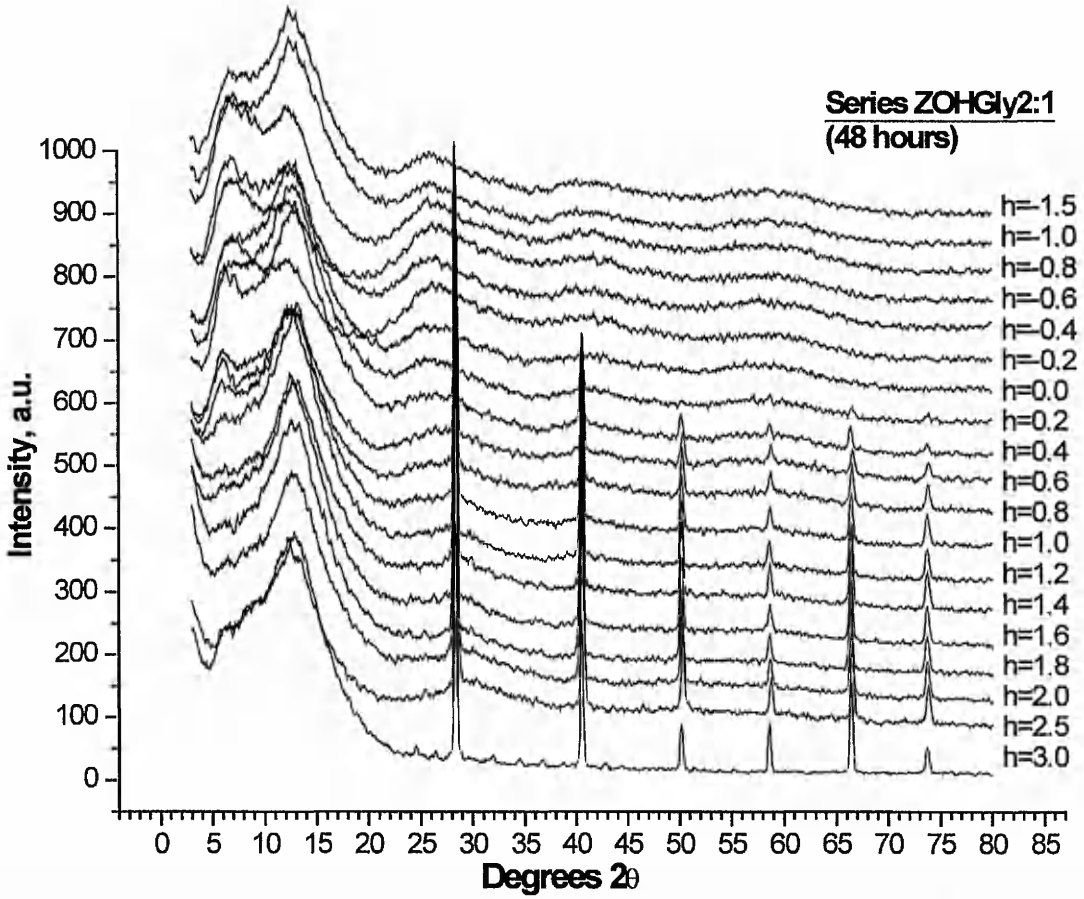


Fig. 5.29. PXRD patterns of the SFD samples prepared from the series **ZrOHGly2:1** after 48 hours of hydrolysis (90°C). Y-offset – 90%. No internal standard.

some extent the reference spectrum of zirconium acetate ($Zr(CH_3COO)_4$, PDF card No 28-1494) which also contains a number of intense lines at low 2θ, e.g. 8.82, 9.48 and 6.4 °, etc., albeit the figure of merit in the JCPDS database was relatively low (>40).

This finding could suggest that at low hydrolysis ratios (h<0.0) along with the well-matched monoclinic zirconia phase there is another phase present in Zr:Gly mixtures, which increases in amount with decreasing hydrolysis ratios down to h=-1.5. This phase probably contains glycine bound to zirconium in a manner similar to $Zr(CH_3COO)_4$.

At higher hydrolysis ratios (h>0.0) the diffractograms of the series **ZrOHGly1:2** (Fig. 5.27) indicate an increasing amount of the sylvite phase, as well as diminishing peak areas belonging to monoclinic zirconia. At h≥1.6 the dffraction pattern resembles the ones at h<0.0 and the sylvite fraction apparently increases with increasing hydrolysis ratios of the samples. Another phase emerges at h≥0.6 and is present in the XRD patterns of **ZrOHGly1:2** up to h~2.5. This phase contains features which differ significantly from those at h<0.0 and at h<1.6, as indicated by new peaks at 21.90, 33.72, 36.02, 44.44, …, °2θ.

The data of Fig. 5.28 and 5.29 suggest that in the presence of equimolar quantities of glycine (series **ZrOHGly1:1**) as well as at a two-fold excess of Zr-ions to glycine (series **ZrOHGly2:1**) the corresponding diffractograms are largely amorphous and contain only the

peaks of crystalline KCl at h>0.0. The quantity of KCl builds up with increase of h, Fig. 5.28 and 5.29. Only at very high hydrolysis ratios (h>1.6 for the series **ZrOHGly1:1** and h=3.0 for the series **ZrOHGly2:1**) Zr-containing crystalline phase emerges, similar to the series **ZrOHGly1:2** (group at h>1.6), and increases with increasing hydrolysis ratio.

The described dynamic changes in the XRD patterns of the glycine-containing series **ZrOHGly** on the hydrolysis ratio scale can be summarised further by the correlation sum (of the squares of correlation coefficients) graph in Fig. 5.30.

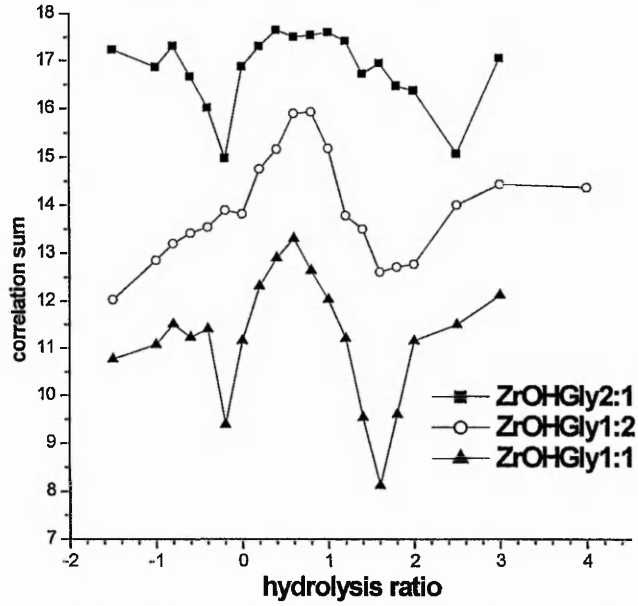


Fig. 5.30. The correlation sums calculated from the XRD patterns of the series **ZrOHGly2:1**, **ZrOHGly1:1** and **ZrOHGly1:2** versus hydrolysis ratio (Y-offset – 40%).

The data of Fig. 5.30 allow for a clear distinction between the ranges of the highest similarity of the XRD patterns for the glycine-containing series. Minima or plateaus on the curves separate the borderlines between the ranges. For instance, for the series **ZrOHGly1:2** a plateau at h=-0.2-0.0 and a minimum at h=1.6 separate three major diffraction regions arising from Zr-containing fractions. The same clear borderline can be observed for the series **ZrOHGly1:1** (h=-0.2 and h=1.6) as well as for the series **ZrOHGly2:1** (h=0.0 and h=2.5).

In order to better understand the distribution of the major crystalline fractions observed in the XRD measurements of the glycine-containing samples, the areas of the most intense peaks have been calculated and the individual peaks were subdivided into groups of highest similarity on the basis of their area variation on the hydrolysis ratio scale obtained by means of correlation analysis. The results of the peak area calculation as well as classification of the individual peaks into groups for the series **ZrOHGly1:2** are shown in Fig. 5.31, for the series **ZrOHGly1:1** and **ZrOHGly2:1** – in Fig. 5.32.

From Fig. 5.31 one can see that four major groups of peaks have been identified in the XRD patterns of the series **ZrOHGly1:2**. The first group with most intense peaks at lower values of 2θ is limited to highly acidic conditions of sample preparation (h<0.0) where the peak area curves of group 1 decrease gradually from a maximum at h=-1.5 to zero at h=0.0.

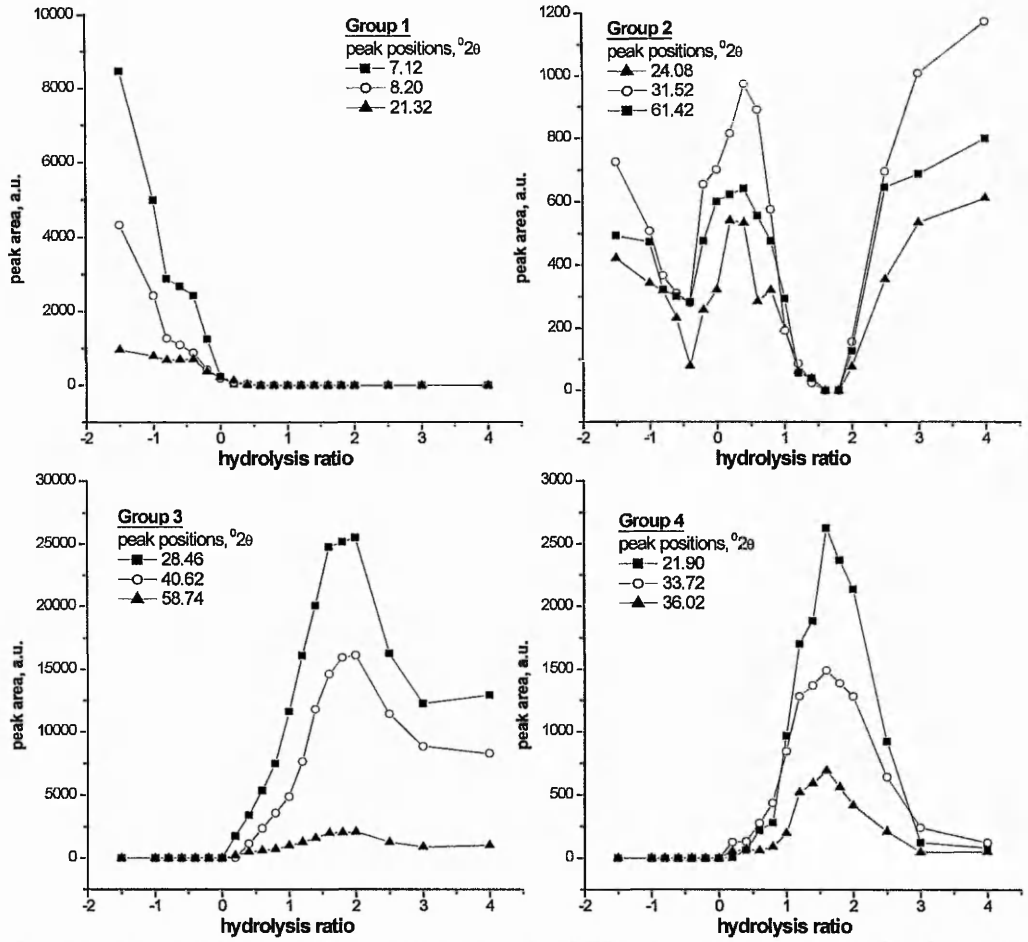


Fig. 5.31. Peak areas of three major peaks of each diffraction peak group identified in the XRD patterns of the series **ZrOHGly1:2**.

The peak area curves of group 2 show a complicated pattern at lower hydrolysis ratios. The peak areas steadily decrease to a minimum at $h \leq -0.4$, after which the presence of the group 2 fraction rises rapidly to a local maximum at h~0.4. Another deep decay of the curves of group 2 at $h>0.4$ leads to a zero-value minimum. The fraction re-emerges at $h\geq1.8$ and becomes the predominant Zr-containing fraction in the XRD patterns of **ZrOHGly1:2** at $h\geq2.0$. Group 3 of the XRD peaks (Fig. 5.31) belongs to the sylvite (KCl) phase. The peak areas of this group increase from zero at $h=0.0$ to a maximum at $h=2.0$ in a monotonic fashion which indicates that most of potassium-ions are free to form KCl crystals upon spray-freeze-drying of the samples. Above $h=2.0$ the peak areas of the sylvite phase rapidly drop to about a half their value. This could provide an indirect hint about the possible release of glycine bound to zirconium oxohydroxopolymers and its interference in the process of KCl crystallisation, or potassium ions could be consumed by the increasingly negative surface of hydrous ZrO_2 at high pH values for charge compensation.

The fourth distinct group of XRD peaks observed in the diffractograms of the series **ZrOHGly1:2** monotonically increases from $h>0.0$ and reaches a maximum at $h=1.6$, after which it descends to zero values at h~3.0.

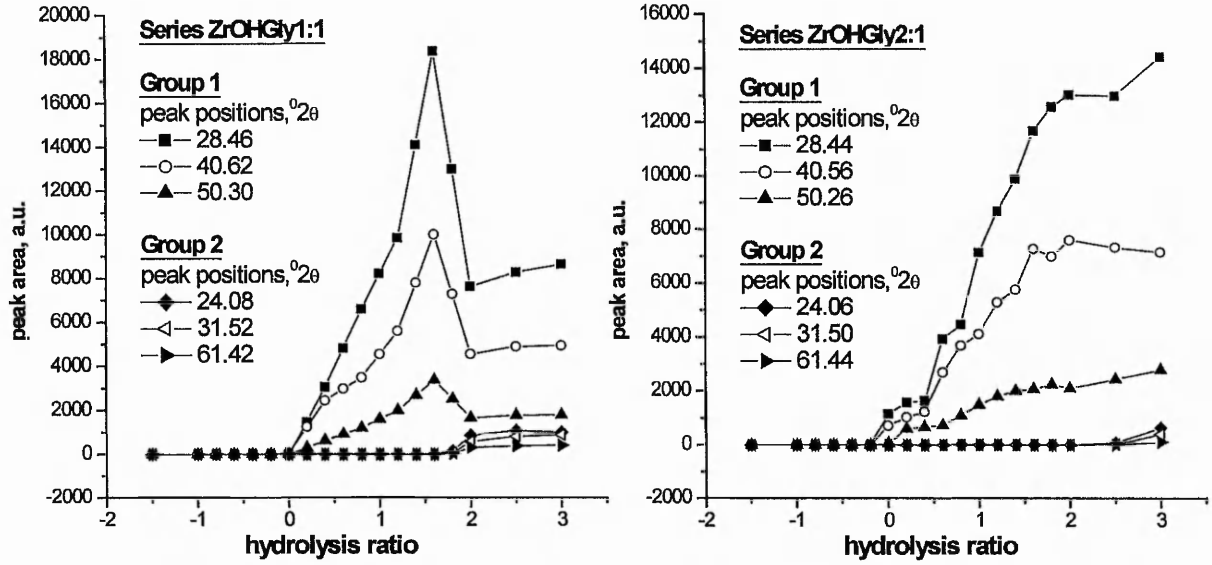


Fig. 5.32. Peak areas of three major peaks of each diffraction peak group identified in the XRD patterns of the series **ZrOHGly1:1** (left) and **ZrOHGly2:1** (right).

The major crystalline phase observed in the XRD data sets of the series **ZrOHGly1:1** and **ZrOHGly2:1** up to h=2.0 is the sylvite (KCl) phase (Fig. 5.32). In both cases, the peak areas of crystalline KCl increase monotonically with increasing hydrolysis ratios of the samples. After reaching a maximum at h=2.0 the peaks of sylvite for the series **ZrOHGly1:1** decrease substantially (more than twice) and remain relatively sable at $h \geq 3.0$. For the series **ZrOHGly2:1** the peaks of sylvite either stabilise, or continue to increase in alkaline conditions (h>2.0).

The second group of diffraction peaks identified in the series **ZrOHGly1:1** and **ZrOHGly2:1** (Fig. 5.32) is similar to those of group 2 of the series **ZrOHGly1:2** (Fig. 5.30) in terms of individual peak positions. This fraction appears at very high hydrolysis ratios ($h \geq 2.0$ for **ZrOHGly1:1** and $h \geq 3.0$ for **ZrOHGly1:2**). The bulk of the Zr-containing material in the series with the lower amount of glycine (Zr:Gly 1:1 and 2:1) is amorphous.

Along with peak areas discussed above, we have calculated the crystallite sizes of the major phases from the glycine-containing series. The results of calculation are shown in Fig. 5.33 for the series **ZrOHGly1:2** and Fig. 5.34 for the series **ZrOHGly1:1** and **ZrOHGly2:1**.

The data of Fig. 5.33 indicate that with increase of hydrolysis ratio the crystallite sizes of the first group of XRD peaks identified in the diffractograms of the series **ZrOHGly1:2** decrease constantly from d~57 nm at h=-1.5 to d~10nm at h=0.4. This variation is in line with the decreasing areas of the peaks of group 1 (Fig. 5.31) and, therefore, correlates with the diminishing presence of a crystalline phase formed at low hydrolysis ratios. The crystallite sizes calculated from the second group of XRD peaks (Fig. 5.33) show an initial fall in values from ca. 20 to 10 nm at very low hydrolysis ratios ($-1.5 \leq h \leq -0.8$), which is followed by a local maximum at h=0.2 (d~19 nm). From h=0.4 the size of the fraction represented by the group 2 peaks monotonically increases from d~10 nm to d~44 nm at h=1.6. At higher values

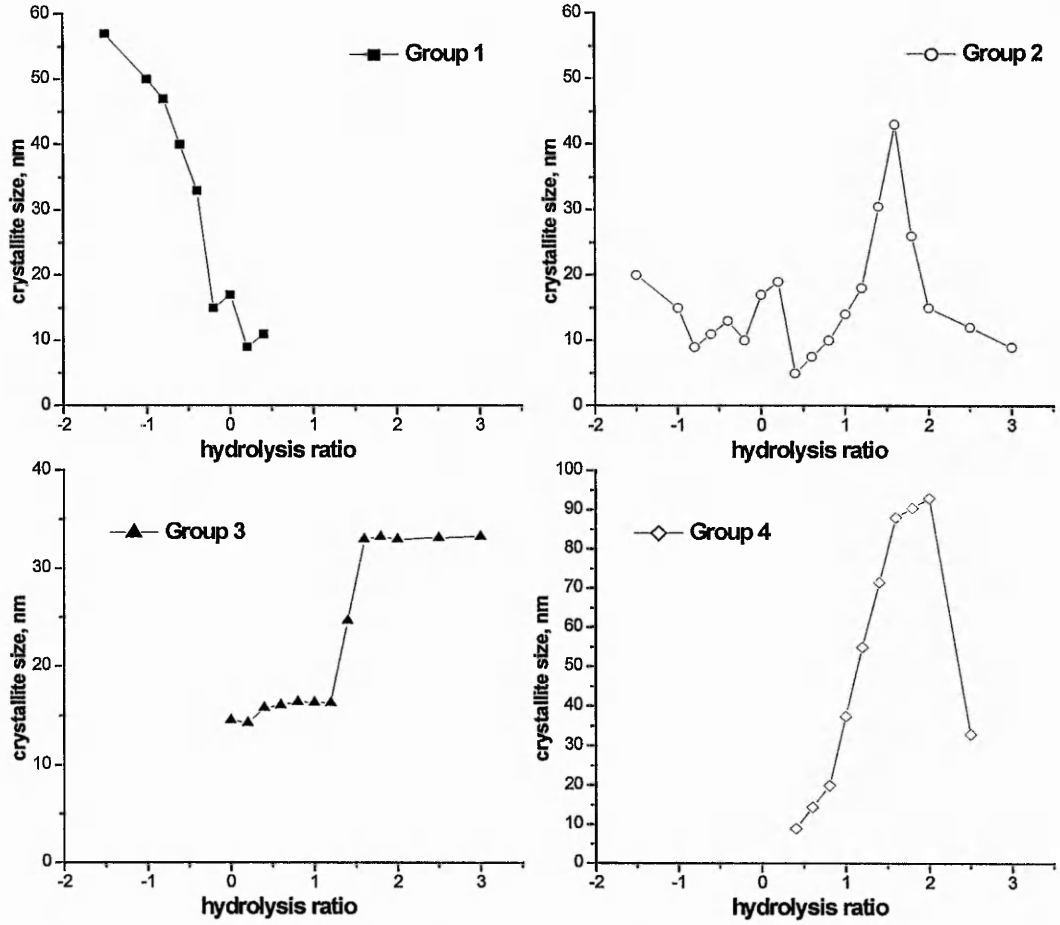


Fig. 5.33. Crystalline domain sizes of the major crystalline phases present in the PXRD patterns of the series **ZrOHGly1:2**.

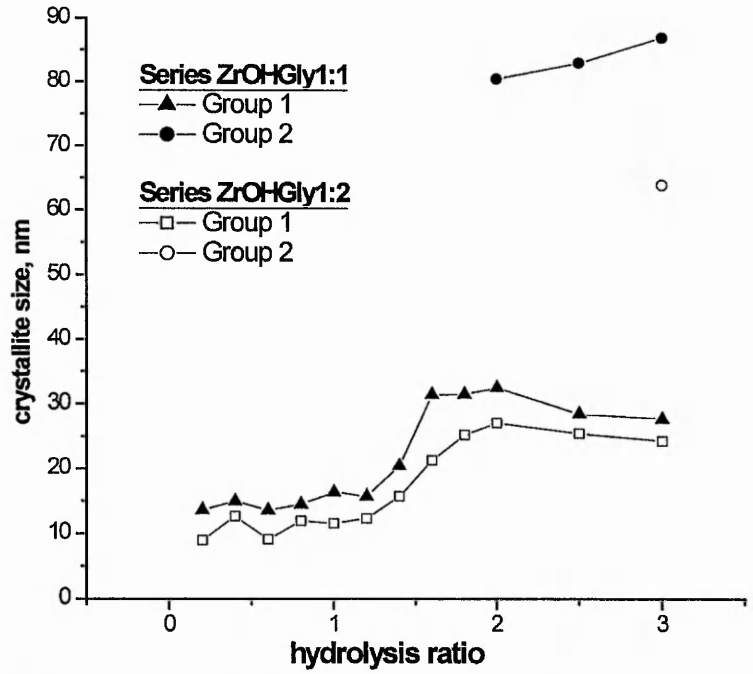


Fig. 5.34. Crystalline domain sizes of the major crystalline phases present in the PXRD patterns of the series **ZrOHGly1:1** and **ZrOHGly2:1**.

of h the particle size gradually reduces to ca. 8 nm at h=3.0.

Group 3 of the XRD peaks of the series **ZrOHGly1:2** (sylvite phase) shows two distinct ranges of relatively constant crystallite sizes (Fig. 5.33). In the range $0.0 \leq h \leq 1.2$ the domain size is 14-15 nm on average, while within $1.6 \leq h \leq 3.0$ it equals ca. 33 nm. The crystallite sizes of the group 4 phase increase from ca. 7 nm to ca. 52 nm within the range of hydrolysis ratios $0.4 \leq h \leq 2.0$ and then diminish at $h > 2.0$.

Only two crystalline phases are observed in the case of the series **ZrOHGly1:1** and **ZrOHGly2:1**. We have calculated the crystallite sizes for both (Fig. 5.34). The domain sizes of the sylvite phase (group 1 in both series) follows the same pattern and are very similar to the data obtained for the series **ZrOHGly1:2**. The curves of group 1 in Fig. 5.34 split into two distinct regions – at $0.0 < h \leq 1.2$ and at $1.6 \leq h \leq 3.0$. At lower hydrolysis ratio an average crystallite size is ca. 10 nm for the series **ZrOHGly1:1** and ca. 13 nm for the series **ZrOHGly2:1**. At higher h the average sizes are d=23 nm (**ZrOHGly1:1**) and d=29 nm (**ZrOHGly1:2**). The crystallite sizes of the Zr-containing phase appearing at high hydrolysis ratios are significantly higher than for the sylvite phase. In the case of the **ZrOHGly1:1** series they vary within $80 \leq d \leq 86$ nm, and for the **ZrOHGly2:1** series– d=64 nm.

5.5. Discussion of SFD and XRD data

5.5.1. Spray-freeze-drying

The method of spray-freeze-drying (SFD) developed specifically for chemical speciation studies in the present study has shown great potential for solution speciation analysis. The closeness of the ^{27}Al solution NMR spectra of re-dissolved spray-freeze-dried samples of the series **AMK1** (Fig. 5.2) to the analogous spectra of the initial as-prepared samples, as well as a good correlation with solid-state ^{27}Al NMR data (Fig. 5.3), which shows all major species as detected in solution, proves the maintenance of the speciation patterns, when transforming samples from solution into solid state using the SFD technique. XRD examination of the solid Al-containing samples of the series **AMK1** and Zr-containing samples of the series discussed in Section 5.3 of the present chapter also proves that variation in structural properties of spray-freeze-dried materials is mainly caused by the conditions of sample preparation in solution and therefore, hydrolysis ratio and pH are the crucial parameters determining the structure, composition and phase distribution of solid SFD materials. A minor drawback of spray-freeze-drying is that it converts into the solid state all species (including foreign ions and molecules) present in solution into solid state can, however be of benefit. For instance, detection of the crystalline phase of KCl (in the form of sylvite) allowed us to monitor whether chloride and potassium ions are free or bound to the target Al-, or Zr-containing species.

5.5.2. Series AMK1

Extensive solid-state characterisation of the solid samples obtained by spray-freeze-drying of solution samples from the multi-batch alkaline titration of Al-ions at high temperature (series **AMK1**) has revealed the following trends. Re-dissolution of the SFD samples of the series **AMK1** combined with ^{27}Al solution NMR spectroscopy along with the preservation of the speciation patterns upon transformation from solution to solid state using the SFD technique, has revealed that for some species, such as Al_{30}-mer (the NMR signal at 70 ppm in Fig. 5.2), their structure and concentration remain practically unchanged (variation in the peak areas is less then 5 % when compared to initial sample solutions), whereas the quantities of Al_{13}-mer, and to a greater extent, Al dimers and Al monomers with signals at 63, 4 and 0 ppm correspondingly are slightly altered (variation between the re-dissolved SFD samples and the initial samples is within ca. 10 %). This alteration in quantities of individual species does not necessarily arise from the spray-freeze-drying procedure itself, but could possibly relate to the re-dissolution procedure which can alter speciation patterns due to the impossibility to match precisely all the conditions of the initial sample preparation. Moreover, the degree of deviation of the quantitative composition in the solid state from the initial solution state could provide qualitative information on the relative stability of the species and in particular, a possibility for them to be transformed into the solid state. The least variation of the concentration observed for Al_{30}-mer (Fig. 5.3) indicates higher stability of this species and shows a possibility to transform the Keggin ion into the solid state structurally unaltered.

High-resolution ^{27}Al MAS NMR characterisation of the solid samples of the series **AMK1** (Fig. 5.3) indicates that Al-monomers exist in the samples after the SFD procedure in a wide range of hydrolysis ratios (up to h~2.0), in agreement with the solution data. Al dimers in the solid state also follow the same pattern as in the solution studies of the series **AMK1** with a maximum of intensity of the corresponding peak ~0-1 ppm at h~1.0. This value corresponds to the theoretical hydrolysis ratio of the Al dimer (OH/Al ratio is equal to 1 for this species). The maximum intensity of the peak at 62 ppm of tetrahedral Al in Al_{13}-mer in the MAS NMR spectra is between h=2.4 and h=2.6, which is again very close to the theoretical ratio of these species (h=2.46). The peak maximum at 68 ppm (the signal from tetrahedral Al of the Al_{30}-mer) exactly matches its theoretical hydrolysis ratio at h=2.40.

PXRD measurements of the SFD samples of the series (Fig. 5.4) indicate that Al monomers are capable of crystallisation into the chloraluminite phase of the initial solid precursor ($AlCl_3$*$6H_2O$). The distribution of the peak areas of this crystalline phase generally follows the Al monomer patterns in solution and solid-state NMR spectra, except that $AlCl_3$*$6H_2O$ is not detected in the XRD patterns above h~1.5 probably due to (*a*) lower sensitivity of XRD patterns comparing to high-resolution (14 Tesla) MAS NMR and solution ^{27}Al NMR spectra, (*b*) the hydrolysis lower content of Al monomers and into monomeric $[Al(OH)(H_2O)_5]^{2+}$ and $[Al(OH)_2(H_2O)_4]^{+}$ species, into oligomers (Al dimer, Al_{13}-mer and

Al_{30}-mer which increasingly hinders formation of chloraluminite at h>0.0; (*c*) increasing amounts of Al hydroxide, formed far below the point of electroneutrality at h=3.0, which force the system to form amorphous phase.

Along with the soluble lower molecular weight species (Al monomers, dimers, Al_{13}-mes and Al_{30}-mers) solid-state ^{27}Al NMR spectra and XRD measurements have also revealed the presence of the gibbsite phase (a relatively sharp peak at ca. 9.5 ppm, Fig. 5.3). The range of the gibbsite formation according to the MAS NMR spectra is at least from h~1.0 to h~3.0. The XRD patterns of the series **AMK1** could detect the gibbsite phase only in the range $h\geq2.8$. This difference may indicate that either the gibbsite particles are too small and their broadening too high to be detected in the standard XRD patterns at h<2.8, or the signal observed in the MAS NMR spectra relates to a soluble direct precursor of gibbsite, isostructural with the final gibbsite phase. In the latter case the signal of such soluble 'proto-gibbsite' particles would be present in the ^{27}Al solution NMR spectra, albeit indistinguishable from the peak at ca. 10 ppm. Careful peak fitting of some solution NMR spectra at h>2.0 (Section 3.3.3) suggests that this could be the case, since a small additional peak at 10-11 ppm can be sometimes uncovered on top of the very broad and large NMR peak relating to octahedral Al of Keggin polycations. The presence of 'proto-gibbsite' would also explain some slight discrepancies between the total amount of soluble Al species detected with solution NMR and the sum of all NMR-identifiable species observed in the 'wet' experiments at high hydrolysis ratios in Chapter 3 of this work.

The relatively low intensity of the gibbsite peaks in the XRD patterns of the series **AMK1** (Fig. 5.4) probably indicates that this crystalline fraction constitutes only a minor fraction of the bulk Al-containing part of the SFD materials which are predominantly amorphous from h~1.75 to h~2.9. This may lead to a conclusion that the pathway of Al hydrolysis-condensation through the formation of Keggin-ions probably hinders formation of crystalline Al hydroxide. One of the possible reasons for this fact is an instant collapse of the Keggin ions at h>2.6 which leads to a structurally disordered amorphous Al hydroxide phase, unable to restructure and to form well-aligned crystalline phase. Another reason could be, as it was mentioned above, the early formation of the amorphous hydroxide phase due to 'local perturbations in Al-ion solutions caused by strong alkali.

The crystalline phase of KCl (sylvite) has been also detected in the PXRD patterns of the series **AMK1** along with chloraluminite and gibbsite. Since the formation of KCl crystals depends exclusively on the concentration of potassium-ions supplied by the increasing portions of alkali (KOH in the series **AMK1**) and on the concentration of unbound chloride-ions available for such crystallisation, areas of the sylvite-related XRD peaks can be a measure of the availability of both ions in solution. From the data of Fig. 5.5 one can find that the peak areas of the KCl phase increase almost linearly with increase of the hydrolysis ratio from h=0.0 to h~2.6, after which the curve for the most intensive peak at 28.5 °2θ becomes

steeper until a maximum at h=3.0 is reached. This may indicate that some portion of chloride remains bound to ionic Al species prevailing at h<2.6 and only after the point of Keggin ion (Al_{13}-mer, Al_{30}-mer) collapse at ca. h~2.6 is it released and becomes available for crystallisation into sylvite upon spray-freeze-drying. The amount of crystalline KCl indicated by the areas of the relevant XRD peaks decreases at h>3.0. One can hypothesise that in this case the decrease is caused by the deficit of free potassium-ions probably bound to the increasing anionic $Al(OH)_4^-$ species or, more probably, to the surface of Al hydroxide that is negatively changed under alkaline conditions [16].

Crystallite sizes calculated from the peak broadening of the XRD patterns of the series **AMK1** (Fig. 5.6) are within quite a narrow range (40-56 nm) for all crystalline phases identified. The crystalline size of chloraluminite reaches a maximum at h=0.0 and decreases both at h<0.0 and at h>0.0. At lower h the decrease is probably caused by the interference of high proton concentration on the growth of crystallites in the solid state. At higher hydrolysis ratios (h>0.0) the crystalline growth of $AlCl_3$ is limited by the decreasing concentration of Al monomers as well as the increasing extent of their hydrolysis. Gibbsite particles are the largest (55.6 nm) at h=3.0 (the point of electroneutrality) and reduce in size below and above this point. Crystallite sizes of the KCl phase detected for the series **AMK1** increase in line with the growing concentration of potassium-ions introduced by alkali and reach a maximum at h~2.9. Beyond this point (h>2.9) the size of KCl crystallites decreases. On the basis of crystallite size distribution of all three phases detected in the series **AMK1** one can notice that the higher the concentration of free ions, the higher the size of the KCl crystallites.

5.5.3. Advanced treatment of XRD spectra

PXRD measurements of the Zr-containing solid samples produced by spray-freeze-drying contain a wealth of crucial structural information on Zr-ion speciation in aqueous solutions, otherwise practically inaccessible from the solution and colloidal data.

The XRD patterns of the Zr-containing solid samples are characterised by a large number of peaks, several phases can be present in the samples simultaneously. In order to identify the major crystalline components of the samples from the multi-batch titration series with Zr-ions, we have developed an algorithm based on 2D-correlation analysis [13] and the method of the correlation sum graphs, proposed in this work. To our knowledge, this is one of the first attempts to implement 2D-COS analysis for the identification of XRD patterns. As a result of its application, significantly larger numbers of the XRD peaks have been unambiguously identified in comparison with a conventional visual analysis.

Areas of the XRD peaks have been chosen as a quantitative parameter for the relative phase distribution analysis due to their advantage over peak intensities which are affected by significant peak broadening, as follows from the crystallite size evaluation. Peak fitting procedure using advanced software (GRAMS, Origin) has been applied in order to determine

peak areas of the overlapped peaks more precisely. Direct integration has been used in the case of well-separated peaks. An advanced procedure for has been implemented for the XRD data set normalisation. Combination of the peak-fitting and the cross-normalisation procedure has enabled us to obtain useful semi-quantitative results on the pH-dependent distribution of crystalline phases in the solid Zr-containing samples prepared by spray-freeze-drying.

5.5.4. Discussion of the PXRD spectra from the series of 'pure' hydrolysed Zr-ions

XRD patterns of the SFD samples from the multi-batch series **ZrHCO3** and **ZrOH**, obtained by titration of (0.2 M) Zr-ion solutions at high temperature (90 °C) with $KHCO_3$ and KOH correspondingly, show a number of similar features (Fig. 5.8 and 5.18). In acidic media (h<1.2) a group of intense XRD peaks is present in the diffractograms of the series **ZrHCO3** and **ZrOH** after 48 hours of hydrolysis which we have assigned to a mixture of 'dehydrated' forms of the precursor $ZrOCl_2*8H_2O$. Several crystalline phases of such kind have been reported in the literature [17-20] and have an overall formula $ZrOCl_2*xH_2O$ where x is the of number of water molecules which varies in the reference phases available in the PDF database from 6 to 2. Some of these crystalline phases have been synthesised by direct heating of solid $ZrOCl_2*8H_2O$ [17, 18] that supports the hypothesis of 'dehydration' of zirconyl chloride. Interestingly, while the initial solid precursor of zirconyl chloride ($ZrOCl_2*8H_2O$) has a tetragonal structure; the 'dehydrated' forms are all monoclinic. Moreover, the monoclinic zirconia phase was also identified in the acidic range (h<1.6) in this study, as well as in other works [21-23]. Therefore, one can hypothesise that the identified 'dehydrated' forms of zirconyl chloride are the result of partial dehydration of tetragonal zirconium tetramers and related polymers (the main structural elements of $ZrOCl_2*8H_2O$ in solution [21]) upon heat and high acidity. This favours the transformation from the thermodynamically more stable tetragonal form of these polymers into a monoclinic form. The transformation requires a decrease of coordination number of Zr-atoms from N=8 (tetragonal) to N=7 (monoclinic) which can be achieved by reducing the number of aquo-ligands in their coordination sphere.

The increase of acidity of the sample solution favours the formation of the monoclinic zirconia in agreement with the literature data [21-23]. Analysing the peak area distribution of this phase obtained from the PXRD patterns of the series **ZrOH** and **ZrHCO3**. However, at the most extreme acidity reached in this work (h=-1.5, pH~0.2-0.3), there is some tendency for the decline of the monoclinic zirconia amount. The results reported in the work [24] indicate a similar trend.

At intermediate hydrolysis ratios (1.0<h<2.0) corresponding to the formation of so-called gels α and β according to solution data in Chapter 4, the SFD samples are practically amorphous (Fig. 5.8, 5.17). The only significant crystalline phase observed in this region is KCl. The presence of the KCl phase increases from zero at h=0.0 to its very intense maximum at h~2.0 and then gradually decreases. As in the case of Al-containing series

AMK1 discussed above, the amount of KCl is an important indicator of the freedom of K^+ and Cl^--ions. It appears that chloride-ions are not bound strongly to Zr hydroxopolymers that is supported by rapid increase of the sylvite phase, while potassium ions become bound to increasingly negative zirconium oxide at very high hydrolysis ratios (h>2.0) which results in a decreasing amount of KCl being detected.

At h≥1.4 another Zr-containing crystalline phase starts to emerge in the XRD patterns of the series **ZrHCO3** and **ZrOH**, which we assign as tetragonal zirconia. This assignment is in general agreement with the literature data which suggests that higher pH should favour the formation of t-ZrO_2 prepared with different alkalis [25]. In the case of the series **ZrHCO3** the relative amount of t-ZrO_2 detected from the corresponding areas of the XRD peaks slowly increases towards a maximum at h=3.0, after which it decreases quite rapidly. In the case of the series **ZrOH** the tetragonal zirconia phase increases quickly and reaches a maximum at h=2.0, after which it decreases relatively slowly. At this point one can observe another significant deviation between the series **ZrOH** and **ZrHCO3** due to varying alkali strength.

The reason for the formation of the tetragonal zirconia phase under conditions of high temperature and high concentration of alkali (h≥1.4) possibly has a kinetic origin, which we have examined on the basis of the XRD patterns of the series **ZrOH** prepared at different sampling times ranging from 3 to 48 hours. The results of examination in the form of peak area dependence on hydrolysis ratio are shown in Fig. 5.18. It seems logical that the higher the amount of alkali added in one shot, the faster the precipitation of purely amorphous hydrated zirconia and the more 'loose' the aggregation of particles in the precipitate. Upon alkaline precipitation, unlike for the slow formation of monoclinic zirconia at low pH, Zr-atoms are not forced to strip off coordinated water and to decrease the coordination number from 8 to 7. Instead, freshly precipitated zirconia possibly restructures into the ordered tetragonal phase, the process being speeded up by the high temperature of solution. The degree of ordering and, therefore, the amount and the crystallite size of tetragonal zirconia depends on the degrees of freedom in the 'loose' zirconia particles which obviously increase with pH and hydrolysis ratio of solution due to faster precipitation of less ordered amorphous phase. Owing to this, the largest amounts of tetragonal zirconia (the highest areas of the relevant XRD peaks in Fig. 5.18) and the largest crystallite sizes (Fig. 5.19) are encountered at the point of the electroneutrality of zirconia (h=2.0) in the series **ZrOH**, where precipitation is very fast. Above the point of electroneutrality the process of zirconia ordering into tetragonal crystals is probably hindered by the increasing negative charge on the surface groups in alkaline conditions [26]. The decreasing peak areas of t-ZrO_2 reflect this trend. The topochemical reaction of the transformation of amorphous zirconia into the tetragonal crystalline phase occurs in the solid state and is, therefore, relatively slow. For instance, from Fig. 5.18 one can see that at h=2.0 the peak area of the **ZrOH** sample at τ=48 hours is twice as large as at τ=3 hours. Varying solubility of the colloidal aggregates of hydrous zirconia can

be another contributing factor of the transformation into *t*-ZrO_2. Higher alkali strength would lead in this case to increasing dissolution rates and faster transformation of amorphous precipitate into *t*-ZrO_2.

In the case of the series **ZrHCO3** the alkali added is weaker ($KHCO_3$) and precipitation at $h \geq 1.4$ is probably not as fast as in the series **ZrOH**. Also, the solubility of hydrous zirconia would be lower in a weaker alkali. In the specific case of $KHCO_3$ as a titrant, there is a third very important factor involved - the formation of soluble Zr carbonate complexes in alkaline conditions [27]. The combined action of the mentioned three factors results in lower amounts of crystalline *t*-ZrO_2 and smaller crystallite sizes.

As follows from the time-resolved XRD data from the series **ZrOH**, the formation of monoclinic zirconia is even slower than that of tetragonal ZrO_2. This is related to the temperature conditions. The authors of the reported work [28] suggest that the temperature of 90°C is 'borderline' between two temperature regions: at T<90°C the formation of monoclinic is restricted kinetically, and at *T*>90 °C this is kinetically more feasible process. On the 'borderline' at 90°C monoclinic zirconia forms very slowly, as supported by our time-dependent XRD data of the series **ZrOH** (Fig. 5.13-5.17).

Analysis of the crystallite size data of the series **ZrHCO3** and **ZrOH** obtained using XRD peak broadening measurements of the most intense peaks of each crystalline phase present in the solid samples shows the following general trend: the larger the amount of the given crystalline phase indicated by its peak areas, the higher the corresponding crystallite size. Most of the identified crystalline phases of the series **ZrHCO3** and **ZrOH** follow this trend, apart from a few exceptions. For instance, the crystallite size of one of the phases relating to the 'dehydrated' forms of zirconyl chloride is larger at higher hydrolysis ratios $h > -0.4$ (Fig. 5.19) which is the reverse of the trend of the peak area curves (Fig. 5.18). The variation of the crystallite sizes with time analysed in Fig. 5.19 for the series **ZrOH** indicates that crystallite sizes of Zr-containing phases such as monoclinic and tetragonal zirconia and, to some extent, 'dehydrated' zirconyl chloride phases show strong time dependence. The domain sizes of all Zr-containing phases tend to increase in conditions close to the optimum for the formation of these phases. For instance, the largest crystallite size increase with time is observed for monoclinic zirconia at $h < -0.4$, for tetragonal zirconia – at $2.0 \leq h \leq 3.0$, for group 1*A* ('dehydrated' $ZrOCl_2$) – at $h < -0.8$ and $-0.6 < h < 0.4$, for group 1*B* (another form of 'dehydrated' zirconyl chloride) – at $h > 0.2$. Interestingly, the crystallite sizes of the 'foreign' phase of KCl does not show significant time-dependent behaviour – which probably is due to appearance of this phase only at the stage of spray-freeze-drying.

Comparing the limits of the formation of monoclinic and tetragonal zirconia with the pH-metric data of Chapter 4 of the present study, one can assume that the division of the amorphous colloidal phases into gels α and β [29] observed quite clearly in the pH-metric data could be a result of the underlying structural motifs. The borderline between monoclinic

and tetragonal zirconia phases is at h~1.6 (Fig. 5.11 and 5.18, group 2) which is very close to the inflexion in the titration curves attributed to the conversion of the colloidal phase in solution from gel α to gel β. Therefore, one can conclude that the reason for such a division of amorphous phases lies in the preferred structural orientation (monoclinic for gel α and tetragonal for gel β) and prevailing coordination numbers of Zr atoms in these phases (N=7 for gel α and N=8 for gel β). Indeed, this hypothesis needs further experimental verification.

Another conclusion arising from the comparison of the solid-state XRD and solution pH-metric data of the series **ZrHCO3** and **ZrOH** is that pH-metric data are relatively insensitive to the structural variations of the polymeric species in Zr-ion hydrolysed solutions, while XRD patterns provide valuable insight into the structural motifs underlying colloidal transformations in solution. Again, the use of spray-freeze-drying has provided quite precise 'fingerprints' of Zr solution species which have helped to elucidate structural transformation going on in solution using solid-state techniques.

5.5.5. Effect of anions and glycine on the solid-state speciation of Zr-containing crystalline phases

In Chapter 4 of the present work we have examined the effects of foreign anion and glycine addition on the speciation of Zr-ions in solution. In this Chapter we have studied the structural effects of these additions on the Zr-containing solid phases obtained from spray-freeze-drying of sample solutions after 48 hours of hydrolysis using X-ray diffraction method.

Sulphate-ions are known to drastically change the structure of Zr-containing solid phases [21, 30]. In the series **ZrOHSO4** where SO_4^{2-}-ions were added to Zr-ion solution in equimolar amounts at high temperature (90 °C) and the adjustment of the hydrolysis ratio with HCl or KOH solution (depending on the sign of h) was made immediately afterwards. Therefore, sulphate-ions were able to react with oligomeric Zr species at low pH, and then faced either increasing acidity or had to compete with hydroxyl-ions at positive h for the coordination sites at Zr-atoms in polymers.

PXRD patterns of the series **ZrOHSO4** discussed in Section 5.4.4 of the present Chapter show that the structure of the solid samples produced by SFD technique differs dramatically from the series with 'pure' zirconyl chloride solutions (**ZrHCO3** and **ZrOH**). At least three Zr-containing phases can match the major crystalline peaks of the series **ZrOHSO4** (Table 5.2): orthorhombic $Zr(SO_4)_2*4H_2O$; monoclinic ZrO_2 and possibly monoclinic basic zirconium sulphate hydrate $Zr_2(OH)_2(SO_4)_3(H_2O)_4$. However, none of the mentioned phases fully matches the individual peak positions and especially the relative peak intensities of the phases detected in the XRD patterns of the series **ZrOHSO4**. This leads us to assumption that a complex mixture of at least two phases is present in these samples.

The crystalline phases identified in the XRD patterns were divided into three groups

on the basis of classification using correlation analysis (Fig. 5.21, 5.22). We assume that the peaks of the first group belong to a Zr- and sulphate-containing phase, the amount of which increases with the increase of acidity of initial solutions (h<-0.4). This is in general agreement with the data of work [31] where the reverse route was used to obtain a system similar to the series **ZrOHSO4** and low hydrolysis ratios – the authors used dissolution of $Zr(SO_4)_2*4H_2O$ in HCl solutions at high temperature (85 and 95 °C) and monitored the development of the precipitate. The precipitation process appeared to intensify with the increase of HCl concentration. Unfortunately, the work [31] does not contain the data on the structure or composition of the resulting solid phase.

We hypothesise that at the lowest pH (pH~0.6-0.7) and hydrolysis ratios (h<-0.6) the formation of $Zr(SO_4)_2*4H_2O$ occurs. According to the Partial charge model calculations (Chapter 1, 3), sulphate-ions are able to form complexes with Zr-ions in a very wide pH range (-0.6≤pH≤10.2). However, due to the initial form of Zr-ions in medium-concentrated solution (0.2 M) as tetrameric species $[Zr_4(OH)_8(H_2O)_{16}]^{8+}$ and analogous higher molecular-weight polymers, sulphate-ions have to replace very stable OH-bridges of these species completely in order to form pure sulphate $Zr(SO_4)_2*4H_2O$. This can only be achieved at very low pH and hydrolysis ratios, as well as high temperature which also increases the acidity of water [32]. Under these conditions OH-bridges are probably less favoured than bidentate sulphate-ions of the pure Zr sulphate which can compensate high zirconium positive charges much more efficiently than OH-bridges, which is important at the conditions of extreme acidity and the exchange takes place. The breakdown of Zr tetramers and complexation with bidentate SO_4^{2-}-ions causes a dramatic change in the structure from tetragonal to orthorhombic (Zr sulphate). The exchange is probably a limiting slow step in the formation of Zr sulphate precipitate. Visual observation suggests that precipitation in highly acidic samples (h<-0.4) occurs some time after preparation of the sample, unlike for the samples at h>0.0 where this process is observed almost immediately after the start of experiment. A precipitate of Zr sulphate occurs initially as a very fine haze and only after ca. 12 hours of near-boiling (90°C) conditions the phase separation is visually accomplished (phase separation occurs in the sample solutions).

As the hydrolysis ratio approaches zero, the $Zr(SO_4)_2*4H_2O$ phase is less likely to form due to higher stability of the hydroxo-bridges of Zr tetramers at milder acidities. This can explain the decrease of areas of the XRD peaks of group 1 and group 3 identified in the series **ZrOHSO4** (Fig. 5.22) at $h\rightarrow$0.0.

At positive hydrolysis ratios (h>0.0) another phase starts to dominate the XRD patterns of the series **ZrOHSO4** (Fig. 5.22). Since the increase of hydrolysis ratio from h=0.0 to ca. h=1.0 leads to a gradual increase of the new phase peak areas (Fig. 5.22, Group 1) one can assume that this phase is basic Zr sulphate, similar to the monoclinic reference phase of

$Zr_2(OH)_2(SO_4)_3(H_2O)_4$ (Table 5.2). However, one can suggest that a mixture of basic sulphates with general formula $Zr_x(OH)_y(SO_4)_z(H_2O)_{7x-y-2z}$ is present at h>0.0 since none of the reference diffractograms fits the experimental XRD patterns 100 %. The process is strongly pH-dependent.The pH-metric data of the series **ZrOHSO4** shows an inflexion at ca. h~1.0. We assume that hydroxyl-ions, being a stronger ligand, replace sulphate-ions in the coordination sphere of Zr-atoms and leads to the formation of basic sulphates. However, from the formula of the basic sulphate $Zr_2(OH)_2(SO_4)_3(H_2O)_4$ one can see that sulphate-ions still bridge adjacent Zr-atoms in this monoclinic structure and the coordination number of Zr-atoms is reduced from N=8 t o N=7. After reaching a maximum of the basic sulphate formation at h~1.0 the XRD peaks possibly related to this phase (group 1, Fig. 5.22) are reduced in their areas at h>1.0 and this phase gradually decreases in the diffractograms of the series **ZrOHSO4**, the decrease being especially notable at h>2.0. The values of pH at h~1.0 are close to pH~3.0 which appears to be the optimal pH for complexation of sulphate-ions with Zr-ions from the point of view of the Partial charge model (Chapter 1). Above h~1.0 OH-ligands start to replace the remaining sulphate-ions from the coordination sphere of Zr-atoms and by the value of h~2.0 this process is intensified. However, since complexation of sulphate-ions is relatively strong, the complete replacement of them with OH-ligands is not complete even at h~3.0, as supported by the peak area curve of Fig. 5.22 (groups 1 and 3).

Group 2 of the XRD peaks in the series **ZrOHSO4** diffractograms (Fig. 5.22) are from the sylvite phase (Table 5.2). The peak areas of this group are practically unchanged at h<0.0 which corresponds to the conditions of sample preparation where equimolar quantities of K_2SO_4 are added as a source of sulphate at h<0.0. Therefore, potassium and chloride-ions present in solution are free to crystallize into KCl phase upon spray-freeze-drying of sample solutions of the series **ZrOHSO4**. At h=0.2 the amount of KCl jumps up significantly, probably, due to introduction of KOH at h>0.0. After the point at h~0.2 the amount of KCl indicated by the peak areas of group 2 XRD peaks in Fig. 5.22 starts to decrease to its local minimum at h~1.0. This supports the idea that some of sulphate-ions are replaced by the increasing amount of OH-ligands and hinder the process of the KCl formation due to stronger interaction of SO_4^{2-} ions with K^+-ions. Above h~1.0 the presence of the KCl phase increases again owing to an increasing concentration of KOH and above h=2.0 the sylvite phase starts to disappear quickly because of either the release of free sulphate-ions, or due to increasingly negatively charged anionic Zr basic sulphate polymers [21, 30].

The crystallite sizes of the Zr-containing phases in the series **ZrOHSO4** are relatively large (Fig. 5.23) compared to the data of the series **ZrOH** and **ZrHCO3**. At conditions close to optimum of zirconium basic sulphate formation 0.0<h<1.0 the crystallite sizes calculated from the group 1 peaks exceed 80 nm, and the same values for group 2 approach 100 nm.

The XRD patterns of the series **ZrOHAc** (Zr:acetate=1:1) at h>0.4 indicate that the

majority of Zr-containing samples are amorphous in this case. Only at $h \leq 0.4$ does a crystalline phase appear in increasing amounts which could be related, by analogy with the series **ZrOHSO4**, to 'pure' zirconium acetate. However, this crystalline phase was not matched in the JCPDS database and ability of acetate-ions to replace hydroxo-bridges in the same way as sulphate-ions is questionable, since the optimum pH for complexation of Zr-ions with acetate-ions is at pseudoneutral conditions (p*H*~6.0-7.8) and acetate-ions would not form complexes below pH~1.5 according to the Partial charge model (Chapter 1).

As follows from the peak area curves in Fig. 5.25, at positive hydrolysis ratios the sylvite (KCl) phase starts to emerge in the diffractograms of the series **ZrOHAc**. This phase is absent at $h<0.0$ in spite of a significant amount (0.2 M) of K^+-ions present. Therefore, at negative *h* there is probably a significant amount of free acetate-ions which completely prevents the formation of the KCl phase. The peak areas of this phase increase steadily with the increase of *h* from $h>0.0$ and reach a maximum at h~2.0, above which the presence of the KCl phase starts to diminish. Such behaviour of the KCl phase indicates that (*a*) most of K^+-ions are free at $h>0.0$, (*b*) all acetate-ions are bound to Zr-ions and do not hinder KCl formation. As the surface of Zr-containing phase becomes more negatively charged above the point of electroneutrality at h~2.0, more K^+-ions are engaged in charge neutralisation and less KCl crystals are formed. There is a point at h~1.6 where the steepness of increase of KCl growth changes to higher slope. This point corresponds to a well-defined inflexion in the pH-metric titration curve of the series **ZrOHAc** (Section 4.2.1).

On the basis of the above one can find that acetate-ions at negative hydrolysis ratios lead to the formation of unidentified crystalline phase with Zr-ions and at $h>0.0$ leads to a predominantly amorphous phase. The latter finding is in a good agreement with the literature data on the formation of Zr-acetate materials [33].

The crystallite size of the Zr-containing phase occurring at $h<0.0$ in the XRD patterns of the series **ZrOHAc** has a maximum at h=-1.0 (d~77 nm) and then starts to decrease as the hydrolysis ratio grows (Fig. 5.26). The size of KCl crystallites increases with the growth of the peak areas and reaches a maximum at h~2.0 (d~67 nm).

The presence of different amounts of glycine in Zr-ion solutions also causes significant changes in the structure of the solid phase detected with powder diffractograms (Fig. 5.27-5.29) compared to the analogous samples prepared with pure Zr-ion solutions in the series **ZrOH** and **ZrHCO3**. The two-fold excess of glycine (series **ZrOHGly1:2**, Zr:Gly=1:2) causes significant alterations in the solid-state speciation of Zr-containing materials. At highly acidic conditions ($h<0.0$) along with a well-defined phase of monoclinic zirconia, another unidentified crystalline phase is formed (Fig. 5.27, 5.31). The peak areas of this phase decrease with the increase of *h* and disappear completely at h~0.0. Considering the fact that the carboxylic group of glycine is more acidic than of acetate-ions (pK_a=2.3 and 4.76

correspondingly) one can assume that glycine is able to form complexes with Zr-ions at lower hydrolysis ratios.

The monoclinic zirconia phase (group 2 of XRD peaks in the diffractograms of the series **ZrOHGly1:2**, Fig. 5.31) at negative hydrolysis ratios follows the same pattern as in the series **ZrOH** and **ZrHCO3**. It decreases from its value from a maximum at h=-1.5 to a minimum at h~-0.4. However, unlike the series with pure Zr-ions, in the diffractograms of the series **ZrOHGly1:2** the peak areas of the monoclinic phase increase again at h>-0.4 and reach another local maximum at h~0.4. Moreover, after an abrupt decrease of the peak areas of monoclinic zirconia it re-appears at h>1.8 and starts to increase with further increase of h. Therefore, Zr-atoms in the complex with glycine are forced to reduce their coordination number and to convert into the monoclinic form of hydrated zirconia. This process can possibly be catalysed at h>1.8 by the amino-groups of glycine which are quite basic (pK_b=9.6).

Two other crystalline phases are detected in the diffractograms of the series **ZrOHGly1:2** (group 3 and 4 in Fig. 5.31). One group of XRD peaks (group 3, Fig. 5.31) belongs to the sylvite phase which steadily increases from zero at h=0.0 to its maximum at h~2.0. The absence of variations in the steep inclining part of the peak area curve between 0.0<h<2.0 indicates that potassium and chloride-ions are free to form crystalline KCl and that all glycine is bound to Zr-ions and does not hinder the process of KCl formation. The surface of the Zr-containing phase becomes increasingly negatively charged at h>2.0 as indicated by growing binding of K^+-ions and a decrease of the KCl phase in the XRD patterns of **ZrOHGly1:2** series. The fourth phase which has not been matched with known phases in the JCPDS database appears at h~0.0 and rapidly reaches a maximum at h~1.6. Then it gradually decreases and completely vanishes at h~3.0. It is necessary to mention that there is an inflexion point in the pH-metric titration curves of the series **ZrOHGly1:2** (Section 4.2.1) which occurs at h~1.6. Therefore, the jump of the pH value is attributed to the appearance of this phase which could relate to another Zr-glycine structure, e.g. basic Zr glycinate or even Zr oxide glycinate. Glycine molecules remain bound to Zr-ions in whatever coordination mode, structure and conditions at least up to h~2.0 as indicated indirectly by the unhindered formation of KCl crystals.

The effect of equimolar and deficient amounts of glycine added to Zr-ion solutions has been examined in the series **ZrOHGly1:1** and **ZrOHGly2:1**. The XRD patterns of these series are quite similar: at lower hydrolysis ratios (h<1.8 for **ZrOHGly1:1** and h<2.5 for **ZrOHGly2:1**, Fig. 5.32) Zr-containing phase of the solid samples is amorphous. Only the KCl phase is present in the XRD patterns, and it increases steadily from zero at h~0.0 to a maximum at h~2.0. The fate of the KCl phase at h>2.0 is different for the samples of the series **ZrOHGly1:1** and **ZrOHGly2:1**: in the first case the amount of KCl drops significantly

(Fig. 5.32), while in the second series it remains almost unchanged. The reason for this difference is unclear.

At very high hydrolysis ratios the diffractograms of the series **ZrOHGly1:1** (h>1.8) and 1:2 (h>2.5) indicate the formation of the same phase as in the series **ZrOHGly1:2** – most probably, monoclinic zirconia. As it has been mentioned above the formation of m-ZrO_2 is possibly catalysed by the protonated amino-groups of glycine.

The crystallite sizes of the four major phases detected in the series **ZrOHGly1:2** with the excess of glycine generally follow the trend of the peak areas of the corresponding XRD peaks (Fig .5.33). The largest domain sizes (d→100 nm) are reached in the case of the unidentified phase of supposedly Zr basic glycinate (group 4 of XRD peaks in Fig. 5.33). In contrary, the crystallite sizes of the KCl phase are relatively small (9≤d≤32 nm). Moreover in the case of KCl phase there are two distinct groups of average crystallite sizes (d~15 nm and d~32 nm) and the switch between them occurs at 1.2<h<1.6. The origin of such a division is probably related to the unidentified phase of group 4 which affects the size of KCl crystallites.

The crystallite sizes of the KCl phase of the series **ZrOHGly1:1** and **ZrOHGly2:1** follow the same trend as the series with the excess of glycine (Fig. 5.34). The few measured sizes of allegedly monoclinic zirconia crystallites (group 2 XRD peaks) of these two series are in the range 62≤d≤84 nm which is significantly higher than in the case of the series **ZrOHGly1:2** 8≤d≤44 nm). Therefore, the concentration of glycine affects the crystallite sizes of the monoclinic zirconia, but it does not affect the crystallite sizes of the KCl phase.

Summarising the effect of complexing anions (sulphate and acetate) and glycine the following important points can be highlighted:

1. Addition of the complexing ligand changes the speciation patterns of Zr-ions in solution, in colloidal and solid state dramatically. At very low pH (pH<1.0) and hydrolysis ratios (h<-0.4) the presence of the ligands studied in the ratio Zr:ligand 1:1 leads to the breakdown of Zr-$(OH)_2$-Zr double hydroxide-bridges of Zr tetramers and larger oligomers and to the formation of highly ordered crystalline phases (precipitates) which most probably contain a normal salt of monomeric Zr-atoms with a ligand (e.g. $Zr(SO_4)_2$*$4H_2O$, $Zr(CH_3COO)_4$, $Zr(Gly)_4$).
2. All ligands studied form complexes with Zr-ions also upon addition of alkali. The extent of the complexation, structural features, crystallinity and other parameters of the resulting phases depend on the strength of the ligands towards Zr-ions and on the optimum pH conditions for the complexation. The major trend is that at positive hydrolysis ratios the ligands studied do not alter the structure of Zr tetramers and tend to form basic salt complexes alongside hydroxide-ligands. The structural motifs of these basic salts can change upon the increase of the hydrolysis ratio due to the ability of the ligands to change

their denticity (e.g., from bidentate to monodentate complex) and position (e.g. chelating or bridging complex). The complexing strength and high charge of sulphate-ions lead to the formation of well-aligned crystalline Zr basic sulphates throughout the hydrolysis ratio scale above h=0.0. Acetate-ions form a prevailingly amorphous Zr basic acetate phase and glycine probably forms crystalline Zr basic glycinate. It was not possible to identify the structure of most of these basic salts. However, on the basis of the analysis of the reference Zr basic sulphates (JCPDS database) one can assume that most of these salts have a monoclinic structure. The monoclinic structure arises from the elimination of one aquo-ligand from the coordination sphere of Zr-atoms by bulky ligands (acetate, sulphate, glycine) and forced reduction of Zr coordination number from 8 to 7. This leads to a change from a tetragonal structure of the initial Zr tetramer to the monoclinic structure of the basic salt.

3. Tetragonal zirconia never forms in the presence of complexing ligands. Instead, monoclinic zirconia can form alongside acidic or basic Zr salts with the ligands. This phenomenon arises from stabilisation of the coordination number N=7 of Zr-atoms described above. Excessive amounts of glycine in the series **ZrOHGly1:2** (Zr:Gly=1:2) favours the formation of monoclinic zirconia.
4. Most of the transformations of Zr complexes with the ligands studied occur in the solid state. Nevertheless, these transformations are highly pH-dependent and correlate well with the pH-metric data in solution (Chapter 4).
5. The crystallite size of all studied solid phases was found to be below 100 nm, for the most of phases – below 60 nm. The limit of the crystallite growth results from the slow kinetics of crystallisation [28] as well as from the cut-off induced by spray-freeze-drying procedure. The domain size of crystallites with a few exceptions correlates well with the amount of the crystalline phase present in the samples.
6. The formation of sylvite (KCl) phase in the majority of the series studied serves as a good indirect indicator of the degree of binding of the ligands in question to Zr-ions, since free ligands (acetate, sulphate, glycine) can hinder the formation of crystalline KCl. Formation of the KCl phase also shows a progressively negative charge of Zr-containing phases above the point of electroneutrality (usually h~2.0), because of the reduction of free K^+-ions and, therefore, amount of crystalline KCl due to the charge compensation effect.
7. Several new crystalline phases have been identified in the multi-batch series in the presence of complexing anions and glycine. These phases have been assigned tentatively on the basis of the analysis of their pH-dependent distribution. Further work is required for the unambiguous determination of the structure and composition of these phases.

5.6. Infrared spectra of solid samples produced by spray-freeze-drying (SFD)

As was mentioned above, implementation of the SFD technique has enabled us to study the produced solid samples using several solid-state techniques. One of them is conventional solid-state infrared spectroscopy, sensitive to functional and structural variations in the solid state.

5.6.1. Infrared spectra of the solid samples from the series AMK1

The KBr disc technique was used to obtain infrared spectra of the series **AMK1** in the mid-IR region (4000-400 cm^{-1}). Details of sample preparation and the infrared spectrum measurement procedure are given in Section 2.9.2. Results of the IR examination of the SFD samples of the series **AMK1** are shown in Fig. 5.35. The series of solid samples produced by the SFD after 6 hours of hydrolysis were chosen for IR characterisation and discussion due to the presence of both the Al_{13}-mer and Al_{30}-mer (Section 3.2) as two species of special interest in this study.

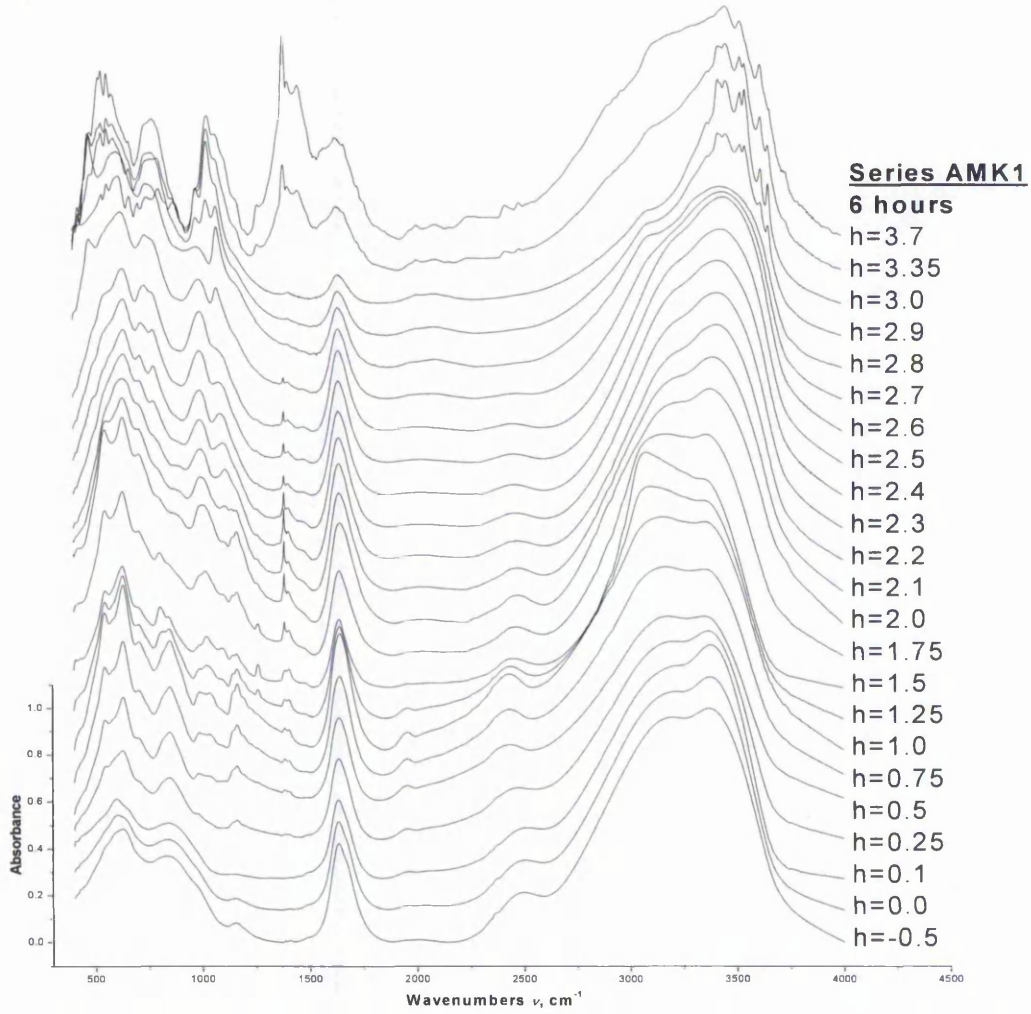


Fig. 5.35. Normalised mid-infrared (KBr disc) spectra of the solid samples of the series **AMK1** spray-freeze-dried after 6 hours of the experiment.

As follows from Fig. 5.35, the mid-IR spectra of the series **AMK1** are highly dependent on the hydrolysis ratio. Identification of the IR-bands in the obtained dynamic set

of spectra for the series **AMK1** (hydrolysis ratio is a dynamic variable) is not a trivial task. Unlike PXRD patterns examined in the previous Section, peak positions in the IR-spectra can vary substantially. Also, the degree of overlap of some very broad peaks and the intrinsic problems associated with baseline correction in IR-spectroscopy [34] contribute to the complexity of spectral band identification. The major problem is an intense signal from water molecules, physically adsorbed on the solid SFD materials as well as chemically bound to Al-ions. Water molecules produce a very broad signal due to antisymmetric and symmetric stretching of OH-bond, appearing the region 3550-3200 cm^{-1}, several bands at 2800-2400 cm^{-1}, bending vibrations at 1630-1600 cm^{-1} and intense "librational modes" due to rotational oscillations in the low-frequency region 600-200 cm^{-1} [35]. For strongly acidic samples the presence of hydronium ions (H_3O^+) and similar positive ions is also possible [36]. The intense and broad signals of water in the solid samples make spectral band identification and baseline correction more difficult.

In order to carry out identification of the spectral bands in the mid-IR spectra of the series **AMK1**, the degree of similarity of the IR-spectra was examined first, using a correlation sum graph for the hydrolysis ratio domain (Fig. 5.36).

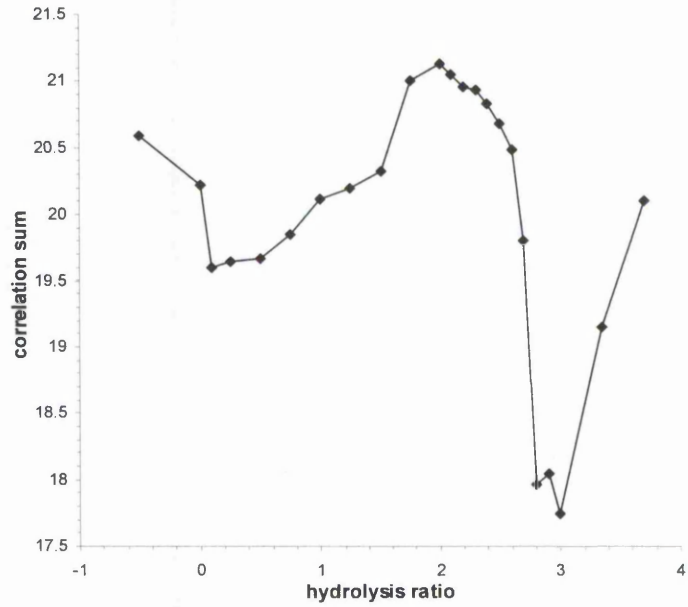


Fig. 5.36. The correlation sum graph calculated on the basis of the mid-IR-spectra of the series **AMK1**.

Analysing the shape of the correlation sum curve in Fig. 5.36 one can see its substantial agreement with pH-metric titration curves (first derivatives) as well as with the correlation data of the XRD measurements (Fig. 5.3). At least four major groups of IR-spectra can be distinguished on the basis of the correlation sum curve: (*1*) $-0.5 \le h \le 0.0$ – the range of predominantly non-hydrolysed Al monomers; (*2*) $0.0 \le h \le 2.0$ – hydrolysis-condensation of Al-ions into polycations; (*3*) $2.0 \le h \le 2.8$ – domination of polycations and colloidal Al hydroxide; (*4*) $h \ge 2.8$ – presence of Al hydroxide only. The defined ranges of h are employed in the

correlation analysis described below.

Pursuing the task of unambiguous assignment of peak positions in the IR-spectra of the series **AMK1**, compared three possible methods of peak identification: (*1*) derivatisation of spectrum (most common technique); (*2*) full 2D-correlation analysis of the dynamic set **AMK1**; (*3*) the method of the correlation sum graph implemented in the spectral domain. Examples of the application of the listed methods are shown in Fig. 5.36, 5.37 and 5.38.

As follows from the data of Fig. 5.37-5.39, the peak positions identified using all three methods are generally in good agreement. Negative maxima of the smoothed second order derivative curve indicate peak positions. Comparing the methods, one can notice that the derivatisation technique is characterised by high resolution and is better for the identification of sharp peaks. However, it sometimes fails to identify band positions when broad peaks are considered (e.g. bands at ca. 3150, 3300 and 3600 cm^{-1} in Fig. 5.37). Additionally, the derivatisation technique may lead to the appearance of 'false' peaks in the derivative curve due to the Lorentzian shape and strong overlapping of adjacent broad peaks [34].

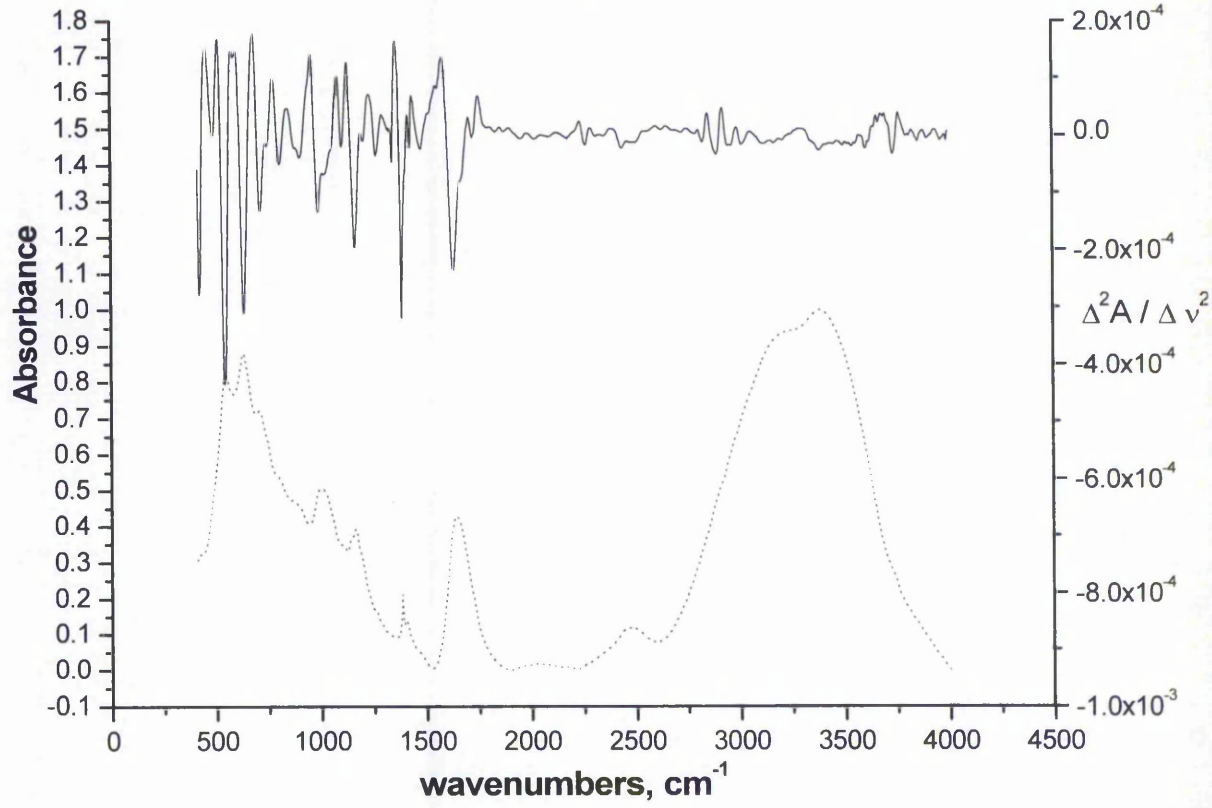


Fig. 5.37. Second derivative curve (solid line) vs. original spectrum of the solid sample **AMK1** (h=2.0; τ = 6 hours) (dotted line).

Correlation-based techniques for spectral identification (Fig. 5.38, 5.39) are practically free from the pitfalls of the derivatisation technique. The correlation sum method developed in this work generates a curve (Fig. 5.38) from a dynamic set of spectra in which peak maxima can be either positive or negative depending on the dynamic variation of the

particular peak. The peak assignment can be easily made by comparison of the correlation sum graph with the original spectrum as in Fig. 5.38. The advantage of the correlation sum method is detection of the broad band maxima (e.g. negative peaks at 3150 and 3300 cm^{-1} in Fig. 5.38) and providing an indication of the possible classification of correlated peaks according to functionalities they may belong to. However, one must be aware of the possible disappearance from the correlation sum graph of the peaks which remain unchanged in the dynamic set of spectra.

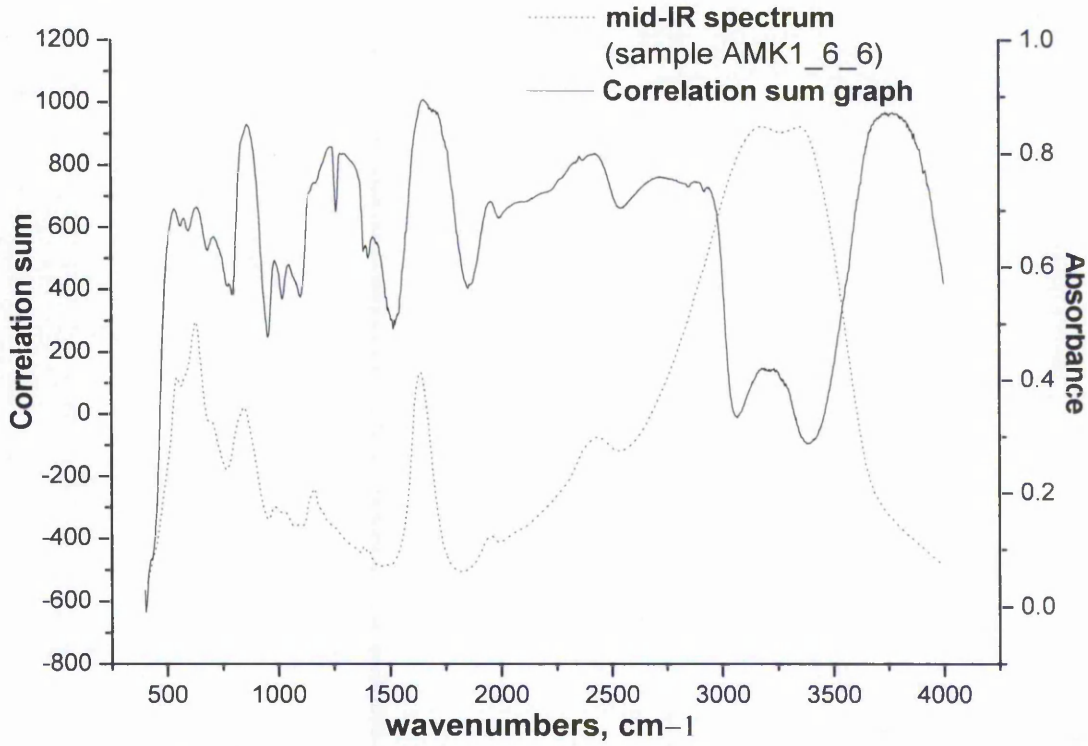


Fig. 5.38. Correlation sum graph of the series **AMK** (wavenumbers domain) vs. the original spectrum of the sample No 6 from the series **AMK1** (h=1.0, τ=6 hours).

Application of the full 2D-correlation analysis (2D-COS method) to the mid-IR spectra of the series **AMK1** enables very high resolution of the identified spectral bands (Fig. 5.39) which is limited only by the initial resolution of the spectrum (in the case of the **AMK1** series – 2 cm^{-1}). Moreover, the 2D-COS method provides information on the band shape and a degree of correlation between all bands indicated by in-phase non-diagonal cross-sections between different bands in the synchronous 2D-spectra (shown in Fig. 5.39) as well as out-of-phase non-diagonal cross-sections in the asynchronous 2D-spectra. Blue lines in Fig. 5.39 indicate that particular spectral bands are anti-correlated (correlation coefficient is negative), while red bands show strong correlation between the spectral bands. The concentric red circles on the diagonal of the 2D-spectra map in Fig. 5.39 give the exact and well-resolved peak positions of all individual spectral bands.

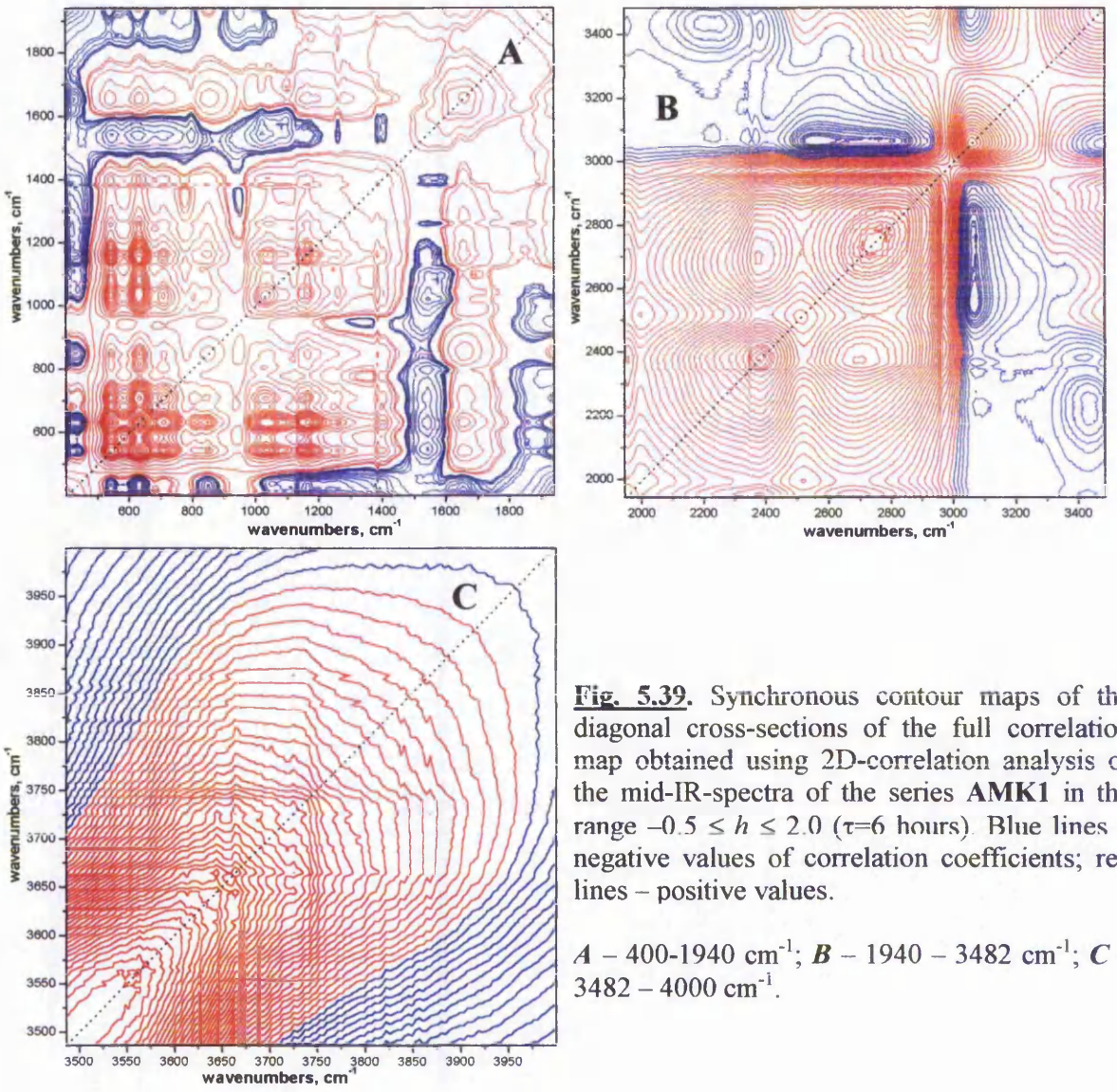


Fig. 5.39. Synchronous contour maps of the diagonal cross-sections of the full correlation map obtained using 2D-correlation analysis of the mid-IR-spectra of the series **AMK1** in the range $-0.5 \leq h \leq 2.0$ (τ=6 hours). Blue lines – negative values of correlation coefficients; red lines – positive values.

A – 400-1940 cm^{-1}; ***B*** – 1940 – 3482 cm^{-1}; ***C*** – 3482 – 4000 cm^{-1}.

The intensities of more than 60 spectral bands identified in the mid-infrared spectra of the series **AMK1** using the three techniques discussed above were submitted to correlation analysis on the hydrolysis ratio scale in order to classify and to divide the bands into groups on the basis of similarity of their pH-dependent behaviour. The PXRD data suggest that along with Al-containing material, the crystalline KCl (sylvite) phase is formed upon spray-freeze-drying of solution samples of the series **AMK1** at h=0.0 (Section 5.3.3). This phase is practically invisible in the mid-IR spectra [37], however, an adjustment of the amount of Al-containing phase has to be made when calculating intensities of the raw IR-spectra. The amount of KCl depends on the initial hydrolysis ratio of solution samples and reaches a maximum at h–3.0. The molecular weight of $Al(OH)_3$ presumably dominating the Al-containing part of the solid sample at h=3.0 is 78 Da. The molecular weight of KCl is 64.5 Da. At h=3.0 approximately 3 moles of KCl and 1 mole of $Al(OH)_3$ are present in the corresponding solid sample. The following formula was applied in order to find an approximate percentage of Al-containing phase in the SFD samples of the series **AMK1**:

$$\frac{m_{total}}{MW_{Al} + MW_{KCl}} = \frac{m_{Al}}{MW_{Al}} + \frac{m_{KCl}}{MW_{KCl}} \tag{5.5}$$

where m_{total} – the total weight of the sample in the KBr table (2 mg) set as 100%; m_{Al} – percent weight of the Al-containing part of the SFD samples; m_{KCl} – percent weight of the KCl part of the SFD samples which is calculated on the basis of the XRD data (Section 5.3.3); MW_{Al} – the molecular weight of Al-containing phase which varies from 243.41 Da at h=0.0 (pure $AlCl_3$*$6H_2O$) to 78 Da at h=3.0 ($Al(OH)_3$), to 95 Da at h=4.0 ($Al(OH)_4^-$). The molecular weights between these points were approximated by linear equations. MW_{KCl} – the molecular weight of KCl (64.5 Da).

Using Eq. (5.5) one can calculate the percentage amount of the Al-containing phase (m_{Al}) and use it for adjustment of the IR-band intensities in the dynamic spectral set for the series **AMK1**. The normalised intensity distributions in the mid-IR spectra of the series **AMK1** are presented in Fig. 5.40.

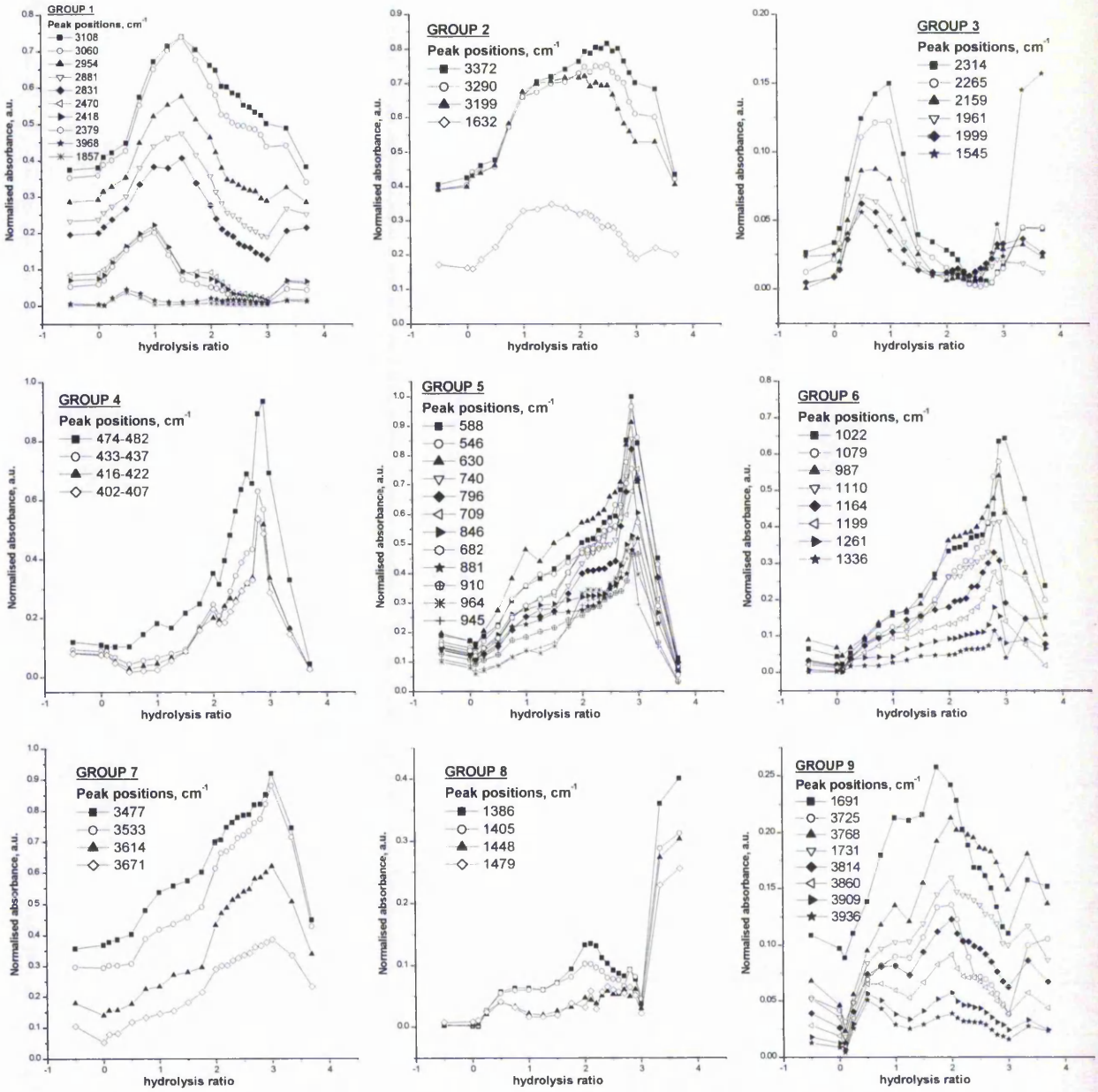


Fig. 5.40. Adjusted and normalised intensities of the IR bands identified in the mid-infrared spectra of the series **AMK1**.

The data of Fig. 5.40 provide a useful qualitative insight into the distribution of peak intensities in the IR spectra of the series **AMK1**, however, it cannot serve for quantification purposes due to: (***a***) the unknown effect of the background water signal on the resulting spectral intensity; (***b***) possible errors associated with preparation of solid samples [37]; (***c***) variability of peak positions of some spectral bands; (***d***) the simplified procedure for evaluation of Al-containing material contribution using Eq. (5.5) above. Nevertheless, the qualitative distribution of the peak intensities can be applied for proving the classification of the IR-bands by correlation analysis as well as for the elucidation of the trends of the spectral bands and their assignment to particular species and functional groups on the basis of Al-ion speciation in solution (Chapter 3) and in the solid state (present Chapter).

As follows from Fig. 5.40, nine major spectral band groups were identified in the IR spectra of the series **AMK1**. The first group contains spectral bands in the IR-region 3110-2800 cm^{-1}. These bands are relatively intense at low hydrolysis ratios ($h \leq 0.0$) and slightly increase with the growth of h up to $h=1.5$. After the maximum at $h=1.5$ all bands of the spectral group 1 steadily decrease in intensity up to $h=3.0$. Above the point of theoretical electroneutrality at $h=3.0$ the higher frequency bands (3080 and 3108 cm^{-1}) continue to decrease, while bands in the region 2881-2831 cm^{-1} start to increase. The band at 2954 cm^{-1} shows intermediate behaviour between the two subgroups mentioned above. In the literature two similar bands at 3150 cm^{-1} (sharp peak, antisymmetric OH-stretching of the Al-OH_2 moiety) and at 2500 cm^{-1} (broad peak, symmetric stretchings of the Al-OH_2 moiety) are described [38]. The distinct band of bending HOH vibrations follows a trend similar to the bands of the group 1 described above. Therefore, most of the water molecules detected in the IR-spectra of the series **AMK1** are coordinatively bound to Al-ions.

The correctness of the assignment of the group 1 spectral bands to aquo ligands of Al-ions is fully supported by the intensity distribution diagrams in Fig. 5.40. During the hydrolysis-condensation of Al-ions, aquo ligands in the inner coordination sphere are gradually replaced by the hydroxyl-ligands. Therefore, the intensity of the corresponding IR-bands should decrease with increase of hydrolysis ratio.

The IR-bands of group 2 in Fig. 5.40 (ν=3372-3199 cm^{-1}) arise from stretching vibrations of the bridging OH-ligands of the polymeric Al-ions [38, 39]. The shape of the corresponding intensity distribution diagrams is in good agreement with this assignment. The intensity of the peaks of group 2 is relatively low at $h \leq 0.0$ and starts to increase at higher hydrolysis ratios reaching a maximum at $h \sim 2.6$ which corresponds to the point of the maximum amount of the polymeric species (Al_{13}-mer and Al_{30}-mer, see Chapter 3). Above this point, Al polycations rapidly collapse into Al hydroxide colloids which correlates well with the decrease of intensity of the corresponding spectral band at ca. 3300 cm^{-1}. The non-zero value of the intensity of the band at $h \leq 0.0$ is probably due to the high intensity of water background in this spectral region.

Broad bands in the regions 2470-2314 and 2265-1999 cm^{-1} as well as lone bands at 3968, 1857 and 1545 cm^{-1} constitute group 3 of the IR-bands of the series **AMK1** (Fig .5.40). The intensity of these bands is very low or close to zero at $h \leq 0.0$. Above $h=0.0$, the bands increase reaching a maximum in the range $0.5 \leq h \leq 1.0$. Above $h=1.0$ the peak intensity declines to very low values at $h=3.0$ and for some bands (e.g. 1545 cm^{-1}) starts to rise rapidly at $h=3.0$. The bands of group 3 have not been unambiguously assigned in the literature available. One can assume that these spectral features for the series **AMK1** could be related either to a particular type of aquo ligand in the coordination sphere of Al-ions which cease to exist at hydrolysis ratios $h=1.0$, or, more likely, to OH stretching of the hydroxyl-bridges of very small oligomers (e.g. dimers or trimers) the concentration of which reaches a maximum at $h \sim 1.0$ and at higher hydrolysis ratios these species tend to disappear gradually. Abrupt increase of some IR-bands in the group 3 at $h=3.0$ is probably related to background effects rather than actual intensity variations.

Group 4 of the IR-bands of the **AMK1** series of solid samples (Fig. 5.40) is located in the low frequency of the dynamic spectral set (ν=490-400 cm^{-1}). The fact that these bands increase from very low values at $h \leq 0.0$ to a sharp maximum at h=2.8-3.0 indicates that they are related to Al hydrolysed species. Again, these bands lack unambiguous assignment in the available literature [38-41]. However, one can hypothesise three possible assignments for this group of IR bands: (***a***) in this region (310-490cm^{-1}) lattice water can show ν(Al-O) symmetric and asymmetric stretching vibrations of Al-OH_2 moieties [38], and the variety and fluctuation of the band positions can be explained by different Al-O distances in aquo-complexes of Al-ions hydrolysed or condensed to a different extent; (***b***) different types of rotation vibrations of lattice water (rocking and wagging) are also possible in this region [35]; (***c***) overtones of the stretching vibrations [38] of the Al-OH moiety of hydrolysed Al-ions and Al polycations. The assignment of the bands in the region 490-400 cm^{-1} to various types of lattice water is highly unlikely due to an increase of band intensity with hydrolysis ratio (actual number of aquo ligands in the coordination sphere of Al-ions gradually decreases with increase of h) and also due to the fact that these bands are at near-zero values below $h=0.0$. Therefore, the set of the IR bands of group 4 of the series **AMK1** is more probably derived from hydroxyl-groups of hydrolysed Al-ions. The fact that the maximum of the group intensities is reached at $h \sim 2.8$ (in some cases $h=3.0$) indicates that the spectral bands of group 4 could be related to Al polycations. At $h \geq 2.8$ all locations of the IR bands of group 4 change significantly. The lower-frequency bands at 400-407, 416-422 and 433-437 cm^{-1} disappear, as indicated in Fig. 5.35, while the new intense and sharp band appears at 454 cm^{-1}. The band at ca 482 cm^{-1} slightly shifts to 486 cm^{-1} and becomes sharper and more intense. Hence, the intensity distribution of the group 4 peaks is not valid at $h \geq 2.8$.

The next three groups of the IR bands of the **AMK1** series spectra (group 5, 6 and 7) have similar shapes for the intensity distribution curves in Fig. 5.40 and can, in fact, be united

into one large group mainly related to OH-groups of the hydrolysed Al-ions.

Groups 5 and 6 in the IR spectra of the series **AMK1** are located in the spectral region 500-1500 cm^{-1} in which deformation (bending) vibrations of the unidentate and bridging hydroxyl-groups of hydrolysed metal ions occur [35]. Therefore, this spectral group contains important information on the Al-ion speciation and should be considered in more detail using an enlarged region of the dynamic spectral set in Fig. 5.41 (full version is shown in Fig.5.35).

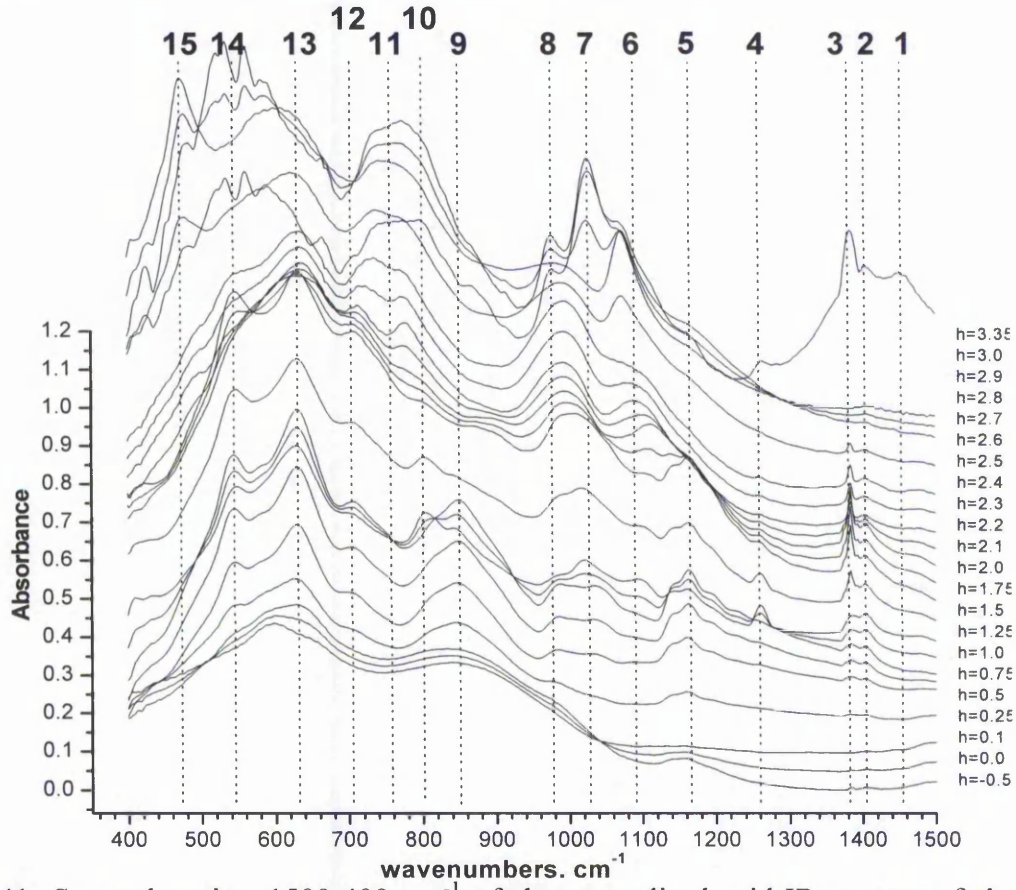


Fig. 5.41. Spectral region 1500-400 cm^{-1} of the normalised mid-IR spectra of the series **AMK1** (6 hours of hydrolysis). Y-offset – 80 %.

There are 15 major IR bands identified in the region 1500-400 cm^{-1} and several other bands observed in Fig. 5.41. The bands No 1-3 at ca. 1490, 1405 and 1384 cm^{-1} belong to the spectral group 8 in Fig. 5.40 and can be most probably related to carbon dioxide absorbed by the solid samples of the series **AMK1** during storage. This assignment is supported by the fact that at alkaline conditions (h=3.0), where absorption of CO_2 is accelerated, these bands dramatically increase in intensity. Another proof of the assignment is that the mentioned IR bands are not observed for acidic samples (h=0.5) where absorption of CO_2 is less likely. The bands No 1-3 (Fig. 5.41) reach a local maximum of intensity at h~2.0-2.2. Therefore, basic salts of Al-ions containing predominantly Al polycations are more susceptible to adsorption of CO_2 than less hydrolysed samples at h=0.5 which can again be related to the increased pH of the initial sample solutions (4<pH=6) at h=2.0. One can also assume that Al dimers are the

major reactive form towards carbon dioxide. Due to frequently encountered bridging nature of carbonate-ions and carbon dioxide [35] this Al species would be additionally stabilised by the complexation with CO_2 from atmosphere.

The IR band No 4 at 1261 cm^{-1} in Fig. 5.41 also can be related either to a particular type of hydroxyl-ligands of hydrolysed Al-ions, or to the complexed form of carbon dioxide (ν_1(M-CO_2)=1120-1260 cm^{-1} [35]). This IR-band is clearly observed in the range of $0.5 \leq h \leq 2.2$ and reappears at h=3.0. The set of the IR bands No 5 at 1194, 1164 and 1151 and cm^{-1} observed clearly in Fig. 5.41 can also belong to either coordinatively bound carbon dioxide, or to hydroxyl-groups of Al-ions. The fact that this group of IR-bands appears again at h=3.0 as a shoulder of the more intense lower-frequency band (Fig. 5.41) supports the first assignment.

The set of IR bands No 6-8 in Fig. 5.41 at 1110, 1080, 1022 and 987 cm^{-1} belongs to group 6 in Fig. 5.40. The IR-bands at 1080 and 970 cm^{-1} have been previously assigned to an Al-O-H bend of the bridging Al-OH-Al groups of Al polymeric species and Al-O-H deformation bend of Al-OH and Al-OH_2 moieties respectively [38]. The data of Fig. 5.40 and 5.41 support this assignment. The intensity distribution of the latter two bands at near-zero values at $h \leq 0.0$, then it reaches maximum at h~2.4-2.6 and tends to decrease at higher hydrolysis ratios. This coincides with the distribution of polymeric Keggin ions in the samples of the **AMK1** series. The assignment of the bands at 1100 and 1090 cm^{-1} is not obvious, however, these bands can be related to polymeric species other than Keggin ions (Al_{13}-mer and Al_{30}-mer), for instance, Al dimers or Al-OH groups of Al hydroxide.

The IR-band No 9 in Fig. 5.41 at ca. 887 cm^{-1} is most distinct and intense at h=1.0, suggesting that this band arises from Al dimers which are also at a maximum at h=1.0 (Chapter 3). The set of IR-bands No 10-12 in Fig. 5.41 at ca. 790-807, 747-754 and 702-710 cm^{-1} have varying peak positions and intensities. The band at 790-807 cm^{-1} is assigned to AlO_4 antisymmetric stretching [39], while the lower-frequency bands at 747-754 and 702-710 cm^{-1} could be related to Al-OH deformation bends from Al hydroxide particles formed at higher hydrolysis ratios. These assignments are supported by the fact that below h~2.4 the band at 790-807 cm^{-1} is the most intense of the three, while at hydrolysis ratios approaching h=3.0 the bands at 747-754 and 702-710 cm^{-1} become dominant (Fig. 5.41). Another possible assignment of the bands at 747-754 and 702-710 cm^{-1} to rocking and twisting vibrations of the coordinatively bound water is based in the literature data of various aquo-complexes reviewed by Nakamoto [35]. However, the letter assignment does not explain the intensity distribution of these bands depicted in Fig. 5.43.

The band No 13 in Fig. 5.41 at 630-632 cm^{-1} has been attributed to AlO_4 symmetric stretches of the Keggin ions [39]. The intensity distribution of this band shows that the maximum of intensity is reached at h~2.6-2.8 which agrees well with the given assignment. The band No 14 in Fig. 5.41 at ca. 542-547 cm^{-1} is not assigned in previous studies; however,

this band is very distinct and intense in Fig. 5.41.

As can be seen from Fig. 5.40, the IR-bands of group 9 at 1691, 1731 cm^{-1} as well as a large group of bands at 3725-3938 cm^{-1} have a distinct intensity distribution with low absorbance values at h~0.0 and the maximum at h~2.0-2.2. Another feature of this spectral group is a minimum of absorbance in the vicinity of h~3.0. One can hypothesise that the group 9 bands are related to physisorbed (or free) water inevitably present in the SFD samples due to the very gentle nature of the spray-freeze-drying technique used to produce solid samples of the series **AMK1**. The amount of physically adsorbed water is probably related (***a***) to the overall charge of the solid SFD materials, and (***b***) degree of saturation of the coordination sphere of Al-ions. At low pH and hydrolysis ratios (h=0.0) a relatively large amount of protons from acidic solutions is probably present in the solid samples. This prevents free water vapour from being absorbed by the samples of the **AMK1** series, e.g. via hydrogen bond formation. At higher hydrolysis ratios an overall charge of Al species (monomers and polymers) is still relatively high, albeit aquo ligands become available for hydrogen-bonding with extraneous water. Above h=2.0, when the Al hydroxide phase emerges in solutions of hydrolysed Al-ions, the overall charge of Al species starts to decrease and aquo ligands become less acidic thus hindering possible adsorption of free water. The minimum charge of the solid SFD samples occurs at h=3.0 where adsorption of free water is also at its minimum.

Returning to the initial IR spectra of the series **AMK1** shown in Fig. 5.35, one can see that at h=3.0 the overall spectral pattern is very close to the analogous spectra of amorphous pseudoboehmite reported in the literature [42]. This is the major product of alkaline hydrolysis of Al-ions [43]. Some minor bands, e.g. at 3616, 1015 and 914 cm^{-1} characteristic of crystalline gibbsite are also present in the spectra of the samples obtained in the vicinity of h=3.0. This fact correlates well with the PXRD patterns of the series **AMK1** discussed in Section 5.3.3.

One should mention that the IR spectra of the samples **AMK1** at low hydrolysis ratios (around h=0.0) are very close to the reference spectrum of solid crystalline $AlCl_3*6H_2O$. This is further evidence that the structure and composition of Al species remains unperturbed by the procedure of spray-freeze-drying.

Summarising the above, the major IR-bands of the series **AMK1** and their possible assignments are presented in Table 5.3. From the data of Table 5.3 one can find that at least three types of IR-bands can be detected in the IR spectra of the series **AMK1**: the bands related to 'lattice water' coordinatively bound to Al-ions; the bands of OH-groups of Al hydrolysed species including monomers, oligomers and Al hydroxide; the bands of coordinatively bound or physically absorbed atmospheric CO_2 and several bands corresponding to Al-O bonds of the polymeric Al species and hydroxide. Some bands remain unassigned and further work is needed in order to attribute them to particular features of Al

speciation.

Table. 5.3. Identification and assignment of the mid-IR bands in the spectra of **AMK1** series.

Method 1*	Method 2	Method 3	Average ν cm^{-1}	±Absolute deviation	Intensity	Shape	Assignment	Ref.
3967.6			**3967.6**	-	Low	Broad	Overtones of Al-OH stretchings in $Al-OH_2$ moiety or overtones of H-OH stretchings of the free water content in the solid samples	[44]
3937.0	3935.5		**3936.2**	0.4	Low	-		
3908.4			**3908.4**	-	Low	-		
3862.4	3859.1		**3860.7**	0.8	Low	-		
3813.8			**3813.8**	-	Low	-		
3771.9		3764.8	**3768.4**	1.8	Medium	Broad		
3729.0	3721.3		**3725.1**	1.9	Medium	Broad		
3674.7	3670.2		**3672.5**	1.1	V. high	Broad	OH stretch vibrations in Al-OH-Al moiety in polymeric Al species	[38]
3611.5	3617.0		**3614.2**	1.4	V. high	Broad		
3536.4	3529.9		**3533.2**	1.6	High	-	OH stretch vibrations in Al-OH-Al moiety in polymeric Al species	
3476.4	3479.0		**3477.7**	0.6	High	-		
3368.4		3377.0	**3372.7**	2.2	V. high	Broad	OH stretch vibrations in Al-OH-Al moiety in polymeric Al species	[39]
3292.0		3289.9	**3290.9**	0.5	V. high	Broad		
3199.8			**3199.8**	-	V. high	Broad	OH antisymmetric stretch vibrations in $Al-OH_2$ group	[42]
3109.2			**3109.2**	-	V. high	Broad		
3061.0	3058.0	3060.2	**3059.7**	0.6	High	-		
2954.0		2953.6	**2953.8**	0.1	Medium	-	Hydrogen-bonded OH-groups of coordinatively bound water (?)	
2881.7			**2881.7**	-	Medium	Broad		
2828.2	2826.0	2836.5	**2830.2**	3.1	Medium	Broad		
2471.1			**2471.1**	-	Medium	Broad	OH symmetric stretch vibrations of the coordinatively bound carbonate species	[35]
2419.3		2416.8	**2418.0**	0.6	Medium	Broad		
2380.2	2383.0	2374.0	**2379.1**	2.0	Low	Broad	CO_2 absorbed by basic Al salts	[35]
2314.2			**2314.2**	-	Low	Broad		
2266.3			**2266.3**	-	Low	-		
2159.5			**2159.5**	-	Low	-	Unassigned	[38]
2005.9	1997.0	1999.1	**2000.7**	2.6	Low	-		
1964.0	1959.0		**1961.5**	1.2	Low	-		
1857.5	1859.0	1853.3	**1856.6**	1.2	Low	Broad	ν_3 stretchings of CO_2 coordinatively bound to Al-ions	[35]
1733.8		1731.1	**1732.4**	0.7	Low	Broad		
1692.0	1693.0	1691.3	**1692.1**	0.4	Low	-		
1633.8	1628.6		**1631.2**	1.3	Medium	Sharp	HOH bending vibration of lattice water	[35]
1546.2	1542.0	1547.7	**1545.3**	1.2	Low	-	Unassigned	
1479.8			**1479.8**	-	Low	Sharp	ν_1 stretchings of CO_2 absorbed on the surface of Al polymers or coordinatively bound to Al-ions	[35]
1447.4			**1447.4**	-	Medium	Sharp		
1406.8		1405.9	**1406.4**	0.2	Medium	Sharp		
1386.4	1384.0	1388.2	**1386.2**	1.0	Medium	Sharp		
1334.6	1342.0	1332.6	**1336.4**	2.8	Low-Med.	-	CO_2 absorbed on the surface of Al polymers or coordinatively bound to Al-ions	
1263.2	1261.0	1261.2	**1261.8**	0.7	Low-Med.	Sharp		
1204.9		1194.1	**1199.5**	2.7	Low-Med.	Sharp	ν_2 stretchings of CO_2 coordinatively bound to Al-ions or Al-OH deformation bends in Al oligomers	[35]
1163.7	1164.8		**1164.2**	0.3	Medium	Sharp		
1115.1	1116.0	1101.2	**1110.8**	2.6	Medium	Sharp	Al-O-H deformation bend of bridging Al-OH-Al moiety	[38]
1079.3			**1079.3**	-	Medium	Sharp		
1022.1	1021.0	1020.2	**1021.1**	0.5	Med.-High	Sharp		
987.8			**987.8**	-	Med.-High	Sharp	Al-O-H deformation bend of Al-OH and $Al-OH_2$ moieties	[39]
963.9			**963.9**	-	Medium	-		
945.0	945.7	944.6	**945.1**	0.3	Medium	-		
910.2			**910.2**	-	Medium	Sharp	Al-OH deformation bends of Al hydroxides	[42]
882.1			**882.1**	-	Med.-High	Sharp		
846.4	848.5		**847.5**	0.5	Med.-High	-		
795.5	795.2	794.5	**795.1**	0.2	High	Sharp	AlO_4 antisymmetric stretch	[38]
741.4		737. 9	**739.6**	0.9	Medium	Sharp	Rocking, twisting and wacking deformation vibrations of the coordinatively bound water	[35]
712.7	708.0		**710.3**	1.2	Low-Med.	Sharp		
683.2	682.7	684.6	**683.5**	0.6	Medium	-		
628.9	632.5		**630.7**	0.9	High	Sharp	AlO_4 symmetric stretch	[39]
589.0	582.4	589.8	**587.1**	1.3	Medium	-	Al-OH deformation bends of Al hydroxides	[42]
548.1	545.0	546.1	**546.4**	0.8	Low	Sharp		
485.2		480.6	**482.9**	1.2	Med.-High	Sharp	$Al-OH_2$ librational and transitional modes	[35]
437.8	433.1	430.1	**433.7**	2.1	Medium	Sharp		
	416.5	417.0	**416.8**	0.1	Low-Med.	Sharp		
407.2	405.4		**406.3**	0.5	Low	Sharp		

* - **method 1** – the second derivative with smoothing; **method 2** –full 2D-correlation analysis; **method 3** – the correlation sum graph (dynamic variable - ν, cm^{-1}).

5.6.2. Mid-infrared spectra of the series ZrHCO3

Infrared spectra of the series **ZrHCO3** prepared by the hydrolysis of Zr-ions with KHCO3 at 90°C were acquired in mid-infrared (KBr pellet) and far–infrared (CsI pellet) regions. Mid-IR spectra (4000-400 cm^{-1}) of the series **ZrHCO3** are presented in Fig. 5.42.

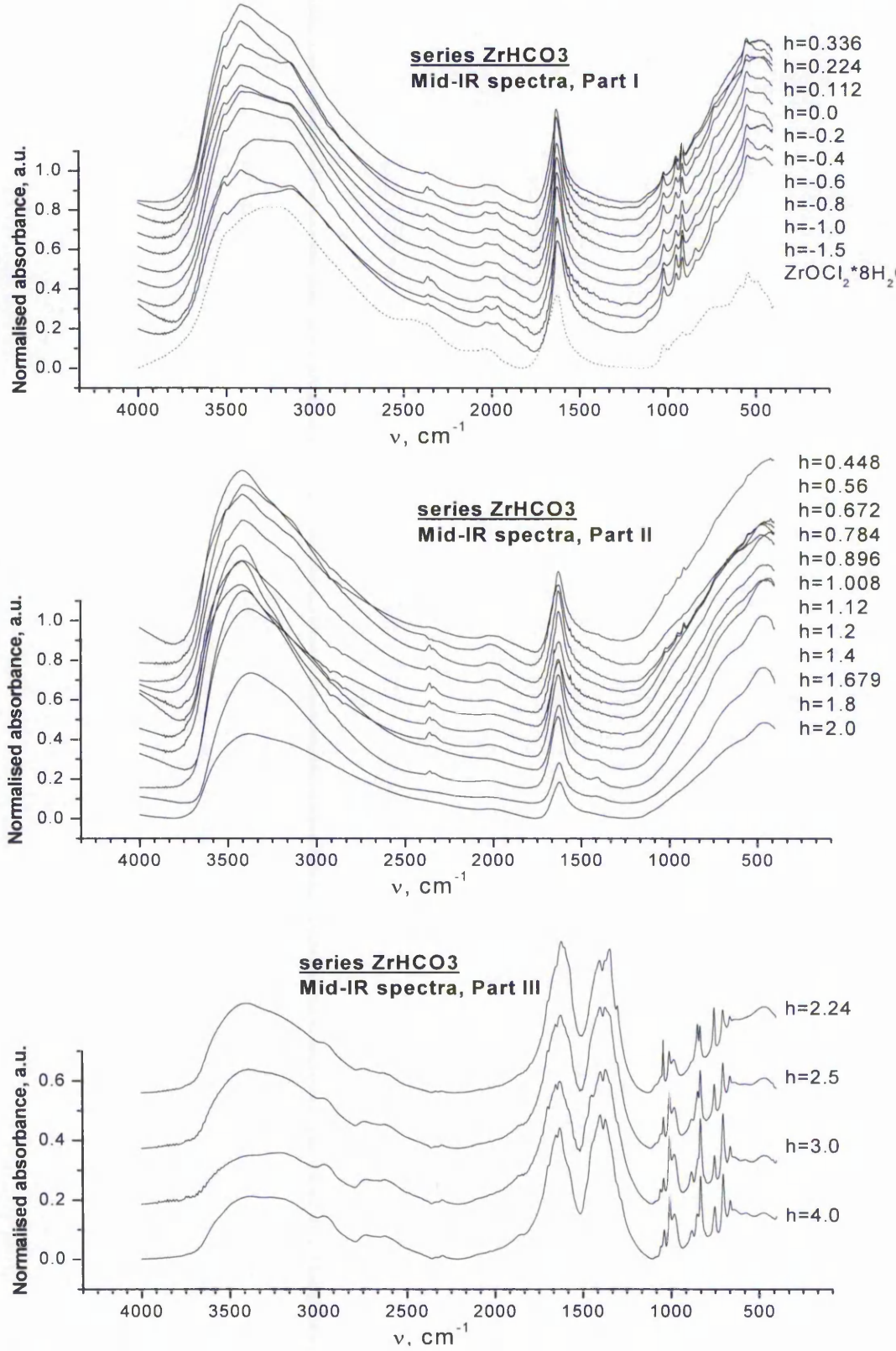


Fig. 5.42. Mid-infrared spectra of the solid samples of the series **ZrHCO3**.

The spectra in Fig. 5.42 are divided into three major groups on the basis of the spectral similarity: strongly acidic ($-1.5 \leq h \leq 0.366$); mildly acidic to neutral ($0.448 \leq h \leq 2.0$) and alkaline samples ($h \geq 2.0$). The division into abovementioned groups is supported by the correlation sum graph in the hydrolysis ratio domain (Fig. 5.43).

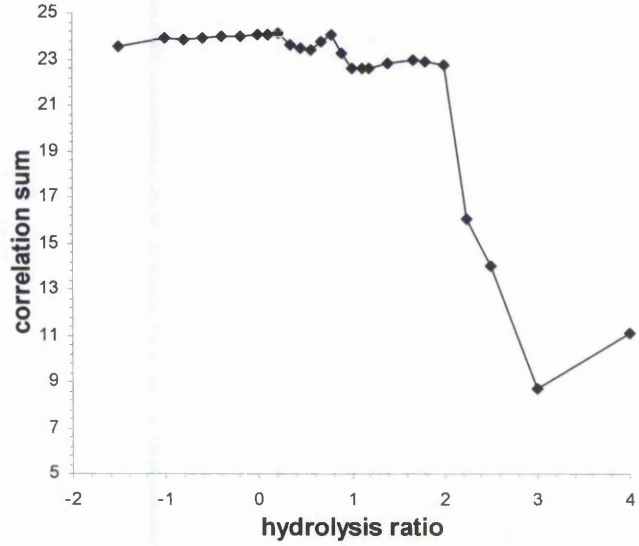


Fig. 5.43. The correlation sum graph calculated on the basis of the mid-IR-spectra of the series **ZrHCO3**.

The data of Fig. 5.43 indicate that below $h \sim 0.6$ the spectra are quite similar, a minor change of spectral patterns occurs in the hydrolysis ratio range $0.48 \leq h \leq 2.0$. Above $h = 2.0$ the spectra change dramatically. Therefore, division of the dynamic IR spectra of the series **ZrHCO3** into three groups is well grounded.

We have subjected all three described groups to a detailed analysis using full 2D-COS spectroscopy. For the sake of briefness, only the diagonal cross-sections of the correlation matrices of the groups 1-3 produced by full 2D-COS analysis are given in Fig. 5.44-5.50, although the data of non-diagonal cross-sections have also been analysed and the results included in the discussion.

From Fig. 5.44 and 5.45 (diagonal cross-sections of the synchronous and asynchronous 2D-correlation matrices correspondingly) a large number of major 'auto-peaks' (the peaks on the diagonal of the contour map) can be identified in the IR-spectra of the samples of group 1 ($h \leq 0.366$). At high frequencies (Fig. 5.44*E* and 5.45*E*) the 2D-COS data indicates the presence of the broad peak beyond the spectral limit of the mid-IR spectra ($\nu > 4000$ cm^{-1}). The literature data suggests that in this range the vibrations of the OH-group of non-bridged Zr-OH group can occur in the near-IR region [45]. According to the study [46], the set of minor peaks in the range ca. 3850-3750 cm^{-1} in Fig. 5.44*E*, 5.45*E* are due to non-bridged Zr-OH moieties. These peaks are not clearly seen in the raw spectra (Fig. 5.42), but appear in the 2D-correlation spectra (Fig. 5.44, 5.45 *E*). The set of strongly out-of-phase peaks at 3705-3610 cm^{-1} (3703, 3684, 3670, 3645 and 3613 cm^{-1}) are clearly observed in the

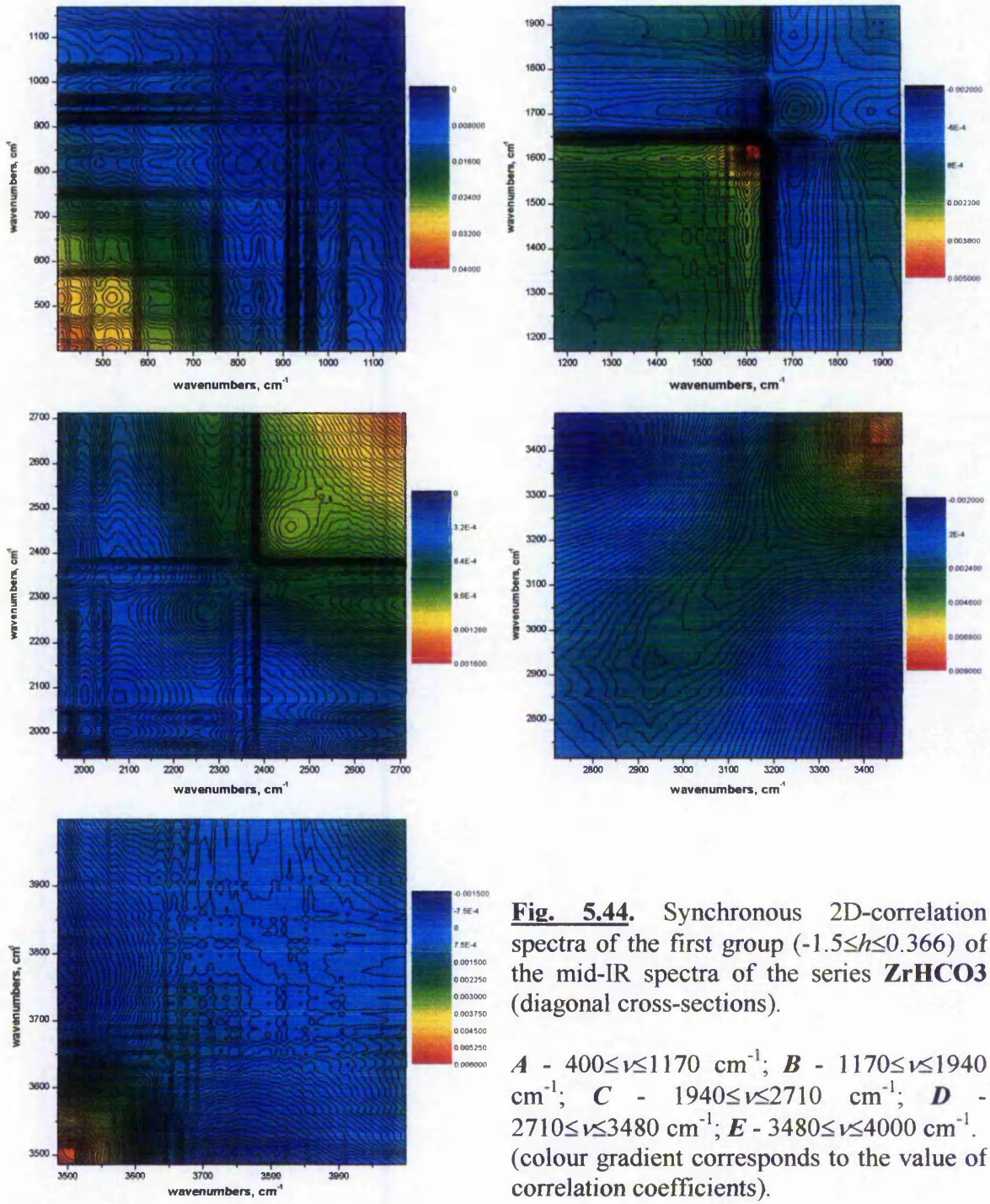


Fig. 5.44. Synchronous 2D-correlation spectra of the first group ($-1.5 \le h \le 0.366$) of the mid-IR spectra of the series **ZrHCO3** (diagonal cross-sections).

A - $400 \le \nu \le 1170$ cm^{-1}; ***B*** - $1170 \le \nu \le 1940$ cm^{-1}; ***C*** - $1940 \le \nu \le 2710$ cm^{-1}; ***D*** - $2710 \le \nu \le 3480$ cm^{-1}; ***E*** - $3480 \le \nu \le 4000$ cm^{-1}. (colour gradient corresponds to the value of correlation coefficients).

asynchronous spectra of Fig. 5.45*E*. According to Jung and Bell [46] and other authors [47, 48], these peaks relate to the broad band of stretching vibrations of tri-bridging Zr-OH groups on the surface of monoclinic zirconia (3650-3670 cm^{-1}) that agrees well with the data of the PXRD studies discussed in Section 5.4.1.1. The intensity of the IR-bands in this region is relatively low (Fig. 5.42), indicating a low concentration of the tri-bridged Zr-OH moieties in the samples of group 1 (series **ZrHCO3**) and quite small amounts of monoclinic zirconia. However, the strong overlap with the intense peaks from water vibrations located at lower frequencies (discussed below) obscures the real intensity of the peaks arising from monoclinic zirconia formed in acidic conditions.

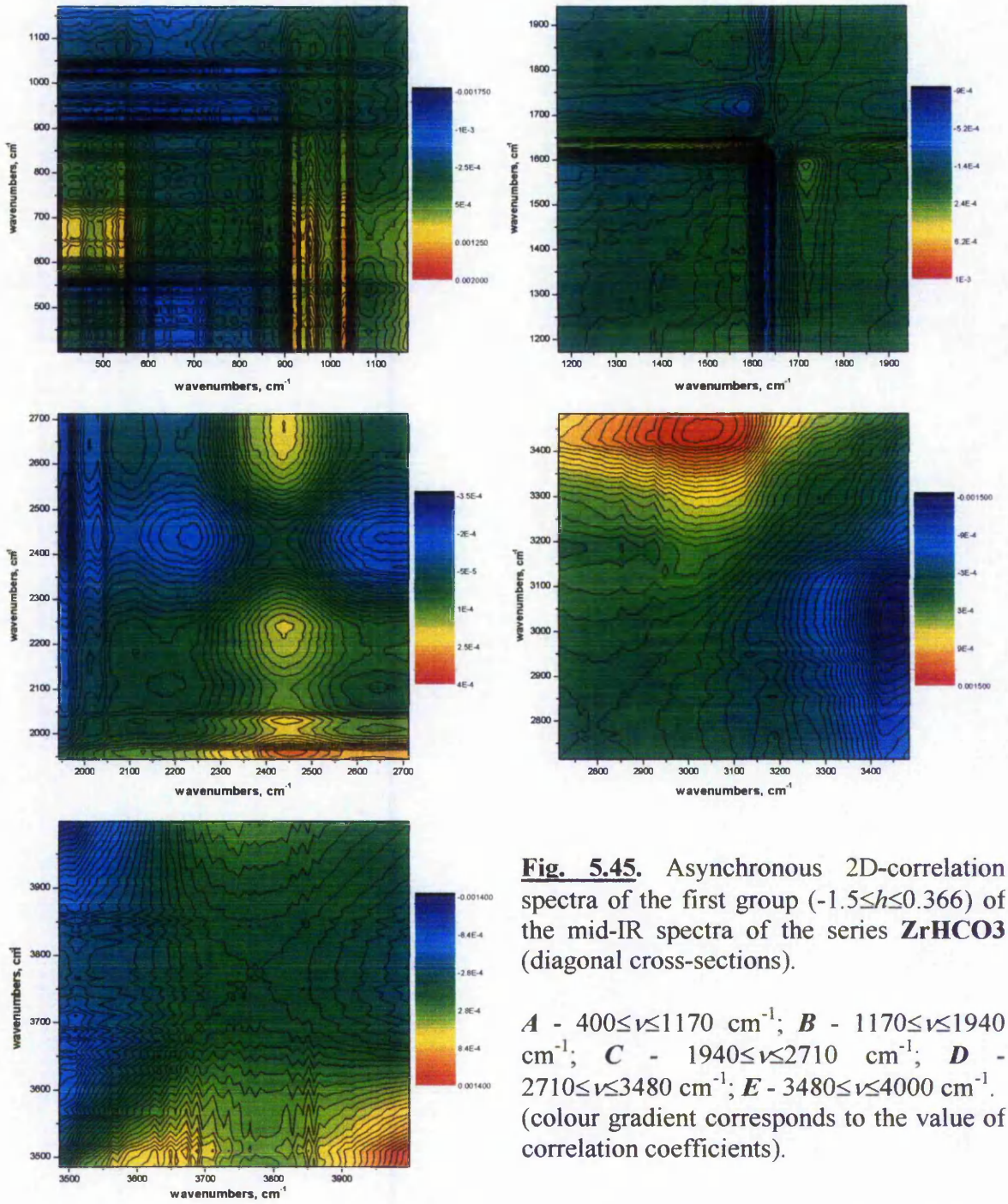


Fig. 5.45. Asynchronous 2D-correlation spectra of the first group ($-1.5 \leq h \leq 0.366$) of the mid-IR spectra of the series **ZrHCO3** (diagonal cross-sections).

A - $400 \leq \nu \leq 1170$ cm^{-1}; ***B*** - $1170 \leq \nu \leq 1940$ cm^{-1}; ***C*** - $1940 \leq \nu \leq 2710$ cm^{-1}; ***D*** - $2710 \leq \nu \leq 3480$ cm^{-1}; ***E*** - $3480 \leq \nu \leq 4000$ cm^{-1}. (colour gradient corresponds to the value of correlation coefficients).

The central feature of Fig. 5.44 (*D*, *E*) is the presence of very intense and strongly autocorrelated peaks at 3507 and 3421 cm^{-1} which occur together with other poorly resolved peaks at 3208; 3267; 3344; 3548; 3560; 3604 and 3621 cm^{-1}. In this region the vibrations of hydronium-ions (H_3O^+) characteristic of highly acidic samples can occur [35] as well as tri-bridging hydroxyl-ligand bands [48] and fundamental stretching vibrations of OH-groups of lattice water [35]. The bands at 3604 and 3621 cm^{-1} are more likely to be related to $Zr(OH)_3Zr$ tri-bridged groups [48], which have been shown to prevail in the case of monoclinic zirconia [46]. Relatively weak bands at 3548 and 3560 cm^{-1} can be assigned either to the ν_1 band of H_3O^+ [49], or to OH-stretchings of lattice water. The rest of the observed features in the range

3430-3200 cm^{-1} with a maximum at 3421 cm^{-1} most probably relates to lattice water [50].

There is controversy between different authors concerning the assignment of the intense bands observed both in IR- and Raman spectra of hydrous zirconia, Zr hydrolytic polymers Zr-based gels, etc. For instance, the band at 3510 cm^{-1} has been assigned to the vibrations of Zr-OH moieties of bi-bridging OH-ligands of the Raman spectra of zirconyl chloride [51]. Other authors attribute the same band either to free water [48], or to lattice water vibrations [47]. A similar controversy exists over assignment of the major band at 3400-3430 cm^{-1}. The data from the 2D-correlation analysis indicate that bands at 3505-3510 and 3430-3400 cm^{-1} are strongly correlated with each other. Therefore, they arise from the same type of functionality in Zr polymers. It is presumed that these bands are attributed to Zr-OH_2-stretchings of lattice water. This assignment agrees well with the fact that both bands are very intense up to quite high hydrolysis ratios (h=1.6), where substantial dehydration of Zr colloids has been reported to occur [52].

A large number of the peaks in the range 2700-3200 cm^{-1} (2776; 2822; 2926; 2982; 3029; 3078; 3116; 3161 cm^{-1}) can be identified in the 2D-COS patterns (synchronous spectrum in Fig.5.44*D*). This array of peaks is anti-correlated with the intense peaks at 3421 and 3507 cm^{-1} (OH-vibrations of Zr-OH_2 groups). The asynchronous spectrum (non-diagonal cross-sections of the correlation matrix not presented) shows out-of-phase maxima at 2982, 3029, 3078, 3116 and 3161 cm^{-1} compared to the lattice water and Zr-OH_2-Zr vibrations at 3421 and 3507 cm^{-1}. The correlation with the group of bands in the region 3740-3600 and 4000-3900 cm^{-1} is also observed for these bands. Therefore, the group of the IR-bands at 2982, 3029, 3078, 3116 and 3161 cm^{-1} is related to terminal or bridging Zr-OH vibrations.

Analysing the raw IR-spectra shown in Fig. 5.42 (Part I) one can find that the peaks at 3550-3560 cm^{-1} probably related to hydronium-ions, rapidly diminish with increase of hydrolysis ratio from h=-1.5 to h=0.336 which is in line with the decreasing acidity of the initial Zr-ion solutions and corresponding solid samples of the series **ZrHCO3**. The sharp and intense band at ~3510 cm^{-1} attributed to Zr-OH_2 moieties is at its highest value at h~0.0 and remains virtually constant with the increase of the hydrolysis ratio up to h~1.6. The broad and intense band at 3421 cm^{-1} shifts to shorter wavenumbers (~3400 cm^{-1}) and, starting from h~1.6, decreases significantly with the increase of h, indicating gradual elimination or replacement of aquo ligands of Zr polymeric ions with OH-ligands. The array of the IR-bands of physisorbed water (2950-2500 cm^{-1}) also tends to decrease with the increase of the hydrolysis ratio (unlike for the series **AMK1** with Al-ions). It means that lower-charged hydrolysed Zr species at high values of h allow for easier removal of physically absorbed water in the process of spray-freeze-drying.

The next IR-region in Fig. 5.44 and 5.45 (*C*) shows the presence of the bands at 1962, 2032, 2262, 2285, 2354, 2371, 2460, 2498, 2526, 2543 and 2583 cm^{-1}. The broad band 2700-2950 cm^{-1} arising from non-lattice water (Fig. 5.44, 5.45 *D*) continues in Fig. 5.44*C* at >2500

cm^{-1} with several local maxima at 2526, 2543 and 2583 cm^{-1}. A distinct doublet of the bands at 2498 and 2460 cm^{-1} is persistently present in the raw IR-spectra of the series **ZrHCO3** throughout the hydrolysis ratio scale investigated at practically constant intensity (Fig. 5.42). These bands are not correlated with any other bands in the IR-spectra of the series **ZrHCO3**. Asynchronous 2D-COS patterns show that the bands at 2498 and 2460 cm^{-1} exhibit strong out-of-phase peaks with the rest of the IR-bands observed in the region (Fig. 5.45*C*). Therefore, they are independent from the hydrolysis ratio and pH and can be attributed to atmospheric water. Another very weak doublet at 2354 and 2371 cm^{-1} corresponds to atmospheric (free) carbon dioxide [35]. The third distinct doublet identified in the 2D-COS patterns is at ca. 2262 and 2285 cm^{-1}. It is related to physically absorbed water since these bands correlate well with the broad set of bands of the same origin at 2500-3200 cm^{-1}. The same assignment can be made for the weak spectral features in the IR-region 1950-2040 cm^{-1}.

The next spectral region in the mid-IR spectra of the samples of group 1 (series **ZrHCO3**) is located at 1180-1950 cm^{-1} (Fig. 5.44, 5.45 *B*). The band of bending vibrations of water molecules with the maximum at ca. 1636 cm^{-1} in the raw IR-spectra (Fig. 5.42) dominates the spectral region. As follows from Fig. 5.44, 5.45 *B*, this peak has a composite structure and consists of the bands at 1705, 1636 and 1600 cm^{-1}. The band at 1705 cm^{-1} is correlated only with a doublet at 2498 and 2460 cm^{-1} assigned to atmospheric moisture. A narrow band at 1636 cm^{-1} is the only part of the composite peak arising from lattice water of Zr-containing samples that is supported by strong correlation with the other distinct lattice water peak at 3420 cm^{-1}. The highly correlated band at ca. 1600 cm^{-1} is accompanied by a large number of weak satellite bands in the region 1600-1200 cm^{-1} (Fig. 5.44, 5,45 *B*). This set of IR-bands is strongly correlated with the bands of non-lattice (free) water at 2300-2150 cm^{-1} and 3200-2500 cm^{-1}. Hence, the set of bands at 1600-1200 cm^{-1} is related to bending and other deformation vibrations of physically absorbed water for the solid samples **ZrHCO3**.

A doublet of bands ventered at 1464 and 1429 cm^{-1} can be distinguished from the set of bands at 1600-1200 cm^{-1} discussed above. These bands are very weak at the low hydrolysis ratios (h=0.366) of samples of group 1 and are related to the complex of carbonate-ions with zirconium polymers as will be described below.

The most important and informative region of the mid-IR-spectra of the series **ZrHCO3** is located at lower frequencies (1180-400 cm^{-1}, Fig. 5.44, 5.45 *A*). In this region the deformation vibrations of Zr-OH moieties of Zr-$(OH)_2$-Zr and Zr-OH_2 can be found [29, 51]. This region also distinguishes the samples of group 1 ($-1.5 \leq h \leq 0.336$) from the rest of the less acidic samples of the series **ZrHCO3**. Three very sharp bands at 1028, 954 and 919 cm^{-1} are clearly seen in the raw spectra of the series in Fig. 5.42 and in the 2D-COS patterns of Fig. 5.44, 5.45 *A*. These bands are observed present in the raw IR-spectra of the series **ZrHCO3** up to h~0.8 and are related to $\delta_{Zr\text{-}OH}$ deformation vibrations of the bi-bridging OH-ligands [51]. The bands are strongly correlated with the stretching vibrations of the same bond at ca.

3750 cm^{-1} and are anti-correlated with the band of OH-stretchings at 3421 and 3507 cm^{-1}. Weaker and broader bands at 893, 845, 818 and 725 cm^{-1} can be also seen in the 2D-COS patterns in Fig. 5.44, 5.45 *A*. These bands are slightly correlated with the abovementioned set of $\delta_{Zr\text{-}OH}$. However, they exhibit a correlation behaviour, which differentiates them from the rest of the IR-bands in the spectra of the series **ZrHCO3**. The band at 725 cm^{-1} agrees well with the position of the Raman band of monoclinic and tetragonal zirconia at ca. 730-750 cm^{-1} [55] and can be attributed to Zr-O-Zr bending motion in the crystalline phase occurring at $h \leq 0.336$ (group 1 of the samples of the series **ZrHCO3**). The rest of the bands in the region 800-900 cm^{-1} are difficult to identify [51].

As follows from Fig. 5.44, 5,45 *A*, the IR-region $1100 \leq \nu \leq 400$ cm^{-1} is heavily populated with bands from the strongly correlated set of librational modes of free and lattice water [35]. The maximum of this set of strongly overlapped broad bands is at ca. 420-440 cm^{-1}. The other bands in the mid-IR spectra of the series **ZrHCO3** occur on top of this broad peak. The librational bands of water occur even in pure crystalline $ZrOCl_2*8H_2O$ (Fig. 5.42) and hinder estimation of other band positions and their relative intensities. Nevertheless, the use of full 2D-correlation analysis enables the allocation of the major bands in the region 1100-400 cm^{-1}. Along with the librational water bands discussed above the low frequency bands at 630, 606, 550-560, 528, 492, 440 and 408 cm^{-1} were identified. Practically the same bands have been observed by Tosan et. al [29] in the Raman spectra of the hydrolysed zirconyl chloride solutions. The bands at 408, 440 and 520-530 cm^{-1} are highly correlated between themselves. They are also highly correlated with the fundamental bands of $Zr\text{-}OH_2$ vibrations at 3510 and 3421 cm^{-1}. The authors [51] also attribute the band at 430 cm^{-1} (which is probably a composite band consisting of two peaks at 408 and 440 cm^{-1}) to either lattice water deformation vibrations or to the Zr-OH vibrations of the complex of different symmetry (comparing to the 'normal' $Zr\text{-}(OH)_2\text{-}Zr$ complex of Zr tetramers [21]). In other study [53] the band at 530 cm^{-1} was assigned to Zr-O-Zr deformation vibrations.

The band at 640 cm^{-1} appears to be a doublet of adjacent bands at 627 and 647 cm^{-1}. This band identified in the 2D-COS patterns of Fig. 5.44, 5.45 A most probably belong to $\delta(Zr\text{-}OH_2)$ vibrations of the aquo ligands of Zr polymers. The peaks at 606 and 493 cm^{-1} probably correspond to the Raman bands at 580 and 456 cm^{-1} observed in the reported work [54] and related to the δ(Zr-OH) vibrations of the bi-bridged $Zr\text{-}(OH)_2\text{-}Zr$ groups.

It is necessary to stress that almost all of the IR-bands described above for the acidic samples (h=0.336) of the series **ZrHCO3** are observed also in the raw spectrum of the crystalline $ZrOCl_2*8H_2O$ solid (Fig. 5.42). The bands at 3421 cm^{-1} and the arrays of the bands at 1600-1200 and 1100-400 cm^{-1} related to stretching, deformation and librational modes of lattice water correspondingly, are somewhat diminished in the spectrum of pure zirconyl chloride (Fig. 5.42). However, the intense band at ca. 3200 cm^{-1} relating to non-coordinated water indicates that even in the pure zirconyl chloride solid there is a relatively large number

of water molecules not bound directly to Zr atoms.

Analysing the results of the 2D-correlation analysis of the mid-IR spectra of the **group 2** solid samples of the series **ZrHCO3** (Fig. 5.42, Part II) obtained in the hydrolysis ratio range $0.48 \leq h \leq 2.0$, one must emphasise that there are some fundamental differences in the spectra of this compared with the mid-IR spectra of samples of group 1:

1. Both stretching vibrations at 3421 and 3507 cm^{-1} of lattice water and non-lattice water vibrations in the range 2950-2500 cm^{-1} have a strong tendency to decrease at higher hydrolysis ratios (h=1.2) to their minimum at h=2.0 (the point of electroneutrality of hydrous zirconia). This indicates that lattice water is being gradually replaced by hydroxyl-ligands upon alkali-forced polymerisation. The presence of non-lattice or physically absorbed water is diminished due to a decreasing overall charge of Zr polymers upon neutralisation with alkali. The peak of bending water vibrations with the maximum at ca. 1636 cm^{-1}, as well as the bands of the deformation vibrations of lattice water at 440 and 408 cm^{-1} follow the same trend as the higher frequency bands described above.
2. The bands of Zr-$(OH)_2$-Zr stretches at 3670-3650 cm^{-1} and $\delta_{Zr\text{-}OH}$ vibrations at 1030, 954 and 919 cm^{-1} gradually disappear at h=0.8. This is indicative of the process of internal oxolation, i.e. transformation of OH-bridges into oxo-bridges of zirconium oxide. This finding agrees well with the pH data discussed in Chapter 4.
3. In spite of the tendency of both Zr-OH and Zr-OH_2 groups to decrease with increase of hydrolysis ratio, even at h=2.0 where Zr-ions are completely neutralised with alkali ($KHCO_3$), there is a significant level of aquo- and hydroxo-ligands present in the solid materials produced at this point. Therefore, alkaline neutralisation does not fully convert Zr-ions into a final hydrated zirconia precipitate, or the surface of hydrated zirconia is large enough to accommodate a significant number of the bridged OH-ligands and water molecules, which agrees well with the literature data [46-48].
4. The major lower-frequency bands in the IR-spectra of the samples produced at $0.48 \leq h \leq 2.0$ are located at ca. 408, 440, 492, 530 and 620-640 cm^{-1}. These bands correspond to surface water and lattice vibrations of amorphous hydrous zirconia [29]. The presence of amorphous zirconia correlates well with the XRD data in Section 5.4.1.1.
5. There is no significant adsorption or complexation of bicarbonate or carbon dioxide. from the alkali used as a titrant ($KHCO_3$) on the surface of Zr hydrolytic polymers of amorphous hydrous zirconia below hydrolysis ratio h=2.0. Therefore, acidic and quasi-neutral conditions do not favour these chemical processes.

The data of the mid-IR spectra of groups 1 and 2 of the samples of the series **ZrHCO3** ($-1.5 \leq h \leq 2.0$) discussed above and their assignments together with the literature data and corresponding references are summarised in Table 5.4.

Table 5.4. Band positions and assignments in the mid-IR spectra of the group 1 and 2 samples of the series **ZrHCO3** ($-1.5 \leq h \leq 2.0$)

ν, cm^{-1}	Intensity	Shape	Assignment	Reference method	Ref.
>4000	Unknown	Broad	Possibly, OH-vibrations of Zr-OH_2 ligands	-	[45]
3903	V. weak	Sharp	-"-	-	-
3870-3750	Vanishing	Sharp	OH-stretchings of the terminal Zr-OH groups of monoclinic zirconia	IR	[47,48]
3745-3700	Weak	Sharp	OH-stretchings of the bi-bridged Zr-OH groups of monoclinic and tetragonal zirconia	IR	[46]
3700-3610	Weak	Broad	OH-stretchings of the tri-bridged Zr-OH groups of monoclinic zirconia	IR	[46]
3560, 3548	Medium		Either OH-stretchings of the hydronium-ion (H_3O^+), or OH-stretchings of coordination water	IR	[35]
3507, 3421	Very high	Sharp, broad	OH-stretchings of lattice water (Zr-OH_2 ligands)	IR	[21]
3510-3200	High	Broad	-"-	IR	[21]
3200-2900	High	Broad	Sretchings of Zr-OH_2 ligands (unknown denticity)	-	-
2950-2500	Med.-high	Broad	OH-stretchings of free, non-lattice water	Raman	[29]
2498, 2460	Weak	Sharp	Atmospheric contaminants (e.g. moisture, atmospheric CO_2, etc.)	IR	[35]
2371, 2354	Weak	Sharp	Vibrations of free atmospheric CO_2	IR	[35]
2300-1900	Weak	Broad	Atmospheric contaminants (e.g. moisture, atmospheric CO_2, etc.)	-	-
1705	Weak	Broad	Atmospheric contaminants	-	-
1636	Medium	Sharp	Bending (HOH) vibrations of lattice water	IR, Raman	[35]
1600-1200	Med.-low	Sharp	Atmospheric moisture (bending vibrations)	-	-
1464, 1429	Low	Sharp	Carbonate ligands bound to Zr polymers	IR	[35]
1028, 954, 919	Med.-low	V. sharp	δ(Zr-OH) vibrations of Zr hydrolytic polymers	(ATR)-IR	[51]
893-818, 725	Weak	Sharp (725 – broad)	ρ_r, ρ_t and ρ_w deformation modes of lattice water	Raman	[51]
640, 606, 555, 528	Medium	Varies	Structural deformations of Zr-O-Zr lattice	Raman	[29, 51]
492, 440, 408	High	Varies	Librations, transitions of lattice water - δ(Zr-OH_2) vibrations	Raman	[29,35]

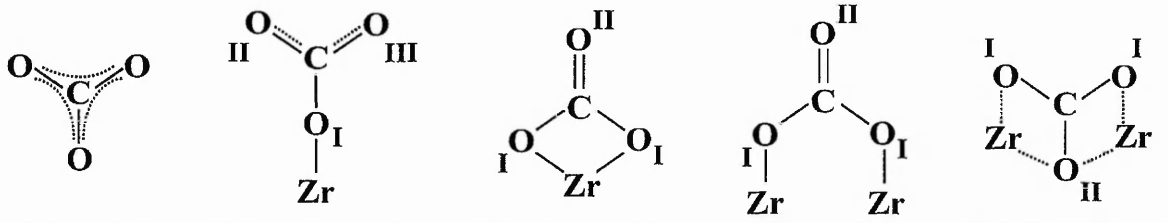
The mid-IR spectra of the **group 3** samples of the series **ZrHCO3** produced at alkaline conditions (h=2.0) exhibit dramatic changes (Fig. 5.42 and Fig. 5.43) due to (***a***) complete formation of Zr hydrous oxide, and (***b***) strong complexation of zirconia with carbonate-ions which becomes possible in alkaline conditions.

Analysis of the raw IR-spectra of the group 3 samples (h=2.0) of the series **ZrHCO3** (Fig. 5.42, Part III) together with the full 2D-correlation analysis (not shown for the sake of brevity) indicates that the stretching vibrations of the coordinated water are red-shifted to lower wavenumbers (ca. 3385 and 3242 cm^{-1}) compared with the samples of groups 1 and 2 obtained at lower hydrolysis ratios. The array of IR-bands at 2950-3200 cm^{-1} is transformed into a single sharp band at 2960-2970 cm^{-1}. There are two new distinct bands at 2728 and 2632 cm^{-1} which have not been clearly observed in the spectra of groups 1 and 2. Three other bands at 2017, 1955 and 1843 of unknown origin are analogous to IR-bands observed in the spectra of samples at lower hydrolysis ratios. 2D-correlation analysis allowed for a clear distinction of the bands at 3650, 3745 and 3810-3905 cm^{-1} arising from tri-, bi- and monodentate hydroxo-groups of the surface of hydrous zirconia [46]. The intensity of these bands follows the order: ν_I(Zr-OH)<<ν_{III}(Zr-$(OH)_3$-Zr)<ν_{II}(Zr-$(OH)_2$-Zr) indicating that bi-

bridging OH-ligands prevail thus supporting the dominance of the tetragonal zirconia phase revealed using XRD patterns in Section 5.4.1.1.

The spectral region 1800-400 cm^{-1} comprises major differences of the spectra of group 3 compared with the other two groups of **ZrHCO3** samples (Fig. 5.42). There are two sets of the most intense bands at 1620-1560 cm^{-1} and 1420-1330 cm^{-1}. These bands are of a composite structure and belong to carbonate species that are coordinatively bound to Zr-atoms. There is a range of very sharp and intense bands in the region 1300-600 cm^{-1} also arising from coordinatively bound carbonate-ions. IR-bands at 1738 cm^{-1} and 1657 cm^{-1} are also observed. The lower-frequency region exhibits vibrations at 640-630, 585-575 cm^{-1} attributed to the lattice Zr-O-Zr vibrations of the oxide phase and a band at 475 cm^{-1} assigned to librational modes of the coordinatively bound water. The band intensity decreases with increase of *h*, indicating replacement of aquo ligands with carbonato-ligands at higher pH.

In-depth correlation analysis of the carbonate-related bands in the region 1750-660 cm^{-1} indicates that there are three major types of complexes of carbonate-ions with zirconium species in the alkaline medium (*h*=2.0) of the **ZrHCO3** series. In general, the following types of carbonate complexes can be determined using IR-spectroscopy [35]:



Free carbonate-ion **Monodentate complex** **Bidentate complex** **Bidentate bridging complex** **Polydentate complex**

Position of the ν(C-O) stretching vibrations allows for identification of the majority of carbonato-complexes of metal ions [35]. On the basis of 2D-correlation analysis, two bidentate complexes with very similar structure were found to co-exist in the IR-spectra of the group 3 samples of the series **ZrHCO3**. Both the complexes are characterised by the following sets of vibrations: $\nu(CO_{II})$ – 1697 and 1675 cm^{-1}; $\nu(CO_I)+\delta(O_ICO_{II})$ – 1365 and 1392 cm^{-1}; $\nu(CO_I)$ – 1014 and 1045 cm^{-1}; π(ring) – 833 and 850 cm^{-1}; δ(ring) – 705 and 756 cm^{-1}; $\delta(O_ICO_{II})$ – 663 cm^{-1}. The differences Δ between $\nu(CO_I)$ and $\nu(CO_{II})$ bands are 278 and 332 cm^{-1} respectively. Therefore, both complexes are of the bidentate (non-bridging) type [35] with the structural differences probably relating to two distinct sites on Zr hydrous oxide [46]. Another possible explanation is the existence of carbonate (CO_3^{2-}) and bicarbonate complexes with slightly different structure. The bands listed above are extremely sharp suggesting that the polymeric Zr-carbonate complexes are well ordered.

Along with the listed bands attributed to the bidentate carbonato-complex with zirconium in the alkaline medium, there is another minor complex with $\nu(CO_{II})$=1489 cm^{-1} and $\nu(CO_I)$=1461 cm^{-1} (Δ=28 cm^{-1}). This complex has a polydentate structure [35]. The bands at 1489 and 1461 cm^{-1} are anti-correlated with the bands of the bidentate complex. This fact is

in agreement with the trend of the bidentate complex amount to increase with increase of pH and hydrolysis ratio, while the fraction of the polydentate complex gradually decreases.

The band at 1657-1666 cm^{-1} identified in the 2D-correlation spectra of the group 3 samples of the series **ZrHCO3** is possibly related to non-complexed (free) carbonate-ion. This species is of minor importance in the spectra of the series **ZrHCO3** at h=2.0 (Fig. 5.42) which indicates that the majority of CO_3^{2-}-ions are bound to the surface of hydrous ZrO_2.

5.6.3. Far-infrared spectra of the solid samples of the series ZrHCO3

Far-IR spectra contain crucial information concerning the speciation of Zr-ions in solid and solution state, since they exhibit bands related to metal-ligand low frequency vibrations only [35]. The far-IR spectra of the series **ZrHCO3** (CsI pellet technique) in the range 700-120 cm^{-1} was examined (Fig. 5.46). Three sample groups in Fig. 5.46 in the range – $1.5 \leq h \leq 0.45$; $0.56 \leq h \leq 1.6$ and $1.8 \leq h \leq 4.0$ are identified in the mid-IR spectra of the series (Fig. 5.42). The spectra in Fig. 5.46 were normalised for presentation purposes.

Division of the far-IR spectral patterns into three groups depicted in Fig. 5.46 was made on the basis of the correlation sum graph presented in Fig. 5.47.

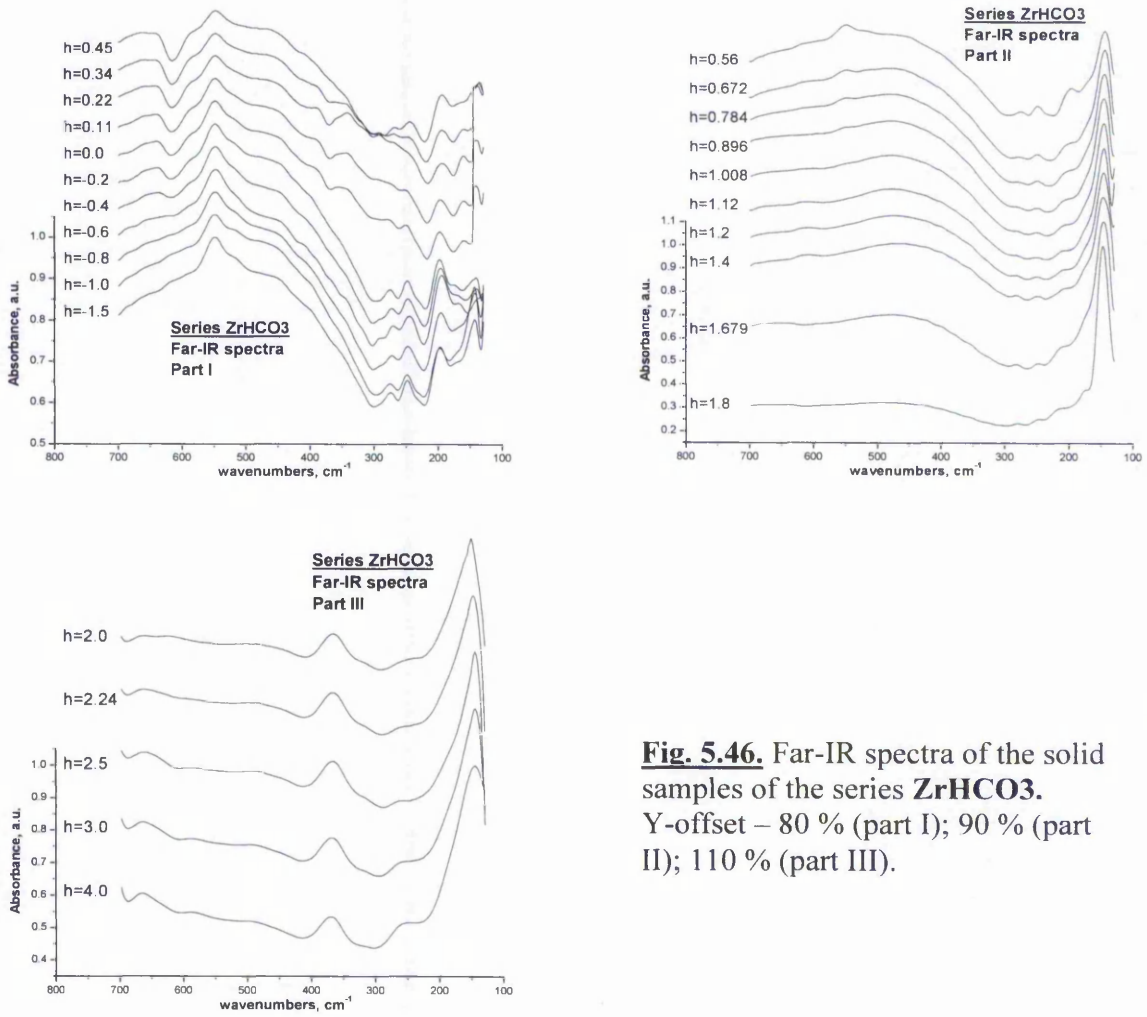


Fig. 5.46. Far-IR spectra of the solid samples of the series **ZrHCO3.** Y-offset – 80 % (part I); 90 % (part II); 110 % (part III).

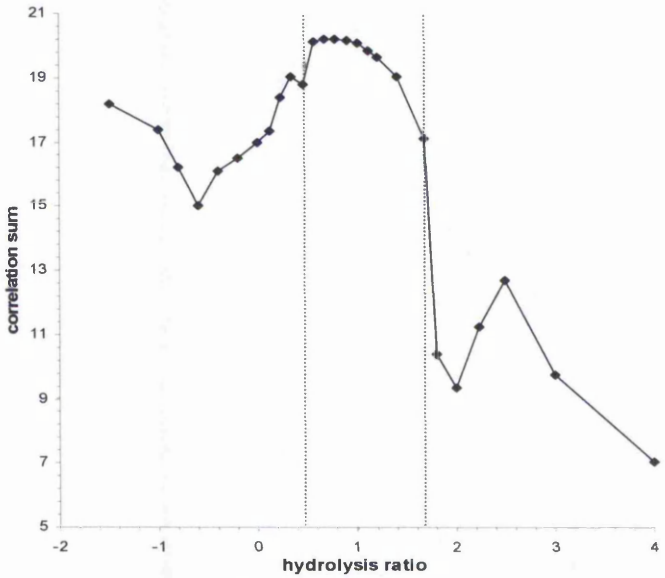


Fig. 5.47. The correlation sum graph in the hydrolysis ratio domain calculated from the far-IR spectra of the solid samples of the series **ZrHCO3**.

As follows from the spectral patterns shown in Fig. 5.46, the far-IR spectra of the spray-freeze-dried samples of the series **ZrHCO3** are quite sensitive to variations of pH and hydrolysis ratios in the solution preparation stage of the corresponding materials.

Comparison of Fig. 5.47 and 5.43 leads to the conclusion that far-IR spectra exhibit completely different correlation patterns compared to those of mid-IR spectra for the series **ZrHCO3** (Fig. 5.43). The correlation behaviour of the far-IR spectra is reminiscent of the PXRD patterns of the same series (Fig. 5.9). This fact confirms structure-related nature of the far-IR spectra of Zr-containing samples.

2D-correlation spectroscopy has enabled us to identify and to relate the bands in the far-IR spectra of the series **ZrHCO3**. The 2D-COS analysis was performed for all three groups of the spectra indicated in Fig. 5.46. As an illustrative example, 2D-contour maps from the 2D-COS analysis of the group 1 samples ($h \leq 0.45$) are shown in Fig. 5.48.

The data of Fig. 5.48*C* indicate the presence of the dominant sharp band at 548 cm^{-1} which is highly auto-correlated (large peak maximum in the 2D-pattern diagonal). Other bands at 642, 603 and 528 cm^{-1} appear to be satellite bands of this major peak. The described set of bands is most likely attributed to structural Zr-O-Zr deformations, as has been shown using Raman spectroscopy [29] and deuterium exchange [51]. The bands of librational modes of lattice water at 456 and 408 cm^{-1} are of minor importance in the far-IR spectra.

Together with weak bands at 685 and 697 cm^{-1} these bands are anti-correlated to structural (Zr-O) vibrations in the range 500-650 cm^{-1} (Fig. 5.48*D*). The latter bands have not been clearly observed in the mid-IR spectra of the group 1 samples (Fig. 5.42, 5.44, 5.45).It is presumed that they are related to the adjacent bands at 725 and 818-883 cm^{-1} which were assigned to rotational modes of the coordinatively bound water (Table 5.4).

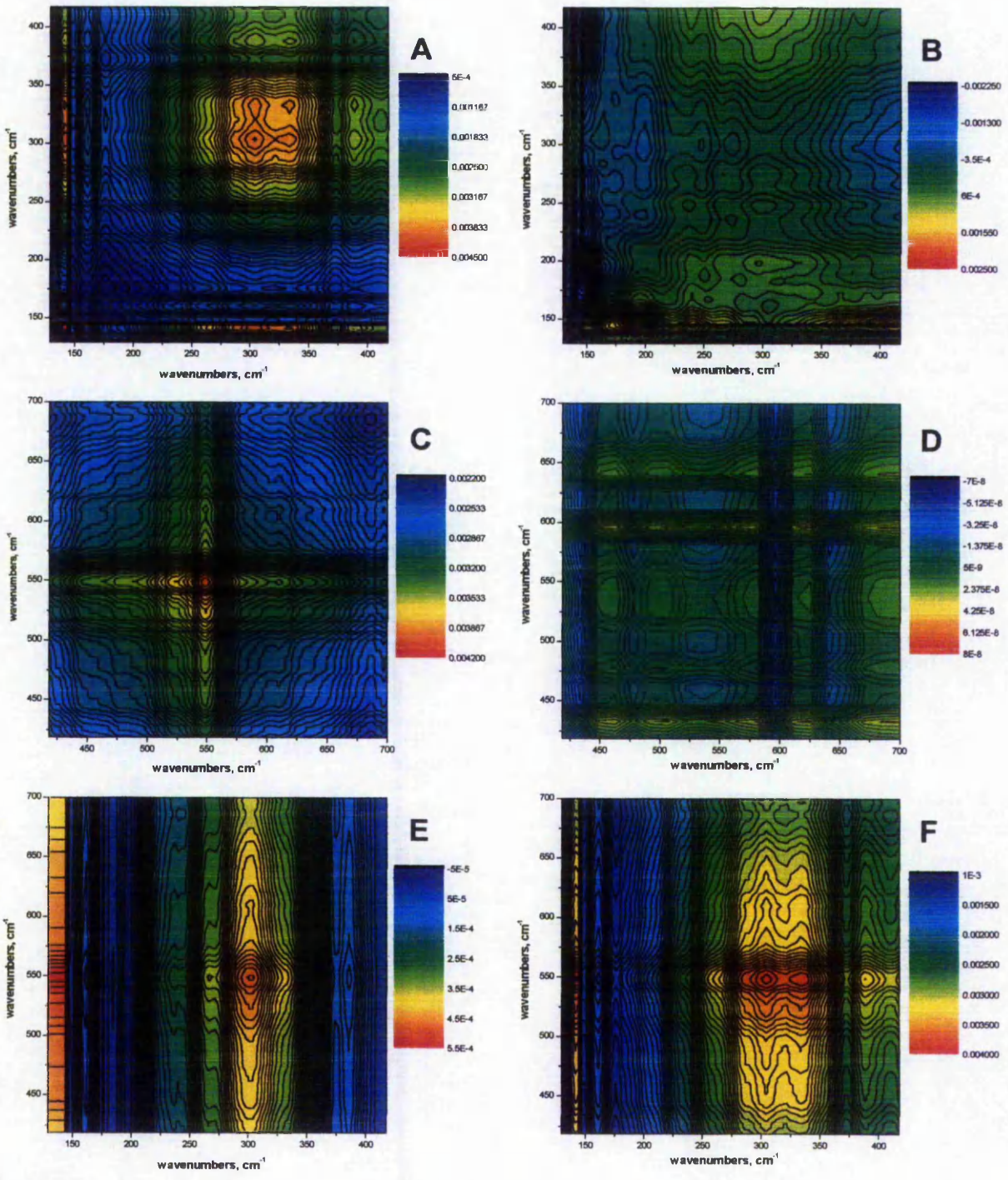


Fig. 5.48. 2D-correlation contour maps of the far-IR spectra of the group 1 samples of the series **ZrHCO3**. ***A, B*** – synchronous and asynchronous diagonal cross-sections in the region 120-400 cm^{-1}; ***C, D*** - synchronous and asynchronous diagonal cross-sections in the region 400-700 cm^{-1}; D, E - synchronous and asynchronous non-diagonal cross-sections of the regions 120-400 $cm^{-1}$and 400-700 cm^{-1}.

At lower frequencies (Fig. 5.48*A*, *B*) major auto-correlated peaks at 334 and 303 cm^{-1} are observed. These high-energy IR-bands have been previously observed in the Raman spectra of hydrous zirconia of monoclinic structure [54]. Therefore, they indicate the presence of this crystalline phase in **ZrHCO3** samples of acidic origin. The raw far-IR spectra of the

series (Fig. 5.46) reveal that both bands are most distinct and intense at lower hydrolysis ratios (h=0.0). At positive values of h, the bands start to decrease their intensity and totally disappear around h=1.68. This is in very good agreement with the PXRD data of Section 5.4.1.1. Another intense auto-correlated band observed in the far-IR spectra of group 1 samples is at 142 cm^{-1} (Fig. 5.48*A*). This band is strongly correlated with the abovementioned bands at 303 and 334 cm^{-1}. It has also been observed in the Raman spectra of monoclinic hydrous zirconia [54]. Additionally, the band at 388 cm^{-1} is probably of the same origin as the bands at 334, 303 and 142 cm^{-1}, although the correlation between the bands is much weaker. All these bands relate to the structural Zr-O vibrations of monoclinic zirconia observed in the far-IR spectra of the most acidic samples of the series **ZrHCO3**.

The data of Fig. 5.48 *D* and *E* indicate that the lower-frequency bands at 142, 303 and 334 cm^{-1} are strongly correlated with the major structural band at 548 cm^{-1} and other bands (528, 603 and 640 cm^{-1}). There is a weak correlation between the bands at 161 and 548 cm^{-1}, as well as a medium intensity correlation of the bands at 388 and 548 cm^{-1} (Fig. 5.48*E*, *F*). It is also clear that all structural (Zr-O) bands are anti-correlated with the bands of librational mode of lattice water (408 and 456 cm^{-1}). There is a distinct set of medium-intensity anti-correlated bands observed in the region 160-300 cm^{-1} (ν=171, 195, 247, 271 and 288 cm^{-1}). These IR-bands probably arise from the structural deformations of tetragonal zirconyl chloride, which are obviously anti-correlated with the bands of monoclinic zirconia and monoclinic "dehydrated" forms of zirconyl chloride as it was shown on the basis of the PXRD patterns in Section 5.4.1.1.

With increase of hydrolysis ratio for the series **ZrHCO3** the spectral patterns in the far-IR region change significantly (Fig. 5.46, 5.47). Analysis of the spectra of the **group 2** samples shows that the band at 548 cm^{-1} constantly diminishes at $0.56 \leq h \leq 1.8$ and becomes of minor importance (Fig. 5.46). The band at 640 cm^{-1} related to δ(Zr-O-Zr) remains quite intense up to h=1.68. The bands of the coordinatively bound water at 456 and 408 cm^{-1} remain in the spectra up to h~1.8, where they disappear. The bands of the tetragonal zirconyl chloride phase, after reaching a maximum at h~0.45-0.56, start to decrease in intensity, albeit their presence is maintained up to h~2.0. Interestingly, that at $h \geq 1.68$ these IR-bands start to regain their intensity, which indicates that from this hydrolysis ratio the overall ordering of Zr hydrolytic polymers becomes closer to the tetragonal phase (compare with the PXRD data of the series **ZrHCO3** in Section 5.4.1.1). The major band of the group 2 far-IR spectra (Fig. 5.46) is at 142-146 cm^{-1}. This peak possibly arises from fundamental (Zr-O) vibrations and depends on the form (monoclinic, amorphous or tetragonal) of zirconia in the samples. The band at 142-146 cm^{-1} continues to increase in intensity with increasing h, which probably indicates progressive formation of more covalent Zr-O-Zr bonds of hydrous zirconia.

Group 3 of the samples of **ZrHCO3** series is characterised by a completely different far-IR pattern (Fig. 5.46). At higher frequencies, the bands at 603 and 585 cm^{-1} relating to

ν(Zr-O) vibrations are present, as well as the band 492 cm^{-1} attributed to deformation vibrations of lattice water. In the shorter-wavenumber region (ν<400 cm^{-1}) there is a new intense and relatively sharp band at ca. 368 cm^{-1} which is assigned to the ν(Zr-O) vibrations of the carbonate complex [35]. Interestingly, in spite of the presence of at least three types of carbonato-complexes detected in the mid-IR spectra above, only one ν(Zr-O) band appears in the far-IR region. This correlates well with literature data indicating that monodentate and bidentate carbonato-complexes of different metal ions exhibit this vibrational mode at a similar frequency [35]. The shoulder at 247 cm^{-1} probably arises from the tetragonal structure of the remaining zirconia arrangements. The fundamental band of Zr-O structural vibrations at 142 cm^{-1} still has a high intensity in the group 3 spectra. Therefore, in spite of extensive complexation with carbonate-ions, the major structural component of the solid samples in the series **ZrHCO3** obtained in alkaline conditions is hydrous zirconia.

5.6.4. Mid-infrared spectra of the samples of ZrOH series

The raw mid-IR spectra of the solid samples of the series **ZrOH** produced with KOH as an alkaline titrant (Section 2.4.3) in the full range of hydrolysis ratios studied are presented in Fig. 5.49. The correlation sum graph calculated on the basis of the mid-IR data is shown in Fig. 5.50.

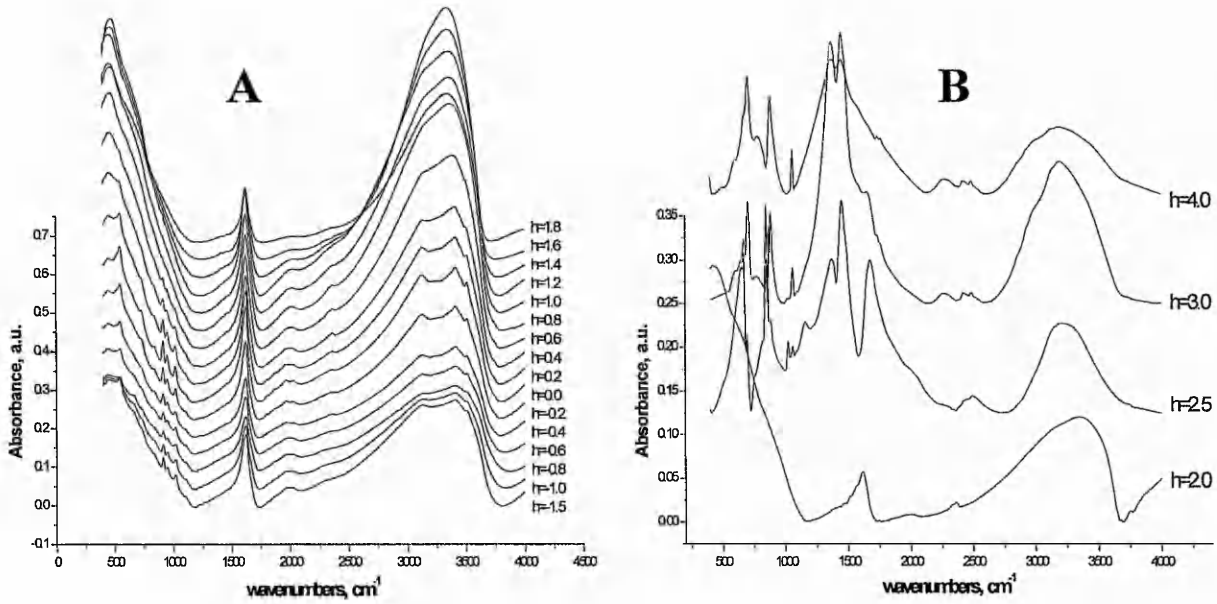


Fig. 5.49. Mid-IR spectra of the solid samples of **ZrOH** series. ***A*** - -1.5≤*h*≤1.8 (Y offset – 80 %); ***B*** – 2.0≤*h*≤4.0.

The data of Fig. 5.49 reveal strong similarity of the mid-IR spectra of the series **ZrOH** at *h*≤2.0 with the analogous spectral patterns of the series **ZrHCO3** discussed in Section 5.5.3. The correlation sum curve for the series **ZrOH** depicted in Fig. 5.50 also resembles that of the series **ZrHCO3** (Fig. 5.43). The results in Fig. 5.49 and 5.50 show that at h≤2.0 the mid-IR spectra of the series **ZrOH** are highly correlated. Three subdomains can

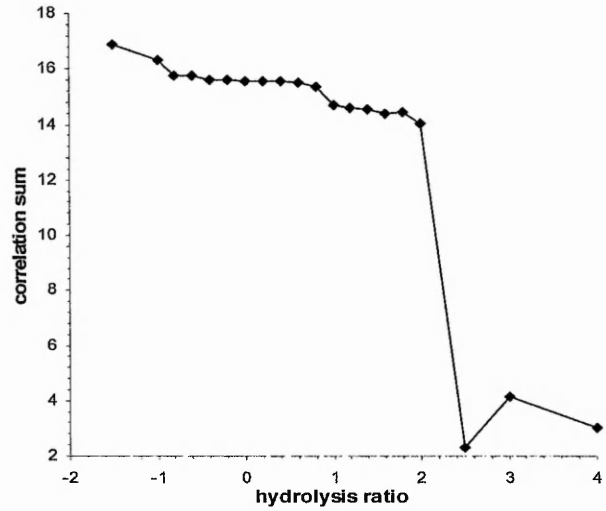


Fig. 5.50. The correlation sum graph in the hydrolysis ratio domain calculated on the basis of the mid-IR spectra of the series **ZrOH**.

be established: the samples produced at very acidic conditions ($-1.5 \leq h \leq 0.0$), and two groups of the milder acidity samples at $0.0 < h \leq 1.0$ and $1.0 < h \leq 2.0$ with slightly different spectral shapes and corresponding correlation sums (Fig. 5.49*A*, 5.50). At alkaline conditions above the hydrolysis ratio h=2.0 the mid-IR spectra exhibit rather different patterns (Fig. 5.49*B*).

In-depth 2D-correlation analysis carried out for the series of mid-IR spectra of **ZrOH** samples (the data are omitted for the sake of brevity) has enabled us to identify all major bands and relationships between them. These bands and the trends of their intensity variations are very close to those of the series **ZrHCO3** (Table 5.4). Here again, the vibrational modes of coordinatively bound water of Zr polymers (ν(Zr-OH_2)=3425-3420 cm^{-1}, 3200-2950 cm^{-1}; δ(HOH)=1636 cm^{-1}; δ(Zr-OH_2)=493, 460-440 and 410 cm^{-1}) are superimposed on the vibrations of hydroxyl-ligands of zirconium polymers (3830-3760 cm^{-1}; ν(Zr-$(OH)_2$-Zr)=3750-3730 cm^{-1}; ν(Zr-$(OH)_3$-Zr)=3560-3550 cm^{-1}; δ(Zr-OH)=1030, 955 and 916 cm^{-1}) and structural Zr-O-Zr vibrations (δ(Zr-O-Zr)=640, 603, 555 and 530 cm^{-1}). From a comparison of the mid-IR spectra of the series **ZrOH** and **ZrHCO3** one can draw a conclusion that the strength and the nature of alkali used for neutralisation of zirconium-ions at high temperature does not effect the overall structure and composition of the produced polymeric species and the resulting solid phases (monoclinic phases at low pH, amorphous hydrous zirconia at higher pH below the point of electroneutrality at h=2.0).

The differences in the mid-IR spectra for the series **ZrOH** and **ZrHCO3** in quasi-neutral and alkaline conditions are not as profound as expected. In IR-spectra of the series **ZrOH** at $h \geq 2.0$ the following intense and sharp bands of two Zr-carbonate complexes are observed with positions and intensities similar to those for the series **ZrHCO3**: $\nu(CO_{II})$ – 1646 and 1677 cm^{-1}; $\nu(CO_I)+\delta(O_ICO_{II})$ – 1359 and 1371 cm^{-1}; $\nu(CO_I)$ – 1154 and 1060 cm^{-1}; π(ring) – 883 and 848 cm^{-1}; δ(ring) – 703 and 772 cm^{-1}; $\delta(O_ICO_{II})$ – 663 and 607 cm^{-1}. The

distances Δ between $\nu(CO_I)$ and $\nu(CO_{II})$ bands for these two complexes are 275 and 318 cm^{-1} respectively. Therefore, these Zr-carbonate complexes detected in the alkaline samples of the series **ZrOH** are bidentate with a structure very similar to the analogous complexes reported for the series **ZrHCO3** above. Unlike the series **ZrHCO3**, the mid-IR spectra of the alkaline samples of the series **ZrOH** show prevailing Zr-carbonate complex of polydentate structure with the major bands at 1429 and 1482 cm^{-1} [35] (in the raw spectra these bands form a single peak at ca. 1450 cm^{-1}) which dominate the spectral patterns of the series at h>2.0. The carbonato-complexes observed in the series **ZrOH** can originate either from solutions where carbon dioxide from the atmosphere can dissolve intensively at pH>7.0 (albeit high temperature decreases the solubility of this acidic gas), or directly from the atmosphere via adsorption of carbon dioxide onto the solid samples during storage and handling. In any case, the carbonato-complexes with the surface of hydrous zirconia dominate the mid-IR spectra at h=2.0. The proportion of polydentate and bidentate carbonato-complexes varies with the hydrolysis ratio. Polydentate complexes after reaching a maximum concentration at h~3.0 appear to diminish at high hydrolysis ratios, while bidentate complexes probably increase in concentration with the increase of pH and the hydrolysis ratio of sample solutions. Aquo ligands are substantially eliminated from the coordination sphere of Zr-atoms, as indicated by the decreased bands of stretching (3400-3420 cm^{-1}), bending (1636 cm^{-1}) and librational vibrations (460-400 cm^{-1}). The stretching vibration $\nu(Zr\text{-}OH_2)$ is red-shifted to 3385 cm^{-1}.

5.6.5. Far-infrared spectra of the series ZrOH

Solid samples of the series **ZrOH** were also studied in the far-IR region (Fig. 5.51). The spectral shapes observed in Fig. 5.51 are analogous to those of the series **ZrHCO3** (Fig. 5.46). The correlation between the far-IR spectra of **ZrOH** samples depicted as a correlation sum graph in Fig. 5.52 is similar to that of the series **ZrHCO3**. However, higher resolution of the far-IR spectra of the series **ZrOH** (2 cm^{-1}) comparing to the series **ZrHCO3** (4 cm^{-1}, Fig. 5.46) has revealed a number of additional features related to pH-dependent structural transformations of Zr hydrolytic polymers and solid materials.

Approximately 18 bands were detected in the far-IR spectra of the series **ZrOH** (600≥ν≥200 cm^{-1}), sixteen of them are marked with numbered dashed lines in Fig. 5.51 in order to enable comparison between samples. The positions of the bands were determined using the 4th derivative of the raw spectra and full 2D-correlation analysis. The bands at ca. 588, 549-547 and 527-523 cm^{-1} identified in the far-IR spectra of the series **ZrOH** (Fig. 5.51) belong to the deformation vibrations of the Zr-OH bond of bridging hydroxyl-ligands. These bands are most intense at lower hydrolysis ratios (maximum around h=0.0) and indicate that a large number of bridging groups of Zr polymers are in the form of hydroxyls. The bands at 493-489, 455-465, 440 and 410-400 cm^{-1} together with the lower-frequency bands at 389-377, 360-355, 334-328 and 305-303 cm^{-1} relate to librational modes of the water coordinatively

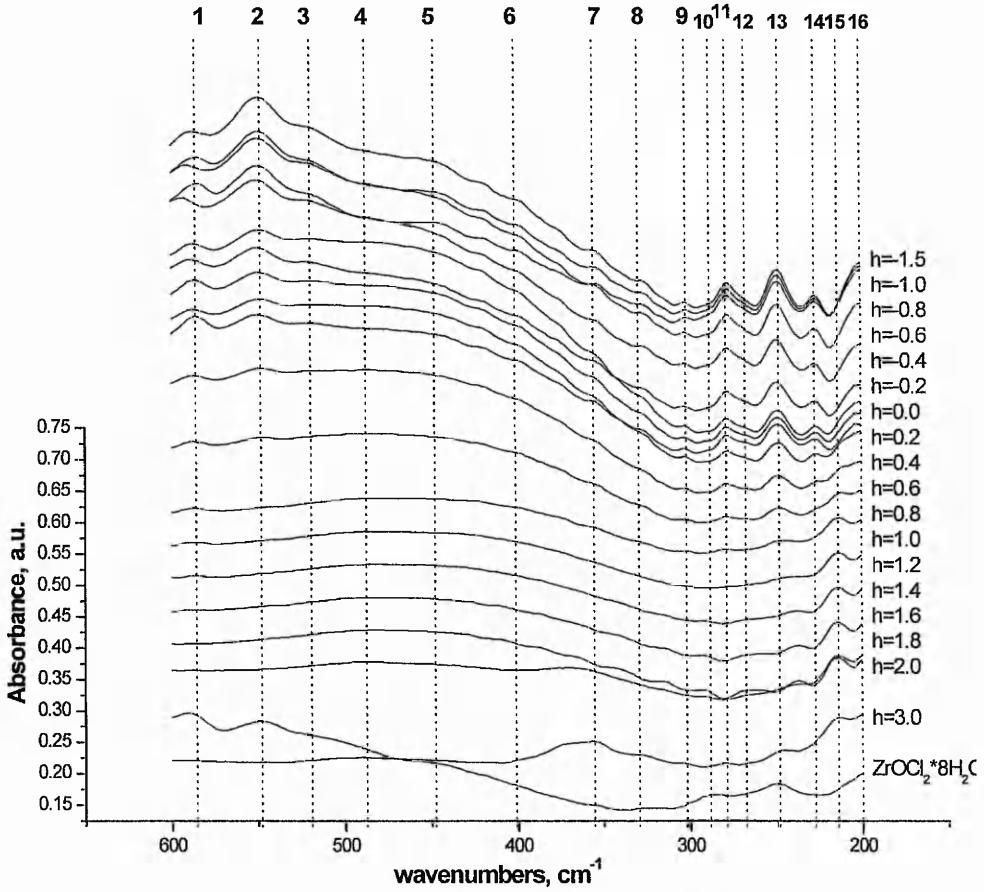


Fig. 5.51. Far-IR spectra of the solid samples of the series **ZrOH** (the spectrum of the initial crystalline precursor $ZrOCl_2*8H_2O$ is given for comparison). Y-offset – 100 %.

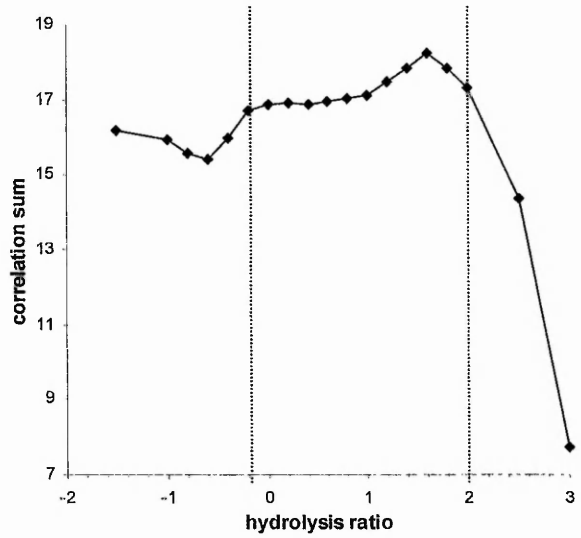


Fig. 5.52. The correlation sum graph in the hydrolysis ratio domain calculated on the basis of the mid-IR spectra of the series **ZrOH**.

bound to Zr-atoms. These bands gradually decrease in intensity with increase of hydrolysis ratio, practically disappearing around h=2.0. The distribution of intensities of these bands also changes with increase of h. The bands at 440 and 410 cm^{-1} are more important at lower hydrolysis ratios (h=1.6), while at higher values of h, the band at ca. 490 cm^{-1} becomes the

dominant band for the aquo ligands in the far-IR region. This is in a good agreement with the decreasing number, structural arrangement and acidity of aquo ligands in the coordination sphere of the hydrolysed Zr-ions, the latter being shown using Partial charge model calculations in Chapter 4.

The bands at 288-285, 278-277, 249-242 and 232-228 cm^{-1} are assigned to the structural vibrations of Zr-O bonds of the hydrolytic Zr polymers as discussed above for the series **ZrHCO3**. Comparison with the far-IR spectrum of the initial precursor to Zr polymers – zirconyl chloride one can find that in the region 300-200 cm^{-1} this tetragonal crystalline salt exhibits only two broad bands (at ca. 278 and 250 cm^{-1}). One can assume that upon transformation of the more ordered tetragonal phase into monoclinic structures, these bands of zirconyl chloride degenerate into four bands which are observed in a wide range of hydrolysis ratios ($-1.5 \leq h \leq 1.6$). Such degeneration has been shown theoretically by Mirgorodsky et. al [55] using Raman spectra of tetragonal and monoclinic zirconia. At hydrolysis ratios above $h=1.6$ the positions and the number of the bands in the region 300-200 cm^{-1} change again (279 and 247 cm^{-1}), which is closer to those expected for the tetragonal structure of Zr hydrous oxide. Here again, a good agreement with the PXRD data discussed in Section 5.4.1.1 was observed. There is one more distinct band in the region at ca. 214 cm^{-1} which is most intense in the hydrolysis ratio range $h \geq 0.0$. The distribution of intensities of this band reaches a maximum at $h \sim 2.0$. On the basis of the position and the intensity distribution, it is believed that the band at 214 cm^{-1} could be attributed to the structural vibrations of amorphous zirconia and could serve as a good indicator of the presence of this phase in the solid samples of Zr-containing materials.

Concluding the discussion of the spectra in the far- and mid-IR region obtained from **ZrOH** samples after 48 hours of hydrolysis at 90°C it is necessary to add that IR-spectra were acquired for the solid samples of the same series produced at other sampling times (e.g. 3, 12 and 24 hours). The results of the IR-analysis of these samples are not shown in this work for the sake of brevity. Due to intrinsic difficulties with quantification of the IR-spectra, kinetic curves have not been constructed on the basis of these spectra. However, two time-dependent features revealed by comparison of the otherwise similar spectra for the different time series must be emphasised here. First is that the peaks of the deformation vibrations of hydroxyl-ligands observed at ca. 1030, 957 and 914 cm^{-1} (δ(ZrO-H)) and in the region 300-200 cm^{-1} (ν(Zr-O)) are generally more intense at earlier times of the experiment **ZrOH**. This fact supports the idea that in the course of the high-temperature hydrolysis reaction the transformation of the (bi)-bridged Zr-OH-Zr into oxo-bridges (oxolation reaction) takes place. The transformation becomes more complete at higher pH and hydrolysis ratios. The second feature of all of the time-dependent series **ZrOH** is the presence of major bands at ca. 1428 and 1489 cm^{-1} in the alkaline ($h=2.0$) samples assigned above to the polydentate complexes of Zr-ions with carbonate. The intensity of the bands generally increases with hydrolysis ratio and the time of experiment. The bands of bidentate Zr-carbonate complexes are of minor

importance in the spectra of samples synthesised after 3 and 12 hours of hydrolysis. This result indicates that the source of Zr-carbonate species dominating the IR-spectra of the alkaline samples of the series **ZrOH** is dissolution of atmospheric carbon dioxide in aqueous medium at high pH. High temperature and vigorous agitation of the sample solutions does not prevent this process. One can assume that the structure of Zr oxide at alkaline conditions is still closer to tetragonal as supported by the XRD data reported above.

5.6.6. Mid-infrared spectra of the series ZrOHSO4

Infrared spectroscopy has proved to be a useful tool in the elucidation of the structure of the metal-ion complexes with anions, especially in the mid-infrared range [35]. The mid-IR spectra of the series **ZrOHSO4** were acquired. In this series Zr-ions were hydrolysed with strong alkali (KOH) in the presence of equimolar quantities of sulphate-ions. The results are shown in Fig. 5.53. On the basis of the raw mid-IR spectra given in Fig. 5.53, the correlation sum graph in the hydrolysis ratio domain was calculated (Fig. 5.53)

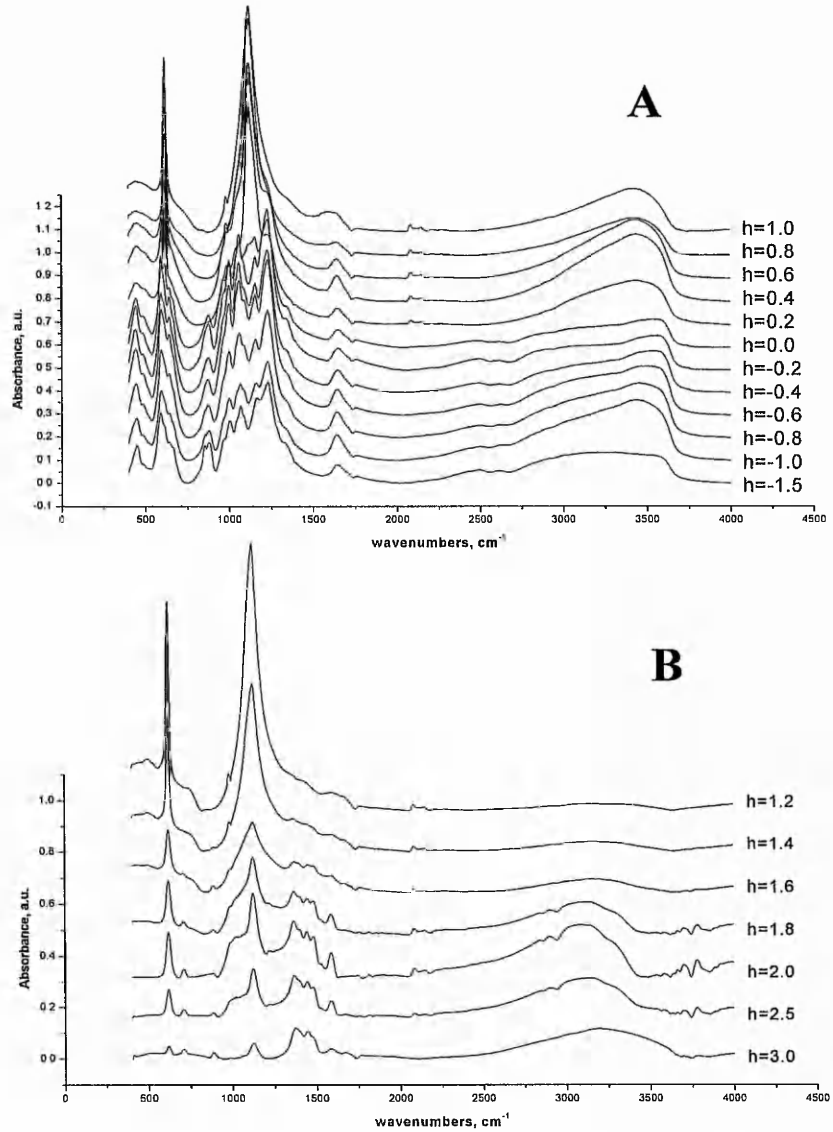


Fig. 5.53. Mid-IR spectra of the solid samples of the series **ZrOHSO4**. ***A*** – samples in the range $-1.5 \leq h \leq 1.0$; ***B*** - $1.2 \leq h \leq 3.0$. Y-offset – 80 %.

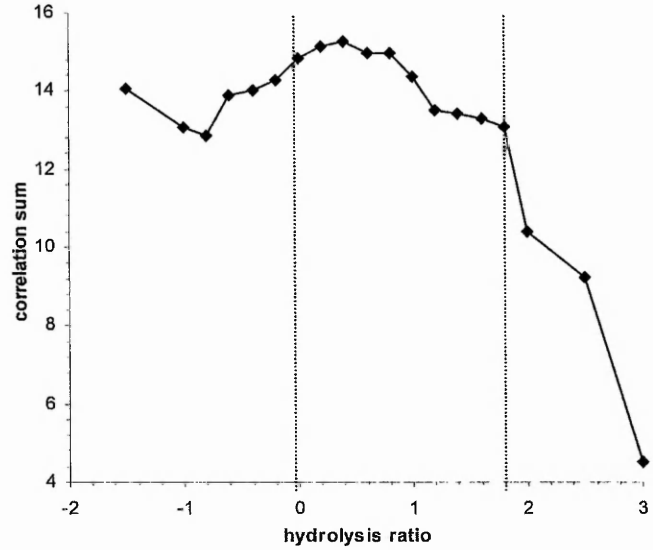


Fig. 5.54. The correlation sum graph in the hydrolysis ratio domain calculated from the mid-IR spectra of the series **ZrOHSO4**.

Three distinct groups of samples can be identified in the dynamic mid-IR patterns of the series **ZrOHSO4** (Fig. 5.53, 5.54): a group with the hydrolysis ratio range $-1.5 \leq h \leq 0.0$, a second group at $0.2 \leq h \leq 1.6$ and a third group at $1.8 \leq h \leq 3.0$. These groups are characterised by the distinct spectral features and exhibit different correlation patterns according to Fig. 5.54.

All acquired mid-IR spectra of the series **ZrOHSO4** are characterised by diminished bands in the region 3600-3000, 2900-2500, 1600-1700 and 500-400 cm^{-1} arising from the coordinatively bound water of Zr species (Fig. 5.53). These ligands are practically absent in the IR-spectra at h=1.2-1.6. Therefore, sulphate-ions force the lattice water out of the coordination sphere of Zr-atoms. The band positions of the OH-stretching vibration of aquo ligands also change significantly in the presence of sulphate-ions. The major stretching vibrations of these moieties occur at 3550-3476 cm^{-1} (Fig. 5.53) in the range of hydrolysis ratios $-1.5 \leq h \leq 0.0$. For the second group of samples of the series **ZrOHSO4** ($0.2 \leq h \leq 1.6$) the position of this band varies from 3445 to 3400 cm^{-1} and is dependent on the value of h. Other intense bands in the higher-frequency range are at 3220-3160 cm^{-1} and 2920-2910 cm^{-1}. These bands probably arise from different types of water in Zr polymers. The band relating to bending HOH vibrations of aquo ligands also changes its intensity and position from ca. 1646 to 1610 cm^{-1} depending on hydrolysis ratio. The bands arising from aquo ligands regain their intensity to some extent at h=1.2 and continue to increase with increasing hydrolysis ratio (maximum intensity at high hydrolysis ratios is observed at h=2.0).

The most important IR-region where the bands related to Zr complexes with sulphate-ions occur is at $1800 \leq \nu \leq 400$ cm^{-1} [35]. This region was examined in detail using 2D-correlation analysis. The results are shown as colour-coded synchronous and asynchronous 2D-contour maps in Fig. 5.55.

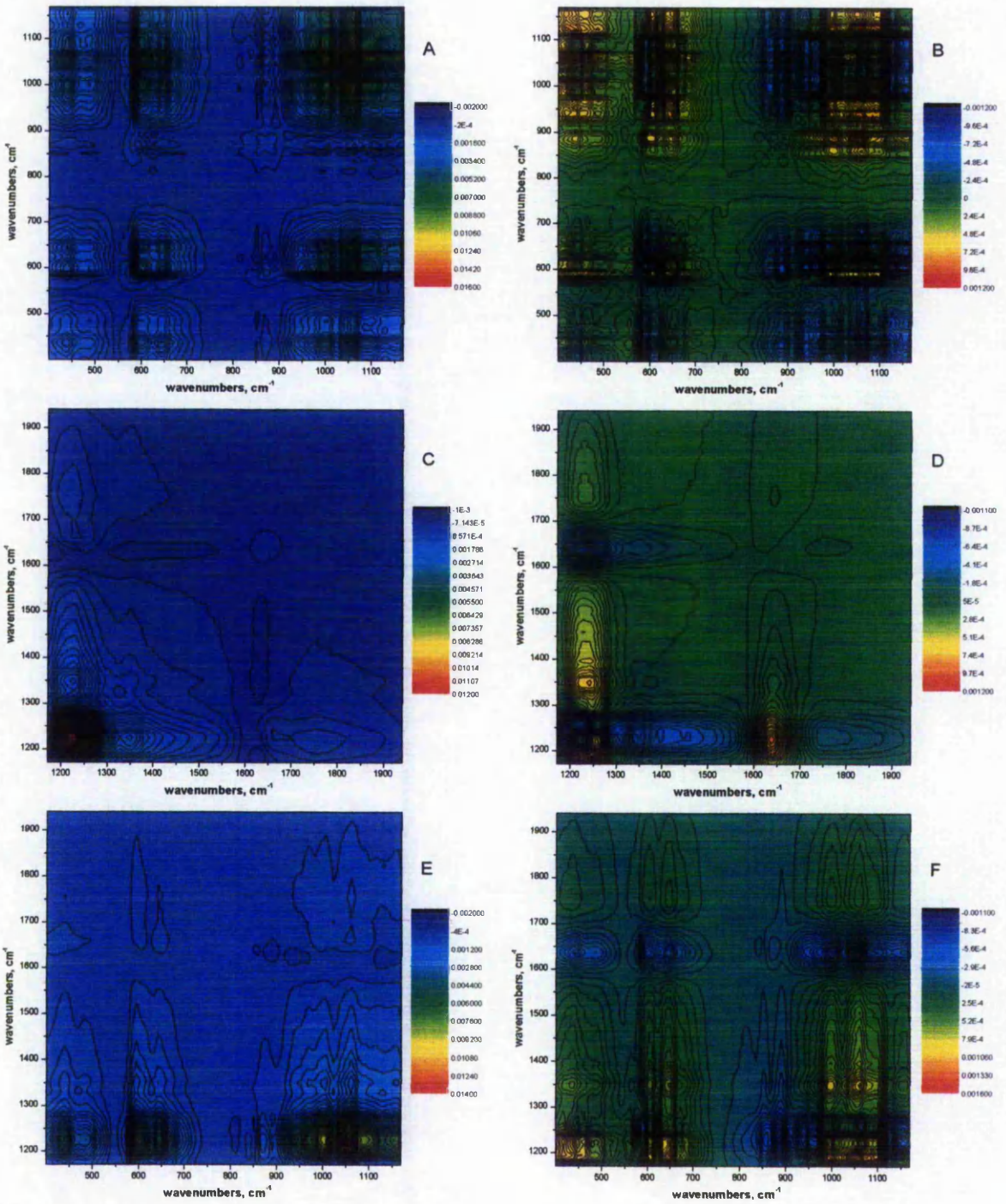
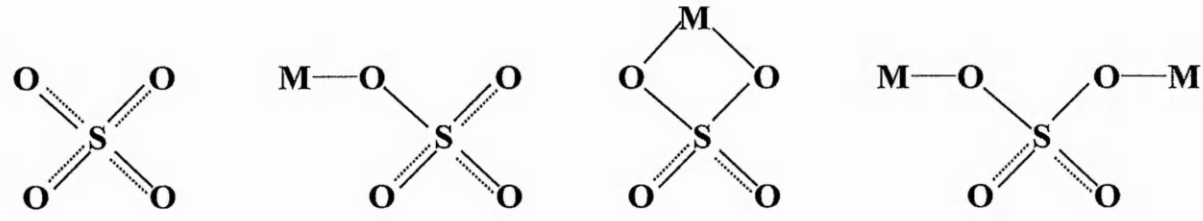


Fig. 5.55. 2D-correlation spectral maps calculated on the basis of the mid-IR spectra of the group 1 samples, series **ZrOHSO4** ($-1.5 \leq h \leq 0.0$) in the IR-region 1940-400 cm^{-1}. ***A***, ***B*** – diagonal synchronous and asynchronous patterns, 1170-400 cm^{-1}; ***C***, ***D*** – diagonal synchronous and asynchronous patterns, 1940-1170 cm^{-1}; ***E***, ***F*** – non-diagonal synchronous and asynchronous patterns 1170-400 cm^{-1} versus 1940-1170 cm^{-1}.

It is well known [35] that free sulphate ion belongs to the high-symmetry point group T_d. Of the four fundamental vibrations, only ν_3 and ν_4 are infrared-active. If the symmetry of the ion is lowered by complex formation, the degenerate vibrations split and Raman-active modes appear in the spectrum. The lowering of symmetry caused by coordination is different for the unidentate and bidentate complexes, as shown below [35]:



Free ion (T_d) | **Unidentate complex (C_{3v})** | **Bidentate complex (C_{2v})** | **Bridged bidentate complex (C_{2v})**

The relative intensity, positions and the number of (degenerate) IR-bands can help to identify a particular complex structure [35].

From the data of 2D-COS analysis of the group 1 samples of the series **ZrOHSO4** (Fig. 5.55) it follows that at least two types of complex are present in Zr-sulphate solutions at very high acidity ($h \leq 0.0$). The first is a chelating bidentate complex with the following fundamental sulphate bands: ν_1 = 1000 cm^{-1}; ν_2 = 438 cm^{-1}; ν_3=1227, 1156, 1061 cm^{-1}; ν_4 = 681, 595 cm^{-1}. The listed bands are highly correlated with each other (Fig. 5.55*A, C, E*) and exhibit strong out-of-phase peaks in the asynchronous spectra (Fig. 5.55*B, D, F*). Another complex is of the bridged bidentate structure with the following bands: ν_1=994-990 cm^{-1}; ν_2=460 cm^{-1}; ν_3=1191, 1066, 960 cm^{-1}; ν_4=643 cm^{-1}. The latter complex contains peaks which are either anti-correlated or non-correlated with the bands of the chelating bidentate Zr-sulphate complex. Therefore, the trends of pH-distribution of these two complexes are different, if not opposite. Analysis of the raw spectra (Fig. 5.53) indicates that the fundamental bands of the bridged bidentate complex tend to decrease with increase of *h*, starting from $h \sim -1.0$, while the fraction of the chelating complex constantly increases from the sample produced at h=-1.5 to the one produced at h=0.0. Hence, one can assume that with increase of *h* the chelating Zr-sulphate complex gradually replaces the bridged one.

There are several other intense bands observed as shoulders in the mid-IR spectra of the series **ZrOHSO4** in the range 1940-400 cm^{-1}. For instance, two bands are observed at 1429 and 1350 cm^{-1}. These bands could be related either to the Zr complex with carbonate-ions, or to another (e.g. polydentate) complex of sulphate-ions with Zr-atoms. However, extensive literature on the subject does not indicate any of such complexes [21, 35]. The doublet of intense and sharp stand-alone bands at 887 and 861 cm^{-1} is not related to any of the bidentate Zr-sulphate complexes, or aquo ligands of Zr polymers. One can assume that these peaks together with a weak band at 940 cm^{-1} can be assigned to δ(Zr-OH) vibrations of hydroxo-groups of Zr species. The fact that the bands at 887 and 861 cm^{-1} are so intense and sharp indicates that only one type of hydroxyl-ligand remains in Zr polymers in the presence of sulphate-ions at very low hydrolysis ratios. The band position also differs significantly from the analogous bands in the spectra of the series **ZrHCO3** and **ZrOH** (1030-915 cm^{-1}). Therefore, structural arrangement and acidity of hydroxyl-ligands are strongly affected by the coordinated sulphate-ions. The weak band at 484 cm^{-1} is probably the only band arising from

the librational modes of lattice water. The peak of bending vibrations of aquo ligands is located at 1646 cm^{-1} and is a distinct sharp band. The absence of physically absorbed water shows the higher hydrophobicity of **ZrOHSO4** samples compared with the samples from the series **ZrOH** and **ZrHCO3**.

Analysing the IR-spectra of the **group 2** samples of the series **ZrOHSO4** ($0.2 \leq h \leq 1.6$) one can see that even tiny additions of alkali cause dramatic changes in the spectral patterns (Fig. 5.53). The major bands of these spectra are at ca. 1120-1115 cm^{-1}($\nu_3(SO_4)$), 978 cm^{-1} (ν_1) and 616-613 cm^{-1} (ν_4). These bands most probably arise from a unidentate Zr-sulphate complex [35]. The bands of the chelating bidentate Zr-sulphate complex at 1228, 1161, 1061-1155 cm^{-1} (ν_3); 1003-995 cm^{-1} (ν_1); 664, 597 cm^{-1} (ν_4) and 440-436 cm^{-1} (ν_2) gradually decrease their intensity with increase of hydrolysis ratio and become almost negligible at h~1.0. The bands related to aquo ligands of Zr polymers (3440-3300; 2950-2500; 1646; 484 and 420 cm^{-1}) also continue to drop in intensity. The bands presumably arising from the deformation vibrations of hydroxyl-ligands (890-860 cm^{-1}) practically disappear from the spectra above h=0.0. On the basis of this spectral information one can conclude that additions of alkali (h=0.0) force sulphate complexed with Zr to transform from chelating bidentate into unidentate form. Hydrolytic condensation inside the precipitates of hydrous zirconia formed upon this transformation, if such process takes place, goes via oxolation reaction (no hydroxyl-bridges are observed in the resulting precipitates). One can say that coordinatively bound unidentate sulphate-ions "catalyse" oxolation process and direct formation of the final hydrous zirconia. Gardener [55] observed a similar effect, when aqueous Zn salts have been transformed directly into ZnO in the presence of sulphate-ions.

Combining the results of the PXRD characterisation of the group 2 samples ($0.2 \leq h \leq 1.6$) and the abovementioned data of infrared spectroscopy, one can conclude that in the specified range of hydrolysis ratios a single basic zirconium sulphate phase dominates after prolonged hydrolysis at high temperature, which is in fact zirconium sulphate oxide with unidentate sulphate ligands and oxo-bridges connecting Zr atoms in the solid material. The type of crystalline structure of this material is yet to be identified, however for the basic salt with a $Zr:SO_4$ ratio 1:1 of empirical formula $Zr(OH_2)SO_4H_2O$ (zirconium hydroxide sulphate hydrate, JCPDS card No 70-1537) with the monoclinic structure is known. The reference XRD reflections of this phase (19.3, 25.5; 29.9 and 31.6 °2θ) are quite close to the reflections observed in the PXRD patterns of **ZrOHSO4** samples in the range $0.0 \leq h \leq 1.6$ (Table 5.2).

The unidentate form of sulphate ligands persists in the solid samples of the series **ZrOHSO4** up to h~3.0, albeit becoming of lesser importance at h=2.0. It is presumed that at higher pH and hydrolysis ratios the sulphate-ligand is gradually eliminated from the coordination sphere of Zr-ions. The resulting Zr oxide phase is probably of monoclinic structure (Section 5.4.1.3) that would agree well with literature data [56] indicating transformation of Zr basic sulphates into monoclinic zirconia upon prolonged heating or hot

water annealing.

Group 3 samples of the series **ZrOHSO4** produced at $h \geq 1.8$ exhibit vibrations related to Zr-carbonate complexes in the corresponding mid-IR spectra, The bands at 1578 and 1394 cm^{-1} are related to bidentate carbonato-complexes (Δ=184 cm^{-1}) and the bands at 1490, 1429 cm^{-1} (Δ=61 cm^{-1}) are most probably related to polydentate Zr-carbonate complexes on the surface of hydrous zirconia. These complexes are formed upon dissolution of atmospheric carbon dioxide in alkaline solutions. The presence of these complexes indirectly supports the monoclinic structure of hydrous zirconia in the given conditions [46]. The bands of unidentate sulphato-complexes decrease in importance with increase of hydrolysis ratio (Fig. 5.53), while the fraction of carbonato-complexes increases. It is not clear whether carbonate-ligands participate in the replacement of sulphate-ions from the coordination sphere of Zr atoms, although it is clear that in alkaline conditions carbonate-ions have an advantage over sulphate-ions due to (*a*) better solubility of carbon dioxide at high pH; (*b*) limitations of sulphate-ion complexation with Zr-ions at pH=10 calculated using the Partial charge model (Chapter 1).

Elimination of sulphate-ions from the solid precipitates at high hydrolysis ratios (h=2.0) also gives way for complexation of aquo ligands and hydroxo-ligands with the surface of hydrous zirconia. This is supported by the increased intensity of the stretching vibration band of aquo ligands in the region 3400-3200 cm^{-1} and water bending vibrations at 1640 cm^{-1} (Fig. 5.53). The presence of terminal and possibly tri-bridged hydroxyl-ligands on the surface of hydrous Zr oxide (which are favoured in the case of monoclinic zirconia [46, 47]) can be clearly seen from the distinct bands at 3778-3770 and 3700-3690 cm^{-1} in the spectra of **ZrOHSO4** samples obtained at h=2.0.

5.6.7. Far-infrared spectra of the solid samples of the series ZrOHSO4

Along with the mid-IR spectra of the series **ZrOHSO4** discussed above, far-IR spectra of the same solid samples were recorded in the region 700-100 cm^{-1} (Fig. 5.56). The acquired spectra can be roughly divided into two main groups – in the hydrolysis ratio range – $1.5 \leq h \leq 0.0$ and at h=0.0. The correlation sum graph depicted in Fig. 5.57 shows that this division is conditional and three hydrolysis ratio domains can be devised on the basis of the correlations between the spectral patterns: at $-1.5 \leq h \leq 0.0$ the spectra show strong similarity (close values of the correlation sums in Fig. 5.57). The spectra in the range $0.2 \leq h \leq 1.6$ show decreasing values of the correlation parameter (the local maximum at $h \sim 1.2$ can be observed on the correlation sum graph). At higher hydrolysis ratios, the far-IR spectra possess another unique shape, well indicated in Fig. 5.57.

The raw far-IR spectra of the series **ZrOHSO4** have been examined in detail using 2D-correlation analysis and 4th derivative spectra. The major bands in the range 600-330 cm^{-1} identified using these techniques belong to the fundamental vibrations of Zr-sulphate complexes (as discussed in the previous section) and to the vibrations relating to librational

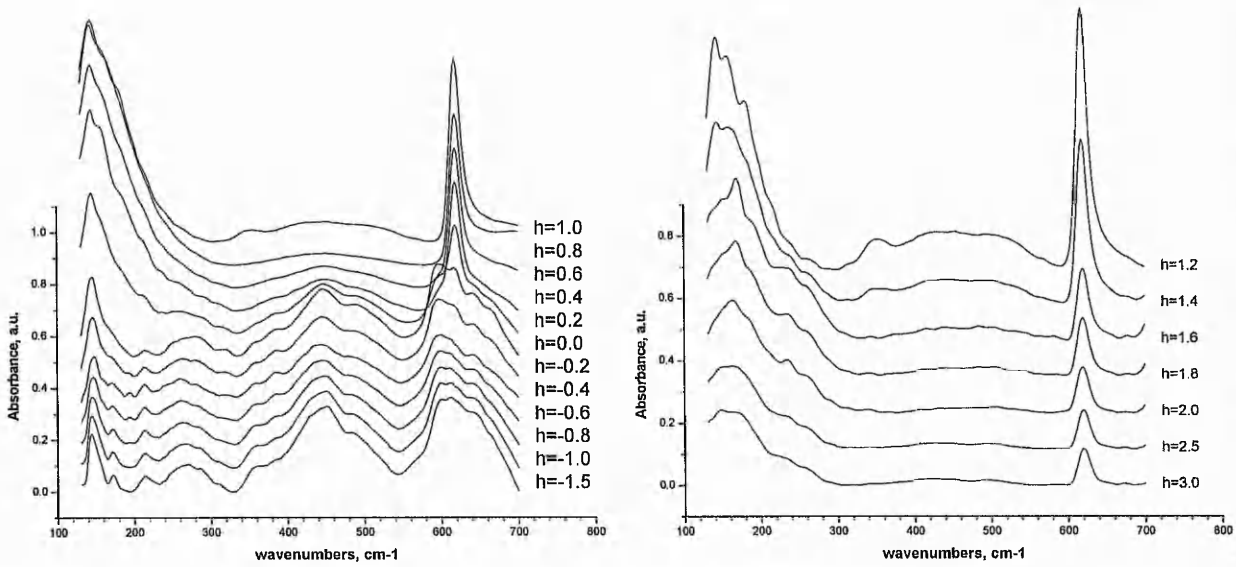


Fig. 5.56. Far-IR spectra of the solid samples of the series **ZrOHSO4**. Y-offset – 80 %.

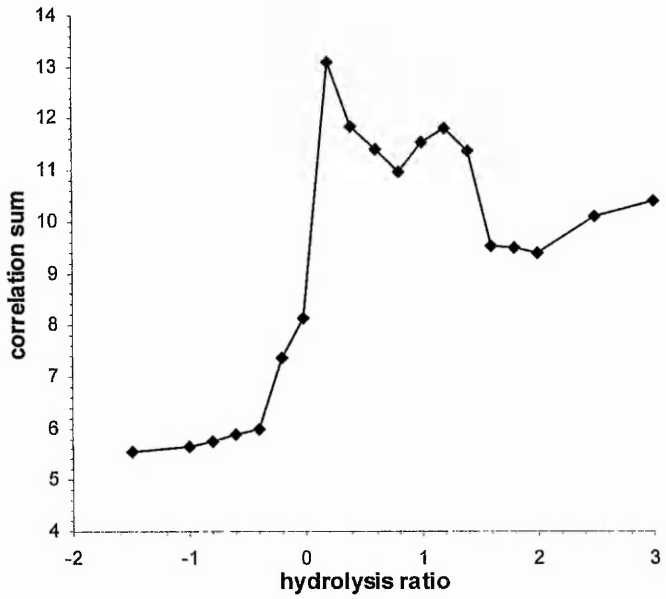


Fig. 5.57. The correlation sum graph in the hydrolysis ratio domain calculated from the data of the far-IR spectra of the series **ZrOHSO4**.

and transitional modes of aquo ligands. In addition to the bands in the region 600-400 cm^{-1}, the majority of which have been assigned in the mid-IR spectra above, there are two other bands of aquo ligand deformations – at 397, 380 and 353 cm^{-1} that can be observed at low hydrolysis ratios (h=0.2) which also belong to the librational modes of aquo ligands.

In the lower-frequency region there is a set of distinct and highly correlated bands at 311, 289, 269, 247 and 213 cm^{-1}. In the discussion of the far-IR spectra of the series **ZrOH** and **ZrHCO3** it was pointed out that these vibrational bands can belong to the structural Zr-O bonds of Zr polymers and solid phases. These bands for the series **ZrOHSO4** are the most intense at h=0.2 and are closer to the bands expected for the monoclinic zirconia phase

observed in very acidic solutions of pure zirconyl chloride (series **ZrHCO3** and **ZrOH**). Above h=0.2 these bands, apart from the peak at 213 cm^{-1}, gradually loose their intensity and become less distinct. Therefore, these bands primarily arise from Zr-O bonds of the hydroxo-complexes of Zr polymers. With increase of hydrolysis ratio the extent of hydroxylation in the samples of the series **ZrOHSO4** gradually diminishes and completely disappears at h~1.2, as shown by the mid-IR spectra above.

In the spectral region 200-130 cm^{-1} a set of bands at 201-198, 182, 161 and 143 cm^{-1} is observed. These bands reflect the structural Zr-O-Zr vibrations in Zr polymers and solid phases. Their intensity is relatively low at h=0.2. At higher hydrolysis ratios it starts to increase and reaches a maximum at h~1.0-1.2. Above this point the relative intensities of the bands constituting the set at 200-130 cm^{-1} starts to vary. At h=1.2 the band at 143 cm^{-1} is the most intense (similar to the series **ZrOH** and **ZrHCO3**). Above h=1.2 bands at 161 and 182 cm^{-1} become more distinct and intense. This change probably reflects electronic and structural fluctuations in Zr basic sulphates relating to densification of the solid phase and its complete separation from solution at h=1.0-1.2 as has been found in the pH-titration curves of the series **ZrOHSO4** (Chapter 4). In the pH-metric data a sharp inflexion has been observed at this point indicating an important point of precipitation.

Two more bands were detected in the far-IR bands in the very low frequency region – at 114 and 106 cm^{-1}. The former band was too intense to be shown in the far-IR spectra of the series **ZrOHSO4** (Fig. 5.56).

5.6.8. Mid-infrared spectra of the solid samples of ZrOHAc series

Another series of experiments where Zr-ions have been hydrolysed at high temperature in the presence of foreign species is the series **ZrOHAc** conducted using Zr:acetate 1:1 solution ratio (Section 2.4.3). The mid-IR spectra of metal-acetate complexes provide wealth of information concerning the structural arrangements of acetate ions [35]. The spectra of the series **ZrOHAc** are shown in Fig. 5.58.

As usual, the correlation sum graph was calculated for the mid-IR spectra of the series **ZrOHAc** (Fig. 5.59) in order to establish the degree of similarity between spectra obtained from solid samples in the range of hydrolysis ratios (-1.5≤h≤4). Fig. 5.59 shows that the mid-IR spectra of the series can be approximately divided into three groups at -1.5≤h≤0.6; 0.8≤h≤1.8 and 2.0≤h≤4.0 according to distinct spectral shapes in these regions.

The higher-frequency part of the spectra from the **ZrOHAc** series contains only one set of unresolved bands in the region 3600-2500 cm^{-1} related to the stretching vibrations of OH-groups of lattice water and hydroxyl-ligands of Zr polymers. There is also a set of bands attributable to ν(CH) vibrations of the methyl group of acetate-ions located at ca. 2988, 21931, 2838 and probably 2771 cm^{-1}.

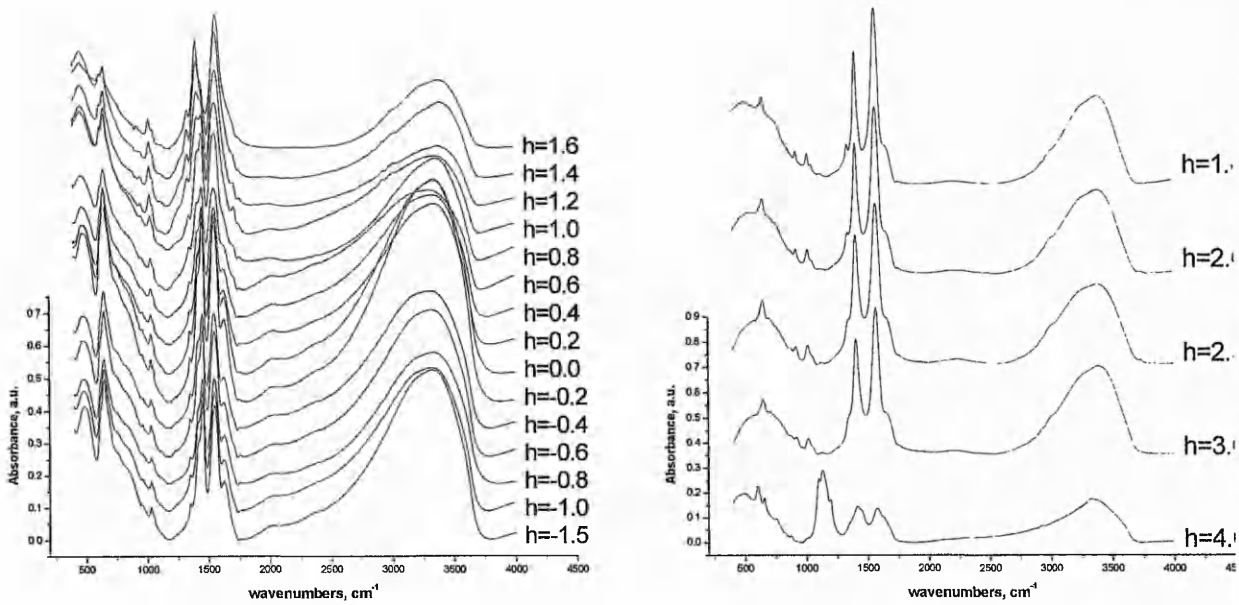


Fig. 5.58. Mid-IR spectra of the solid samples from the series **ZrOHAc**. Y-offset = 80 %.

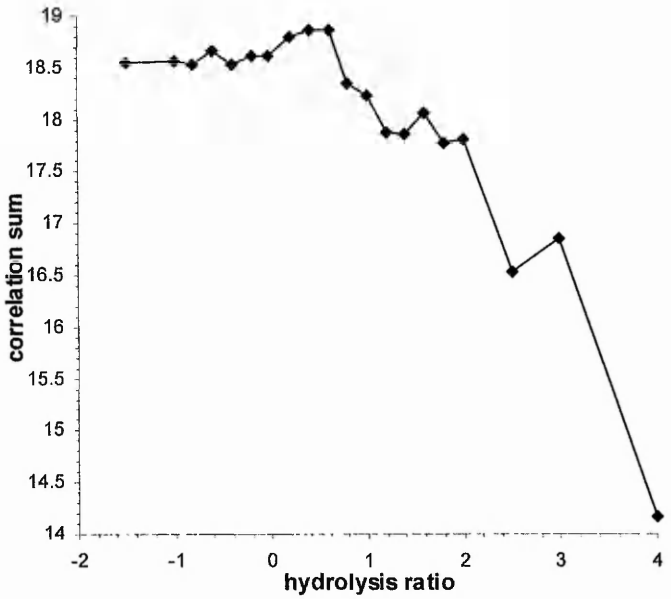


Fig. 5.59. The correlation sum graph in the hydrolysis ratio domain calculated from the data of the mid-IR spectra of the series **ZrOHAc**.

The lower-frequency range at 1900-400 cm^{-1} in the mid-IR spectra of the series **ZrOHAc** is most important for elucidation of interactions of acetate-ions and Zr polymers. An in-depth analysis of this region has been performed using the 2D-correlation method. The results are given in Fig. 5.60 as colour-coded spectral contour maps.

The 2D-COS data presented in Fig. 5.60*A*, *B* and derivatisation (4^{th} derivative) of the mid-IR spectra of the acidic samples ($(-1.5 \leq h \leq 0.8)$ of the series **ZrOHAc** indicate that in the lower-wavenumber part of the spectrum (1170-400 cm^{-1}) the band at ca. 435 cm^{-1} is assigned

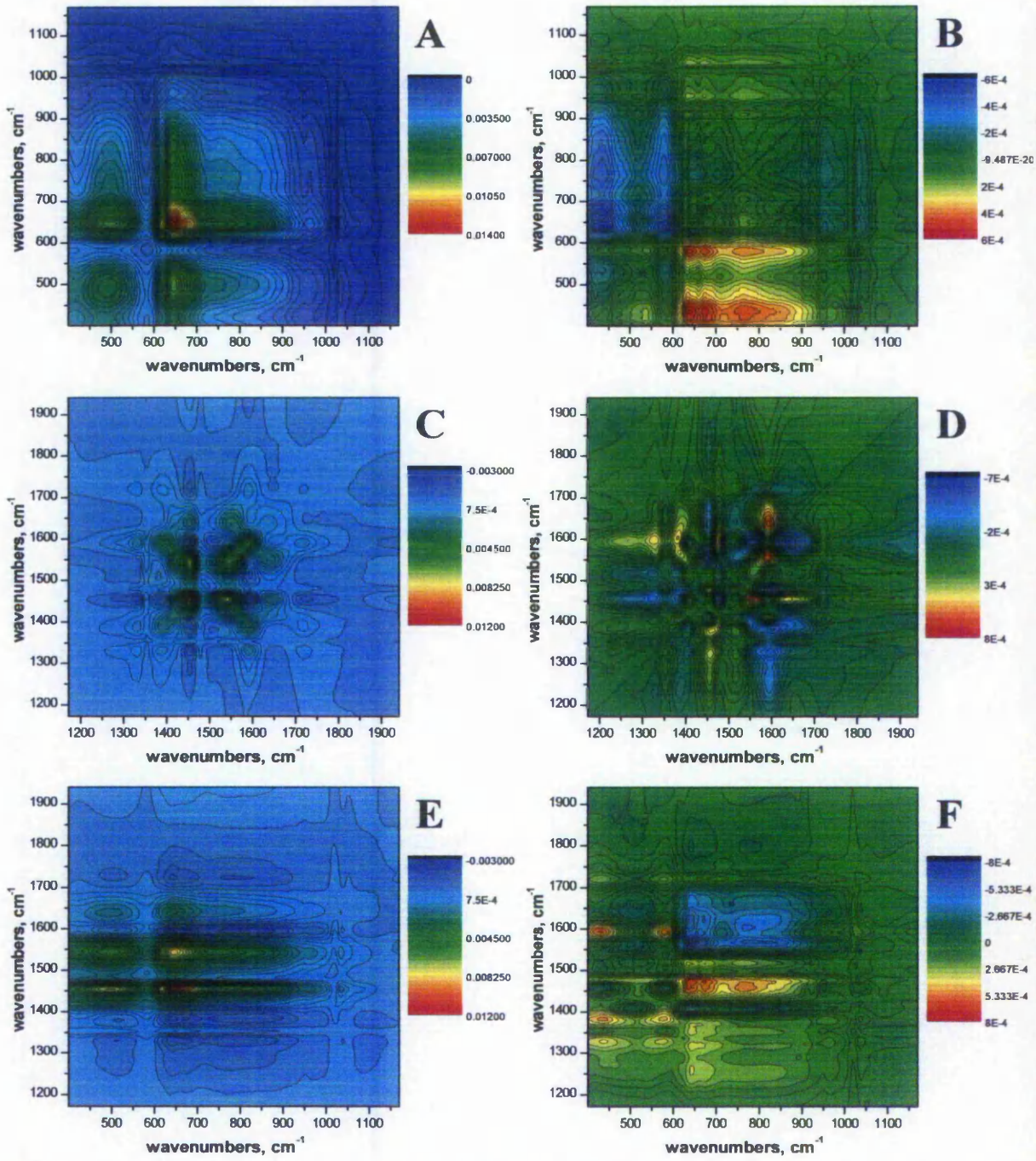
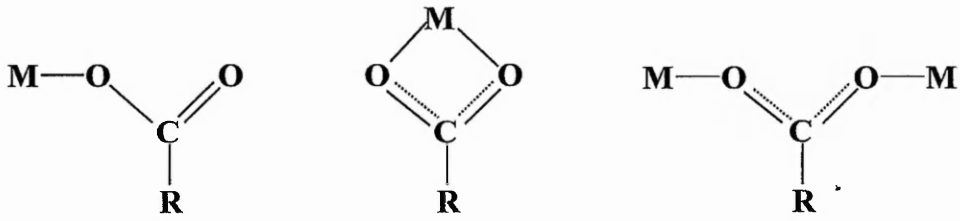


Fig. 5.60. 2D-correlation spectral maps calculated on the basis of the mid-IR spectra of the group 1 samples, series **ZrOHAc** ($-1.5 \leq h \leq 0.8$) in the IR-region 1940-400 cm^{-1}. ***A***, ***B*** – diagonal synchronous and asynchronous patterns, 1170-400 cm^{-1}; ***C***, ***D*** – diagonal synchronous and asynchronous patterns, 1940-1170 cm^{-1}; ***E***, ***F*** – non-diagonal synchronous and asynchronous patterns 1170-400 cm^{-1} versus 1940-1170 cm^{-1}.

to librational modes of lattice water. The band at 457 cm^{-1} can belong to δ(CH) or ρ_r(COO) vibrations [35] or to librational modes of water. The high intensity of this band favours the second assignment. The band at ca. 503 cm^{-1} appears as a shoulder of the band at 547 cm^{-1} and is clearly seen in Fig. 5.60*A*. This band as well as the weak peak at 530-520 cm^{-1} is most probably attributable to the ν(ZrOH) stretchings observed at >500 cm^{-1} [51].

The intense and sharp bands at 650 and 621 cm^{-1} are assigned to δ(OCO) and π(COO) vibrations in the spectra of the acidic samples of the series **ZrOHAc** [35]. These bands exhibit highly correlated behaviour (Fig. 5.60*A*). There is also a band at ca. 688 cm^{-1} (a shoulder of the band at 650 cm^{-1}) and a set of weak bands at 888, 840 and 769 cm^{-1} correlated with the band at 650 cm^{-1} (Fig. 5.60). The bands at 1052, 1023 and 920 cm^{-1} can be attributed to $\rho_r(CH_3)$ and ν(CC) vibrations [35]. The origin of the band at 951 cm^{-1} is quite unclear, since it is not observed in the spectra of acetate-ions [35]. This band can probably belong to the δ(ZrOH) vibrations of hydroxyl-ligands in Zr polymers. A weak broad band at ca. 1116 cm^{-1} is unassigned. All the described bands above ca. 900 cm^{-1} are not correlated with the bands of deformational and rotational vibrations in the region 600-900 cm^{-1} (Fig. 5.60*A*). In fact, as the asynchronous spectrum shows (Fig. 5.60*B*), the bands at >900 cm^{-1} are 'out-of phase' with the highly correlated bands in the region 600-900 cm^{-1}.

Generally, carboxylate-ions may coordinate to metal ions in the following modes [35]:



Unidentate complex | **Chelating bidentate complex** | **Bridged bidentate complex**

Careful examination of IR spectra of many acetates have led to the following conclusions:

1. Unidentate complexes exhibit the Δ values (Δ = $\nu(COO)_a$ - $\nu(COO)_s$ where $\nu(COO)_a$ and $\nu(COO)_s$ are antisymmetric and symmetric stretchings of the carboxyl group correspondingly) which are much greater than the ionic complexes;
2. Chelating (bidentate) complexes exhibit Δ values which are significantly less than the ionic Δ.
3. The Δ values for bridging (bidentate) complexes are greater than those of chelating ones, and close to ionic values ($\nu(COO)_a$=1578 cm^{-1}, $\nu(COO)_b$=1414 cm^{-1}; Δ=164 cm^{-1} for free acetate ion).

Summarising these empirical rules one may write:

$$\Delta(\text{chelating}) < \Delta(\text{bridging}) \sim \Delta(\text{free Ac}) << \Delta(\text{unidentate}) \qquad \textbf{(5.6)}$$

In the range of wavenumbers 1940-1170 cm^{-1} (Fig. 5.60*C*, *D*) several intense acetate-derived bands are observed. The analysis of correlation behaviour clearly presented by the sharp and symmetric synchronous 2D-pattern of Fig. 5.60*C* allows for easy classification of these bands. The strong and sharp peaks at 1547 ($\nu(COO)_a$) and 1453 cm^{-1} ($\nu(COO)_b$) are

very strongly correlated and dominate the region 1940-1170 cm^{-1} in the spectra of acidic samples from the series **ZrOHAc**. Another pair of COO-stretchings is located at 1591 and 1393 cm^{-1}. The distance between the COO-stretchings Δ=94 cm^{-1} and the position of the $\nu(COO)_a$ vibration (1547 cm^{-1}) enable us to assign the first complex to a chelating bidentate Zr-acetate complex. The second complex with Δ=198 cm^{-1} can be attributed to a bridged complex. The chelating Zr-acetate complex is anti-correlated to bending water vibrations at ca. 1636 cm^{-1} as clearly indicated in Fig. 5.60*C*. It is also anti-correlated with the bridging bidentate complex (these complexes are superimposed on the hydrolysis ratio scale).

The intensity distribution of the fundamental bands of the two Zr-acetate complexes in the mid-IR patterns of the acidic samples (series **ZrOHAc**) can be traced from the raw spectra (Fig. 5.58). At low hydrolysis ratios (h=-1.0) the bidentate chelating Zr-acetate complex significantly prevails over the bridged complex. However, with increase of hydrolysis ratio from h=-1.5 to ca. h=0.8 (this trend is followed by a slow increase of the correlation sum in Fig. 5.59), the intensity of the bands at ca. 1547 and 1453 cm^{-1} relating to the acetate chelate diminishes, while the bands from the bridging complex steadily increase. At h=1.0 the bridging bidentate complex of acetate ions with zirconium is predominant (Fig. 5.58). There is no evidence for the presence of free acetate-ions in Zr ion solutions in the range of hydrolysis ratios $-1.5 \leq h \leq 1.0$ (ν(COO) bands at 1578 and 1414 cm^{-1}) which proves that all acetate-ions are complexed with zirconium.

In very acidic conditions (h<0.0) a relatively weak bands at 1713 and 1284 cm-1 arise from minor quantities of unidentate Zr-acetate complex. These bands disappear from the mid-IR spectra at h~0.4-0.6.

Above h=1.0, the concentration of both bidentate Zr-acetate complexes begin to decrease rapidly with the growth of h. (Fig 5.58). The bands of free acetate ($\nu(COO)_a$=1578 cm^{-1}, $\nu(COO)_b$=1414 cm^{-1}) start to dominate the spectra. Therefore, at these conditions Zr-acetate complexes are being replaced by the hydroxyl-ion of alkali.

At hydrolysis ratio h=4.0, new extremely intense and sharp bands occur in the IR-spectra of the series **ZrOHAc** at 1193, 1132, 1102, 1061 and 602 cm^{-1} (Fig. 5.58). The bands at 3383, 3322, 874, 828, 750 and cm^{-1} become sharper. Perhaps most of these bands arise from a complex of carbonate-ions with Zr-ions usually observed in alkaline conditions. The presence of free acetate ions appears to assist the formation of this complex.

5.6.9. Far-infrared spectra of the solid samples from the series ZrOHAc

The solid samples of the series **ZrOHAc** were characterised in the far-IR region (700-100 cm^{-1}). The recorded spectra are shown in Fig. 5.61. The corresponding correlation sum graph is presented in Fig. 5.62.

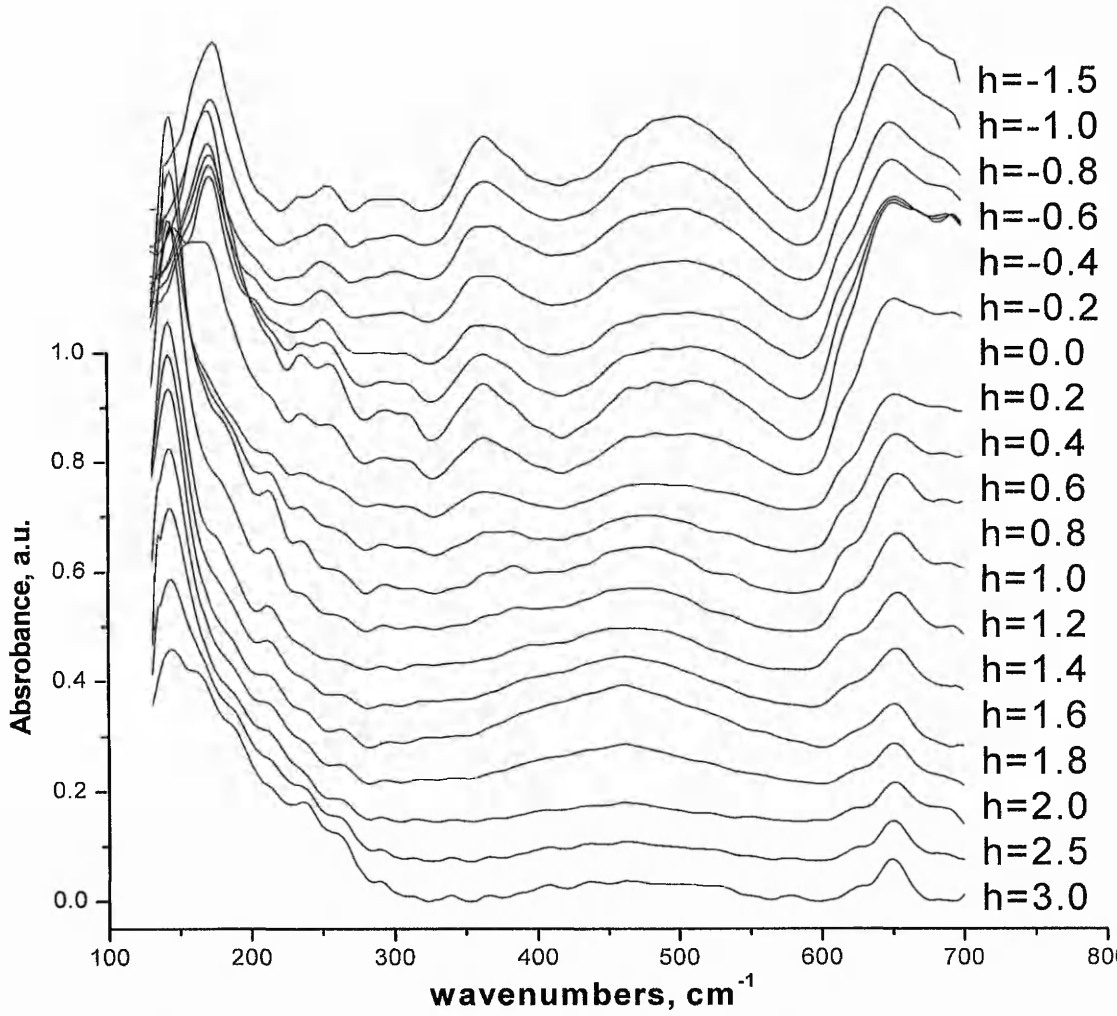


Fig. 5.61. Far-IR spectra of the solid samples of the series **ZrOHAc**. Y-offset – 90 %.

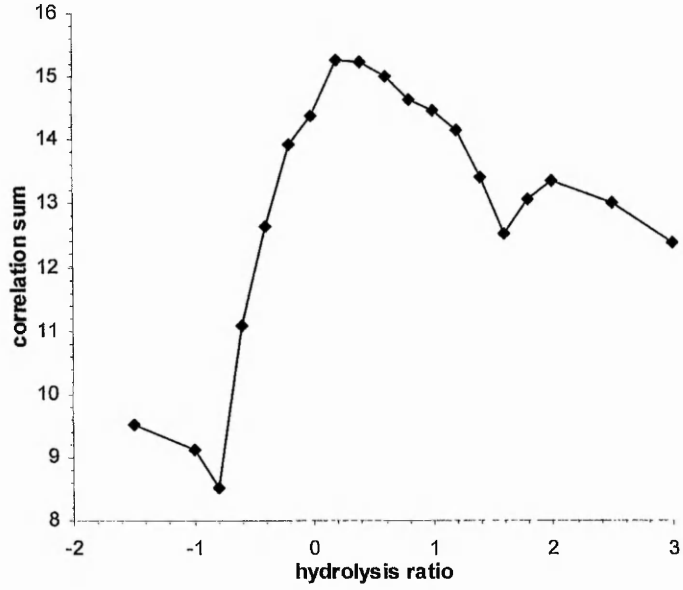


Fig. 5.62. The correlation sum graph in the hydrolysis ratio domain calculated from the data of the far-IR spectra of the series **ZrOHAc**.

The raw far-IR spectra from Fig. 5.61 can be roughly divided into two distinct groups on the basis of their correlation patterns depicted in Fig. 5.62 – at $-1.5 \leq h \leq 0.0$ and $0.2 \leq h \leq 3.0$. The spectra of the samples produced in acidic conditions ($h \leq 0.0$) are characterised by the presence of intense bands at 650 and 688 cm^{-1}. As mentioned above, the first of these bands can be assigned to bridging bidentate Zr-acetate complex (δ(OCO) vibrations [35]), This band reaches its maximum in the range $0.2 \leq h \leq 1.0$ (Fig. 5.61) and steadily decreases in intensity with the further increase of hydrolysis ratio in line with the rest of the bands arising from the bridging complex detected in the mid-IR spectra of the series **ZrOHAc**. The band at 688 cm^{-1} can be related either to the chelating bidentate Zr-acetate complex, or to the vibrations of structural hydroxyl-ligands. In any case, this band decreases in intensity with increasing hydrolysis ratio faster than the band at 650 cm^{-1}.

The bands with maxima at 503 and 334 cm^{-1} possess a composite structure as revealed by the 4th derivative spectra of acidic samples of the series **ZrOHAc**. The band at 503 cm^{-1} actually consist of the overlapped bands at 541, 523, 483, 462 and 428 cm^{-1}, while the composite band at 334 cm^{-1} contains peaks at 386, 365, 348 and 304 cm^{-1}. The synchronous behaviour of these bands is observed in the 2D-correlation maps (omitted). The bands above 500 cm^{-1} most probably belong to the vibrations of structural hydroxyls of Zr hydrolytic polymers (as has been shown for the series **ZrOH**, **ZrHCO3** and **ZrOHSO4**), while the peaks at lower frequencies are derived from librational modes of aquo ligands. Both sets of bands at 503 and 334 cm^{-1} are most intense at lower hydrolysis ratios (h=0.0) and gradually decrease upon the increase of h. At h~0.8 the positions of these composite bands start to change. The maximum of the lower-frequency band blue-shifts towards 400 cm^{-1}, while the band at 503 cm^{-1} is red-shifted towards ~460 cm^{-1}. At h~1.6 both bands overlap completely and form a single very broad band with a maximum at ~465 cm^{-1}.

In the range of frequencies 300-200 cm^{-1} the set of bands arising from the Zr-O vibrations of hydrous zirconia and Zr polymers are located as for the series **ZrOH** and **ZrHCO3**. The region contains four major bands in the case of the acidic **ZrOHAc** samples ($h \leq -0.6$) at 307, 283, 257 and 234 cm^{-1} with comparable intensities. The fact that the bands in the region are highly degenerate is indicative of the presence of the monoclinic phase in the solid samples produced at low pH. With the increase of hydrolysis ratios (h=0.0) the lower-frequency bands of the region increase in intensity, while the bands at 307 and 283 cm^{-1} decrease. This feature may reflect a gradual transformation of ol-bridges into oxo-bridges (oxolation) upon alkaline hydrolysis of Zr-ions in the presence of acetate-ions.

At very low frequencies (<200 cm^{-1}) two major bands are observed in the far-IR

spectra of the series **ZrOHAc** at 177 and 144 cm^{-1}. The first band is very intense for the acidic samples ($h \leq 0.0$). Above hydrolysis ratio $h=0.0$, the band at 144 cm^{-1} starts to dominate. One can assume that these bands are fundamentals of Zr-O stretchings in the structural units of the solid products. Hence, the band at 177 cm^{-1} is probably associated with ν(Zr-O) of bridged hydroxyls, and the band at 144 can be attributed to ν(Zr-O) of oxo-bridges. This assignment could offer an easy explanation of the processes occurring upon the hydrolysis of Zr-acetate complexes.

The presence of aquo ligands in the samples of the series **ZrOHAc** indicated by the ν(OH) vibrations at 3600-3200 cm^{-1} and at $500 \leq \nu \leq 400$ cm^{-1} arise from librational and translational modes of lattice water. The presence of hydroxyl-ligands of any kind is still of doubt, since no clear indications of these ligands are detected in the corresponding IR spectra. One of the reasons is the strong overlapping of the bands with the bands arising from acetate-ions.

The acetate-ion is considered a relatively weak ligand, compared, for instance, with sulphate. Therefore, the formation of pure zirconium acetate hydrate, even in acidic conditions and at high temperatures is questionable. At higher hydrolysis ratios, basic zirconium oxohydroxide acetate hydrate can be hypothesised as a major component of Zr-containing materials of the series **ZrOHAc**. Acetate-ions are in the chelating form for complexes at $h \leq 0.8$. At higher pH and hydrolysis ratios, transformation of acetate-ions from chelating into the bridging form leads to a crystalline product, unlike the precipitate produced under strongly acidic conditions with chelating acetate-ligands. The bridged form of acetate-ions probably forces this due to the better alignment of Zr tetramers or other building blocks. The structure of hydrous zirconia or basic acetate is probably closer to monoclinic at acidic conditions (the samples are XRD-amorphous). At very high hydrolysis ratios the structure of the solid product may be closer to the tetragonal phase, although this tentative assignment is based only on the far-IR data in the region 300-200 cm^{-1}.

5.6.10. Mid-infrared spectra of the solid samples from the series ZrOHGly2:1, ZrOHGly1:1 and ZrOHGly1:2

We have examined infrared spectra of the solid samples of the series "**ZrOHGly**" with different ratios of Zr-ions and glycine in the precursor solutions (Zr:Gly = 2:1; 1:1; 1:2). Mid-IR spectra of the series **ZrOHGly1:2**, **ZrOHGly1:1** and **ZrOHGly2:1** are shown in Fig. 5.63-5.65 (Fig. 5.64 and 5.65 are presented in APPENDIX 3), and the corresponding correlation sum graphs are given in Fig. 5.66.

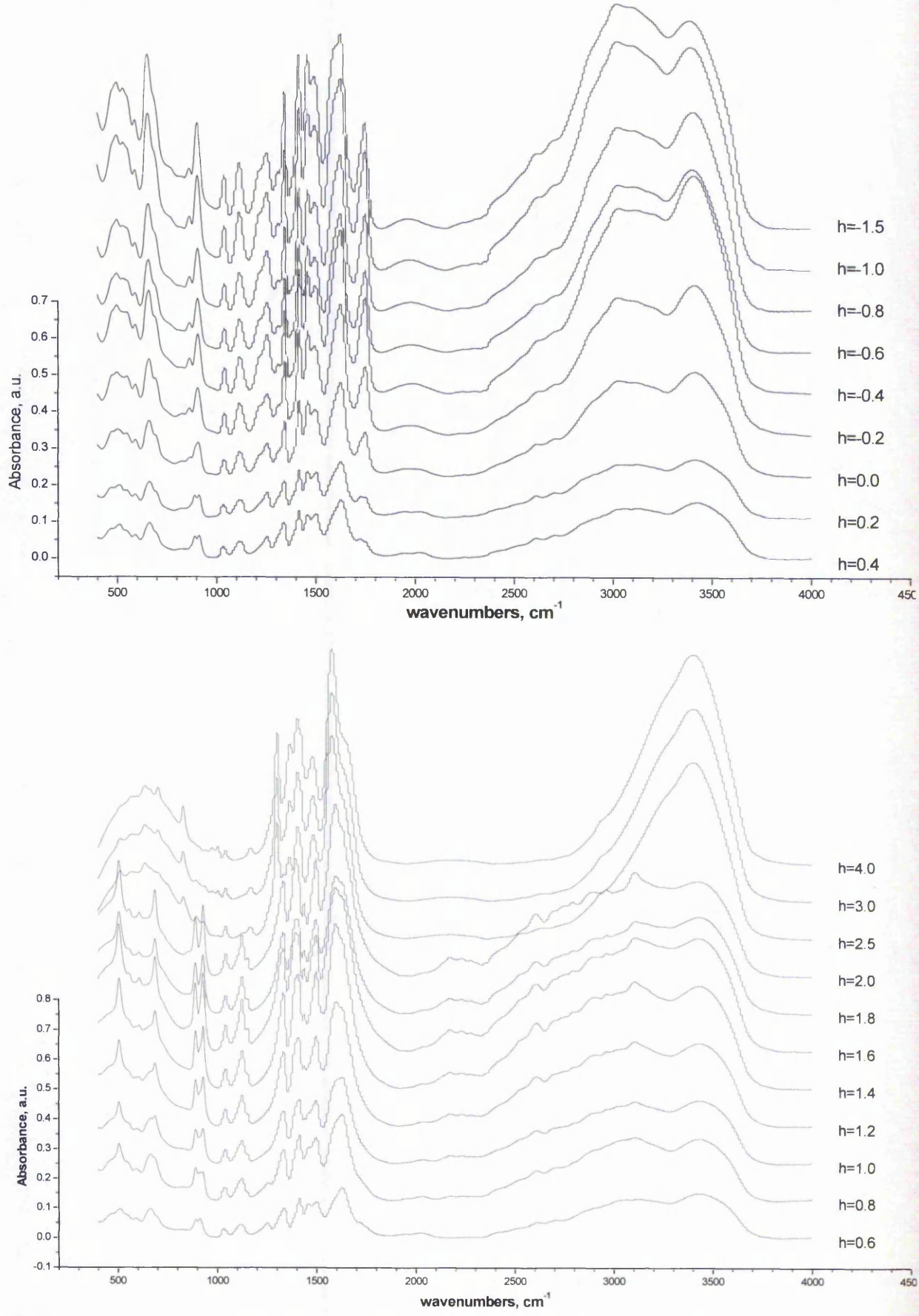


Fig. 5.63. Mid-IR spectra of the solid samples of the series **ZrOHGly1:2**. Y-offset – 120%.

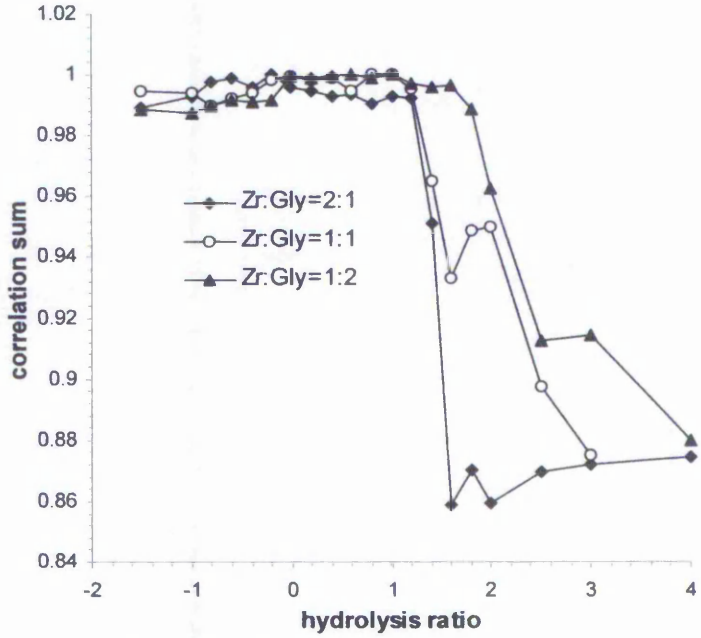


Fig. 5.66. The correlation sum graphs in the hydrolysis ratio domain (values normalised to unity) calculated from the data of the mid-IR spectra of the series **ZrOHGly1:2**; **ZrOHGly1:1** and **ZrOHGly2:1**.

2D-COS analysis of the IR-region 4000-3230 cm^{-1} reveals the composite nature of the band at ca. 3400-3380 cm^{-1} (Fig. 5.67, 5.68, 5.69).

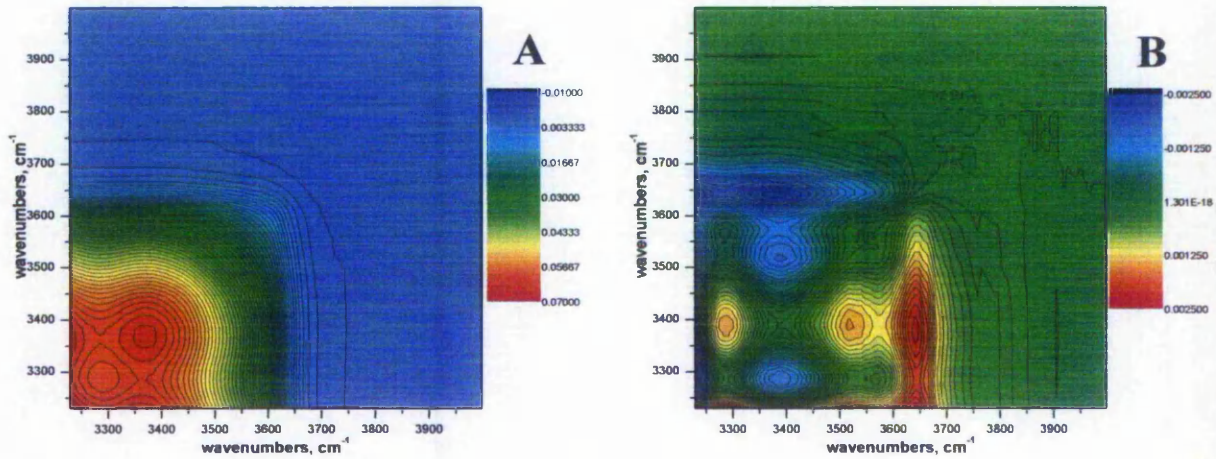


Fig. 5.67. 2D-correlation maps of the IR-region 4000-3230 cm^{-1} for the series **ZrOHGly1:2** in (***A***) synchronous and (***B***) asynchronous modes.

From the synchronous correlation map in the region 4000-3230 cm^{-1} in Fig. 5.67*A* it can be seen that the broad band at ca. 3400-3380 cm^{-1} consists of three bands - ca. 3384, 3286 and 3168 (the actual maximum of the latter band is outside the synchronous map in Fig. 5.67*A*). These highly correlated bands presumably arise from aquo ligands in the coordination sphere of Zr-ions (3384 cm^{-1}), protonated amino-groups of glycine (3286 cm^{-1} and physically absorbed water in the solid samples of the series **ZrOHGly1:2**. The asynchronous correlation

map in Fig. 5.67*B* reveals that the listed bands are accompanied by a narrow band at 3640-3650 cm^{-1} which corresponds to tri-bridged hydroxyl-ligands of Zr-ion in the monoclinic zirconia phase [46]. The bands arising from water and the NH_3^+-groups (3384, 3286 and 3168 cm^{-1}) and hydroxyl-ligands (3645 cm^{-1}) are superimposed, Fig. 5.67*B*. The IR--bands corresponding to bi-bridged and terminal OH-groups of Zr polymers [47] are virtually absent in the correlation graphs calculated from the mid-IR data of the series **ZrOHGly1:2**. It is necessary to add that in the higher-frequency region of the mid-IR spectra of the series **ZrOHGly1:2** a range of intense bands arising from NH_2-group stretching vibrations is detected at 3168-2750 cm^{-1}, $\nu(CH_2)$ bands are located in the region 2750-2400 cm^{-1}.

In the case of the series with equimolar quantities of zirconium and glycine (**ZrOHGly1:1**) the higher-frequency region shows the presence of three slightly differing bands of hydroxyl-groups of Zr-polymers (Fig. 5.68*B*) at 3642, 3651 and 3674 cm^{-1} (tri-bridged OH-ligands) along with the bands at 3746 and 3816 cm^{-1} which arise from bi-bridged and terminal OH-ligands of Zr polymers [48]. As follows from the raw-IR spectra of the series **ZrOHGly1:1** (Fig. 5.64), the bands of tri-bridged hydroxyls are more intense than those of bi-bridged OH-groups, and the terminal OH band shows the smallest intensity.

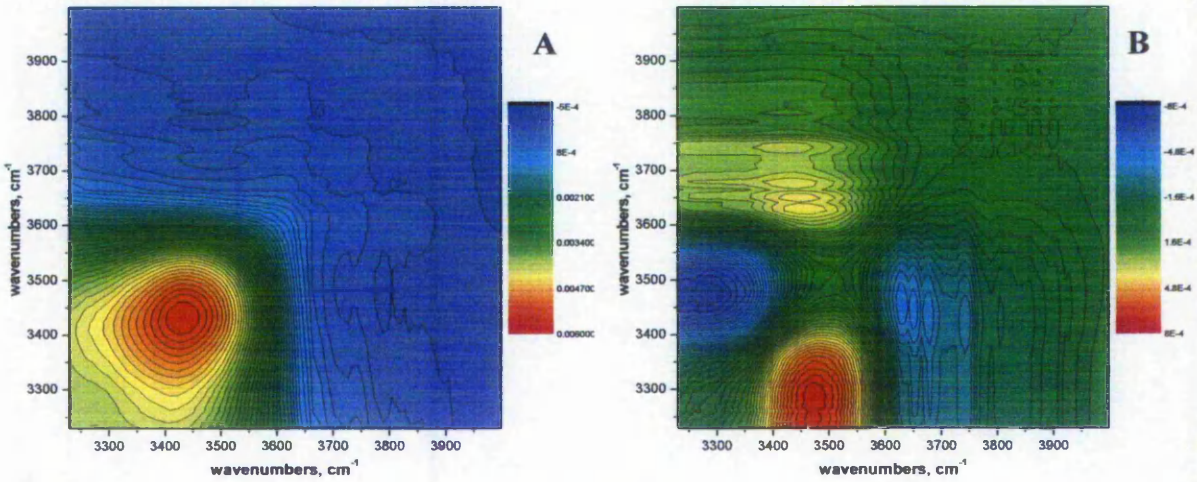


Fig. 5.68. 2D-correlation maps of the IR-region 4000-3230 cm^{-1} for the series **ZrOHGly1:1** in (***A***) synchronous and (***B***) asynchronous modes.

The 2D-correlation maps of the higher-frequency region of the IR-spectra of the series with deficient glycine (**ZrOHGly2:1**) show a slightly different distribution of bands (Fig. 5.69). The synchronous pattern (Fig. 5.69*A*) shows a dominance of the intense and broad band at ca. 3400-3421 cm^{-1}, quite similar to that observed for the analogous pattern for the series **ZrOHGly1:1** (Fig. 5.68*A*). The asynchronous correlation map in Fig. 5.69*B* indicates that the weak band of the tri-bridged OH-ligands at ca. 3606 cm^{-1} is not superimposed with the band from the ν(OH) stretching vibrations of water at 3400-3421 and 3286 cm^{-1}, in contrast to what was observed for **ZrOHGly1:2** and **ZrOHGly1:1**. However, the band at 3606 cm^{-1} remains

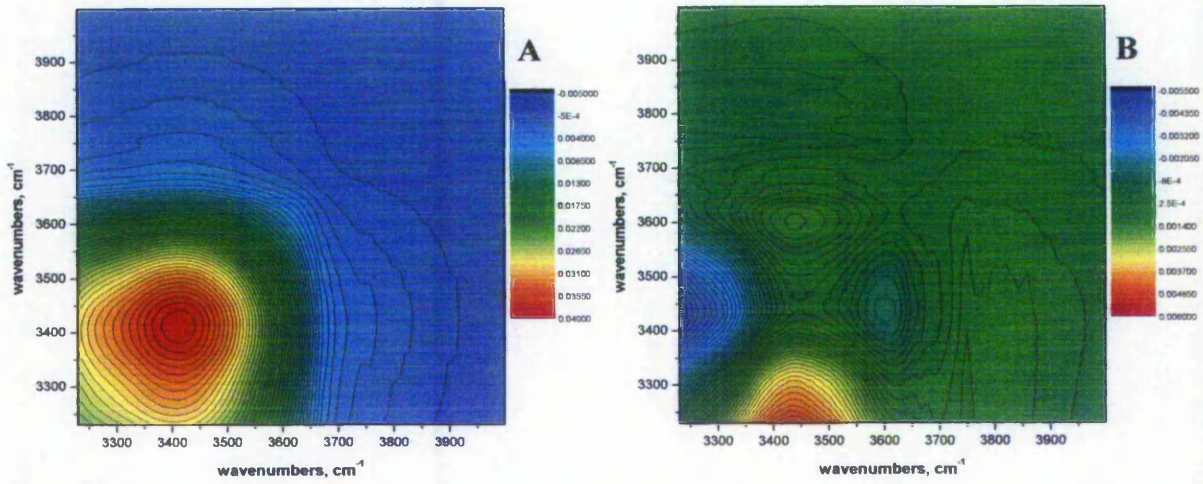


Fig. 5.69. 2D-correlation maps of the IR-region 4000-3230 cm^{-1} for the series **ZrOHGly2:1** in (***A***) synchronous and (***B***) asynchronous modes.

superimposed with the band from the protonated amino-group of glycine at ca. 3160 cm^{-1}.

Analysing the pH-dependent behaviour of the IR-bands in the higher-frequency range, it is clear that the major band at 3420-3380 cm^{-1} arising from aquo ligands of Zr polymers remains at a very high intensity up to a hydrolysis ratio of h=4.0 for all glycine-containing studied (Fig. 5.63-5.65). The intensity of these bands starts to decrease at h>1.6. The bands arising from different forms of hydroxyl-ligands at 3816-3645 cm^{-1} have their highest intensity at h<1.2-1.6 and tend to decrease with increase of hydrolysis ratio (exact variation patterns for these IR-bands are difficult to obtain due to the strong overlap with bands of OH-stretching of water). The bands at 3170-2750 cm^{-1} arising from the protonated amino-group of glycine possess highest intensity at low hydrolysis ratios h<1.2. The intensity of the bands arising from amino-groups of glycine decrease strongly in the range $1.2 \leq h \leq 2.0$. At h>2.0 these bands practically disappear from the mid-IR spectra of the series **ZrOHGly** for the different Zr:Gly ratios investigated. The major bands arising from the protonated amino-group at ca. 3150-1360 cm^{-1} disappear from the spectra of all three glycine-containing series at h>1.8 indicative of depronotation of this functional group. The IR-bands arising from methylene groups (2750-2400 cm^{-1}) follow pH-dependent patterns similar to that observed for the amino-groups.

According to Nakamoto [35], the region at 1900-400 cm^{-1} represents the most important part of the IR-spectra of glycine-containing complexes, since it provides a wealth of information concerning the form of glycine and the type of complex formed with metal ions. On the basis of the full 2D-COS contour maps and 4th derivative spectra this region was analysed and the results of the 2D-correlation analysis are shown in Fig. 5.71-5.73.

In order to assign the numerous glycine-associated bands in this spectral region, a spectrum of pure crystalline glycine was also recorded for comparison (Fig. 5.70). The band positions in Fig.5.70 match the reference band positions [35].

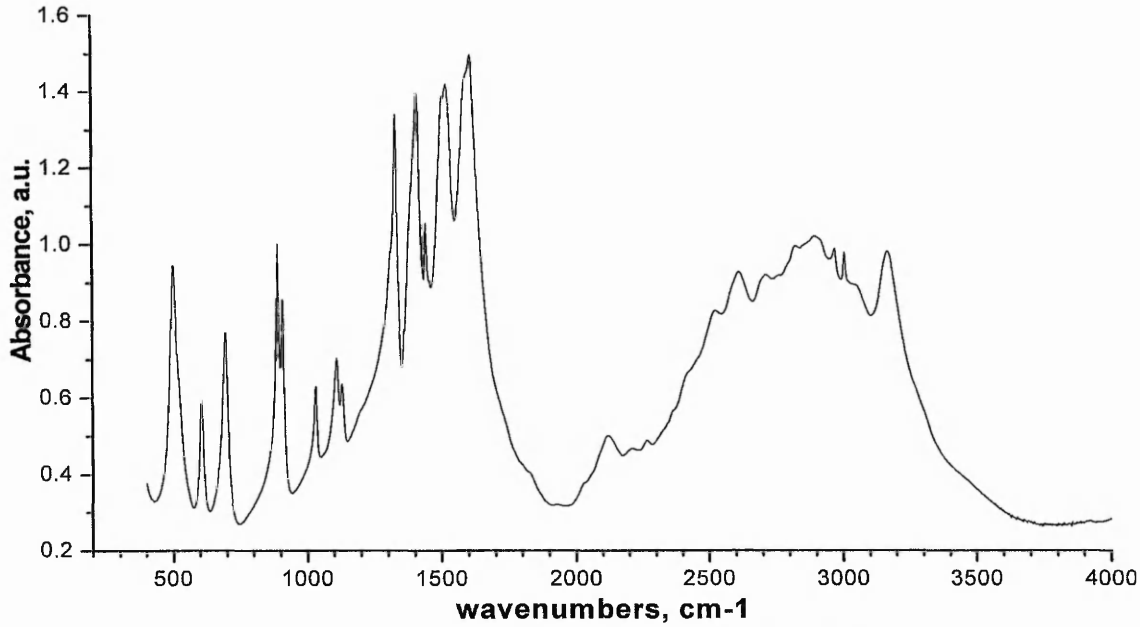


Fig. 5.70. Mid-infrared spectrum of crystalline glycine (zwitter-ionic form).

Results of the 2D-correlation analysis of the IR-spectra for the series **ZrOHGly1:2**, **ZrOHGly1:1** and **ZrOHGly2:1** in the region 1940-1170 cm^{-1} revealed the presence of three major sets of bands superimposed on each other (Fig. 5.71-5.73). The first set of bands is most clearly observed in the synchronous map for the series **ZrOHGly1:2** (Fig. 5.71) and contains the bands correlated to the diagonal peak at 1759-1752 cm^{-1}. On the basis of the appearance of this set of bands in acidic media (h<1.2), the complete disappearance of the bands at higher hydrolysis ratio, as well as the relative band positions (explained below), these bands are assigned to the free protonated form of glycine $HOOC\text{-}CH_2\text{-}NH_3^+$: 1756 cm^{-1} - $\nu_a(COOH)$; 1256 (1220) cm^{-1} - $\nu_s(COOH)$; 1620-1610 cm^{-1} - $\delta_d(NH_3^+)$; 1462 cm^{-1} - $\delta_s(NH_3^+)$; 1446 cm^{-1} - $\delta(CH_2)$; 1331 cm^{-1} -$\rho_w(CH_2)$. Comparing the listed assignments with the positions of analogous bands from the spectrum of pure solid glycine (zwitterion) in Fig. 5.70 (1611 cm^{-1} - $\nu_a(COOH)$; 1410 cm^{-1} - $\nu_s(COOH)$; 1585 cm^{-1} - $\delta_d(NH_3^+)$; 1507 cm^{-1} - $\delta_s(NH_3^+)$; 1445 cm^{-1} - $\delta(CH_2)$; 1333 cm^{-1} -$\rho_w(CH_2)$), one can conclude that the methylene group of glycine does not change significantly upon transformation into the protonated form. The bands from the protonated NH_3^+-group vary more substantially for the two forms of glycine, probably, due to the effect of the protonated carboxylic group on the acidity of the protonated amine. The largest variation is observed for bands arising from the carboxylic group of glycine, for which the separation of symmetric and asymmetric vibrations increases from Δ=198 cm^{-1} (zwitter-ion) to Δ~500 cm^{-1} (protonated COOH-form) as observed in the spectra of the series **ZrOHGly1:2**. A similar large separation has been observed for unidentate complexes of carboxylic acids and glycine with metal ions [35].

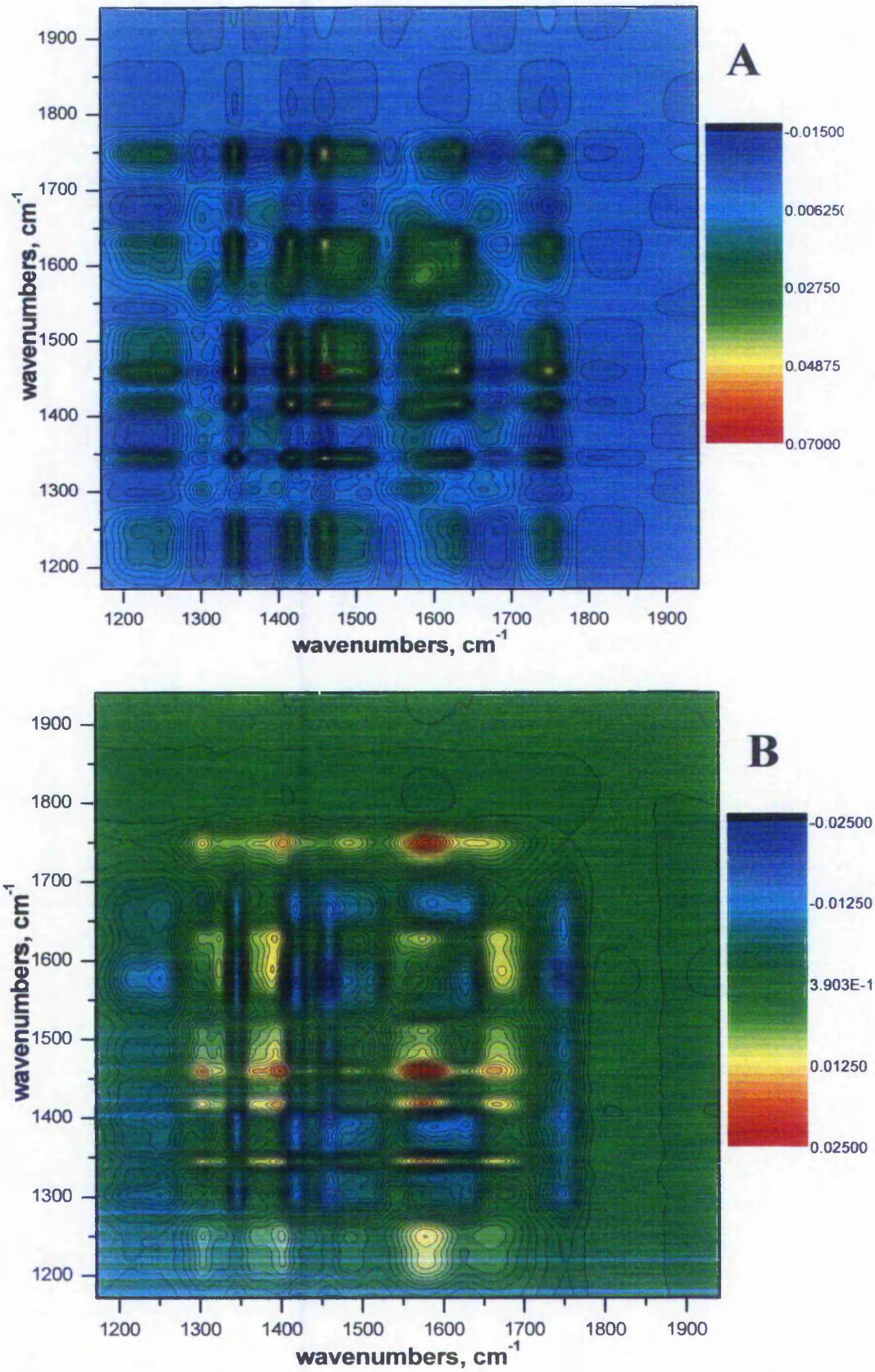


Fig. 5.71. Synchronous (*A*) and asynchronous (*B*) 2D-correlation contour maps of the diagonal cross-section 1940-1170 cm^{-1} calculated from the full set of the mid-IR spectra of the series **ZrOHGly1:2**.

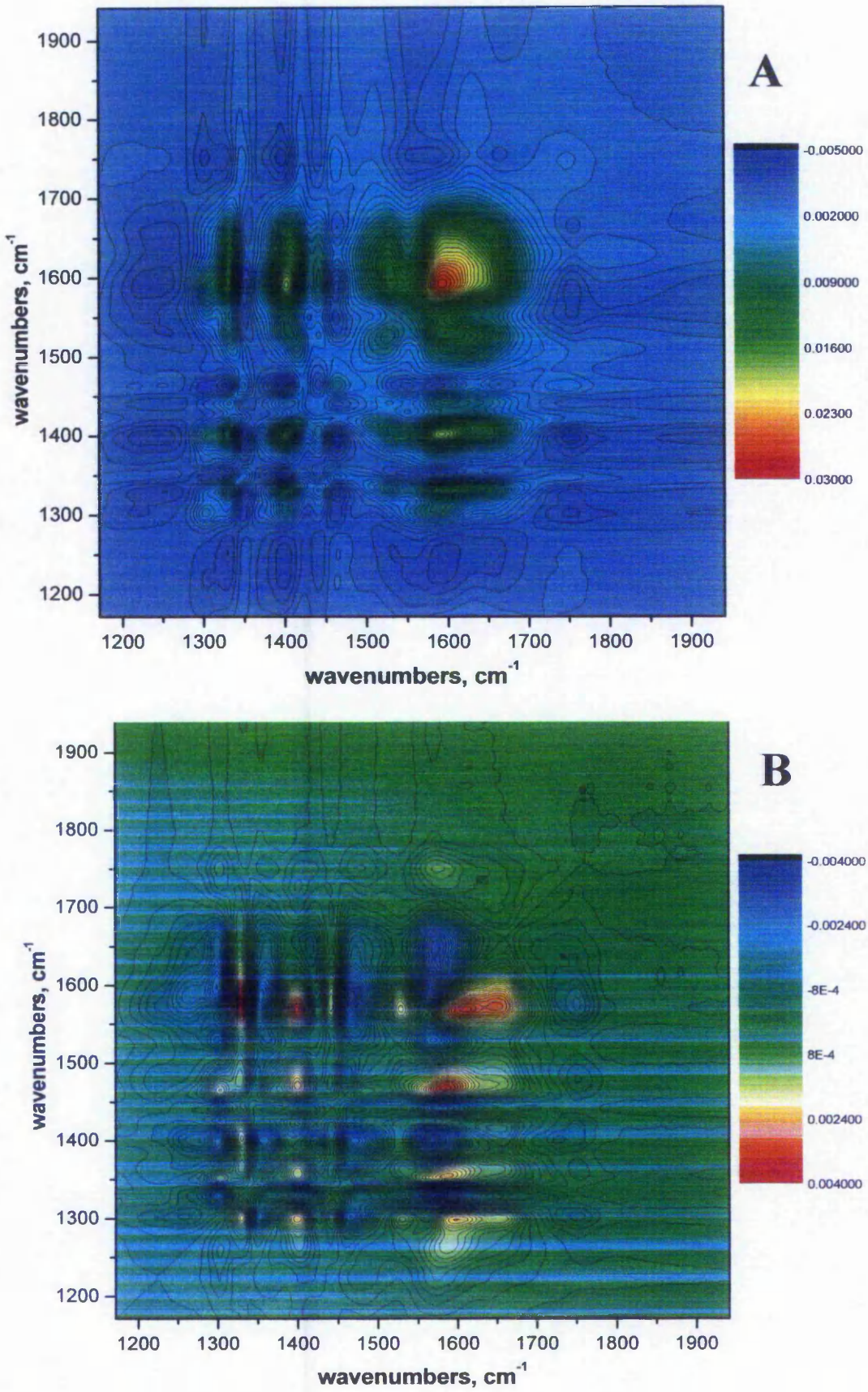


Fig. 5.72. Synchronous (*A*) and asynchronous (*B*) 2D-correlation contour maps of the diagonal cross-section 1940-1170 cm^{-1} calculated from the full set of the mid-IR spectra of the series **ZrOHGly1:1**.

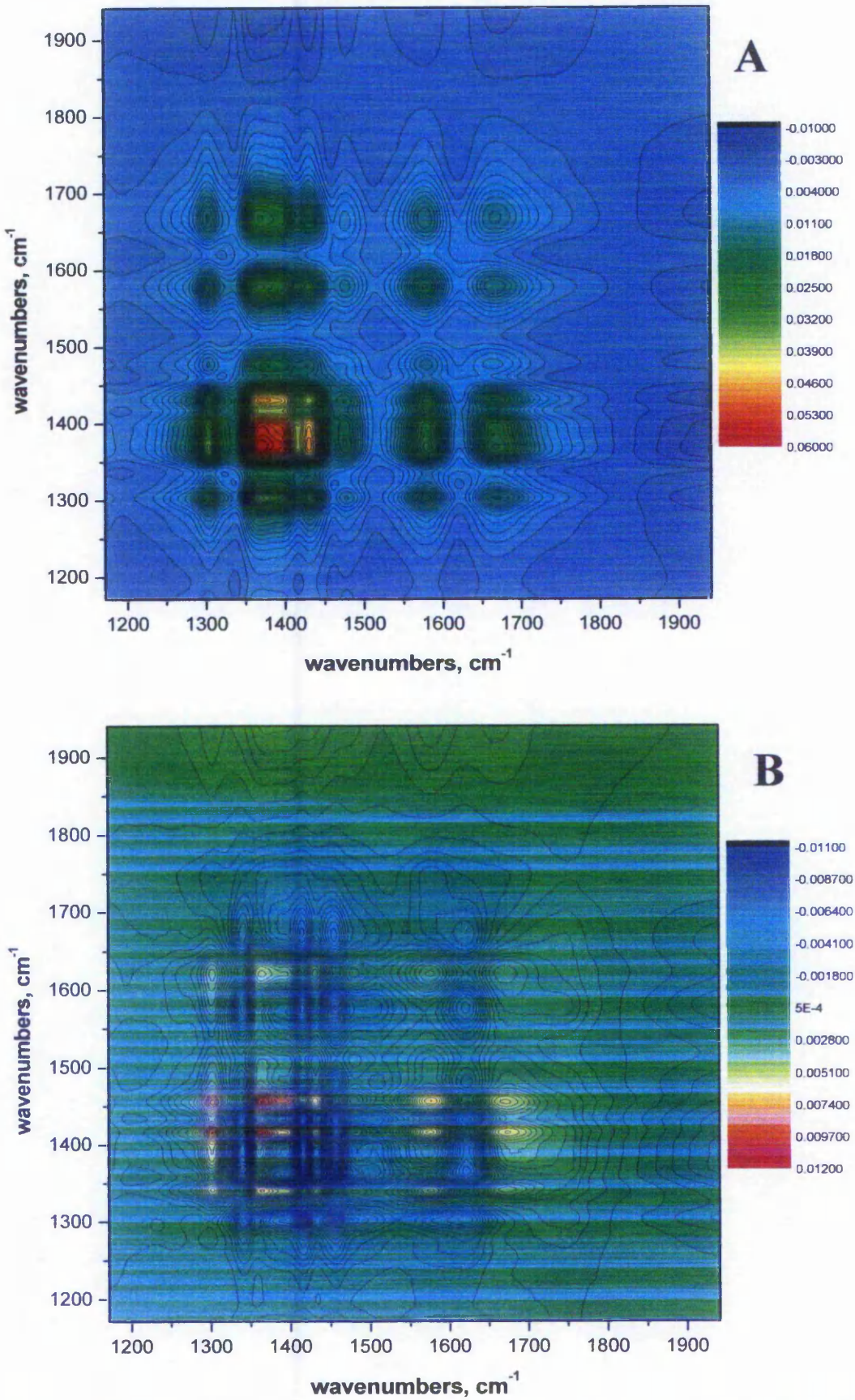


Fig. 5.73. Synchronous (***A***) and asynchronous (***B***) 2D-correlation contour maps of the diagonal cross-section 1940-1170 cm^{-1} calculated from the full set of the mid-IR spectra of the series **ZrOHGly2:1**.

Therefore, one can assume that the formation of a unidentate Zr-glycine complex in acidic media cannot be completely ruled out. Unidentate complexes of glycine usually occur in the case of "soft" metal ions (Pt (II), Pd(II)) and involve neutral amino-groups as the donor. Zr-ions are hard acids with a high affinity to oxygen-containing ligands and the protonated amino-group is virtually impossible in the conditions of high acidity. Therefore, only carboxylic group of glycine is bound to Zr-atoms in the complex.

For the unidentate complex of protonated form of glycine is probably an indication of the incomplete complexation of glycine in samples from the series **ZrOHGly1:2**, where glycine is present in a two-fold excess. For the series **ZrOHGly1:1** with equimolar quantities of Zr-ions and glycine the intensity of the IR-bands at 1756 and 1256 cm^{-1} (major indicators of the protonated form of glycine) are significantly lower (Fig. 5.64). In the series **ZrOHGly2:1** with a deficit of glycine compared to Zr-ion concentration these bands are absent at $h<1.2$. Therefore, one may draw an important preliminary conclusion that the actual ratio of Zr to glycine in the complex is lower than 1, at least for materials prepared under highly acidic conditions. One presumes that protons are unlikely to compete with Zr-ions for glycine, since this has also not been observed for the complexation of acetic acid, which is a weaker base than glycine. Therefore, complexation of glycine with zirconium in solution is limited by other factors that are discussed below.

The presence of free zwitter-ionic form of glycine could not be identified unambiguously from the mid-IR spectra of the glycine-containing series. The band arising from the bending vibrations of water, normally located at 1630-1640 cm^{-1}, becomes identifiable only at higher hydrolysis ratios ($h>1.6$). Therefore, most of glycine molecules are bound to Zr-ions. Glycine replaces aquo ligands in the coordination sphere of zirconium.

Another set of IR-bands extracted from the 2D-correlation data in Fig. 5.71-5.73 correlates with the band at ca. 1632 cm^{-1}. This set of bands is attributed to the bidentate bridging complex of glycine with Zr-ions on the basis of the Δ(COO) value of Δ=193 cm^{-1} for this set as compared with the value for pure glycine (Δ=198 cm^{-1} for the zwitter-ionic form). The following band assignments can be made for this set of bands: 1632-1628 cm^{-1} - $\nu_a(COO^-)$; 1439 cm^{-1} - $\nu_s(COO^-)$; 1590 cm^{-1} - $\delta_d(NH_3^+)$; 1482 cm^{-1} - $\delta_s(NH_3^+)$; 1446 cm^{-1} - $\delta(CH_2)$; 1331 cm^{-1} -$\rho_w(CH_2)$. Exact positions of the listed bands vary slightly between the series with different amounts of glycine (Fig. 5.71-5.73). The IR-bands of the bridged Zr-glycine complex are partially correlated with the set of bands for the protonated free form of glycine. This is possibly due to the shared positions of some bands (e.g., the bands arising from the CH_2-group) and due to some similarity of the pH-dependent patterns in the intensity behaviour of both sets. The bridged bidentate Zr-glycinate complex also dominates in acidic medium ($h<1.2$).

As follows from the raw IR data (Fig. 5.63-5.65), at higher hydrolysis ratios ($h \geq 1.2$) other types of Zr-glycine complexes are present. Using 2D-correlation analysis, identified the complex with $\nu_a(COO^-)$=1606-1597 cm^{-1} and $\nu_s(COO^-)$=1392 cm^{-1} was identified with the value of Δ~202-212 cm^{-1}, close to that expected for the bridging bidentate complex. With increase of hydrolysis ratio from h~1.2 to h=4.0 the band positions of this complex change to $\nu_a(COO^-)$=1578 cm^{-1} and $\nu_s(COO^-)$=1416 cm^{-1} with Δ=162 cm^{-1}, which is closer to that expected for a chelating bidentate type of Zr-glycine complex, according to the empirical classification for carboxylate ligands described in the previous section for the series with acetate-ions (**ZrOHAc**). Gradual transformation of one complex into another possibly occurs due to deprotonation of the amino-group of glycine or to the structural rearrangement of the glycine moiety in the complex from a bridging to a chelating form.

Another type of Zr-glycine complex detected in the mid-IR spectra of the glycine-containing series of samples using 2D-COS analysis at higher hydrolysis ratios (h>1.0) possesses bands at ca. 1668 cm^{-1} ($\nu_a(COO^-)$) and 1368 cm^{-1} ($\nu_s(COO^-)$). The relatively large value of Δ (300 cm^{-1}) makes it difficult to assign this complex to a particular type. One can suggest that in this complex glycine acts either as an asymmetric bidentate ligand characterised by unusually large values of Δ [35], or a unidentate ligand. In any case, this complex appears to be of minor importance judging by the intensities of the corresponding bands (Fig. 5.63-5.65).

2D-correlation analysis of the mid-IR spectra of the series with various Zr:Gly ratios has shown that the amino-group of glycine, completely protonated at h<1.4, is not involved in the complexation of this ligand with zirconium-ions. This fact is supported by the presence of deformation vibrations of the NH_3^+-moiety (1485 and 1592 cm^{-1}) up to very high hydrolysis ratios (h~1.8-2.0).

At high hydrolysis ratios (h>1.2-1.4) it is possible to observe the gradual transformation of the protonated free amino-group of glycine into the unprotonated form, which is followed by a steady red shift of $\delta_s(NH_3^+)$ band from 1485 cm^{-1} to ca. 1524 cm^{-1}. A new band probably associated with the neutral amino-group also appears at high hydrolysis ratios at ca. 1302-1304 cm^{-1} (Fig. 5.63-5.65).

As follows from the mid-IR spectra of the series with glycine, around hydrolysis ratio h~1.6 the bidentate complexes start to disappear and the bands of free glycine start to dominate the spectra. Therefore, glycine molecules are gradually replaced with hydroxyl-ions of alkali at h>1.6. This process occurs at significantly higher h and pH, which is indicative of increased stability of Zr-glycine complex copared with the acetate complex.

The initial concentration of glycine in the samples of the series ZrOHGly plays a minor role in the intensity distribution and positions of the IR-bands of various forms of

glycine. Only the amount of unidentate complex with glycine changes significantly. In acidic conditions the concentration of this complex reaches significant amounts for the series with the two-fold excess of glycine. When the ratio Zr:glycine is 2:1, the unidentate complex is virtually absent in the spectra. For bidentate complexes, in the range of Zr:Gly ratios from 0.5 to 2, the complexation of zirconium with glycine proceeds in a uniform fashion. The complexes produced also react to variations of pH in the same way, regardless of Zr:Gly ratio.

The data of other studies on the Raman and IR-spectra of Zr-glycine complexes generally agree with the data of this work. The work [57] suggests that several forms of glycine are present in 50% (weight) solutions of Zr and Al basic chloride with glycine (Zr:Gly ratio 1:1). The IR spectra were consistent with the presence of the glycine zwitter-ion. The authors have shown that glycine binds to Zr polymeric species through its carboxylic group only. Solid materials contained 100% of glycine bound to Zr polymers, while only 58 to 75 % of glycine was bound to a metal ion in Zr (Al) solutions.

The work [58] reports a synthesis of the complex of glycine with another 'hard' metal ion – yttrium. On the basis of the IR spectra they have postulated that the ratio of Y-glycine complex was Y:Gly=1:3, and glycine was bound to yttrium as N,O-bidentate ligand. However, the presence of bands arising from protonated amino-groups of glycine (1507, 1123, 1100 cm^{-1}) is in apparent contradiction with the proposed structure of the Y-glycine complex. The absence of the bands of neutral or complexed amino-groups in the list of the detected IR-bands is also in disagreement with the assigned yttrium-glycine complex.

Detailed studies of Zr-glycine complexation have been conducted using solution and solid-state ^{13}C NMR [59]. Free glycine solutions exhibit two major signals in the ^{13}C NMR spectra – at δ=40-45 ppm (CH_2-group) and δ=170-182 ppm (COO-group). The latter signal varies strongly depending on which of the three forms of glycine are present in solution (the form *B2* is more stable in the gas phase [60]):

$$\underset{(A)}{{}^{+}NH_3CH_2COOH} \overset{pK=2.3}{\leftrightarrow} \underset{(B1)}{{}^{+}NH_3CH_2COO^{-}} \overset{pK=9.6}{\leftrightarrow} \underset{(C)}{NH_2CH_2COO^{-}}$$

$$\updownarrow$$

$$\underset{(B2)}{NH_2CH_2COOH}$$

The authors of the review [60] have reported the presence of at least four signals of the carboxylate group of glycine in the ^{13}C NMR spectra of a solution with Zr:Gly ratio 1:1. Two of these signals (δ=171.9 and δ=172.1 ppm) were close to zwitter-ionic and protonated free (*A* and *B1*) forms of glycine (δ=170.36 and δ=172.1 ppm correspondingly). At least one of the other two forms with signals at (δ~172.5 and δ~173.2 ppm) has been assigned to coordinatively bound glycine. There is one more peak apparently present in ^{13}C NMR spectra

at δ~173.1 ppm as a shoulder of the peak at δ~173.2 ppm, that is not discussed by the author. On the basis of the peak areas of the described NMR peaks the author has concluded that depending on the pH value, from 58 to 75 % of glycine is bound to zirconium in the 1:1 Zr-glycine solutions. Lower acidity allowed for a higher percentage of bound glycine. The identification of at least four ^{13}C NMR signals corresponding to different forms of glycine (free and coordinatively bound to zirconium) greatly supports the assignments in the mid-IR spectra made in the present study. Solid-state ^{13}C NMR spectra of Zr-glycine solutions have been previously acquired [59]. The signal from the Zr-glycine complex is broad and is located between the signal of the protonated form of free glycine and the zwitter-ionic form. On the basis of the NMR characterisation, the author concluded that all of the glycine is bound to Zr-ions in the solid state. However, the way the samples containing the Zr-glycine complex were transformed from solution into solid state is unclear.

Another significant contribution in studies of the interactions of glycine and zirconium has been made using size-exclusion chromatographic separations of 10% wt. aqueous mixtures of Zr and Al basic chloride with glycine [61]. This work has revealed a low-molecular weight species related to a Zr-glycine complex of the size smaller than ca. 1 nm. This is in a good agreement with the DLS data (Chapter 4) where the major Zr-glycine species was sub-nanometre in size. Therefore, the hydrolytic condensation of Zr polymeric species containing coordinatively bound glycine is strongly hindered, as will be discussed below.

The lower-frequency region of the mid-IR spectra (<1170 cm^{-1}) of the series **ZrOHGly1:2**, **ZrOHGly1:1** and **ZrOHGly2:1** shown in Fig. 5.63-5.65 also provides important information concerning the forms of glycine in Zr-glycine solutions and on the possible structure of the complex. The bands at ca. 1135 and 1108 cm^{-1} present in the IR-spectra of all three series with glycine arise from $\rho_r(NH_3^+)$ vibrations. They represent a very good indicator of the presence of the protonated amino-group of glycine in the samples. These bands are observed in the spectra up to very high hydrolysis ratio (for the series **ZrOHGly1:2** - up to h~2.0, for the series **ZrOHGly1:1** – up to h~3.0 and for the series **ZrOHGly2:1** – up to h~1.8). The bands strongly overlap at lower hydrolysis ratios in the series with Zr:Gly ratio 1:2 and 1:1 and split into two distinct bands from h~1.0-1.2. A very distinct and sharp band is located at 1049-1033 cm^{-1} and corresponds to νa(CCN) vibrations [35]. The band is present in the mid-IR spectra of all three series with glycine throughout the whole hydrolysis ratio range studied, and can possibly serve for quantification of the total amount of glycine in the sample (however this needs calibration).

Another distinct and intense band in the mid-IR spectra in question has a maximum at 903-907 cm^{-1} in all three glycine-containing series of samples. At lower hydrolysis ratios (h<1.0) this band represents an unresolved doublet of bands at ca. 905 and 894 cm^{-1}

attributable to rocking motions of the methylene-group of glycine and ν_s(CCN) vibrations correspondingly [35]. These bands become separate from one other in the series **ZrOHGly1:2** and **ZrOHGly1:1** at higher hydrolysis ratios (h~1.0-1.4).

At ca. 695-691 cm^{-1} is located a band associated with $\rho_w(COO^-)$ vibrations is found [35]. The band persists throughout the whole hydrolysis ratio range investigated. This band is overlapped with another peak at 668-656 cm^{-1} of unknown origin. The latter band is observed only at lower hydrolysis ratios (h<1.2). One can assume that the band at 668-656 cm^{-1} arises from the protonated free form of glycine (A) and can be attributed either to $\rho_w(COO^-)$, or to the π(COO) vibrations [35] normally observed at 608-595 cm^{-1}. At frequencies below 600 cm^{-1} several major bands can be identified at lower hydrolysis ratios (h<1.2) with maxima at 560, 529-520, 510-493, 477-463, 435 and 406 cm^{-1}. The bands at 560, 468 and 411 cm^{-1} are not strongly correlated with the remaining bands arising from glycine. One could suggest that these bands belong to aquo- and hydroxyl-ligands of Zr polymers. The bands at 529-520 cm^{-1} and at 510-493 cm^{-1} have analogues in the spectrum of pure glycine (Fig. 5.70) at 528 and 502 cm^{-1} which are derived from $\rho_r(NH_3^+)$ and $\rho_r(COO^-)$ correspondingly [35]. The band at 510-493 cm^{-1} is relatively weak at h<1.0 and starts to increase at higher hydrolysis ratios. At h>1.6 this band dominates the lower-frequency region, while the bands tentatively attributed above to vibrations of aquo- and hydroxyl-ligands start to decrease their intensity in the spectra of all three glycine-containing series of samples. The band at ca. 529-520 cm^{-1} is possibly red-shifted to ca. 545-550 cm^{-1} at h>1.0. The origin of the band at 435 cm^{-1} is unclear. It must be stressed that all the described lower-frequency bands are located on top of the broad and quite intense band of librational and translational modes of water according to the 2D-correlation data. This peak gradually decreases in the spectra at h>1.2.

5.6.11. Far-infrared spectra of the series ZrOHGly1:2, 1:1 and 2:1

In an attempt to clarify the bonding of glycine to Zr-ions, far-IR spectra of all three series of Zr-ions with glycine were recorded. The acquired spectra are shown in Fig. 5.74-5.76. A comparison of the correlation sum graphs calculated from the far-IR data can be made from Fig. 5.77.

The variation of the shapes of the far-IR spectra of the glycine-containing series (Fig 5.77) is smallest at highest glycine content (Zr:Gly=1:2) and largest at lowest glycine content (Zr:Gly=2:1). The far-IR spectra of all three series exhibit roughly the same correlation domains: $-1.5 \le h \le -0.6$; $-0.4 \le h \le 1.6$ and $h \ge 1.8$. The changes in shape of the far-IR spectra in strongly acidic and alkaline domains become stronger with decrease of glycine concentration, the middle domain narrows in the same order from $-0.4 \le h \le 1.8$ for the ratio Zr:Gly=1:2 to $-0.2 \le h \le 1.4$ for Zr:Gly=1:1.

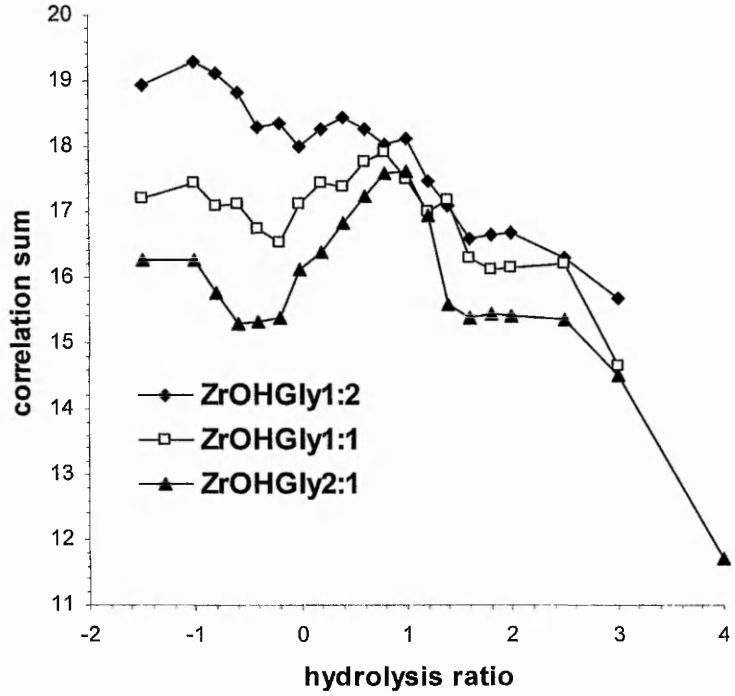


Fig. 5.77. The correlation sum graphs in the hydrolysis ratio domain calculated from the far-IR spectra of the series **ZrOHGly1:2**, **ZrOHGly1:1** and **ZrOHGly2:1**.

The raw far-IR spectra of the series **ZrOHGly1:2** in the region 600-130 cm^{-1} (Fig. 5.75) enable us to identify the following bands at low hydrolysis ratios ($h \leq 0.8$). The bands at 695, 6689, 592, 562, 522, 498-502, 476, 459-454 and 418-411 cm^{-1} have been detected and assigned in the mid-IR spectra of the same series above. In the region 400-330 cm^{-1} there is an intense composite band in the far-IR spectra of the series with the two-fold excess of glycine which contains bands at 397-390, 385-380, 373-365 and 353-343 cm^{-1}. The 2D-COS data show (omitted here for the sake of brevity) that the bands at 369 and 347 cm^{-1} are correlated with the band at 454 cm^{-1} and probably arise from the deformation vibrations of the functional groups of glycine, since they are strongly correlated with the band at 503 cm^{-1} of $\rho_r(COO^-)$ vibrations. The IR-band at ca. 383 cm^{-1} is independent from the rest of the bands relating to glycine and can be assigned to the one of the librational modes of aquo ligands as in the case of the series **ZrOH**, **ZrHCO3** and **ZrOHAc** above.

The band at ca. 301 cm^{-1} is also of composite structure and comprises bands at 323, 301 and 280 cm^{-1} (Fig. 5.75). The band at 301-302 cm^{-1} in the far-IR spectra of the series **ZrOHGly1:2** increases its intensity in the hydrolysis ratio range $-1.5 \leq h \leq 0.8$ and is the most intense at $h=0.8$ above which it diminishes significantly. This band could arise from either to Zr-O structural bond of the Zr-glycine complex, or to ν(Zr-O) vibrations of Zr polymers. The pH-dependent distribution of the intensity of this band allows for its association with the bridged bidentate Zr-glycine complex which appears in the same hydrolysis ratio domain.

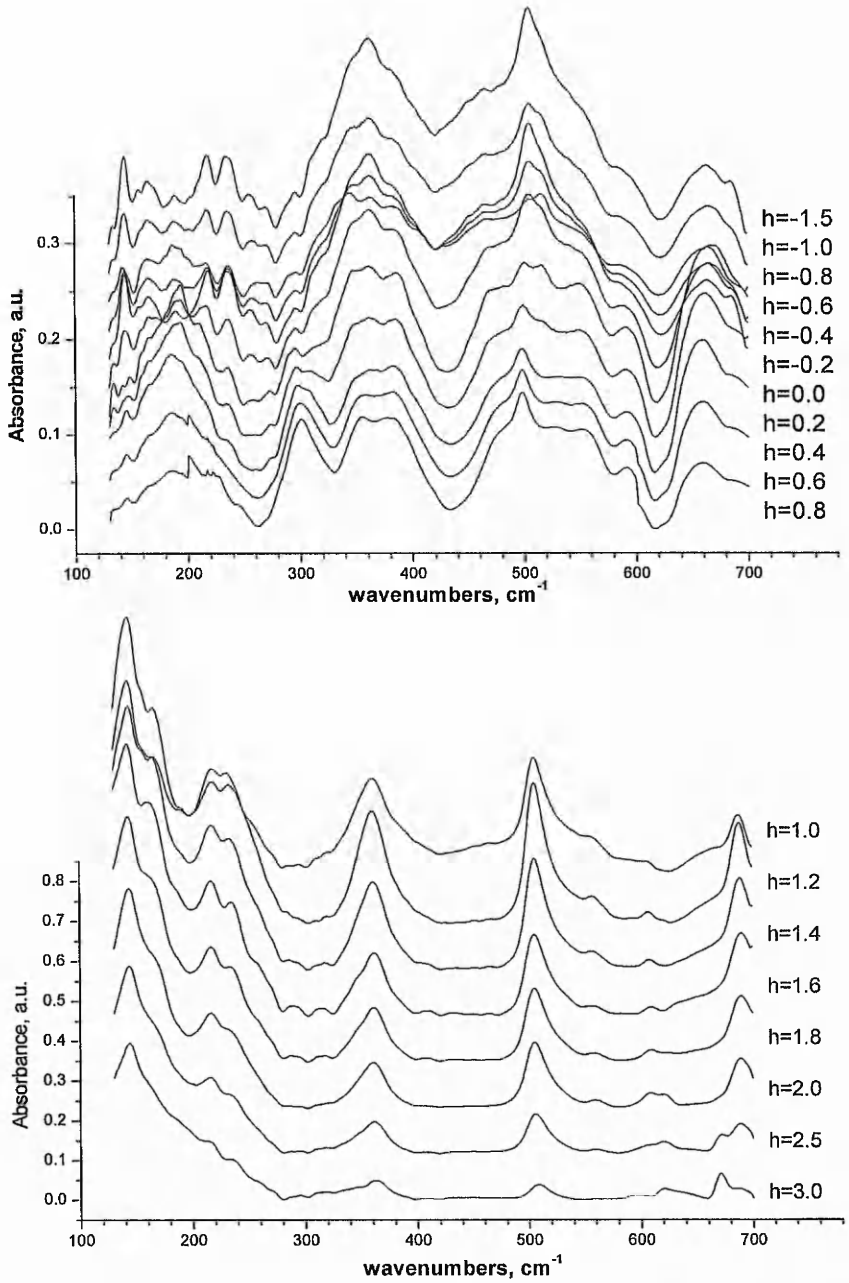


Fig. 5.74. Far-infrared spectra of the series **ZrOHGly1:2**. Y-offset (upper graph) – 120 %; (lower graph) – 100 %.

Bands in the region 300-200 cm^{-1} of the series **ZrOHGly1:2** (Fig. 5.75) relating to the structural features of Zr polymers are located at ca. 273, 255, 237, 218 and 203 cm^{-1}. The degree of degeneration of the bands in this region indicates the presence of the monoclinic form of Zr polymers. However, the increased intensity of the bands at 237 and 218 cm^{-1} may indicate that the tetragonal form of Zr oligomers is dominant. Moreover, with increase of hydrolysis ratio above h~0.8 the bands at 273, 255 and 203 cm^{-1} decrease, while the bands at 237 and 218 cm^{-1} maintain their relatively high intensity up to h~3.0. Therefore, the tetragonal form of Zr polymers dominate the quasi-neutral region of pH and hydrolysis ratios.

At very low frequencies the far-IR spectra of the series with the two-fold excess of glycine

(Fig. 5.75) exhibit an intense composite band with a maximum at 199-193 cm^{-1}. The peak consists of the bands at 193, 187 and 166 cm^{-1} and is most intense at $-0.4 \leq h \leq 0.2$, where it overlaps with bands of structural Zr-O vibrations at 237 and 218 cm^{-1}. The origin of the band is not clear, however it indicates some important changes occurring in Zr polymers in the vicinity of hydrolysis ratio h=0.0. The band at ca. 144 cm^{-1} is observed in all far-IR spectra of the series **ZrOHGly1:2** (Fig. 5.75) and is attributable to structural Zr-O-Zr vibrations of hydrous zirconia. The increasing intensity of the band with increase of hydrolysis ratio indicates a steady transformation of aquo-hydroxo forms of Zr polymers with bound glycine to oxo-forms inherent in the final Zr oxide. An absorbance at 144 cm^{-1} is weak in acidic conditions up to h~0.8 above which this band starts to dominate the far-IR spectral patterns of the series **ZrOHGly1:2**.

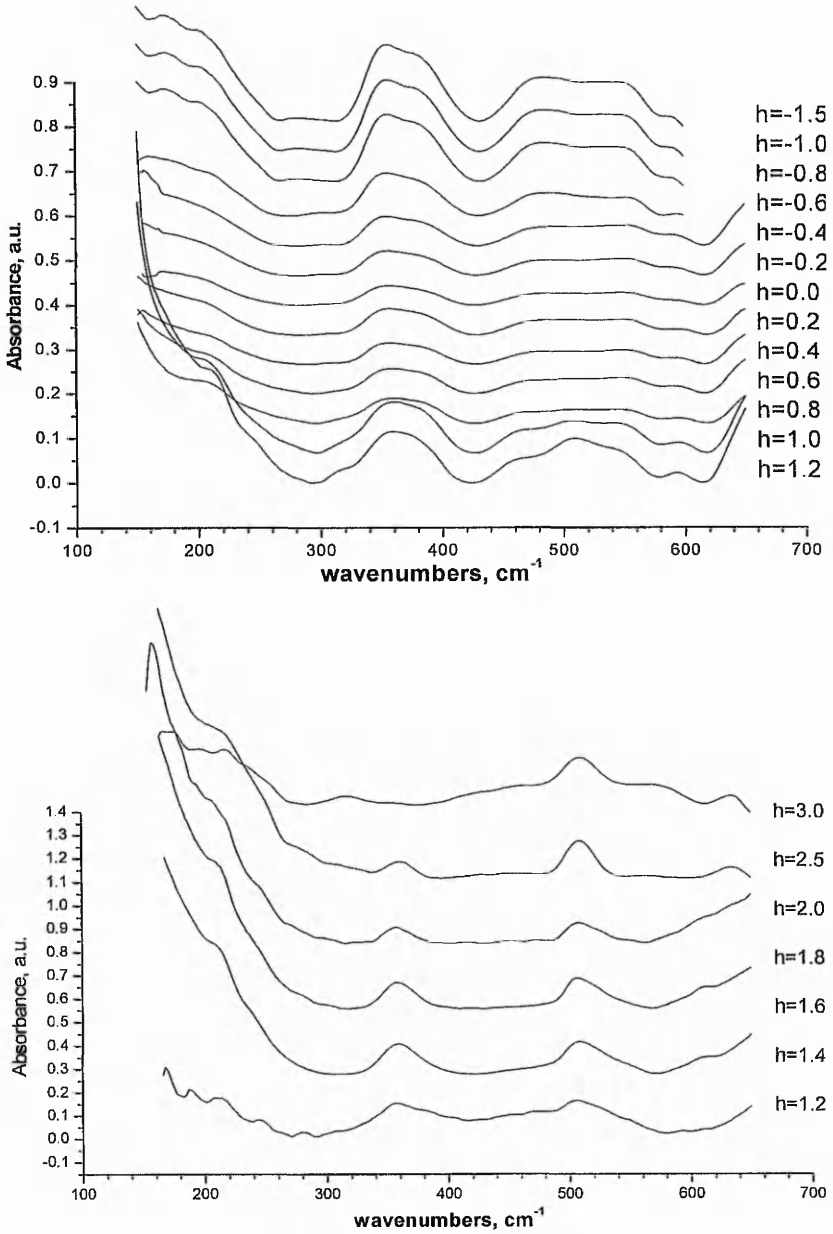


Fig. 5.75. Far-infrared spectra of the series **ZrOHGly1:1**. Y-offset (upper graph) – 100 %; (lower graph) – 80 %.

The far-IR spectra of the series with equimolar quantities of glycine and Zr-ions in the region 700-200 cm^{-1} are shown in Fig. 5.76.

Spectral resolution of the spectra in Fig. 5.76 is significantly lower (4 cm^{-1}) than for the previous series (2 cm^{-1}). Owing to this, the spectra appear to be much 'smoother' than in the case of the series **ZrOHGly1:2**. However, the analysis of the fourth derivative spectra of the series **ZrOHGly1:1** give a very similar set of IR-bands to that for the series with the two-fold excess of glycine. The differences between the series **ZrOHGly1:1** and **ZrOHGly1:2** are as follows:

(1) There is no indication of the monoclinic structure of polymers for the series **ZrOHGly1:1** due to the absence of intense and degenerate bands in the region 300-200 cm^{-1}. Therefore, amorphous Zr polymers dominate the whole region of the hydrolysis ratios studied which agrees well with the lack of long-range order in the PXRD patterns of the same series;

(2) The bands arising from aquo ligands in the range 500-330 cm^{-1} appear to be more persistent over a wider range of hydrolysis ratios for the series **ZrOHGly1:1**.

(3) The band at ca. 303-301 cm^{-1} is weak throughout the series **ZrOHGly1:1** and the highest intensity of this band is reached at h~1.2.

(4) Unlike for the series **ZrOHGly1:2**, in the case of equimolar quantities of glycine the doublet of bands at 347 and 368 cm^{-1} is more intense that the band of ρ(COO-) vibrations (503 cm^{-1}) in the hydrolysis ratio range ($-1.5 \leq h \leq 1.2$).

The far-IR patterns of the series **ZrOHGly2:1** with a deficient amount of glycine (Zr:Gly=2:1) are given in Fig. 5.77. The differences between the series **ZrOHGly1:2** and **ZrOHGly1:1** become more pronounced in this series. The doublet of bands at 347 and 368 cm^{-1} has significantly higher intensity than the set of bands at 590-440 cm^{-1}. Moreover, the band at 347 cm^{-1} is more intense in the spectra of the series **ZrOHGly2:1** than in the previous two glycine containing series. The band at 301 cm^{-1} emerges at h~-0.6 and is clearly observed up to h~1.2, above which it completely vanishes. Three bands dominate the region at 300-200 cm^{-1} at 258, 241 and 221 cm^{-1} in the range of hydrolysis ratios $-0.6 \leq h \leq 1.2$, however, the most intense band is probably located around ca. 144 cm^{-1} (outside the scanned spectral region) indicative of significant amounts of hydrous zirconia present. Comparison with the PXRD patterns of the series **ZrOHGly2:1** indicates that there is an amount of basic Zr-glycinate salts present in the solid samples investigated. However, the structure of this crystalline phase is unclear and does not match any of the known patterns for hydrous zirconia and zirconium basic salts. At higher hydrolysis ratios (h>1.2) only three sets of bands remain in the spectra of the series **ZrOHGly2:1** – the broad band centred at ca. 503 cm^{-1}, the doublet of bands at 347 and 368 cm^{-1} and the set of bands arising from structural Zr-O-Zr vibrations of an hydrous zirconia phase.

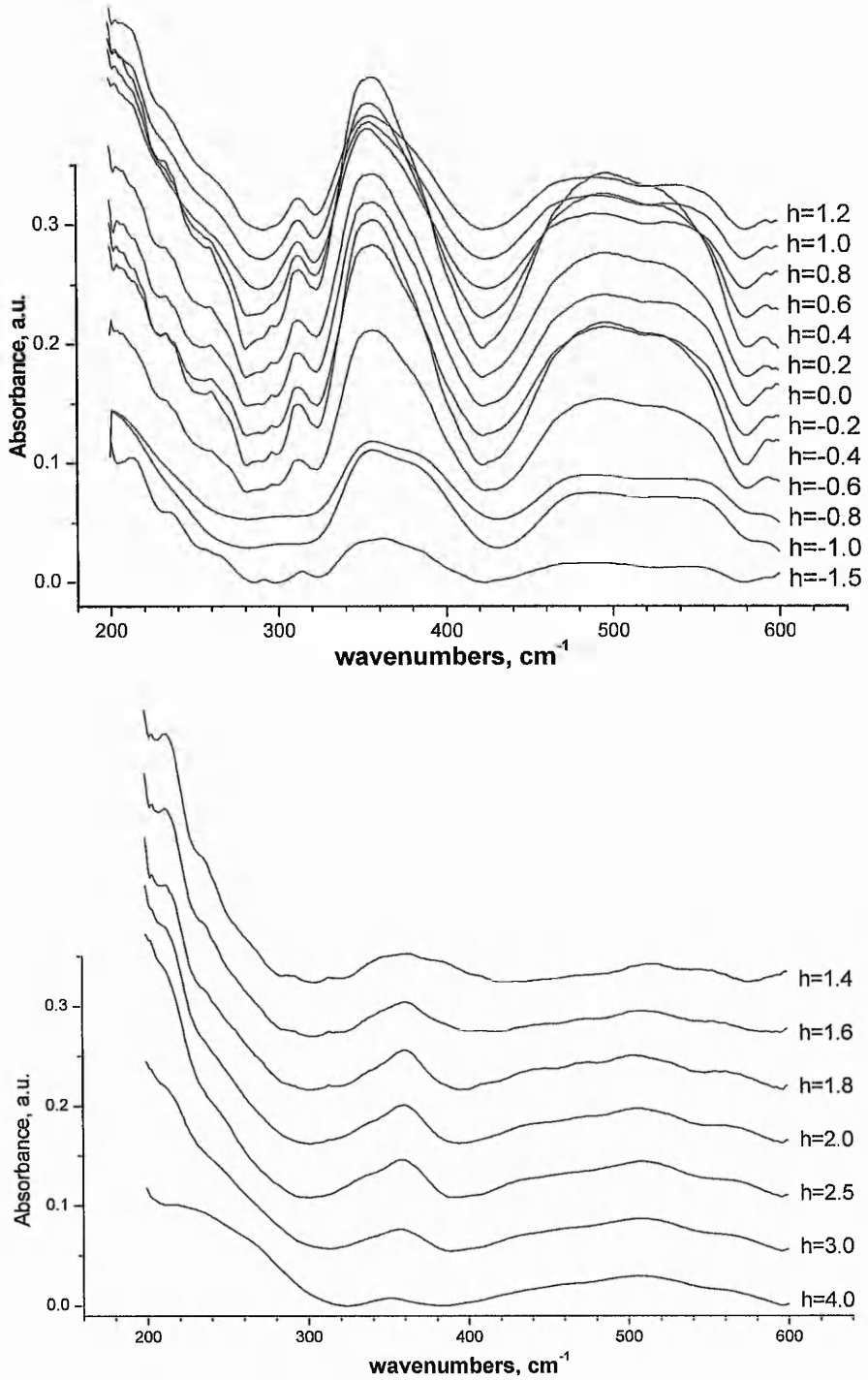


Fig. 5.76. Far-infrared spectra of the series **ZrOHGly2:1**. Y-offset (upper graph) – 120 %; (lower graph) – 100 %.

Integrating together the results of solution studies (dynamic light scattering, Xylenol Orange assay, dynamic light scattering, Chapter 4), the data of PXRD characterisation and the IR-studies of the glycine-containing series described above, it is possible to propose a rational explanation for the phenomenon that prevents the hydrolytic condensation of Zr polymers by glycine in a wide range of hydrolysis ratios and pH, as observed in this work and other studies [60].

Due to premixing of zirconyl chloride solutions with glycine they are allowed to react in a uniform fashion producing bidentate chelating or bridging complexes depending on the conditions of reaction and the 'history' of the zirconyl chloride solution (hydrolysis, ageing, heating, etc.). The following additions of strong alkali or acid do not react with a mixture of pure zirconyl chloride and glycine, but with quite stable complexes of the two reagents. Glycine is unlikely to break down the structure of Clearfield's tetramer. Instead, this ligand partially replaces aquo ligands remaining in the coordination sphere of zirconium-ions, but not completely, as clearly indicated from the IR-data presented here. Glycine binds to Zr oligomers existing in solution and stabilises them.

Two key points should be emphasised in order to explain further events upon addition of alkali or acid: (*1*) zwitter-ionic glycine solutions represent a natural buffer containing both basic and acidic sites; (*2*) the presence of protonated free amino-groups in acidic conditions is another crucial point.

The buffering property of glycine ensures that the pH of solutions of Zr-glycine mixtures is effectively increased. This increase of pH value depends on the concentration of Zr-ions (and, therefore, the initial pH of solution) and the ratio of Zr-ions and glycine. As follows from the data of Table 4.1 (Chapter 4), as a result of addition of glycine to 0.2 M Zr-ion solutions, the value of pH increases from an initial pH~0.7 to pH~1.05 (Zr:Gly=2:1), pH~1.7 (Zr:Gly=1:1) and pH~2.4 (Zr:Gly=1:2). However, due to complexation of Zr-ions with the carboxylic group of glycine this shift of pH does not lead to substantial condensation, as would be observed in pure Zr-ion solutions. Glycine is a relatively strong acid (pK_a=2.3) compared, for instance, with acetic acid (pK_a=4.76). Complexation with Zr-ions effectively reduces the positive charge on Zr-atoms of oligomeric Zr species and makes any remaining aquo ligands significantly less acidic thus leading to the reduced ability of Zr species to hydrolyse in response to increasing pH. As a consequence, no significant amounts of terminal hydroxyl-groups have been detected in the IR-spectra of Zr-glycine complex at ca. 3750 cm^{-1}.

The presence of free protonated amino-group in the complex with Zr-ions plays a crucial role. First, it prevents nucleophilic attack of OH-ligands of hydrolysed Zr species on the electrophilic Zr-atoms of oligomers, either by providing a more available proton of its own, or by the simple electrostatic repulsion between oligomers. This repulsion is the reason for the prevention of condensation events in solutions of Zr-glycine complexes.

With further additions of alkali the pH slowly increases. However, even above the point of zirconia electroneutralisation at h=2.0, the pH of solutions is between 8 and 10 depending on the concentration of glycine. This again demonstrates the buffering properties of the zwitter-ionic glycine. In order to increase pH, the hydroxyl ions of the added alkali

have to neutralise all amino-groups of the bound glycine (pK_b=9.6). The complexation of glycine with zirconium should increase the basicity of the NH_3^+-group even further. Eventually, when all protonated amino-groups are neutralised (deprotonated), hydroxyl-ligands of the alkali are able to complete with glycine for the coordination sites on Zr polymers, albeit this reaction does not occur up to very high hydrolysis ratios (h=3.0-4.0), i.e. at two-fold excess of alkali against Zr-ion concentration.

In the present study zirconyl chloride and glycine solutions have been mixed without any pre-treatment of Zr-ions. This led to the formation of very small oligomeric species containing coordinatively bound bidentate glycine, as observed by the dynamic light scattering measurements (Chapter 4). The presence of the protonated amino-group on the surface of Zr oligomers also effectively protects these species against crystallisation, in spite of a relatively high overall charge of the species, as supported by the absence of long-range ordering in the corresponding PXRD patterns of the glycine-containing series with the ratios Zr:Gly 1:1 and 2:1.

Concluding the discussion on Zr-glycine complexes it is necessary stress that this experimental system could be a promising precursor for interesting Zr-containing materials, and the approach of complexation (with glycine) for adjustment of the properties of the inorganic precursor could be extended on other easily hydrolysing metal ions. The attempts to understand the complex chemistry of Zr-glycine systems would highly favour this direction.

References:

1. Modern Fourier Transform Infrared Spectroscopy / Ed. by A.A. Christy et. al. (2001) Amsterdam: Elsevier, 376 p.
2. J.-J. Max, C. Chapados. Appl. Spectrosc. (1999) **9** 1045-1053.
3. A. Hennessy et. al. J. Synchrotron Radiat. (2002) **9** 323-324.
4. F. Iskandar et. al. J. Colloid Interf. Sci. (2003) **265** 296-303.
5. L.M. Bull et. al. Stud. Surf. Sci. Catal. (1994) **84** 429-434.
6. O.V. Pupysheva et. al. Inorg. Mater. (1997) **33** 951-955.
7. S.V. Kalinin et. al. J. Sol-Gel Sci. Technol. (1995) **4** 31-35.
8. J. Rowsell, L.F. Nazar. J. Am. Chem. Soc. (2000) **122** 3777-3778.
9. S.M. Bradley et. al. Inorg. Chem. (1992) **31** 1181-1185.
10. J.W. Akitt. Prog. Nucl. Mag. Res. Sp. (1989) **21** P. 1-2, 1-149.
11. T.J. Bastow et. al. Mater. Lett. (1994) **18** 197-200.
12. X.S. Zhao et. al. J. Mol. Catal. A (2003) **191** 67-74.
13. I. Noda. J. Am. Chem. Soc. (1989) **111** 8116-8118.

14. D. Adachi (Kwansei Gakuin Univ.,Japan). Computer program 2D-Pocha for Windows 95.
15. Science and technology of zirconia / Ed. by A.H. Heuer and L.W. Hobbs (1981) Columbus, The American Ceramic Society, 479 p.
16. S.M. Bradley, J.V. Hanna. Chem. Comm. (1993) 1249-1251.
17. JCPDS Powder diffraction file, card No 47-0815 ($ZrOCl_2*6H_2O$)
18. JCPDS Powder diffraction file, card No 18-1497 ($ZrOCl_2*4H_2O$)
19. JCPDS Powder diffraction file, card No 15-0440 ($ZrOCl_2*2H_2O$)
20. JCPDS Powder diffraction file, card No 15-0337 ($ZrO(ClO_4)_2*3H_2O$)
21. A. Clearfield. Rev. Pure and Appl. Chem. (1964) **14** 91-108.
22. J.I. Tosan et. al. J. Non-Cryst. Solids (1993) **160** 167-176.
23. A.A.M. Ali, M.I. Zaki. Thermochim. Acta (2002) **387** 29-38.
24. K. Matsui, M. Ohgai. J. Ceram. Soc. Jpn. (1998) **106** 1232-1237.
25. H.-J. Noh et. al. Mater. Lett. (2003) **57** 2425-2431.
26. G.K. Chuah. Catal. Today (1999) **49** 131-139.
27. I.C. Smith, B.L. Carson. Trace Metals in the Environment (1978) V. 3 (Zirconium) 373-383.
28. A. Singhal et. al. J. Colloid Interf. Sci. (1997) **194** 470-481.
29. J.L. Tosan, B. Durand, M. Roubin, F. Bertin, H. Loiseleur. Eur. J. Solid State Inorg. Chem. (1993) **30** 179-193.
30. G.M. Muha, P.A. Vaughan. J. Chem. Phys. (1960) **33** 194.
31. H. Cölfen et. al. Langmuir (2002) **18** 3500-3509.
32. W. Stumm, J.J. Morgan. Aquatic Chemistry. An Introduction Emphasizing Chemical Equilibria in Natural Waters. (1981) New York, Wiley andSons, 780 p.
33. M. Yashima et. al. J. Mater. Res. (1997) **12** 2575- 2583.
34. M.J. Adams. Chemometrics in Analytical Spectroscopy (1995) London, RSC, 216 p.
35. K. Nakamoto. Infrared and Raman spectra of inorganic and coordination compounds. Parts A, B (1997) New York – Chichester, John Wiley.
36. S. Sjoberg, L.O. Ohman. J. Chem. Soc. Dalton (1985) 2665-2669.
37. The infrared spectra handbook of inorganic compounds (1984) Philadelphia, Sadtler Research Laboratories.
38. J.J. Fitzgerald. Chemistry of aluminium hydrolysis complexes. In: Antiperspirants and Deodorants (1988) New York, Marcel Dekker, 119-296.
39. D.A. Riesgraf, M.L. May. Appl. Spectrosc. (1978) **32** 362.
40. J.T. Kloprogge, R.L. Frost. Spectrochim. Acta A (1999) **55** 163-169.
41. J.T. Kloprogge, R.L. Frost. Thermochim. Acta (1998) **320** 245-252.

42. K. Wefers, C. Misra. Oxides and Hydroxides of Aluminum. Alcoa Technical Paper No 19, Revised (1987) Acoa, 92 p.
43. A. Aboulayt et. al. J. Chem. Soc. - Faraday Transac. (1995) **91** 2913-2920.
44. C.K. Loong et. al. Journal of Catalysis, (1995) **157** 636-644.
45. K.T. Jung, A.T. Bell. Journal of Molecular Catalysis A (2000) **163** 27-42.
46. M. Maczka et.al. Journal of physics and chemistry of solids (1999) **60** 1909-1914.
47. P. Bouvier et. al. Int. J. Inorg. Mater. (2001) **3** 647-654.
48. R.C. Taylor, G.L. Vidale. J. Am. Chem. Soc. (1956) **78** 5999.
49. J.I. Tosan et. al. Annal. Chim. Sci. Mater. (1991) **16** 595-606.
50. G.V. Kozhevnikova et. al. Izvestiya Akademii Nauk SSSR, Neorganicheskie Materialy (1988) **24** 470-473.
51. P. Jakubus et. al. J. Thermal Anal. Calorim. (2003) **72** 299-310.
52. Burkov K. A. et al. Russ. J. Inorg. Chem. (1982) **27** 1427-1431.
53. K. Matsui, H. Suzuki, M. Ohgai, P. Arashi. J. Am. Ceram. Soc. (1995) **78** 146-152.
54. A.P. Mirgorodsky et. al. J. Phys. Chem. Solids (1999) **60** 985-992.
55. M. Gardener. Ph.D. thesis (2000) The Nottingham Trent University, Nottingham, UK.
56. A. Nagai et. al. J. Mater. Sci. (1995) **30** 3333-3338.
57. R.P. Oertel, M.R. Rush. Appl. Spectrosc. (1979) **33** 14.
58. I.M. Hodzic, S.R. Niketic. J. Serb. Chem. Soc. (2001) **66** 331-334.
59. 6. H. Rosenberg, J.J. Fitzgerald. Chemistry of Aluminum-Zirconium-Glycine (AZG) complexes Chlorohydrates. In: Antiperspirants and Deodorants / Ed. by K. Laden (1999) New York, Marcel Dekker, 83-136.
60. F.R. Tortonda, et. al. J. Mol. Struct. - THEOCHEM (2003) **623** 203-210.
61. D.T. Callaghan, A.M. Phipps. (1985) Antiperspirants, Bitish UK Patent Application GB2, 144, 992A.

CHAPTER VI Summary

The aim of this Chapter is to summarise in a systematic fashion the experimental findings on aluminium and zirconium speciation in solutions and colloidal state described in Chapters 3 and 4 of the present study, as well as the results of investigation of the solid materials reported in Chapter 5. The discussion will be divided into modules according to major processes occurring in aqueous solutions of aluminium and zirconium ions: hydrolysis and condensation of Al and Zr ions, colloid formation of the corresponding Al hydroxides and Zr hydrous oxides, structural arrangement of the solid materials obtained from the hydrolysed solutions of the metal ions in question, as well as the effect of anions and complexing agents on the hydrolytic processes occurring in solutions, colloidal and solid state.

6.1. Aqueous chemistry of aluminium ions

The studies of hydrolysis-condensation of aluminium-ions in the present study were limited mainly to medium aluminium concentrations in solutions (0.05-0.2 mol/L). Alkaline titration was chosen as a major method for carrying out hydrolysis-condensation experiment. Strongly acidic pH values were achieved by the additions of different amount of acids (mainly HCl). In the conditions of medium to high concentration of Al-ions several oligomers (dimers and possibly trimers) and larger polycations (Al_{13} and Al_{30}) are known form [1-3].

The majority of the experimental findings in the present study were presented on the hydrolysis ratio scale (h=[OH^-]/Me^{z+}]). This scale has several advantages over the commonly used pH-scale: (*a*) it is virtually unlimited, convenient and universal; (*b*) it does not depend on the concentrations of metal ion and alkali; (*c*) it maintains a link with the structure of the hydrolytic complexes of metal ions which depends on the number of metal ions and hydroxyl-ligands [4]; (*d*) precision of the hydrolysis ratio parameter and resolution of the corresponding scale depends only on the experimental error associated with the concentrations of metal ion and alkali and can be easily optimised, e.g. by a careful standardisation of stock solutions; (*e*) acidic and alkaline scales can be easily unified into a single scale by replacing the formula h=[OH^-]/Me^{z+}] with h=[H^+]/Me^{z+}]. However, the latter feature does not bear physical meaning and serves mainly for presentation purposes. The relationship between hydrolysis ratio and pH of aqueous solutions of metal ions, albeit not straightforward, nonetheless can be simplified by considering the fact that at hydrolysis ratios equal to the formal ratio of the corresponding metal hydroxide ($Al(OH)_3$, h=3.0 and $Zr(OH)_4$, h=4.0) pH values are close to neutral. Below this point pH is acidic, and above – alkaline. The use of the hydrolysis ratio scale is slightly more convenient than the ligand number scale widely used in the thermodynamic studies [5], since the former does not contain a term related to 'intrinsic' acidity (or basicity) of metal ion solution due to autohydrolysis which has to be known or measured experimentally.

6.1.1. Monomeric hydrolysis of Al-ions

Hydrolysis of Al-ions can proceed spontaneously to some extent ($pQ_{1,1}$=4.97 [5]). Acidity of the native solution of Al-ions in the presence of non-complexing anions (chloride, nitrate, perchlorate) increases (e.g. pH~2.73 in 0.1 M solutions of $AlCl_3$) thus preventing further autohydrolysis. Therefore, initial medium-concentrated Al-ion solutions contain a mixture of hexaaquo-cation $[Al(H_2O)_6]^{3+}$ and hydrolysed monomeric species (mainly $[Al(H_2O)_5OH]^{2+}$) (Eq. 1.25): Some amount of Al dimers $[Al_2(OH)_2(H_2O)_4]^{4+}$ can be also detected in the initial Al-ion solutions depending on the concentration of Al-ions and the time span between solution preparation and the start of actual experiment (measurement).

Even upon tiny additions of alkali, Al-ions start to hydrolyse extensively. Potentiometric measurements of the present work reflect this process by the inflexion point at h<0.3, in good agreement with the other studies [6, 7]. This inflexion is mainly attributed to further formation of the hydrolysed monomeric Al species. The ^{27}Al solution NMR data indicates (Chapter 3) that the inflexion at h<0.3 is primarily related to the monomeric hydrolysis of Al-ions, since no large amounts of oligomeric species are detected in these conditions by ^{27}Al NMR. Moreover, as our investigations have shown [9], the signal from the monomeric Al species at ca. 0.0 ppm fluctuates upon titration with alkali showing the trend to increase from δ ca. –0.3 - -0.2 ppm at h≤2.0 to δ~0.2 ppm at h>2.0 (titration of 0.1 M $AlCl_3$ solution with 1 M NH_4OH, cf. Fig. 3.15, Chapter 3). It can be assumed that the signal at ca. 0.0 ppm is of a composite structure and contains signals from all monomeric Al species observed in solutions. A practical conclusion also arises from the trend described above that the use of the signal at ca. 0.0 ppm as a reference for calibration of the chemical shift scale is irrelevant due to these fluctuations. Application of the highly stable signal from the internal standard of at 80 ppm is a better choice.

The monomeric Al species are observed in solutions of hydrolysed Al-ions in a very wide range of hydrolysis ratios (h≤2.6-2.8, Chapter 3). The presence of this species is important for the formation of Al polycations as discussed below.

6.1.2 Formation of large aluminium polycations

The Partial charge model calculations (cf. Table 1.4, Chapter 1) indicate that the monohydrolysed species $[Al(H_2O)_5OH]^{2+}$ is a reactive nucleophile. This species is primarily involved in the formation of oligomeric Al species [10]. When the pH of the solution increases, substantial amounts of this species are accumulated. Condensation then starts to proceed via formation of the smallest oligomers (Al dimers) first (Eq. 1.29). This process appears to be reversible and slower than monomeric hydrolysis. Quantitative ^{27}Al solution NMR measurements show (section 3.3.3) that the optimum conditions for the formation of Al dimers appear to be in the vicinity of h~1.0 which corresponds to the formal hydrolysis ratio of this species (OH/Al=1.0). The fraction of Al dimers never exceeds ca.30-35 % of the total Al-ion concentration. Optimum pH conditions for the formation of Al dimers are

approximately within 3.5≤pH≤4.0.

Further increase of hydrolysis ratios (h>1.0) and pH (pH>4.0) leads to the increasing predominance of the Al_{13}-mer. An extensive discussion of the possible mechanistic pathways for the formation of this species can be found in the literature [3, 10-12]. Two major models have been proposed. In the first model Al trimers condense around Al monomer that is initially 6-coordinated, but that looses coordinated oxygens as the Al_{13} molecule forms (Fig. 6.1).

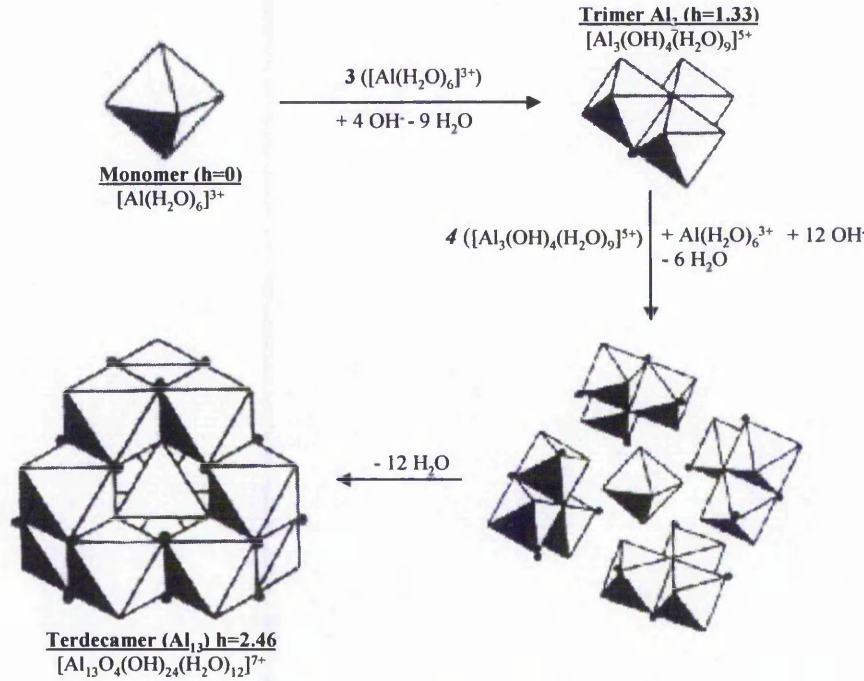


Fig. 6.1. The possible pathway of the Al_{13}-mer polycation formation according to [4, 10].

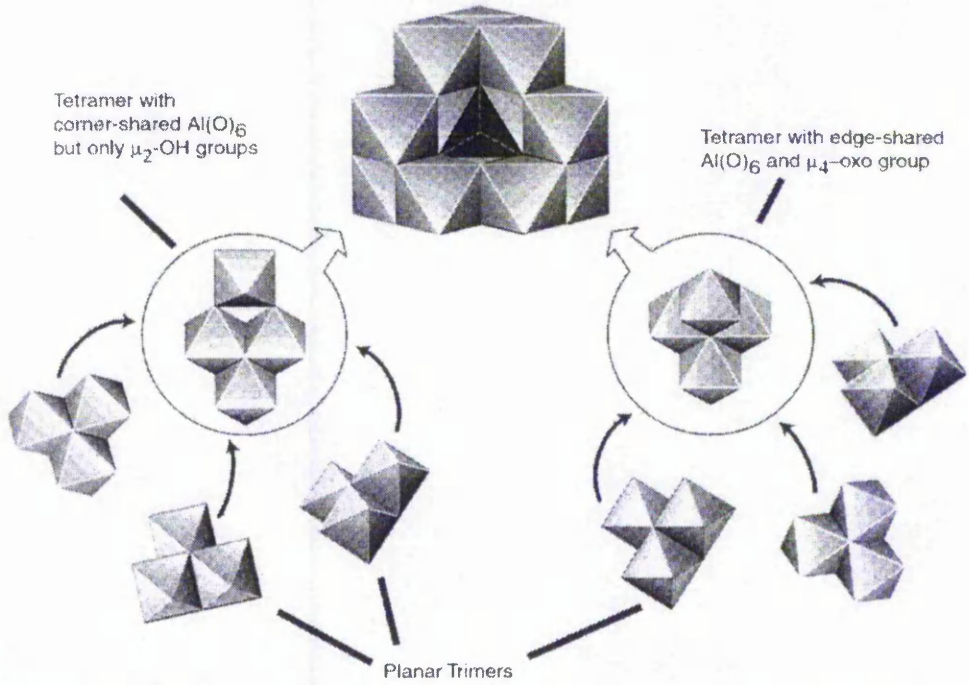


Fig. 6.2. Two pathways of the Al_{13}-mer formation proposed by Michot et. al [12].

Michot et. al [12] have developed further this concept postulating that the key reactants are sets of planar trimers that react with a yet-unidentified tetramer to form the ε-Keggin structure (Fig. 6.2). One tetramer consists of a corner-shared AlO_6 octahedra bonded to a planar trimer (Chapter 1). Such tetramer has been detected in EXAFS spectra [12]. The other tetramer shown in Fig. 6.2 contains a AlO_6 group that shares edges with a planar trimer. This tetramer, yet to be identified spectroscopically, contains a μ_4-group that may facilitate the formation of ε-Keggin molecule of the Al_{13}-mer, since the AlO_6 group can become the central AlO_4 core of the Al_{13}-mer molecule by loss of two bound waters and rotation [3].

The second model of the Al_{13}–mer formation invokes the presence of excess of the $Al(OH)_4^-$ ion in solution during synthesis [13,14] as a source of AlO_4 in the Keggin ion. In this model Al trimers condense around aluminate-ion created locally at the site of poor titrant mixing. The relevance of the second model has been questioned by Brinker and Scherer [11] who doubted the existence of the $Al(OH)_4^-$ ion in acidic solution. In the recent review [3] Casey et. al summarise that both models are reasonable.

Most authors agree that the planar trimers $[Al_3(OH)_4]^{5+}$ are the fundamental building blocks for the ε-Keggin molecules. However, this species is yet to be identified directly [3, 10]. Early potentiometric studies, though, are consistent with the presence of this moiety in Al-ion solutions [5]. Casey et. al. [3] indicate that there is some spectroscopic hint of the presence of trimers in concentrated Al(III) solutions as there is sometimes a relatively narrow peak that is evident at ca. 11 ppm. Authors suggest that the assignment of this peak to the planar Al trimer is supported by the similarity of the chemical shift to that of the AlO_6 'shell' of the Al_{13} complex. However, the authors of the study [15] assign this peak to very fine colloidal particles of aluminium hydroxide. A similar peak at ca. 15-16 ppm in the ^{27}Al NMR spectra of hydrolysed solutions was also observed in this work (Chapter 3). The peak can be distinguished more clearly after peak fitting procedure carried out with the NMR spectrum (Fig. 3.21).

Another important question arising from the mechanistic studies of the Al_{13}-mer formation is concerning the role of Al dimers in the formation of hypothetical Al trimer and ε-Keggin ion: is the $[Al_2(OH)_2(H_2O)_8]^{4+}$ ion involved in the formation of larger polynuclear species, or it is just a 'side product' on the pathway leading to the Al_{13}-mer ? Some authors doubt the presence of this species itself in solutions [10,16]. Akitt and Elders [17] have re-dissolved in dilute solutions the crystalline Al sulphate containing Al dimers [18] and observed a signal at ca. 4 ppm in the ^{27}Al NMR spectra. They concluded, however, that the dimer decomposes in solution and hydrolyses to form a higher order complex, such as trimer and monomeric species. Casey et. al [3] has emphasised that like most polynuclear oxo- or hydroxo complexes and the surfaces of oxide minerals, Al dimers are amphoteric in water and can dissociate by pathways that involve either proton uptake at a hydroxyl-bridge or proton release from a bound water molecule.

From the electrostatic point of view the Al dimer species are quite inert both towards hydrolysis and condensation. As follows from the PCM parameters calculated in the present study (Table 1.4, species 1), mean electronegativity of the $[Al_2(OH)_2(H_2O)_8]^{4+}$ ion is χ_t=2.716 that corresponds to preferably acidic conditions for the existence of this species (pH_{H2O}=0.5). For comparison, the closest values of χ_t are those of the Al hexaaquo-cation and mono-hydrolysed monomer (χ_t=2.757 and χ_t=2.679 respectively). The Al dimer possesses relatively inert bridging hydroxyl-groups (δ(OH)=0.001) and quite acidic aquo ligands ($\delta(H_2O)$=0.105). Therefore, dissociation of this complex via cleavage of the bridging OH-groups is not favoured. Further hydrolysis of the Al dimer can be tested by the assumption that $[Al_2\mu_2(OH)_2\mu_1(OH)(H_2O)_7]^{3+}$ (species I) or $[Al_2\mu_2(OH)_2\mu_1(OH)(H_2O)_7]^{3+}$ (species II) ion are formed. The PCM calculation in this case leads to the following results (species I: χ_t=2.666; δ(OH)=-0.0068; $\delta(H_2O)$= 0.081; pH_{H2O}=1.9; species II: χ_t=2.612; δ(OH)= -0.0111; $\delta(H_2O)$= 0.056; pH_{H2O}=3.4). Hence, further hydrolysis of Al dimers leads to more basic species with increasingly negative average partial charges on hydroxyl-ligands. Therefore, upon hydrolysis Al dimers become (*a*) less stable; (*b*) more reactive, which makes this process unfavourable. One can assume that Al dimers could rather participate in the following reaction leading to the trimer species:

$$[Al_2(OH)_2(H_2O)_8]^{4+} + [Al(H_2O)_5OH]^{2+} \rightarrow [Al_3(OH)_4(H_2O)_9]^{5+} + 3H_2O + H_3O^+ \quad \textbf{(6.1)}$$

Electronic properties of the Al trimer closely resemble those for the Al dimer (Table 1.4), albeit only average values are available for the μ_2 and μ_3 OH-groups of the trimer. Alam and Henry [19] have shown that electronic properties of silicates calculated by the Partial charge model are closely related to the corresponding ^{29}Si NMR parameters. By analogy, one can assume that Al dimers and trimers possess similar ^{27}Al NMR signals at ca. 4 ppm. Moreover, from the ^{27}Al solution NMR spectra acquired in the present study one can find that the peak at ca. 4 ppm actually fluctuates between ca. 2.3 and 4.3 ppm. Due to strong overlap of this signal with highly intense signal from the sum of monomeric species at ca. 0.0 ppm at lower hydrolysis ratios (h<1.0) and with the signal from octahedral Al shell of the polycations at ca. 10 ppm at higher hydrolysis ratios, exact identification of the peak position at ca. 4 ppm is a difficult task. However, there is a certain trend for this signal to shift with increase of hydrolysis ratio. One can hypothesise that the peak at 4 ppm is of composite structure and contains a signal from both dimer and trimer. This would explain fluctuation of the signal position with increase of hydrolysis ratio as well as the data of Akitt and Elders on the re-dissolution of the dimer-containing aluminium basic sulphate [17]. The 'disproportionation' of dimers observed in the work [17] was probably caused by strong dilution of the samples which led to destabilisation of the Al dimer molecule and to the occurrence of both acidic cleavage into the monomer as well as condensation into the trimer.

Analysis of the electronic properties of Al trimer also suggests that this species is relatively stable in mildly acidic solutions (pH_{H2O}=0.6), at least in terms of the mean

electronegativity. This fact probably led the authors of the work [10] to consider the formation of more reactive trimeric species which can attack hexacoordinated Al monomer with the formation of AlO_4 core of the Al_{13}-mer (described in detail in section 1.3.5). One can also assume that in ideal conditions with no local perturbations due to insufficient mixing of alkali, the trimeric species would be stable up to hydrolysis ratios around h~1.33 which corresponds to the theoretical ratio for the Al trimer. At this point all dimers would convert into trimers with little or no Al_{13}-mer present. Incomplete transformation of Al monomers into dimers and then into trimers could arise from high lability and easy dissociation of small oligomers into monomers. The average value of δ(OH) for the trimer is close to zero (Table 1.4), which can indicate that highly acidic character of the μ_3 hydroxo-bridge (partial charge of μ_3 OH-group is expected to be positive) is probably compensated by slightly positive charges of three μ_2 OH-bridges. This makes μ_2 OH-bridges of the Al trimer susceptible to the protonation and subsequent cleavage which may lead to the dissociation of the trimeric species. In practice, the signal of the Al_{13}-mer is observed very early in the course of alkaline titrations (h~0.5). The reason for this apparent discrepancy will be explained below. The PCM calculations also show that further hydrolysis of the planar Al trimer is quite unlikely due to extreme acidity of the hydrolysed products.

Above the hydrolysis ratio h=1.33 (the formal ratio of the $[Al_3(OH)_4(H_2O)_9]^{5+}$) the trimeric species starts to convert into Al_{13}-mers. It is well known [3,5] that the ε-Keggin ion forms very quickly (from seconds to minutes according to the review [3]). The observations using ^{27}Al NMR spectroscopy suggest the same (Chapter 3). If to assume the formation of the Al_{13}-mer from 3 trimers and 1 tetramer [12], it is clear that the process schematically depicted in Fig. 6.2 requires the presence of the precursor molecules in abundance in order to maintain such a high formation rate of the Al_{13}-mer (the formal order of the reaction via 3 trimers and 1 tetramer is 4). This would be the case if all species relating to the signal at 4 ppm in ^{27}Al NMR spectra would be trimers. The incomplete formation of the tridecameric species after several minutes of the alkali addition even at 90°C observed in the time-resolved *in-situ* ^{27}Al NMR spectra (section 3.2.4) indicates that the amount of trimers at this point of the process is insufficient for conversion of all Al-ions into Al_{13}-mers. Longer times are required in order to complete this transformation (from one hour at room temperature to 15-30 min at 90°C, Chapter 3). Therefore, the concentration of the Al trimer limits the extent and the rate of the Al_{13}-mer formation.

NMR measurements of Al speciation in this study (Chapter 3) detected the presence of Al dimers (or a mixture of dimers and trimers according to the remarks above) in the hydrolysis ratio range $0.0 \leq h \leq 2.4$. Quantitative analysis of the NMR data indicates that the fraction of Al dimers exhibits behaviour reciprocal to that of the Al_{13}-mers in the range $1.5 \leq h \leq 2.4$. However, a relatively low value of the correlation coefficient ($R^2 = -0.68$) does not allow for unequivocal conclusion on the direct consumption of small Al oligomers during the formation of Al_{13}-mer. One can suggest that due to highly labile nature of the Al dimer and

trimer these species at relatively low pH can either convert into the Al_{13}-mer, or dissociate to form monomers.

Concerning the formation of the tetrameric Al oligomer from the trimeric species [12], the Partial charge model allows for evaluation of feasibility of this hypothesis. Electronic parameters of two hypothetical tetramers [3]: edge-sharing $[Al_4(OH)_4(H_2O)_{13}]^{8+}$ (h=1.0) and corner-sharing $[Al_4(OH)_6(H_2O)_{11}]^{6+}$ (h=1.5) were calculated for this purpose. For the edge-sharing isomer the PCM parameters are: χ_t=2.755; $\delta(OH)$= 0.0049; $\delta(H_2O)$= 0.123; pH_{H2O}= -0.6. The corner-sharing tetramer has the following parameters: χ_t= 2.697; $\delta(OH)$= -0.001; $\delta(H_2O)$= 0.096; pH_{H2O}= 1.0. From the comparison of two possible isomers of the tetrameric complex, one can easily derive that the corner-sharing configuration is preferable. The edge-sharing unit possesses a highly positive average partial charge on hydroxyl groups which makes this species unlikely to exist [4,10]. The corner-sharing configuration exhibits electronic parameters very close to those of the dimer and trimer. The value of mean electronegativity is somewhat lower which leads to a lower value of pH_{H2O} = 1.0. The partial charge of the corner-sharing tetramer is slightly more negative comparing to nearly zero-values of dimer and trimer, nonetheless it is quite close to zero value as well indicating that this species are fairly stable. The value of hydrolysis ratio of the corner-sharing tetramer is h=1.5 which is in between h=1.33 for the trimer and h=2.46 for the Al_{13}-mer, which also makes it a feasible candidate for an intermediate in the synthesis of the ε-Keggin ion.

Considering the remarks above, one can hypothesise the following order of the species appearance on the hydrolysis ratio scale (Fig. 6.3):

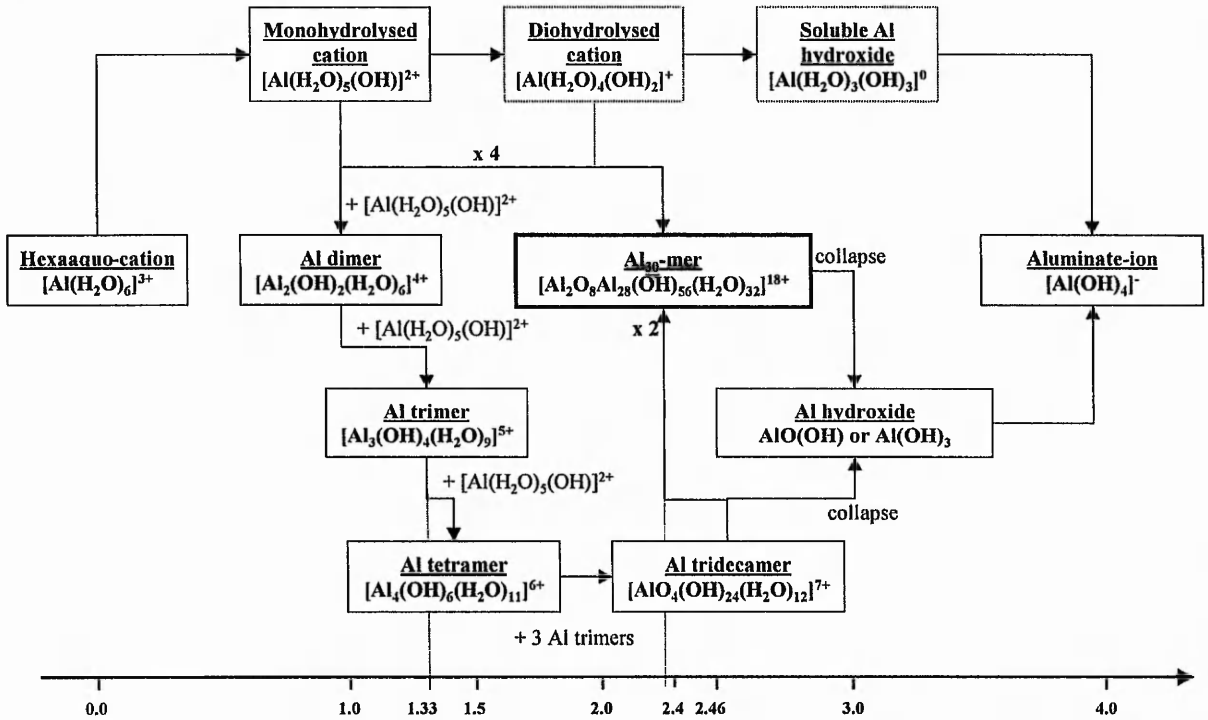


Fig. 6.3. Schematic speciation pathways of Al-ion hydrolysis-condensation (dashed frames indicate tentative ions at high Al-ion concentrations; bold frame indicates that ion is present at high temperatures; dashed lines show the hydrolysis ratio of the species or tentative involvement in the reaction pathway).

From Fig. 6.3 one can see that the value of hydrolysis ratio dictates the species distribution. Another important feature follows from the scheme in Fig. 6.3 is that monohydrolysed $[Al(H_2O)_5(OH)]^{2+}$ species are involved in the formation of all known and hypothetic polycations. Therefore, the presence of this species is crucial in the synthesis of larger oligomers. One can see that the corner-sharing Al tetramer (h=1.5) proposed in the work [12] well fits the gap between Al dimers, trimers and Al_{13}-mers on the hydrolysis ratio scale.

In order to form the Al_{13} moiety, trimers or tetramers must convert into more acidic state, such as edge-sharing tetramer containing highly acidic μ_4-bridges. These acidic species then react with a single monomer by removing two waters from its coordination sphere and converting it into tetrahedral AlO_4 unit.

Electronic properties obtained from PCM calculations exhibit strong dependence on the formal hydrolysis ratio of the species involved in hydrolysis-condensation reactions of Al-ions. As an example, the relationship between the value of mean electronegativity and formal hydrolysis ratio of Al monomers and polycations is presented in Fig. 6.4.

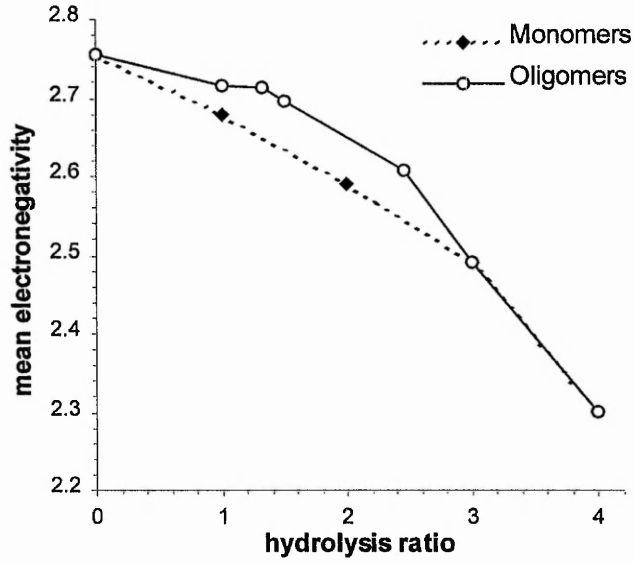


Fig. 6.4. Relationship between mean electronegativity of the Al species (monomers and oligomers) and their formal hydrolysis ratio.

From Fig. 6.4 one can find that although mean electronegativities of Al monomers and oligomers follow the same trend on the hydrolysis ratio scale, there is a significant gap between two curves in the range $0.0<h<3.0$. The reason for this gap is not identified yet, however, once explained, it would greatly assist fundamental understanding of the formation of the metal polynuclear species and related phenomena.

The formation of the Al_{30}-mer species has been discussed in the recent publications [3, 20, 21]. This species dominates the speciation patterns of Al-ions at high temperatures as shown in Fig. 3.41 (Chapter 3). The hydrolysis ratio range of the Al_{30}-mer existence is somewhat more acidic than that of the Al_{13}-mer. This fact arises from slightly lower value of the formal hydrolysis ratio of the Al_{30}-mer (h=2.40) compared with the same value for the

Al_{13}-mer (h=2.46). The formation of Al_{30}-mers proceeds directly from 4 equivalents of the monomeric species and 2 equivalents of the Al_{13}-mer without any intermediates detectable in the ^{27}Al NMR spectra. Authors of the study [21] have detected a signal at ca.64.5 ppm and assigned it to the δ-form of the Al_{13}-mer postulated as a direct intermediate to the Al_{30}-mer molecule. A similar signal in the ^{27}Al NMR spectra of Al-ion solutions hydrolysed at high temperature in the range $2.0<h<3.0$ was also observed in this work (Fig. 3.36). However, the signal was very weak and inconsistent due to relatively low resolution of the NMR spectrometer and strong noise mainly arising from the presence of significant amounts of Al hydroxide at high hydrolysis ratios. Nevertheless, it is quite clear that Al monomers and Al_{13}-mers are the major synthons for the synthesis of the Al_{30}-mer.

6.1.3. Kinetics of the formation of large Al polycations

The data of the time-resolved speciation diagrams calculated on the basis of quantitative ^{27}Al NMR measurements show the importance of kinetics in the transformation of Al_{13}-mers into larger species (Fig. 3.41). The Al_{13}-mer ion dominates the diagrams in quite wide range of hydrolysis ratios ($1.6\leq h\leq 2.6$) and pH ($3.8\leq pH\leq 5.9$) at the early stages of the high-temperature time-resolved experiments up to ca. 6 hours. After this time period, Al_{30}-mer ions start to dominate the dynamic equilibrium. This species is extremely thermally stable, is supported by virtually constant concentration of the Al_{30}-mer in mildly acidic conditions over 48 hours of the experiment at 90°C. The possible reason for such high stability is structural stabilisation of the δ-form of the Al_{30}-mer [20] compared with the strained ε-form of the Al_{13}-mer. Obviously, significantly longer experimental monitoring of the Al_{30}-mer breakdown is required in order to estimate corresponding kinetic rate.

Estimation of the kinetic rates of the formation-dissociation of the large Al polycations reveals the differences in the dynamics of the Al_{13}-mer and Al_{30}-mer. Both species exhibit the highest formation rates in the range of hydrolysis ratios $2.0<h<2.8$, however, the rate of the Al_{13}-mer formation is at least 2 orders higher than a similar value for the Al_{30}-mer. The rate of the Al_{13}-mer breakdown in acidic pH is also very high and the process is reciprocal to the evolvement of the monomer in the early time of experiment. It was impossible to estimate the rates of the Al_{30}-mer dissolution due to high stability of this species. At hydrolysis ratios below ca. h~1.0 the signal arising from the Al_{30}-mer was too weak to be detected and evaluated kinetically.

The kinetics of the Al monomer evolvement in the optimum conditions for the synthesis of Al_{13} and Al_{30} ($2.0<h<3.0$) indicate a complex behaviour which arises from the fact that this is the only species produced from the acidic dissociation of the Al_{13}-mer and probably from the Al_{30}-mer. On the other hand, the monomer is the synthon for the formation of the Al_{30}-mer. Somewhat complicated shape of the resulting kinetic curves reflects the competition of these two processes.

Interestingly, the signal arising from the small Al oligomers (allegedly, the mixture of dimers an trimers) does not change profoundly in the time-resolved speciation diagrams given in Fig. 3.41. This fact indicates that small oligomeric species are stable in acidic conditions ($3.2<pH<3.8$) over relatively long periods of time even at high temperatures.

Summarising the discussion on the possible mechanism of the large Al polycation formation, it is possible to draw the following conclusions:

1. Condensation of Al-ions in aqueous solutions upon alkaline titration at room temperature most probably proceeds via the following species: Al monomers → Al dimers → Al trimers → (Al tetramers) → Al tridecamers (→ Al_{30}-mers, at high temperature).
2. Al trimers and probably tetramers are possible candidates as direct precursors for the formation of the Al_{13}-mer.
3. Al dimers are neither 'side products' of the hydrolytic processes, nor direct precursor to any larger polycations apart from the trimer.
4. Condensation of Al-ions into polynuclear species involves monomeric species on all stages of the process.
5. Kinetics of the formation of the Al_{13}-mer and the Al_{30}-mer differ more than 2 orders of magnitude.
6. The major species in mildly acidic conditions are monomers, Al_{13}-mers and Al_{30}-mers. Their mutual transformations in time determine dynamic equilibrium in Al-ion solutions.

6.1.4. Factors affecting speciation of Al-ions

The most important factors of Al speciation investigated in the present study were pH/hydrolysis ratio discussed above as well as temperature, ionic strength, effect of complexing anion (sulphate) and effect of alkali.

6.1.4.1. Effect of temperature

The studies of Al-ion speciation in aqueous solutions were conducted at two temperatures – room temperature (25±1 °C) and elevated temperature of 90°C (Chapter 3). In spite of the different experimental strategies adopted for these temperatures (predominantly monotonic single-batch titrations at room temperature and multi-batch titrations at high temperature), some parallels can be established between the observed speciation patterns of Al-ions. The overall distribution of Al species including monomers, small oligomers, large polycations and Al hydroxide is similar at both temperatures. Similar shapes of the potentiometric titration curves and the results of the ^{27}Al NMR measurements support this fact. The major difference was the amount of the Al_{30}-mer which dominated the speciation patterns at 90°C and was present in negligible amounts at high hydrolysis ratios ($2.0<h<3.0$) in the room-temperature experiments as follows from the corresponding ^{27}Al NMR signal comparable with the spectral noise. It was found that pH-scale shifts to lower values at high

temperatures making it difficult to compare the results using this parameter. On the contrary, the hydrolysis ratio scale used throughout the present study displayed virtual independence from the temperature effects. Another difference between the experiments at 25 and 90°C is the amount of Al hydroxide which was found to be substantially lower for the high-temperature experiments. The major consequence of the temperature effect was acceleration of the formation-dissolution rates of Al oligomeric species which is in agreement with the thermodynamic data analysed in Fig. 1.6 (Chapter 1). The data in Fig. 1.6 indicate that small oligomeric species (Al dimers and trimers) are less susceptible to the variations of temperature than large Al polycations, in this case – Al_{13}-mers. The temperature effect on the Al_{13}-mer ion results in the drop of the $pQ_{13,32}$ value almost 2 times. As follows from Fig. 1.4 reproduced from [25], aluminium monomers are less susceptible to the temperature variations on a large temperature scale (up to 500 K). The most susceptible stage of monomeric hydrolysis is the first stage.

The data on the temperature dependence of the formation-dissolution reaction of the Al_{30}-mer are not available in the literature. However, it has long been known that the optimum conditions for the formation of this species are prolonged boiling of the hydrolysed Al-ion solutions at high Al concentration in the hydrolysis ratio range $2.0<h<2.5$ [22]. Authors of the work [3] also indicated that instead of prolonged boiling of Al-ion solutions for 2-3 days it is possible to obtain considerable quantities of the Al_{30}-mer simply by leaving a solution for a decade. In the present study the amounts of the Al_{30}-mer were negligible after 24 hours of stirring a solution of hydrolysed Al-ions at room temperature.

6.1.4.2. Effect of ionic strength

Application of the extended Debye-Davies equation (1.2) along with the evaluation of the temperature effects allows for the effect of ionic strength to be considered on the basis of available thermodynamic data. In the case of aluminium, the coefficients a, b of the equation (1.2) responsible for the evaluation of ionic strength are known [5]. Results of plotting the calculated values of concentration quotients versus ionic strength of solution for the established Al species are shown in Fig. 1.3*C*. The data of Fig. 1.3*C* indicate that for 0.1 M Al-ion solutions the Al_{13} species are most affected by increase of ionic strength. With increase of this parameter from I=0 to I=3 mol/L the $-\log Q_{13,32}$ value falls ca. 10 % which is equivalent to the 10 order of magnitude change of the concentration quotient $Q_{13,32}$. Similar trend, albeit on a smaller scale is observed for all four monomeric forms of Al-ions, particularly at low values of I. Interestingly, the ionic strength dependent variation of the concentration quotient for the $[Al_3(OH)_4(H_2O)_9]^{5+}$ species is reciprocal to that of the Al_{13}-mer and is close to the variation of the solubility product of Al hydroxide.

Potentiometric titration data at room temperature (Section 3.1.1.2) revealed that the peak on the first derivative titration curve corresponding to the collapse of Al polycations at

h~2.5-2.6 is the inflexion most affected by the increase of ionic strength (1 M NaCl). This inflexion merges with the major peak at *h*~3.0 arising from the bulk precipitation of Al hydroxide. Therefore, the effect of ionic strength on the Al_{13}-mer molecule is a higher probability of this species to break down or to collapse and then transform into colloidal phase of amorphous hydroxide. This fact indicates that large Al polycations behave similarly to colloidal particles, although structurally, they are not direct precursors to colloidal or crystalline hydroxide [4]. ^{27}Al NMR spectroscopy did not reveal significant changes in the speciation patterns of Al-ions at room temperature upon introduction of highly concentrated electrolyte (section 3.1.2) apart from deviations observed in the potentiometric measurements.

6.1.4.3. Effect of alkali

Alkali type and strength are important parameters for the Al-ion speciation. Three alkalis of different strength were investigated in the present study at room temperature (section 3.1.1.2): KOH, NH_4OH and $KHCO_3$. The link of the Al-ion speciation pattern with the strength of alkali is not straightforward, especially in the case of ammonia as a titrant (Chapter 3). Potentiometric titrations have shown that ammonia acting as a structure-breaking agent in aqueous solutions [23] induces changes in the corresponding titration curves similar to those discussed above for high ionic strength.

Potassium hydroxide is the strongest alkali in the range. The use of this alkali as a titrant leads to appearance of a distinct inflexion at *h*~2.5-2.6 which arises from the collapse of Al polycations. This inflexion has been clearly observed in other works (e.g. Bradley et. al. [24]) and it was assigned to the Al_{13}-mer moiety plus other possible large polycations (e.g. Al_{30}-mers). However, the exact origin of the inflexion at ca. 2.5-2.6 has not been emphasised. On the basis of the extensive potentiometric and ^{27}Al NMR data in this work, it is concluded that this inflexion is related to the collapse of the polycations when after reaching a critical hydrolysis ratio slightly above the theoretical value (h=2.46 for the Al_{13}-mer) the system transforms abruptly into highly disordered colloidal phase of amorphous Al hydroxide. The collapse of the Keggin polycations occurs due to mismatch of the purely octahedral structure of the hydroxide phase and mixed tetrahedral-octahedral structure of polycations. In the case of KOH as a titrant, the inflexion at *h*~2.5-2.6 can be easily discerned from the adjacent major inflexion relating to bulk precipitation of Al hydroxide at *h*~3.0.

The use of potassium bicarbonate as a titrant leads to dramatic increase of the inflexion arising from the collapse of the Al_{13}-mer (Fig. 3.4). In this case, the amount of polycations formed in the mild acidic range of h is significantly higher than in the case of KOH. The system follows the rules established by the Principle of Hard and Soft Acids and Bases (HSAB) proposed by Pearson [25]. According to this principle soft acids prefer soft bases, hard acids prefer hard bases, aluminium hexaaquocation and its hydrolysed monomeric derivatives are soft acids. Therefore, they prefer a soft base ($KHCO_3$) to a strong one (KOH).

This preference leads to lesser perturbations in the Al-ion-$KHCO_3$ system and significantly increased concentrations of the transient species such as Al polycations. The latter feature, in turn, results in the formation of gel-like colloids in the range of $2.5<h<3.0$ due to very large surface areas of Al polycations (more than 1000 m^2/g according to some estimations [28]) which upon collapse into colloidal state tend to form a 3D-hydrogel rather than dense particulates [11].

Interestingly, ^{27}Al NMR spectra of all three systems containing Al-ions hydrolysed with KOH, NH_4OH and $KHCO_3$ aged for 24 hours at room temperature show no significant differences arising from the strength or type of alkali applied. Therefore, the differentiation between alkalis occurs on the short-time scale and is caused by so called 'local perturbations' induced by alkali additions to medium concentrated Al-ion solutions discussed below.

6.1.4.4. 'Local' alkali-induced perturbations

The use of strong alkalis for the titrations of medium and highly concentrated Al-ions is known to produce 'local perturbations' induced by inadequate mixing of reactants [11]. The problem arises from high degree of solution supersaturation [26] at concentrations of Al-ions well above the solubility limit of Al hydroxide (~$1\text{-}6*10^{-6}$ mol/L depending on the type of Al hydroxide formed [11, 27, 28]. When alkali is added to such solutions, formation of colloidal hydroxide is so fast, that it occurs practically at any stirring rate leading to solution heterogeneity even at low pH values. Obviously, higher stirring rates, elevated temperatures, dilution of Al-ion and alkali solutions and other measures can significantly reduce the extent of the colloid formation. Attempts to overcome the 'local perturbation' problem have been described in the literature [29, 30]. For instance, the authors [29] propose to use urea as a source of OH^--ions. At temperatures around 75°C urea thermodissociates producing ammonium-ion and carbon dioxide. Therefore, metal ion and urea solutions can be carefully premixed at room temperature and heated up to induce alkaline hydrolysis. Although, the route described in [29] and other works seems to lead to very homogeneous hydrolysis, the problem associated with the presence of structure-breaking ammonium-ions acting as coagulating agents at higher hydrolysis ratios ($h>2.0$ for Al-ions) remains.

Another way to overcome the problem of alkaline hydrolysis is to use electrochemical route to produce Al basic salts of different compositions [31]. The synthesis is normally carried out by oxidation-reduction reaction of aluminium metal in aqueous HCl or $AlCl_3$ solution according to the redox equation:

$$10Al(s) + 2AlCl_3\,(aq) + 30\,H_2O \rightarrow 6\,Al_2(OH)_5Cl\,(aq) + H_2\,(g) \qquad \textbf{(6.2)}$$

Varying the ratio of Al metal and acid (HCl or ACl_3) can lead to basic Al salts (aluminium chlorohydrates) of different basicity. The reaction temperature is usually kept near 96°C for up to 30 hours depending on the starting aluminium solution and concentration. Tiny amounts of mercury are added to Al metal to induce better solubility in deficient amounts of HCl or

$AlCl_3$ [31]. The method is free from effects of alkali, foreign anions and varying ionic strength. However, preliminary tests have shown that laboratory scale experiments without use of toxic mercury prove somewhat cumbersome due to a problem to achieve a complete dissolution of Al metal in highly deficient amounts of HCl (significantly less than 1:3 ratio required for the formation of $AlCl_3$). Another problem with this method that it cannot be used for the real-time kinetic experiments on Al speciation implemented in the present study due to limitation of solution kinetics by the rate of Al metal dissolution. On the contrary, the normal alkaline hydrolysis route is free from this problem hence the hydrolysis is initiated immediately after first addition of alkali.

Summarising the above remarks on 'local perturbations' it is necessary to mention that, to the author's belief, the problem of the improper mixing of Al and alkali solution is one of the main roots to the majority of discrepancies and uncertainties available in the literature. The actual hydrolysis ratio in the system containing Al-ions neutralised with alkali, therefore is an weighed average of the hydrolysis ratio of soluble species and h~3.0 for the colloidal fraction. In the present study the amount of the colloidal phase could be quantified indirectly from the ^{27}Al NMR data considering that it measures the sum of all soluble species present in solutions. Useful observations concerning the extent and conditions for the colloid formation in Al-ion solutions were made using the analysis of the first derivative potentiometric titration curves as (Chapter 3) and dynamic light scattering measurements. Combined use of time-resolved potentiometric measurements and correlation analysis can also assist understanding of colloid formation, since the time-resolved pH profiles in this method primarily originate from the heterogeneity of the titrated solutions. The shape of these pH-profiles was found to vary in agreement with the dynamic speciation in the titrated Al-ion solutions which includes rapid formation and following dissolution of the colloidal phase.

One can hypothesise than detection of Al_{13}-mers in the experiments of Chapter 3 at rather low hydrolysis ratios h~0.25-0.5 is also a manifestation of the alkaline perturbation problem, since from the thermodynamic point of view this species are not supposed to form at h<1.0 and pH<3.6-3.8.

As the present investigation and other works have shown, the problem of alkaline perturbations cannot be overcome completely by vigorous stirring, temperature increase, minimisation of the alkali concentration, introduction of much softer alkalis, minimisation of ionic strength, and other measures attempted in this work. Substantial dilution of Al-ion solutions would make these systems irrelevant to the concentration range usually applied in materials chemistry. Two possible ways to overcome this problem can be foreseen:

1. Attempt the quantification of formation-dissolution processes for the colloidal Al hydroxide phase.
2. Devise radically new strategies for pH adjustments not based on the direct additions of alkali.

The first pathway can prove to be quite difficult due to high variability of the colloidal phase parameters (size, morphology, short-order structure, surface properties, etc.) depending on numerous factors (e.g. concentration of Al-ions, pH, ionic strength, temperature, etc.). The second way to eliminate the effect of alkaline perturbations has not been explored so far.

In spite all the criticism, alkaline hydrolysis will remain one of the major methods for modelling of Al-ion speciation in aqueous media in the nearest future owing to its convenience, simplicity and the possibility to conduct kinetic experiments.

6.1.5.5. Effect of anions

The effect of anions on speciation patterns of Al-ions in solutions was examined on example of chloride, nitrate and sulphate as counter-ions. The results of Chapter 3 show that there are only tiny differences between the speciation of Al-ion in chloride and nitrate media. The differences arise from the higher acidity of Al nitrate solutions compared to Al chloride, which are indicative of some weak interactions between chloride and Al-ions suggested in the literature [10].

The detrimental effect of sulphate-ions on the formation of the Al_{13} ion has been shown in several works [32,33] including our study [9, 34]. Sulphate ions completely prevent the formation of this species in all pH conditions studied (Chapter 3). Nevertheless, it is clearly observed that some polynuclear species do form in Al sulphate solution upon increase of hydrolysis ratio. Potentiometric titrations described in section 3.1.1.2 show that an inflexion arising from the collapse of some polynuclear species appears at h~2.1-2.2 which is lower than for the analogous titrations of Al chloride and nitrate.

The ^{27}Al NMR data in this study are consistent with the presence of the peak relating to Al monomers at ca.0.34 and 0.77 ppm, peak of small Al oligomers at ca. 3-4 ppm as well as broad peak associated with unidentified octahedral Al based polynuclear species. Interestingly, the peak of monomers is shifted considerably compared to Al-ion solutions in the presence of non-complexing ions. Unlike for Al chloride or nitrate, the NMR peak arising from Al dimers or trimers occurs at higher hydrolysis ratios (h>0.75). Only the peak of large polynuclear species of unknown structure at ca. 40-50 ppm remains in the NMR spectra at h>2.0.

DLS measurements reported in Chapter 3 indicate that below hydrolysis ratio ca. 2.0, the size of the species was too small to be detected with this technique. Above h~2.0 large particles start to form extensively that agrees well with the inflexion in the pH titration curves.

The experimental findings described above raise a question above an alternative mechanism of Al-ion condensation in the presence of sulphate-ions. One can assume that the major reason for such profound difference between sulphate and non-complexing ligands lies in the complexation of this anion with aluminium. The occurrence of the monomeric Al-sulphate complex could be clearly detected in the ^{27}Al NMR spectra in this work on the basis

of the peaks at ca. –3.68 and –3.32 ppm. The different behaviour of the Al dimer allows the hypothesis to be proposed that the complexation in the Al-sulphate systems causes a delay in the formation of this species up to h~0.75-1.0. The Partial charge model calculations on the system aluminium(III)-sulphate have shown that outer-sphere complexes with Al dimers are possible. These complexes can stabilise the otherwise labile dimeric ion and lead to further condensation pathway into Al hexamer $[Al_6(OH)_{12}(H_2O)_{12}]^{6+}$ and its higher homologues. The highly symmetric hexameric species contain only octahedral al atoms and have a formal hydrolysis ratio h=2.0 which does not change upon further condensation via cyclisation [27] as shown in Chapter 1 (p. 27). This hypothesis agrees well with the potentiometric data which renders an inflexion in the vicinity of h~2.0.

The formation of Al-sulphate complexes has been reported in the literature on the basis of NMR data [32], IR-spectroscopy [34] and potentiometry [35].

6.1.4.6. Formation of colloidal phases. The fate of Al polycations at higher pH

According to Jolivet [4], the transient polymeric species formed in solutions of hydrolysed metal ions cases are not the direct precursors to colloidal and solid phases. This fact arises from the following properties of the polycations: (*a*) high charge of the species (e.g. z = +7 for the Al_{13}-mer and z = +18 for the Al_{30}-mer); (*b*) extremely small size often incomparable with the size of primary nuclei reported for colloidal processes; (*c*) structural mismatch between polycations and colloids / solid phases.

Metastable Al polycations are transient species which can be defined as temporary arrangements of hydrolysed Al-ions into structurally distinct forms in order to minimise free energy of the system on the way to the formation of stable hydroxide phases. In order to transform into Al hydroxide phase these species possessing Keggin-like structures have to rearrange completely. The experimental evidence for such rearrangement is disappearance of the tetrahedral AlO_4 core of Al Keggin ions in the ^{27}Al NMR spectra (Chapter 3) upon conversion of Keggin ions into final hydroxide phase which consists only of octahedral Al atoms. Two possible arrangements of octahedral Al atoms are possible leading to two major classes of Al hydroxide [4,10,11,27]. The first class has an overall formula $Al(OH)_3$ and consists of well-ordered crystalline gibbsite and bayerite which are formed outside the quasi-neutral range of pH. The basic structural unit of these phases is planar Al hexameric ring which forms planar sheets. Bayerite and gibbsite exhibit very close structural and chemical properties, the only difference in their structure is the relative arrangement of Al atoms in the adjacent sheets which is ABAB for bayerite and ABBA for gibbsite [27,28]. Another class of Al hydroxides (overall formula AlO(OH)) includes boehmite (γ-AlO(OH)) and related structures. The basic structural unit of this class of hydroxides is Al edge-sharing tetramer. Most reports on the conversion of Al polycations into hydroxide phase upon forced alkaline neutralisation are consistent with the so called 'pseudoboehmite' phase which has the same

structural motif as boehmite, albeit being a highly frustrated, amorphous solid. Depending on the treatment the second type of Al hydroxides which is considered as metastable can transform into more stable phases of gibbsite or bayerite.

Hydrolysed aluminium chloride and nitrate solutions transform in to crystalline (γ-AlO(OH)) upon ageing at higher temperatures (>80°C) [11]. Formation of γ-AlO(OH) has been discussed by Jolivet [4]. A mechanism has been proposed based on the formation of the $[Al_4O(OH)_{10}(H_2O)_5]^0$, condensation of which via olation and oxolation leads to corrugated sheets of γ-AlO(OH) as depicted schematically in Fig. 6.5.

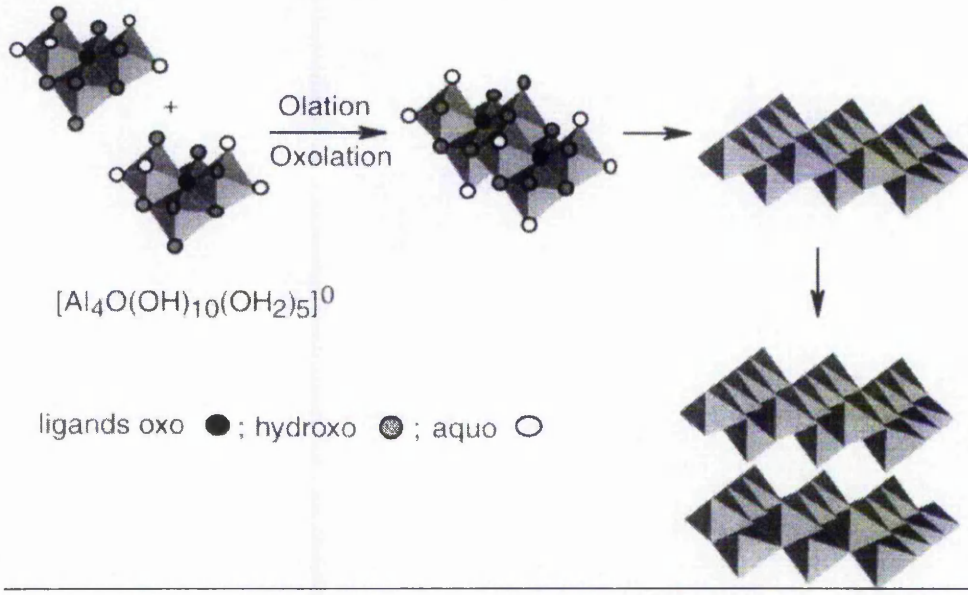


Fig. 6.5. Possible formation mechanism of boehmite γ-AlOOH by thermohydrolysis.

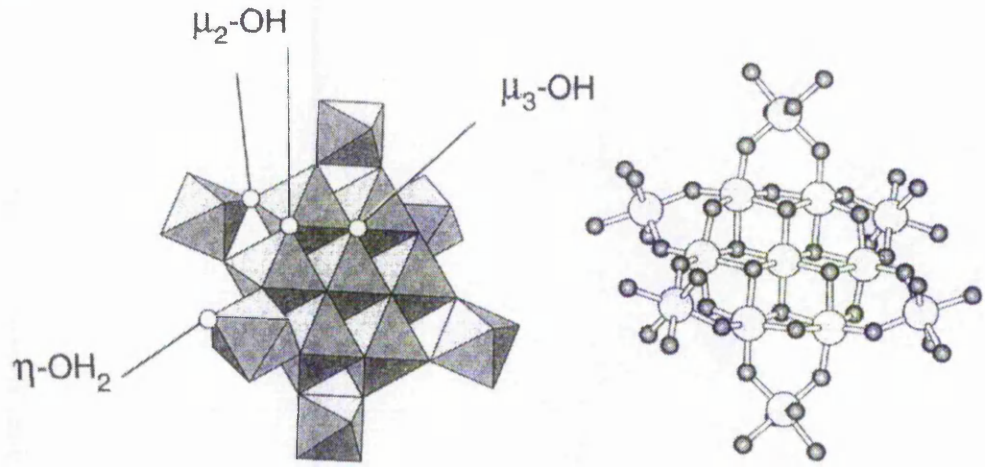
On the basis of the above one can conclude that the transformation of Al Keggin ions (Al_{13} and Al_{30}) into tetramer-based hydroxides of boehmite structure is supposed to proceed via rearrangement of these moieties into neutral tetramer-like species (e.g. $[Al_4O(OH)_{10}(H_2O)_5]^0$) upon charge cancellation in the vicinity of h~3.0. Al_{13}-mers can produce directly only one tetramer (combining one trimer and AlO_4 core which converts into octahedral form). Conversion of the AlO_4 unit of Keggin ions is probably the major reason for the formation of partially dehydrated Al oxohydroxide γ-AlO(OH). In the conditions of neutral pH the formation of the hydroxide phase via re-dissolution is quite unlikely (Al hydroxides are most stable around pH~7 [5]). Therefore, the core tetrahedral unit of Keggin ions is not able to 'rehydrate' completely in solid-state conditions upon transformation into octahedral form. The other three trimers have to undergo more substantial structural changes in order to become tetramers. At high temperatures this topochemical rearrangement is speeded up, leading to a well defined crystalline γ-AlO(OH) phase [27,28]. At temperatures below ca. 80 °C the rate of the process is insufficient and the collapse of the polycations results in the poorly ordered pseudoboehmite phase [27].

The mechanism of charge cancellation causing the collapse of Al_{13}-mers and Al_{30}-

mers is not described yet. As follows from the potentiometric studies conducted in the present work (Chapter 3) one can see that Al-ion solutions 'accumulate' hydroxyl ions as suggested by a prolonged plateau in the titration curves in the range $0.5<h<2.0$ with relatively small change of pH values ($4.0<pH<5.0$). Above h~2.0 the inflexion arising from charge cancellation takes place. As it was mentioned above, this inflexion is close to the formal hydrolysis ratios of Al polycations (h=2.4 for Al_{30} and h=2.46 for Al_{13}) Therefore, charge cancellation and simultaneous collapse of Keggin ions does not occur on a large scale, before the theoretical hydrolysis ratio for these species existence is reached. When all possibilities to form Keggin ions are exhausted, even tiny additions of alkali cause a dramatic shift in pH values indicating that alkali is not consumed anymore by hydrolysis-condensation reactions.

Dynamic light scattering measurements of solutions of hydrolysed Al-ions have shown (Chapter 3) that above h~2.0 the formation of Al hydroxide colloids significantly increases. Several ranges of particle sizes were observed including nano-sized (10-80 nm) as well as submicron and micron-sized particles (ca. 100 to ca. 2500 nm). The particle formation and aggregation processes occur in the narrow hydrolysis ratio range $2.6\leq h\leq 3.0$ indicating the trend to increase particle sizes with increase of h. The pH-dependent increase of the particle sizes of Al hydroxide colloids allows suggesting that the major driving force for the colloid formation in the vicinity of the point of electroneutrality (h=3.0) is continuing charge cancellation on the surface of the colloidal particulates.

The formation of $Al(OH)_3$-type of Al hydroxide (gibbsite, bayerite) has been explained in terms of dissolution-re-precipitation of boehmite preliminary formed upon alkaline neutralisation [4]. Acidic or alkaline conditions ($pH<5$ or $pH>8$) assist such mechanism. Well-aligned phases of gibbsite and bayerite are more thermodynamically stable than boehmite [27], however at quasi-neutral conditions the γ-AlO(OH) phase is probably stabilised kinetically [4]. Hexamer-based model has been proposed in order to explain direct formation of the $Al(OH)_3$ phase in some cases [27], including sulphate-based solutions of Al-ions discussed above. Another possible candidate as a direct precursor to gibbsite or bayerite is recently identified flat Al tridecamer $[Al_{13}(OH)_{24}(H_2O)_{24}]^{16+}$ (h=1.85) of the following structure [3]:



This structure represents a central flat Al_7-mer containing edge-sharing Al atoms surrounded by 6 out-of-plane corner-sharing Al atoms. The PCM calculations of these species lead to following electronic values (χ_t=2.722; $\delta(OH)$ = 0.0002; $\delta(H_2O)$ = 0.108; pH_{H2O}=0.3). The species are quite acidic compared to other polynuclear Al species and contain very stable OH-groups ($\delta(OH)$ is close to zero). However, partial charges on μ_3 and μ_2 hydroxo-bridges must be somewhat different (μ_3 bridges are assumed to be more negative). Aquo ligands of the flat tridecamer possess quite high average partial charge which enables them to hydrolyse further. The fact that the structure of this species appeared to be highly twinned [3] favours the assumption that the flat Al_{13} can easily hydrolyse and form a reactive flat surface leading to reaction of the surfaces between adjacent molecules.

There are some common structural motifs in the flat Al_{13} and gibbsite as well as the formal hydrolysis ratio of the species (h=1.85) quite close to the inflexion at h=2.1-2.2 (titration of Al sulphate) However, the acidic character of the species makes their assignment as direct precursor to the $Al(OH)_3$ phase quite unlikely. Moreover, this species were synthesised using a specific route, namely, direct heating of the $AlCl_3$ crystallohydrate [36] which is difficult to compare with solution-based synthesis conditions. The same species were also obtained as complexes with multidentate amino-carboxylate ligands [37]. Perhaps, the direct formation of gibbsite and bayerite can proceed directly from molecular precursors only when facilitated by highly charged weakly complexing anions such as sulphate. Such reaction probably occurs via hexamer-related mechanism as supported by the studies of Al-sulphate system (Chapter 3).

In the solid-state studies of the materials produced by spray-freeze-drying from solutions of hydrolysed Al-ions (Chapter 5) it was found that in the range of hydrolysis ratios $1.0<h<4.0$ where the formation of Al_{13}-mers and Al_{30}-mers is expected from the data of solution studies (Chapter 3) the samples were X-ray amorphous. Tiny amounts of gibbsite were detected in the vicinity of h=3.0. One can suggest that gibbsite is formed from amorphous colloidal non-Keggin material produced by local alkali-induced perturbations. Therefore, X-ray diffraction combined with spray-freeze-drying can become another useful method for estimation of the non-equilibrium colloid formation observed in alkaline titrations of Al-ions.

The literature data show similar findings [22] indicating that solid materials produced from basic Al chloride solutions by spray-drying were predominantly amorphous. The reason of the formation of amorphous solids from highly charged Al polycations is not clear, especially how the charge compensation of these species occurs in the solid state. The solid-state NMR results show (Chapter 5) that polycations maintain their structure in the solid state. Crystalline products containing Keggin ions can be obtained by precipitation with sulphate-ions. Rowsell and Nazar [20] suggest that sodium-ions are included in the crystalline structure of the Al_{30}-mer for charge compensation and they may play important role in the ordering and

stabilisation of the Al_{30}-mer in the solid state. Upon re-dissolution both amorphous (section 5.2) and crystalline products [3] containing Al_{13}-mers and Al_{30}-mers are easily transferred into soluble state.

Another important point in the discussion of structural transformations of Keggin ions and hydroxides is the presence of penta-coordinated Al atoms detected by solid state NMR [38,39]. Smith et. al [39] observed thermoinduced transformation of solid aluminates into bayerite and gibbsite using high-field ^{27}Al solid-state NMR. The authors have shown that the signal of tetrahedral Al arising from aluminate diminishes upon thermal treatment and the signal of gibbsite or bayerite increases. Such mechanism can be important for the solid-state transformations of Al Keggin ions into hydroxide phases.

6.2. Aqueous chemistry of zirconium ions

Solution speciation patterns of zirconium ions in medium concentrated aqueous solutions have been described and discussed in detail in Chapter 4 of the present study. Solid state speciation patterns of Zr-ions ha been investigated in Chapter 5 on the basis of X-ray and infrared characterisation of the solid samples produced by spray-freeze-drying. In this section the major findings of these studies will be emphasised

6.2.1. Hydrolysis of zirconium ions

In Chapter 1 of the present work it was shown that the major species present in medium-concentrated Zr-ion solutions are Clearfield's tetramers $[Zr_4(OH)_8(H_2O)_{16}]^{8+}$ [40] and their derivatives of higher molecular weight [41]. It is considered as proved that Zr tetramers are transferred into solutions from solid zirconyl chloride salt ($ZrOCl_2*8H_2O$) without alteration of their structure (coordination number of Zr N=8, bipyramid anti-prism configuration). These extremely acidic species ($pK_{4,4}$=-0.3) define hydrolytic processes occurring in Zr-ion solutions in the absence of complexing anions. Clearfield [40] postulates that initial step in the formation of Zr hydrolytic polymers from Zr tetramers is hydrolysis of the latter:

$$[Zr(OH)_2{\cdot}4H_2O]_4^{8+} \leftrightarrow Zr(OH)_{2+x}{\cdot}(4-x)H_2O]^{(8-4x)+} + 4xH^+ \qquad (6.3)$$

The reaction in Eq. (6.3) would explain why equimolar quantities of protons compared to Zr concentration are produced upon dissolution of zirconyl chloride as observed in pH measurements of pure Zr-ion solutions (in the presence of chloride) made in the this work (e.g. Table 4.1). The extent of tetramer hydrolysis is still unknown. One can calculate electronic parameters for the $[Zr(OH)_{2+x}{\cdot}(4-x)H_2O]^{(8-4x)+}$ species in attempt to elucidate hydrolysis pathways of the tetramer (Table 6.1).

Table 6.1. Results of the Partial charge model calculations for hydrolysed Zr tetramers

No	Species	*h*	*z*	χ_t	δ(Zr)	δ(O)	δ(H)	δ(H_2O)	δ(OH)	pH_{H2O}
1	$Zr_4(OH)_8(H_2O)_{16}^{8+}$	2.00	8	|	0.923	-0.308	0.312	0.105	0.0002	0.5
2	$Zr_4(OH)_9(H_2O)_{15}^{7+}$	2.25	7	2.693	0.909	-0.317	0.301	0.094	-0.0009	1.1
3	$Zr_4(OH)_{10}(H_2O)_{14}^{6+}$	2.50	6	2.671	0.894	-0.326	0.290	0.084	-0.0018	1.7
4	$Zr_4(OH)_{11}(H_2O)_{13}^{5+}$	2.75	5	2.648	0.879	-0.335	0.278	0.073	-0.0026	2.4
5	$Zr_4(OH)_{12}(H_2O)_{12}^{4+}$	3.00	4	2.624	0.863	-0.344	0.266	0.062	-0.0033	3.1

The data of Table 6.1 indicate that with increase of hydrolysis ratio of Zr tetramers the species become less feasible as judged by the increasingly negative values of average partial charges on hydroxyl-groups (δ(OH)). The value pH_{H2O} relating to the lower limit of the species existence (pH_{H2O} is a pH limit above which aquo ligands become able to deprotonate [10]) grows significantly at higher hydrolysis ratios, reciprocally to the decreasing value of mean electronegativity χ_t. This trend is evidence of rising basicity of the hydrolysed tetramer. Therefore, from electrostatic point of view the process of Zr tetramer hydrolysis via deprotonation of aquo ligands is unlikely, which is in contrast to the models proposed in the literature [40]. In acidic conditions, another mechanism seems to be more appropriate which is based on the direct olation condensation of two $[Zr_4(OH)_8(H_2O)_{16}]^{8+}$ tetramers involving $H_3O_2^+$-bridged intermediate [4, 10, 11].

6.2.2. Condensation of zirconium ions

Further condensation of hydrolysed tetramers, according to the classical review by Clearfield [40], proceeds via olation reaction between Zr tetramers leading to a potentially indefinite three-dimensional phases. It is generally accepted that in the growing Zr polymer chain two adjacent tetrameric units are connected by four μ_2 OH-bridges, since such structure is common for tetragonal zirconia. Clearfield speculates that since all Zr atoms in the tetramer are identical, condensation can proceed in any direction. However, more recent reports [41, 42] challenge this postulate showing that unidirectional growth of tetramer-based polymeric units is likely to occur. The initial bipyramid antiprism configuration of Zr atoms in the tetramer changes upon stacking condensation to distorted cubic configuration [40].

On the basis of the detailed SAXS study of zirconyl chloride solutions allegedly containing tetrameric Zr species it is suggested that above the ratio HCl:Zr =0.6 stacked octamers $[Zr_8(OH)_{20}(H_2O)_{24}Cl_{12}]^{4+}$ dominate solution equilibrium [41] which have been discussed in Chapter 1 of this study. The authors [41] have deliberately included twelve chloride ions into the formula of the octamer emphasising that these anions only the results of SAXS measurement and do not interfere in solution equilibria. Analysis of the electronic properties of stacked Zr octamer has shown (PCM parameters: (χ_t=2.689; δ(OH)= -0.0005;

$\delta(H_2O)$= 0.092; pH_{H2O}=1.2) that this species in the free form $[Zr_8(OH)_{20}(H_2O)_{24}]^{16+}$ is more basic than initial Zr tetramer (Table 6.1). This would explain the fact that forced alkaline hydrolysis or thermolysis is required in order to induce further condensation of Zr polymers [40]. The value of $\delta(OH)$ is only slightly negative and very close to zero, and the value of $\delta(H_2O)$ is decreased showing diminished propensity of aquo ligands to hydrolyse further. For higher homologues evaluated in Table 1.6 (Chapter 1) the parameter of $\delta(OH)$ remains very close to zero indicating that the species are generally stable. The values of mean electronegativity continue to decrease with the growth of molecular weight of the tetramer-based polymers, while the parameters $\delta(H_2O)$ and pH_{H2O} are gradually reduced. Interestingly, this trend steadies when the number of Zr-atoms in the polymer reaches ca. 60-64 atoms which roughly corresponds to a polymer size of ca. 10 nm. The value of hydrolysis ratio increases more rapidly at initial stages of condensation from h=2.0 for the tetramer and h=2.5 for the octamer and then slows down at N(Zr)>48 (h=2.93 for the Zr_{60} polymer), approaching the value of h=3.0. The value of pH_{H2O} follows a similar trend asymptotically reaching absolute maximum at ca. pH_{H2O}=2.2-2.3. Therefore by the critical size of ca. 50-60 Zr atoms further hydrolytic condensation via olation becomes unlikely. The value of pH ca. 2.2-2.3 and the theoretical hydrolysis ratio h=3.0 (equivalent to the value h=1.0 in this work; hydrolysis ratio of Zr tetramer was arbitrarily chosen as a reference point) probably defines a borderline for the olation-based condensation of hydrolytic Zr polymers.

Numerous experimental observations [40-44] including the results in Chapter 4 support the results of PCM calculations described above, showing that above hydrolysis ratio h~1.0 and pH~2 completely different process dominates speciation patterns of Zr-ions, namely, the formation of colloidal hydrous zirconia. Estimated particle sizes also agree well with the results of colloidal studies of Zr-ion solutions [45, 46]. Dynamic light scattering measurements of this study also reveal the presence of hydrous zirconia nanoparticles of ca.2-3 nm and 40-50 nm in the vicinity of the hydrolysis ratio h=1.0. The minimum domain size of monoclinic zirconia and related crystalline phases calculated from the XRD data of the present work (Chapter 5, series **ZrOH** and **ZrHCO3**) is also close to ca. 10-12 nm.

6.2.3. Structural features of Zr-ion condensation

The majority of authors investigating polymerisation of Zr-ions in aqueous media concentrated on the size of the species arising from this process rather than on the structure of the intermediates. The effect of structural transformations of the tetragonal Zr tetramer in the course of polymerisation on the resulting polymers, colloidal phases and solid products is, to author's mind, a cornerstone problem of aqueous chemistry of Zr-ions. The model of stacked condensation of tetramer-based polymers via acid-catalysed olation described above leads to a conclusion that tetragonal form of zirconia would dominate in the solid state. However, a

large number of studies carried out in the conditions of acidic reflux of zirconyl chloride solutions show that monoclinic zirconia is produced [47, 48]. Moreover, tetragonal zirconia also slowly converts into monoclinic phase in the solid state in the absence of stabilising cations [49]. These facts are extremely important for elucidation of solution patterns of Zr-ions. Monoclinic structure of zirconia is expected to contain two distinct types of Zr atoms in 7-fold and 8-fold configuration as shown in Fig. 6.6.

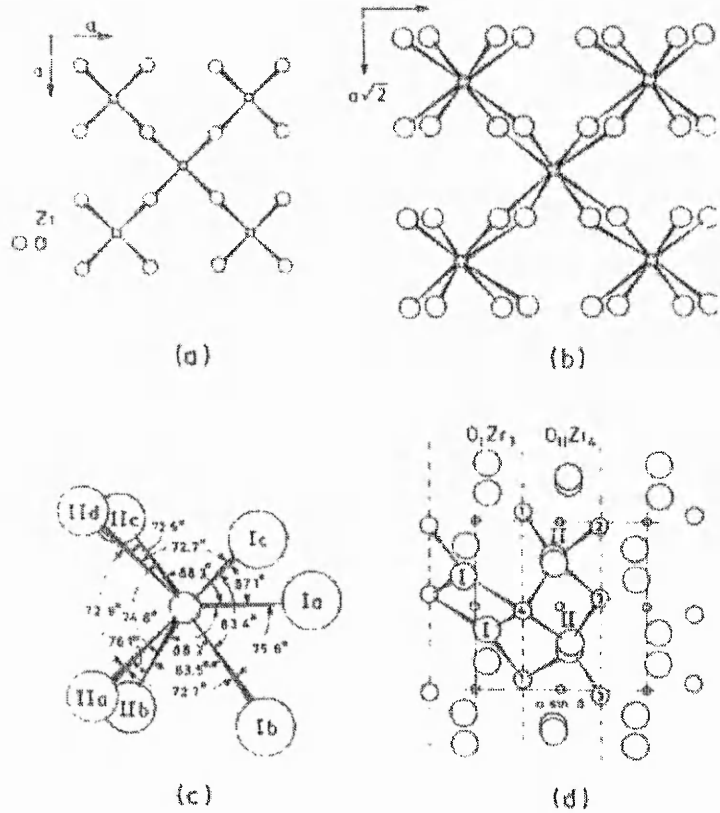


Fig. 6.6. Crystal structure of Zr polymorphs [50]: (*a*) projection of a layer of ZrO_8 groups in the cubic ZrO_2 on the (100) pane; (*b*) projection of a layer of ZrO_8 groups on the (110) plane of tetragonal ZrO_2; (*c*) angles and interatomic distances in the ZrO_7 polyhedron of monoclinic ZrO_2; (d) projection of the crystal structure of monoclinic ZrO_2 along the c_m-axis.

As follows from Fig. 6.6*d*, monoclinic zirconia contains periodic layers of triangular O_IZr_3 (μ_3) and tetrahedral $O_{II}Zr_4$ (μ_4) polyhedra unlike uniformly distributed oxygens of tetragonal and cubic zirconia (Fig. 6.6*a*, *b*). The bond Zr-O is expected to be more covalent [50] and the corresponding hypothetical solution species with 7-fold coordination of Zr-atoms are most probably more basic than tetramer-based polymers due to the presence of μ_3 and μ_4 hydroxyl- or oxo-bridges. The bond distances and angles in the monoclinic structure have large variety of values, in contrast with uniform bond angles of tetragonal zirconia and only two possible Zr-O distances 0.2455 and 0.2065 nm. The oxygen layer thickness of monoclinic zirconia caries for triangular O_I and distorted tetrahedral O_{II} atoms, and is equal for tetragonal zirconia [50]. The differences between monoclinic and tetragonal zirconia phase are also observed in terms of surface chemistry. For instance in the IR spectra of the hydrated

monoclinic zirconia the bands of both tri-bridging and terminal surface hydroxyls dominate in the region 3850-3600 cm^{-1} [51]. A single band arising from bi-bridging hydroxyls in the same spectral region dominates the surface of the hydrated tetragonal zirconia.

XRD spectra acquired in the present study (Chapter 5) show the presence of the monoclinic phase for the solid samples produced using spray-freeze-drying of 0.2 M Zr-ion solutions aged for 48 hours in the nearly boiling (90°C) and highly acidic ($h \leq 0.0$) conditions. With increase of HCl concentration (negative values of h) the amount of monoclinic zirconia continued to build up. Therefore, tetramer-based model is not relevant at extremely low pH. The tetramers should restructure under conditions of high acidity into completely other species which (*a*) are isostructural to monoclinic zirconia phase; (*b*) contain 7-fold coordinated Zr polyhedron; (*c*) do not contain bi-bridging hydroxyl-groups. This dramatic rearrangement seems unlikely to be topochemical, i.e. occurring in the solid state without dissolution of Zr-ions. At this point one can consider the formation of Zr trimers such as $Zr_3(OH)_5(H_2O)_{12}^{7+}$ reported in the potentiometric studies of strongly acidic Zr solutions [5]. These species are substantially more acidic than Zr tetramers (Table 1.7, Chapter 1) and stable at very low pH. Chloride-ions entering coordination sphere of Zr-atoms at extremely high acidity [40] can play a certain role in stabilisation of the monoclinic intermediates.

The layered structure of the monoclinic zirconia can cause either unidirectional growth of crystals or platelet crystal formation. Large cubic crystals of this phase have been reported [52] as well as platelets and layered sheets [53, 54]. Higher covalency of Zr-O bond as well as higher coordination of oxygens in monoclinic zirconia probably makes it easier to transform into final hydrous zirconia phase. Transient species occurring upon transformation of Zr tetramer from zirconyl chloride solutions into monoclinic zirconia have not been revealed yet. However, one can assume that several crystalline phases arising from 'dehydrated' zirconyl chlorides ($ZrOCl_2 * xH_2O$ where x is between 2 and 6) compiled in the JCPDS Powder diffraction file can be precursors to the final monoclinic zirconia. All these phases are monoclinic and increase their presence in the solid samples produced in this work with increase of hydrolysis ratio at which the samples were obtained, as shown by XRD and IR method in the present study.

6.2.4. Effect of pH and temperature

As was mentioned above, the change from highly symmetric tetragonal or distorted cubic orientation of ZrO_8 coordination polyhedron into the monoclinic ZrO_7 unit with large diversity of bond angles and distances is probably a dramatic event. One can assume that in acidic conditions the excess of protons catalyses this process. Apparent incompatibility of the tetragonal tetramer or its higher homologues with the monoclinic structure forces them to

loose one aquo ligand and to rearrange bi-bridging OH-ligands in order to create μ_3 and μ_4 bridges of the monoclinic structures. High acidity possibly assists this step of the 'tetragonal-to-monoclinic' transformation by protonation of the leaving H_2O-group. If a stepwise dehydration of the tetragonal units on the conversion into the monoclinic phase is assumed , the μ_3 and μ_4 bridges of the partially dehydrated Zr-atoms are initially hydroxyls, which should be highly acidic and deprotonate to give rise to final oxo-bridges of *m*-ZrO_2. On the other hand, the excess of protons would slow down the deprotonation of the μ_3 and μ_4 OH-bridges, which is observed experimentally from the potentiometric data showing very slow decrease of pH in highly acidic conditions.

It is clearly indicated in the literature on the surface properties of the monoclinic zirconia [55], that this zirconium oxide polymorph possesses quite basic terminal Zr-OH groups able to adsorb acidic carbon dioxide. Upon the 'tetragonal-to-monoclinic' transformation this groups are inevitably formed on the surface of oligomers with monoclinic structure and can serve as nucleophilic agents inducing condensation of the basic structural units of the monoclinic phase. Again, the excess of protons may slow down this process. One can notice that acidity of solution plays a dual role. On one hand, low pH values force the degradation of the tetragonal tetramers and their conversion into yet unidentified monoclinic intermediates. On the other hand, the excess of protons strongly limits the rate of the condensation at low pH.

Since the increase of Zr-ion concentration leads to equimolar release of protons, this factor affects hydrolysis-condensation in acidic media similarly to acid additions. Additions of strong acid with non-complexing anions (e.g. HCl) below ca. 2 mol/L lead to increase of the particle size of the resulting Zr polymers. Above this value strong acid probably leads to breakdown of Zr tetramers. Increase of Zr-ion concentration acts in a similar fashion.

In the conditions of forced alkaline hydrolysis (h>0.0) the presence of crystalline phases with the monoclinic structure diminishes (Chapter 5). Instead, amorphous phase is obtained in the range of hydrolysis ratios up to h~1.6. The structure of these amorphous solids has been investigated by the WAXS method [56], Raman spectroscopy [57] and electron microscopy [58]. The majority of authors come to a conclusion that amorphous solids produced in mildly acidic to quasi-neutral pH conditions represent a mixture of monoclinic and tetragonal phases. Starting from h~1.6 the tetragonal zirconia phase occurs in the XRD and far-IR spectra of the spray-freeze-drying samples obtained from hydrolysed zirconyl chloride solutions (Chapter 5). Literature data suggest [59] that tetragonal zirconia can be formed only in highly alkaline conditions. One can assume that the early formation of the tetragonal zirconia is strongly assisted by the presence of potassium-ions from alkali (KOH). This cation plays stabilising role in analogy with other metal cations such as Ca^{2+}, Mg^{2+} and Y^{3+} [50]. The role of the cation is to maintain the tetragonal structure which otherwise

converts spontaneously into *m*-ZrO_2 during storage at room temperature [59] probably by charge compensation of the highly acidic Zr-O^- sites which form occasionally on the surface of *t*-ZrO_2. Usually higher charge of cation is required for efficient charge compensation, however, it can be compensated by significant excess of potassium ions at high pH. The involvement of K^+-ions in the formation of tetragonal zirconia at high pH is supported indirectly by the fact that the amount of the sylvite (KCl) phase formed from the excess of potassium and chloride ions stops growing in the vicinity of h~2.0 and above this point starts to decrease.

On the basis of the experimental findings discussed above one can conclude that solid-state chemistry of hydrous zirconia at high temperatures is dominated by the monoclinic phase in acidic conditions and by the tetragonal phase in basic conditions. In between lies an amorphous zirconia phase with features of both tetragonal and monoclinic zirconia. The apparent borderline of the monoclinic and tetragonal structural domains is in the vicinity of the hydrolysis ratio h~1.5-1.6.

Solution data reported in the literature [43] and potentiometric measurements in this work (Chapter 4) are consistent with the presence of two distinct types of colloids or gels at h~1.3 and h~1.7 which have been designated as gel α and gel β in the study [43]. These colloidal phases visually differ in their density, gel α being more viscous and gel β - denser and finely grained. Although Raman spectroscopic measurements of these colloidal phases in the work [43] did not reveal significant differences in the range 700-100 cm^{-1}, one can hypothesise that the appearance of two distinct colloidal phases is probably a result of the fact that they occur on the opposite sides of the monoclinic-tetragonal borderline at h~1.5 proposed above.

Results of dynamic light scattering in the present study (Chapter 4) indicate that the particle size of the species present in the hydrolysed Zr-ion solutions evolves progressively with increase of hydrolysis ratio. The apparent discrepancy between the particle size predicted from the PCM calculations and the results of the DLS measurements can probably be explained by the rod-like shape of the polymers formed through the olation of Zr-tetrameric units as described above. In the systematic SAXS study of thermoinduced polymerisation of hydrolysed Zr-ions [60] fine and uniform rod-like particles have been detected with dimensions ca 0.4 x 6 nm. It is practically impossible to discern between these dimensions using DLS measurements. As a consequence an average peak at ca. 2-3 nm is observed. The maximum length of ca. 6 nm for the primary nuclei of hydrous zirconia colloids according to the work of Singhal et. al [60] is relatively close to the limit of olation condensation at ca. 8-10 nm roughly estimated by the PCM calculations above.

The work [60] and similar important studies provide an abundant and highly

consistent evidence for the elongated growth of Zr polymers on early stages of condensation, however, it does not provide a mechanistic explanation for this phenomenon. Simple considerations can clarify the problem. Let us consider the smallest elongated oligomer – Zr_{12}-mer of the formula $[Zr_{12}(OH)_{36}(H_2O)_{48}]^{18+}$ (check) schematically depicted in Fig. 6.7.

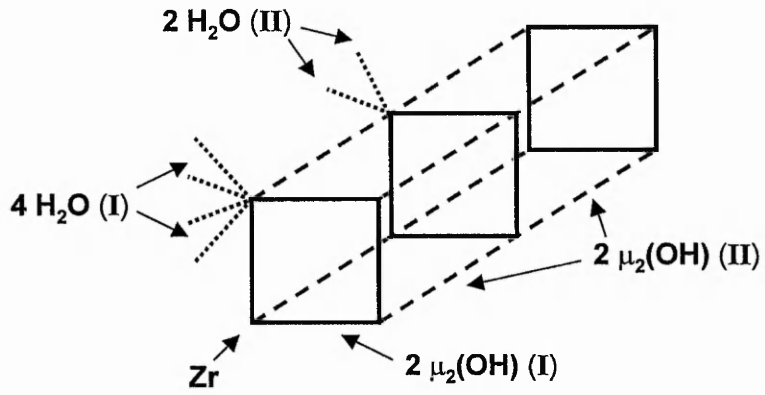


Fig. 6.7. Schematic presentation of the Zr_{12}-mer. Bold lines – 'intrinsic' $2\mu_2$ (OH) bridges of Zr tetramers (I); dashed lines – 'extrinsic' μ_2 (OH) ligands; dotted lines - examples of aquo ligands of the front tetrameric unit (H_2O (I)) and central tetrametic unit (H_2O(II)).

The central Zr tetrameric unit of the hypothetic Zr_{12}-mer, formed according to the olation model described above, possesses only two aquo ligands (type II) left, the other 6 positions of the ZrO_8 polyhedron are occupied by four 'intrinsic' bridging μ_2 (OH) ligands (I) and two 'extrinsic' bridging μ_2 (OH) ligands (II). Unlike the central tetramer, face and rear tetramers contain 4 aquo ligands of type (I) and 4 μ_2 (OH) bridging ligands (I) The aquo ligand of the face tetrameric unit would be stronger acid (higher positive values $\delta(H_2O)$) then the same moiety of the central Zr_4 unit. Higher value of $\delta(H_2O)$ makes aquo ligands of the face tetramers better leaving groups [10] and enables easier hydrolysis with the formation of reactive terminal hydroxyl-ligands. Therefore, hydrolysis-condensation becomes preferable at the face plane of Zr_{12}-mer. As the condensation process progresses, the difference between two types of aquo ligands would become more profound for larger Zr polymers. Such uniaxial growth of Zr polymers would last until all possibilities for acid-catalysed olation are exhausted (h~3.0, pH~2.0).

Apparently, condensation via olation does not result in any significant inflexions in the potentiometric titration curves of zirconyl chloride solutions acquired in the present study in the range $-1.5 \leq h \leq 0.8$. This is indicative of the gradual progression of the condensation reaction up to h~1.0, consistent with the model of acid-catalysed olation discussed above. Time-resolved pH-measurements clearly indicate the extent of reaction showing slowly decreasing pH values over the whole period of monitoring (48 hours, Chapter 4).

The work of Singhal et al. [60] has demonstrated that when olation reaction is

finished, rod-like polymeric particles start to stick to each other in a relatively random order, as depicted in Fig. 1.12. Rearrangement and alignment of the rods along a preferential axis can proceed under conditions of long-term ageing at high pH and temperatures. If the reaction goes too fast or the temperature is not fast enough to facilitate topochemical restructuring of the precipitate, the resulting solid material is amorphous, which is the case for the experiments conducted in this study as indicated by the inflexions arising from gels α and β occurring in the range $1.0<h<2.0$. Well-aligned arrays of the tetramer-based polymer rods lead eventually to the formation of tetragonal zirconia phase. As was mentioned above, this phase needs to be stabilised with highly electropositive cations, which were supplied in the experiments in this work by the excess of alkali.

One must note, that in the case of $KHCO_3$ as a titrant, solid materials produced at high hydrolysis ratios ($h\geq2.0$), albeit containing some minor crystalline tetragonal-like phase, exhibit completely different structure due to extensive complexation of Zr-ions with carbonate. This feature will be discussed below. In the case of KOH as a titrant the resulting phase is increasingly crystalline with increase of hydrolysis ratio above $h=2.0$

Another hypothesis helping to explain the distinction between gels α and β with corresponding potentiometric inflexions at $h\sim1.3$ and $h\sim1.7$ can be proposed:

Upon aggregation of rod-like particulates of the primary (0.4x6 nm) and secondary (40-50 nm) another chemical process occurs, namely, internal oxolation leading to deprotonation of bi-bridging hydroxyl-ligands of tetragonal zirconia and gradual formation of oxo-bridges of the final hydrous zirconia phase. In between two inflexions of gels α and β may lie a critical point triggering the internal oxolation process. As was shown on the basis of PCM calculations in order to complete acid-catalysed olation the hydrolysis ratio should reach the value of ca. $H=3.0$ ($h=1.0$). One can assume that during the early stages, the aggregation of the primary particles into 3D-aggregates the process can still proceed via olation of the aquo ligands located on the long edges of the rods. It has been shown [60] that under conditions of forced alkaline hydrolysis initial rod alignment is quite poor. As a consequence, ramification' of the rods can occur leading to fern-like structures. Therefore, face-sided aquo ligands of the primary rod particles still continue to play important role due to their higher reactivity compared with the edge-sided aquo ligands, as discussed above. At $h\sim1.5$ all possibilities for edge-sided olation to occur are probably exhausted, as schematically illustrated in Fig. 4.5 (Chapter 4). Further process is bulk internal oxolation of the hydroxyl-bridges of the colloidal aggregates eventually leading to hydrous zirconia. This hypothesis would help to explain high concentration of bridging hydroxyls in the vicinity and above the point of electroneutrality of hydrous zirconia at $h=2.0$ observed in the infrared spectra of this work (Chapter 5). Internal oxolation in this case is incomplete due to mismatch of the fast zirconia precipitation in the narrow region $1.5\leq h\leq2.0$ with alkali and slow oxolation process. The occurrence of 'gel β' is probably a result of densification of the amorphous aggregates

due to oxolation process leading to shorter and more covalent Zr-O-Zr bridges [4].

In the work [60], the authors have shown that temperature is a crucial parameter ensuring kinetic feasibility of the condensation and aggregation processes of the elongated particles of tetramer-based Zr polymers. Their temperature-dependent data suggests that the critical point for making the process feasible is around the temperature of ca. 90°C. The majority of the experiments in the study [60] are conducted at 92°C which is quite close to the temperature of 90°C chosen for multi-batch experiments with Zr-ion solutions in the present work.

Summarising the above one can conclude that in the case of Zr-ions structural arrangements can affect colloidal processes at h>0.0, which can result either in gels (e.g. gel α at h~1.3), or in highly aggregated dense particulate colloids ('gel' β at h~1.7), or in the precipitation of bulk hydrous zirconia which can be either amorphous or crystalline (tetragonal structure). A particular outcome of the colloidal processes is defined to a great extent by the kinetics of the solid-state alignment of the rod-like primary particles into well-ordered 2D-arrays. Kinetic rate of this process depends on pH and temperature, increase of which favours better alignment and subsequently crystalline structure of the resulting material.

6.2.5. Effect of anions

Combined characterisation of the series of multi-batch alkaline titrations using solution-based (pH-metry), colloidal (DLS) and solid state techniques (infrared and XRD) has enabled us to acquire a systematic picture of the effect of anions and glycine on the speciation patterns of Zr-ions in medium-concentrated solutions at high temperature. Results of the integrated characterisation are discussed in detail in Chapters 4 and 5. The following features of complexation with Zr-ions must be emphasised.

Chloride ions. According to the PCM calculations complexation of Cl^--ions with zirconium is unlikely on the normal pH scale (pH=0-14). The possibility of complex formation is predicted only in extremely acidic media. Such complexes of Zr-ions with chloride are known [61]. Clearfield [40] has proposed that at very low pH Zr tetramers are neutralised first, and then gradually transformed into (a) mixed chloro-hydroxo-complexes and finally, chloro-complexes with negative charge. The final species in this pH-dependent equilibrium is $ZrCl_6^{2-}$ which has been identified experimentally [40]. In this complex the coordination number of Zr is reduced to 4. In the present study no signs of the effect of chloride-ions on the equilibria in Zr-ion solutions have been observed over the whole range of hydrolysis ratios studies.

Sulphate-ions are able to complex Zr-ions in whatever coordination mode over a wide range of pH and hydrolysis ratios according to the Partial charge model. Acidity of the medium plays significant role in the extent and type of complexation by sulphate. Two major

complexes have been detected in the solid samples of the sulphate-containing series **ZrOHSO4** ($Zr:SO_4^{2-}=1:1$) using IR-spectroscopy and 2D-correlation analysis : bridging and chelating bidentate complexes. The first complex dominates acidic region ($-1.0\leq h\leq 0.4$-0.6) being taken over by the chelating complex at $h>0.2$-0.4. XRD data show that bridging sulphate ligands can possibly substitute the structural hydroxyls of the tetramer-based Zr polymers as supported by the crystalline phase closely resembling that of zirconium sulphate $Zr(SO_4)_2*4H_2O$. However, the amount of sulphate (equimolar quantities) is not sufficient to replace all hydroxyls and to form a complex with only sulphate ligands. As a result, a mixture of Zr sulphate, basic sulphate and monoclinic zirconia is detected. At higher hydrolysis ratios ($h>0.0$) native hydroxyl groups of Zr polymers are probably two stable and sulphate can only replace aquo ligands. Structurally this effect results in the precipitation of the basic sulphate of the approximate formula $Zr(OH)_2SO_4*H_2O$. As follows from the potentiometric data, above hydrolysis ratio $h\sim 1.0$ the charge compensation of the tetramer-based polymers is completed due to the complexation with sulphate. Further increase of the hydrolysis ratio does not lead to profound changes in the highly insoluble solid product (Chapter 5).

Acetate-ion is considered as a soft ligand according to PCM (Chapter 1). Nonetheless, in very acidic solutions acetate-ions are still able to form complexes with Zr oligomers. At very low pH and h ($h<-0.6$) there is a minor amount of the supposedly unidentate complex of protonated acetate with Zr-ions detected in the IR-spectra. At higher hydrolysis ratios $-1.0\leq h\leq 1.0$-1.2 two types of the Zr-acetate bidentate complex occur: bridging and chelating. Unlike for the complexation wit sulphate, bridging complex appears to be more stable at higher pH. Both complexes virtually vanish from the IR spectra of the corresponding solid samples of the series ZrOHAc at $h\sim 0.8$-1.2. This point coincides with the inflexion observed in the pH-metric titration curves. The complex of unidentate and bidentate chelating acetate-ligands with Zr-ions does not lead to any crystalline phase in the acidic region. Complexation via bridging mechanism leads to the formation of a minor unidentified crystalline phase at $0.0<h<1.6$ which is probably basic zirconium acetate. Due to intrinsic softness of acetate-ions, they are easily removed from the solid precipitates at $h>1.0$ by hydroxyl-ions.

Carbonate-ion is able to form stable complexes with Zr-ions at pseudoneutral and alkaline conditions ($h\geq 2.0$). This feature arises from the limited stability of this anion at lower pH. Two bidentate chelating complexes with slightly different structures have been identified using IR-spectroscopy of the solid samples of the series **ZrHCO3** (Chapter 5) probably corresponding to two distinct sites on the surface of hydrous zirconia precipitate. The precipitate tends to dissolve according to the DLS data (Chapter 4) indicating that carbonate-ions are capable of replacing hydroxyl-ligands even in the conditions of high alkalinity. The overall charge of the complexes is expected to be negative which is in contrary with the cationic stabilisation required for the tetragonal zirconia phase. Therefore, carbonate-ions strongly hinder the formation of t-ZrO_2 as clearly follows from the comparison of the XRD

data of the series with $KHCO_3$ and KOH as titrants.

Glycine is a harder acid than acetate according to the thermodynamic considerations and PCM predictions. As a result complexation occurs in much wider hydrolysis ratio range than in the case of acetate-ions. As follows from the IR-data, at highly acidic conditions a unidentate complex of the glycine molecule with Zr-ions occurs, similarly to the acetate-ion, albeit the extent of the complexation in the case of glycine is significantly higher (this complex is assigned as free protonated glycine in Chapter 5). At higher acidities at least two types of the bidentate complex of glycine with zirconium polymers can be identified using advanced treatment of the IR-spectra by means of 2D-correlation analysis. Allegedly bridging complex is slightly more stable in acidic medium similarly to sulphate. Chelating complex apparently dominates at higher hydrolysis ratios (up to h~1.6). Above h~1.6 both complexes are replaced by hydroxyl-ions. Complexation of Zr-ions strongly depends on the Zr:glycine ratio in solutions. At higher ratio (Zr:glycine=1:2) the formation of all types of complexes with glycine is more profound. In the conditions of the two-fold excess of glycine, monoclinic zirconia is present in the XRD spectra of very acidic samples. Positive values of h result in the formation of basic zirconium glycinate of yet unidentified structure. Buffering property of glycine zwitter-ionic molecule plays significant role in the speciation patterns. Glycine strongly increases pH of Zr-ion solutions, the increase being higher at higher glycine concentrations. In spite of high pH values (pH=2.4 at h=0.0 comparing to pH=0.69 at h=0.0 for "pure" Zr-ion solutions), condensation of tetramers via olation does not occur to a large extent as evidenced by the DLS data in Chapter 4. Stronger complexation with carboxylic group and protonated amino-group of glycine protect small Zr oligomers from condensation and aggregation by alkali. Only at h~1.6 (substantially higher than h~0.8-1.0 for acetate-ions) glycine is abruptly replaced by hydroxyl ions as supported by the peaks of free ligands in the corresponding mid-IR spectra.

It is important to note that except for chloride-ions, none of the studied anions led to the tetragonal phase of zirconia. Monoclinic phase is diminished too, probably due to increase of pH by the replacement of the structural hydroxyls with anions in very acidic conditions.

6.3. Future work

From the results summarised above one can find that the combination of rational experimental design, an integrated multi-phase characterisation approach and advanced treatment of the data have resulted in a significantly improved understanding of complex processes occurring in aqueous solutions of aluminium and zirconium ions. In order to achieve an exhaustive level of understanding of these systems the following measures are needed in the future:

1. Further automation of 'wet' chemistry and characterisation techniques would allow

stronger penetration of the combinatorial chemistry approach into the research of fundamental phenomena such as aqueous chemistry of metal ions. It would also improve quality (better precision and resolution) and enable larger scale investigations involving multiple factors.

2. Introduction of the methods of factorial design for the optimum productivity and enabling of statistical modelling for the systems in question in multi-factorial dimensions.
3. Expanding and improving the analytical base for the characterisation of heterogeneous aqueous systems as a whole would allow for the establishment of reliable relationships between solution, colloidal and solid-state chemistry of these systems. Further attention should be paid to the introduction of new analytical techniques, in particular, separation methods, electro-spray mass-spectrometry and other highly informative techniques. Solid-state characterisation must be improved in terms of throughput and quantification (particularly structural and microscopic techniques), since application of such methods as spray-freeze-drying offers a convenient way to obtain solution species in the solid state and to characterise them extensively. Traditional solid-state characterisation methods such as thermo-analysis would also contribute to the understanding of the multi-phase speciation of metal ions.
4. Data treatment is to be improved dramatically, since combinatorial methods such as real-time multi-batch titrations implemented in the present study allow for large libraries of samples and large sets of data to be obtained. Along with such statistical tools such as correlation analysis successfully applied in previous Chapters identification and classification, multivariate quantitative techniques would be beneficial for better quantification and, subsequently, better modelling of complex aqueous systems.
5. Several 'white spots' still exist in the aqueous chemistry of aluminium and zirconium. Mechanistic studies of the transformations of large polynuclear aluminium and zirconium species upon their dissociation and conversion into colloidal and solid state, will require additional effort in order to provide experimental evidence for the possible pathways predicted by theoretical methods (see above). More complicated, realistic and diverse systems derived on the basis of the models explored in the present study and other works can be investigated on a radically new level of depth. Such systems would include aqueous media of biological and environmental relevance, as well as the systems of industrial potential relevant to materials science.
6. Mixed aluminium-zirconium aqueous systems represent a new level of challenge and would require dedicated studies. However, the present work together with other studies has laid the foundation for the systematic in-depth analysis of such systems.

References:

1. J.W. Akitt. Prog. Nucl. Mag. Res. Sp. (1989) **21** P. 1-2, 1-149.
2. P.M. Bertsch, D.R. Parker. Aqueous Polynuclear Aluminum Species In: The environmental chemistry of aluminum / Ed. by G. Sposito (1996) Boca Raton, Lewis, 117-168.
3. W. Casey et. al. Aqueous Aluminum Polynuclear Complexes and Nanoclusters: A Review. In: Nanoparticles in the Environment / Ed. by J.F. Banfield, A. Navrotsky (2001). 167-190.
4. J.-P. Jolivet. Metal Oxide Chemistry and Synthesis. From Solution to Solid State. (2000) Chichester, Wiley and Sons, 321 p.
5. D.F. Baes Jr., R.E. Mesmer. Boron, aluminium and scandium. In: The hydrolysis of cations. (1976) New York, Wiley-Interscience, 152-158.
6. S.M. Bradley et. al. J. Chem. Soc. Dalton (1990) 413-417.
7. N.B. Milic, Z.D. Bugarcic, S.R. Niketic. Gazz. Chim. Ital. (1991) **121** 45-48.
8. L.P. Holmes, D.L. Cole, E.M. Eyring. J. Phys. Chem. (1968) **72** 301-310.
9. C.C. Perry, K.L. Shafran. J. Bioinorg. Chem. (2001) **87** 115-124.
10. M. Henry, J.P. Jolivet, J. Livage. Aqueous Chemistry of Metal Cations - Hydrolysis, Condensation and Complexation. (1992) Structure And Bonding **77**, 153-206.
11. C.J. Brinker, G.W. Scherer. Sol-gel science: the physics and chemistry of sol-gel processing (1990) New York, Academic Press, 908 p.
12. L.J. Michot et. al. J. Am. Chem. Soc. (2001) **122** 6048-6056.
13. J.W. Akitt, A. Farthing. J. Chem. Soc. Dalton Trans. (1981) 1617-1623.
14. P.M. Bertsch. Soil Soc. Am. J. (1987) **51** 825-828.
15. S.M. Bradley, R.A. Kydd, R.F. Howe (1993) J. Colloid Interf. Sci. **159** 2, 405-412.
16. J.W. Akitt et. al. J. Chem. Soc. Dalton (1989) 1897-1901.
17. J.W. Akitt, J.M. Elders (1988) J. Chem. Soc. Dalton, 5, 1347-1355.
18. G. Johansson. Acta Chem. Scand. (1962) **16** 403.
19. T.M. Alam, M. Henry. PCCP (2000) **2** 23-28.
20. J. Rowsell, L.F. Nazar. J. Am. Chem. Soc. (2000) **122** 3777-3778.
21. L. Allouche, C. Gerardin, T. Loiseau, G. Ferey, F. Taulelle. Agew. Chem. Int. Edit. (2000) **39** 511-514.
22. J.J. Fitzgerald. Chemistry of aluminium hydrolysis complexes. In: Antiperspirants and Deodorants (1988) New York, Marcel Dekker, 119-296.
23. J. Burgess. Metal ions in solution (1978) Chichester, Ellis Horwood, 481 p.
24. S.M. Bradley, R.A. Kydd, R. Yamdagni. J. Chem. Soc. Dalton (1990) 413-417.
25. R.G. Pearson. Chemical Hardness (1997) Weinheim – Chichester, Wiley-VCH, 198 p.
26. W. Stumm, J.J. Morgan. Aquatic Chemistry. An Introduction Emphasizing Chemical Equilibria in Natural Waters. (1981) New York, Wiley and Sons, 780 p.
27. K. Wefers, C. Misra. Oxides and Hydroxides of Aluminum. Alcoa Technical Paper No 19, Revised (1987) Alcoa, 92 p.
28. Chemistry of aluminium, gallium, indium and tallium / Ed. by A.J Downs.(1993) London, Chapman and Hall, 526 p.

29. P. Mishra. Mater. Lett. (2002) **55** 425-429.
30. F. Kara, G. Sahin. J. Eur. Ceram. Soc. (2000) **20** 689-694.
31. J.J. Fitzgerald, A.H. Rosenberg. Chemistry of Aluminum Chlorohydrate and Activated Aluminum Chlorohydrates. In Antiperspirants and Deodorants / Ed. by K. Laden (1999) New York, Marcel Dekker, 83-136.
32. G.L. Kerven, P.L. Larsen, F.P.C. Blamey. Soil Sci. Soc. Am. J. (1995) **59** 765-771.
33. A. Benyattou et. al. B. Soc. Chim. Fr. (1995) **132** 1103-1108.
34. J.T. Kloprogge, R.L. Frost. Thermochim. Acta (1998) **320** 245-252.
35. M.K. Ridley et. al. Geochim. Cosmochim. Acta (1999) **63** 459-472.
36. W. Seichter et. al. Eur. J. Inorg. Chem. (1998) 795-797.
37. S.L. Heath et. al. J. Inorg. Biochem. (1995) **59** 785-794.
38. L.F. Nazar e.t al. Chem. Comm. (1992) 251-253.
39. K.J. D. MacKenzie et. al. Thermochim. Acta (2000) **359** 87-94.
40. A. Clearfield. Rev. Pure and Appl. Chem. (1964) **14** 91-108.
41. A. Singhal, L.M. Toth, J.S. Lin, K. Affholter. J. Am. Chem. Soc. (1996) **118** 11529-11534.
42. J.A. Jutson et. al. Materials Research Society Symposium Proceedings (1990) **180** (Better Ceramics through Chemistry 4) 123-128.
43. J.L. Tosan, B. Durand, M. Roubin, F. Bertin, H. Loiseleur. Eur. J. Solid State Inorg. Chem. (1993) **30** 179-193.
44. B.H. Davis. Comm. Am. Ceram. Soc. (1984) C-168.
45. A. Bleier, R.M. Cannon. In: Better Ceramics Through Chemistry II / Mater. Res. Soc. Symp. Proc. **73** / Ed. by C.J. Brinker, D.E. Clark, D.R. Ulrich (1986)Pittsburgh,Pa., 71-77.
46. R.C. Garvie, M.F. Goss. J. Mater. Sci. (1986) **21** 1253-1257.
47. T. Uchikoshi et. al. J. Mater. Res. (1998) **13** 840-843.
48. K. Lee et. al. J. Am. Ceram. Soc. (1999) **82** 338-342.
49. A. Gulino et. al. J. Mater. Chem. (1997) **7** 1023–1027.
50. E.C. Subbarao. Zirconia – An Overview. In: Science and technology of zirconia (Advances in Ceramics, Vol. 3) / Ed. by A.H. Heuer, L.W. Hobbs (1987) Columbus, The American Ceramic Society 1-24.
51. K.T. Jung, A.T. Bell. J. Mol. Catal. A (2000) **163** 27-42.
52. R. Ramamoorthy et. al. Bull. Mater. Sci. (1997) **20** 573-578.
53. P.D. Southon et. al. Chem. Mater. (2002) **14** 4313-4319.
54. E. Zhao et. al. J. Mater. Chem. (1998) **8** 1635–1640.
55. E. Djurado et. al. J. Solid State Chem. (2000) **149** 399-407.
56. A.C. Geiculescu, H.J. Rack. J. Sol-Gel Sci. Technol. (2001) **20** 13-26.
57. G.K. Chuah et. al. J. Catal. (1998) **175** 80-92.
58. M. Daturi et. al. J. Chem. Soc. - Faraday Trans. (1998) **94** 1143-1147.
59. H.-J. Noh et. al. Mater. Lett. (2003) **57** 2425-2431.
60. A. Singhal et. al. J. Colloid Interf. Sci., 1997, V. 194, 2, pp. 470-481.
61. R.K. Bajaj et. al. Polyhedron (1984) **3** 883-887.

APPENDIX 1. Table 4.3. PCM calculations of Zr polycation complexes with glycine

No	Species	*h*	Ligand*	*z*	χ_t	$\delta(H_2O)$	δ(OH)	δ(Gly)**	$pH_{opt.}$
Tetramers									
1	$Zr_4(OH)_8(H_2O)_{16}$	*2.00*	$Gly^+(\mu_1)$	8	2.6913	0.093	-0.0011	-	*1.16*
2	$Zr_4(OH)_8(H_2O)_{15}(Gly^+)$	*2.00*	$Gly^+(\mu_1)$	9	2.7257	0.109	0.0008	0.0315	*0.18*
3	$Zr_4(OH)_8(H_2O)_{14}(Gly^+)_2$	*2.00*	$Gly^+(\mu_1)$	10	2.7542	0.123	0.0024	0.0222	*-0.63*
4	$Zr_4(OH)_8(H_2O)_{13}(Gly^+)_3$	*2.00*	$Gly^+(\mu_1)$	11	2.7782	0.134	0.0037	0.0184	*-1.32*
5	$Zr_4(OH)_8(H_2O)_{12}(Gly^+)_4$	*2.00*	$Gly^+(\mu_1)$	12	2.7987	0.143	0.0049	0.0161	*-1.91*
6	$Zr_4(OH)_8(H_2O)_{10}(Gly^+)_6$	*2.00*	$Gly^+(\mu_1)$	14	2.8318	0.159	0.0067	0.0132	*-2.85*
7	$Zr_4(OH)_8(H_2O)_8(Gly^+)_8$	*2.00*	$Gly^+(\mu_1)$	16	2.8574	0.171	0.0082	0.0114	*-3.58*
8	$Zr_4(OH)_8(H_2O)_6(Gly^+)_{10}$	*2.00*	$Gly^+(\mu_1)$	18	2.8778	0.180	0.0093	0.0100	*-4.17*
9	$Zr_4(OH)_8(H_2O)_4(Gly^+)_{12}$	*2.00*	$Gly^+(\mu_1)$	20	2.8944	0.188	0.0102	0.0090	*-4.64*
10	$Zr_4(OH)_8(H_2O)_2(Gly^+)_{14}$	*2.00*	$Gly^+(\mu_1)$	22	2.9082	0.194	0.0110	0.0081	*-5.03*
11	$Zr_4(OH)_8(Gly^+)_{16}$	*2.00*	$Gly^+(\mu_1)$	24	2.9199	0.200	0.0117	0.0074	*-5.37*
12	$Zr_4(OH)_8(H_2O)_{15}$(Z-Gly)	*2.00*	Z-Gly(μ_1)	8	2.7063	0.100	-0.0003	0.0948	*0.73*
13	$Zr_4(OH)_8(H_2O)_{14}$(Z-Gly)$_2$	*2.00*	Z-Gly(μ_1)	8	2.7191	0.106	0.0004	0.0504	*0.37*
14	$Zr_4(OH)_8(H_2O)_{13}$(Z-Gly)$_3$	*2.00*	Z-Gly(μ_1)	8	2.7300	0.111	0.0011	0.0353	*0.06*
15	$Zr_4(OH)_8(H_2O)_{12}$(Z-Gly)$_4$	*2.00*	Z-Gly(μ_1)	8	2.7396	0.116	0.0016	0.0276	*-0.22*
16	$Zr_4(OH)_8(H_2O)_{10}$(Z-Gly)$_6$	*2.00*	Z-Gly(μ_1)	8	2.7554	0.123	0.0025	0.0196	*-0.67*
17	$Zr_4(OH)_8(H_2O)_8$(Z-Gly)$_8$	*2.00*	Z-Gly(μ_1)	8	2.7680	0.129	0.0032	0.0154	*-1.03*
18	$Zr_4(OH)_8(H_2O)_6$(Z-Gly)$_{10}$	*1.50*	Z-Gly(μ_1)	10	2.8142	0.151	0.0077	0.0145	*-2.35*
19	$Zr_4(OH)_8(H_2O)_4$(Z-Gly)$_{12}$	*1.00*	Z-Gly(μ_1)	12	2.8546	0.169	0.0160	0.0136	*-3.50*
20	$Zr_4(OH)_8(H_2O)_2$(Z-Gly)$_{14}$	*0.50*	Z-Gly(μ_1)	14	2.8903	0.186	0.0400	0.0129	*-4.52*
21	$Zr_4(OH)_8$(Z-Gly)$_{16}$	*0.00*	Z-Gly(μ_1)	16	2.9221	0.201	-	0.0122	*-5.43*
22	$Zr_4(OH)_8(H_2O)_{14}$(Z-Gly)	*2.00*	Z-Gly(μ_2)	8	2.7153	0.105	0.0002	0.0990	*0.48*
23	$Zr_4(OH)_8(H_2O)_{12}$(Z-Gly)$_2$	*2.00*	Z-Gly(μ_2)	8	2.7373	0.115	0.0015	0.0546	*-0.15*
24	$Zr_4(OH)_8(H_2O)_{10}$(Z-Gly)$_3$	*2.00*	Z-Gly(μ_2)	8	2.7576	0.124	0.0026	0.0396	*-0.73*
25	$Zr_4(OH)_8(H_2O)_8$(Z-Gly)$_4$	*2.00*	Z-Gly(μ_2)	8	2.7764	0.133	0.0036	0.0319	*-1.27*
26	$Zr_4(OH)_8(H_2O)_4$(Z-Gly)$_6$	*2.00*	Z-Gly(μ_2)	8	2.8100	0.149	0.0055	0.0238	*-2.23*
27	$Zr_4(OH)_8$(Z-Gly)$_8$	*2.00*	Z-Gly(μ_2)	8	2.8392	0.162	0.0072	0.0196	*-3.06*
28	$Zr_4(OH)_8(H_2O)_{15}(Gly^-)$	*2.00*	$Gly^-(\mu_1)$	7	2.6863	0.091	-0.0014	0.1935	*1.31*
29	$Zr_4(OH)_8(H_2O)_{14}(Gly^-)_2$	*2.00*	$Gly^-(\mu_1)$	6	2.6820	0.089	-0.0016	0.0957	*1.43*
30	$Zr_4(OH)_8(H_2O)_{13}(Gly^-)_3$	*2.00*	$Gly^-(\mu_1)$	5	2.6782	0.087	-0.0018	0.0632	*1.54*
31	$Zr_4(OH)_8(H_2O)_{12}(Gly^-)_4$	*2.00*	$Gly^-(\mu_1)$	4	2.6748	0.086	-0.0020	0.0470	*1.64*
32	$Zr_4(OH)_8(H_2O)_{10}(Gly^-)_6$	*2.00*	$Gly^-(\mu_1)$	2	2.6690	0.083	-0.0023	0.0308	*1.80*
33	$Zr_4(OH)_8(H_2O)_8(Gly^-)_8$	*2.00*	$Gly^-(\mu_1)$	0	2.6643	0.081	-0.0026	0.0229	*1.93*
34	$Zr_4(OH)_8(H_2O)_6(Gly^-)_{10}$	*2.00*	$Gly^-(\mu_1)$	-2	2.6604	0.079	-0.0028	0.0181	*2.04*
35	$Zr_4(OH)_8(H_2O)_4(Gly^-)_{12}$	*2.00*	$Gly^-(\mu_1)$	-4	2.6571	0.077	-0.0030	0.0149	*2.14*
36	$Zr_4(OH)_8(H_2O)_2(Gly^-)_{14}$	*2.00*	$Gly^-(\mu_1)$	-6	2.6543	0.076	-0.0032	0.0127	*2.22*
37	$Zr_4(OH)_8(Gly^-)_{16}$	*2.00*	$Gly^-(\mu_1)$	-8	2.6519	0.075	-0.0033	0.0110	*2.29*
38	$Zr_4(OH)_8(H_2O)_{14}(Gly^-)$	*2.00*	$Gly^-(\mu_2)$	7	2.6946	0.095	-0.0009	0.1975	*1.07*
39	$Zr_4(OH)_8(H_2O)_{12}(Gly^-)_2$	*2.00*	$Gly^-(\mu_2)$	6	2.6977	0.096	-0.0007	0.0995	*0.98*
40	$Zr_4(OH)_8(H_2O)_{10}(Gly^-)_3$	*2.00*	$Gly^-(\mu_2)$	5	2.7007	0.098	-0.0006	0.0668	*0.89*
41	$Zr_4(OH)_8(H_2O)_8(Gly^-)_4$	*2.00*	$Gly^-(\mu_2)$	4	2.7035	0.099	-0.0004	0.0505	*0.81*
42	$Zr_4(OH)_8(H_2O)_4(Gly^-)_6$	*2.00*	$Gly^-(\mu_2)$	2	2.7087	0.102	-0.0001	0.0341	*0.66*
43	$Zr_4(OH)_8(Gly^-)_8$	*2.00*	$Gly^-(\mu_2)$	0	2.7135	0.104	0.0001	0.0258	*0.53*
Zr octamers									
44	$Zr_8(OH)_{20}(H_2O)_{24}$	*2.50*	-	12	2.6619	0.080	-0.0011	-	*2.00*
45	$Zr_8(OH)_{20}(H_2O)_{23}(Gly^+)$	*2.50*	$Gly^+(\mu_1)$	13	2.6839	0.090	-0.0006	0.0126	*1.37*
46	$Zr_8(OH)_{20}(H_2O)_{22}(Gly^+)_2$	*2.50*	$Gly^+(\mu_1)$	14	2.7036	0.099	-0.0002	0.0108	*0.81*
47	$Zr_8(OH)_{20}(H_2O)_{20}(Gly^+)_4$	*2.50*	$Gly^+(\mu_1)$	16	2.7373	0.115	0.0006	0.0092	*-0.15*
48	$Zr_8(OH)_{20}(H_2O)_{18}(Gly^+)_6$	*2.50*	$Gly^+(\mu_1)$	18	2.7652	0.128	0.0012	0.0082	*-0.95*
49	$Zr_8(OH)_{20}(H_2O)_{16}(Gly^+)_8$	*2.50*	$Gly^+(\mu_1)$	20	2.7886	0.139	0.0017	0.0075	*-1.62*

APPENDIX 1 Table 4.3. (continued)

No	Species	*h*	Ligand	*z*	χ_t	$\delta(H_2O)$	$\delta(OH)$	$\delta(Gly)$	$pH_{opt.}$
50	$Zr_8(OH)_{20}(H_2O)_{14}(Gly^+)_{10}$	*2.50*	$Gly^+(\mu_1)$	**22**	**2.8085**	0.148	0.0022	0.0069	*-2.19*
51	$Zr_8(OH)_{20}(H_2O)_{12}(Gly^+)_{12}$	*2.50*	$Gly^+(\mu_1)$	**24**	**2.8257**	0.156	0.0026	0.0064	*-2.68*
52	$Zr_8(OH)_{20}(H_2O)_{10}(Gly^+)_{14}$	*2.50*	$Gly^+(\mu_1)$	**26**	**2.8407**	0.163	0.0029	0.0060	*-3.10*
53	$Zr_8(OH)_{20}(H_2O)_8(Gly^+)_{16}$	*2.50*	$Gly^+(\mu_1)$	**28**	**2.8538**	0.169	0.0032	0.0056	*-3.48*
54	$Zr_8(OH)_{20}(H_2O)_{23}$(Z-Gly)	*2.50*	Z-Gly(μ_1)	**12**	**2.6721**	0.084	-0.0009	0.0790	*1.71*
55	$Zr_8(OH)_{20}(H_2O)_{22}$(Z-Gly)$_2$	*2.50*	Z-Gly(μ_1)	**12**	**2.6814**	0.089	-0.0007	0.0416	*1.44*
56	$Zr_8(OH)_{20}(H_2O)_{20}$(Z-Gly)$_4$	*2.50*	Z-Gly(μ_1)	**12**	**2.6977**	0.096	-0.0003	0.0227	*0.98*
57	$Zr_8(OH)_{20}(H_2O)_{18}$(Z-Gly)$_6$	*2.50*	Z-Gly(μ_1)	**12**	**2.7115**	0.103	0.0000	0.0162	*0.59*
58	$Zr_8(OH)_{20}(H_2O)_{16}$(Z-Gly)$_8$	*2.50*	Z-Gly(μ_1)	**12**	**2.7233**	0.108	0.0003	0.0128	*0.25*
59	$Zr_8(OH)_{20}(H_2O)_{14}$(Z-Gly)$_{10}$	*2.50*	Z-Gly(μ_1)	**12**	**2.7335**	0.113	0.0005	0.0108	*-0.04*
60	$Zr_8(OH)_{20}(H_2O)_{12}$(Z-Gly)$_{12}$	*2.50*	Z-Gly(μ_1)	**12**	**2.7425**	0.117	0.0007	0.0093	*-0.30*
61	$Zr_8(OH)_{20}(H_2O)_{10}$(Z-Gly)$_{14}$	*2.50*	Z-Gly(μ_1)	**12**	**2.7504**	0.121	0.0009	0.0082	*-0.53*
62	$Zr_8(OH)_{20}(H_2O)_8$(Z-Gly)$_{16}$	*2.50*	Z-Gly(μ_1)	**12**	**2.7574**	0.124	0.0010	0.0074	*-0.73*
63	$Zr_8(OH)_{20}(H_2O)_{22}$(Z-Gly)	*2.50*	Z-Gly(μ_2)	**12**	**2.6765**	0.087	-0.0008	0.0810	*1.59*
64	$Zr_8(OH)_{20}(H_2O)_{20}$(Z-Gly)$_2$	*2.50*	Z-Gly(μ_2)	**12**	**2.6904**	0.093	-0.0005	0.0437	*1.19*
65	$Zr_8(OH)_{20}(H_2O)_{16}$(Z-Gly)$_4$	*2.50*	Z-Gly(μ_2)	**12**	**2.7163**	0.105	0.0001	0.0249	*0.45*
66	$Zr_8(OH)_{20}(H_2O)_{12}$(Z-Gly)$_6$	*2.50*	Z-Gly(μ_2)	**12**	**2.7399**	0.116	0.0006	0.0184	*-0.23*
67	$Zr_8(OH)_{20}(H_2O)_8$(Z-Gly)$_8$	*2.50*	Z-Gly(μ_2)	**12**	**2.7615**	0.126	0.0011	0.0151	*-0.84*
68	$Zr_8(OH)_{20}(H_2O)_4$(Z-Gly)$_{10}$	*2.50*	Z-Gly(μ_2)	**12**	**2.7814**	0.135	0.0016	0.0130	*-1.41*
69	$Zr_8(OH)_{20}$(Z-Gly)$_{12}$	*2.50*	Z-Gly(μ_2)	**12**	**2.7998**	0.144	0.0020	0.0115	*-1.94*
70	$Zr_8(OH)_{20}(H_2O)_{23}(Gly^-)$	*2.50*	$Gly^-(\mu_1)$	**11**	**2.6602**	0.079	-0.0011	0.1808	*2.05*
71	$Zr_8(OH)_{20}(H_2O)_{22}(Gly^-)_2$	*2.50*	$Gly^-(\mu_1)$	**10**	**2.6586**	0.078	-0.0012	0.0900	*2.10*
72	$Zr_8(OH)_{20}(H_2O)_{20}(Gly^-)_4$	*2.50*	$Gly^-(\mu_1)$	**8**	**2.6557**	0.077	-0.0012	0.0447	*2.18*
73	$Zr_8(OH)_{20}(H_2O)_{18}(Gly^-)_6$	*2.50*	$Gly^-(\mu_1)$	**6**	**2.6532**	0.076	-0.0013	0.0296	*2.25*
74	$Zr_8(OH)_{20}(H_2O)_{16}(Gly^-)_8$	*2.50*	$Gly^-(\mu_1)$	**4**	**2.6510**	0.075	-0.0013	0.0220	*2.31*
75	$Zr_8(OH)_{20}(H_2O)_{14}(Gly^-)_{10}$	*2.50*	$Gly^-(\mu_1)$	**2**	**2.6491**	0.074	-0.0014	0.0175	*2.37*
76	$Zr_8(OH)_{20}(H_2O)_{12}(Gly^-)_{12}$	*2.50*	$Gly^-(\mu_1)$	**0**	**2.6474**	0.073	-0.0014	0.0145	*2.42*
77	$Zr_8(OH)_{20}(H_2O)_{10}(Gly^-)_{14}$	*2.50*	$Gly^-(\mu_1)$	**-2**	**2.6458**	0.072	-0.0015	0.0124	*2.46*
78	$Zr_8(OH)_{20}(H_2O)_8(Gly^-)_{16}$	*2.50*	$Gly^-(\mu_1)$	**-4**	**2.6444**	0.072	-0.0015	0.0108	*2.50*
79	$Zr_8(OH)_{20}(H_2O)_{22}(Gly^-)$	*2.50*	$Gly^-(\mu_2)$	**11**	**2.6643**	0.081	-0.0010	0.1828	*1.93*
80	$Zr_8(OH)_{20}(H_2O)_{20}(Gly^-)_2$	*2.50*	$Gly^-(\mu_2)$	**10**	**2.6666**	0.082	-0.0010	0.0920	*1.87*
81	$Zr_8(OH)_{20}(H_2O)_{16}(Gly^-)_4$	*2.50*	$Gly^-(\mu_2)$	**8**	**2.6710**	0.084	-0.0009	0.0465	*1.74*
82	$Zr_8(OH)_{20}(H_2O)_{12}(Gly^-)_6$	*2.50*	$Gly^-(\mu_2)$	**6**	**2.6751**	0.086	-0.0008	0.0313	*1.62*
83	$Zr_8(OH)_{20}(H_2O)_8(Gly^-)_8$	*2.50*	$Gly^-(\mu_2)$	**4**	**2.6790**	0.088	-0.0007	0.0237	*1.51*
84	$Zr_8(OH)_{20}(H_2O)_4(Gly^-)_{10}$	*2.50*	$Gly^-(\mu_2)$	**2**	**2.6827**	0.089	-0.0006	0.0192	*1.41*
85	$Zr_8(OH)_{20}(Gly^-)_{12}$	*2.50*	$Gly^-(\mu_2)$	**0**	**2.6862**	0.091	-0.0006	0.0161	*1.31*
Zr octamers with glycine-bridges									
86	$Zr_8(OH)_{19}(H_2O)_{24}$(Z-Gly)	*2.38*	Z-Gly(μ_2)	**14**	**2.6955**	0.095	-0.0004	0.0179	*1.04*
87	$Zr_8(OH)_{18}(H_2O)_{24}$(Z-Gly)$_2$	*2.25*	Z-Gly(μ_2)	**16**	**2.7250**	0.109	0.0003	0.0156	*0.20*
88	$Zr_8(OH)_{16}(H_2O)_{24}$(Z-Gly)$_4$	*2.00*	Z-Gly(μ_2)	**20**	**2.7747**	0.132	0.0018	0.0134	*-1.22*
89	$Zr_8(OH)_{16}(H_2O)_{20}$(Z-Gly)$_6$	*2.00*	Z-Gly(μ_2)	**22**	**2.8100**	0.149	0.0028	0.0116	*-2.23*
90	$Zr_8(OH)_{16}(H_2O)_{16}$(Z-Gly)$_8$	*2.00*	Z-Gly(μ_2)	**24**	**2.8419**	0.164	0.0037	0.0105	*-3.14*
91	$Zr_8(OH)_{19}(H_2O)_{24}(Gly^-)$	*2.38*	Gly-(m2)	**12**	**2.6721**	0.084	-0.0009	0.1866	*1.71*
92	$Zr_8(OH)_{18}(H_2O)_{24}(Gly^-)_2$	*2.25*	Gly-(m2)	**12**	**2.6814**	0.089	-0.0007	0.0956	*1.44*
93	$Zr_8(OH)_{16}(H_2O)_{24}(Gly^-)_4$	*2.00*	Gly-(m2)	**12**	**2.6977**	0.096	-0.0004	0.0498	*0.98*
94	$Zr_8(OH)_{16}(H_2O)_{24}(Gly^-)_6$	*2.00*	Gly-(m2)	**10**	**2.7007**	0.098	-0.0003	0.0334	*0.89*
95	$Zr_8(OH)_{16}(H_2O)_{24}(Gly^-)_8$	*2.00*	Gly-(m2)	**8**	**2.7035**	0.099	-0.0002	0.0252	*0.81*
Zr 12-mers									
96	$Zr_{12}(OH)_{32}(H_2O)_{32}$	*2.67*	-	**16**	**2.6503**	0.074	-0.0008	-	*2.33*
97	$Zr_{12}(OH)_{32}(H_2O)_{31}(Gly^+)$	*2.67*	$Gly^+(\mu_1)$	**17**	**2.6613**	0.079	-0.0007	0.0024	*2.02*
98	$Zr_{12}(OH)_{32}(H_2O)_{30}(Gly^+)_2$	*2.67*	$Gly^+(\mu_1)$	**18**	**2.6718**	0.084	-0.0005	0.0036	*1.72*

APPENDIX 1 Table 4.3. (continued)

No	Species	*h*	Ligand	*z*	χ_t	$\delta(H_2O)$	δ(OH)	δ(Gly)	$pH_{opt.}$
99	$Zr_{12}(OH)_{32}(H_2O)_{28}(Gly^+)_4$	*2.67*	$Gly^+(\mu_1)$	20	2.6914	0.093	-0.0003	0.0040	*1.16*
100	$Zr_{12}(OH)_{32}(H_2O)_{26}(Gly^+)_6$	*2.67*	$Gly^+(\mu_1)$	22	2.7096	0.102	0.0000	0.0040	*0.64*
101	$Zr_{12}(OH)_{32}(H_2O)_{24}(Gly^+)_8$	*2.67*	$Gly^+(\mu_1)$	24	2.7263	0.110	0.0002	0.0040	*0.16*
102	$Zr_{12}(OH)_{32}(H_2O)_{22}(Gly^+)_{10}$	*2.67*	$Gly^+(\mu_1)$	26	2.7419	0.117	0.0004	0.0039	*-0.28*
103	$Zr_{12}(OH)_{32}(H_2O)_{20}(Gly^+)_{12}$	*2.67*	$Gly^+(\mu_1)$	28	2.7563	0.124	0.0006	0.0038	*-0.69*
104	$Zr_{12}(OH)_{32}(H_2O)_{31}$(Z-Gly)	*2.67*	Z-Gly(μ_1)	16	2.6493	0.074	-0.0009	0.0684	*2.36*
105	$Zr_{12}(OH)_{32}(H_2O)_{30}$(Z-Gly)$_2$	*2.67*	Z-Gly(μ_1)	16	2.6483	0.073	-0.0009	0.0339	*2.39*
106	$Zr_{12}(OH)_{32}(H_2O)_{28}$(Z-Gly)$_4$	*2.67*	Z-Gly(μ_1)	16	2.6465	0.073	-0.0009	0.0168	*2.44*
107	$Zr_{12}(OH)_{32}(H_2O)_{26}$(Z-Gly)$_6$	*2.67*	Z-Gly(μ_1)	16	2.6448	0.072	-0.0009	0.0110	*2.49*
108	$Zr_{12}(OH)_{32}(H_2O)_{24}$(Z-Gly)$_8$	*2.67*	Z-Gly(μ_1)	16	2.6432	0.071	-0.0009	0.0082	*2.54*
109	$Zr_{12}(OH)_{32}(H_2O)_{22}$(Z-Gly)$_{10}$	*2.67*	Z-Gly(μ_1)	16	2.6418	0.070	-0.0010	0.0065	*2.58*
110	$Zr_{12}(OH)_{32}(H_2O)_{20}$(Z-Gly)$_{12}$	*2.67*	Z-Gly(μ_1)	16	2.6405	0.070	-0.0010	0.0054	*2.62*
111	$Zr_{12}(OH)_{32}(H_2O)_{30}$(Z-Gly)	*2.67*	Z-Gly(μ_2)	16	2.6486	0.074	-0.0009	0.0680	*2.38*
112	$Zr_{12}(OH)_{32}(H_2O)_{28}$(Z-Gly)$_2$	*2.67*	Z-Gly(μ_2)	16	2.6470	0.073	-0.0009	0.0336	*2.43*
113	$Zr_{12}(OH)_{32}(H_2O)_{24}$(Z-Gly)$_4$	*2.67*	Z-Gly(μ_2)	16	2.6438	0.071	-0.0009	0.0164	*2.52*
114	$Zr_{12}(OH)_{32}(H_2O)_{20}$(Z-Gly)$_6$	*2.67*	Z-Gly(μ_2)	16	2.6407	0.070	-0.0010	0.0107	*2.61*
115	$Zr_{12}(OH)_{32}(H_2O)_{16}$(Z-Gly)$_8$	*2.67*	Z-Gly(μ_2)	16	2.6377	0.068	-0.0010	0.0079	*2.69*
116	$Zr_{12}(OH)_{32}(H_2O)_{12}$(Z-Gly)$_{10}$	*2.67*	Z-Gly(μ_2)	16	2.6349	0.067	-0.0011	0.0062	*2.77*
117	$Zr_{12}(OH)_{32}(H_2O)_8$(Z-Gly)$_{12}$	*2.67*	Z-Gly(μ_2)	16	2.6322	0.066	-0.0011	0.0050	*2.85*
118	$Zr_{12}(OH)_{32}(H_2O)_{31}(Gly^-)$	*2.67*	$Gly^-(\mu_1)$	15	2.6373	0.068	-0.0010	0.1697	*2.71*
119	$Zr_{12}(OH)_{32}(H_2O)_{30}(Gly^-)_2$	*2.67*	$Gly^-(\mu_1)$	14	2.6249	0.062	-0.0012	0.0818	*3.06*
120	$Zr_{12}(OH)_{32}(H_2O)_{28}(Gly^-)_4$	*2.67*	$Gly^-(\mu_1)$	12	2.6015	0.052	-0.0015	0.0381	*3.73*
121	$Zr_{12}(OH)_{32}(H_2O)_{26}(Gly^-)_6$	*2.67*	$Gly^-(\mu_1)$	10	2.5800	0.042	-0.0018	0.0236	*4.34*
122	$Zr_{12}(OH)_{32}(H_2O)_{24}(Gly^-)_8$	*2.67*	$Gly^-(\mu_1)$	8	2.5601	0.032	-0.0021	0.0165	*4.91*
123	$Zr_{12}(OH)_{32}(H_2O)_{22}(Gly^-)_{10}$	*2.67*	$Gly^-(\mu_1)$	6	2.5417	0.024	-0.0024	0.0123	*5.44*
124	$Zr_{12}(OH)_{32}(H_2O)_{20}(Gly^-)_{12}$	*2.67*	$Gly^-(\mu_1)$	4	2.5246	0.016	-0.0026	0.0096	*5.93*
125	$Zr_{12}(OH)_{32}(H_2O)_{30}(Gly^-)$	*2.67*	$Gly^-(\mu_2)$	15	2.6433	0.071	-0.0009	0.1726	*2.53*
126	$Zr_{12}(OH)_{32}(H_2O)_{28}(Gly^-)_2$	*2.67*	$Gly^-(\mu_2)$	14	2.6358	0.068	-0.0011	0.0845	*2.75*
127	$Zr_{12}(OH)_{32}(H_2O)_{24}(Gly^-)_4$	*2.67*	$Gly^-(\mu_2)$	12	2.6190	0.060	-0.0013	0.0402	*3.23*
128	$Zr_{12}(OH)_{32}(H_2O)_{20}(Gly^-)_6$	*2.67*	$Gly^-(\mu_2)$	10	2.5992	0.050	-0.0016	0.0252	*3.79*
129	$Zr_{12}(OH)_{32}(H_2O)_{16}(Gly^-)_8$	*2.67*	$Gly^-(\mu_2)$	8	2.5757	0.040	-0.0019	0.0175	*4.47*
130	$Zr_{12}(OH)_{32}(H_2O)_{12}(Gly^-)_{10}$	*2.67*	$Gly^-(\mu_2)$	6	2.5473	0.026	-0.0023	0.0126	*5.28*
131	$Zr_{12}(OH)_{32}(H_2O)_8(Gly^-)_{12}$	*2.67*	$Gly^-(\mu_2)$	4	2.5121	0.010	-0.0028	0.0091	*6.28*
Zr 16-mers									
132	$Zr_{16}(OH)_{44}(H_2O)_{40}$	*2.75*	-	20	2.6441	0.071	-0.0007	-	*2.51*
133	$Zr_{16}(OH)_{44}(H_2O)_{39}(Gly^+)$	*2.75*	$Gly^+(\mu_1)$	21	2.6526	0.075	-0.0006	-0.0015	*2.27*
134	$Zr_{16}(OH)_{44}(H_2O)_{38}(Gly^+)_2$	*2.75*	$Gly^+(\mu_1)$	22	2.6609	0.079	-0.0005	0.0011	*2.03*
135	$Zr_{16}(OH)_{44}(H_2O)_{36}(Gly^+)_4$	*2.75*	$Gly^+(\mu_1)$	24	2.6767	0.087	-0.0003	0.0023	*1.58*
136	$Zr_{16}(OH)_{44}(H_2O)_{34}(Gly^+)_6$	*2.75*	$Gly^+(\mu_1)$	26	2.6915	0.093	-0.0002	0.0027	*1.16*
137	$Zr_{16}(OH)_{44}(H_2O)_{32}(Gly^+)_8$	*2.75*	$Gly^+(\mu_1)$	28	2.7054	0.100	-0.0001	0.0028	*0.76*
138	$Zr_{16}(OH)_{44}(H_2O)_{30}(Gly^+)_{10}$	*2.75*	$Gly^+(\mu_1)$	30	2.7184	0.106	0.0001	0.0028	*0.39*
139	$Zr_{16}(OH)_{44}(H_2O)_{28}(Gly^+)_{12}$	*2.75*	$Gly^+(\mu_1)$	32	2.7307	0.112	0.0002	0.0028	*0.04*
140	$Zr_{16}(OH)_{44}(H_2O)_{26}(Gly^+)_{14}$	*2.75*	$Gly^+(\mu_1)$	34	2.7424	0.117	0.0003	0.0028	*-0.30*
141	$Zr_{16}(OH)_{44}(H_2O)_{24}(Gly^+)_{16}$	*2.75*	$Gly^+(\mu_1)$	36	2.7534	0.122	0.0004	0.0027	*-0.61*
142	$Zr_{16}(OH)_{44}(H_2O)_{22}(Gly^+)_{18}$	*2.75*	$Gly^+(\mu_1)$	38	2.7638	0.127	0.0005	0.0027	*-0.91*
143	$Zr_{16}(OH)_{44}(H_2O)_{20}(Gly^+)_{20}$	*2.75*	$Gly^+(\mu_1)$	40	2.7737	0.132	0.0006	0.0027	*-1.19*
144	$Zr_{16}(OH)_{44}(H_2O)_{39}$(Z-Gly)	*2.75*	Z-Gly(μ_1)	20	2.6434	0.071	-0.0007	0.0656	*2.53*
145	$Zr_{16}(OH)_{44}(H_2O)_{38}$(Z-Gly)$_2$	*2.75*	Z-Gly(μ_1)	20	2.6427	0.071	-0.0007	0.0327	*2.55*
146	$Zr_{16}(OH)_{44}(H_2O)_{36}$(Z-Gly)$_4$	*2.75*	Z-Gly(μ_1)	20	2.6415	0.070	-0.0007	0.0162	*2.59*
147	$Zr_{16}(OH)_{44}(H_2O)_{34}$(Z-Gly)$_6$	*2.75*	Z-Gly(μ_1)	20	2.6403	0.070	-0.0007	0.0107	*2.62*
148	$Zr_{16}(OH)_{44}(H_2O)_{32}$(Z-Gly)$_8$	*2.75*	Z-Gly(μ_1)	20	2.6392	0.069	-0.0007	0.0080	*2.65*

APPENDIX 1 Table 4.3. (continued)

No	Species	*h*	Ligand	*z*	χ_t	$\delta(H_2O)$	δ(OH)	δ(Gly)	$pH_{opt.}$
149	$Zr_{16}(OH)_{44}(H_2O)_{30}(Z\text{-}Gly)_{10}$	*2.75*	Z-Gly(μ_1)	**20**	**2.6382**	0.069	-0.0007	0.0063	*2.68*
150	$Zr_{16}(OH)_{44}(H_2O)_{28}(Z\text{-}Gly)_{12}$	*2.75*	Z-Gly(μ_1)	**20**	**2.6372**	0.068	-0.0008	0.0052	*2.71*
151	$Zr_{16}(OH)_{44}(H_2O)_{26}(Z\text{-}Gly)_{14}$	*2.75*	Z-Gly(μ_1)	**20**	**2.6363**	0.068	-0.0008	0.0044	*2.74*
152	$Zr_{16}(OH)_{44}(H_2O)_{24}(Z\text{-}Gly)_{16}$	*2.75*	Z-Gly(μ_1)	**20**	**2.6354**	0.067	-0.0008	0.0039	*2.76*
153	$Zr_{16}(OH)_{44}(H_2O)_{22}(Z\text{-}Gly)_{18}$	*2.75*	Z-Gly(μ_1)	**20**	**2.6346**	0.067	-0.0008	0.0034	*2.78*
154	$Zr_{16}(OH)_{44}(H_2O)_{20}(Z\text{-}Gly)_{20}$	*2.75*	Z-Gly(μ_1)	**20**	**2.6338**	0.067	-0.0008	0.0031	*2.81*
155	$Zr_{16}(OH)_{44}(H_2O)_{38}(Z\text{-}Gly)$	*2.75*	Z-Gly(μ_2)	**20**	**2.6428**	0.071	-0.0007	0.0653	*2.55*
156	$Zr_{16}(OH)_{44}(H_2O)_{36}(Z\text{-}Gly)_2$	*2.75*	Z-Gly(μ_2)	**20**	**2.6416**	0.070	-0.0007	0.0324	*2.58*
157	$Zr_{16}(OH)_{44}(H_2O)_{32}(Z\text{-}Gly)_4$	*2.75*	Z-Gly(μ_2)	**20**	**2.6392**	0.069	-0.0007	0.0159	*2.65*
158	$Zr_{16}(OH)_{44}(H_2O)_{28}(Z\text{-}Gly)_6$	*2.75*	Z-Gly(μ_2)	**20**	**2.6369**	0.068	-0.0008	0.0104	*2.72*
159	$Zr_{16}(OH)_{44}(H_2O)_{24}(Z\text{-}Gly)_8$	*2.75*	Z-Gly(μ_2)	**20**	**2.6347**	0.067	-0.0008	0.0077	*2.78*
160	$Zr_{16}(OH)_{44}(H_2O)_{20}(Z\text{-}Gly)_{10}$	*2.75*	Z-Gly(μ_2)	**20**	**2.6325**	0.066	-0.0008	0.0061	*2.84*
161	$Zr_{16}(OH)_{44}(H_2O)_{16}(Z\text{-}Gly)_{12}$	*2.75*	Z-Gly(μ_2)	**20**	**2.6304**	0.065	-0.0008	0.0050	*2.90*
162	$Zr_{16}(OH)_{44}(H_2O)_{12}(Z\text{-}Gly)_{14}$	*2.75*	Z-Gly(μ_2)	**20**	**2.6284**	0.064	-0.0008	0.0042	*2.96*
163	$Zr_{16}(OH)_{44}(H_2O)_8(Z\text{-}Gly)_{16}$	*2.75*	Z-Gly(μ_2)	**20**	**2.6264**	0.063	-0.0009	0.0036	*3.02*
164	$Zr_{16}(OH)_{44}(H_2O)_4(Z\text{-}Gly)_{18}$	*2.75*	Z-Gly(μ_2)	**20**	**2.6245**	0.062	-0.0009	0.0032	*3.07*
165	$Zr_{16}(OH)_{44}(Z\text{-}Gly)_{20}$	*2.75*	Z-Gly(μ_2)	**20**	**2.6226**	0.061	-0.0009	0.0028	*3.13*
166	$Zr_{16}(OH)_{44}(H_2O)_{39}(Gly^-)$	*2.75*	$Gly^-(\mu_1)$	**19**	**2.6341**	0.067	-0.0008	0.1681	*2.80*
167	$Zr_{16}(OH)_{44}(H_2O)_{38}(Gly^-)_2$	*2.75*	$Gly^-(\mu_1)$	**18**	**2.6245**	0.062	-0.0009	0.0817	*3.07*
168	$Zr_{16}(OH)_{44}(H_2O)_{36}(Gly^-)_4$	*2.75*	$Gly^-(\mu_1)$	**16**	**2.6063**	0.054	-0.0011	0.0386	*3.59*
169	$Zr_{16}(OH)_{44}(H_2O)_{34}(Gly^-)_6$	*2.75*	$Gly^-(\mu_1)$	**14**	**2.5891**	0.046	-0.0012	0.0244	*4.08*
170	$Zr_{16}(OH)_{44}(H_2O)_{32}(Gly^-)_8$	*2.75*	$Gly^-(\mu_1)$	**12**	**2.5731**	0.038	-0.0014	0.0173	*4.54*
171	$Zr_{16}(OH)_{44}(H_2O)_{30}(Gly^-)_{10}$	*2.75*	$Gly^-(\mu_1)$	**10**	**2.5579**	0.031	-0.0016	0.0131	*4.97*
172	$Zr_{16}(OH)_{44}(H_2O)_{28}(Gly^-)_{12}$	*2.75*	$Gly^-(\mu_1)$	**8**	**2.5436**	0.025	-0.0017	0.0103	*5.38*
173	$Zr_{16}(OH)_{44}(H_2O)_{26}(Gly^-)_{14}$	*2.75*	$Gly^-(\mu_1)$	**6**	**2.5301**	0.018	-0.0018	0.0084	*5.77*
174	$Zr_{16}(OH)_{44}(H_2O)_{24}(Gly^-)_{16}$	*2.75*	$Gly^-(\mu_1)$	**4**	**2.5174**	0.012	-0.0020	0.0070	*6.13*
175	$Zr_{16}(OH)_{44}(H_2O)_{22}(Gly^-)_{18}$	*2.75*	$Gly^-(\mu_1)$	**2**	**2.5053**	0.007	-0.0021	0.0059	*6.48*
176	$Zr_{16}(OH)_{44}(H_2O)_{20}(Gly^-)_{20}$	*2.75*	$Gly^-(\mu_1)$	**0**	**2.4938**	0.001	-0.0022	0.0050	*6.81*
177	$Zr_{16}(OH)_{44}(H_2O)_{38}(Gly^-)$	*2.75*	$Gly^-(\mu_2)$	**19**	**2.6386**	0.069	-0.0007	0.1703	*2.67*
178	$Zr_{16}(OH)_{44}(H_2O)_{36}(Gly^-)_2$	*2.75*	$Gly^-(\mu_2)$	**18**	**2.6328**	0.066	-0.0008	0.0837	*2.83*
179	$Zr_{16}(OH)_{44}(H_2O)_{32}(Gly^-)_4$	*2.75*	$Gly^-(\mu_2)$	**16**	**2.6201**	0.060	-0.0009	0.0403	*3.20*
180	$Zr_{16}(OH)_{44}(H_2O)_{28}(Gly^-)_6$	*2.75*	$Gly^-(\mu_2)$	**14**	**2.6059**	0.054	-0.0011	0.0257	*3.60*
181	$Zr_{16}(OH)_{44}(H_2O)_{24}(Gly^-)_8$	*2.75*	$Gly^-(\mu_2)$	**12**	**2.5898**	0.046	-0.0012	0.0183	*4.06*
182	$Zr_{16}(OH)_{44}(H_2O)_{20}(Gly^-)_{10}$	*2.75*	$Gly^-(\mu_2)$	**10**	**2.5713**	0.037	-0.0014	0.0138	*4.59*
183	$Zr_{16}(OH)_{44}(H_2O)_{16}(Gly^-)_{12}$	*2.75*	$Gly^-(\mu_2)$	**8**	**2.5500**	0.028	-0.0016	0.0106	*5.20*
184	$Zr_{16}(OH)_{44}(H_2O)_{12}(Gly^-)_{14}$	*2.75*	$Gly^-(\mu_2)$	**6**	**2.5250**	0.016	-0.0019	0.0082	*5.91*
185	$Zr_{16}(OH)_{44}(H_2O)_8(Gly^-)_{16}$	*2.75*	$Gly^-(\mu_2)$	**4**	**2.4955**	0.002	-0.0022	0.0063	*6.76*
186	$Zr_{16}(OH)_{44}(H_2O)_4(Gly^-)_{18}$	*2.75*	$Gly^-(\mu_2)$	**2**	**2.4600**	-0.014	-0.0025	0.0046	*7.77*
187	$Zr_{16}(OH)_{44}(Gly^-)_{20}$	*2.75*	$Gly^-(\mu_2)$	**0**	**2.4166**	-0.035	-0.0030	0.0031	*9.01*

* - three forms of glycine are denoted as Gly^+ - positively charged form ($HOOC\text{-}CH_2\text{-}NH_3^+$) with protonated amino-group and carboxylic group; Z-Gly – zwitter-ion form ($^-OOC\text{-}CH_2\text{-}NH_3^+$) with deprotonated carboxylic and protonated amino-group; Gly^- - negatively charged form ($^-OOC\text{-}CH_2\text{-}NH_2$) with neutral amino-group and deprotonated carboxylic group. μ_1 is for unidentate ligand, μ_2 – bidentate (bridging) ligand.

** - partial charge on complexed glycine indicates the value corresponding to one of the listed forms of glycine indicated in the third column

APPENDIX 2. Powder diffractograms of the series ZrOH ar different sampling times

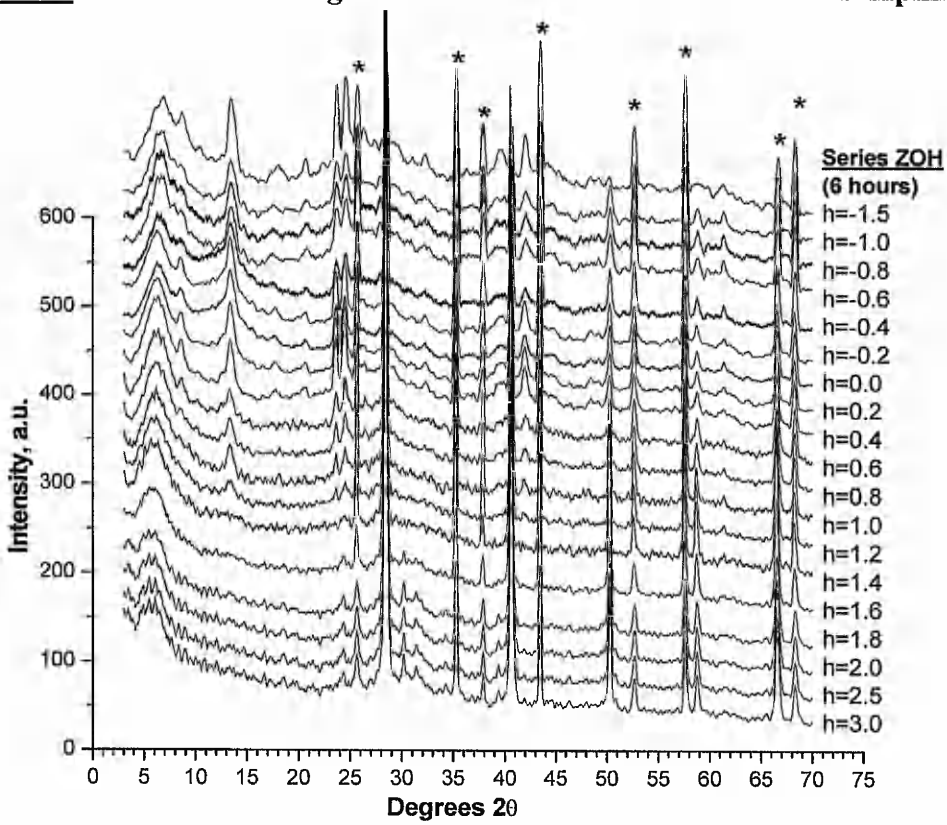


Fig. 5.14. PXRD patterns of the SFD samples prepared from the series **ZrOH** after 6 hours of hydrolysis (90°C). Y-offset – 75%.

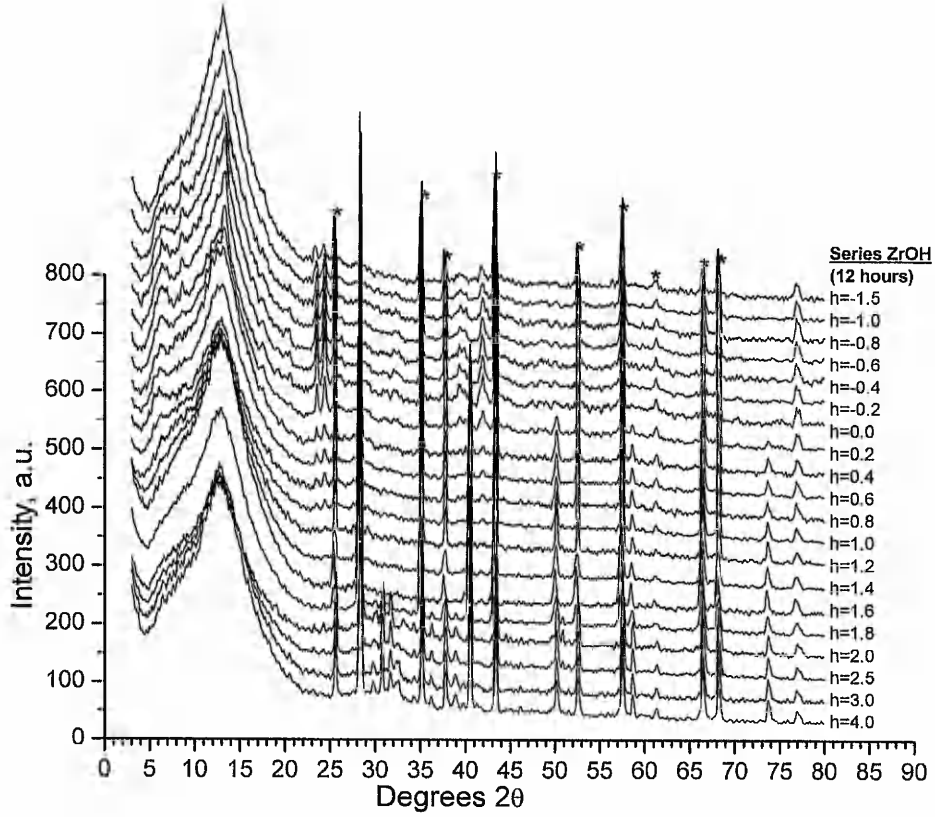


Fig. 5.15. PXRD patterns of the SFD samples prepared from the series **ZrOH** after 12 hours of hydrolysis (90°C). Y-offset – 60%.

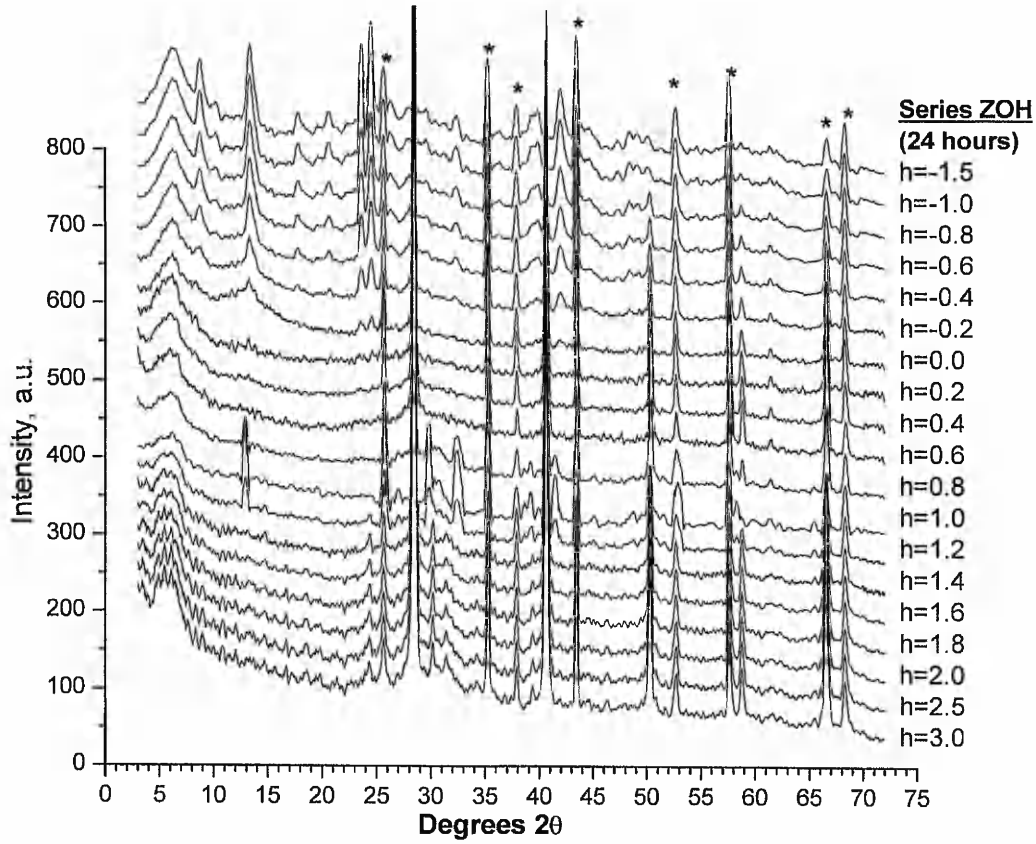


Fig. 5.16. **PXRD patterns of the SFD samples prepared from the series** ZrOH **after 24 hours of hydrolysis (90°C). Y-offset – 70%.**

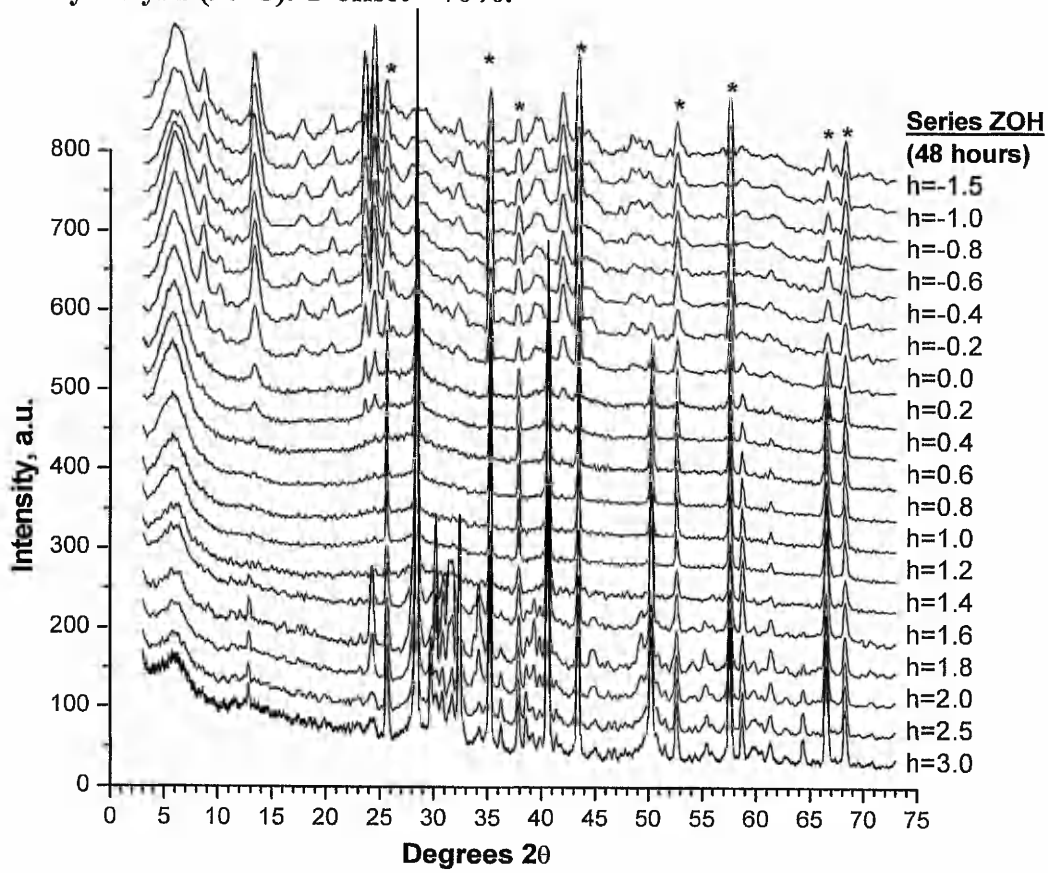


Fig. 5.17. **PXRD patterns of the SFD samples prepared from the series** ZrOH **after 48 hours of hydrolysis (90°C). Y-offset – 80%.**

APPENDIX 3. FT-IR spectra of the series 'ZrOHGly'

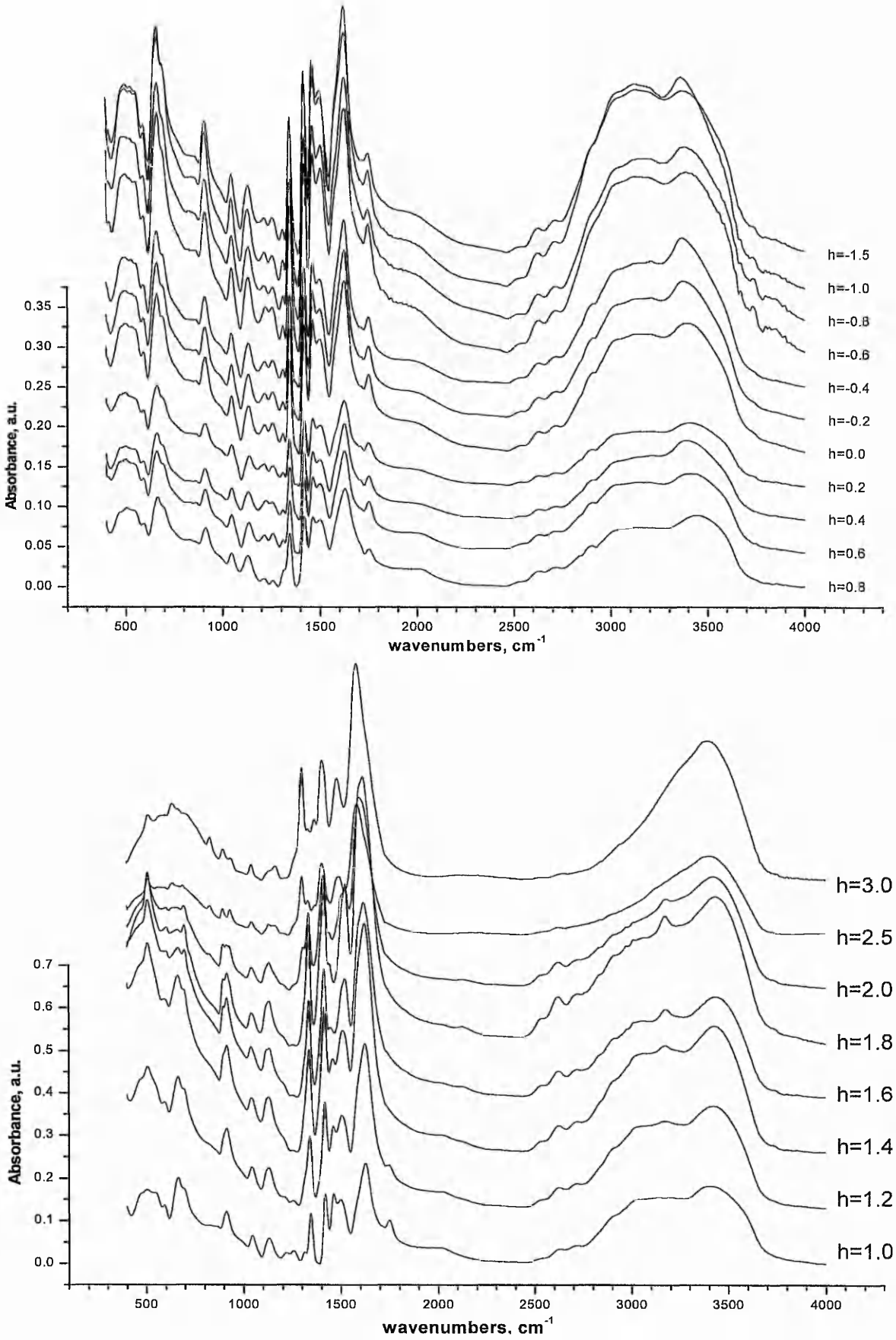
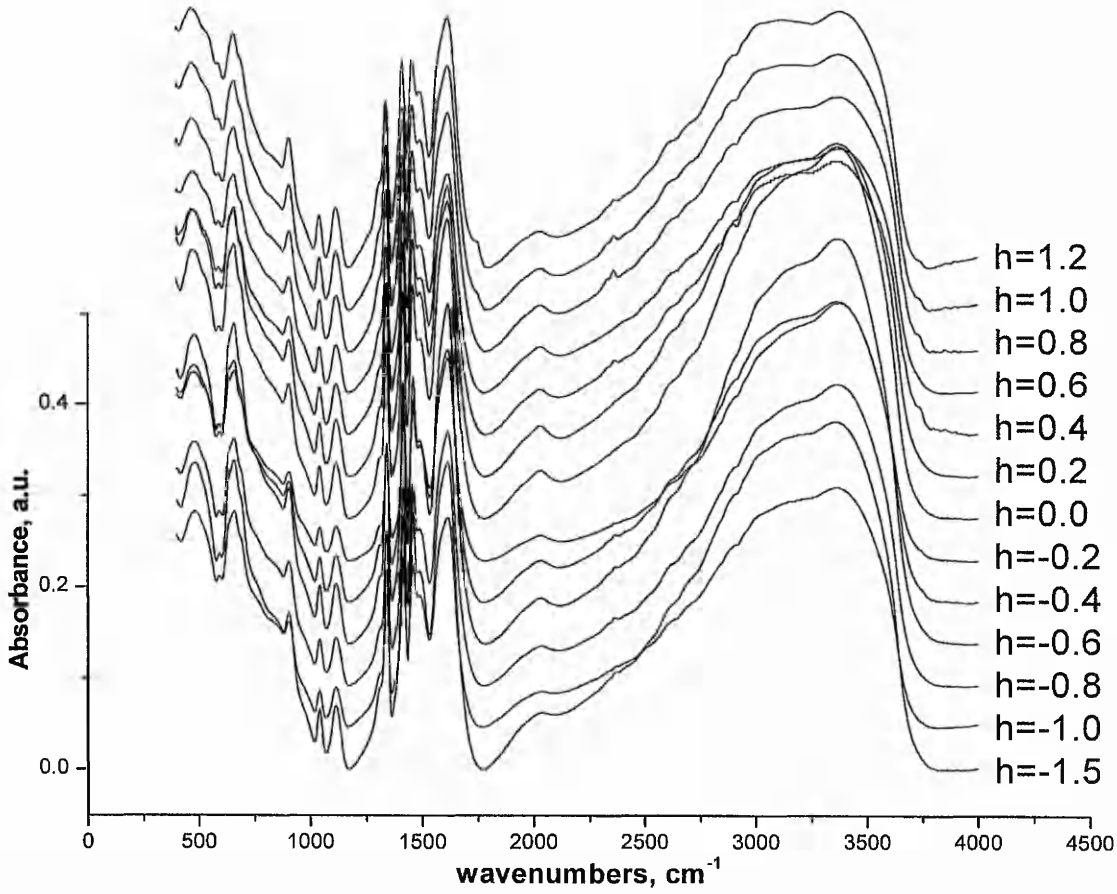


Fig. 5.64. Mid-IR spectra of the solid samples of the series **ZrOHGly1:1**. Y-offset – 110 %.



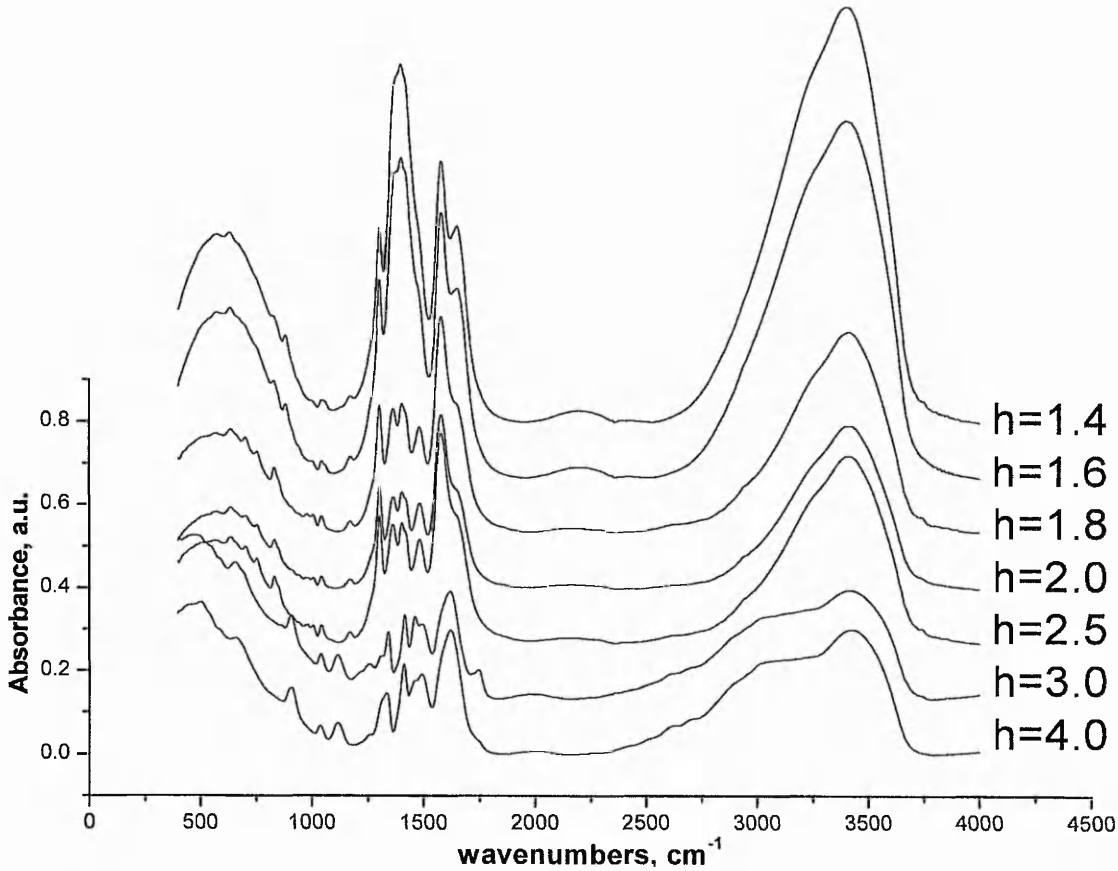


Fig. 5.65. Mid-IR spectra of the solid samples from the series **ZrOHGly1:1**. Y-offset – 80 %.